UNIVERSITÀ DEGLI STUDI DELLA BASILICATA

PhD Programme in

Sciences – Chemical Sciences

TITLE OF THE THESIS:

"**Design, Characterization, and Electrospinning of Hyaluronic Acid Bioconjugated for Biomedical Applications"**

Scientific Disciplinary Sector

CHEM-05/A – Organic Chemistry

PhD Coordinator

Prof. Patrizia Falabella

PhD Candidate

Dr. Francesca Armiento

PhD Tutor

Prof. Brigida Bochicchio

PhD Co-Tutors

Prof. Antonietta Pepe

Dr. Antonio Laezza

XXXVIII Cycle

To my nephew Valerio,
with all my love.

Index

Abbreviations 1

Abstract 6

Chapter 1 – Chemical Modifications in Hyaluronic Acid-Based Electrospun Scaffolds

Abstract 11

1. Introduction 12

2. In Situ Crosslinking 15

3. Off-Site Crosslinked HA Electrospun Scaffolds 22

3.1 Carbodiimide-Promoted Crosslinking of Electrospun HA-Based Scaffolds 24

3.2 Photo-Crosslinking of Electrospun HA-Based Scaffolds 24

3.3 Alternative Crosslinking Methodologies for HA-Based Scaffolds 26

4. Electrospun Scaffolds Based on Hyaluronic Acid Derivatives 27

4.1 Small Molecule-Decorated HA Derivatives 27

4.2 C6-Decorated Hyaluronic Acid for Enhanced Resistance to Hyaluronidase-Mediated Digestion 28

4.3 Peptide-Decorated HA Electrospun Scaffolds 30

4.4 Peptide Bioconjugation by Bioorthogonal Chemistry 32

5. Summary 37

6. Outlook 38

References 39

Chapter 2 – Sequential Electrospinning of Asymmetric PDLLA/PVP-HA Scaffolds Functionalized with Glycine for Medical Devices

Abstract 45

1. Introduction 46

2. Materials and Methods 49

2.1 Materials 49

2.2 Methods 49

2.2.1 Nuclear Magnetic Resonance (NMR) Spectroscopy 49

2.2.2 Attenuated Total Reflectance Fourier Transform Infrared (ATR-FT-IR) Spectroscopy 49
2.2.3 Scanning Electron Microscopy (SEM) 50
2.2.4 Atomic Force Microscopy (AFM) 50
2.2.5 Semi-Synthesis of HA-Gly-OEt 51
2.2.6 Semi-Synthesis of HA-Gly-OH 51
2.2.7 Electrospinning 51
2.3 Wettability (Water Contact Angle Measurement) 53
2.4 Cell Culture and Biocompatibility Evaluation 53
2.5 Sol (SF) Gel Fraction (GF) Calculation 54
2.6 Calibration Curve for CTAB Assay 54
2.7 CTAB Assay for Cumulative Release 55
2.8 Phenol Assay 55
3. Results and Discussion 57
3.1 Semi-Synthesis and Characterization of HA-Gly-OH 57
3.2 Electrospinning and Morphological Analysis of Electrospun Composites 60
3.3 Water Contact Angle Measurements 66
3.4 Mechanical Properties of Electrospun Composites 69
3.5 Evaluation of Cytocompatibility of Electrospun Scaffolds 74
3.6 Sol (SF) Gel Fraction (GF) 79
3.7 Cumulative Release 81
4. Conclusions 83
Supporting Information 85
References 102

Chapter 3 – Design, Characterization, and Electrospinning of Hyaluronic Acid-Arginine Bioconjugates

1. Introduction 109
2. Materials and Methods 112
2.1 Materials 112
2.2 Methods 112
2.2.1 General Methods 112
2.2.2 Nuclear Magnetic Resonance (NMR) Spectroscopy 112

2.2.3 Attenuated Total Reflectance Fourier Transform Infrared (ATR-FT-IR) Spectroscopy 113
2.2.4 Scanning Electron Microscopy (SEM) 113
2.2.5 Synthesis of Arg(Pbf)-OH 113
2.2.6 Synthesis of Arg(di-Z)-OH 114
2.2.7 Bioconjugation of Arg(Pbf)-OH with HA 114
2.2.8 Bioconjugation of Arg(di-Z)-OH with HA 115
2.2.9 Deprotection of HA-Arg(Pbf)-OH 115
2.2.10 Deprotection of HA-Arg(di-Z)-OH 115
2.2.11 Synthesis of Arg-OH 116
2.2.12 Bioconjugation of Synthetic Arg-OH with HA 116
2.2.13 Bioconjugation of Commercial Arg-OH with HA 117
2.2.14 Intrinsic Viscosity Measurements 117
2.2.15 Electrospinning 118
2.2.16 Raman Spectroscopy 119
2.2.17 Circular Dichroism (CD) Spectroscopy 119
2.2.18 Evaluation of Cytocompatibility of Electrospun Scaffolds 120
3. Results and Discussion 121
3.1 Semi-Synthesis of HA-Arg-OH 121
3.2 Comparison of the Molecular Weight of HA-Arg-OH Derivatives 146
3.3 Raman Spectroscopy 155
3.4 Circular Dichroism (CD) 158
3.5 Electrospinning and Morphological Analysis of Electrospun Composites 162
3.6 Biocompatibility Assessment 167
4. Conclusions 169
Supporting Information 171
References 186

Chapter 4 – Design, Characterization, and Electrospinning of Hyaluronic Acid-Cysteine Bioconjugates

1. Introduction 190
2. Materials and Methods 192
2.1 Materials 192
2.2 Methods 192

2.2.1 General Methods 192
2.2.2 Nuclear Magnetic Resonance (NMR) Spectroscopy 192
2.2.3 Attenuated Total Reflectance Fourier Transform Infrared (ATR-FT-IR) 193
Spectroscopy
2.2.4 Scanning Electron Microscopy (SEM) 193
2.2.5 Bioconjugation of Cys-OEt with HA 193
2.2.6 Deprotection of HA-Cys-OEt 193
2.2.7 Bioconjugation of Cys-OH with HA 194
2.2.8 Electrospinning 194
2.2.9 Evaluation of Cytocompatibility of Electrospun Scaffolds 195
3. Results and Discussion 197
3.1 Semi-Synthesis of HA-Cys-OH 197
3.2 Electrospinning and Morphological Analysis of Electrospun Composites 205
3.3 Biocompatibility Assessment 210
4. Conclusions 212
Supporting Information 214
References 219

Chapter 5 – Characterization of Electrospun Hyaluronic Acid-Based Bioconjugate Scaffolds

1. Introduction 222
2. Materials and Methods 223
2.1 Materials 223
2.2 Methods 224
2.2.1 Scaffold Fabrication and Composition 224
2.2.2 Sterility Test 225
2.2.3 Water Contact Angle Measurement 226
2.2.4 Raman Spectroscopy and Principal Component Analysis (PCA) 226
2.2.5 Cell Seeding and Culture Conditions 227
2.2.6 Immunofluorescence 228
3. Results and Discussion 229
3.1 Sterilization of Electrospun Scaffolds 229
3.2 Final Scaffolds Compositions 230
3.3 Water Contact Angle Measurement 232

3.4 Raman Spectroscopy and Principal Component Analysis (PCA) 240
3.5 Biological Evaluation of the Electrospun Scaffolds 254
4. Conclusions 258
Supporting Information 260
References 290

Chapter 6 – Design and Characterization of Hyaluronic Acid-Amino Acid Bioconjugates

1. Introduction 292
2. Materials and Methods 293
2.1 Materials 293
2.2 Methods 293
2.2.1 General Methods 293
2.2.2 Nuclear Magnetic Resonance (NMR) Spectroscopy 293
2.2.3 Attenuated Total Reflectance Fourier Transform Infrared (ATR-FT-IR) 293
Spectroscopy
2.2.4 Bioconjugation of Val-OMe with HA 294
2.2.5 Deprotection of HA-Val-OMe 294
2.2.6 Bioconjugation of Val-OH with HA 294
2.2.7 Bioconjugation of Met-OEt with HA 295
2.2.8 Deprotection of HA-Met-OEt 295
2.2.9 Bioconjugation of Leu-OMe with HA 296
2.2.10 Deprotection of HA-Leu-OMe 296
2.2.11 Bioconjugation of Leu-OH with HA 296
2.2.12 Bioconjugation of Phe-OH with HA 297
3. Results and Discussion 298
3.1 Semi-Synthesis of HA-Val-OH 298
3.2 Semi-Synthesis of HA-Met-OH 305
3.3 Semi-Synthesis of HA-Leu-OH 309
3.4 Semi-Synthesis of HA-Phe-OH 316
4. Conclusions 320
Supporting Information 321
References 332

Chapter 7 – A Study on Thiol-Michael Addition to Semi-Synthetic Elastin-Hyaluronan Material for Electrospun Scaffolds

Abstract 334

1. Introduction 335

2. Results and Discussion 337

2.1 Semi-Synthesis of Polysaccharide Derivatives 337

2.2 ATR-FTIR Analysis 343

2.3 Morphological Analysis 344

2.4 Cytotoxicity Assay 346

3. Conclusions 348

4. Experimental Section 349

Supporting Information 352

References 383

Conclusions and Future Perspectives 388

Acknowledgements 390

Abbreviations

The following abbreviations are used in this thesis:

AA : Amino acid

AD : Adamantane

AFM : Atomic force microscopy

AMPs : Antimicrobial peptides

ANOVA : Analysis of variance

ATCC : American Type Culture Collection

ATR-FTIR : Attenuated total reflectance Fourier transform infrared spectroscopy

AUC : Area under the curve

BDDE : 1,4-Butanediol diglycidyl ether

BMP-2 : Bone morphogenetic protein-2

Boc : tert-Butoxycarbonyl

CA : Citric acid

Cbz (Z) : Benzyloxycarbonyl

CD : Circular dichroism

CD44 : Cluster of differentiation 44

CDMT : 2-Chlorodimethoxy-1,3,5-triazine

CH_2Cl_2 : Dichloromethane

CMPI : 2-Chloro-1-methylpyridinium iodide

CTL : Lactose-modified chitosan

Cys : L-Cysteine

Cys-OEt : L-Cysteine ethyl ester

CR : Crosslinked

D_2O : Deuterium oxide

DAPI : 4′,6-Diamidino-2-phenylindole

DEX : Dexamethasone

DM : Degree of modification

DMEM : Dulbecco's Modified Eagle Medium

DMF : Dimethylformamide

DMSO : Dimethyl sulfoxide

DMSO-d_6 : Deuterated dimethyl sulfoxide

DMT : Derjaguin–Muller–Toporov

DOX : Doxorubicin

DPBS : Dulbecco's phosphate-buffered saline

DS : Degree of substitution

DSA : Drop shape analyzer

DSS : Sodium 3-(trimethylsilyl)propane-1-sulfonate

DTP : Dithiobis(propanoic dihydrazide)

DTPH : Thiolated dithiobis(propanoic dihydrazide)

DTT : Dithiothreitol

DVS : Divinyl sulfone

EAHP : Elastin-conjugated hyaluronic acid/poly-D,L-lactide scaffold

ECM : Extracellular matrix

EDC·HCl : *N*-(3-Dimethylaminopropyl)-*N*′-ethylcarbodiimide hydrochloride

EDTA : Ethylenediaminetetraacetic acid

EL : Elastin-derived peptide

ELHA : Elastin–hyaluronic acid bioconjugate

ELAHA : Elastin–hyaluronan bioconjugate

Et_2O : Diethyl ether

EtOH : Ethanol

FBS : Fetal bovine serum

FITC : Fluorescein isothiocyanate

FLIM : Fluorescence lifetime imaging microscopy

Fmoc : Fluorenylmethoxycarbonyl

FTIR : Fourier transform infrared spectroscopy

GAG : Glycosaminoglycan

GAGs : Glycosaminoglycans

GE : Gelatin

Gly-OEt·HCl : Glycine ethyl ester hydrochloride

Gly-OH : Glycine

GlcA : D-Glucuronic acid

GlcNAc : *N*-acetyl-D-glucosamine

GTA : Glutaraldehyde

HA : Hyaluronic acid

HA-AA : Hyaluronic acid–amino acid bioconjugate

HA-Arg-OH : Hyaluronic acid–arginine bioconjugate

HA-Bn : Benzyl-esterified hyaluronic acid

HA-Cys-OH : Hyaluronic acid–cysteine bioconjugate

HA-DTPH : Thiol-modified hyaluronic acid

HA-Gly-OEt : Glycine ethyl ester–functionalized hyaluronic acid

HA-Gly-OH : Glycine-functionalized hyaluronic acid

HA-Leu-OH : Hyaluronic acid–leucine bioconjugate

HA-Met-OH : Hyaluronic acid–methionine bioconjugate

HA-Phe-OH : Hyaluronic acid–phenylalanine bioconjugate

HA-TCO : trans-Cyclooctene-modified hyaluronic acid

HA-Tz : Tetrazine-modified hyaluronic acid

HA-Val-OH : Hyaluronic acid–valine bioconjugate

HAMA : Methacrylated hyaluronic acid

HDFs : Human dermal fibroblasts

HFP : 1,1,1,3,3,3-Hexafluoro-2-propanol

HHA : High molecular weight hyaluronic acid

HHA-S : Thioether-grafted hyaluronic acid

HOBT : 1-Hydroxybenzotriazole

HP : Hyaluronic acid/poly-D,L-lactide scaffold

HPβCD : Hydroxypropyl-β-cyclodextrin

HTE : Human tropoelastin

IBU : Ibuprofen

IGF-1 : Insulin-like growth factor-1

IGF-1C : IGF-1-derived peptide

IR : Infrared spectroscopy

ISO : International Organization for Standardization

L929 : Murine fibroblast cell line

Leu-OH : L-Leucine

Leu-OMe : L-Leucine methyl ester

LMW : Low molecular weight

LSM : Laser scanning microscope

Lys : Lysine

MA : Maleic anhydride

MAAHA : Methacrylamide-decorated hyaluronic acid

MAHA : Methacrylate-decorated hyaluronic acid

MAHP : Methacrylamide-decorated hyaluronic acid/poly-D,L-lactide scaffold

MaPVA : Methacrylated poly(vinyl alcohol)

MDI : Methylene diphenyl diisocyanate

MES : 2-(N-Morpholino)ethanesulfonic acid

Met-OEt : L-Methionine ethyl ester

MHA : Maleilated hyaluronic acid

MMP : Matrix metalloproteinase

MTS : 3-(4,5-Dimethylthiazol-2-yl)-5-(3-carboxymethoxyphenyl)-2-(4-sulfophenyl)-2H-tetrazolium

MTT : 3-(4,5-Dimethylthiazol-2-yl)-2,5-diphenyltetrazolium bromide

NAcCys : *N*-acetyl-L-cysteine

NAD(P)H : Nicotinamide adenine dinucleotide (phosphate)

NFM : Nanofibrous membrane

NHS : N-Hydroxysuccinimide

NMR : Nuclear magnetic resonance

NO : Nitric oxide

NONOate : N-Diazeniumdiolate

OMe : Methyl ester

PBS : Phosphate-buffered saline

Pbf : 2,2,4,6,7-Pentamethyl-2,3-dihydrobenzofuran-5-sulfonyl

PC : Principal component

PCA : Principal component analysis

PCL : Polycaprolactone

PDLLA : Poly(D,L-lactic acid)

PEG : Poly(ethylene glycol)

PEGDA : Poly(ethylene glycol) diacrylate

PEO : Poly(ethylene oxide)

PFA : Paraformaldehyde

PGA : Polyglycolic acid

PGS : Poly(glycerol sebacate)

PLA : Poly(lactic acid)

PLGA : Poly(lactic-co-glycolic acid)

PLLA : Poly(L-lactic acid)

PSA : Penicillin/streptomycin/amphotericin B

PVA : Poly(vinyl alcohol)

PVP : Polyvinylpyrrolidone

RGD : Arginine–glycine–aspartic acid peptide sequence

ROS : Reactive oxygen species

RT : Room temperature

s-NHS : *N*-Hydroxysulfosuccinimide

SD : Standard deviation

SEM : Scanning electron microscopy

SDA : Sabouraud dextrose agar

SDB : Sabouraud dextrose broth

SPPS : Solid phase peptide synthesis

TBA : Tetrabutylammonium

TCEP : Tris(2-carboxyethyl)phosphine

TCEP·HCl : Tris(2-carboxyethyl)phosphine hydrochloride

TCO : trans-Cyclooctene

TFA : Trifluoroacetic acid

THF : Tetrahydrofuran

TIS : Triisopropylsilane

TLC : Thin-layer chromatography

TSA : Tryptic soy agar

TSB : Tryptic soy broth

UPW : Ultrapure water

UV : Ultraviolet

Abstract

L'acido ialuronico (HA) è un polisaccaride di origine naturale ampiamente utilizzato in applicazioni biomediche grazie alla sua eccellente biocompatibilità e al suo ruolo biologico chiave nei processi di rigenerazione tissutale e di guarigione delle ferite. Tuttavia, la sua elevata idrofilicità, la limitata stabilità meccanica e la scarsa processabilità rappresentano importanti criticità per la sua lavorazione mediante elettrofilatura finalizzata alla realizzazione di scaffold nanofibrosi. Pertanto, la modifica chimica rappresenta una strategia efficace per modulare le proprietà fisico-chimiche dell'HA preservandone al contempo la rilevanza biologica.

In questa tesi è stato sviluppato un approccio chimico sistematico e modulare per la funzionalizzazione dell'acido ialuronico mediante reazioni di accoppiamento mediato da carbodiimmide. Amminoacidi strutturalmente diversi e motivi peptidici bioattivi sono stati covalentemente introdotti lungo la catena dell'HA in condizioni acquose blande. I bioconiugati di HA ottenuti sono stati caratterizzati mediante spettroscopia NMR e ATR-FTIR, confermando l'avvenuta bioconiugazione e la preservazione dell'integrità della catena polisaccaridica, con un grado di sostituzione dipendente sia dalla struttura molecolare dei sostituenti sia dalla strategia di coniugazione adottata.

Alcuni derivati selezionati di HA sono stati successivamente processati in scaffold nanofibrosi mediante elettrofilatura. Per superare le limitazioni intrinseche della processabilità dell'HA, il polivinilpirrolidone è stato impiegato in combinazione con l'HA, e sono state sviluppate architetture sia a strato singolo sia bilayer asimmetriche, ottenute combinando strati idrofili a base di HA con un supporto in poli(D,L-acido lattico). Gli scaffold risultanti hanno mostrato morfologie fibrose continue e proprietà superficiali modulabili.

Le proprietà superficiali degli scaffold sono state investigate mediante misure dell'angolo di contatto, che hanno dimostrato come la bagnabilità superficiale fosse governata dall'architettura dello scaffold e dalla chimica di superficie. La spettroscopia Raman, supportata da analisi multivariata, ha consentito di discriminare tra sistemi a base di HA non funzionalizzati e funzionalizzati. È stato inoltre dimostrato che la sterilizzazione UV è efficace senza indurre modifiche chimiche rilevabili. La valutazione biologica preliminare ha evidenziato l'influenza dell'idratazione superficiale e della stabilità del materiale sulle interazioni cellula–materiale, sottolineando la necessità di bilanciare bioattività e robustezza strutturale.

Nel complesso, questo lavoro fornisce una piattaforma versatile per la modifica chimica controllata dell'acido ialuronico e la sua integrazione in sistemi di scaffold elettrofilati, offrendo principi di progettazione per lo sviluppo di biomateriali a base di HA destinati ad applicazioni nella guarigione delle ferite.

Abstract

Hyaluronic acid (HA) is a naturally occurring polysaccharide widely used in biomedical applications due to its excellent biocompatibility and its key biological role in tissue regeneration and wound healing. However, its high hydrophilicity, limited mechanical stability, and poor processability represent major challenges for its processing by electrospinning for the fabrication of nanofibrous scaffolds. Therefore, chemical modification presents an effective strategy to tailor the physicochemical properties of HA while preserving its biological relevance.

In this thesis, a systematic and modular chemical approach for the functionalization of hyaluronic acid was developed using carbodiimide-mediated coupling. Structurally diverse amino acids and bioactive peptide motifs were covalently introduced along the HA backbone under mild aqueous conditions. The resulting HA bioconjugates were characterized by NMR and ATR-FTIR spectroscopy, confirming successful bioconjugation while preserving the integrity of the polysaccharide backbone, with a substitution degree depending on both the molecular structure of the substituents and the conjugation strategy.

Selected HA derivatives were subsequently processed into nanofibrous scaffolds by electrospinning. To overcome the intrinsic limitations of HA processability, polyvinylpyrrolidone was employed in combination with HA, and both single-layer and asymmetric bilayer architectures were developed by combining hydrophilic HA-based layers with a poly(D,L-lactic acid) support. The resulting scaffolds exhibited continuous fibrous morphologies and tunable surface properties.

Scaffold surface properties were investigated by contact angle measurements, which demonstrated that surface wettability was governed by scaffold architecture and surface chemistry. Raman spectroscopy, supported by multivariate analysis, enabled the discrimination between non-functionalized and functionalized HA-based systems. Importantly, UV sterilization was shown to be effective without inducing detectable chemical modifications. Preliminary biological evaluation highlighted the influence of surface hydration and stability on cell–material interactions, underscoring the need to balance bioactivity and structural robustness.

Overall, this work provides a versatile platform for the controlled chemical modification of hyaluronic acid and its integration into electrospun scaffold systems, offering design principles for the development of HA-based biomaterials for wound-healing applications.

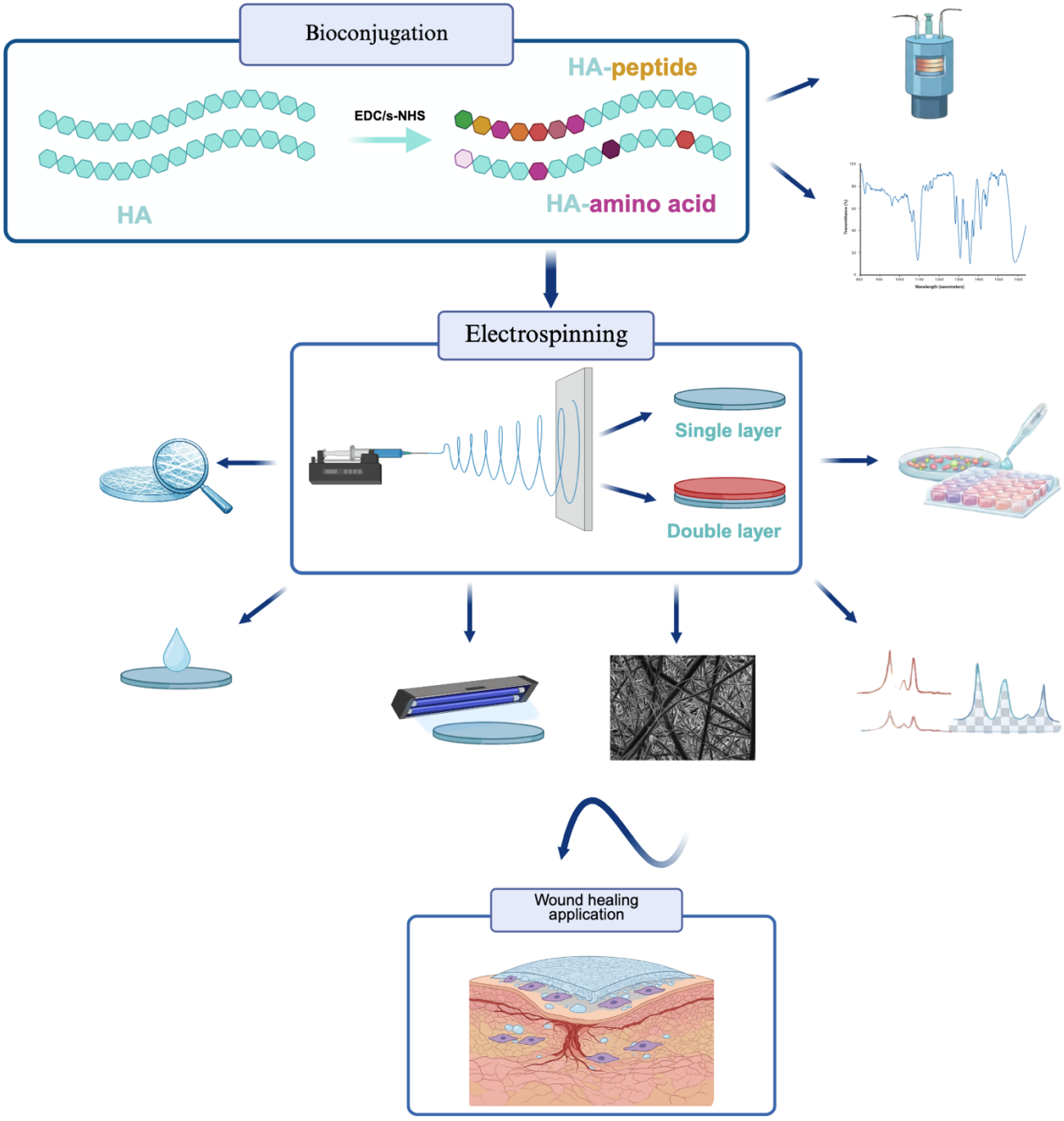

Figure 1. Overview of the chemical modification of hyaluronic acid via carbodiimide-mediated bioconjugation, characterized by NMR and ATR-FTIR spectroscopy, and its processing into single-layer and bilayer electrospun scaffolds, followed by physicochemical characterization and application-oriented evaluation for wound healing.

Chapter 1

Chemical Modifications in Hyaluronic Acid-Based Electrospun Scaffolds

Antonietta Pepe [a], Antonio Laezza [a], Francesca Armiento [a] and Brigida Bochicchio*[a]

[a] Department of Science, University of Basilicata, Via Ateneo Lucano, 10, 85100 Potenza, Italy

The content of this chapter has been published in ChemPlusChem
DOI: 10.1002/cplu.202300599

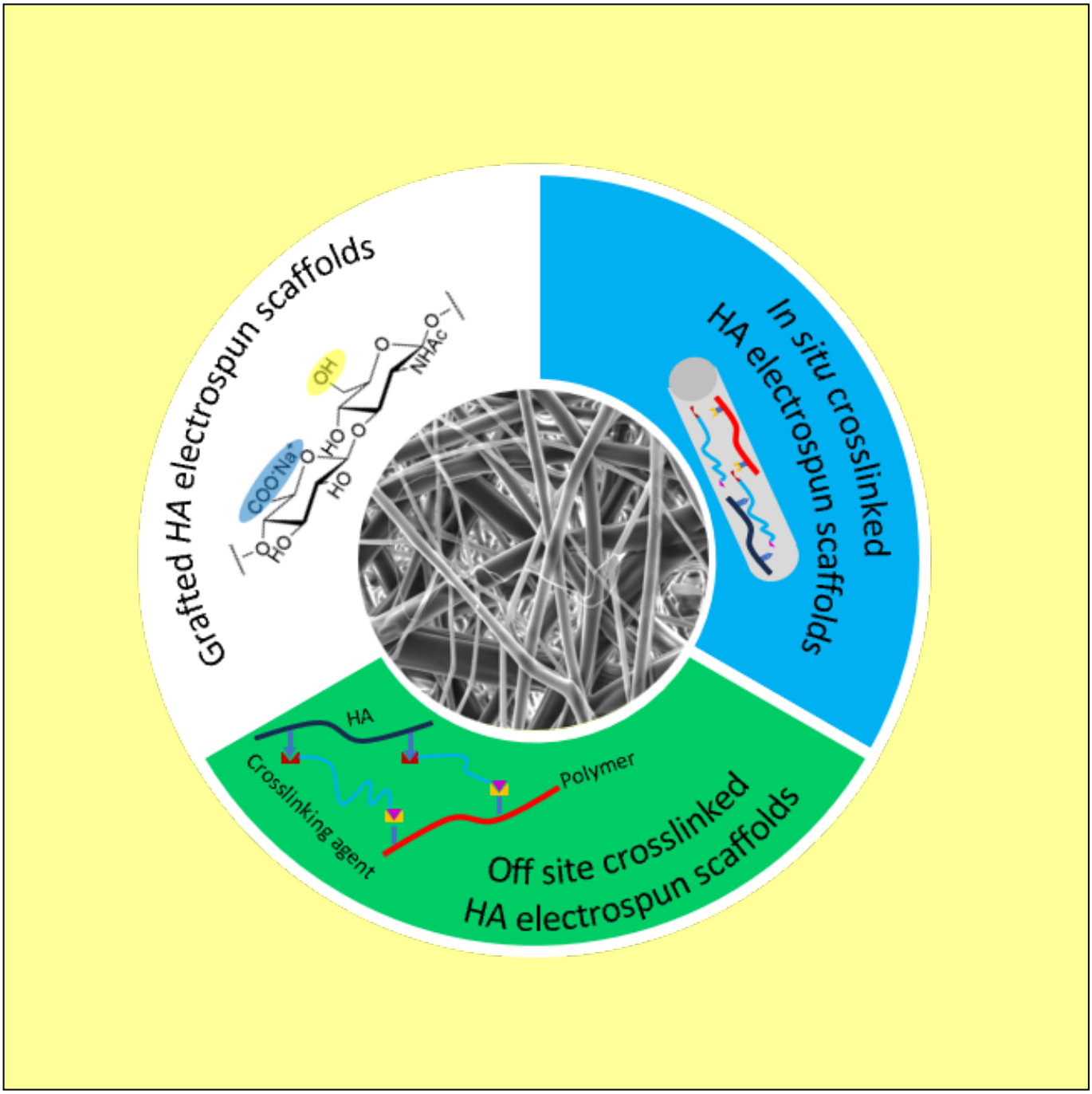
Grafted HA electrospun scaffolds
In situ crosslinked
HA electrospun scaffolds
Off site crosslinked
HA electrospun scaffolds
HA
Crosslinking agent
Polymer

Abstract

Hyaluronic acid (HA) is a natural, non-sulfated glycosaminoglycan (GAG) present in the ECM. It is involved in different biological functions with appealing properties in cosmetics and pharmaceutical preparations as well as in tissue engineering. Generally, HA has been electrospun in blends with natural or synthetic polymers to produce fibers having diameters in the order of nano and micro-scale whose pores can host cells able to regenerate damaged tissues. In the last decade, a rich literature on electrospun HA-based materials arose. Chemical modifications were generally introduced in HA scaffolds to favour crosslinking or conjugation with bioactive molecules. Considering the high solubility of HA in water, HA-based electrospun scaffolds are cross-linked to increase the stability in biological fluids. Crosslinking is necessary also to avoid the release of HA from the hybrid scaffold when implanted *in vivo*. Furthermore, to endow the HA based scaffolds with new chemical or biological properties, conjugation of bioactive molecules to HA was widely reported. Herein, we review the existing research classifying chemical modifications on HA and HA-based electrospun fibers into three categories: i) *in situ* crosslinking of electrospun HA-based scaffolds; ii) off-site crosslinking of electrospun HA-based scaffolds; iii) conjugation of biofunctional molecules to HA with focus on peptides.

1. Introduction

Hyaluronic acid (HA) is a glycosaminoglycan which is a linear polysaccharide found in skin, cartilage, vitreous humor, and synovial liquid [1]. This natural polymer consists of alternating disaccharide units of β-1,4-D-glucuronic acid and β-1,3-*N*-acetyl-D-glucosamine *n*-fold repeated (Figure 1). One of the main drawbacks in HA use is source limitations as well as high production costs. Generally, the production of HA has been based in the past on its extraction from bovine vitreous humor, umbilical cord, or rooster comb, while microbial HA from *Streptococcus* strains is currently the main valid alternative to traditional methods. HA is one of the most appealing macromolecules not only for cosmetics and pharmaceutical formulations but also for regenerative medicine with applications ranging from myocardial tissue engineering to neural growth to wound healing. HA is a natural hydrogel owning a physiological water holding capacity and raising deep interest also in cancer therapy considered its ability to target receptors overexpressed in cancer cells, i.e. CD44 [2]. However, the debate concerning HA inflammatory reactions is still challenging. Recent studies have demonstrated pro-inflammatory functions of low molecular weight (LMW) HA and its capability to promote the activation of macrophages [3]. That finding undoubtedly deserves to be kept under consideration in the formulations of HA-based nanodevices. Natural hydrogels have physicochemical and biological properties superior to synthetic ones. The most important advantages in the use of natural hydrogels are low immunogenicity, excellent biocompatibility and cytocompatibility, biodegradability, specific cellular/tissue response, adequate stability, superior structural design, controllable solubility, and 3D geometry [4]. On the other hand, weak mechanical properties, rapid *in vivo* degradation, and clearance [5] must be taken into account too. An answer is offered by the versatility of HA structure containing different functional groups such as acetamide, carboxyl, hydroxyl, and terminus aldehyde affording a multitude of potential functionalization strategies. In Figure 1, the most common functionalization sites are highlighted [6]. Commonly, HA esterification or amidation were employed to introduce functional groups able to form covalent bonds with different biomolecules through Michael-type addition or Schiff-base synthetic methodologies. HA functionalization is also useful to the formation of cross-links conferring stability to HA in aqueous solution. The most diffuse crosslinkers are dihydrazide, dialdehyde, butanediol-diglycidyl ether (BDDE), divinyl sulfone (DVS), and genipin [7]. Furthermore, HA has been widely photo-crosslinked by preliminary introduction of methacrylic groups [8]. However, great attention deserves the cross-linker choice which must be operated in the perspective of ensuring HA stability and preserving the cytocompatibility of the final scaffolds. Recent studies have demonstrated that the esterification of HA through carbodiimide induced self-esterification equivalent to a self-crosslinking [9]. The main advantage herein is represented by the exclusive presence of HA as a bridged molecule.

Self-crosslinked HA has great potential in applications such as drug release where the simultaneous release of drug and side-reaction products derived from commercial cross-linkers is avoided.

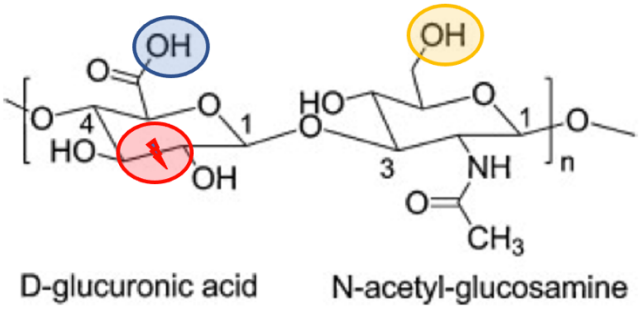

Figure 1. Chemical structure of hyaluronic acid and target sites for chemical modification.

In addition, cross-linking confers to HA a 3D structure able to mimic the extracellular matrix and hosting cells for regenerative purposes. Higher is the relationship between surface area and volume of pores in 3D structure of the hydrogel, better would be the performance as biomaterial. Electrospinning is a valuable technique aimed at the production of micro- and nano-fibers hierarchically organized in interconnected porous structures assuring nutrients and waste exchanges essential for the survival of cells. Electrospinning is an electrohydrodynamic process where a liquid drop from a polymer solution is electrified to produce a jet elongating in a straight-line direction and undergoing thinning and solidification onto a grounded collector. The schematic set-up of electrospinning consists of a high-voltage supply, a syringe-pump, a spinneret consisting of a needle and a ground collector. The solvent evaporates during the path from spinneret to the collector and then the solid appears as a web of fibers. Therefore, volatile organic solvents are preferred in electrospinning because solvent evaporation induces fiber solidification. However HA is not soluble in organic solvents while it is soluble in aqueous solution characterized by high surface tension, low evaporability and high viscosity level which significantly hinders the process of electrospinning. Also HA concentration is a critical issue in spinnability, given that hyaluronan concentration can be used only in a narrow range in order to successfully realise fibrous structures. At high polymer concentration, the electric field may not be able to overcome the high viscosity of the solution, and thus a continuous jet stream from the polymer solution is not obtained and fiber production fails. On the other hand, at low polymer concentrations an excess amount of solvent must be removed between the jet fluid stream leaving the spinneret and the fiber reaching the ground with the consequence that

the process turns into the formation of particles instead of fibers. The contradiction could be overcome by accurate tuning of concentration and electrospinning parameters such as voltage, tip to collector distance, needle gauge diameter, flow rate. Additionally, another parameter worthy of attention is HA molecular weight. Low molecular weight HA is less viscous than that of high molecular weight HA at the same concentration. However, the electrospinning results from the lower molecular weight HA do not produce nanofibers as the polymer chains are not sufficiently entangled to form fibrous morphology. Overcoming the high viscosity to successfully find the threshold between molecular weight, viscosity, and spinning parameters, is one of the main challenges faced in fabricating nanofibers of HA. A successful attempt was the introduction of electro-blowing assisted electrospinning where solvent evaporation was accelerated by blowing air at high temperature [10]. Alternatively, to improve the electrospinnability, HA has been widely electrospun with other synthetic or natural polymers for the production of hybrid scaffolds as recently highlighted in several reviews [11]. Finally, chemical modifications of HA functional groups are extensively carried out to improve electrospinnability by changing HA viscosity. In this way, intermolecular hydrogen bond network found in the hyaluronan solution is interrupted with beneficial effects on the viscosity. This review focuses on the electrospinning of properly designed chemical modifications on hyaluronans. Indeed, even if a rich literature on chemical modifications of hyaluronic acid exists, few are the examples of electrospun scaffolds obtained from HA-derivatives containing covalent bonds between hyaluronic acid and bioactive molecules. In this review, we survey the recent research carried out on the chemical modifications made on hyaluronan-based electrospun scaffolds through the classification into three main categories: i) *in situ* crosslinked HA electrospun scaffolds; ii) off-site crosslinked HA electrospun scaffolds; iii) (peptide)-decorated HA electrospun scaffolds.

2. In Situ Crosslinking

In situ crosslinking of hyaluronan-based electrospun fibers is defined as a process consisting of a single crosslinking step carried out during electrospinning with instruments equipped with multi-syringe apparatus. The syringes contain either crosslinker or electrospinnable polymer(s) solutions which are mixed and ejected simultaneously. Herein, some examples are presented (Table 1). Arnald-Pastòr *et al*. reported bilayered *in situ* crosslinked electrospun HA/PLLA scaffolds. Poly-L-lactic acid (PLLA) is FDA approved polymer widely used for applications in biomedicine. It is easily electrospun alone or blended with other polymers as HA. In this example, bilayered HA/PLLA crosslinked electrospun scaffolds were produced (Figure 2a). Crosslinked electrospun HA scaffolds were obtained in a single step by combining HA with a divinylsulfone (DVS) crosslinker solution in sodium hydroxide in a three-way valve (Figure 2b). They were electrospun and deposited onto previously electrospun PLLA materials in order to obtain bilayered HA/PLLA membranes. These membranes showed two distinct faces with complementary properties: the PLLA side was cell friendly promoting cell attachment and spreading, while the HA face hindered cell adhesion and thus may prevent post-surgical adherences. Bilayered membranes made up of polymers and HA are widely described in literature with potential applications in wound dressing and tissue engineering [12]. Kim *et al*. described the dual syringe reactive electrospinning.

Table 1: Summary of main characteristics of *in situ* cross-linked HA-based electrospinning methodologies

Chemical modification	Crosslinker/Modifier[a]	Polymer Blend[b]/ Drug	Methodology	Proposed Application	References
In situ cross-linking	Divinylsulfone (DVS)	HA+PLLA	Bilayered Scaffold	Patch for preventing post-surgical adhesions	[12]
	PEGDA	HA-DTPH/PEO	PEO removing after electrospinning	soft-tissue scaffold in 3D cell cultures for tissue engineering.	[14]
	Citric acid (CA)	HA/PVA/L-Arg HA/PVA/CNCs/L-Arg	Additional thermal treatment (100°C , 6h)	Multifunctional wound dressings	[15]
	EDC/NHS	HA/PVA/HPβCD	multi-needles emitter Additional annealing (60°C, 24h)	Drug delivering wound dressings	[18]
	Maleic Anhydride (MA)	HA/PVA	Additional Photo-crosslinking (UV)	Controlled release modulated devices	[19]

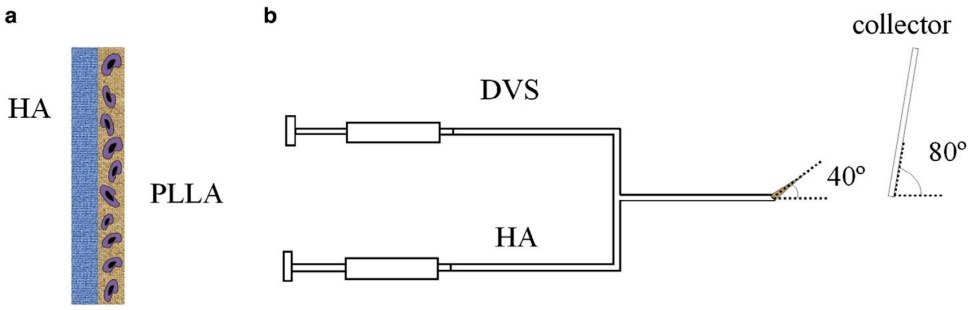

Figure 2. Schematic representation of: a) bilayer membrane b) electrospinning apparatus setup (Adapted from [12]. Copyright (2013) with permission from Elsevier).

The *in situ* or reactive electrospinning allows the crosslinking reaction to occur simultaneously during the electrospinning process [13]. In the example herein reported, HA was previously chemically modified with dithiobis(propanoic dihydrazide) (DTP) by carbodiimide chemistry.

Next, disulfide bonds were reduced using dithiothreitol (DTT) to give, after exhaustive dialysis, the corresponding thiol-modified macromolecular derivatives HA-DTPH (Figure 3). The HA-derivative containing thiol groups (HA-DTPH) has been electrospun (Figure 3a) and simultaneously crosslinked with a homobifunctional poly(ethylene glycol)diacrylate (PEGDA), shown in Figure 3b, through a dual-syringe apparatus. The crosslinking reaction occurred at room temperature in approximately ten minutes and in aqueous solution at pH 7.4 giving rise to HA-PEGDA-HA electrospun scaffold (Figure 3c). The electrospinning apparatus is schematized in Figure 4 [14]. Electrospinning in water is highly recommended in terms of the adoption of harmless practices for the environment and sustainability, even if the electrospinning of HA in water is a huge task given the high viscosity of the biopolymer. This limit was here successfully addressed by adding a viscosity modifier as PEG which facilitated fiber formation. HA-PEGDA-HA electrospun scaffold was proposed as a potential soft-tissue scaffold material for tissue engineering. Another example is represented by electrospun polyvinyl alcohol (PVA)/Hyaluronic acid/L-arginine nanofibers *in situ* crosslinked by citric acid. L-arginine-loaded citric acid (CA) crosslinked poly(vinyl alcohol)/Hyaluronic Acid (PVA-HA) nanofibers were fabricated by electrospinning and proposed for potential wound healing purposes. These nanofibrous scaffolds were prepared by dissolving first L-arginine and CA in PVA/HA solution and then by electrospinning them. CA is a tri-dentated crosslinker showing the advantages of being water soluble and harmless. CA started the crosslinking reaction during electrodeposition, whereas a final heating treatment of electrospun nanofibers at 100 °C for 6 h was applied to ensure complete

crosslinking. L-arginine loading was expected to accelerate wound healing process through nitric oxide (NO) release stimulating angiogenesis, collagen synthesis, and cell proliferation [15].

Tomihata *et al*. reported the *in situ* crosslinking of hyaluronic acid/cyclodextrin nanofibers electrospun in aqueous solution. In order to broaden the scope of potential applications, the incorporation of functional compounds such as cyclodextrins in the electrospun fibers is one of the novel strategies envisaged.

Herein, HA was electrospun in water with a natural polysaccharide as hydroxypropyl-β-cyclodextrin (HPβCD) in presence of poly-vinyl alcohol (PVA) as carrier polymer. *In situ* crosslinking was carried out simultaneously to electrospinning by adding *N*-(3-Dimethylaminopropyl), *N*′-ethylcarbodiimide hydrochloride and *N*-hydroxysuccinimide (EDC/NHS) to the polymeric solution (Figure 5a). In general terms, carbodiimide derivatives are widely used because they are water soluble and atoxic [16]. The coupling of EDC with NHS allows to form ester bonds between carboxylic acid groups and hydroxyl groups of HA itself or of other molecules present at its side giving rise to an extensive self-crosslinking which stabilizes the molecule (Figure 5b) [17]. In order to preserve the bioactivity of such compounds that could be lost during harvest heating, the mildest annealing conditions allowing an efficient crosslinking were sought. An annealing step at 60 °C during 24 h was necessary to ensure the efficient crosslinking for which the reaction scheme and the proposed resulting structure of the nanofibers are shown in Figure 5c. It has been demonstrated that the nanostructure of the final membrane as revealed by SEM was not altered by annealing, highlighting the role of HPβCD in ensuring an efficient crosslinking reaction mainly due to the combination of the electrospinning and freeze-drying steps [18]. An envisaged application for these scaffolds is the drug delivery system exploiting cyclodextrin structure.

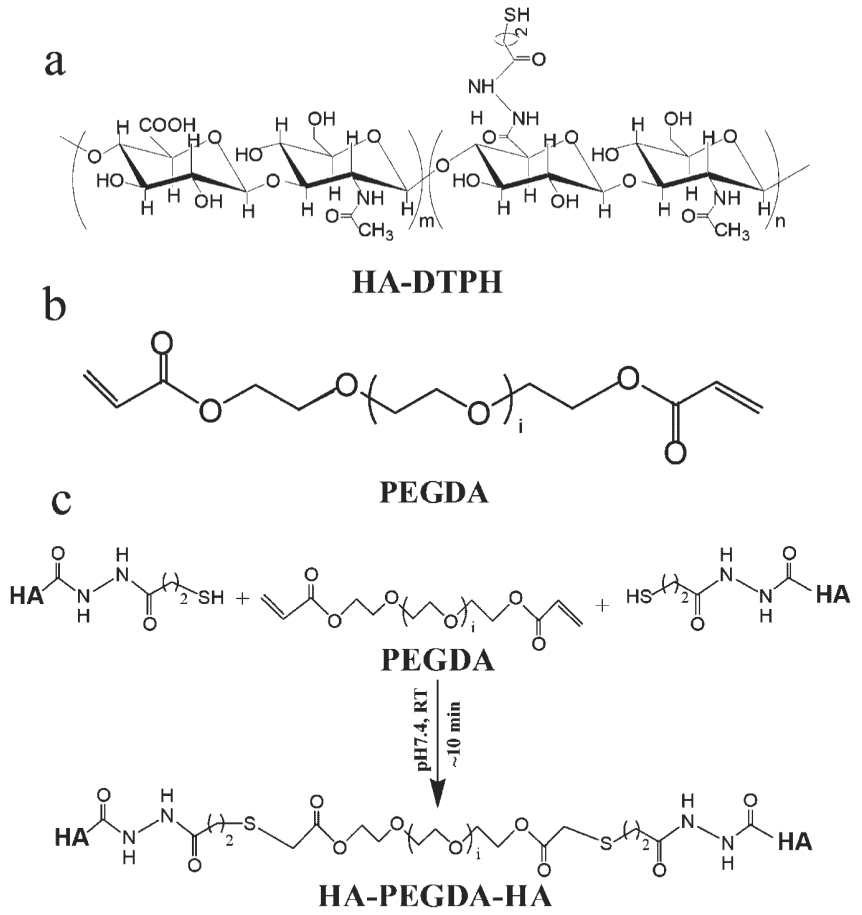

Figure 3. a) Structure of HA-DTPH. b) Structure of PEGDA. c) Crosslinking reaction to form HA-PEGDA-HA linkages. Reprinted from [14]. Copyright (2006) with permission from Wiley.

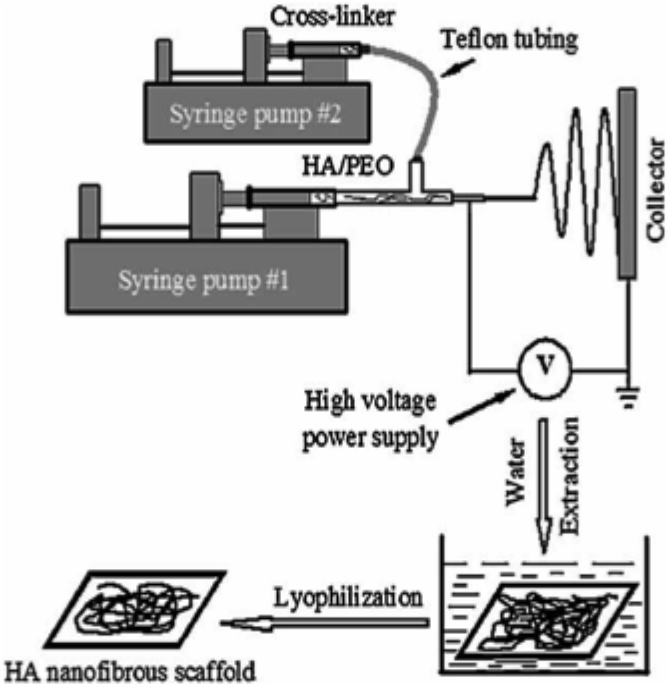

Figure 4. Schematic illustration of the electrospinning setup and the procedure for the fabrication of HA-DTPH nanofibrous scaffolds. HA-DTPH/PEO blend solution was loaded into the primary syringe (#1). A PEGDA solution was loaded into the secondary syringe (#2) and delivered to the primary syringe (#1) using Teflon tubing. A 'T'-shaped three-way steel adapter was designed to mix the solutions and transport them to the spinneret. The electrospun HA-DTPH/PEO blend scaffold was soaked in deionized water for 24 h to extract PEO, followed by lyophilization to obtain an electrospun HA-DTPH nanofibrous scaffold. Reprinted from [14]. Copyright (2006) with permission from Wiley.

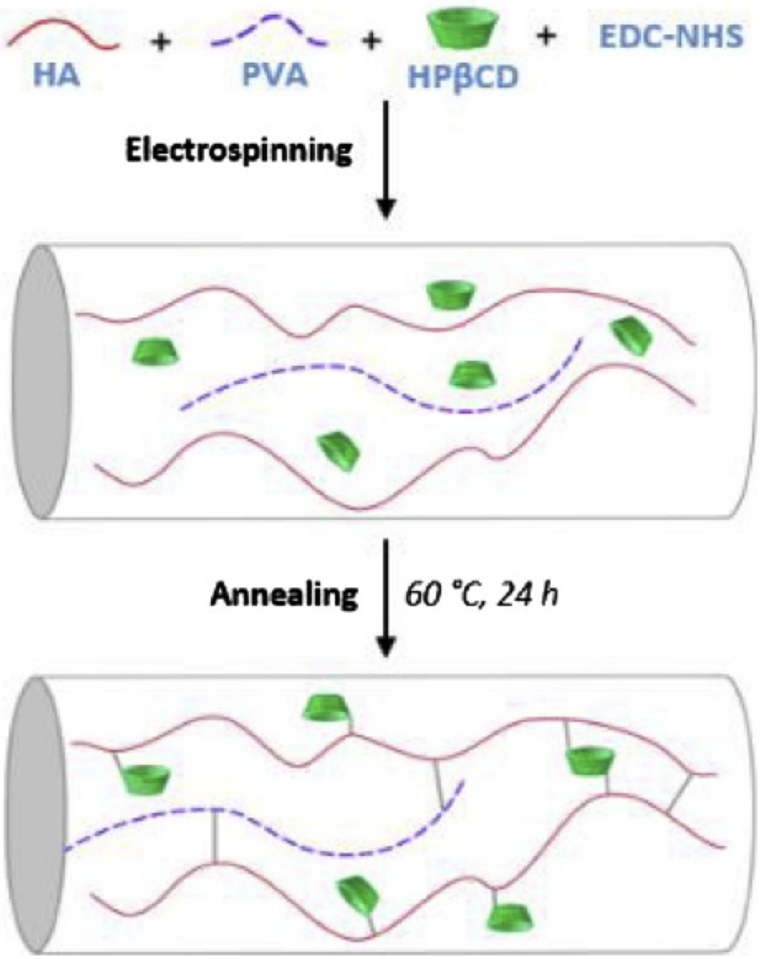

Figure 5. Schematic illustration of the processing to obtain crosslinked HA-PVA-HPβCD fibers. Adapted from [18]. Copyright (2018) with permission from Elsevier.

Finally, the production of crosslinked HA/PVA electrospun membranes free from organic solvent was reported as another example of environmentally-friendly procedure. The membranes were crosslinked during electrospinning through maleic anhydride (MA) addition improving also the electrospinning performances. To ensure the stability of the membranes, since PVA and HA functional groups compete for the possible active reaction sites as shown in Figure 6, a final crosslinking step was performed through photo-crosslinking by exposure to a UV light reactor for 40 min [19]. Previously, Yang *et al*. showed that PVA hydroxyl and MA acyl groups efficiently reacted giving rise to a crosslinking during the electrospinning process, without the need of heat treatment or UV radiation [20]. PVA and MA reacted to form mono esters or bis-esters during electrospinning thanks to the high electric field that can stimulate the chemical activity of the molecules and causing the rapid evaporation of water can accelerate the esterification reaction.

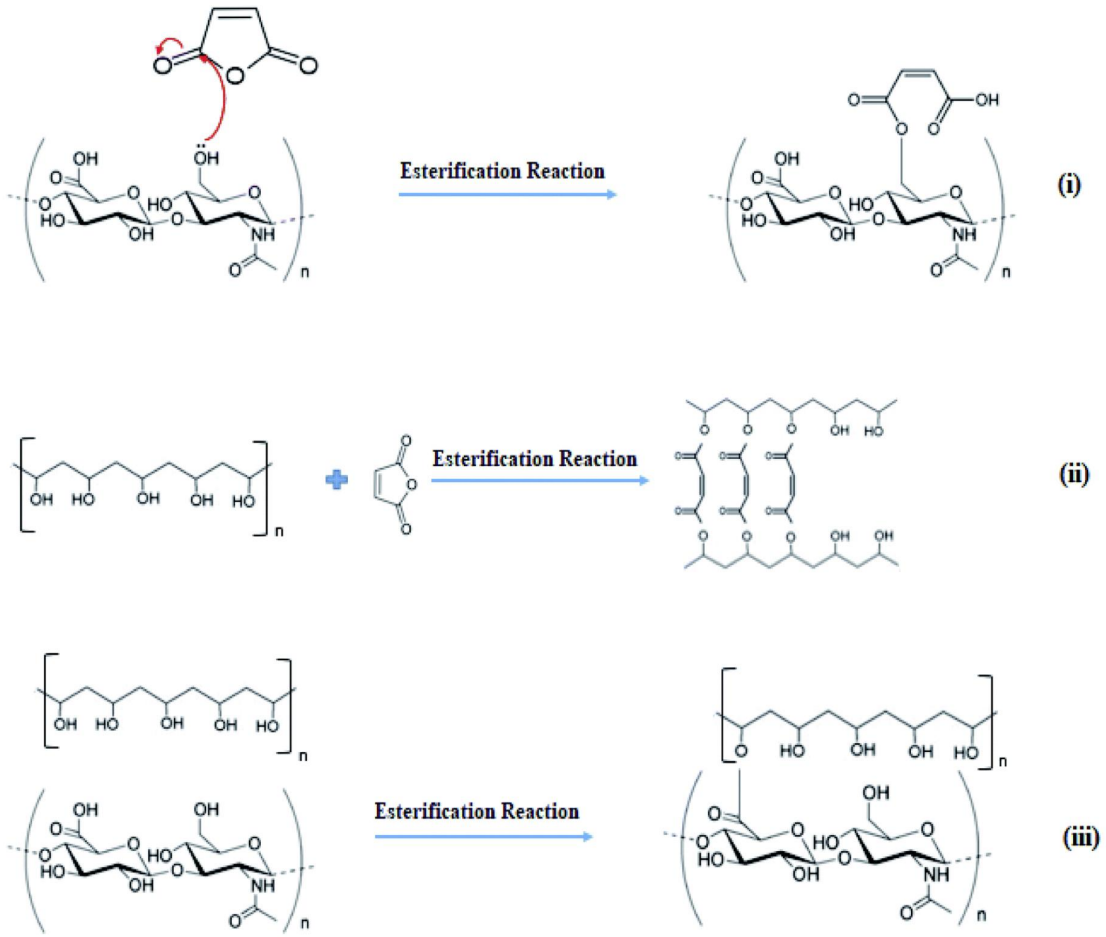

Figure 6. Schematic representation of possible esterification reactions between (i) HA and MA, (ii) PVA and MA, (iii) PVA and HA. Reprinted from [19], copyright (2020) with permission from RSC.

3. Off-Site Crosslinked HA Electrospun Scaffolds

In this section some examples of crosslinking reactions carried out on blended HA scaffolds after electrospinning are reviewed (Table 2). In many cases a modification step of HA before its processing by electrospinning has been reported to promote the crosslinking of HA electrospun fibers [21]. In some cases, HA was used as a crosslinker by forming amide or ester bonds with other electrospun polymers. For example, hybrid Gelatin/Poly-L–Lactide Scaffolds (GE/PLA) were crosslinked by tethering HA to electrospun nanofibers through carbodiimide and *N*-hydroxysuccinimide (NHS). The high-water solubility of GE in the electrospun scaffolds made the crosslinking mandatory before any use in aqueous solutions. Hyaluronate crosslinking by EDC/NHS reaction to GE/PLA electrospun scaffolds was performed also to control hydrophilicity and cell adhesion. The scaffolds after crosslinking and sterilization in 70 % ethanol solution were allowed to stay overnight at r.t. to complete evaporation of any residual solvent. Fluorescence lifetime imaging microscopy (FLIM) was used to image human dermal fibroblasts (HDFs) seeded on the hybrid scaffolds. Besides cell imaging, FLIM enabled the measurement of the HDF glycolytic activity by assessing the ratios between free and protein-bound NAD(P)H [22].

Table 2: Summary of main characteristics of off-site cross-limking HA-based electrospinning methodologies

Chemical modification	Crosslinker/Modifier[a]	Polymer Blend[b]/ Drug	Methodology	Proposed Application	Ref.
Off-site cross-linking	HA + EDC/NHS	GE/PLLA	Pouring and crosslinking	in vitro drug testing system	[11]
			Nanofiber dispersion crosslinking	Superadsorbent scaffolds for Cartilage Tissue Engineering	[22]
	Methacrylated HA	Aminolyzed PCL	Michael reaction and photocrosslinking	Cell culture matrix	[23]
	EDC	HA/Gelatin	Pouring in crosslinking solution	Biomedical materials	[24]
		HA/collagen	Salt leaching of NaCl particulates	Scaffolds for tissue engineering	[25]
	UV-irradiation	Maleilated-HA/Methacrylated PVA	Photo-crosslinking	wound dressings	[26]
	UV-irradiation	Methacrylated HA/PEO	Photopatterning	scaffolds with channels for tissue engineering	[27]
	UV-irradiation	Methacrylated HA/PCL/IGF-1	Blended or shell(PCL)/core(HAMA+IGF-1)	artificial dura mater for application in neurosurgery.	[28]
	UV-irradiation	PCL/poly(glycerol sebacate) (PCL-PGS) + HAMA/PEO/Pluronic F127	Bilayered scaffold	artificial nerve grafts as tubular nerve guide conduit	[29]
	UV-irradiation	NO-releasing methacrylated HA/PEO	Photo-crosslinking	Wound healing applications	[30]
	Genipin, Glutaraldehyde, EDC/NHS	HA/CTL/PEO	Different chemical crosslinking methodologies	wound dressings	[32]
	$FeCl_3$ BDDE	HA/Ibuprofen	ionic crosslinking + covalent crosslinking	Prevention of post surgery tendon adhesion	[33]
	Methylene diisocyanate (MDI)	HA/zein//PVP		Scaffolds for tissue engineering and wound healing	[34]

Chen *et al*. crosslinked a dispersion of homogenized GE/PLA electrospun nanofibers by addition of HA and EDC/NHS activating agents. After freeze-drying, a superabsorbent 3D scaffold based on electrospun nanofibers for cartilage tissue engineering was obtained [23]. In another report Cho *et al*. decorated PCL nanofibers on the surface with methacrylated HA via Michael type addition and by photo-crosslinking with the aim to reduce hydrophobicity and improve cell viability and proliferation of the scaffold [24].

3.1. Carbodiimide Promoted Crosslinking of Electrospun HA-Based Scaffolds

Water soluble carbodiimide EDC was frequently employed as activating agent of carboxyl groups, both in protein-based or uronic acid -based biopolymers. Further reaction with amine or hydroxyl groups introduces amide or ester linkages, respectively. HA solubility in water permits to avoid organic solvents in electrospun scaffolds. Gelatin (GE) outstanding biocompatibility and water solubility characteristics induced the fabrication of GE/HA nanofibrous membranes. The addition of HA improved the electrospinnability of GE solutions. Electrospun scaffolds showing aligned nanofibers were fabricated. The crosslinking of GE/HA electrospun scaffolds was carried out by immersion of electrospun scaffolds in EDC solution [25].

The same crosslinking methodology was employed by Kim *et al*. for the production of HA/collagen electrospun scaffolds for cartilage tissue engineering. In order to avoid collapse of HA/collagen electrospun scaffolds at the end of electrospinning and to create macropores facilitating cell infiltration NaCl salt particulates were deposited on electrospun scaffolds. After EDC crosslinking the scaffolds were exposed to a salt leaching process with deionized water. Collagen introduction triggered a slow degradation of scaffolds as demonstrated by *in vitro* studies. Furthermore, chondrocyte adhesion was greatly enhanced in presence of collagen showing 4.5-fold higher cell number. This work demonstrated that HA/collagen scaffolds after crosslinking process and salt leaching treatment gave rise to biomaterials with strong potentialities in tissue engineering [26].

3.2. Photo-Crosslinking of Electrospun HA-Based Scaffolds

Photo-crosslinking is largely employed as a crosslinking strategy both *in situ* and off-site as well. Below, some examples of off-site photo-crosslinking procedures are reported.

Maleilated hyaluronate (MHA) and methacrylated poly-vinylalcohol (MaPVA) were synthesized. Afterwards, MHA/MaPVA bicomponent nanofibrous scaffolds were prepared using water as solvent for electrospinning and subsequently photo-polymerized. The nanofibers were irradiated directly under the Hg lamp. The application proposed is a hydrogel useful in wound dressing [27]. Another example of off-site crosslinking is represented by the photo-patterning strategy to fabricate scaffolds with pore size useful to enhance cell infiltration. Patterns are obtained through the introduction of masks between the light source and the scaffold (Figure 7).

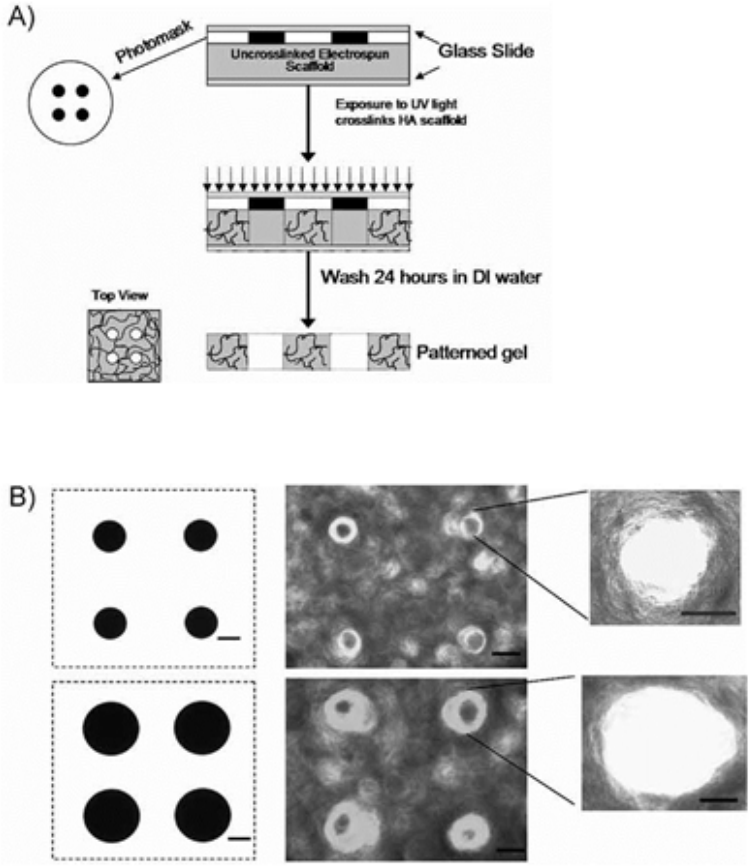

Figure 7. Schematic representation of photopatterned macro-channels into electrospun scaffolds using light transmittance through masks. (B) Light micrographs of photomasks and top-view of patterned HA scaffolds (scale bars = 100 μm) Adapted from [27], copyright 2010 with permission from Wiley.

Herein, methacrylated HA (MAHA), PEO, and the photoinitiator electrospun scaffolds were photo-crosslinked by 365 nm light in nitrogen chamber because the oxygen can inhibit crosslinking [28].
An additional example of off-site photo-crosslinking was carried out on PCL and methacrylated HA electrospun scaffolds proposed as scaffolds for patients suffering from traumatic brain injury. Crosslinking was accomplished after electrospinning by UV irradiation for 20 s time. The encapsulation of insulin-like growth factor IGF-1, essential for improving the survival and neurite outgrowth of neural cells after traumatic brain injury, ensured a controlled release and a higher survival of neurons [29]. Other reports describe off-site photo-crosslinking of methacrylated HA/PEO/Pluronic F127 blend as layer of a scaffold deposited on polycaprolactone-poly(glycerol sebacate) (PCL-PGS) layer. The produced bilayered scaffolds self-folds into tubular structures in aqueous solutions forming nerve guide conduit as artificial nerve grafts [30].

In the work of Gwon *et al*. hyaluronic acid was functionalized with methacrylic groups for UV photo-crosslinking and with N-diazeniumdiolate (NONOate)-NO donor groups as bioactive molecule developing NO-releasing HA-based nanofibers with the potential application in wound healing [31]. Multifunctional HA derivatives were also prepared by Miller *et al*. starting from methacrylated HA (HAMA) by conjugating separately adamantane (AD) and β-cyclodextrin (CD) for the development of a host-guest system. In electrospun scaffolds containing both AD-HAMA and CD-HAMA a strong association of hydrophobic AD (guest) groups with the hydrophobic core of CD (host) molecules is observed, resulting in a stable, yet reversible, supramolecular guest–host interaction that could mechanically stabilize the UV photo-crosslinked nanofibers [32].

3.3. Alternative Crosslinking Methodologies for HA-Based Electrospun Scaffolds

Electrospun membranes prepared using hyaluronic acid, a bioactive lactose-modified chitosan (CTL), and polyethylene oxide (HA/CTL/PEO) have been produced. The obtained scaffolds showed weak mechanical properties, thus they have been crosslinked following different protocols using glutaraldehyde (GTA), genipin, EDC/NHS or thermal treatments and the results have been discussed in terms of scaffold stability and fiber loss [33].

Chen *et al*. prepared a multi-functional nanofibrous membrane (NFM) for prevention of postoperative tendon adhesion by electrospinning hyaluronic acid (HA)/ibuprofen (IBU) (HAI), followed by dual ionic crosslinking with FeCl3 and covalent crosslinking with 1,4-butanediol diglycidyl ether (BDDE) to produce nanofibers endowed with abilities to prevent fibroblast attachment and penetration and contextually exert anti-inflammation effects. Results of the studies showed that the presence of HA in the multifunctional scaffold was able to prevent fibroblast penetration, while at appropriate concentration IBU imparted anti-inflammation response [34].

Other biopolymers were blended with HA and electrospun. For example, zein is the major corn protein and gained some interest in tissue engineering because it is electrospinnable from ethanol aqueous solutions. In this study, blended zein/HA solutions were electrospun after the introduction of polyvinylpyrrolidone (PVP) in aqueous ethanol solution and zein/HA/PVP scaffolds were fabricated. The scaffolds were crosslinked by methylene diphenyl diisocyanate (MDI) in THF solution. The crosslinked scaffold morphology was characterized by SEM and the mechanical properties were assessed by stress-strain measurements. The results have suggested that the combination of three different polymers such as zein, HA and PVP was successful for the fabrication of electrospun scaffolds with good mechanical properties with great potential in tissue engineering and wound healing [35].

4. Electrospun Scaffolds Based on Hyaluronic Acid Derivatives

In general terms, the modification of a polymer backbone to impart a variety of functional groups through chemical methodologies is referred to as decoration [36]. The final aim of polymer decoration is to improve physico-chemical properties such as conductivity, solubility, mechanical characteristics, as well as bioactivity [37]. HA decoration is widely carried out mainly to improve electrospinnability by changing HA viscosity. However, other reasons for grafting have to be also considered. In the following, some examples of electrospun grafted HA will be discussed (Table 3).

Table 3: Summary of main characteristics of grafted HA-based-electrospinning methodologies

Chemical modification	Grafted molecules	Polymer Blend[b]/ Drug	Methodology	Proposed Application	Ref.
Grafting	2-(methylthio)ethylamine	thioether grafted HA/	EDC/HOBT ionic crosslinking (Fe^{3+})	wound-dressing for chronic diabetic wounds	[37]
	benzyl bromide	HA-benzyl ester/Doxorubicin	Doxorubicin encapsulation	anti-melanoma drug delivery system	[38]
	$C_8/C_{12}/C_{18}$ Alkyl Amine+ EDA	alkylated-HA/PVA/HPβCD/dexa-methasone	EDC/NHS crosslinking	scaffold for periodontal regeneration	[39]
	Temporin Ra	HA/Chitosan/PVA	Peptide Loading	Antimicrobial wound healing dressing	[51]
	REDV peptide (P1)	PCL	Layer-by-layer deposition of PDDA[a], SePEI[b] and P1-HA	Small diameter vascular graft with catalytic NO generation and promoted EC adhesion	[60]
	G**C**GYGRGDSPG peptide (P2)	P2-HA/PEO Or HAMA/PEO	P2 conjugation by Thio-ene to methacrylated HA+ UV crosslinking	electrospun scaffolds with mechanical and adhesive gradients	[71]
	CAAAAAAAAAAKAAKYGAAAGL (P3)	PDLLA/P3-HA	P3 conjugation by Thio-ene to methacrylated HA	wound dressings	[75]
	RGD-TCO[c] (P4)	PCL-Tz[d]	LbL deposition of HA-TCO and HA-Tz+ final P4-TCO deposition	therapeutic implants for the treatment of vocal fold scarring	[79]
	Ac-KGGPQVTRGDVFTMP (P5)	PVA/HA	P5 conjugation with EDC/NHS on glutaraldehyde crosslinked nanofibers	Scaffold for iPSCs growth and proliferation	[80]

[a]PDDA: Polydiallyldimethylammonium chloride; [b]SePEI: organoselenium immobilized polyethyleneimine; [c]TCO : trans-cyclooctene; [d]Tz: *s*-tetrazine;.

4.1. Small Molecule Decorated HA Derivatives

With the aim to produce an absorbable bioactive wound dressing device, thioether grafted HA (HHA-S) was synthesized from high molecular weight HA (HHA) and 2-(methylthio)ethylamine using EDC and 1-hydroxybenzotriazole (HOBT) as condensation reagents. Afterwards, decorated HHA-S was electrospun into nanofibers and further crosslinked by ferric ions (Fe^{3+}). The thioether moiety was shown to scavenge the ROS quickly in the early inflammation phase, conferring to the matrix

significant antioxidant properties, while the Fe^{3+} showed broad-spectrum antibacterial action [38]. Moreover, high molecular weight HA (HHA) was able to promote the transformation of macrophages from a pro-inflammatory M1 to a reparative M2 phenotype, thus reducing inflammation and promoting proliferation by releasing anti-inflammatory cytokines and growth factors [3]. The electrospun thioether decorated HHA-S nanofibrous hydrogel was shown to accelerate the healing phase transition from inflammation to proliferation and remodeling and could be proposed as improved dressing for chronic diabetic wounds.

Nowadays, the employment of HA electrospun scaffolds in tissue regeneration and regenerative medicine is largely assessed. Additionally, they play an additional role as therapeutic agents acting as vehicles in drug delivery. Doxorubicin (DOX) is a widely employed anticancer drug also used in the treatment of melanoma. One of the main limits in its use is the rapid release affecting the efficacy of the treatment. Han *et al*. esterified HA with benzyl-bromide in presence of tetrabutylammonium (TBA) and electrospun the resulting product in order to obtain HA-benzyl ester (HA-Bn) nanofibers. The anticancer drug doxorubicin (DOX) was encapsulated into nanofibers via electrospinning. Taking advantage of the π–π* stacking interactions between the benzene ring of DOX and the benzyl group of HA-Bn, the scaffolds were designed in order to favor a sustained release of DOX resulting in an efficiency of about 90 %, achieved within 7 days. *In vitro* cell experiments demonstrated that HA-DOX nanofiber had a considerable inhibitory effect on murine melanoma cell lines [39].

The introduction of alkylamine pendant moieties at different lengths (C_x) to HA (HA-EDA-C_x) was carried out by Federico *et al*. and the osteoinductive potential of HA-based electrospun scaffolds was evaluated [40]. HA derivatives were blended with PVA and 2-hydroxypropylcyclodextrin to improve electrospinning process. The polymeric solutions were also loaded with dexamethasone (DEX) before electrospinning in order to stimulate an osteoinductive effect [41]. Finally, the electrospun scaffolds were crosslinked with EDC/NHS. The main purpose of this study was to assess if the increasing hydrophobicity of the growing alkyl chains provided superior resistance to enzymatic hydrolysis without affecting surface properties of the scaffolds, important for cell adhesion and proliferation. The results of cell cultures on DEX-loaded alkylated HA scaffolds showed high cytocompatibility and induced osteogenic response with improved mineralization, thus holding great potential for periodontal regeneration.

4.2. C_6-Decorated Hyaluronic Acid for Enhanced Resistance to Hyaluronidase-Mediated Digestion

The hyaluronidase enzyme (Hyal-2) and the CD44 (Cluster of Differentiation-44) cell surface receptors are involved in HA degradation [42]. Molecular modeling based on crystallographic studies

indicated that the recognition sites of the Hyal-2 enzymes and CD44 receptors are the carboxylate group of HA [43]. As a consequence, the functionalization of HA carboxylic groups into ester or amide, could affect enzymatic recognition and stability of HA towards hyaluronidase-mediated hydrolysis. Vandamme and co-workers evaluated the effect of conjugating alanine onto HA through the amidation of HA carboxyl group [44]. They demonstrated that for higher degree of modification slower HA enzymatic degradation was observed. One of the most popular methods to link amines to HA carboxylic acid is the activation with EDC, because it can be carried out in aqueous solution, which is the native solvent for HA, and at slightly acidic pH [45]. EDC first reacts with the carboxylic acid to form a highly reactive O-acyl isourea intermediate (Figure 8a) which can react with the N-terminal amino group of an aminoacid residue or of a peptide. However, the stable *N*-acyl urea product could be formed by reaction of O-acyl isourea intermediate with competitive water nucleophile thus precluding the amide formation (Figure 8) [17, 46]. One of the strategies to avoid this collateral reaction, is the use of *N*-hydroxysuccinimide (NHS) at pH = 7.5. Also in that case, as reported by Vandamme and co-workers, the degree of substitution (DS), defined as a percentage value expressing the number of HA molecules esterified at carboxyl groups, was relatively low being in the range of 10 to 13 %, according to literature data [47]. An alternative strategy which avoided the use of NHS and pH monitoring was performed in water/acetonitrile mixture using 2-chlorodimethoxy-1,3,5-triazine (CDMT) with a final increased DS value of 50 % (Figure 8b) [47d, 48]. To obtain a complete substitution at the HA carboxylic acid, the reaction was carried out in anhydrous conditions using 2-chloro-1-methylpyridinium iodide (CMPI) in *N*,*N*-dimethylformamide (DMF) after conversion of HA into a tetrabutylammonium (TBA) salt (Figure 8c) [49]. The results indicated that amidation of hyaluronic acid in an anhydrous solvent was carried out with a degree of substitution of the carboxylic groups up to 100 %. They also demonstrated the hyaluronamides obtained through amino acid conjugation to HA enhanced resistance towards enzymatic digestion while forming solutions with viscosities similar to the solutions of hyaluronic acids of similar lengths [47d]. However, to the best of our knowledge amino acid-decorated hyaluronamides were not electrospun.

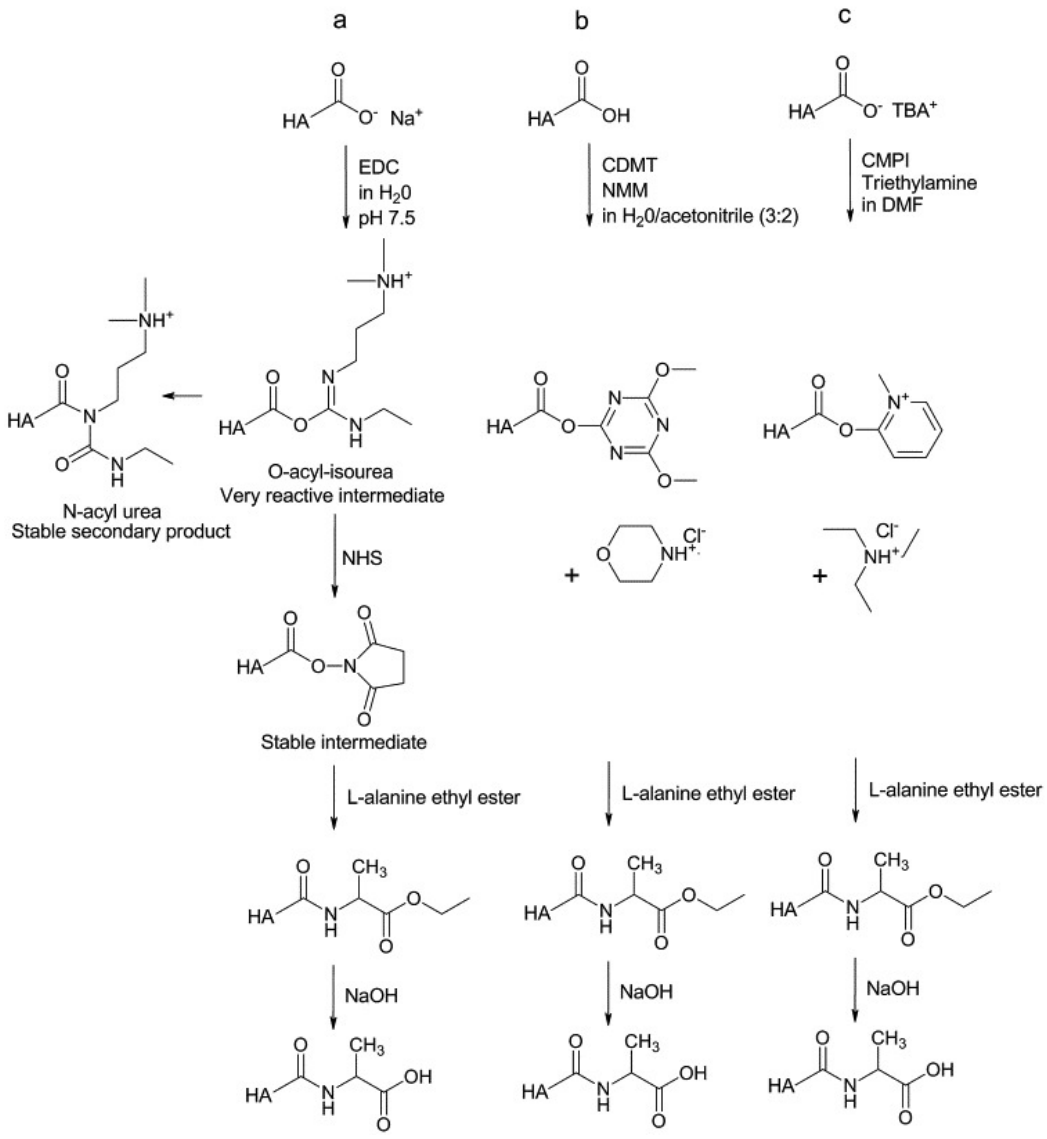

Figure 8. Synthetic routes to N-alanyl hyaluronamide. Reprinted from [43], Copyright (2011), with permission from Elsevier.

4.3. Peptide-Decorated HA Electrospun Scaffolds

Peptides were widely employed as bioactive components in tissue engineering and regenerative medicine. Indeed, peptides able to self-assemble into nanofibers are generally used as biomaterials with a wide range of applications from tissue engineering, biosensors to drug delivery systems [50]. Peptides are produced on medium scale by Solid Phase Peptide Synthesis (SPPS) with affordable costs and the possibility to introduce bioactive sequences and non-proteinogenic or modified amino acid residues such as L–DOPA, ornithine, hydroxyproline, and methoxyproline inside the primary structure improved their versatility [51]. On the other hand, synthetic polymers are easily available at low cost while natural polymers like gelatin promise better biocompatibility. A successful strategy

representing a good compromise is the electrospinning of peptides in combination with polymers. Some examples are described in literature where the polymeric solutions were loaded with bioactive peptides. Koohzad and Asoodeh produced by electrospinning a nanofibrous scaffold composed of HA/Chitosan/PVA adding temporin-Ra peptide as antimicrobial agent for improved wound healing dressing [52]. The main drawback of blended mixtures consisting of peptides and polymers is represented by the fast release of the peptides when the scaffolds are implanted *in vivo.* To avoid this problem, the covalent link between the peptide and the polymers represents a valid alternative. A general overview of peptide conjugation strategies to diverse polymers before and after electrospinning was reviewed by Bucci *et al* [53]. A less explored, however full potential route, is peptide conjugation to HA through its functional groups for endowing novel biological/pharmacological properties to HA electrospun scaffolds. Generally, the main strategy currently used to covalently bind peptides, consists of the modification of the polymer prior to electrospinning [54]. Different methodologies were used to link peptides. In the following we summarize the main synthetic strategies aimed to peptide conjugation on chemically modified HA.

As previously shown for the conjugation of amino acids to HA, a high number of reports described peptide grafting to the C_6 carboxylic group of glucuronic acid of HA by amidation. The most explored route envisaged the activation of the COOH with water-soluble carbodiimide (EDC) in presence of NHS or HOBT for the synthesis of the intermediate activated esters. The following reaction with the *N*-terminal amino group, or eventual ε-amino group of lysine residues caused the formation of the amide linkage. In this way antimicrobial peptides (AMPs) like nisin, [55] or colistin, [56] cell penetrating peptides G_4R_8, [57] fibronectin-derived cell adhesive peptides, like $G_{1/4}$RGDS peptides, [58] BMP-2 peptide, [59] acne alleviating peptide, [60] as well as endothelial cell specific peptide REDV [61] were successfully conjugated to HA. In some cases EDC alone was employed as activating agent for conjugating peptides like the cell penetrating peptide SS-31 the cell binding peptide, [62] GRGDSY, [63] or the collagen binding peptide LSELRLHNN [64]. In these conditions the degree of substitution (DS) was very low, due to the competitive side reaction that took to the stable *N*-acyl urea by-product.

With the aim to avoid reaction of amino acid side chain functional groups with the activated COOH, alternative chemo-selective methodologies were developed. Some of these reactions are based on the coupling of aldehyde moieties with amine- or aminoxy- groups forming Schiff's base or oxime, respectively. Usually, aldehydes were introduced on the HA by coupling of small molecule containing masked-aldehyde moieties using carbodiimide-mediated coupling. For example, aminoacetaldehyde dimethyl acetal was easily conjugated to HA and then converted to aldehyde by mild acidic treatment [45a]. Alternatively, periodate oxidation of the C_2, C_3 diols function of the glucuronic acid was

performed. The oxidation of HA by periodate treatment on the proximal hydroxyl groups at C_2 and C_3 carbons of glucuronic acid moiety generates two aldehyde groups, thereby opening the sugar ring to form a linear chain. An antimicrobial peptide (KR12) was successfully conjugated onto periodate oxidized HA by reductive amination, [65] while Insulin growth factor-1 derived peptide (IGF-1C) with potential effect on neovascularization was conjugated by Schiff's base linkage [66]. While periodate oxidation allows for the formation of a large number of functional groups, the disadvantage is the loss of the native backbone structure that could be responsible for limited biological activity of HA. Consequently, the generated derivative presumably could not be recognized as HA by cells [45a].

4.4. Peptide Bioconjugation by Bioorthogonal Chemistry

Biologists were historically involved in the study of biomolecules in their native state. Nowadays, the interest to study biological processes is growing also among chemists and it is finalized to the chemical modification of proteins, carbohydrates, nucleic acids. The reaction of compounds with bioorthogonal functional groups is required to proceed in the presence of all functional groups present in living systems such as carboxylic, thiol, aldehyde, hydroxyl groups. In other terms,"bioorthogonal reactions should be mutually and selectively reactive, and neither interact nor interfere with the biological system" [54]. Such reactions must be inert toward the multitude of functional groups of biomolecules. Bioorthogonal chemistry well fits peptide conjugation to HA because the two components to be linked-peptide and carbohydrate- share most of the functional groups that could interfere in common reactions. Accordingly, to promote bioorthogonal chemistry, specific functional groups have to be introduced on both molecules. Commonly, HA was decorated with electron-poor activated unsaturated groups by adding (meth)acrylate or maleimide moieties in order to exploit the thiol-ene reaction, in both its radical and base/nucleophilic forms. The thiol-ene click reaction has already been demonstrated to be a powerful and versatile method for site specific functionalization also for biopolymers, and as a convenient conjugation tool [67].Methacrylic anhydride was preferentially reacted with C_6 primary hydroxyl group of *N*-acetyl glucosamine sugar ring of HA to obtain methacrylated HA (HAMA). Peptides, containing a cysteine residue in the sequence, preferentially at the *N*- or C- terminus, were then grafted by thiol-ene click reaction, through a Michael-type addition. The insertion of cysteine in the peptide sequence by SPPS is straightforward, rendering this chemical strategy widely explored. He and Li conjugated a tumor recurrence inhibiting peptide, juxtamembrane 2 peptide (JM2), to HAMA by triethanolamine nucleophile catalyzed thiol-ene reaction [68] while Teng *et al*. conjugated a RGD peptide in a similar manner [69]. *N*-cadherin mimetic peptides were also grafted to HAMA to promote the osteogenesis of human mesenchymal stem cells [70]. In another report, Deng *et al*. employed tris(2-carboxyethyl) phosphine (TCEP) as

nucleophilic catalyst to bioconjugate cysteine-containing Wnt5a mimetic ligand (Foxy5 hexapeptide) to HAMA with the aim to promote the chondrogenesis of hMSCs [71]. Furthermore, HAMA was decorated by thiol-ene Michael addition with an adhesive peptide showing G**C**GYG**RGD**SPG sequence and subsequently co- electrospun with PEO to fabricate HA scaffolds with adhesive gradient. Adhesive gradients in the HA-based electrospun scaffold were created by programming the flow rate of two solutions where one with high concentration of Peptide conjugated HAMA/PEO increases in concentration, whereas the other solution composed by HAMA /PEO decreases in concentration over the scaffold collection period. In this way the incorporation of an adhesive peptide was modulated [72]. In all these reports the methacrylic group was exploited for peptide grafting as well as for hydrogel production by UV photo- crosslinking. Accordingly, the reagents ratios (HAMA/peptide) were carefully determined to have a DS of peptide conjugation in the order of 20% with respect to methacrylic groups. To improve enzymatic degradation resistance the functionalization of HA with activated ene groups was also performed at the glucuronic C_6 COOH site using two-step synthetic methods.

In the first step a molecule containing the activated -ene group was anchored to HA usually by amidation. As an example, 2-aminoethyl maleimide was conjugated with carboxylic function of HA by EDC/NHS activation. The subsequent Michael addition by thiol containing peptides determined peptide anchoring. In this way a collagen mimetic peptide [73], and GRGDSPC cell adhesive peptide [74] were added. In a recent report, an elastin-derived peptide was grafted to glucuronic C_6 methacrylated HA by thiol-ene chemistry.

The peptide sequence -(C)AAAAAAAAAAKAAKYGAAAGL- was modified by the insertion of a cysteine at C-terminal end (EL) and corresponds to the region 302–322 of human tropoelastin (HTE) promoting cell attachment and spreading [75]. In the first step, the carboxyl groups of HA activated by EDC/NHS reacted in water with 2- aminoethyl methacrylate hydrochloride (2-AEMA · HCl), affording the C_6-methacrylated hyaluronic acid (MAHA). In the second step, the electron-poor double bond of MAHA was linked to the thiolated elastin-peptide via Michael-type addition (Scheme 1b) to produce an elastin-hyaluronan bioconjugate (ELHA) as a bioactive component of electrospun scaffolds [76]. The authors demonstrated by circular dichroism conformational studies that the linkage to HA preserved the native α-helix conformation of the peptide, considered important for bioactivity. The ELHA bioconjugate was successfully electrospun with poly-D,L-lactide (PDLLA) giving rise to a nanofibrous structure. Interestingly, SEM micrographs of ELHA/PDLLA electrospun scaffolds notably showed improved morphology with absence of defects in comparison to electrospun scaffolds composed of HA/PDLLA. In summary, the bioconjugation facilitated the electrospinning process of HA in aqueous solution thus rendering more appealing the obtained scaffolds in terms of

biocompatibility through the elimination of organic solvents. Other examples of bioorthogonal click chemistry used for peptide conjugation to HA are presented below. HA polymers were first modified at glucuronic C_6 carboxyl groups with masked aldehyde groups and then with methylfuran moieties. HA-methylfuran groups were conjugated with maleimide-functionalized bioactive peptides via Diels–Alder reaction to introduce biochemical properties, whereas the HA-aldehyde groups were crosslinked with bis(oxyamine)-poly(ethylene glycol) (PEG) via oxime ligation to control hydrogel mechanical properties [77]. Maleimide-functionalized peptides were also conjugated by Fowler *et al*. to thiol- functionalized HA derivatives by thiol-ene chemistry [78]. By this route, biomimetic, hyaluronic acid (HA)-based hydrogel platform containing covalently immobilized bioactive peptides derived from perlecan domain IV (TWSKV), laminin-111 (YIGSR, IKVAV), and fibronectin (RGDSP) were produced.

Recently, peptide decoration to HA was at the basis of the fabrication of a tunable hydrogel platform having protease susceptibility and cell adhesive properties employing bioorthogonal inverse electron tetrazine ligation with strained alkenes like *trans*-cyclooctene (TCO) [79]. In this study, tetrazine-functionalized HA (HA-Tz) was first crosslinked by a bis- norbornene-functionalized protease susceptible peptide used as crosslinker to obtain the hydrogel. Then the hydrogel was modified via a diffusion-controlled method using a *trans*- cyclooctene-functionalized cell adhesive peptide reacting to HA-Tz by cycloaddition (Figure 9). The reaction was extremely fast and highly selective, and succeeded in producing an innovative hydrogel platform that supports the growth, assembly, and migration of cancer cells in 3D.

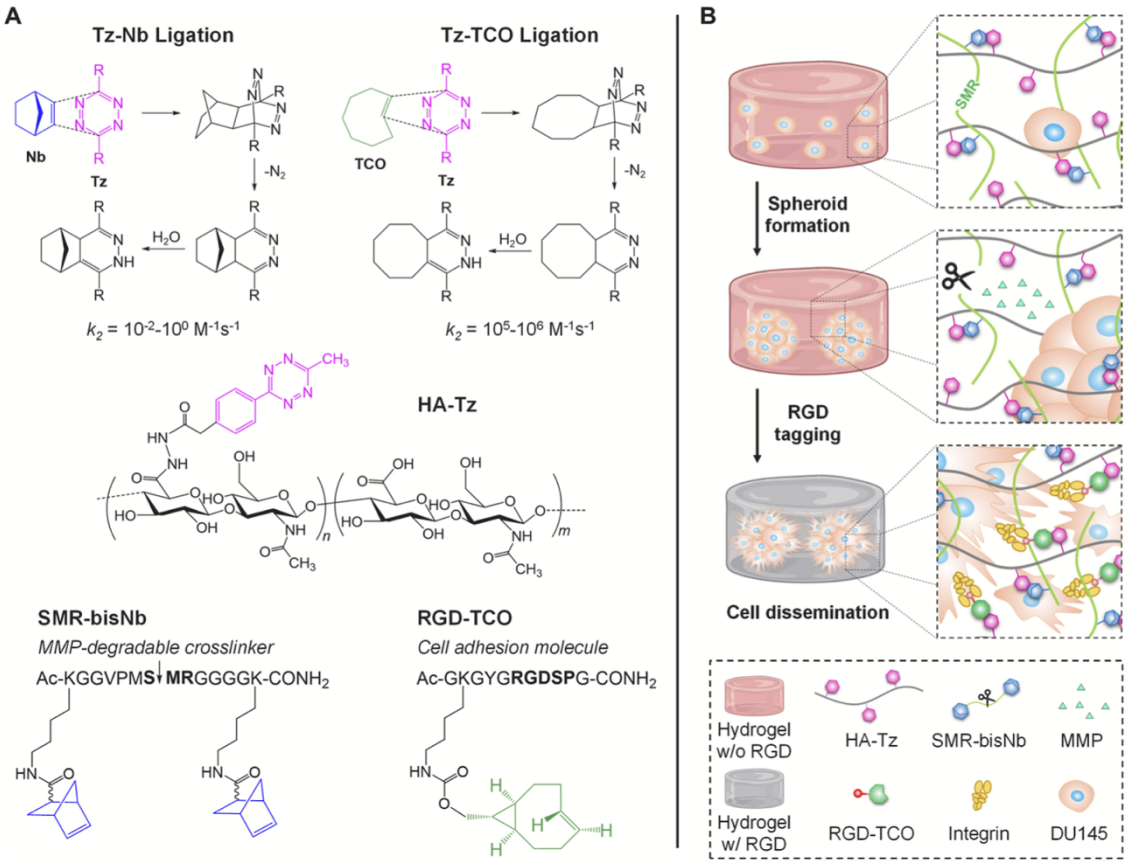

Figure 9. Bioorthogonal tuning of hydrogel properties to induce EMT. (A) Hydrogels were fabricated via slow Tz-Nb cycloaddition reaction using tetrazine modified HA (HA-Tz) and an MMP-degradable crosslinker (SMR-bisNb) at a Tz/Nb molar ratio of 2/1. RGD ligand was covalently conjugated to the synthetic ECM via fast Tz-TCO ligation through a diffusion-controlled mechanism. RGD density was tuned by varying the molar ratio of RGD-TCO and RGE-TCO. (B) DU145 cells in MMP-degradable HA gels spontaneously assembled into multicellular spheroids in 3D. Seven days post encapsulation, the RGD signal was introduced. RGD tagging promoted decompaction of spheroids and invasive processes were developed around the spheroids. Reprinted from [78], copyright (2023) with permission from Elsevier.

The bioorthogonal inverse electron tetrazine ligation with strained alkenes was also employed to form core-shell microfibers by layer-by-layer assembly of decorated HA-Tz and HA- TCO as outer shells of electrospun PCL microfibers. The outermost layer constituted of HA-Tz was reacted with TCO-conjugated RGD peptide, to promote cell adhesion. The scaffolds fostered the attachment and growth of primary porcine vocal fold fibroblasts limiting the induction of the myofibroblast phenotype. The electrospun microfibers, consisting of a stiff PCL core and a soft HA based shell, were considered promising as therapeutic implants for the treatment of vocal fold scarring [80].

Finally, peptide conjugation performed on scaffolds after electrospinning was reported by Deng *et al* [81]. PVA/HA electrospun nanofibers were crosslinked by glutaraldehyde vapors and thereafter Vitronectin peptide (VP) was immobilized onto the electrospun mats through EDC/NHS chemistry.

Decoration of scaffolds with VP peptide was able to promote proliferation of human induced pluripotent stem cells (hiPSCs).

5. Summary

This review focuses on electrospun hyaluronic acid-based materials commonly used in various applications, from cosmetics to tissue engineering. Nowadays, electrospinning techniques have raised great interest in the field of biomedical devices. On that basis, hyaluronic acid has been generally electrospun in blends with other polymers for optimizing the performance of the final scaffold, sharing complementary properties such as the biocompatibility deriving from the use of polysaccharide and the mechanical strength of nanofibers. Electrospun polymers are characterized by porous structures that facilitate the exchange of nutrients and the elimination of waste products by cells populating the scaffolds.

Hyaluronic acid is highly versatile thanks to the presence of different functional groups, which give rise to the possibility of achieving chemical modifications on the glycosaminoglycan backbone to anchor bioactive molecules and functionalized polymers as well. Furthermore, the glycosaminoglycan structure is also functional for the crosslinking of hyaluronic acid-inspired scaffolds, which is mandatory to prolong the half-life when implanted *in vivo*.

Analogously, decorated HA biomolecules such as peptides are also worthy of note because the covalent bond slows HA's degradation rate, as the crosslinking does. Recent advances in the field have been herein reviewed and discussed.

6. Outlook

Over the last years, great interest has been devoted to the production of hyaluronic acid derived products because they are appealing as biomedical devices and cosmetics as well. Besides, the electrospinning technique has attracted a great attention to produce nonwoven scaffolds made of nanofibers. However, electrospinning of hyaluronan-based biomaterials is still a challenging process that requires from the research community peculiar attention and further efforts forwarded in the direction of implementing sustainable and eco-friendly processes especially in the perspective of extending electrospinning adoption to large-scale production. Therefore, the material and production cost, and societal and environmental concerns need to be considered too. Bioorganic chemistry could be the answer to this difficult task because it enables the tuning of the properties of hyaluronan through the creation of covalent bonds with proper bioactive molecules using mild conditions. This review is an anthology of the recent findings in the field and opens new perspectives in terms of innovative and smart chemical strategies on hyaluronan.

With the outlook of smart biomaterials production, the future perspective is represented by the set-up of crosslinking methodologies to be carried out during electrospinning both on plain HA and HA-based scaffolds. While several literature data exist, in fact, on HA fibers crosslinked after electrospinning, few data are present on crosslinking carried out simultaneously with electrospinning.

Acknowledgements

F. A. acknowledges support from INPS within PhD Programme Industry 4.0.

Conflict of Interests

The authors declare no conflict of interest.

Keywords: Hyaluronic acid; electrospinning; cross-linking; bioconjugation; peptide

References

[1] a) K. T. Dicker, L. A. Gurski, S. Pradhan-Bhatt, R. L. Witt, M. C. Farach-Carson, X. Jia, *Acta Biomater.* **2014**, *10*, 1558–1570; b) J. R. Fraser, T. C. Laurent, U. B. Laurent, *J. Intern. Med.* **1997**, *242*, 27–33.

[2] F. Della Sala, A. Fabozzi, M. di Gennaro, S. Nuzzo, P. Makvandi, N. Solimando, M. Pagliuca, A. Borzacchiello, *Macromol. Biosci.* **2022**, *22*, 2100304.

[3] J. E. Rayahin, J. S. Buhrman, Y. Zhang, T. J. Koh, R. A. Gemeinhart, *ACS Biomater. Sci. Eng.* **2015**, *1*, 481–493.

[4] a) M. C. Catoira, L. Fusaro, D. Di Francesco, M. Ramella, F. Boccafoschi, *J. Mater. Sci. Mater. Med.* **2019**, *30*, 115; b) M. Gomez-Florit, A. Pardo, R. M. A. Domingues, A. L. Graça, P. S. Babo,R. L.Reis, M. E. Gomes, *Molecules* **2020**, *25*, 5858.

[5] a) T. Segura, B. C. Anderson, P. H. Chung, R. E. Webber, K. R. Shull, L. D. Shea, *Biomaterials* **2005**, *26*, 359–371; b) G. Pitarresi, P. Pierro, F. S. Palumbo, G. Tripodo, G. Giammona, *Biomacromolecules* **2006**, *7*, 1302– 1310.

[6] a) C. E. Schante, G. Zuber, C. Herlin, T. F. Vandamme, *Carbohydr. Polym.* **2011**, *85*, 469–489; b) H. Samadian, H. Maleki, Z. Allahyari, M. Jaymand, *Coord. Chem. Rev.* **2020**, *420*, 213432.

[7] S. Khunmanee, Y. Jeong, H. Park, *J. Tissue Eng.* **2017**, *8*, 2041731417726464.

[8] L. A. Pérez, R. Hernández, J. M. Alonso, R. Pérez-González, V. Sáez-Martínez, *Biomedicine* **2021**, *9*, 1113.

[9] E. Bedini, E. Cassese, A. D'Agostino, M. Cammarota, M. A. Frezza, M. Lepore, M. Portaccio, C. Schiraldi, A. La Gatta, *Int. J. Biol. Macromol.* **2023**, *236*, 123873.

[10] I. C. Um, D. Fang, B. S. Hsiao, A. Okamoto, B. Chu, *Biomacromolecules* **2004**, *5*, 1428–1436.

[11] a) K. C. Castro, M. G. N. Campos, L. H. I. Mei, *Int. J. Biol. Macromol.* **2021**, *173*, 251–266; b) M. F. P. Graça, S. P. Miguel, C. S. D. Cabral, I. J. Correia, *Carbohydr. Polym.* **2020**, *241*, 116364; c) P. Snetkov, S. Morozkina, M. Uspenskaya, R. Olekhnovich, *Polymer* **2019**, *11*, 2036; d) Humaira, S. A. Raza Bukhari, H. A. Shakir, M. Khan, S. Saeed, I. Ahmad, K. Muzammil, M. Franco, M. Irfan, K. Li, *Front. Chem.* **2022**, *10*.

[12] M. Arnal-Pastor, C. Martínez Ramos, M. Pérez Garnés, M. Monleón Pradas, A. Vallés Lluch, *Mater. Sci. Eng. C* **2013**, *33*, 4086–4093.

[13] S. H. Kim, S.-H. Kim, S. Nair, E. Moore, *Macromolecules* **2005**, *38*, 3719– 3723.

[14] Y. Ji, K. Ghosh, B. Li, J. C. Sokolov, R. A. F. Clark, M. H. Rafailovich, *Macromol. Biosci.* **2006**, *6*, 811–817.

[15] Y. Hussein, E. M. El-Fakharany, E. A. Kamoun, S. A. Loutfy, R. Amin, T. H. Taha, S. A. Salim, M. Amer, *Int. J. Biol. Macromol.* **2020**, *164*, 667–676.

[16] a) Z. Ahmad, J. H. Shepherd, D. V. Shepherd, S. Ghose, S. J. Kew, R. E. Cameron, S. M. Best, R. A. Brooks, J. Wardale, N. Rushton, *Regener. Biomater.* **2015**, *2*, 77–85; b) K. G. Cornwell, P. Lei, S. T. Andreadis, G. D. Pins, *J. Biomed. Mater. Res. Part A* **2007**, *80 A*, 362–371.

[17] K. Tomihata, Y. Ikada, *J. Biomed. Mater. Res.* **1997**, *37*, 243–251.

[18] M. Séon-Lutz, A.-C. Couffin, S. Vignoud, G. Schlatter, A. Hébraud, *Carbohydr. Polym.* **2019**, *207*, 276–287.

[19] K. C. d. Castro, J. Burga-Sánchez, M. G. Nogueira Campos, L. H. I. Mei, *RSC Adv.* **2020**, *10*, 31271–31279.

[20] E. Yang, X. Qin, S. Wang, *Mater. Lett.* **2008**, *62*, 3555–3557.

[21] a) Y. Ji, K. Ghosh, X. Z. Shu, B. Li, J. C. Sokolov, G. D. Prestwich, R. A. F. Clark, M. H. Rafailovich, *Biomaterials* **2006**, *27*, 3782–3792; b) J. A. Burdick, C. Chung, X. Jia, M. A. Randolph, R. Langer, *Biomacromolecules* **2005**, *6*, 386–391.

[22] G. Piccirillo, N. Feuerer, D. A. Carvajal Berrio, S. L. Layland, S. Reimer Hinderer, B. Bochicchio, K. Schenke-Layland, *Tissue Eng.* **2021**, *27*, 589–604.

[23] W. Chen, S. Chen, Y. Morsi, H. El-Hamshary, M. El-Newhy, C. Fan, X. Mo, *ACS Appl. Mater. Interfaces* **2016**, *8*, 24415–24425.

[24] W. Cho, Y. Park, Y. M. Jung, J. H. Park, J. Park, H. S. Yoo, *ACS Omega* **2022**, *7*, 40355–40363.

[25] J. Li, A. He, J. Zheng, C. C. Han, *Biomacromolecules* **2006**, *7*, 2243–2247.

[26] T. G. Kim, H. J. Chung, T. G. Park, *Acta Biomater.* **2008**, *4*, 1611–1619.

[27] X. Chen, B. Lu, D. Zhou, M. Shao, W. Xu, Y. Zhou, *Int. J. Biol. Macromol.* **2020**, *155*, 903–910.

[28] H. G. Sundararaghavan, R. B. Metter, J. A. Burdick, *Macromol. Biosci.* **2010**, *10*, 265–270.

[29] Y. Wang, Q. Guo, W. Wang, Y. Wang, K. Fang, Q. Wan, H. Li, T. Wu, *Nanoscale* **2022**, *14*, 18217–18230.

[30] I. Apsite, G. Constante, M. Dulle, L. Vogt, A. Caspari, A. R. Boccaccini, A. Synytska, S. Salehi, L. Ionov, *Biofabrication* **2020**, *12*, 035027.

[31] K. Gwon, W. I. Choi, S. Lee, J. S. Lee, J. H. Shin, *Biomater. Sci.* **2021**, *9*, 8160–8170.

[32] B. Miller, A. Hansrisuk, C. B. Highley, S. R. Caliari, *ACS Biomater. Sci. Eng.* **2021**, *7*, 4164–4174.

[33] M. Gruppuso, F. Iorio, G. Turco, E. Marsich, D. Porrelli, *Carbohydr. Polym.* **2022**, *288*, 119375.

[34] C.-T. Chen, C.-H. Chen, C. Sheu, J.-P. Chen, *Int. J. Mol. Sci.* **2019**, *20*, 5038.

[35] C. Yao, X. Li, T. Song, *J. Biomater. Sci. Polym. Ed.* **2007**, *18*, 731–742.

[36] A. Bhattacharya, B. N. Misra, *Prog. Polym. Sci.* **2004**, *29*, 767–814.

[37] P. Purohit, A. Bhatt, R. K. Mittal, M. H. Abdellattif, T. A. Farghaly, *Front. Bioeng. Biotechnol.* **2023**, *10*, 1-22.

[38] S. Liu, Q. Zhang, J. Yu, N. Shao, H. Lu, J. Guo, X. Qiu, D. Zhou, Y. Huang, *Adv. Healthcare Mater.* **2020**, *9*, 2000198.

[39] X. Han, M. Zhao, R. Xu, Y. Zou, Y. Wang, J. Liang, Q. Jiang, Y. Sun, Y. Fan, X. Zhang, *Int. J. Mol. Sci.* **2023**, 24, 7023.

[40] S. Federico, G. Pitarresi, F. S. Palumbo, C. Fiorica, F. Yang, G. Giammona, *Colloids Surf. B* **2021**, *197*, 111438.

[41] S.-M. Kim, Y.-G. Kim, J.-W. Park, J.-M. Lee, J.-Y. Suh, *J. Periodontal Implant Sci.* **2013**, *43*, 168–176.

[42] A. Aruffo, I. Stamenkovic, M. Melnick, C. B. Underhill, B. Seed, *Cell* **1990**, *61*, 1303–1313.

[43] S. Banerji, A. J. Wright, M. Noble, D. J. Mahoney, I. D. Campbell, A. J. Day, D. G. Jackson, *Nat. Struct. Mol. Biol.* **2007**, *14*, 234–239.

[44] C. Schanté, G. Zuber, C. Herlin, T. F. Vandamme, *Carbohydr. Polym.* **2011**, *86*, 747–752.

[45] a) P. Bulpitt, D. Aeschlimann, *J. Biomed. Mater. Res.* **1999**, *47*, 152–169; b) I. Danishefsky, E. Siskovic, *Carbohydr. Res.* **1971**, *16*, 199–205.

[46] N. Nakajima, Y. Ikada, *Bioconjugate Chem.* **1995**, *6*, 123–130.

[47] a) V. Crescenzi, A. Francescangeli, A. Taglienti, D. Capitani, L. Mannina, *Biomacromolecules* **2003**, *4*, 1045–1054; b) M. Kurisawa, J. E. Chung, Y. Y. Yang, S. J. Gao, H. Uyama, *Chem. Commun.* **2005**, 4312–4314; c) J.-J. Young, K.-M. Cheng, T.-L. Tsou, H.-W. Liu, H.-J. Wang, *J. Biomater. Sci. Polym. Ed.* **2004**, *15*, 767–780; d) C. E. Schanté, G. Zuber, C. Herlin, T. F. Vandamme, *Carbohydr. Polym.* **2012**, *87*, 2211–2216.

[48] K. Bergman, C. Elvingson, J. Hilborn, G. Svensk, T. Bowden, *Biomacromolecules* **2007**, *8*, 2190–2195.

[49] A. Magnani, R. Rappuoli, S. Lamponi, R. Barbucci, *Polym. Adv. Technol.* **2000**, *11*, 488–495.

[50] a) C. Ligorio, J. A. Hoyland, A. Saiani, *Gels* **2022**, *8*, 211; b) Y. Huo, J. Hu, Y. Yin, P. Liu, K. Cai, W. Ji, *ChemBioChem* **2023**, *24*, e202200582; c) A. Levin, T. A. Hakala, L. Schnaider, G. J. L. Bernardes, E. Gazit, T. P. J. Knowles, *Nat. Chem. Rev.* **2020**, *4*, 615–634; d) C. Sinthuvanich, L. A. Haines-Butterick, K. J. Nagy, J. P. Schneider, *Biomaterials* **2012**, *33*, 7478– 7488.

[51] a) M. J. O'Donnell, C. Zhou, W. L. Scott, *J. Am. Chem. Soc.* **1996**, *118*, 6070–6071; b) A. Pepe, M. A. Crudele, B. Bochicchio, *New J. Chem.* **2013**, *37*, 1326–1335; c) B. Bochicchio, A. Laurita, A. Heinz, C. E. H. Schmelzer, A. Pepe, *Biomacromolecules* **2013**, *14*, 4278–4288.

[52] F. Koohzad, A. Asoodeh, *ACS Appl. Mater. Interfaces* **2023**, *15*, 15172– 15184.

[53] R. Bucci, F. Vaghi, E. Erba, A. Romanelli, M. L. Gelmi, F. Clerici, *Acta Biomater.* **2021**, *122*, 82–100.

[54] J. Zheng, G. Hua, J. Yu, F. Lin, M. B. Wade, D. H. Reneker, M. L. Becker, *ACS Macro Lett.* **2015**, *4*, 207–213.

[55] a) J.-B. Paris, D. Seyer, T. Jouenne, P. Thébault, *Colloids Surf. B* **2017**, *156*, 186–193; b) I. Lequeux, E. Ducasse, T. Jouenne, P. Thebault, *Eur. Polym. J.* **2014**, *51*, 182–190.

[56] N. V. Dubashynskaya, A. N. Bokatyi, E. R. Gasilova, A. V. Dobrodumov, Y. A. Dubrovskii, E. S. Knyazeva, Y. A. Nashchekina, E. V. Demyanova, Y. A. Skorik, in *Int. J. Biol. Macromol., Vol. 215*, **2022**, pp. 243–252.

[57] H. Yagi, T. Tomono, Y. Handa, N. Saito, M. Ukawa, K. Miyata, K. Shigeno, S. Sakuma, *Mol. Pharmaceutics* **2023**, *20*, 303–313.

[58] a) O. Bernstein-Levi, G. Ochbaum, R. Bitton, *Colloids Surf. B* **2016**, *137*, 214–220; b) I. P. Monteiro, D. Gabriel, B. P. Timko, M. Hashimoto, S.
Karajanagi, R. Tong, A. P. Marques, R. L. Reis, D. S. Kohane, *Acta Biomater.* **2014**, *10*, 4928–4938.

[59] S. Magdziarz, M. Boguń, J. Frączyk, *Polymer* **2023**, *15*, 1551.

[60] Z. Su, Y. Zhang, J. Cao, Y. Sun, Y. Cai, B. Zhang, L. He, Z. Zhang, J. Xie, Q. Meng, L. Luo, F. Li, J. Li, J. Zhang, X. Chen, A. Hong, *J. Nanobiotechnol.* **2023**, *21*, 55.

[61] Y. Wang, S. Chen, Y. Pan, J. Gao, D. Tang, D. Kong, S. Wang, *J. Mater. Chem. B* **2015**, *3*, 9212–9222.

[62] H. Zhao, M. Wu, L. Zhu, Y. Tian, M. Wu, Y. Li, L. Deng, W. Jiang, W. Shen, Z. Wang, Z. Mei, P. Li, H. Ran, Z. Zhou, J. Ren, *Theranostics* **2018**, *8*, 1892–1910.

[63] H. Tian, L. Lin, J. Chen, X. Chen, T. G. Park, A. Maruyama, *J. Controlled Release* **2011**, *155*, 47–53.

[64] S. Federico, U. Nöchel, C. Löwenberg, A. Lendlein, A. T. Neffe, *Acta Biomater.* **2016**, *38*, 1–10.

[65] S. H. Jeong, S. Cheong, T. Y. Kim, H. Choi, S. K. Hahn, *ACS Appl. Mater. Interfaces* **2023**, *15*, 16471–16481.

[66] X. Wang, J. Zhang, W. Cui, Y. Fang, L. Li, S. Ji, D. Mao, T. Ke, X. Yao, D. Ding, G. Feng, D. Kong, *ACS Appl. Mater. Interfaces* **2018**, *10*, 4481–4493.

[67] A. B. Lowe, *Polym. Chem.* **2010**, *1*, 17–36.

[68] D. He, H. Li, *Adv. Funct. Mater.* **2020**, *30*, 2004709.

[69] B. Teng, S. Zhang, J. Pan, Z. Zeng, Y. Chen, Y. Hei, X. Fu, Q. Li, M. Ma, Y. Sui, S. Wei, *Acta Biomater.* **2021**, *122*, 145–159.

[70] a) M. Zhu, S. Lin, Y. Sun, Q. Feng, G. Li, L. Bian, *Biomaterials* **2016**, *77*, 44–52; b) M. Y. Kwon, S. L. Vega, W. M. Gramlich, M. Kim, R. L. Mauck, J. A. Burdick, *Adv. Healthcare Mater.* **2018**, *7*, 1701199.

[71] Y. Deng, X. Zhang, R. Li, Z. Li, B. Yang, P. Shi, H. Zhang, C. Wang, C. Wen, G. Li, L. Bian, *Biomaterials* **2022**, *281*, 121316.

[72] H. G. Sundararaghavan, J. A. Burdick, *Biomacromolecules* **2011**, *12*, 2344–2350.

[73] Y. Ren, H. Zhang, W. Qin, B. Du, L. Liu, J. Yang, *Mater. Sci. Eng. C* **2020**, *108*, 110276.

[74] A. Mazzocchi, K. M. Yoo, K. G. Nairon, L. M. Kirk, E. Rahbar, S. Soker, A. Skardal, *Biomed. Mater.* **2022**, *17*, 025001.

[75] a) P. Lee, G. C. Yeo, A. S. Weiss, *FEBS J.* **2017**, *284*, 2216–2230; b) B. Bochicchio, G. C. Yeo, P. Lee, D. Emul, A. Pepe, A. Laezza, N. Ciarfaglia, D. Quaglino, A. S. Weiss, *FEBS J.* **2021**, *288*, 4024–4038.

[76] A. Laezza, A. Pepe, B. Bochicchio, *Chem. Eur. J.* **2022**, *28*, e202201959.

[77] A. E. G. Baker, R. Y. Tam, M. S. Shoichet, *Biomacromolecules* **2017**, *18*, 4373–4384

[78] E. W. Fowler, A. Ravikrishnan, R. L. Witt, S. Pradhan-Bhatt, X. Jia, *ACS Biomater. Sci. Eng.* **2021**, *7*, 5749–5761.

[79] M. Pol, H. Gao, H. Zhang, O. J. George, J. M. Fox, X. Jia, *Biomaterials* **2023**, *299*, 122180.

[80] A. Ravikrishnan, H. Zhang, J. M. Fox, X. Jia, *ACS Macro Lett.* **2020**, *9*, 1369–1375.

[81] Y. Deng, X. Zhang, Y. Zhao, S. Liang, A. Xu, X. Gao, F. Deng, J. Fang, S. Wei, *Carbohydr. Polym.* **2014**, *101*, 36–39.

Chapter 2

Sequential Electrospinning of Asymmetric PDLLA/PVP-HA Scaffolds Functionalized with Glycine for Medical Devices

Antonio Laezza[1†], Francesca Armiento[1†], Luigi Fabiano[2], Serena Munaò[3], Paola Campione[2], Matteo Carrozzino[1], Ileana Ielo[3], Katja Schenke-Layland[4,5],Giovanna De Luca[2], Grazia Maria Lucia Messina[2], Giovanna Calabrese[3], Antonietta Pepe[1*], Brigida Bochicchio[1*]

1. Department of Basic and Applied Sciences (DISBA), University of Basilicata, Via Ateneo Lucano 10, 85100 Potenza, Italy; (A.L.); (F.A.); (M.C.)
2. Department of Chemical Sciences, University of Catania and CSGI, Viale A. Doria 6, 95125 Catania, Italy; (L.F.); (P.C.); (G.M.L.M.)
3. Department of Chemical, Biological, Pharmaceutical and Environmental Sciences (ChiBioFarAm), University of Messina, Viale F. Stagno d'Alcontres 31, 98166 Messina, Italy; (S.M); (I.I.); (G.D.L.); (G.C.)
4. NMI Natural and Medical Sciences Institute at the University of Tübingen, 72770 Reutlingen, Germany; (K.S.-L.)
5. Department of Women's Health, Research Institute for Women's Health, Eberhard-Karls-University Tübingen, 72076 Tübingen, Germany; (K.S.-L.)

†These authors contributed equally to this work

The content of this chapter has been accepted

Abstract

In this study we engineered bilayered electrospun scaffolds consisting of hydrophobic PDLLA and hydrophilic PVP layer which incorporate either native HA or semi-synthetic HA-Gly-OH at concentrations of 1% and 3% w/w. Generally, bilayer scaffolds electrospun on different days delaminated, while herein they maintained their integrity because electrospun on the same day. Sequential electrospinning enabled the bilayer structure, characterized via Scanning Electron Microscopy (SEM), Atomic Force Microscopy (AFM), and Young's modulus measurements to assess morphology and mechanics. In vitro cytotoxicity and cell viability assays with fibroblast cells confirmed good biocompatibility for both the individual layers and bilayer system. Among the tested formulations, the bilayer PDLLA/PVP–HA-Gly-OH 1% showed the most promising performance, attributed to the synergistic effects of HA and Gly-OH in promoting adhesion and proliferation.

Keywords: Bilayer scaffolds; hyaluronic acid; glycine; electrospun scaffolds; biocompatibility

1. Introduction

Skin is a complex three-layered organ representing the body's primary barrier against external risks, including pathogenic microorganisms, physical trauma, and chemical stressors [1-4]. It plays a critical role in immune surveillance and maintaining homeostasis, acting as the body's frontline defense and preserving overall health. When this barrier is compromised due to injury, the body initiates a dynamic and highly regulated wound healing process, which involves overlapping stages of hemostasis, inflammation, proliferation, and maturation [5]. The final remodeling phase results in the formation of scar tissue mainly composed of collagen fibers [6].

Traditional wound dressings are primarily designed to protect clean and dry wounds from external contamination; however, they lack the ability to actively promote tissue regeneration or accelerate the healing process. To overcome these limitations, recent research has been focused on advanced wound care strategies that incorporate bioactive components and functional materials. Among these innovations, biomaterial scaffolds have emerged as a particularly promising approach [7, 8]. These scaffolds function as temporary templates that facilitate cell infiltration, proliferation, and tissue regeneration by mimicking the native extracellular matrix (ECM) and providing a supportive microenvironment favorable to new tissue formation. Within this context, various fabrication methods and compositions have been investigated [9]. Particularly, electrospinning has gained attention for its ability to produce well-organized nanofibrous structures with high surface/volume ratios and interconnected porosity. These structural features are essential for maintaining a moist wound environment, allowing gas exchange, and controlling bleeding, important factors that contribute to effective wound healing [10-12].

To mimic the structural and functional features of the epidermal and dermal layers of the skin, a bilayer system has emerged as a promising strategy for enhancing wound healing [13, 14]. These systems are typically engineered with an asymmetric architecture that mimics the skin's natural barrier and regenerative properties. The external layer, designed to simulate the epidermis, is typically fabricated by hydrophobic nanofibers, acting as a protective shield against external agents, such as pathogens and environmental stressors [15]. In contrast, the inner layer consists of hydrophilic nanofibers closely resembling the ECM, thereby supporting cellular activities essential for tissue regeneration [16]. Among the methods for developing asymmetric scaffolds, sequential electrospinning is widely used [17]. It refers to one-by-one electrospinning of different material solutions or melts. In our case, it consists of fabricating hydrophobic and hydrophilic layers, through one-spinneret per step, leading to a bilayer architecture which provides a moist wound environment that facilitates cellular adhesion, migration and proliferation, which are key processes in effective wound healing.

As a principal component of the ECM, hyaluronic acid (HA), also known as hyaluronan, has gained great attention for the development of innovative wound dressings [18]. HA is a non-sulfated component of glycosaminoglycans (GAGs) which is composed of D-glucuronic acid (GlcA) and *N*-acetyl-D-glucosamine (GlcNAc), linked by alternating β-1→3 and β-1→4 glycosidic bonds, resulting in 4)-β-GlcA-(1→3)-β-GlcNAc-(1→ disaccharide repeating unit. HA plays important roles in the healing process, participating in inflammation modulation, angiogenesis, and tissue remodeling [19, 20]. In addition to its biocompatibility and biodegradability, the presence of functional groups along its polysaccharide backbone, specifically, hydroxyl and carboxyl groups, confers high hydrophilicity that facilitates exudates absorption [21]. Moreover, these functional groups also enable the functionalization of the backbone for obtaining tailored derivatives [18, 22].

Pure and functionalized HA have been investigated for nanofibrous wound dressing production. However, the high viscosity of their solutions limits the polysaccharide spinnability, a drawback that has been addressed by blending HA with different natural and synthetic polymers [23-25]. Among them, polyvinylpyrrolidone (PVP) presents water solubility, chemical inertness, thermal stability, pH resistance, non-toxic nature, and non-ionic character. These features have made PVP a valuable component in electrospun materials for wound dressings and a wide range of other biomedical applications [26, 27].

This work aims to fabricate, by sequential electrospinning, an asymmetric or bilayer scaffold containing poly-D,L-lactide (PDLLA) and a PVP/HA-Gly-OH blend serving as hydrophobic and hydrophilic layers, respectively. Without a doubt, since many years L-alpha amino acid residues of certain biological relevance have been grafted with HA in aqueous solution via amide bond formation through carbodiimide/N-hydroxysuccinimide chemistry in order to synthesize HA-derivatives empowered in terms of biocompatibility with added value in tissue engineering and regenerative medicine [28, 29]. At the same time, electrospinning is a precious technique aimed at the production of microfibers hierarchically organized in interconnected porous structures assuring nutrients and waste exchanges essential for the survival of cells. On this basis, HA has been widely electrospun with synthetic or natural polymers for the production of hybrid scaffolds with several applications in biomedicine.

Although the literature widely reports the use of native HA in the fabrication of electrospun asymmetric scaffolds [24, 30-32], the application of suitably functionalized glycosaminoglycans in the design of these materials has not yet been fully explored. The novelty of this work consists in the electrospinning of covalently functionalized HA [23].

A strategic localization of semi-synthetic HA-Gly-OH exclusively within the hydrophilic layer could create a spatially defined bioactive interface for cells, while the external PDLLA layer remains an

unmodified mechanical barrier. While polysaccharide-glycine peptide conjugates have been incorporated into biomaterials [33-36], this study aims to address the gap in current knowledge by examining the functionalization of HA with the single amino acid glycine. Our approach involves the functionalization of HA with this small molecule to investigate its impact on the scaffolds' physico-chemical properties while introducing beneficial chemical motifs, without the added complexity and cost associated with peptide synthesis.

The developed scaffold will be thoroughly characterized in terms of its morphological properties using scanning electron microscopy (SEM). Additionally, its biocompatibility will be assessed through *in vitro* assays, including cell viability (MTT or Live/Dead staining), cell adhesion, and proliferation studies using fibroblast cell lines, to evaluate its potential for clinical wound healing applications.

2. Materials and Methods

2.1 Materials

Commercial-grade reagents and solvents were used without further purification, except where otherwise indicated. The term "ultrapure water (UPW)" refers to water purified by a Millipore Milli-Q Gradient system. HA (Mw=186 KDa) medical device grade was a generous gift of Altergon Italia SrL. Hydrochloric acid 37% (HCl) and sulfuric acid 95% (H_2SO_4) were purchased from VWR. 2-(*N*-Morpholino)ethanesulfonic acid hydrate (MES), 3-(Trimethylsilyl)propionic-2,2,3,3-d_4 acid sodium salt (DSS), glycine ethyl ester hydrochloride (Gly-OEt·HCl), cetyltrimetyl ammonium bromide (CTAB), glacial acetic acid (AcOH), phenol, PVP (Mw ~ 1300 KDa), sodium acetate trihydrate ($AcONa·3H_2O$), sodium chloride (NaCl), sodium hydroxide pellets (NaOH) were purchased from Sigma Aldrich. 1,1,1,3,3,3-Hexafluoro-2-propanol (HFP) and *N*-(3-(Dimethylamino)propyl)-*N*'-ethylcarbodiimide hydrochloride (EDC·HCl) were purchased from Iris Biotech GmbH, and *N*-Hydroxysulfosuccinimide sodium salt (s-NHS) was purchased from TCI Chemicals. PDLLA (EasyFil PLA, transparent pellets, molecular weight: 126 KDa, density: 1240 kg/m^3) was obtained from Form-Futura.

2.2. Methods

2.2.1. Nuclear Magnetic Resonance (NMR) Spectroscopy

NMR spectra were recorded on 500 MHz (^{1}H: 500 MHz, ^{13}C:125 MHz) and 400 MHz (^{1}H: 400 MHz, ^{13}C: 100 MHz) Varian Inova instruments in D_2O or 9:1 v/v H_2O/D_2O (DSS 0.1 mM as internal standard, δ_H=0 ppm). The degree of substitution (DS) of HA-Gly-OEt is attributed to disaccharide repeating units.

2.2.2. Attenuated Total Reflectance Fourier Transform Infrared (ATR-FT-IR) Spectroscopy

ATR-FT-IR spectra were carried out on J-460 (Jasco Europe Srl) equipped with an ATR PRO ONE Single-reflection ATR accessory using a single crystal diamond ATR prism. Spectra were acquired in the region from 4000 to 450 cm-^{1} with a spectral resolution of 2 cm^{-1} and 256 scans. Background spectra were recorded each time and then subtracted from the sample spectra.

2.2.3. Scanning Electron Microscopy (SEM)

SEM images were acquired with a voltage of 20 kV and different magnifications, after gold sputter-coating on a FEI Quanta 400 high resolution field emission scanning electron microscope (ESEM) instrument. The diameter of the fibers and the porosity were evaluated using ImageJ software supplied with the DiameterJ plug-in. The sample size considered corresponds to 50 individual fibers measured from three different images obtained from one scaffold, for a total of 150. For the cross-section analysis, the samples were secured on plotted stubs and cut using fine scissors. The images were acquired with at 20 kV and different magnifications, after gold sputter-coating on a Philips-Fei ESEM XL30-LaB6 instrument.

2.2.4. Atomic Force Microscopy (AFM)

The mechanical properties of the electrospun fibers were evaluated by force spectroscopy using an NTEGRA II AFM (NT-MDT, Moscow, Russia). Force–distance curves were collected, and the Young's modulus was extracted from the elastic portion of the curves. Stiff single-crystal silicon cantilevers with a symmetric tip geometry were employed (model Tap300AI-G, BudgetSensors, Sofia, Bulgaria; nominal resonance frequency 300 kHz, nominal spring constant 40 N m^{-1}, and tip radius < 10 nm). The spring constant of each cantilever was calibrated using the Sader method [37].

The Young's modulus was obtained by fitting the experimental force–distance curves in the elastic regime with the Derjaguin–Muller–Toporov (DMT) model [38], according to the equation (1):

$$F + F_{ad} = \frac{4E_s}{3(1-\nu_s^2)}\sqrt{R\delta^3} \quad (1)$$

where F is the applied force; F_{ad} is the adhesion force; E_s is Young's modulus; ν_s is Poisson's ratio for the sample; R is the radius of the spherical indenter; and δ is the elastic indentation depth. A Poisson's ratio of 0.40 was chosen based on values commonly reported for amorphous polymers such as PVP under standard conditions[39, 40]. It was used for all samples to enable consistent comparison among formulations; possible small variations in ν due to HA or HA–Gly–OH incorporation are not expected to affect the relative trends discussed in this work. Measurements were carried out at ambient temperature and a relative humidity of 44.72%. More than 300 force–distance curves were acquired, on each sample, in three independent measurements by collecting the curves along the fiber length, thereby ensuring that the probe indented the uppermost regions of the fibers and reducing artifacts arising from abrupt height variations of the fibrous matrix. The elastic modulus was determined from the distribution of the collected data and analyzed using Origin 2018 software. Statistical

evaluation of the datasets was subsequently performed by one-way ANOVA followed by Welch's t-tests, in order to assess global and pairwise differences among the different formulations.

2.2.5. Semi-synthesis of derivative HA-Gly-OEt

HA (101.19 mg, 0.25 mmol) was suspended in pure H_2O (15.0 mL) and stirred at room temperature up to complete dissolution, then treated with a 208.30 mM EDC·HCl (2.41 mL, 0.50 mmol) and 103.29 mM s-NHS (2.43 mL, 0.25 mmol) solution. After 40 minutes MES·xH_2O (44.25 mg) and 250.0 mM Gly-OEt·HCl (2 mL, 0.50 mmol) were added to the reaction mixture obtaining a clear solution. Few drops of freshly prepared 1.0 M NaOH solution were then added to adjust pH to 6, and stirring was continued overnight. After ~ 20 h, the crude was neutralized by HCl 1.0 M and dialyzed against NaCl 150 mM solution for 2 days, and against H_2O for further 2 days. The subsequent freeze-drying yielded a white solid (81.74 mg, yield = 77%). ^{1}H-NMR (500 MHz, D_2O): δ_{DSS} = 4.55 (H-1 GlcNAc), 4.46 (H-1 GlcA), 4.24 (CH_2 Gly-OEt), 4.00-3.20 (H-2, H-3, H-4, H-5 GlcA, H-2, H-3, H-4, H-5, H-6 GlcNAc), 2.01 (CH_3 GlcNAc), 1.27 (CH_3 Gly-OEt).

2.2.6. Semi-synthesis of derivative HA-Gly-OH

HA-Gly-OEt (81.04 mg, 0.19 mmol) was treated with a 1.0 M NaOH (10 mL) solution to adjust pH to 12. The solution was stirred for 6 h at rt and then 1 M HCl was added until neutralization. Dialysis and subsequent freeze-drying yielded a white solid (59.68 mg, yield = 70%). ^{1}H-NMR (500 MHz, D_2O): δ_{DSS} = 4.55 (H-1 GlcNAc), 4.46 (H-1 GlcA), 4.00-3.20 (H-2, H-3, H-4, H-5 GlcA, H-2, H-3, H-4, H-5, H-6 GlcNAc), 2.01 (CH_3 GlcNAc).

2.2.7 Electrospinning

Electrospinning was performed on a Linari Engineering Gamma-High-Voltage generator electro-spinning system and the composition of the electrospinning solutions is reported in Table 1.

Table 1. Composition of the electrospinning solution.

Hydrophobic layer						
Scaffold	**PDLLA (% w/V)**		**HFP (mL)**			**Final volume (mL)**
PDLLA	12.0		2.0			2.0
Hydrophilic layer						
Scaffold	**PVP (% w/V)**	**HA (% w/w)**	**HA-Gly-OH (% w/w)**	**H_2O (mL)**	**EtOH (mL)**	**Final volume (mL)**
PVP	10.0	-	-	0.4	1.6	2.0
PVP-HA 1%	10.0	1.0	-	0.4	1.6	2.0
PVP-HA 3%	10.0	3.0	-	0.4	1.6	2.0
PVP-HA-Gly-OH 1%	10.0	-	1.0	0.4	1.6	2.0
PVP-HA-Gly-OH 3%	10.0		3.0	0.4	1.6	2.0

In the case of the hydrophobic layer, PDLLA (240 mg) was dissolved in HFP (2.0 mL) and kept under magnetic stirring overnight at T = 37 °C. The solution was loaded into a 10 mL glass syringe with a 20 G stainless-steel needle (N) and then electrospun at an applied voltage (V) of 17 kV with a flow rate (F) of 1.0 mL/h of the pump. The target was a round copper plate having 90 mm diameter coated with aluminum foils and the distance (d) between the collector and the needle was set to 19 cm.

For the hydrophilic layer, the preparation of the electrospinning solutions was performed by the following general protocol: HA (2.0 mg) or HA-Gly-OH (2.0 mg), when present, were dissolved in H_2O (0.4 mL), then left to stand for 2 h at room temperature with stirring. In parallel, PVP (200 mg) was dissolved in EtOH (0.6 mL) and also stirred for 2 h at room temperature. Subsequently, the HA or HA-Gly-OH were combined with PVP and diluted with additional EtOH (1.0 mL). The resulting mixture was stirred overnight at the temperature of 37 °C. The solution was loaded into a 10 mL glass syringe with a 20 G stainless-steel needle and then electrospun at 19 kV with a flow rate of 0.5 mL/h of the pump. The target was a round copper plate having 90 mm diameter coated with aluminum foils and the distance between the collector and the needle was set to 19 cm. To avoid the complete dissolution in ultrapure water of the neat PVP layer as well as of those composed of PVP and HA or PVP and HA-Gly-OH, the resulting scaffolds were irradiated with ultraviolet radiation (254 nm) in a multiray reactor (Helios Italquartz, Milan, Italy) for 60 minutes, corresponding to an UV dose of 169.2 mJ/cm^2. To evaluate scaffold biocompatibility, the samples were electrospun directly onto 13 mm glass coverslips. The electrospun volume was reduced to 1.0 mL for both layers, maintaining the concentration reported above and the electrospinning conditions. Considering the reduced volume, the resulting scaffolds were irradiated for 15 minutes, corresponding to an UV dose of 42.3 mJ/cm^2.

2.3. Wettability (Water-Contact Angle Measurement)

Surface wettability of the electrospun scaffolds was evaluated by static water contact angle (SWCA) measurements by using a Drop Shape Analyzer (DSA25E, KRÜSS) operated in sessile drop mode. A droplet of ultrapure water (2 μL) was deposited onto the scaffold surface using an automated syringe system. All measurements were performed at 20 °C. Results were calculated from nine measurements obtained from three different scaffold pieces for each sample.

The contact angle was recorded 10 s after droplet deposition to standardize the measurement and minimize the influence of rapid absorption phenomena occurring on highly hydrophilic fibrous surfaces.

2.4 Cell Culture and Biocompatibility Evaluation

To evaluate scaffold biocompatibility, L929 murine fibroblasts were used. The cells were acquired from the American Type Culture Collection (ATCC, Rockville, MD, USA) and cultured in Dulbecco's Modified Eagle Medium High Glucose (DMEM, Merck Life Science S.r.l., Milan, Italy) supplemented with 10% fetal bovine serum (FBS, Merck Life Science S.r.l., Milan, Italy), 1% penicillin/streptomycin/amphotericin B (PSA, Merck Life Science S.r.l., Milan, Italy). Cultures were maintained at 37 °C in a humidified atmosphere containing 5% CO_2 and sub-cultured upon reaching 80%-90% confluence. Electrospun scaffolds deposited onto 13 mm glass coverslips were sterilized by UV irradiation for 30 minutes prior to use. L929 fibroblasts were seeded onto each scaffold at a density of 3×10^4 cells per sample using a dropwise technique to ensure uniform initial adhesion. The seeded scaffolds were incubated for two hours under standard culture conditions (37 °C, 5% CO_2, humidified atmosphere). Following this adhesion period, 500 μL of fresh complete culture medium was carefully added to each well to fully immerse the scaffolds and support subsequent cell growth.

Cell viability was assessed using the MTT assay [3-(4,5-dimethylthiazol-2-yl)-2,5-diphenyltetrazolium bromide] test (Merck Life Science S.r.l., Milan, Italy) at 24- and 48-hours post-seeding as previously reported [41, 42].

For each time point, 500 μL of a 1 mg/mL MTT solution prepared in serum-free high-glucose DMEM was added to each well and incubated at 37 °C for 2 hours. The resulting formazan crystals were solubilized in 500 μL of dimethyl sulfoxide (DMSO; Merck Life Science S.r.l., Milan, Italy). Absorbance was measured at 540 nm using a microplate reader (AMR-100, Biosigma, Verona, Italy). Viability data were normalized to cells cultured without scaffolds, which served as the internal control.

Live/Dead staining was performed on L929 fibroblasts cultured on electrospun scaffolds for 24 and 48 hours to assess cell viability and distribution, providing qualitative insights into cell proliferation and scaffold cytocompatibility. After incubation, the culture medium was carefully removed, and each

scaffold was rinsed three times with phosphate-buffered saline (PBS, pH 7.4; Merck Life Science S.r.l., Milan, Italy) to eliminate residual media. A 2× working solution of the LIVE/DEAD Cell Imaging Kit (Invitrogen, Cat. No. R37601; excitation/emission: 488/570 nm; Thermo Fisher Scientific, Waltham, MA, USA) was prepared according to the manufacturer's protocol and applied to the samples. The scaffolds were then incubated with the staining solution for 30 minutes at room temperature in the dark to ensure optimal dye uptake and minimize photobleaching. Fluorescence imaging was performed using a NEXCOPE NE 900 inverted fluorescence microscope equipped with a digital camera (TiEsseLab S.r.l., Milan, Italy). Viable cells were visualized by green fluorescence from Calcein AM, while non-viable cells were identified by red fluorescence from BOBO-3 Iodide, enabling qualitative assessment of scaffold cytocompatibility.

2.5. Sol (SF) Gel fraction (GF) calculation

To evaluate the SF and GF for each sample, four pieces from three different crosslinked scaffolds (a total of 12 samples) were investigated. Each sample was immersed in UPW (10 mL) and shaken at 60 rpm on an orbital shaker at room temperature for 24 h. Thereafter, the liquid was gently removed and the samples were freeze-dried, then the SF was calculated according to the following equations (2) and (3):

$$SF\ (\%) = \frac{W_s - W_d}{W_s} 100 \quad (2)$$

$$GF\ (\%) = 100 - SF\ (\%) \quad (3)$$

where Ws and Wd are the weights of starting and freeze-dried scaffolds, respectively.

2.6. Calibration curve for CTAB assay

To construct a calibration curve, a 0.2 M sodium acetate buffer (pH 5.5) containing NaCl 0.15 M was freshly prepared, as well as a 2.5% w/v CTAB solution in 2% w/v NaOH aqueous solution. The latter was stirred at 37°C up to complete dissolution.

HA (15.0 mg) was dissolved in buffer to obtain a 3 mg/mL stock hyaluronic acid solution. Serial dilutions with the buffer were performed to obtain solutions with a final volume of 3.0 mL and with concentrations between 1.7 μg/mL to 0.4 mg/mL. From each solution, 500 μL were collected and treated with 1.0 mL of CTAB solution. Samples were incubated at 37°C for 20 minutes and the absorbance was measured at 37°C within 10 minutes at λ = 570 nm using an Agilent Cary 60

ultraviolet−visible (UV−Vis) spectrophotometer. Thus, a calibration curve with the following equation (4) was constructed:

$$Absorbance = 3.54762 * concentration \quad (4)$$

2.7. CTAB Assay for Cumulative Release

PVP-HA 1% and PVP-HA-Gly-OH 1% scaffolds have been analyzed for evaluating the native and semi-synthetic derivative release profiles. Four pieces from three different scaffolds (a total of 12 samples) were investigated, by immersing each sample in a 0.2 M sodium acetate buffer (pH 5.5) containing NaCl 0.15 M (5.0 mL) and left stirring at 37°C. At regular intervals, 500 µL of the solution was collected and treated with 1.0 mL of 2.5% w/v CTAB solution in 2% w/v NaOH aqueous solution. Samples were incubated at 37°C for 20 minutes and the absorbance was measured within 10 minutes at λ = 570 nm using an Agilent Cary 60 UV−Vis spectrophotometer. PVP scaffold as negative control was analyzed under the same conditions and a solution of sodium acetate buffer and CTAB was used as a blank. To maintain constant total volumes of the solutions, after each sampling, 500 µL of fresh buffer was added.

The concentration of the released HA and HA-Gly-OH were calculated from a standard calibration curve; then, the cumulative release as a function of time was calculated according to the following equation (5):

$$Cumulative\ release\ (\%) = \left(C_t V_{tot} + \sum_{t=0}^{k=1} f_s m_k \right) \frac{100}{Q_{tot}} \quad (5)$$

where C_t, V_{tot}, f_s, m_k, and Q_{tot} are the measured concentration at time t, the total volume used for the release test, the collected solution fraction, the amount of drug released at time k, and the theoretical drug quantity in the scaffold, respectively.

2.8. Phenol assay

Following cumulative release, PVP-HA 1% scaffolds have been analyzed, by way of example, for hyaluronic acid content evaluation employing the phenol assay. The scaffolds have been suspended in UPW (1 mL), treated with a 5% w/v phenol aqueous solution (1 mL) and with 95% H_2SO_4 (5 mL). Samples have been incubated 30°C for 20 minutes and the absorbance was measured at λ = 490 nm using an Agilent Cary 60 UV−Vis spectrophotometer. PVP scaffold as negative control was analyzed

under the same conditions and a solution of UPW, aqueous phenol and concentrated H_2SO_4 was used as a blank.

3. Results and discussion

3.1. Semi-synthesis of HA-Gly-OH

The amidation of HA with glycine amino acid was accomplished with Gly-OEt·HCl, in a MES buffered water (pH = 6) by employing carbodiimide chemistry for the GlcA carboxylate activation (Scheme 1). After overnight reaction at room temperature, dialysis and freeze-drying furnished derivative HA-Gly-OEt in 77% mass yield. The subsequent hydrolysis of ethyl ester group under alkaline aqueous conditions afforded derivative HA-Gly-OH in 70% mass yield after dialysis and freeze-drying.

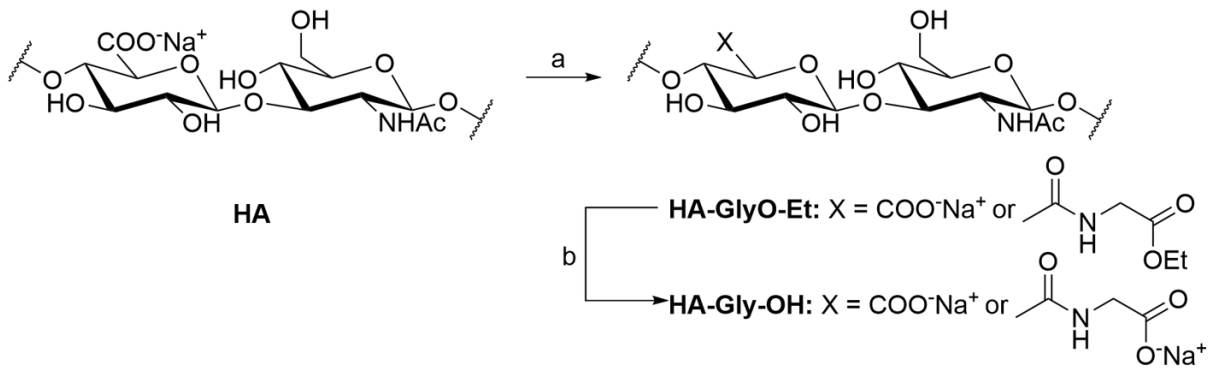

Scheme 1. Semi-synthesis of derivative HA-Gly. a: GlyOEt·HCl, EDC·HCl, s-NHs, MES, H_2O, pH = 6, RT, overnight, yield = 77%, DS = 0.25; b: NaOH, H_2O, pH = 12, RT, 6h, yield = 70%, DS = quantitative.

^{1}H NMR analysis in D_2O confirmed the functionalization of HA thanks to the presence of signals at δ_{DSS} = 4.25 ppm and δ_{DSS} = 1.29 ppm, associated with the CH_2 and CH_3 of amino acid ester protecting group, respectively (Figure 1, red spectrum). The DS for HA-Gly-OEt derivative, with a value of 0.25, was calculated by comparing the integration of the Gly-OEt residue CH_3 signal with respect to those of HA anomeric protons (δ_{DSS} = 4.64-4.38 ppm) (Figure S1) with the following equation (6):

$$DS = \frac{\frac{2}{3} I_{CH_3(GlyOEt)}}{I_{CH\ (GlcA)+CH\ (GlcNAc)}} \quad (6)$$

The subsequent quantitative removal of ethyl ester on GlyOEt was confirmed by the absence of signals associated with the protecting group in the ^{1}H-NMR spectrum of derivative HA-Gly-OH (Figure 1, blue spectrum).

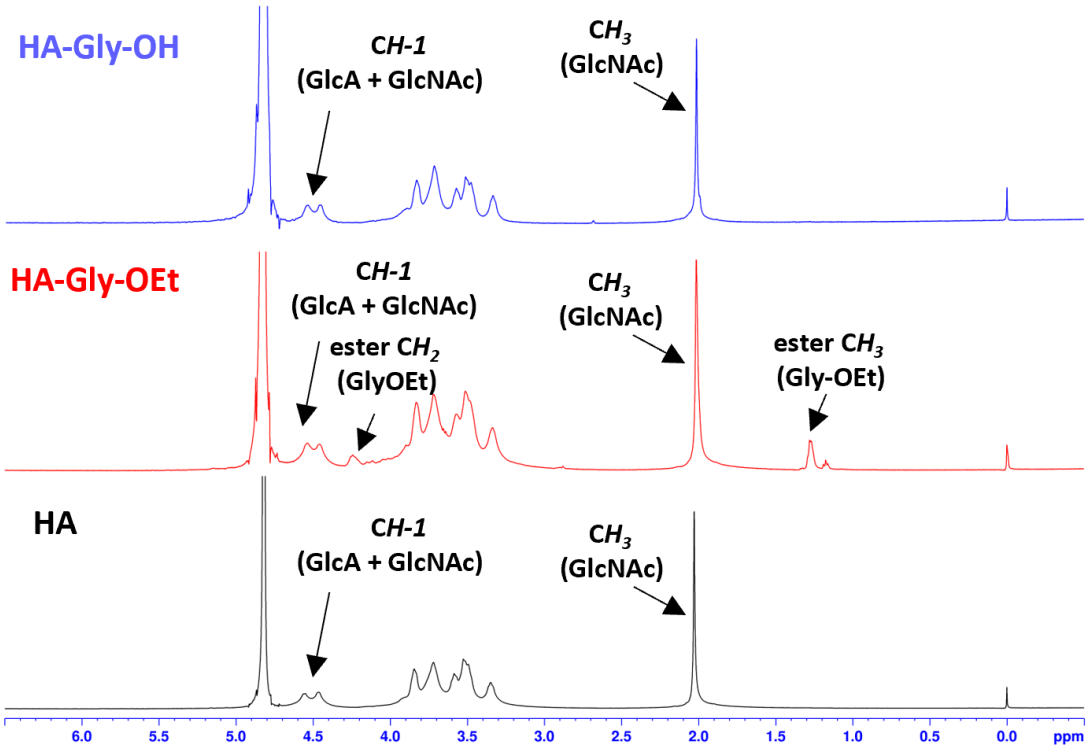

Figure 1. ^{1}H NMR spectra of HA (black), HA-Gly-Oet (red), and HA-Gly-OH (blue) (500 MHz, D2O, 25 °C).

Furthermore, the amide region of the ^{1}H-NMR spectrum recorded in H_2O/D_2O 9:1 v/v, of underivatized HA was compared with that of HA–Gly–OH to confirm the presence of the amino acid after global deprotection (Figure S2). The spectrum of native HA (black spectrum) displayed a signal at δ_{DSS} = 8.05 ppm, attributable to the amide proton of the GlcNAc residue, in agreement with literature data [43, 44]. Upon functionalization with Gly–OH (Figure S2, red spectrum), an additional peak appeared at δ_{DSS} = 8.65 ppm, which can be assigned to the newly formed amide proton following HA modification (Figure S2, red spectrum). A slight downfield shift of the GlcNAc amide proton to δ_{DSS} = 8.10 ppm was also detected, suggesting a change in the local conformation of the polysaccharide backbone. Day and co-workers recently reported an opposite trend following the chemical modification of hyaluronan oligosaccharides [45].

The characterization of HA, and semi-synthetic derivatives was further carried out by ATR-FT-IR (Figure 2), allowing the assignment of specific functional groups on the polysaccharide backbones. In the HA spectrum (black curve) several regions can be distinguished: the stretching vibrations of carbohydrate O-H and acetamido N-H are visible between 3500–3000 cm^{-1} (red circle), as well as the stretching vibration of C-H and C-H_2 groups that are visible between 2950-2863 cm^{-1} (blue circle).

In addition, it is visible the 1630-1700 cm^{-1} region corresponding to the asymmetric stretching vibrations of carboxylate and to the C=O vibrations of acetamido group (amide I, green circle). At ~ 1559 cm^{-1} is present the band corresponding to symmetric stretching of carboxylate and C-N (amide II, orange circle) band of acetamido group stretching vibrations.

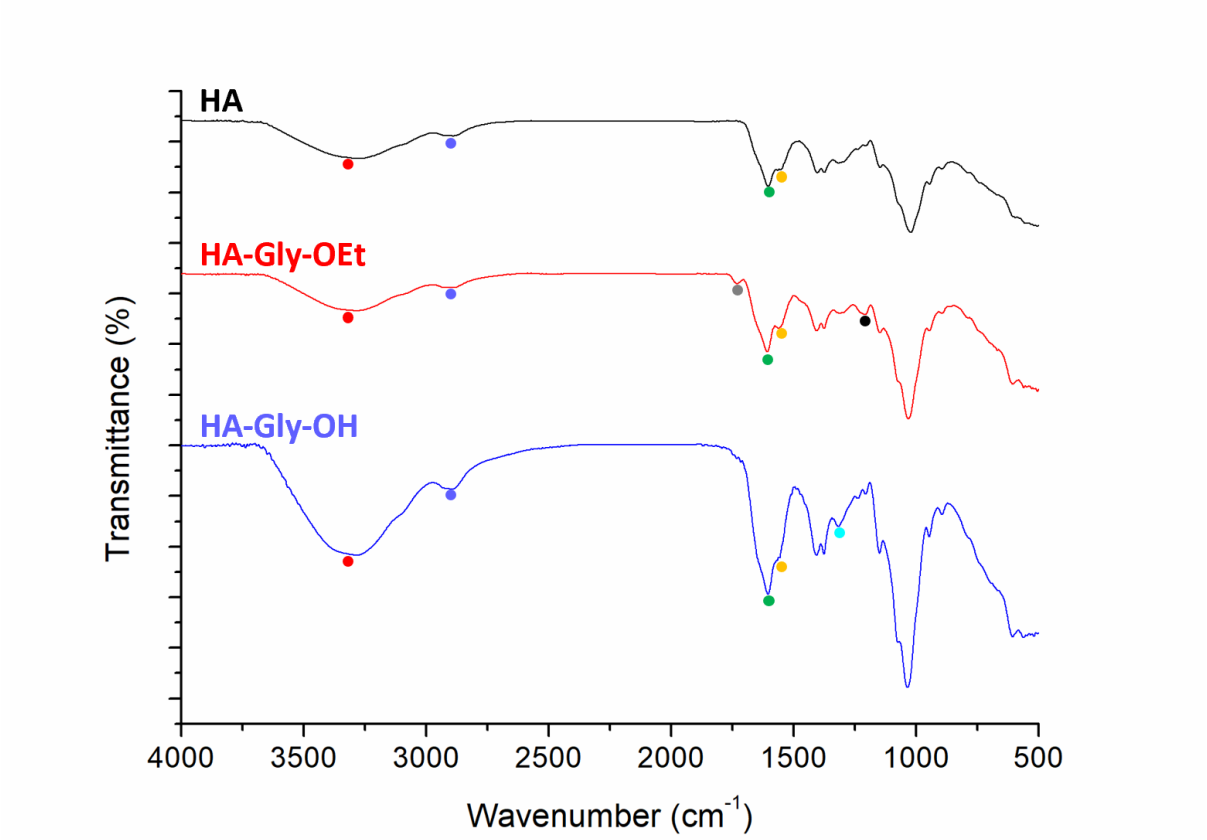

Figure 2. ATR FT-IR spectra of HA (black), HA-Gly-OEt (red), and HA-Gly-OH (blue). O-H and N-H stretching vibration band (red circle), C-H and C-H_2 stretching vibration (blue circle), ester C=O stretching vibration (grey circle), amide and carboxylate C=O stretching vibration (green circle), amide C-N and carboxylate C=O stretching vibration (orange circle), C-H_2 bending vibration (turquoise circle), ester C-O stretching vibration (black circle).

In the spectrum of HA-Gly-OEt (Figure 2, red spectrum), besides the above-mentioned bands, it is evident the occurrence of the amidation due to the band at ~ 1730 cm^{-1} (grey circle) and ~ 1210 cm^{-1} (black circle), corresponding to C=O and C-O stretching vibrations of the ester protecting group of Gly-OEt [46]. Finally, the spectrum of HA-Gly-OH (Figure 2, blue spectrum), confirms the alkaline deprotection of ethyl ester, characterized by the strong band at ~1730 cm^{-1}, and at the same time the presence of the amino acid on the polysaccharide backbone thanks to the intense band at 1316 cm^{-1} associated with the bending of C-H_2 group (turquoise circle).

3.2 Electrospinning and Morphological Analysis of Electrospun Composites

Our aim is to produce asymmetric, or bilayer, electrospun scaffolds that meet the requirements of tissue engineering by the sequential electrospinning of biodegradable and bioactive polymers. Sequential electrospinning, in fact, allows the controlled deposition of different layers (Scheme 2) with distinct biological and mechanical functions [47]. As reported in Table 1, the external hydrophobic layer was prepared by dissolving neat PDLLA in HFP, to a final concentration of 12.0% w/v solution.

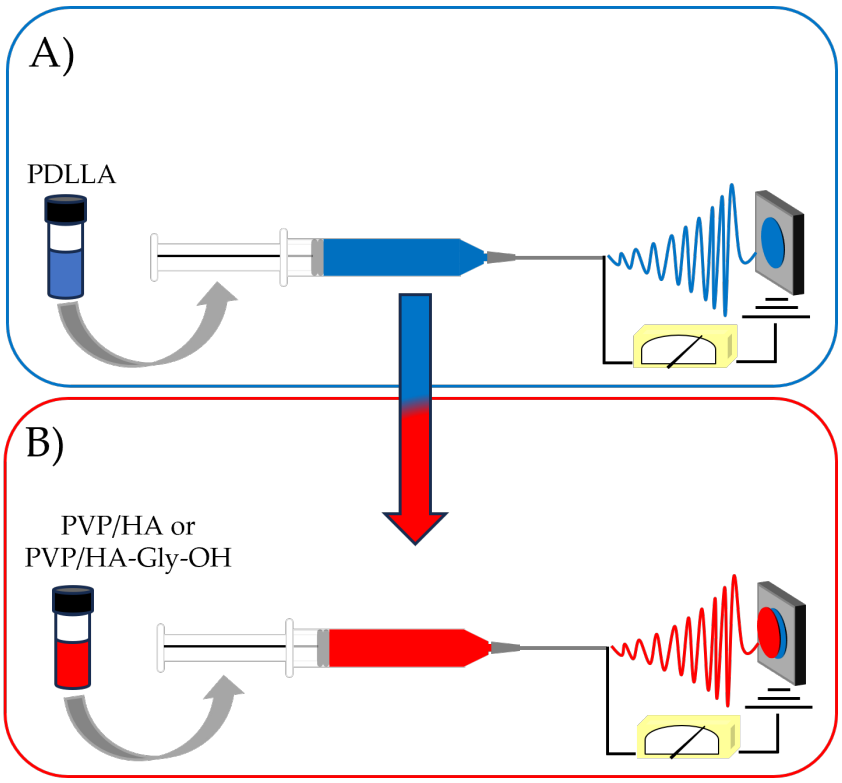

Scheme 2. Sequential electrospinning for the production of asymmetric scaffolds. A): N = 20 G, V = 17 kV, F = 1.0 mL/h, d = 19 cm; B) N = 18 G, V = 19 kV, F = 0.5 mL/h, d = 19 cm.

In contrast, the inner hydrophilic layers were fabricated by blending the semi-synthetic HA-Gly-OH with PVP in ethanolic aqueous solution (80% v/v). HA-Gly-OH was prepared at 1% and 3% w/w weight ratios while PVP at 10% w/v. Electrospinning process parameters were optimized in different conditions for the hydrophobic and hydrophilic layers to assure the process stability and afford membranes with characteristics of uniformity at macroscopic level.

On the other hand, at microscopy level, the final aim was to obtain defect free scaffolds. Therefore, SEM was used to investigate the scaffolds' morphology in terms of fiber orientation, size diameter distribution. As a matter of fact, SEM images of all electrospun scaffolds revealed three-dimensional

microstructures characterized by interconnected pores. In particular, the PDLLA scaffold (Figure 3A) displayed nearly linear, defect-free fibers with an average diameter of 1.23 ± 0.64 μm (Figure S3).

Table 2. Average fibers diameter reported as mean value ± st. deviation.

Scaffold	**Diameter (μm)**	**Porosity (%)**	**Pore area(μm^2)**
PDLLA	1.23 ± 0.64	75 ± 4	14.42 ± 3.87
PVP	1.56 ± 0.79	61 ± 9	37.6 ± 9.90
PVP-HA 1%	1.31 ± 0.51	69 ± 4	21.68 ± 4.86
PVP-HA 3%	0.95 ± 0.24	66 ± 9	7.53 ± 3.86
PVP-HA-Gly-OH 1%	1.44 ± 0.46	65 ± 5	11.31 ± 4.26
PVP-HA-Gly-OH 3%	0.79 ± 0.18	77 ± 1	30.19 ± 3.56

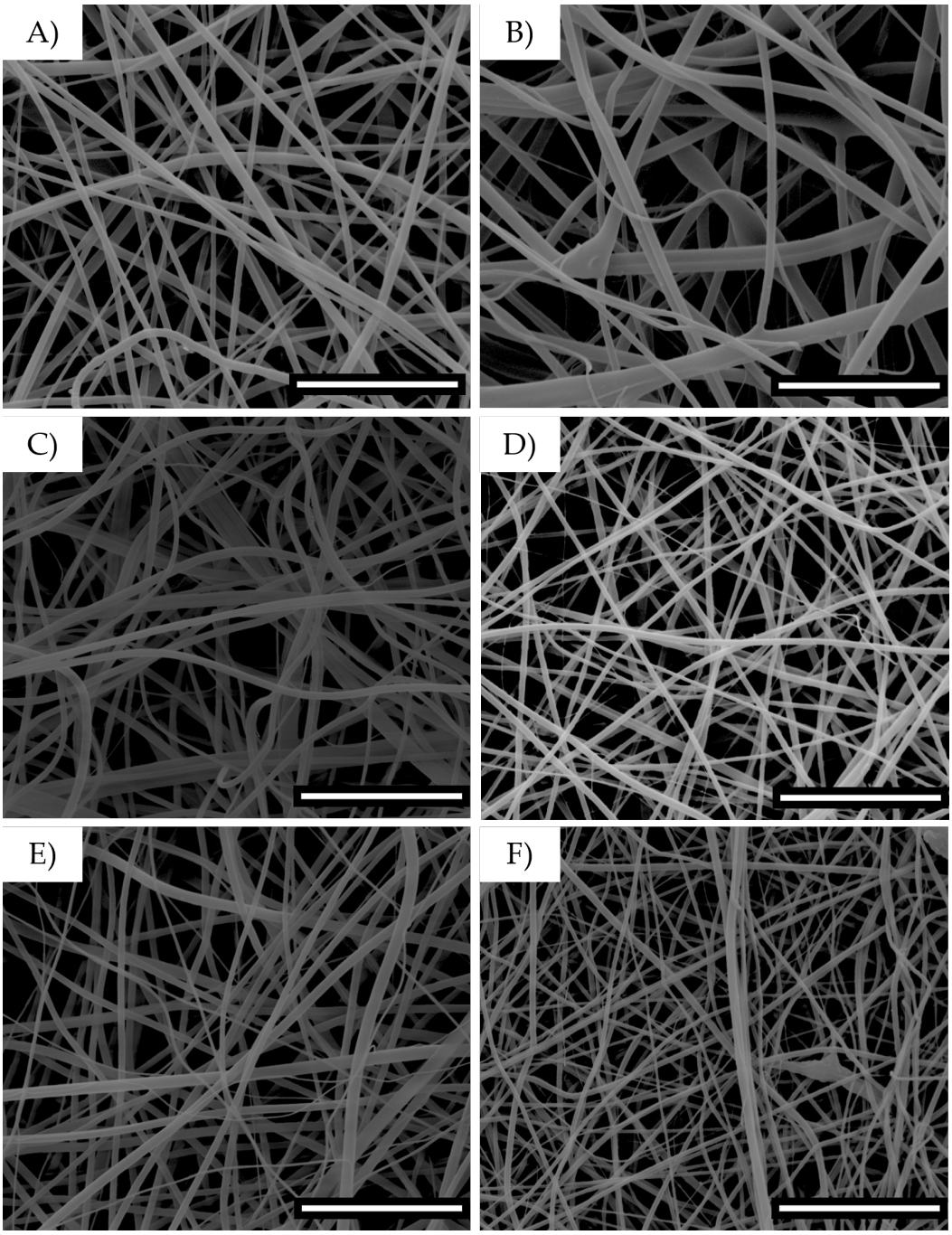

Figure 3. SEM images of electrospun scaffolds (bar: 20 μm). PDLLA (A), PVP (B), PVP-HA 1% (C), PVP-HA 3% (D), PVP-HA-Gly-OH 1% (E), PVP-HA-Gly-OH 3% (F).

Regarding the morphology of the hydrophilic layers, the scaffolds exhibited a generally homogeneous fiber distribution, which appeared slightly curled after the addition of HA or HA-Gly-OH to PVP (Figure 3B–F). Regarding fiber size, there is an evident limitation of this study due to the lack of independent scaffold replicates, because all 150 measurements are essentially technical replicates. On that basis, fiber analysis is a qualitative study. However, the average diameters of fibers as function of frequency (Figures S3) showed a normal distribution around mean values of 1.56 ± 0.79, 1.31 ±

0.51, and 0.95 ± 0.24 μm for PVP, PVP-HA 1%, and PVP-HA 3%, respectively, as reported in Table 2. Moreover, the incorporation of HA-Gly-OH to PVP at concentration of 1% w/w and 3% w/w concentration, resulted in a decrease in average diameter dimension, specifically of 1.44 ± 0.46 and 0.79 ± 0.18 μm respectively. Interestingly, PVP-HA 3% and PVP-HA-Gly-OH 3% w/w showed the smallest average fibers diameter (0.95 ± 0.24, 0.79± 0.18, respectively) and the smallest standard deviation values as well among electrospun scaffolds (Figure 4).

This behavior can be attributed to both the chemical composition and electrospinning process parameters used for the hydrophobic and hydrophilic layers. When the hydrophilic layers are compared, the PVP scaffold exhibited a higher average fiber diameter (1.56 ± 0.79 μm) than those containing HA and HA-Gly-OH. Specifically, for PVP-HA 1% and PVP-HA-Gly-OH 1% was observed an average fiber diameter of 1.31 ± 0.51 μm, and 1.44 ± 0.46, respectively. When the concentration of HA and HA-Gly-OH reached 3% w/w within the scaffold was observed an average fiber diameter of 0.95 ± 0.24 μm and 0.79 ± 0.18 μm, respectively. It is worth noting that for 1% concentration the standard deviation was twice that calculated for 3% scaffolds thus suggesting more dispersion in the group. Taking these considerations into account, it is suggested that a general decrease of diameter values was observed upon addition of hyaluronic acid. A possible explanation for that could be found in the increased conductivity of HA-containing solutions, a phenomenon previously reported in the electrospinning of ethanolic–aqueous solutions containing HA [48]. As a proof of concept, the bioconjugation of the hydrophilic small zwitterionic amino acid Gly-OH to HA induced a further reduction of average diameter length.

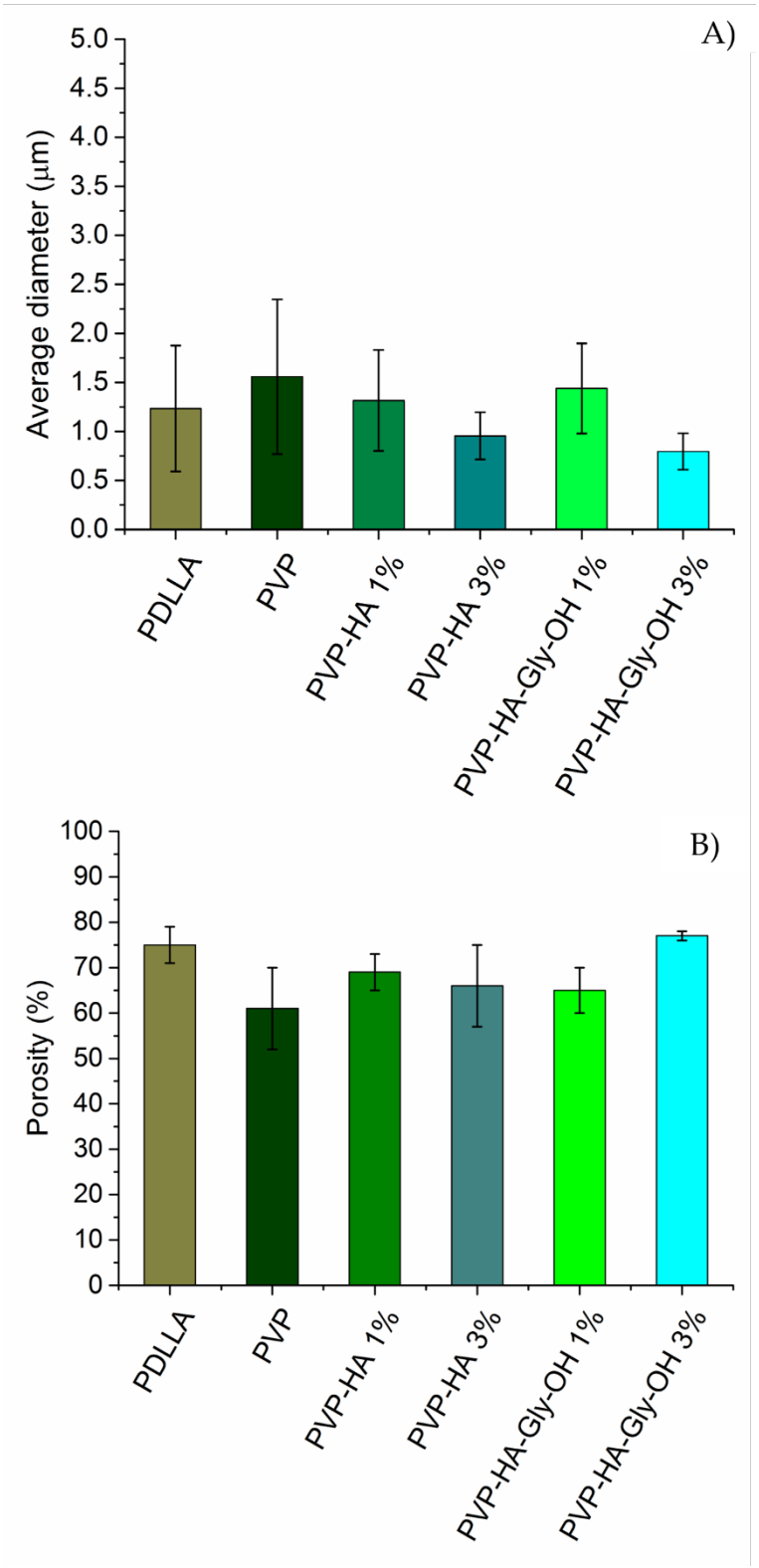

Figure 4. Mean fibers diameter (A) and porosity (B) values (± standard deviation) of electrospun scaffolds (n = 1 per group).

The addition of HA-Gly-OH resulted in a slight, variation in diameters, showing an increase at 1% w/w and a decrease at 3% w/w, when compared with scaffolds containing HA at the same concentrations. Conversely, when the concentration of HA and HA-Gly-OH as well increased from 1% w/w to

3% w/w, a decrease in diameter was observed. This feature could be attributed to the higher conductivity of the electrospinning solution associated with the increased concentration of the glycosaminoglycan.

Porosity is a critical parameter that dictates cellular infiltration and tissue ingrowth into fibrous scaffolds [49]. The porosity values obtained for the scaffolds in this study are summarized in Table 2 and illustrated in Figure 4B. PDLLA scaffold displayed a porosity value of 75 ± 4%. The hydrophilic layers showed lower porosity, with values moving from 61 ± 9% for PVP scaffold to 69 ± 4% and 66 ± 9% for PVP-HA 1% and PVP-HA 3%, respectively. In comparison, when HA-Gly-OH has been blended to PVP the measured porosity increased from 65 ± 5% to 77 ± 1% for PVP-HA-Gly-OH 1% and PVP-HA-Gly-OH 3%, respectively.

The area of pores was also investigated, and the data distribution showed a similar trend across the five scaffolds (Figure S4). Since the values followed a log-normal distribution (data not shown), the mean pore area for each scaffold was calculated using the geometric mean [50]. The mean pore areas for PDLLA and PVP were 14.42 ± 3.87 μm^2 and 37.6 ± 9.90 μm^2, respectively. When HA was blended with PVP, the pore area decreased as the HA concentration increased from 1% w/w to 3% w/w. Specifically, the values were 21.68 ± 4.86 μm^2 and 7.53 ± 3.86 μm^2, respectively. When HA-Gly-OH was blended with PVP, instead, the pore area increased with the concentration. Specifically, values of 11.31 ± 4.26 μm^2 and 30.19 ± 3.56 μm^2 were observed for PVP-HA-Gly-OH 1% and PVP-HA-Gly-OH 3%, respectively. Although the porosity values are in good agreement with the literature on electrospun scaffolds for wound healing applications [51], the pore sizes observed in this study are below the optimal threshold for deep cellular infiltration, they fall within a range that is particularly suitable for controlled drug delivery applications [52]. However, for proposing the herein discussed electrospun scaffolds as wound dressing, a water vapor transmission rate measurement remains a crucial parameter to evaluate. It is well known that the absence of this test could be a limitation.

To investigate the morphology of the bilayer PDLLA/PVP HA-derived electrospun scaffolds, with particular attention to the layer thickness, cross-sections were imaged by SEM (Figures S5-S9) and the data has been reported in Table 3. This approach was also applied in experiments where cell cultures on bilayer scaffolds having hydrophilic and hydrophobic sides, in order to discern better adhesion and integration over one of the two sides of the electrospun scaffold. In general, it is well established that cells preferentially adhere to hydrophilic layers [53]. Not only cross-sectional analysis is commonly used to investigate the internal morphology of a material, offering a direct magnified observation of interfaces, layer thickness, and potential subsurface defects, but also to investigate interfacial adhesion and identify microscopic delamination of the two layers. In this work, the two layers were electrospun on the same day to avoid interfacial delamination. Preliminary observations

showed that delamination occurred when the bilayer scaffolds were fabricated sequentially over two consecutive days (Figure S10).

Table 3. Mean Layer thickness (± standard deviation) of bilayer electrospun scaffolds.

Scaffold	l_{PDLLA} (μm)	l_{PVP} (μm)	$l_{PVP\text{-}HA\ 1\%}$ (μm)	$l_{PVP\text{-}HA\ 3\%}$ (μm)	$l_{PVP\text{-}HA\text{-}Gly\text{-}OH\ 1\%}$ (μm)	$l_{PVP\text{-}HA\text{-}Gly\text{-}OH\ 3\%}$ (μm)
PDLLA/PVP	241.15 ± 8.51	312.26 ± 15.29	-	-	-	-
PDLLA/PVP-HA 1%	420.29 ± 15.04	-	309.57 ± 31.10	-	-	-
PDLLA/PVP-HA 3%	526.14 ± 10.59	-	-	341.57 ± 32.91	-	-
PDLLA/PVP-HA-Gly-OH 1%	168.57 ± 5.91	-	-	-	222.57 ± 13.59	-
PDLLA/PVP-HA-Gly-OH 3%	217.86 ± 6.77	-	-	-		85.04 ± 5.18

3.3 Water Contact Angle Measurements

To evaluate changes in the wettability of PVP scaffolds after HA-glycine conjugation, static water contact angle (SWCA) measurements were performed. The results shown in Figure 5, Table S1 and Figure S11. As shown in Table S1, the single-layer PDLLA scaffold exhibited a contact angle of 131.50 ± 10.71°, confirming the intrinsic hydrophobic character of the polymer. In contrast, the PVP surface displayed markedly lower contact angle of 57.07 ± 17.51°, indicating that the introduction of PVP significantly decreases the hydrophobicity of the scaffold. When HA was incorporated into the PVP layer at a concentration of 3% (w/w), the contact angle further decreased to 36.75 ± 19.41°, suggesting an enhancement in surface hydrophilicity. This trend is consistent with previous studies on HA-coated electrospun scaffolds, which reported the increasing HA content generally leads to more hydrophilic surfaces due to the highly polar nature of HA [54]. Interestingly, when HA-Gly-OH was used as an additive in the PVP layer at the same concentration (3% w/w) a significant increase in SWCA was observed (128.20 ± 12.61°), indicating a more hydrophobic apparent surface behavior. This result may be related to changes in surface organization and fiber morphology induced by the modified HA derivative, which can influence how water droplets interact with the scaffold surface. It should also be considered that electrospun mats are highly porous and typically exhibit considerable surface roughness. Under these conditions, the apparent contact angle is not determined solely by

surface chemistry but can also be strongly affected by the fibrous architecture and by the presence of air pockets trapped within the scaffold. These morphological features can lead to deviations from intrinsic wettability of the materials, often resulting in higher apparent contact angles. In addition, this behavior may partially associated with the shrinkage of the PVP-HA-Gly-OH 3% layer on the PDLLA substrate after processing. This effect, suggested by the reduced thickness of the electrospun layer (Table 3), may lead to a lower effective surface coverage on the top layer. In the bilayer configuration, this could expose a larger fraction of the intrinsically hydrophobic-PDLLA substrate, thereby increasing its contribution to the measured contact angle. Overall, the trends observed here are consistent with previous studies on PCL scaffolds fabricated by-melt-extrusion 3D printing and subsequently functionalized for conjugation with HA-glycine peptides, where surface architecture and coverage were also reported to influence the apparent wettability [33].

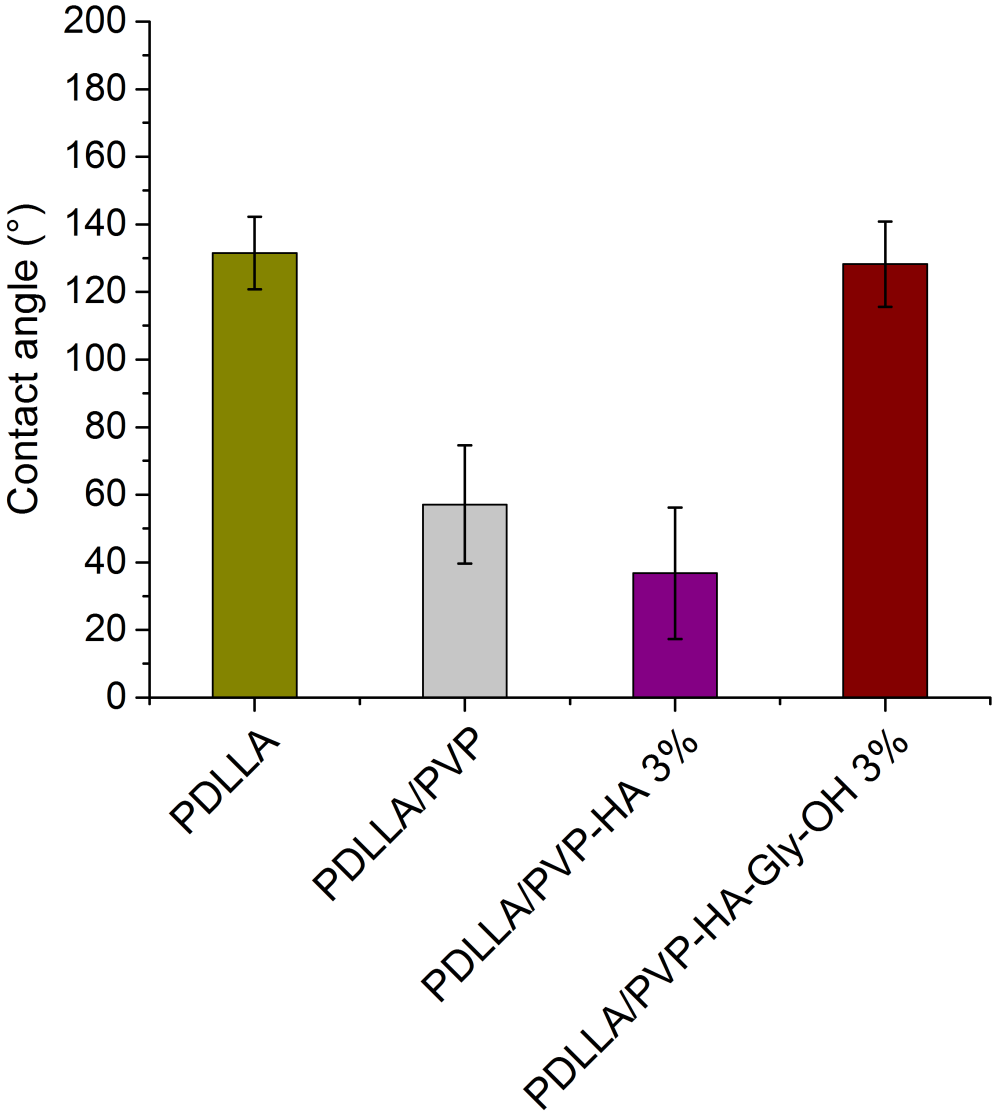

Figure 5. Mean contact angle values (± standard deviation) for electrospun mats of PDLLA, PDLLA/PVP, PDLLA/PVP-HA 3%, and PDLLA/PVP-HA-Gly-OH 3%.

3.4 Mechanical Properties of Electrospun Composites

Figure 6 and Table S2 show the Young's modulus of the electrospun composites materials, calculated by statistically analyzing over 300 force-distance curves for each sample. Although each distribution corresponds to a single scaffold formulation, the measurements were collected from multiple independent AFM acquisitions performed across different regions of the electrospun substrates. Consequently, the reported standard deviations mainly reflect intrinsic spatial heterogeneity of the samples. This extensive data collection enhances the accuracy and reproducibility of the mechanical properties' evaluation and accounts for the inherent heterogeneity and anisotropy of fibrous network, providing a robust characterization of the composite's elastic properties.

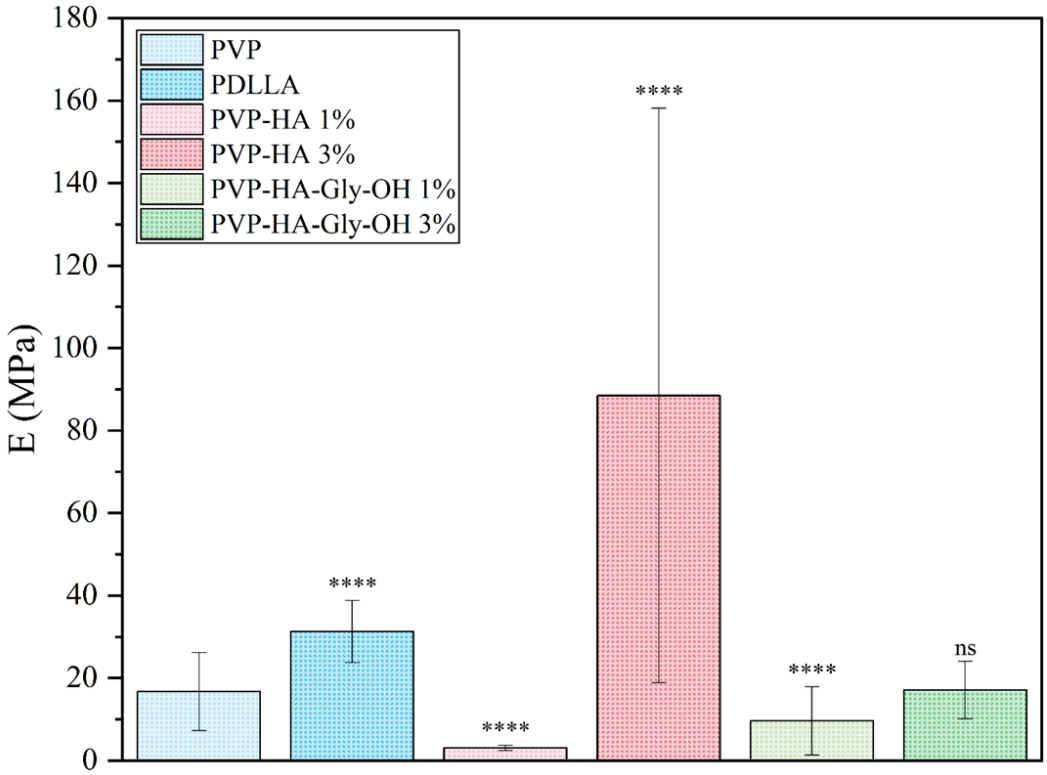

Figure 6. Mean Young's modulus values (± standard deviation) for electrospun mats of PVP, PDLLA, and their blends with HA or HA-Gly-OH at different concentrations (n = 300 per group). Asterisks indicate the level of statistical significance among groups (ns, not significant; *, $p < 0.05$; **, $p < 0.01$; ***, $p < 0.001$; ****, $p < 0.0001$) with PVP as reference sample. All the statistical comparison results are reported in Table S2.

The results clearly demonstrate distinct mechanical behaviors between the internal and external layers of the material. Specifically, PVP fibers, which constitute the internal layer, exhibit a significantly lower Young's modulus compared to the external layer composed of PDLLA fibers. Quantitatively,

the Young's modulus of the PVP fibers is approximately half that of the PDLLA fibers, indicating a much lower stiffness and a higher degree of flexibility.

The mixed solution of HA and PVP induces notable changes in the mechanical properties of the resulting electrospun fibers, with the effect strongly dependent on the concentration of HA present in the blend. At low HA content (1% w/w), a pronounced reduction in Young's modulus was observed in comparison to fibers composed of pure PVP. This behavior could be attributed to the ability of HA chains to disrupt interchain interactions among PVP molecules. Specifically, the introduction of HA increases the free volume within the polymer network, as confirmed by diameter dimensions and enhances the hydrophilicity of the system, leading to a more hydrated and loosely packed fiber structure [55, 56].

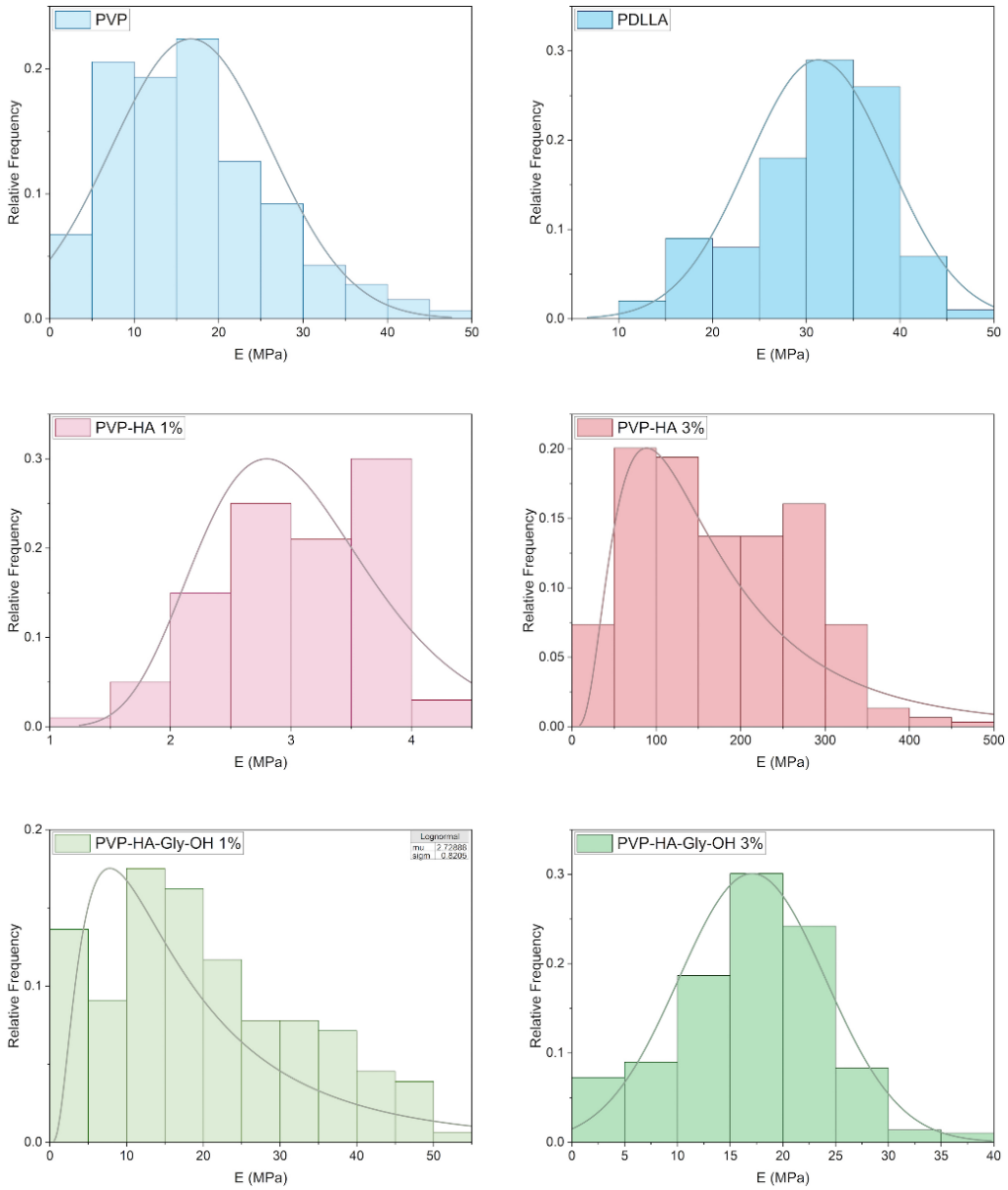

Figure 7. Histogram of electrospun scaffolds Young Modulus (E) distributions for pristine PVP, pristine PDLLA, PVP-HA 1%, PVP-HA 3% and PVP-HA-Gly-OH 1%, and PVP-HA-Gly-OH 3%. Every distribution is based on 300 acquisitions.

These morphological changes collectively contribute to a reduction in overall stiffness, i.e., the fibers become softer and less cohesive. Interestingly, when the HA concentration increases to 3% w/w, an inverse trend can be observed: the modulus increases significantly, albeit with a high degree of variability. This suggests that at higher loadings, HA no longer acts as a simple softening component, but it likely induces the formation of localized, HA-rich microdomains within the fibrous matrix. These microdomains act as rigid inclusions under mechanical load, thereby increasing the stiffness of the composite fibers. However, the heterogeneous distribution of soft and stiff domains results in

mechanical inconsistency, which is reflected in the variability of the measured modulus values as suggested by mean standard deviation values (± 69.65). Such behavior is consistent with reports on other polymer blends containing polysaccharides, in which phase separation and microstructural heterogeneity lead to complex mechanical responses [57]. As further support for this finding, the datasets exhibit asymmetric distributions. Statistical analysis was performed to evaluate differences in the Young's modulus among the various sample groups. Initially, a one-way analysis of variance (ANOVA) was conducted to assess whether overall differences existed between formulations. Considering the potential heterogeneity of variance among groups, pairwise comparisons were subsequently performed using Welch's t-test, which does not assume homogeneity of variances and is therefore more suitable for this dataset. This combined approach allowed us to identify both the overall effect of formulation on mechanical properties and the specific differences between individual groups with high degree of statistical robustness.The conjugation of Gly-OH to HA significantly alters the mechanical response of the fiber system. At a lower concentration (HA-Gly-OH 1% w/w), the Young's modulus increases compared to the PVP-HA 1% formulation, yet it remains substantially lower than that of bare PVP fibers. This indicates that Gly-OH conjugation helps to restore the network's coherent structure, providing limited reinforcement of the polymer matrix. Because Gly-OH contains reactive groups that can interact electrostatically and generate hydrogen bonds with both PVP and HA, its presence decreases chain mobility and increases interfacial adhesion. The resulting network is more compact and uniformly connected, somewhat offsetting the stiffness reduction caused by HA at low concentrations. In contrast, when the HA concentration increases, i.e. HA-Gly-OH 3% w/w, the mechanical behavior shifts markedly.

The Young's modulus reaches that of bare PVP, and no statistically significant difference was observed. This result implies that Gly-OH effectively prevents the formation of rigid, HA-rich microdomains typically associated with high HA content, thereby promoting a more uniform and homogeneous phase distribution within the fiber network. Gly-OH enhances the uniform distribution of HA within the PVP matrix, minimizing local stress peaks and resulting in a steadier and more consistent mechanical behavior. In general, these results indicate that Gly-OH functions as a network modifier. Its presence optimizes the chemical and physical interactions between PVP and HA, adding binding motifs that enhance miscibility and interfacial compatibility. As a result, the rigidity of the fibers can be modified by simultaneously managing the HA concentration and Gly-OH content, leading to materials with tunable and reproducible mechanical properties. This interpretation is consistent with earlier research demonstrating that covalent functionalization or modification of pendant groups on HA greatly influences the viscoelastic and mechanical properties of hybrid networks [58-60]. Statistical analysis confirms that the Young's modulus of the electrospun mats is significantly influenced by

both HA concentration and the presence of Gly-OH, as demonstrated by a two-way ANOVA ($p \ll 0.001$). The pairwise comparisons reveal highly significant differences among most formulations (****), with the only exception being the comparison between bare PVP and PVP–HA–Gly-OH 3%, which do not reach statistical significance. This further supports the observation that Gly-OH conjugation at higher HA concentrations effectively restores the mechanical properties to levels comparable with the unmodified polymer.

The pronounced difference in mechanical properties is crucial for applications requiring a gradient in mechanical performance, such as in layered scaffolds for tissue engineering, where the mechanical mismatch can be tailored to mimic the native tissue architecture or to enhance the integration between layers.

In this context, the local Young's modulus values measured by AFM nanoindentation for the present electrospun scaffolds fall within the broad range reported for skin and skin-mimicking materials at comparable scales. The elastic properties of native human skin span, a very wide range depending on anatomical location, hydration state, age, and, most importantly, on the measurement technique and length scale considered. Reported Young's modulus values range from a few kPa to several tens, or even over one hundred MPa, reflecting the highly anisotropic and viscoelastic nature of skin tissue. For instance, suction-based measurements typically yield elastic moduli in the range of approximately 0.05–0.15 MPa, torsional tests report values around 0.4–0.9 MPa, while uniaxial tensile tests on excised skin commonly result in Young's modulus values between 4 and 20 MPa [61, 62]. At smaller length scales or under localized indentation, higher apparent moduli—reaching several tens of MPa—have also been reported [61, 63]. Overall, this mechanical compatibility, combined with the bilayer architecture, suggests that the developed scaffolds are particularly suitable for superficial and partial-thickness wounds, where conformability, flexibility, and local mechanical cues supporting fibroblast activity are critical.

.

3.5 Evaluation of Cytocompatibility of Electrospun Scaffolds

The cytocompatibility of single/double-layer electrospun scaffolds was evaluated by assessing L929 fibroblast viability at 24 and 48 hours post-seeding. Untreated cells served as the control group, with viability normalized to 100% (Figure 6).

Cells cultured on PVP-only scaffolds exhibited a slight but statistically significant reduction in cell viability at 24 hours (**$p < 0.01$), while no significant difference was observed. However, this effect was no longer evident at 48 hours, suggesting a transient cytotoxic response that may be mitigated over time as cells adapt to the scaffold microenvironment. In contrast, PDLLA scaffolds, widely employed in biomedical applications due to their biodegradability and mechanical strength, showed no statistically significant difference in cell viability compared to untreated cells at either time point, confirming their acceptable biocompatibility. Scaffolds incorporating 1% w/w hyaluronic acid (PVP-HA 1%) maintained viability levels significantly higher than untreated cells at both time points, highlighting HA's contribution to scaffold biocompatibility. HA is known to support cell adhesion and proliferation through interactions with CD44 receptors, while and its hydrophilic nature, which improves scaffold hydration and mimics ECM properties thereby creating a favorable environment for fibroblast growth [64]. Interestingly, increasing the HA concentration to 3% w/w (PVP-HA 3%) resulted in a significant decrease in cell viability (**,°°$p < 0.01$), suggesting that excessive HA may disrupt scaffold architecture or osmotic balance, thereby impairing cell–material interactions [23, 65]. Similar trends have been reported in literature, where high HA content led to scaffold swelling and reduced mechanical integrity ultimately compromising cellular compatibility [66]. The addition of Gly-OH to HA-modified scaffolds significantly enhanced cell viability at both time points. PVP-HA-Gly-OH 1% scaffolds showed the highest cell proliferation, even surpassing untreated cells. Rather than acting as a cell-adhesion motif, glycine is more likely to influence scaffold performance through its physicochemical properties. As a small zwitterionic amino acid, glycine can act as humectant and plasticizer, improving moisture retention, flexibility, and hydrophilicity of the scaffold. These features help stabilize the membrane structure, reduce cytotoxic stress, and facilitate nutrient exchange, thereby indirectly supporting cell growth. This interpretation is consistent with previous studies demonstrating that bioactive additives can modulate scaffold hydration and mechanical behavior to enhance biocompatibility. For instance, Pepe et al. highlighted how chemical modifications in HA-based electrospun scaffolds and highlighted the role of functional groups in enhancing cell adhesion and proliferation by improving hydrophilicity and mimicking the ECM-like environment, promoting cell adhesion and proliferation [23]. Additionally, Niu and Galluzzi demonstrated that HA/collagen nanofiber scaffolds support endothelial cell proliferation and phenotypic maintenance, due to HA's physicochemical properties [67].

Although PVP-HA-GlyOH 3% scaffolds also showed increased viability compared to PVP-HA 3% alone, they remained significantly lower than untreated cells, suggesting that glycine's beneficial effects may be limited when paired with higher HA concentrations. These results reinforce the importance of balanced scaffold composition. The PVP-HA-GlyOH 1% formulation consistently demonstrated superior cytocompatibility and was therefore selected for further development in bilayer scaffold design.

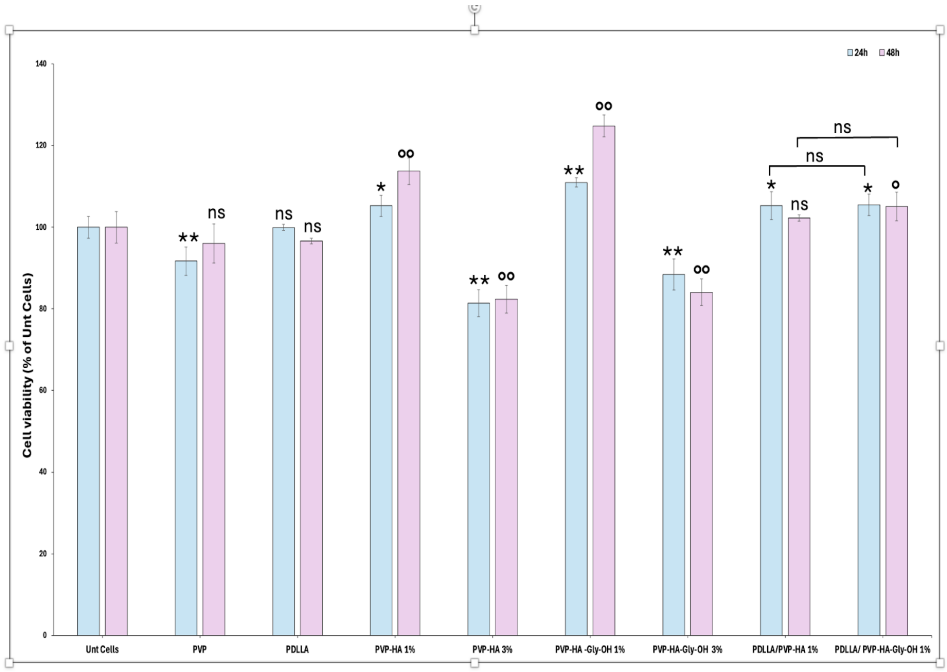

	24h	48h
Unt Cells vs PVP	**p<0.01	ns
Unt Cells vs PDLLA	ns	ns
Unt Cells vs PVP-HA 1%	*p<0.05	°°p<0.01
Unt Cells vs PVP-HA 3%	**p<0.01	°°p<0.01
Unt Cells vs PVP-HA Gly-OH 1%	**p<0.01	°°p<0.01
Unt Cells vs PVP-HA-Gly-OH 3%	**p<0.01	°°p<0.01
Unt Cells vs PDLLA/PVP-HA 1%	*p<0.05	ns
Unt Cells vs PDLLA/ PVP-HA -Gly-OH 1%	*p<0.05	°p<0.05
PDLLA/PVP-HA 1% vs PDLLA/ PVP-HA-Gly-OH 1%	ns	ns

Figure 8. Cell viability of L929 fibroblasts cultured on various electrospun scaffold formulations at 24 and 48 hours. Bar graph showing cell viability (% of untreated cells) for seven treatment groups: Untreated Cells, PVP, PDLLA, PVP-HA 1%, PVP-HA 3%, PVP-HA-Gly-OH 1%, and PVP-HA-Gly-OH 3%, PDLLA/PVP-HA1%, and PDLLA/PVP-HA-Gly-OH 1%. Blue bars represent viability at 24 hours; pink bars represent viability at 48 hours. Error bars indicate standard deviation. Statistical significance is denoted as follows: **,°°p < 0.01, *,°p < 0.05, ns = not significant.

Cells cultured on PDLLA/PVP-HA1% scaffolds exhibited viability levels comparable to untreated cells at both time points, with no statistically significant differences observed at 48 h (ns). This suggests that the combination of PDLLA and 1% w/w of hyaluronic acid provides a biocompatible environment favorable to cell survival. PDLLA is widely recognized for its biodegradability and mechanical strength, while HA contributes to scaffold hydration and cell–matrix interactions, making this blend suitable for biomedical applications [66].

In contrast, the PDLLA/PVP-HA-Gly-OH 1% scaffolds demonstrated a statistically significant increase in cell viability at both 24 hours (*p< 0.05) and 48 hours (°p < 0.05). However, no significant differences were observed when compared to the PDLLA/PVP-HA 1% scaffolds at either time point.

This enhancement indicates a synergistic effect between HA and Gly-OH, where glycine likely improves moisture retention and scaffold flexibility, thereby promoting membrane stability and reducing oxidative stress [68]. The sustained increase in viability over time suggests that the bilayer structure not only supports initial cell attachment but also facilitates ongoing proliferation.

These findings are consistent with previous studies showing that bilayer electrospun scaffolds can mimic the extracellular matrix and provide a favorable microenvironment for cell growth. For instance, Petrova et al. demonstrated that bilayer chitosan/alginate scaffolds enhanced mesenchymal stem cell proliferation due to their high porosity and layered architecture [66]. Similarly, Mohammadalizadeh et al. emphasized the importance of blending synthetic and natural polymers to improve scaffold biocompatibility and mechanical performance [68]. Overall, the PDLLA/PVP-HA-Gly-OH 1% formulation emerged as the most promising candidate for further development, offering superior cytocompatibility and potential for tissue engineering applications.

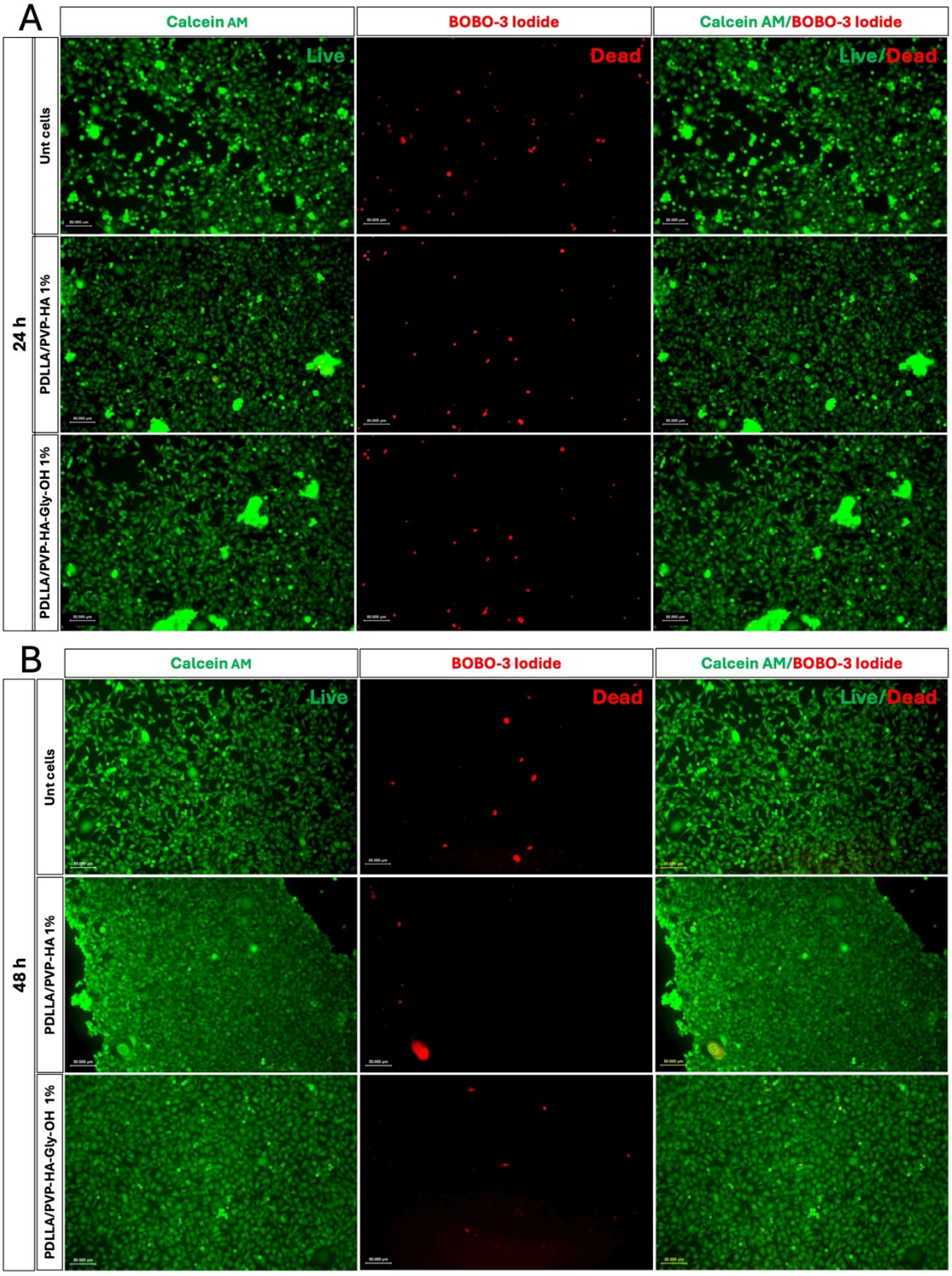

Figure 9. Live/dead fluorescence imaging of L929 fibroblasts cultured on bilayer electrospun scaffolds. Representative fluorescence microscopy images showing cell viability after 24h (panel A) and 48h (panel B), under three conditions: Untreted cells (control), PDLLA/PVP-HA 1%, and PDLLA/PVP-HA-Gly-OH 1%. Columns display staining with Calcein AM (green, viable cells), BOBO-3 Iodide (red, non-viable cells), and merged images.

To further assess the cytocompatibility of the bilayer electrospun scaffolds, live/dead staining was performed using Calcein AM and BOBO-3 Iodide to visualize viable and non-viable L929 fibroblasts, respectively (Figure 9). Both scaffold formulations, PDLLA/PVP-HA 1% and PDLLA/PVP-HA-Gly-OH 1%, exhibited strong green fluorescence with minimal red signal, comparable to untreated cells, confirming high cell viability across all conditions. Cells appeared well spread and uniformly distributed, indicating favorable scaffold architecture and optimal culture conditions. Notably, the PDLLA/PVP-HA-Gly-OH 1% scaffold demonstrated a slightly more pronounced enhancement in cell viability relative to PDLLA/PVP-HA 1% alone. This suggests that the incorporation of glycine may have beneficially influenced the scaffold's physicochemical properties. These modifications are critical for promoting cell adhesion, reducing oxidative stress, and maintaining integrity during culture. Enhanced wettability and porosity resulting from glycine incorporation may also facilitate nutrient diffusion and waste removal, further supporting cell survival and proliferation. These observations align with previous findings that glycine-modified electrospun scaffolds can improve cellular responses by mimicking native ECM characteristics and enhancing biocompatibility. For instance, Niemczyk-Soczynska et al. highlighted that hydrophilic surface functionalization of electrospun nanofibers significantly improves cell adhesion and proliferation by enhancing bioactivity and ECM mimicry [69]. Additionally, Ruccolo et al. reviewed the role of electrospun bio-scaffolds in promoting mesenchymal stem cell differentiation, emphasizing the importance of scaffold surface chemistry and architecture in modulating cell behavior [70]. Furthermore, El-Ghoul et al. reported that bioactive additives in electrospun scaffolds, such as natural compounds and amino acids, can enhance wound healing and cellular compatibility by improving scaffold hydrophilicity and mechanical properties [71].

Taken together, the fluorescence imaging results reinforce the quantitative viability data and confirm that the PDLLA/PVP-HA-Gly-OH 1% bilayer scaffold offers a more favorable microenvironment for fibroblast growth. This formulation holds promise for further development in tissue engineering applications where scaffold biocompatibility and cellular integration are crucial.

3.6. Sol (SF) and Gel Fraction (GF)

SF and GF were calculated to evaluate the stability of the individual electrospun layers and the material loss following immersion in an aqueous environment. This analysis allows the distinction between the soluble fraction (sol fraction), consisting of non-crosslinked or weakly bound material released into the solution, and those insoluble (gel fraction), which represents the stable polymeric network responsible for maintaining the structural integrity of the scaffold.

Table 4. Mean sol and gel fraction values (± standard deviation).

Scaffold	Sol-fraction (%)	Gel fraction (%)
PVP	42 ± 16	58 ± 16
PVP-HA 1%	57 ± 5	43 ± 5
PVP-HA-Gly-OH 1%	30 ± 5	71 ± 5

As reported in Table 4, PVP, PVP-HA 1%, and PVP-HA-Gly-OH 1% displayed SF values of 42 ± 16%, 57 ± 5%, and 30% ± 5%, respectively. Statistical analysis, including one-way ANOVA followed by Tukey's post-hoc test, revealed significant differences among the different scaffold types (Figure 10). In particular, PVP-HA 1% showed a significantly higher material loss compared to pure PVP, with a statistically significant difference (**, $p < 0.01$). This result indicates reduced stability of HA-containing scaffolds in aqueous environments.

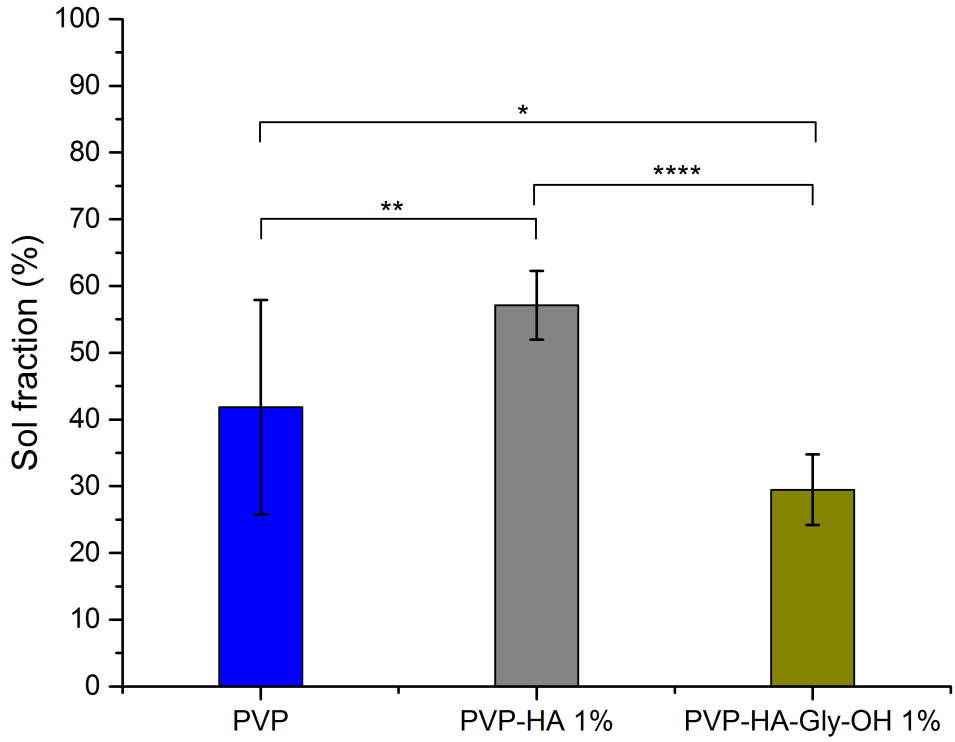

Figure 10 Mean Sol-fraction values (± standard deviation) for electrospun scaffolds of PVP, PVP-HA 1% and, PVP-HA-Gly-OH 1%. Asterisks indicate the level of statistical significance among groups (*, $p < 0.05$; **, $p < 0.01$; ****, $p < 0.0001$).

In contrast, PVP-HA-Gly-OH 1% exhibited the lowest sol fraction, resulting in significantly higher stability compared to both PVP scaffolds (*, $p < 0.05$) and PVP-HA 1% w/w scaffolds (****, $p < 0.0001$). Consequently, GF values were 58 ± 16%, 43% ± 5%, and 71% ± 5% for the same type of scaffolds. The data obtained for PVP are in agreement with results published by Catalani and co-workers [72], as well the values obtained for PVP-HA 1% could be associated with the hydrophilicity of native polysaccharide. Surprisingly, the behavior of PVP-HA-Gly-OH 1% suggests that functionalization of hyaluronic acid with glycine contributes to improving material stability by reducing dissolution in aqueous environments. It is important to acknowledge that the conditions employed for sol and gel fraction calculations are to be regarded as initial screening. However, to overcome this limitation and to confirm the degradation behavior in a more physiological environment, such as in phosphate buffer solution, future analyses are necessary.

3.7. Cumulative Release

The cumulative release of HA and HA-Gly-OH was investigated by UV−Vis spectroscopy in a pH 5.5 sodium acetate solution at 570 nm. The cumulative drug release was expressed in terms of percentage according to a convenient calibration curve and showed values compatible between PVP-HA 1% and PVP-HA-Gly-OH 1%. The maximum degree of release was obtained after 2 h, when PVP-HA 1% and PVP-HA-Gly-OH 1% displayed percentages of 15 ± 4% and 14 ± 2%, respectively. Moreover, a nearly linear sustained release was observed from 4h to 24h (Figure 11), where the absorbance value reached a plateau.

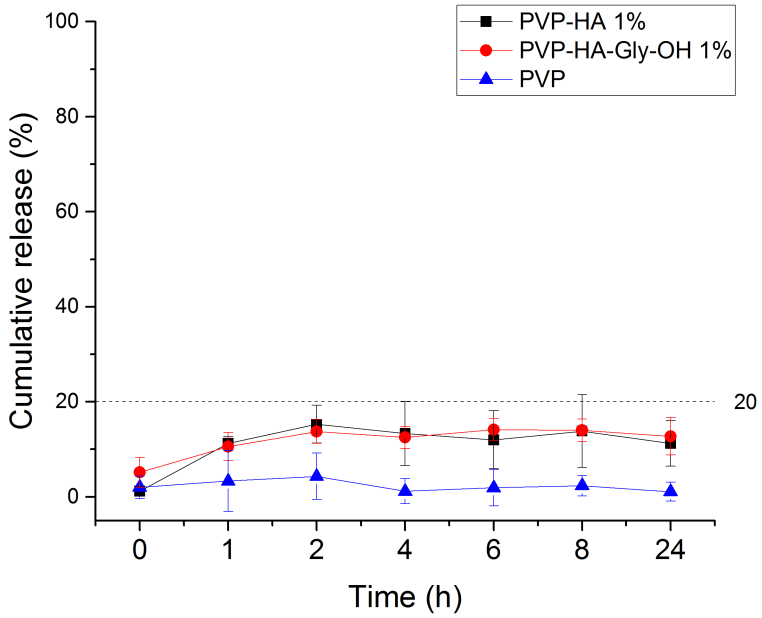

Figure 11. Cumulative release (± standard deviation) of HA, and HA-Gly-OH and PVP from 0 to 24h.

The rate of both HA and HA-Gly-OH release is hypothesized to be related to entrapped native and semi-synthetic polysaccharide within the polymer network of the crosslinked electrospun scaffold, providing resistance to the diffusion out of the swollen matrix. It is worth noting that during the photochemical crosslinking of the electrospun scaffolds, a reaction between PVP and both HA and HA-Gly-OH may occur, potentially reducing their cumulative release. This phenomenon has been observed during the UV irradiation of chitosan/PVP blends, where polysaccharide hydroxyl radicals can react with PVP to form a crosslinked structure [73].

After the cumulative release, the presence of hyaluronic acid within PVP-HA 1% fibers has been qualitatively evaluated by the phenol colorimetric assay. The scaffolds have been suspended in water,

then treated with a 5% aqueous phenolic solution and concentrated sulfuric acid. Finally, the absorbance was measured at 490 nm. As it can be seen in Figure S12, the sample containing HA is characterized by a yellow-brown solution, differently from the PVP sample and the blank. This colour is attributed to HA that is still present within the fibers and that could be available after a degradation. Moreover, a further evaluation of HA presence within the fibers, the cumulative release was conducted on an uncrosslinked PVP-HA 1% electrospun scaffold. In this case, the maximum degree of release was obtained after 1h, where a percentage of 85 ± 2% was observed. (Figure S13). It is worth noting that this analysis has been performed in pH 5.5 acetate buffer, providing a relevant proof-of-concept for the intended application. However, the medium does not fully replicate the complex ionic composition of a physiological environment. Therefore, future release studies in phosphate buffer solution are needed to confirm the release profile.

4. Conclusions

This study reports the successful fabrication and characterization of an electrospun bilayer wound dressing system, consisting of the external PDLLA layer and an internal PVP-based layer incorporating either native HA or semi-synthetic HA-Gly-OH at concentrations of 1% and 3% w/w. While bilayer scaffolds electrospun on different days delaminated, they maintained their integrity when electrospun on the same day. The cross section imaged by SEM images reveal intimate interfaces between PDLLA and PVP layers with achieved thickness suggesting the absence of layer mixing. Sol-gel testing on photochemically crosslinked scaffolds proved the stability in aqueous solution of the scaffolds which is functional to the obtention of the slow release of hyaluronic acid tested at the maximum level of 20%. Mechanical testing revealed distinct behaviors between the two layers, with both native HA and HA-Gly-OH significantly modulating scaffold stiffness in a concentration-dependent manner. Biocompatibility assays demonstrated that while each layer was individually compatible with fibroblasts, higher concentrations of HA and HA-Gly-OH induced a dose-dependent cytotoxic response. Based on these findings, formulations containing 1% w/w of polysaccharide additives were selected for bilayer scaffold development. Notably, the PDLLA/PVP-HA-Gly-OH 1% bilayer demonstrated increased cell viability, highlighting the beneficial role of glycine in improving scaffold physicochemical properties and supporting cellular responses. Overall, the results highlight the potential of this bilayer electrospun system for application as a medical device. Future *in vitro* and *in vivo* studies are required to further validate its therapeutic efficacy, biocompatibility, and long-term stability under physiological conditions.

Supplementary Materials: The following supporting information can be downloaded at: https://www.mdpi.com/article/doi/s1

Author Contributions: A.L., F.A., M.C. K.S.-L.: Investigation, methodology, data curation, and writing—original draft; L.F., S.M., P.C., and I.I: Methodology, writing—original draft; G.D.L: writing—review and editing; G.M.L.M, G.C.: Conceptualization, formal analysis, writing—review and editing, funding acquisition and resources; A.P., and B.B.: Conceptualization, project administration, supervision, resources, funding acquisition, and writing—review and editing. All authors have read and agreed to the published version of the manuscript.

Funding: This work was supported by Ecosistema di Innovazione “Rome Technopole” funded by MUR,– Spoke 3-University education, industrial PhD courses, internationalization. Project BEST-DRESS—Biomimetic Electrospun Scaffold as susTainable wound DRESSing device, CUP F33C24000360006, ECS_0000024 Rome Technopole—PNRR Mission 4, Component 2, Investment 1.5, funded by the European Union—NextGenerationEU.

Institutional Review Board Statement: Not applicable

Data Availability Statement: Data is contained within the article or Supplementary Materials.

Acknowledgments: The authors thank Tania Ruspandini and the Laboratory of Electron Microscopy and Microanalysis of the Department of Earth Sciences, Sapienza University of Rome, for the SEM analysis, performed with FEI Quanta 400 high resolution field ESEM instrument. The authors thank Alessandro Laurita of the University of Basilicata for the cross-section analyses performed with Philips-Fei ESEM XL30-LaB6 instrument.

Conflicts of Interest: The authors declare no conflicts of interest.

Abbreviations

The following abbreviations are used in this manuscript:

AFM	Atomic force microscopy
ATCC	American Type Culture Collection
ATR-FT-IR	Attenuated total reflectance Fourier transform infrared spectroscopy
CTAB	Cetyltrimethyl ammonium bromide
DMEM	Dulbecco's Modified Eagle Medium High Glucose
DMSO	Dimethylsulfoxide
DMT	Derjaguin–Muller–Toporov
DS	Degree of substitution
DSS	3-(Trimethylsilyl)propionic-2,2,3,3-d_4 acid sodium salt
ECM	Extracellular matrix
EDC·HCl	*N*-(3-(Dimethylamino)propyl)-*N*'-ethylcarbodiimide hydrochloride
FBS	Fetal bovine serum
GAGs	Glycosaminoglycans
GlcA	D-glucuronic acid
GlcNAc	*N*-acetyl-D-glucosamine
Gly-OEt ·HCl	Glycine ethyl ester hydrochloride
HA	Hyaluronic acid
HFP	1,1,1,3,3,3-Hexafluoro-2-propanol
MES	2-(*N*-Morpholino)ethanesulfonic acid hydrate
MTT	3-(4,5-dimethylthiazol-2-yl)-2,5-diphenyltetrazolium bromide
NaCl	Sodium chloride
NaOH	Sodium hydroxide
NMR	Nuclear magnetic resonance
PBS	Phosphate-buffered saline
PDLLA	Poly-D,L-lactide
PSA	Penicillin/streptomycin/amphotericin B
PVP	Polyvnylpyrrolidone
SEM	Scanning electron microscopy
SWCA	Static water contact angle
s-NHS	*N*-Hydroxysulfosuccinimide sodium salt
UPW	Ultra-pure water

Supporting Information

Sequential Electrospinning of Asymmetric PDLLA/PVP-HA Scaffolds Functionalized with Glycine for Medical Devices

Antonio Laezza[1†], Francesca Armiento[1†], Luigi Fabiano[2], Serena Munaò[3], Paola Campione[2], Matteo Carrozzino[1], Ileana Ielo[3], Katja Schenke-Layland[4,5] Giovanna De Luca[2], Grazia Maria Lucia Messina[2], Giovanna Calabrese[3], Antonietta Pepe[1*], Brigida Bochicchio[1*]

Table of contents

Figure S1. ^{1}H-NMR spectrum of HA-Gly-OEt in D_2O	**87**
Figure S2. ^{1}H-NMR spectrum of HA-Gly in H_2O/D_2O 9:1 v/v	**88**
Figure S3. Fibers diameter distribution for neat PVP, neat PDLLA, PVP-HA 1%, PVP-HA 3%, PVP-HA-Gly-OH 1%, and PVP-HA-Gly-OH 3% electrospun scaffolds	**89**
Figure S4. Pore area distribution for neat PVP, neat PDLLA, PVP-HA 1%, PVP-HA 3%, PVP-HA-Gly-OH 1%, and PVP-HA-Gly-OH 3% electrospun scaffolds	**90**
Figure S5. Cross-section SEM images of PDLLA/PVP bilayer electrospun scaffolds	**91**
Figure S6- Cross-section SEM images of PDLLA/PVP-HA 1% bilayer electrospun scaffolds	**92**
Figure S7. Cross-section SEM images of PDLLA/PVP-HA 3% bilayer electrospun scaffolds	**93**
Figure S8. Cross-section SEM images of PDLLA/PVP-HA-Gly-OH 1% bilayer electrospun scaffolds	**94**
Figure S9. Cross-section SEM images of PDLLA/PVP-HA-Gly-OH 3% bilayer electrospun scaffolds	**95**
Figure S10. Effect of electrospinning timing on delamination of bilayer electrospun scaffolds	**96**
Figure S11. Contact angle measurement for neat PDLLA, PDLLA/PVP, PDLLA-PVP-HA 3%, and PDLLA-PVP-HA-Gly-OH 3%	**97**
Table S1. Contact angle values for neat PDLLA, PDLLA/PVP, PDLLA/PVP-HA 3%, and PDLLA/PVP-HA-Gly-OH 3%	**98**
Table S2. Young's Modulus (E) values of the electrospun scaffolds	**98**
Table S3. Pairwise statistical comparisons of Young's modulus values	**99**
Figure S12. Phenol assay results for PVP and PVP-HA 1% electrospun scaffolds	**100**
Figure S13. Cumulative release of HA from uncrosslinked PVP-HA 1% electrospun scaffolds	**101**

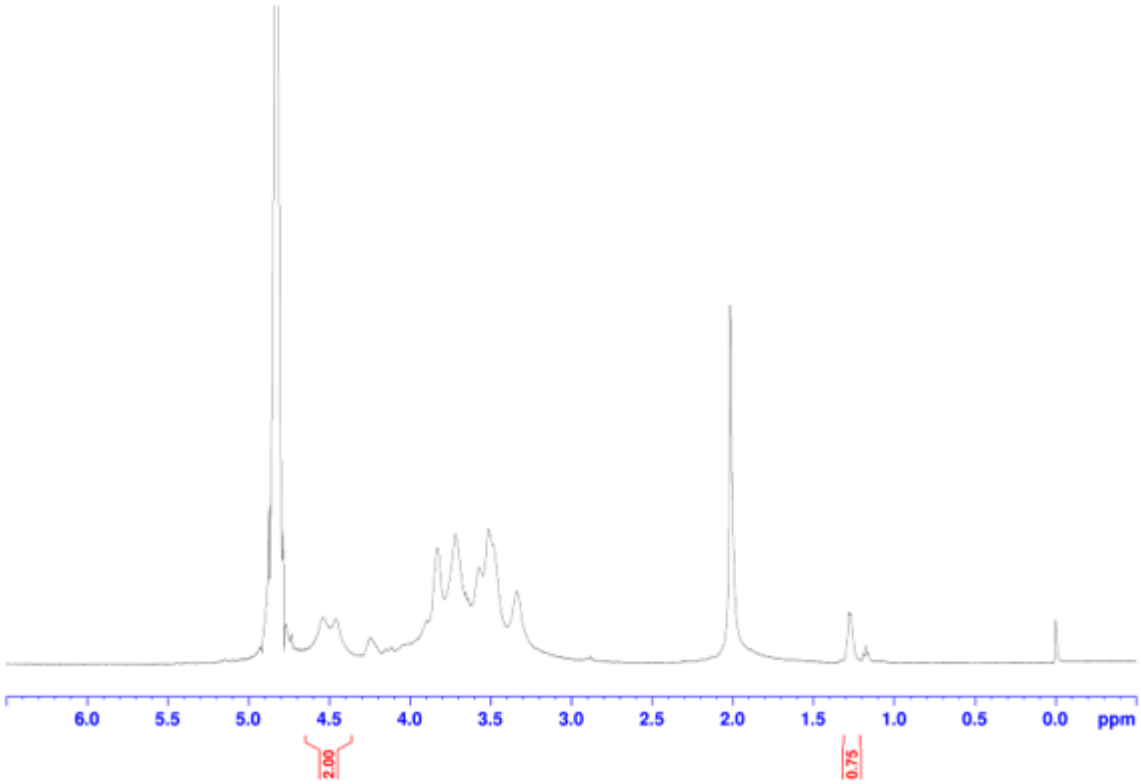

Figure S1. ^{1}H-NMR spectrum of HA-Gly-OEt (500 MHz, D_2O, 25 °C).

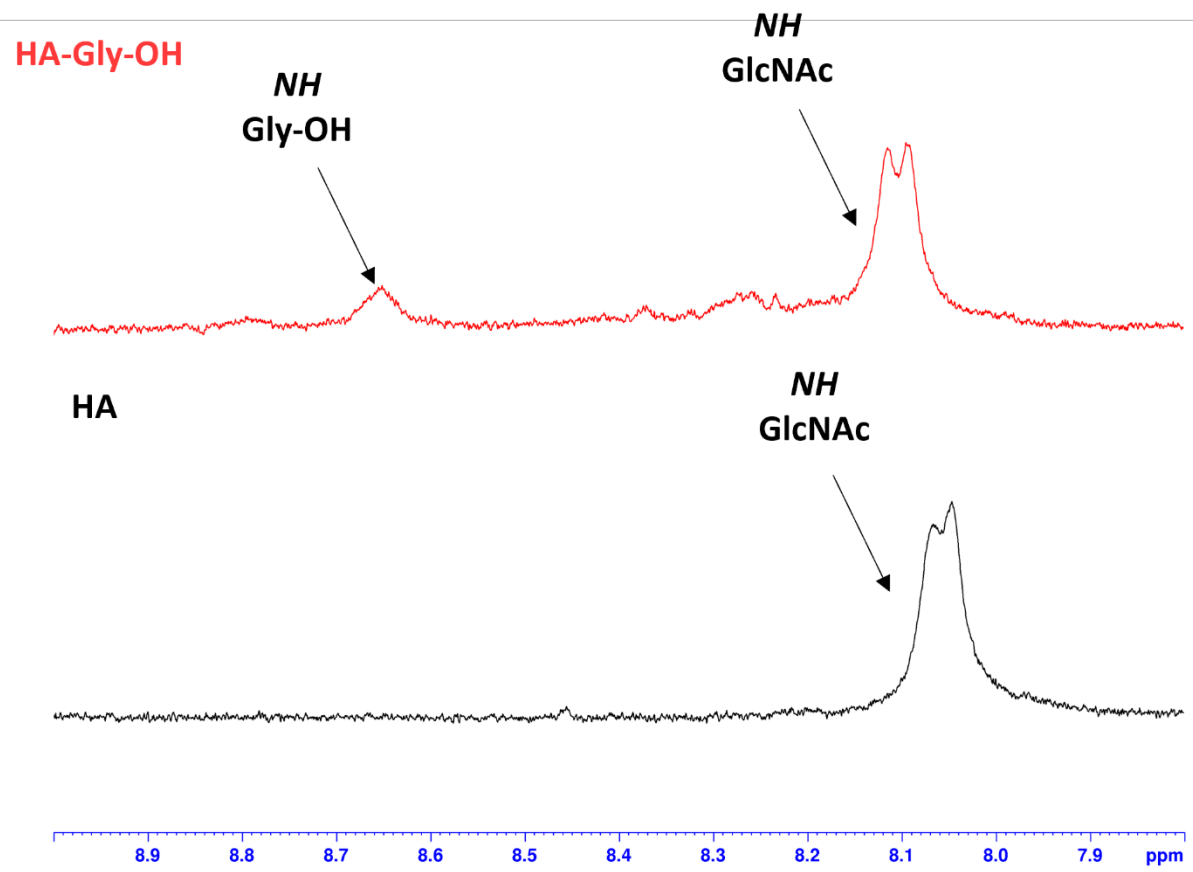

Figure S2. ^{1}H-NMR spectrum of HA (black), and HA-Gly-OH (400 MHz, H_2O/D_2O 9:1 v/v, 25 °C).

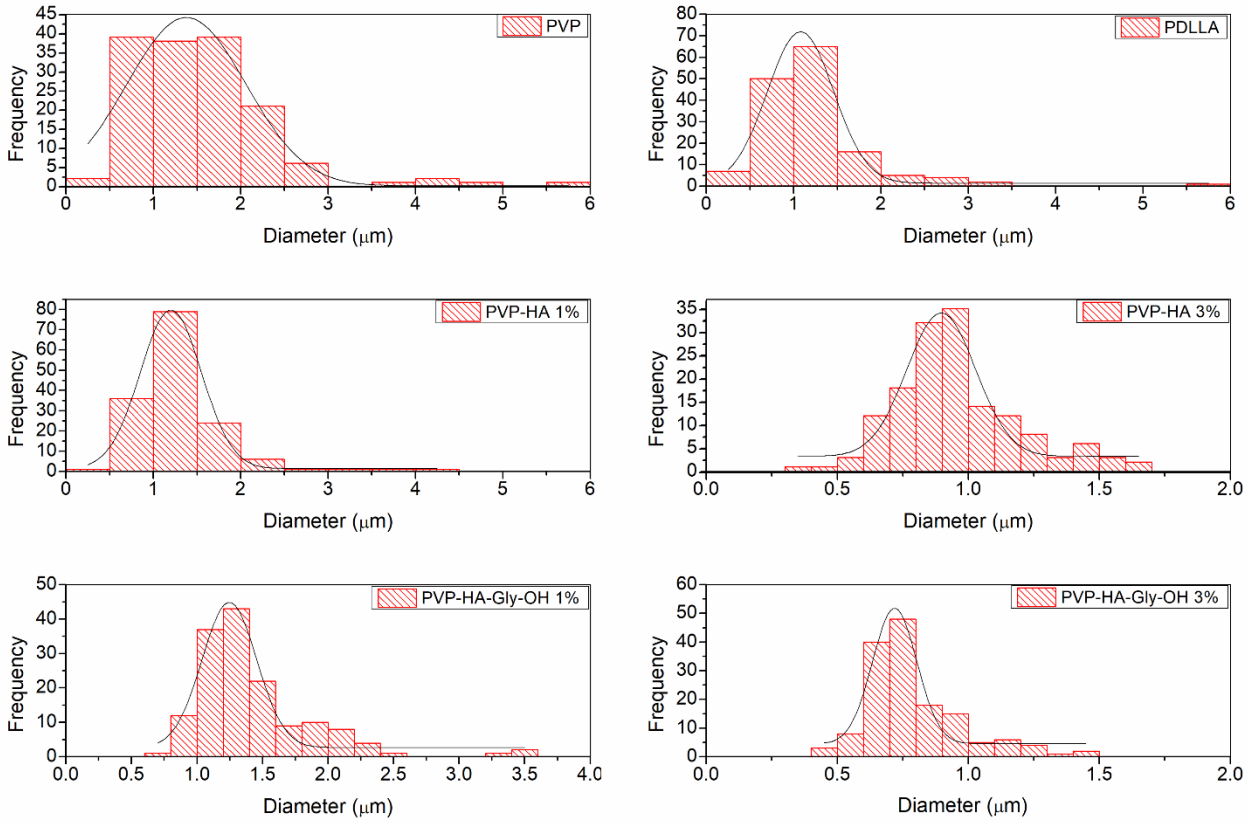

Figure S3. Fibers diameter distribution for neat PVP, neat PDLLA, PVP-HA 1%, PVP-HA 3%, PVP-HA-Gly-OH 1%, and PVP-HA-Gly-OH 3%. Every distribution is based on 50 individual fibers measured from three different images obtained from one scaffold, for a total of 150.

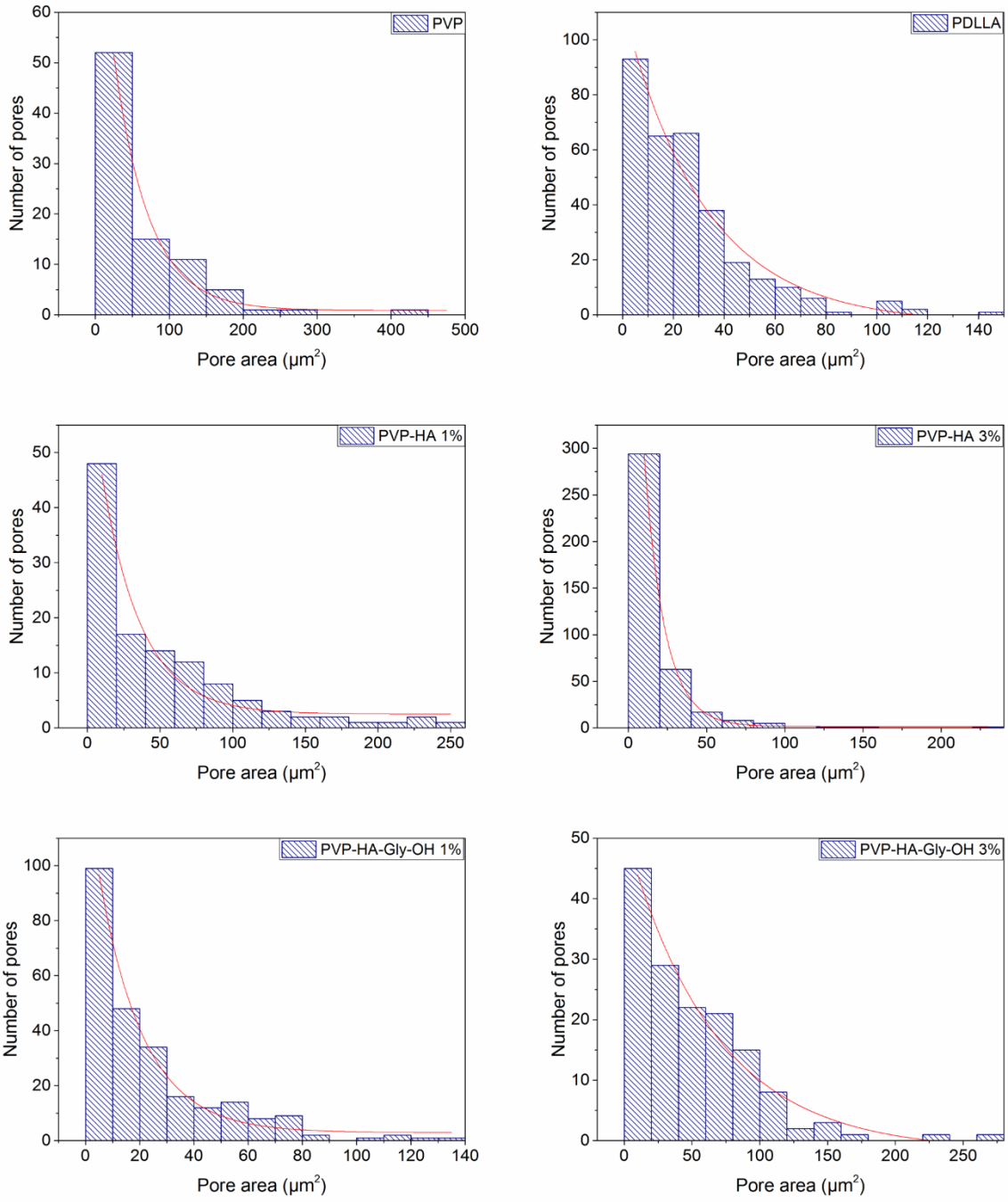

Figure S4. Pore area diameter distribution for neat PVP, neat PDLLA, PVP-HA 1%, PVP-HA 3%, PVP-HA-Gly-OH 1%, and PVP-HA-Gly-OH 3% electrospun scaffolds.

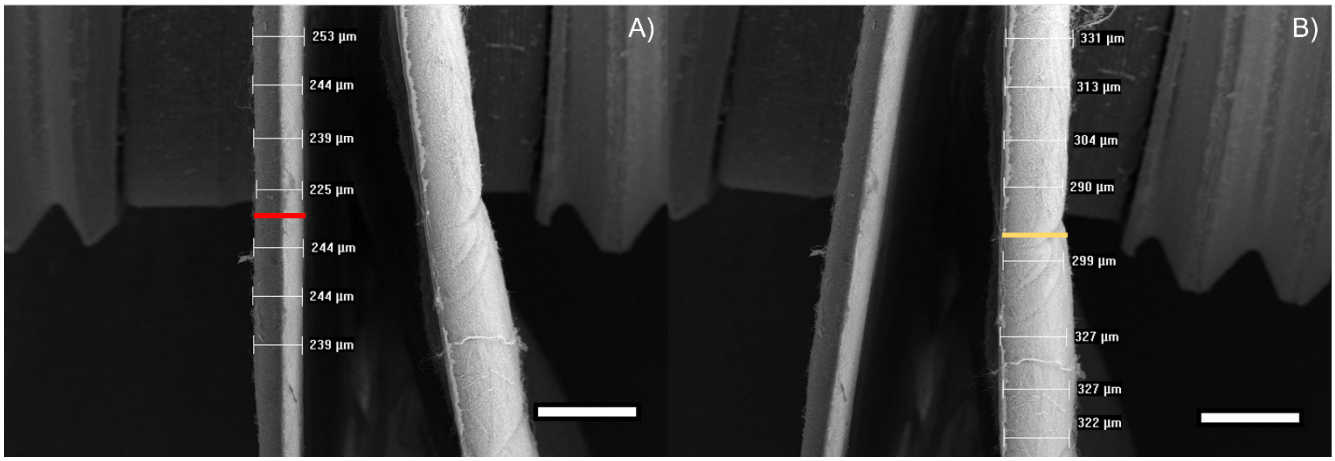

Figure S5. Cross-section SEM images of PDLLA/PVP bilayer electrospun scaffolds (bar: 500 µm). PDLLA (A), PVP (B).

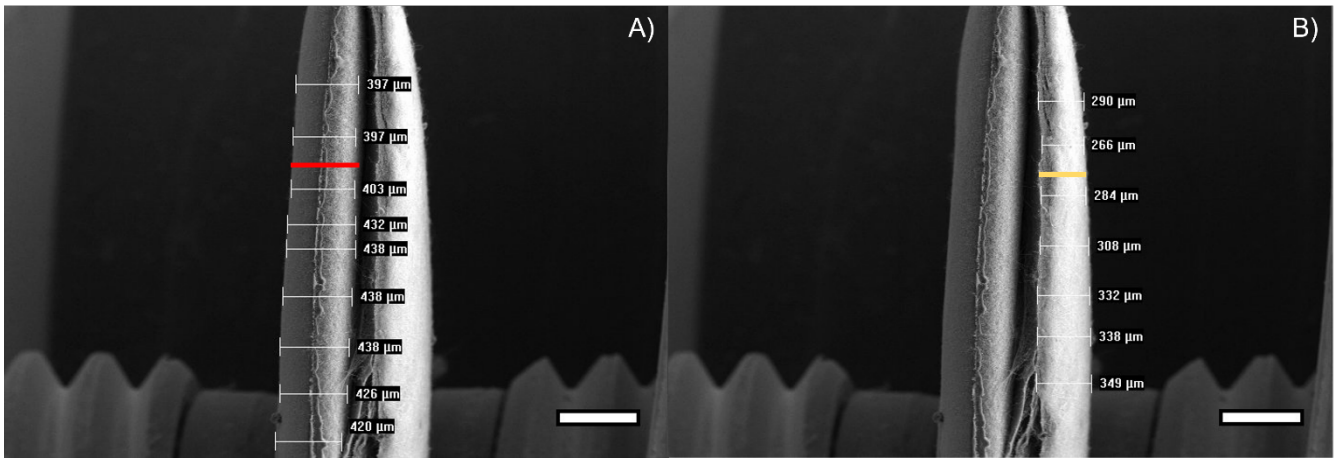

Figure S6. Cross-section SEM images of PDLLA/PVP-HA 1% bilayer electrospun scaffolds (bar: 500 µm). PDLLA (A), PVP-HA 1% (B).

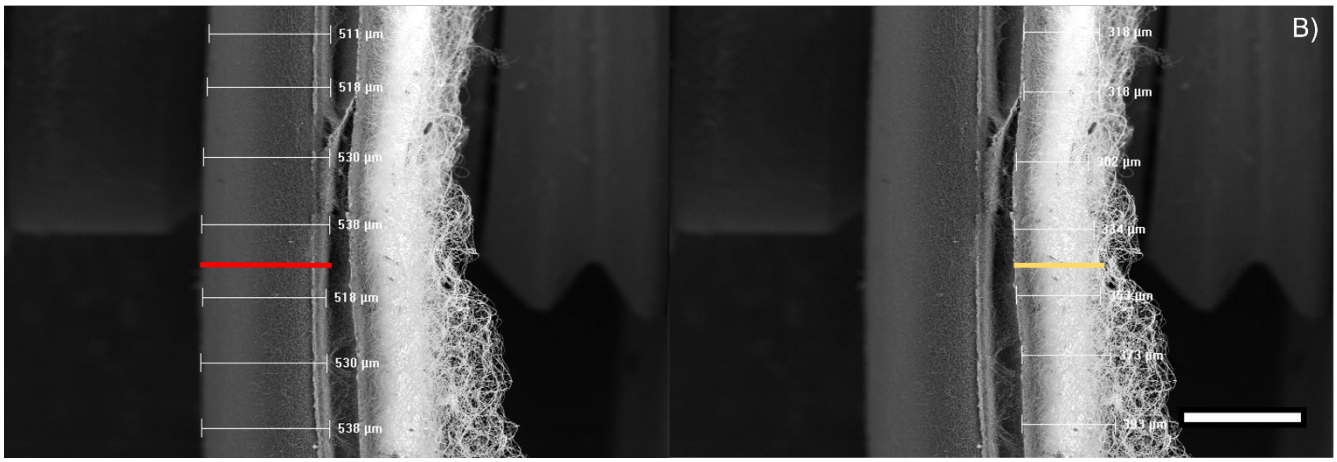

Figure S7. Cross-section SEM images of PDLLA/PVP-HA 3% bilayer electrospun scaffolds (bar: 500 µm). PDLLA (A), PVP-HA 3% (B).

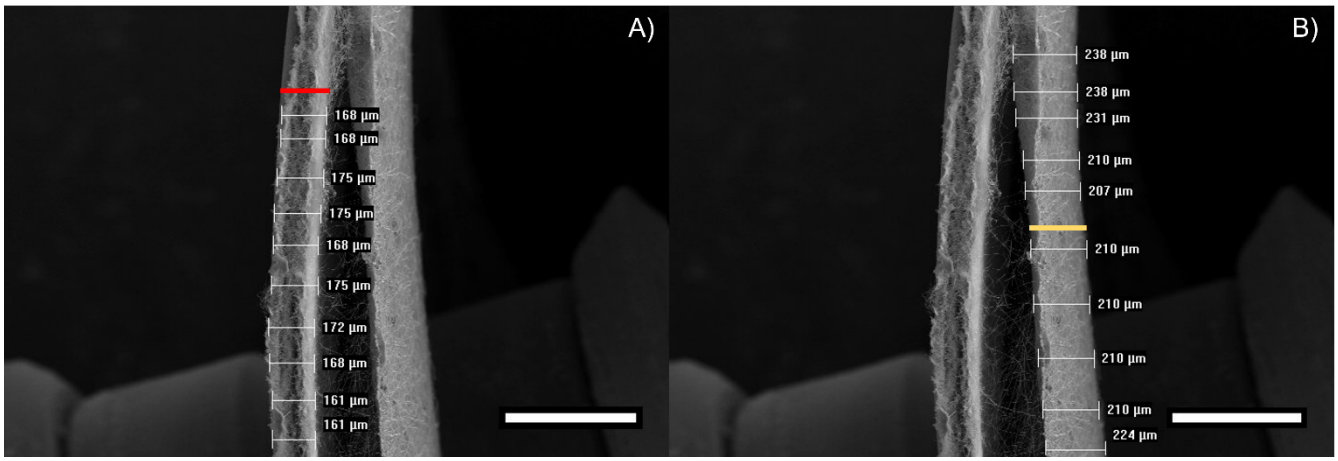

Figure S8. Cross-section SEM images of PDLLA/PVP-HA-Gly-OH 1% bilayer electrospun scaffolds (bar: 500 µm). PDLLA (A), PVP-HA-Gly-OH 1% (B).

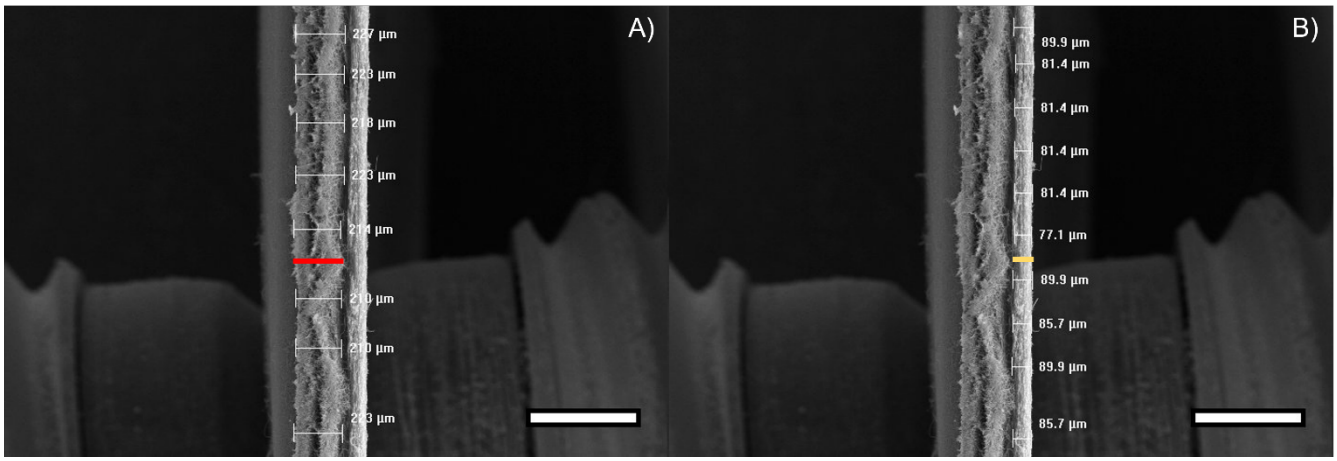

Figure S9. Cross-section SEM images of PDLLA/PVP-HA-Gly-OH 3% bilayer electrospun scaffolds (bar: 500 µm). PDLLA (A), PVP-HA-Gly-OH 3% (B).

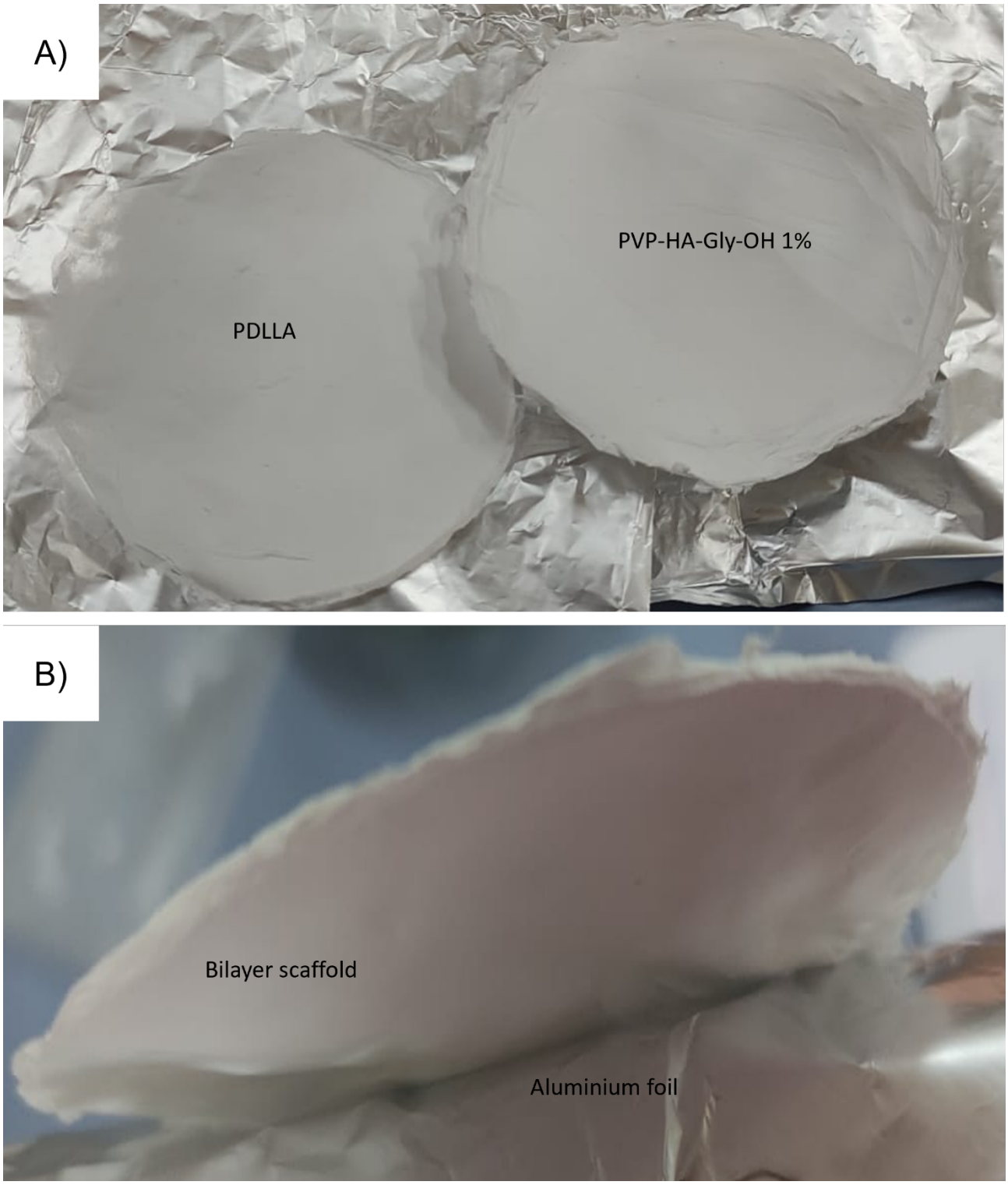

Figure S10. Effect of electrospinning timing on delamination. Bilayer prepared on consecutive days (A), and on the same day (B).

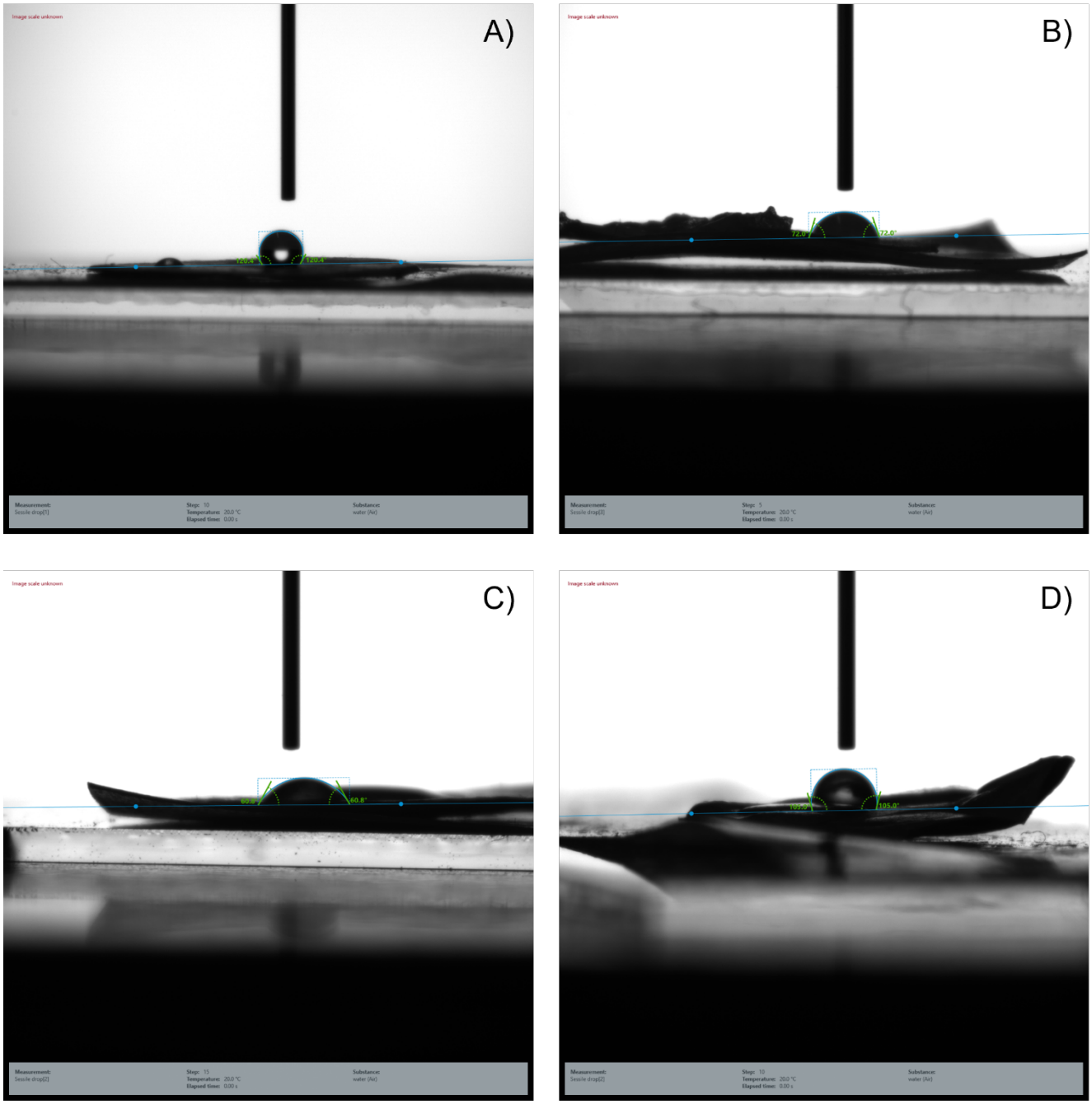

Figure S11. Contact angle measurement for: A) neat PDLLA, B) PDLLA/PVP, C) PDLLA/PVP-HA 3%, and D) PDLLA/PVP-HA-Gly-OH 3%.

Table S1. Contact angle values reported as mean value ± st. deviation (n = 3).

Scaffold	Contact angle (°)	Standard deviation (°)
PDLLA	131.50	10.71
PDLLA/PVP	57.07	17.51
PDLLA/PVP-HA 3%	36.75	19.41
PDLLA/PVP-HA-Gly-OH 3%	128.20	12.61

Table S2. Young Modulus (E) values reported as mean value ± st. deviation (n = 300).

Scaffold	E (MPa)	Standard deviation (MPa)
PDLLA	31.29	7.56
PVP	16.70	9.49
PVP-HA 1%	3.06	0.68
PVP-HA 3%	88.49	69.65
PVP-HA-Gly-OH 1%	33.97	16.19
PVP-HA-Gly-OH 3%	17.08	6.97

Table S3. Pairwise statistical comparisons of Young's modulus values among all sample groups. Reported p-values were calculated using Welch's t-test, and levels of significance are indicated as follows: ns = not significant, * = $p < 0.05$, ** = $p < 0.01$, *** = $p < 0.001$, **** = $p < 0.0001$.

Sample 1	**Sample 2**	**p-value**	**Significance**
PVP	PDLLA	4.4E-37	****
PVP	PVP-HA 1%	4.7E-75	****
PVP	PVP-HA 3%	6.7E-49	****
PVP	PVP-HA-Gly-OH 1%	8E-18	****
PVP	PVP-HA-Gly-OH 3%	0.576	ns
PDLLA	PVP-HA 1%	1.3E-60	****
PDLLA	PVP-HA 3%	5.6E-35	****
PDLLA	PVP-HA-Gly-OH 1%	0.136	ns
PDLLA	PVP-HA-Gly-OH 3%	1.7E-36	****
PVP-HA 1%	PVP-HA 3%	1.1E-61	****
PVP-HA 1%	PVP-HA 1%_GlyOH	5.5E-35	****
PVP-HA 1%	PVP-HA-GlyOH 3%	1.2E-108	****
PVP-HA 3%	PVP-HA-GlyOH 1%	1.7E-30	****
PVP-HA 3%	PVP-HA-Gly-OH 3%	1.3E-48	****
PVP-HA-Gly-OH 1%	PVP-HA-Gly-OH 3%	1.8E-17	****

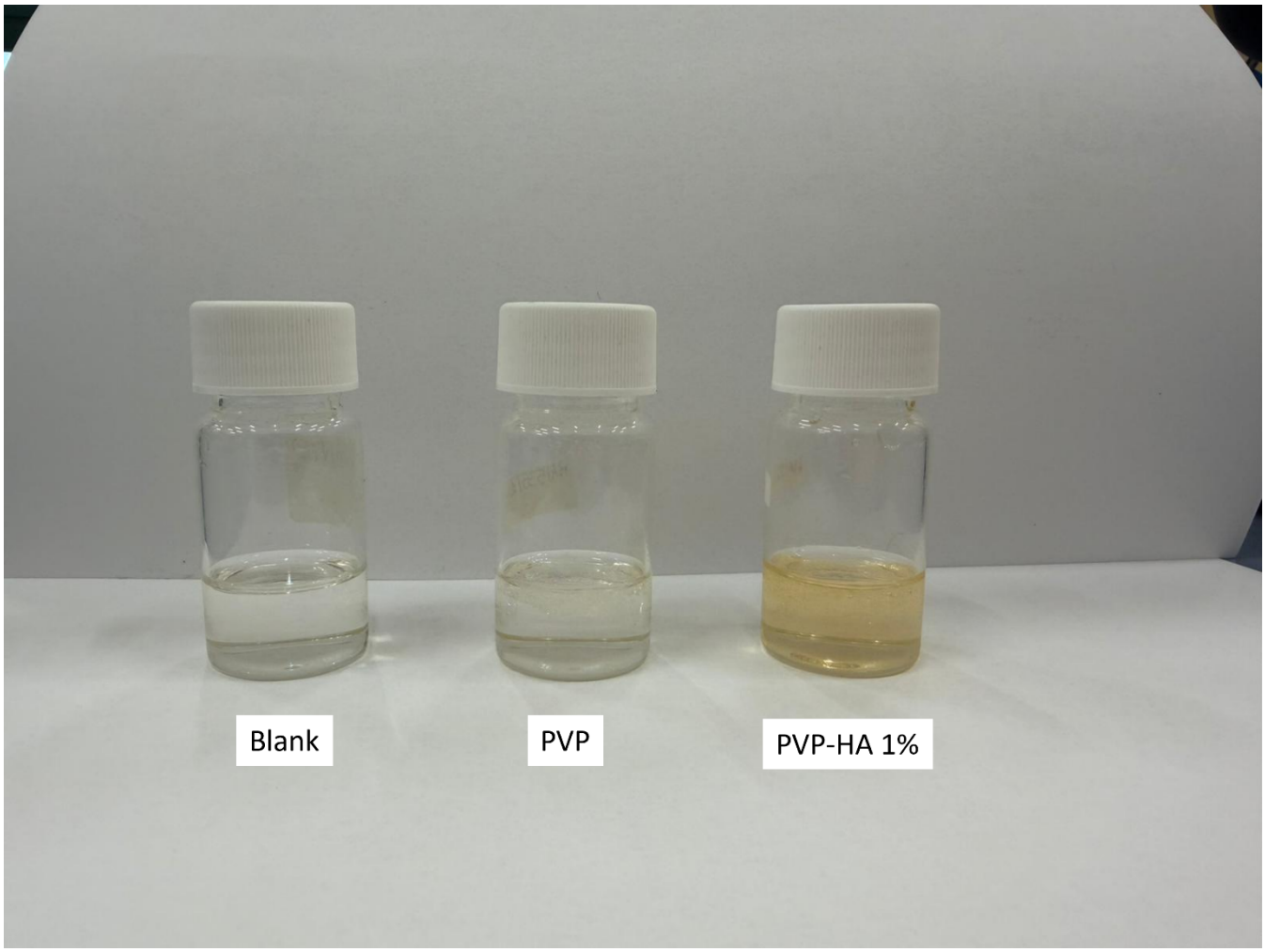

Figure S12. Phenol assay results for PVP and PVP-HA 1% electrospun scaffolds.

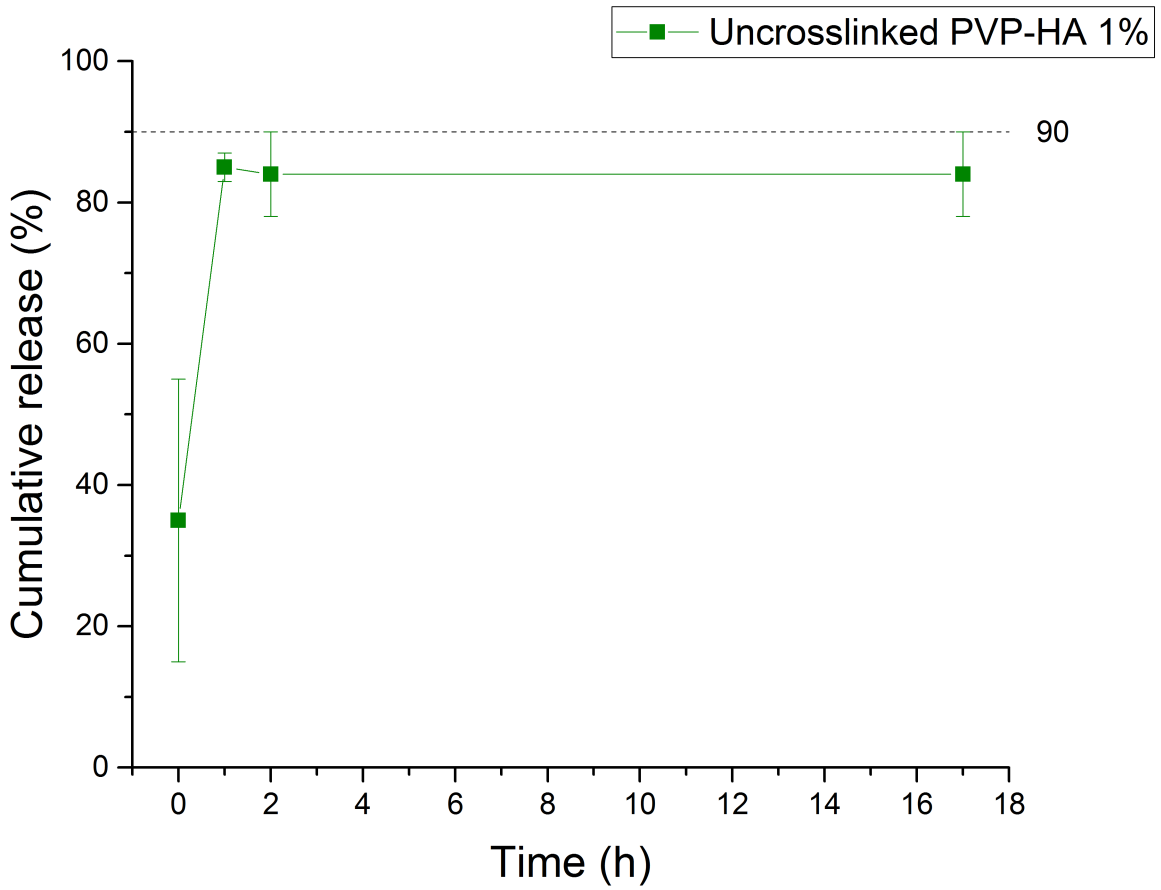

Figure S13. Cumulative release of HA from uncrosslinked PVP-HA 1% electrospun scaffolds**.**

References

[1] Byrd, A. L.; Belkaid, Y.; Segre, J. A., *The human skin microbiome.* Nat. Rev. Microbiol. **2018**, 16, (3), 143–155.

[2] Kabashima, K., *Overview: Immunology of the Skin.* In Immunology of the Skin: Basic and Clinical Sciences in Skin Immune Responses, Kabashima, K., Ed. Springer Japan: Tokyo, **2016**; pp 1–11.

[3] Takeo, M.; Lee, W.; Ito, M., *Wound healing and skin regeneration.* Cold Spring Harb. Perspect. Med. **2015**, 5, (1), a023267.

[4] Nestle, F. O.; Di Meglio, P.; Qin, J. Z.; Nickoloff, B. J., *Skin immune sentinels in health and disease.* Nat. Rev. Immunol. **2009**, 9, (10), 679–91.

[5] Negut, I.; Grumezescu, V.; Grumezescu, A. M., *Treatment Strategies for Infected Wounds.* Molecules **2018**, 23, (9).

[6] Gurtner, G. C.; Werner, S.; Barrandon, Y.; Longaker, M. T., *Wound repair and regeneration.* Nature **2008**, 453, (7193), 314–21.

[7] Calvanese, L.; Brun, P.; Messina, G. M. L.; Russo, T.; Zamuner, A.; Falcigno, L.; D'Auria, G.; Gloria, A.; Vitagliano, L.; Marletta, G.; Dettin, M., *EAK Hydrogels Cross-Linked by Disulfide Bonds: Cys Number and Position Are Matched to Performances.* ACS Biomater. Sci. Eng. **2020**, 6, (2), 1154–1164.

[8] Manso Silván, M.; Messina, G. M. L.; Montero, I.; Satriano, C.; Ruiz, J. P. G.; Marletta, G., *Aminofunctionalization and sub-micrometer patterning on silicon through silane doped agarose hydrogels.* J. Mater. Chem. **2009**, 19, (29), 5226–5233.

[9] Farahani, M.; Shafiee, A., *Wound Healing: From Passive to Smart Dressings.* Adv. Healthc. Mater. **2021**, 10, (16), e2100477.

[10] Memic, A.; Abudula, T.; Mohammed, H. S.; Joshi Navare, K.; Colombani, T.; Bencherif, S. A., *Latest Progress in Electrospun Nanofibers for Wound Healing Applications.* ACS Appl. Bio Mater **2019**, 2, (3), 952–969.

[11] Haik, J.; Kornhaber, R.; Blal, B.; Harats, M., *The Feasibility of a Handheld Electrospinning Device for the Application of Nanofibrous Wound Dressings.* Adv Wound Care (New Rochelle) **2017**, 6, (5), 166–174.

[12] Abrigo, M.; McArthur, S. L.; Kingshott, P., *Electrospun nanofibers as dressings for chronic wound care: advances, challenges, and future prospects.* Macromol. Biosci. **2014**, 14, (6), 772–92.

[13] Graca, M. F. P.; de Melo-Diogo, D.; Correia, I. J.; Moreira, A. F., *Electrospun Asymmetric Membranes as Promising Wound Dressings: A Review.* Pharmaceutics **2021**, 13, (2).

[14] Mousavi, S. M.; Zarei, M.; Hashemi, S. A.; Ramakrishna, S.; Chiang, W.-H.; Lai, C. W.; Gholami, A.; Omidifar, N.; Shokripour, M., *Asymmetric Membranes: A Potential Scaffold for Wound Healing Applications.* Symmetry **2020**, 12, (7), 1100.

[15] Zhang, T.; Xu, H.; Zhang, Y.; Zhang, S.; Yang, X.; Wei, Y.; Huang, D.; Lian, X., *Fabrication and characterization of double-layer asymmetric dressing through electrostatic spinning and 3D printing for skin wound repair.* Mater. Des. **2022**, 218, 110711.

[16] Yu, B.; He, C.; Wang, W.; Ren, Y.; Yang, J.; Guo, S.; Zheng, Y.; Shi, X., *Asymmetric Wettable Composite Wound Dressing Prepared by Electrospinning with Bioinspired Micropatterning Enhances Diabetic Wound Healing.* ACS Appl. Bio Mater. **2020**, 3, (8), 5383–5394.

[17] Xing, J.; Zhang, M.; Liu, X.; Wang, C.; Xu, N.; Xing, D., *Multi-material electrospinning: from methods to biomedical applications.* Mater. Today Bio **2023**, 21, 100710.

[18] Graca, M. F. P.; Miguel, S. P.; Cabral, C. S. D.; Correia, I. J., *Hyaluronic acid-Based wound dressings: A review.* Carbohydr. Polym. **2020**, 241, 116364.

[19] Frenkel, J. S., *The role of hyaluronan in wound healing.* Int. Wound J. **2014**, 11, (2), 159–63.

[20] Chen, W. Y. J., *FUNCTIONS OF HYALURONAN IN WOUND REPAIR.* In Hyaluronan, Kennedy, J. F.; Phillips, G. O.; Williams, P. A., Eds. Woodhead Publishing: **2002**; pp 147–156.

[21] Voigt, J.; Driver, V. R., *Hyaluronic acid derivatives and their healing effect on burns, epithelial surgical wounds, and chronic wounds: a systematic review and meta-analysis of randomized controlled trials.* Wound Repair Regen. **2012**, 20, (3), 317–31.

[22] Hintze, V.; Schnabelrauch, M.; Rother, S., *Chemical Modification of Hyaluronan and Their Biomedical Applications.* Front. Chem. **2022**, 10, 830671.

[23] Pepe, A.; Laezza, A.; Armiento, F.; Bochicchio, B., *Chemical Modifications in Hyaluronic Acid-Based Electrospun Scaffolds.* Chempluschem **2024**, 89, (7), e202300599.

[24] Chanda, A.; Adhikari, J.; Ghosh, A.; Chowdhury, S. R.; Thomas, S.; Datta, P.; Saha, P., *Electrospun chitosan/polycaprolactone-hyaluronic acid bilayered scaffold for potential wound healing applications.* Int. J. Biol. Macromol. **2018**, 116, 774–785.

[25] Ebrahimi-Hosseinzadeh, B.; Pedram, M.; Hatamian-Zarmi, A.; Salahshour-Kordestani, S.; Rasti, M.; Mokhtari-Hosseini, Z. B.; Mir-Derikvand, M., *In vivo evaluation of gelatin/hyaluronic acid nanofiber as Burn-wound healing and its comparison with ChitoHeal gel.* Fibers Polym. **2016**, 17, (6), 820–826.

[26] Ielo, I.; Bauso, L. V.; Laezza, A.; Campione, P.; Fabiano, L.; Pastorello, M.; Marino, A.; Laurita, A.; Pepe, A.; Bochicchio, B.; De Luca, G.; Messina, G. M. L.; Calabrese, G., *In Vitro Assessment of Electrospun PVP+AgNPs Scaffolds for Bioactive Medical Use.* Int. J. Mol. Sci. **2025**, 26, (18).

[27] Kurakula, M.; Koteswara Rao, G. S. N., *Moving polyvinyl pyrrolidone electrospun nanofibers and bioprinted scaffolds toward multidisciplinary biomedical applications.* Eur. Polym. J. **2020**, 136, 109919.
[28] Schanté, C. E.; Zuber, G.; Herlin, C.; Vandamme, T. F., *Improvement of hyaluronic acid enzymatic stability by the grafting of amino-acids.* Carbohydr. Polym. **2012**, 87, (3), 2211–2216.
[29] Schanté, C. E.; Zuber, G.; Herlin, C.; Vandamme, T. F., *Chemical modifications of hyaluronic acid for the synthesis of derivatives for a broad range of biomedical applications.* Carbohydr. Polym. **2011**, 85, (3), 469–489.
[30] Adhikari, J.; Dasgupta, S.; Das, P.; Gouripriya, D. A.; Barui, A.; Basak, P.; Ghosh, M.; Saha, P., *Bilayer regenerated cellulose/quaternized chitosan-hyaluronic acid/collagen electrospun scaffold for potential wound healing applications.* Int. J. Biol. Macromol. **2024**, 261, 129661.
[31] Petrova, V. A.; Chernyakov, D. D.; Poshina, D. N.; Gofman, I. V.; Romanov, D. P.; Mishanin, A. I.; Golovkin, A. S.; Skorik, Y. A., *Electrospun Bilayer Chitosan/Hyaluronan Material and Its Compatibility with Mesenchymal Stem Cells.* Materials **2019**, 12, (12), 2016.
[32] Arnal-Pastor, M.; Martínez Ramos, C.; Pérez Garnés, M.; Monleón Pradas, M.; Vallés Lluch, A., *Electrospun adherent–antiadherent bilayered membranes based on cross-linked hyaluronic acid for advanced tissue engineering applications.* Mat. Sci. Eng. C **2013**, 33, (7), 4086–4093.
[33] Mohan, T.; Gürer, F.; Bračič, D.; Lackner, F.; Nagaraj, C.; Maver, U.; Gradišnik, L.; Finšgar, M.; Kargl, R.; Kleinschek, K. S., *Functionalization of Polycaprolactone 3D Scaffolds with Hyaluronic Acid Glycine-Peptide Conjugates and Endothelial Cell Adhesion.* Biomacromolecules **2025**, 26, (3), 1771–1787.
[34] Laezza, A.; Pepe, A.; Solimando, N.; Armiento, F.; Oszust, F.; Duca, L.; Bochicchio, B., *A Study on Thiol-Michael Addition to Semi-Synthetic Elastin-Hyaluronan Material for Electrospun Scaffolds.* Chempluschem **2024**, 89, (3), e202300662.
[35] Laezza, A.; Pepe, A.; Bochicchio, B., *Elastin-Hyaluronan Bioconjugate as Bioactive Component in Electrospun Scaffolds.* Chem. Eur. J. **2022**, 28, (58), e202201959.
[36] Tan, X.; Jain, E.; Barcellona, M. N.; Morris, E.; Neal, S.; Gupta, M. C.; Buchowski, J. M.; Kelly, M.; Setton, L. A.; Huebsch, N., *Integrin and syndecan binding peptide-conjugated alginate hydrogel for modulation of nucleus pulposus cell phenotype.* Biomaterials **2021**, 277, 121113.
[37] Sader, J. E.; Chon, J. W. M.; Mulvaney, P., *Calibration of rectangular atomic force microscope cantilevers.* Rev. Sci. Instrum. **1999**, 70, (10), 3967–3969.
[38] Derjaguin, B. V.; Muller, V. M.; Toporov, Y. P., *Effect of contact deformations on the adhesion of particles.* J. of Coll. Interface Sci. **1975**, 53, (2), 314–326.

[39] Tüfekci, M.; Durak, S. G.; Pir, İ.; Acar, T. O.; Demirkol, G. T.; Tüfekci, N., *Manufacturing, Characterisation and Mechanical Analysis of Polyacrylonitrile Membranes.* Polymers-Basel **2020**, 12, (10), 2378.

[40] Bruno, T. J. L., D.R., Jr, *CRC Handbook of Chemistry and Physics.* 95th ed ed.; CRC Press: Boca Raton, FL, USA, **2014**.

[41] D'Amora, U.; Ronca, A.; Scialla, S.; Soriente, A.; Manini, P.; Phua, J. W.; Ottenheim, C.; Pezzella, A.; Calabrese, G.; Raucci, M. G.; Ambrosio, L., *Bioactive Composite Methacrylated Gellan Gum for 3D-Printed Bone Tissue-Engineered Scaffolds.* Nanomaterials **2023**, 13, (4), 772.

[42] Szychlinska, M. A.; Calabrese, G.; Ravalli, S.; Parrinello, N. L.; Forte, S.; Castrogiovanni, P.; Pricoco, E.; Imbesi, R.; Castorina, S.; Leonardi, R.; Di Rosa, M.; Musumeci, G., *Cycloastragenol as an Exogenous Enhancer of Chondrogenic Differentiation of Human Adipose-Derived Mesenchymal Stem Cells. A Morphological Study.* Cells **2020**, 9, (2), 347.

[43] Nestor, G.; Sandström, C., *NMR study of hydroxy and amide protons in hyaluronan polymers.* Carbohydr. Polym. **2017**, 157, 920–928.

[44] Blundell, C. D.; DeAngelis, P. L.; Almond, A., *Hyaluronan: the absence of amide-carboxylate hydrogen bonds and the chain conformation in aqueous solution are incompatible with stable secondary and tertiary structure models.* Biochem. J. **2006**, 396, 487–498.

[45] Dodd, R. J.; Blundell, C. D.; Sattelle, B. M.; Enghild, J. J.; Milner, C. M.; Day, A. J., *Chemical modification of hyaluronan oligosaccharides differentially modulates hyaluronan-hyaladherin interactions.* J. Biol. Chem. **2024**, 300, (9), 107668.

[46] Otto, K. E.; Hesse, S.; Wassermann, T. N.; Rice, C. A.; Suhm, M. A.; Stafforst, T.; Diederichsen, U., *Temperature-dependent intensity anomalies in amino acid esters: weak hydrogen bonds in protected glycine, alanine and valine.* Phys. Chem. Chem. Phys. **2011**, 13, (31), 14119–14130.

[47] Morgado, P. I.; Aguiar-Ricardo, A.; Correia, I. J., *Asymmetric membranes as ideal wound dressings: An overview on production methods, structure, properties and performance relationship.* J. Membr. Sci. **2015**, 490, 139–151.

[48] Grimaudo, M. A.; Concheiro, A.; Alvarez-Lorenzo, C., *Crosslinked Hyaluronan Electrospun Nanofibers for Ferulic Acid Ocular Delivery.* Pharmaceutics **2020**, 12, (3).

[49] Rnjak-Kovacina, J.; Weiss, A. S., *Increasing the pore size of electrospun scaffolds.* Tissue Eng. Part. B Rev. **2011**, 17, (5), 365–72.

[50] Schwartz, J. B., *Log-Normal Distribution of Tablet Pore Diameters.* J. Pharm. Sci. **1974**, 63, (5), 774–776.

[51] Ambekar, R. S.; Kandasubramanian, B., *Advancements in nanofibers for wound dressing: A review.* Eur. Polym. J. **2019**, 117, 304–336.

[52] Saghazadeh, S.; Rinoldi, C.; Schot, M.; Kashaf, S. S.; Sharifi, F.; Jalilian, E.; Nuutila, K.; Giatsidis, G.; Mostafalu, P.; Derakhshandeh, H.; Yue, K.; Swieszkowski, W.; Memic, A.; Tamayol, A.; Khademhosseini, A., *Drug delivery systems and materials for wound healing applications.* Adv. Drug Deliv. Rev. **2018**, 127, 138–166.

[53] Kitsara, M.; Blanquer, A.; Murillo, G.; Humblot, V.; De Braganca Vieira, S.; Nogues, C.; Ibanez, E.; Esteve, J.; Barrios, L., *Permanently hydrophilic, piezoelectric PVDF nanofibrous scaffolds promoting unaided electromechanical stimulation on osteoblasts.* Nanoscale **2019**, 11, (18), 8906–8917.

[54] Piccirillo, G.; Feuerer, N.; Carvajal Berrio, D. A.; Layland, S. L.; Reimer Hinderer, S.; Bochicchio, B.; Schenke-Layland, K., *Hyaluronic Acid-Functionalized Hybrid Gelatin–Poly-L-Lactide Scaffolds with Tunable Hydrophilicity.* Tissue Eng. Part C: Methods **2021**, 27, (11), 589–604.

[55] Di Mola, A.; Landi, M. R.; Massa, A.; D'Amora, U.; Guarino, V., *Hyaluronic Acid in Biomedical Fields: New Trends from Chemistry to Biomaterial Applications.* Int. J. Mol. Sci. **2022**, 23, (22), 14372.

[56] Lewandowska, K.; Szulc, M., *Characterisation of Hyaluronic Acid Blends Modified by Poly(N-Vinylpyrrolidone).* Molecules **2021**, 26, (17), 5233.

[57] Burdick, J. A.; Prestwich, G. D., *Hyaluronic Acid Hydrogels for Biomedical Applications.* Adv. Mater. **2011**, 23, (12), H41–H56.

[58] Drobota, M.; Ursache, S.; Aflori, M., *Surface Functionalities of Polymers for Biomaterial Applications.* Polymers-Basel **2022**, 14, (12), 2307.

[59] Kim, M.; Cha, C., *Modulation of functional pendant chains within poly(ethylene glycol) hydrogels for refined control of protein release.* Sci. Rep. **2018**, 8, (1), 4315.

[60] Liang, Y.; Li, L.; Scott, R. A.; Kiick, K. L., *50th Anniversary Perspective: Polymeric Biomaterials: Diverse Functions Enabled by Advances in Macromolecular Chemistry.* Macromolecules **2017**, 50, (2), 483–502.

[61] Ní Annaidh, A.; Bruyère, K.; Destrade, M.; Gilchrist, M. D.; Otténio, M., *Characterization of the anisotropic mechanical properties of excised human skin.* J. Mech. Behav. Biomed. Mater. **2012**, 5, (1), 139–148.

[62] Flynn, C.; Taberner, A.; Nielsen, P., *Mechanical characterisation of in vivo human skin using a 3D force-sensitive micro-robot and finite element analysis.* Biomech. Model. Mechanobiol. **2011**, 10, (1), 27–38.

[63] Joodaki, H.; Panzer, M. B., *Skin mechanical properties and modeling: A review.* Proc. Inst. Mech. Eng. H **2018**, 232, (4), 323–343.

[64] Chen, H.; Xue, H.; Zeng, H.; Dai, M.; Tang, C.; Liu, L., *3D printed scaffolds based on hyaluronic acid bioinks for tissue engineering: a review.* Biomater. Res. **2023**, 27, (1), 137.

[65] Humaira; Raza Bukhari, S. A.; Shakir, H. A.; Khan, M.; Saeed, S.; Ahmad, I.; Muzammil, K.; Franco, M.; Irfan, M.; Li, K., *Hyaluronic acid-based nanofibers: Electrospun synthesis and their medical applications; recent developments and future perspective.* Front. Chem. **2022**, 10, 1092123.
[66] Petrova, V. A.; Golovkin, A. S.; Mishanin, A. I.; Romanov, D. P.; Chernyakov, D. D.; Poshina, D. N.; Skorik, Y. A., *Cytocompatibility of Bilayer Scaffolds Electrospun from Chitosan/Alginate-Chitin Nanowhiskers.* Biomedicines **2020**, 8, (9), 305.
[67] Niu, Y.; Galluzzi, M., *Hyaluronic Acid/Collagen Nanofiber Tubular Scaffolds Support Endothelial Cell Proliferation, Phenotypic Shape and Endothelialization.* Nanomaterials (Basel) **2021**, 11, (9), 2334.
[68] Mohammadalizadeh, Z.; Bahremandi-Toloue, E.; Karbasi, S., *Synthetic-based blended electrospun scaffolds in tissue engineering applications.* J. Mater. Sci. **2022**, 57, (6), 4020–4079.
[69] Niemczyk-Soczynska, B.; Gradys, A.; Sajkiewicz, P., *Hydrophilic Surface Functionalization of Electrospun Nanofibrous Scaffolds in Tissue Engineering.* Polymers-Basel **2020**, 12, (11), 2636.
[70] Ruccolo, L.; Evangelista, A.; Benazzo, M.; Conti, B.; Pisani, S., *Electrospun Bio-Scaffolds for Mesenchymal Stem Cell-Mediated Neural Differentiation: Systematic Review of Advances and Future Directions.* Int. J. Mol. Sci. **2025**, 26, (19), 9528.
[71] El-Ghoul, Y.; Altuwayjiri, A. S.; Alharbi, G. A., *Synthesis and characterization of new electrospun medical scaffold-based modified cellulose nanofiber and bioactive natural propolis for potential wound dressing applications.* RSC Adv. **2024**, 14, (36), 26183–26197.
[72] Lopérgolo, L. C.; Lugão, A. B.; Catalani, L. H., *Direct UV photocrosslinking of poly(N-vinyl-2-pyrrolidone) (PVP) to produce hydrogels.* Polymer **2003**, 44, (20), 6217–6222.
[73] Sionkowska, A.; Wisniewski, M.; Skopinska, J.; Vicini, S.; Marsano, E., *The influence of UV irradiation on the mechanical properties of chitosan/poly(vinyl pyrrolidone) blends.* Polym. Degr. Stab. **2005**, 88, (2), 261–267.

Disclaimer/Publisher's Note: The statements, opinions and data contained in all publications are solely those of the individual author(s) and contributor(s) and not of MDPI and/or the editor(s). MDPI and/or the editor(s) disclaim responsibility for any injury to people or property resulting from any ideas, methods, instructions or products referred to in the content.

Chapter 3

Design, Characterization, and Electrospinning of Hyaluronic Acid-Arginine Bioconjugates

1. Introduction

Wound healing is a highly regulated and dynamic process that progresses through distinct yet interdependent phases: inflammation, proliferation, re-epithelialization, and maturation. These stages are driven by complex interactions among cells, biochemical mediators, and extracellular matrix (ECM) components [1]. In tissue engineering, biomaterials play a fundamental role in supporting damaged tissues by providing temporary three-dimensional scaffolds capable of guiding cell adhesion, organization, proliferation, and ECM production [2]. Scaffold materials can be broadly classified into synthetic and naturally derived biomaterials. Synthetic polymers, such as poly(lactic-co-glycolic acid) (PLGA), poly(ethylene glycol) (PEG), and polyglycolic acid (PGA), offer high reproducibility and precise control over mechanical properties, architecture, and degradation rates, although they often lack intrinsic bioactivity. In contrast, naturally derived biomaterials, including ECM proteins and glycosaminoglycans (GAGs), provide inherent biological cues that support cell adhesion, migration, and tissue remodeling, more closely resembling the native ECM microenvironment, which plays a central role in regulating cellular behavior during tissue regeneration [3].

Glycosaminoglycans (GAGs), including hyaluronic acid (HA), play a key role in tissue homeostasis and regeneration due to their hydrophilicity and ability to modulate cell signaling [4].

Among GAGs, HA plays a central role in wound healing. Its concentration rapidly increases at the wound site, and its degradation fragments actively modulate inflammation, cell migration, and tissue regeneration [1,5]. Owing to its biocompatibility, biodegradability, viscoelasticity, and mucoadhesive properties, HA has been widely employed in advanced wound-care materials, including membranes, sponges, thin films, and electrospun nanofibrous scaffolds (Figure 1) [6].

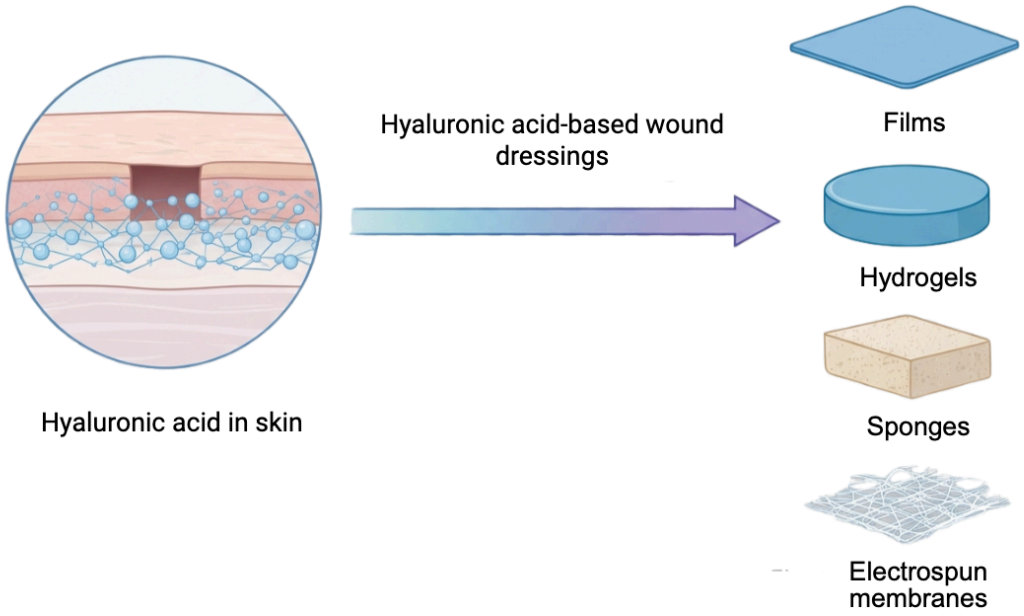

Figure 1. Graphical summary of hyaluronic acid-based wound healing dressings and the main application formats.

Electrospinning has emerged as a powerful technique for the fabrication of nanofibrous scaffolds that closely mimic the architecture of the native ECM, providing high surface-area-to-volume ratios and interconnected porosity that support cell adhesion, proliferation, and nutrient exchange. However, the electrospinning of HA remains challenging due to its high hydrophilicity and solution viscosity, which limit fiber formation and compromise structural stability [7].

Despite its advantages, native HA exhibits poor mechanical properties and undergoes rapid *in vivo* degradation. For this reason, extensive efforts have been devoted to its chemical modification through crosslinking or conjugation strategies to improve stability, biological performance, and processability [8].

Among the molecules explored for HA functionalization, L-arginine (Arg) has attracted attention due to its cationic nature and its involvement in key regenerative pathways, including nitric oxide production and collagen synthesis [9-11]. However, the direct administration of free arginine may not ensure sustained local availability, thus motivating its incorporation into biomaterials [9,12].

Based on these considerations, HA-Arg-OH bioconjugates were developed to combine the intrinsic properties of HA with the biological functionality of arginine, while improving its processability for electrospinning applications. The introduction of cationic groups along the HA backbone is expected to enhance physicochemical properties, intermolecular interactions, and fiber formation.

In this context, this chapter describes the semi-synthesis of HA-Arg-OH bioconjugates obtained via carbodiimide-mediated amidation, followed by their processing into electrospun scaffolds. Both single-layer and bilayer architectures were developed to elucidate the role of scaffold architecture on the

physicochemical and biological performance of the materials. In particular, bilayer scaffolds were designed to better replicate the hierarchical structure of the skin, consisting of a hydrophobic outer layer based on poly(D,L-lactide) (PDLLA) and a hydrophilic inner bioactive layer composed of HA-based bioconjugates blended with poly(vinylpyrrolidone) (PVP). Sequential electrospinning was employed to enable controlled deposition of the different layers and integration of bioactive components, while single-layer systems were used as simplified models to evaluate the intrinsic properties of the bioconjugates.

The resulting materials were characterized in terms of chemical structure (^{1}H-NMR, ATR-FTIR), molecular properties (viscometry, Raman spectroscopy, circular dichroism), morphology (SEM), and cytocompatibility through fibroblast viability assays.

2. Materials and Methods

2.1 Materials

Sodium hyaluronate (HA, Mw = 186 kDa) was a generous gift of Altergon Italia S.r.l. *N*-(tert-butoxycarbonyl)-L-arginine (Boc-Arg-OH), L-arginine hydrochloride, 2-(*N*-morpholino)ethanesulfonic acid monohydrate (MES·H_2O, ≥ 99.5%), palladium on carbon (Pd/C), piperidine, thioanisole, triisopropylsilane, phenol crystals, diethyl ether (Et_2O, ≥ 99.5%), sodium hydroxide (NaOH, ≥ 98%), polyvinylpyrrolidone (PVP), sodium 3-(trimethylsilyl) propane-1-sulfonate (98.0%, DSS) and deuterium oxide (D_2O) were purchased from Sigma-Aldrich. N^{α}-Boc-N^{G},N^{G}-Cbz-L-arginine was purchased from Novabiochem, while N^{α}-Fmoc-N^{G}-Pbf-L-arginine was supplied by INBIOS. 1-Ethyl-3-(3-dimethylaminopropyl) carbodiimide hydrochloride (EDC·HCl) and 1,1,1,3,3,3-Hexafluoro-2-propanol (HFP) were obtained from Iris Biotech GmbH, while *N*-Hydroxysulfosuccinimide sodium salt (s-NHS) from Tokyo Chemical Industry (TCI). Trifluoroacetic acid (TFA, ≥ 99.0%) and dichloromethane (CH_2Cl_2, ≥ 99.8%) were purchased from LabScan Ltd.
Dimethylformamide (DMF) was purchased from Delchimica Scientific Glassware. Ethanol (EtOH, 96%) was obtained from VWR Chemicals, methanol (MeOH, >99.9%) from ROMIL, and sodium chloride (NaCl, ≥ 99.5%) from Fluka. Milli-Q water was produced using a Millipore Milli-Q Gradient System. Poly(D,L-lactic acid) (PDLLA) was purchased from Formfutura.

2.2 Methods

2.2.1 General Methods

Centrifugation was performed using a Hermle (LaborTechnik GmbH) centrifuge (6000 rpm, room temperature, 40 min). Dialysis was carried out using a Slide-A-Lyzer™ Dialysis Cassette G2 with a molecular weight cut-off of 3.5 kDa. Lyophilization was conducted using a Christ Alpha 1-4 LD plus freeze dryer.

2.2.2 Nuclear Magnetic Resonance (NMR) Spectroscopy

NMR spectra were recorded using Varian Inova 500 MHz (^{1}H: 500 MHz, ^{13}C: 125 MHz) and 400 MHz (^{1}H: 400 MHz, ^{13}C: 100 MHz) spectrometers. Samples were prepared in D_2O, in 9:1 v/v H_2O/D_2O mixtures, or in deuterated dimethyl sulfoxide (DMSO-d_6, Sigma-Aldrich). DSS (0.1 mM) was used as an internal standard for chemical shift calibration and referenced at δ_H = 0.00 ppm. The

degree of substitution (DS) for the HA-Arg-OH derivatives was calculated relative to the disaccharide repeating unit.

2.2.3 Attenuated Total Reflectance Fourier Transform Infrared (ATR-FTIR) Spectroscopy

ATR-FTIR analyses were performed using a Jasco J-460 spectrometer (Jasco Europe Srl) equipped with an ATR PRO ONE single-reflection accessory fitted with a diamond crystal. Spectra were collected in the range of 4000-450 cm^{-1} with a spectral resolution of 2 cm^{-1}, averaging 256 scans for each measurement. A background spectrum was recorded prior to each acquisition and automatically subtracted from the corresponding sample spectrum.

2.2.4 Scanning Electron Microscopy (SEM)

SEM micrographs were obtained using a FEI Quanta 400 high-resolution field-emission scanning electron microscope (ESEM) operated at 20 kV and at various magnifications. Samples were sputter-coated with a thin layer of gold prior to imaging. The diameter of the fibers was evaluated using ImageJ software supplied with the DiameterJ plug-in. The sample size considered corresponds to 50 individual fibers measured from three different scaffolds, for a total of 150.

2.2.5 Synthesis of N^G-(2,2,4,6,7-pentamethyl-2,3-dihydrobenzofuran-5-sulfonyl)-arginine (Arg(Pbf)-OH, 2)

N^{α}-Fluorenylmethoxycarbonyl-N^G-2,2,4,6,7-pentamethyl-2,3-dihydrobenzofuran-5-sulfonyl-arginine (Fmoc-Arg(Pbf)-OH) (2.07 g, 3.08 mmol) was dissolved in 10 mL of a 20% (v/v) piperidine solution in DMF. The resulting light-yellow solution was stirred overnight at room temperature to ensure complete removal of the Fmoc protecting group. The reaction progress was monitored by thin-layer chromatography (TLC) using hexane/ethyl acetate mixtures (3:1, v/v). At the end of the reaction, 50 mL of cold diethyl ether was added as a precipitating agent, leading to the formation of a white solid. The suspension was centrifuged (40 min, 6000 rpm, room temperature), and the resulting precipitate was washed with additional cold diethyl ether (2.03 g, quantitative yield).

^{1}H-NMR (400 MHz, DMSO-d_6, 298K): δ_{DSS} = 8.23 ppm (NH), 6.00-5.16 ppm (NH), 3.21 ppm (1H, m, C*H* (H2)), 3.03 ppm (2H, m, CH_2 (H3')), 2.96 ppm (2H, s, CH_2 (H13')), 2.48 ppm (3H, s, CH_3 (H18')), 2.42 ppm (3H, s, CH_3 (H17')), 2.08 ppm (3H, s, CH_3 (H19')), 1.60-1.50 ppm (4H, m, CH_2 (H1') + CH_2 (H2')), 1.48 ppm (6H, s, C(CH_3)$_2$ (H20')).

^{13}C-NMR (100 MHz, DMSO-d_6, 298K): δ_{DSS} = 162.4 ppm (C1), 157.4 ppm (C5'), 156.7 ppm (C15'), 137.3 ppm, 134.4 ppm, 131.4 ppm, (C9'-14'-16'), 124.3 ppm (C8'), 116.3 ppm (C10'), 86.3 ppm (C12'), 54.0 ppm (C2), 45.0 ppm (C3'), 42.6 ppm (C13'), 28.4 ppm (C20'), 25.1 ppm (C1'), 24.5 ppm (C2'), 19.03 ppm (C18'), 17.7 ppm (C17'), 12.3 ppm (C19').

2.2.6 Synthesis of N^G, N^G-bis(benzyloxycarbonyl)-arginine (Arg(di-Z)-OH, 4)

N^α-tert-butoxycarbonyl-N^G,N^G-benzyloxycarbonyl-arginine (Boc-Arg(di-Z)-OH) (300.56 mg; 0.553 mmol) was dissolved in 10 mL of a 50% (v/v) TFA solution in CH_2Cl_2. The resulting clear solution was stirred at room temperature. The reaction progress was monitored by TLC using dichloro-methane/methanol (9:1, v/v). The solvent was then removed under reduced pressure using a rotary evaporator (408.28 mg, quantitative yield).

^{1}H-NMR (500 MHz, DMSO-d_6, 298K): δ_{DSS} = 9.25 ppm (NH), 8.21 ppm (NH), 7.45-7.28 ppm (10H, m, C*H* (H12-H17), + C*H* (H11'-H16')), 5.24 ppm (2H, s, CH_2 (H11)), 5.05 ppm (2H, s, CH_2 (H9')), 3.88 ppm (3H, m, C*H* (H2) + CH_2 (H5)), 1.82-1.56 ppm (4H, m, CH_2 (H3) + CH_2 (H4)).

^{13}C-NMR (125 MHz, DMSO-d_6, 298K): δ_{DSS} = 171.0 ppm (C1), 159.5 ppm (C7'), 158.3 ppm (C9), 137.0 ppm (C12), 135.0 ppm (C10'), 128.0-127.9 ppm (C13-C17 + C11'-C16'), 68.3 ppm (C11), 66.3 ppm (C9'), 51.8 ppm (C2), 43.9 ppm (C5), 27.3 ppm (C3), 24.2 ppm (C4).

2.2.7 Bioconjugation of Arg(Pbf)-OH with HA (9-i)

HA (114.68 mg, 0.286 mmol) was dissolved in 15 mL of H_2O and stirred at room temperature until complete dissolution, then treated with aqueous solutions of EDC·HCl (2.86 mL, 0.572 mmol) and s-NHS (2.85 mL, 0.286 mmol). After 40 minutes of activation, MES·H_2O (40 mg) and an aqueous solution of Arg(Pbf)-OH (2 mL, 0.63 mmol) were added. Upon addition of the amino acid, the reaction mixture became slightly opaque. The pH was carefully adjusted to 6 using a few drops of freshly prepared 1.0 M NaOH, and the mixture was stirred at room temperature overnight. After approximately 20 hours, the reaction was brought to pH 7 with 1.0 M NaOH and subjected to dialysis, first against a 342 mM NaCl solution and subsequently against ultrapure water. The dialyzed solution was frozen and lyophilized to afford a white solid (175.8 mg, quantitative yield).

^{1}H-NMR (500 MHz, D_2O, 298 K): δ_{DSS} = 4.54 ppm (H-1, GlcNAc), 4.45 ppm (H-1, GlcA), 4.00-3.20 ppm (H-2, H-3, H-4, H-5 GlcA; H-2, H-3, H-4, H-5, H-6 GlcNAc), 3.21 ppm (1H, m, C*H* (H2)), 3.07 ppm (2H, m, CH_2 (H3')), 2.54 ppm (3H, s, CH_3 (H18')), 2.47 ppm (3H, s, CH_3 (H17')), 2.09 ppm (3H, s, CH_3 (H19')), 2.01 ppm (NHAc, GlcNAc), 1.48 ppm (6H, s, C(CH_3)$_2$ (H12′ + H20')).

2.2.8 Bioconjugation of Arg(di-Z)-OH with HA (9-ii)

HA (100.20 mg, 0.249 mmol) was dissolved in 15 mL of H_2O and stirred at room temperature until complete dissolution, then treated with aqueous solutions of EDC·HCl (2.49 mL, 0.498 mmol) and s-NHS (2.49 mL, 0.249 mmol). After 40 minutes of stirring at room temperature, MES·H_2O (40 mg) and an aqueous solution of Arg(di-Z)-OH (2 mL, 0.498 mmol) were added to the reaction mixture, which turned slightly cloudy upon addition of the α-amino acid. A few drops of freshly prepared 1.0 M NaOH solution were added to adjust the pH to 6, and stirring was continued overnight. After ~20 h, the reaction was brought to pH 7 with 1.0 M NaOH and subjected to dialysis, first against a 342 mM NaCl solution and subsequently against ultrapure water. The dialyzed solution was frozen and lyophilized to afford a white solid (142.91 mg, quantitative yield).

^{1}H-NMR (400 MHz, D_2O, 298K): δ_{DSS} = 7.53-7.30 ppm (m, C*H* (H12-H17) + C*H* (H11'-H16')), 5.33-5.06 ppm (CH_2 (H9') + CH_2 (H11)), 4.54 ppm (H-1, GlcNAc), 4.45 ppm (H-1, GlcA), 4.00-3.20 ppm (H-2, H-3, H-4, H-5 GlcA; H-2, H-3, H-4, H-5, H-6 GlcNAc), 2.01 ppm (NHAc, GlcNAc).

2.2.9 Deprotection of HA-Arg(Pbf)-OH (10)

HA-Arg(Pbf)-OH (100.91 mg, 0.169 mmol) was treated with a solution containing phenol crystals (755 mg, 8.02 mmol), thioanisole (500 μL, 4.2 mmol), triisopropylsilane (TIS; 250 μL, 1.22 mmol), H_2O (500 μL), and trifluoroacetic acid (TFA, 10 mL). The reaction mixture was transferred to a 100 mL glass flask placed in an ice-water bath and stirred using a magnetic stirrer. The cooling bath was then removed, and the mixture was allowed to stir at room temperature for 3 h. The reaction was diluted with H_2O (100 mL) and neutralized to pH 7 using 5.0 M NaOH. Purification was carried out by dialysis, first against a 342 mM NaCl solution and then against H_2O. Freeze-drying afforded a white solid (339.1 mg, quantitative yield).

^{1}H-NMR (500 MHz, D_2O, 298 K): δ_{DSS} = 4.54 ppm (H-1, GlcNAc), 4.45 ppm (H-1, GlcA), 4.00-3.20 ppm (H-2, H-3, H-4, H-5 GlcA; H-2, H-3, H-4, H-5, H-6 GlcNAc), 2.01 ppm (NHAc, GlcNAc).

2.2.10 Deprotection of HA-Arg(di-Z)-OH (11)

HA-Arg(di-Z)-OH (50.71 mg, 0.137 mmol) was dissolved in 25 mL of a 50% (v/v) ethanol/water solution. Pd/C (40 wt %, 20.0 mg, 0.188 mmol) was then added as catalyst, and the mixture was stirred overnight at room temperature under a hydrogen atmosphere. After completion, the catalyst was removed by filtration, and the filtrate was concentrated under reduced pressure. The residue was purified by dialysis, first against a 342 mM NaCl solution and then against H_2O. The resulting solution was frozen and lyophilized to afford a white solid (46.26 mg, 59% yield).

^{1}H-NMR (500 MHz, D_2O, 298K): δ_{DSS} = 7.53-7.30 ppm (m, C*H* (H12-H17) + C*H* (H11'-H16')), 5.33-5.06 ppm (4H, CH_2 (H9') + CH_2 (H11)), 4.54 ppm (H-1, GlcNAc), 4.45 ppm (H-1, GlcA), 4.00-3.20 ppm (H-2, H-3, H-4, H-5 GlcA; H-2, H-3, H-4, H-5, H-6 GlcNAc), 2.01 ppm (NHAc, GlcNAc).

2.2.11 Synthesis of Arg-OH (6)

N-(tert-butoxycarbonyl)-arginine (Boc-Arg-OH) (300.6 mg, 1.10 mmol) was dissolved in 10 mL of a 50% (v/v) TFA solution in CH_2Cl_2. The resulting clear solution was stirred at room temperature. The reaction progress was monitored by TLC using dichloromethane/methanol (7:3, v/v). After completion, 50 mL of cold diethyl ether was added to the reaction mixture, resulting in the precipitation of the deprotected product. The solid was collected by centrifugation, dissolved in water, and lyophilized to afford a white solid (334.7 mg, quantitative yield).

^{1}H-NMR (400 MHz, D_2O, 298 K): δ_{DSS} = 3.95 ppm (1H, t, C*H* (H2)), 3.24 ppm (2H, t, CH_2 (H5)), 1.95 ppm (2H, m, CH_2 (H3)), 1.70 ppm (2H, m, CH_2 (H4)).

^{13}C-NMR (100 MHz, D_2O, 298 K): δ_{DSS} = 172.5 ppm (C1), 156.9 ppm (C6), 53.0 ppm (C2), 40.4 ppm (C5), 27.1 ppm (C4), 23.6 ppm (C3).

2.2.12 Bioconjugation of synthetic Arg-OH with HA (12-i)

HA (101.5 mg, 0.253 mmol) was dispersed in 15 mL of H_2O and stirred at room temperature until complete dissolution. The resulting solution was then supplemented with aqueous EDC·HCl (2.43 mL, 0.506 mmol) and s-NHS (2.45 mL, 0.253 mmol), and the mixture was stirred for an additional 40 minutes. MES·H_2O (40.2 mg) and an aqueous solution of synthetic Arg-OH (2 mL, 0.506 mmol) were added. The pH was carefully adjusted to 6.0 using freshly prepared 1 M NaOH. A pale-yellow solution was obtained, which was stirred overnight at room temperature. After approximately 22 hours, the reaction was brought to pH 7 with 1.0 M NaOH and subjected to dialysis, first against a 342 mM NaCl solution and subsequently against ultrapure water. The dialyzed solution was frozen and lyophilized to afford a white solid (64.2 mg, 54% yield).

^{1}H-NMR (500 MHz, D_2O, 298 K): δ_{DSS} = 4.54 ppm (H-1, GlcNAc), 4.46 ppm (H-1, GlcA), 4.25 ppm (1H, m, C*H* (H2)), 4.00-3.20 ppm (H-2, H-3, H-4, H-5 GlcA; H-2, H-3, H-4, H-5, H-6 GlcNAc), 3.20 ppm (2H, t, CH_2 (H5)), 2.01 ppm (NHAc, GlcNAc), 1.89 ppm (2H, m, CH_2 (H3)), 1.64 ppm (2H, m, CH_2 (H4)).

2.2.13 Bioconjugation of commercial Arg-OH with HA (12-ii)

HA (100.32 mg, 0.250 mmol) was dissolved in 15 mL of H_2O and stirred at room temperature until complete dissolution. The solution was then treated with aqueous EDC·HCl (2.40 mL, 0.500 mmol) and s-NHS (2.42 mL, 0.250 mmol), and activation was allowed to proceed for 40 minutes. MES·H_2O (40 mg) and an aqueous solution of commercial arginine hydrochloride (2 mL, 0.500 mmol) were subsequently added, and the pH was adjusted to 6.0 using freshly prepared 1.0 M NaOH. The reaction mixture was stirred overnight at room temperature. After ~20 h, the reaction was brought to pH 7 with 1.0 M NaOH and subjected to dialysis, first against a 342 mM NaCl solution and subsequently against ultrapure water. The dialyzed solution was frozen and lyophilized to afford a white solid (89.05 mg, 80% yield).

^{1}H-NMR (400 MHz, D_2O, 298 K): δ_{DSS} = 4.54 ppm (H-1, GlcNAc), 4.46 ppm (H-1, GlcA), 4.24 ppm (1H, m, C*H* (H2)), 4.00-3.20 ppm (H-2, H-3, H-4, H-5 GlcA; H-2, H-3, H-4, H-5, H-6 GlcNAc), 3.21 ppm (2H, t, CH_2 (H5)), 2.01 ppm (NHAc, GlcNAc), 1.90 ppm (2H, m, CH_2 (H3)), 1.65 ppm (2H, m, CH_2 (H4)).

2.2.14 Intrinsic Viscosity Measurements

To determine the molecular weight of the semisynthetic HA-Arg-OH derivatives, stock solutions were prepared at a concentration of 1 mg/mL for native HA and for the HA-arginine bioconjugate (**derivatives 11** and **12-i**), dissolving each sample in 0.15 M NaCl aqueous solution. For the **derivative 10**, a more concentrated stock solution (10 mg/mL in 0.15 M NaCl) was prepared due to its lower viscosity. All stock solutions were filtered through a 0.45 μm syringe filter prior to use. From these stock solutions, additional dilutions were prepared to obtain final concentrations of 0.75, 0.50, and 0.25 mg/mL for HA, **derivatives 11** and **12-i**, and 7.5, 5.0, and 2.5 mg/mL for **derivative 10**.

Intrinsic viscosity measurements were performed using an Ostwald capillary viscometer. For each measurement, the viscometer was filled with 7 mL of solvent (0.15 M NaCl) or the polymer solution. Using gentle aspiration with a propipette applied to the narrow capillary, the liquid was drawn above the upper timing mark and then allowed to flow freely. The efflux time required for the meniscus to travel between the two calibrated marks was recorded with a stopwatch. Each solution was measured in triplicate. From the recorded flow times, relative viscosity (η_{rel}), specific viscosity (η_{sp}), reduced viscosity (η_{red}), were calculated according to the standard relationships:

$$\eta_{rel} = \frac{t_{solution}}{t_{solvent}} \quad (1) \qquad \eta_{sp} = \eta_{rel} - 1 \quad (2) \qquad \eta_{red} = \frac{\eta_{sp}}{C} \quad (3)$$

Reduced viscosity values were plotted as a function of polymer concentration, and the intrinsic viscosity [η] was obtained by extrapolating the linear fit to zero concentration. The molecular weight (M) was then determined using the Mark-Houwink-Sakurada equation:

$$[\eta] = KM^a \rightarrow M = \left(\frac{[\eta]}{K}\right)^{\frac{1}{a}} \quad (4)$$

The Mark-Houwink-Sakurada constants K and a are not universal parameters but depend on the polymer–solvent–temperature system and on the hydrodynamic regime of the polymer chains. These constants are determined from the dependence of intrinsic viscosity on molecular weight for well-characterized samples with low polydispersity. For sodium hyaluronate dissolved in 0.15 M NaCl aqueous solution at 298 K, two distinct molecular-weight regimes are reported in the literature. For high-molecular-weight sodium hyaluronate dissolved in 0.15 M NaCl at 298 K, the literature values K=0.029 $cm^3 \cdot g^{-1}$ and a = 0.80, whereas the constants K = 6.54 × 10^{-4} $cm^3 \cdot g^{-1}$ and a = 1.16 were applied to the low-molecular-weight **derivative 10.** The transition between these two hydrodynamic regimes occurs at a molecular weight of approximately 40,000 g/mol. [14].

2.2.15 Electrospinning

Electrospinning was carried out using a Gamma High Voltage generator (Linari Engineering, Italy) integrated into a horizontal electrospinning system. The composition of the electrospinning solutions is reported in Table 1.

Table 1. Composition of the electrospinning solutions.

Hydrophobic layer						
Scaffold	**PDLLA (% w/V)**		**HFP (mL)**			**Final volume (mL)**
PDLLA	12.0		3.0			3
Hydrophilic layer						
Scaffold	**PVP (% w/V)**	**HA (% w/w)**	**HA-Arg-OH (% w/w)**	**H_2O (mL)**	**EtOH (mL)**	**Final volume (mL)**
PVP-HA-Arg-OH 1%	10.0	-	1.0	0.6	2.4	3
PVP-HA-Arg-OH 3%	10.0	-	3.0	0.6	2.4	3

In the case of the hydrophobic layer, PDLLA (360 mg) was dissolved in HFP (3 mL) and kept under magnetic stirring overnight at 310 K. The solution was loaded into a 10 mL glass syringe with a 20 G stainless-steel needle, and electrospun at 17 kV with a flow rate of 1.0 mL/h. The collector consisted

of a circular copper plate (90 mm diameter) covered with aluminum foil and positioned 19 cm from the needle tip.

For the hydrophilic layer, the preparation of the electrospinning solutions followed the general protocol described below. HA-Arg-OH (**derivative 12-ii**; 1.0 or 3.0 mg), corresponding to 1% or 3% (w/w) with respect to PVP, was dissolved in H_2O (0.6 mL) and stirred for 2 h at room temperature. In parallel, PVP (100 or 300 mg) was dissolved in EtOH (0.9 mL) under the same conditions. The two solutions were then combined and further diluted with EtOH (1.5 mL). The mixture was then stirred overnight at 310 K, loaded into a 10 mL glass syringe fitted with a 20 G stainless-steel needle, and electrospun at 19 kV with a flow rate of 0.5 mL/h. The collector consisted of a circular copper plate (90 mm diameter) covered with aluminum foil and positioned 19 cm from the needle tip.

To prevent the complete dissolution of the electrospun PVP-based layers, including those containing HA-Arg-OH, in ultrapure water, the obtained scaffolds were subjected to ultraviolet (UV) irradiation (254 nm) using a multiray reactor (Helios Italquartz, Milan, Italy) for 60 minutes, corresponding to a UV dose of 169.2 mJ/cm^2.

For cytocompatibility evaluation, the scaffolds were directly electrospun onto 13 mm glass coverslips. In this case, the electrospun volume was reduced to 1.0 mL for each layer, while maintaining the same solution composition and electrospinning parameters described above. Due to the reduced volume, the resulting scaffolds were exposed to UV irradiation for 15 minutes, corresponding to a UV dose of 42.3 mJ/cm^2.

2.2.16 Raman Spectroscopy

Raman spectra were recorded in backscattered configuration using a Jobin Yvon LABRAM HR 800 micro-Raman spectrometer equipped with two gratings (600 and 1800 g/mm) and an Olympus microscope with 10×, 50× and 100× objectives. A He-Ne laser (λ = 632.8 nm, 20 mW) was employed for sample excitation. Spectra were acquired using the 600 g/mm grating and the 100× objective, resulting in an estimated spectral resolution of approximately ~40 cm^{-1}. The Raman spectra were collected in three spectral regions: 400-1500 cm^{-1}, 1500-2500 cm^{-1} and 2500-3500 cm^{-1}.

2.2.17 Circular Dichroism (CD) Spectroscopy

CD spectra were acquired using a JASCO J-815 Spectropolarimeter equipped with a HAAKE temperature controller. Samples were dissolved at a concentration of 0.02 mg/mL in 10 mM PBS at pH 7.0 and subsequently in H_2O for arginine hydrochloride, and at 0.04 mg/mL in 10 mM PBS at pH 7.0 and then in H_2O for HA and HA-Arg-OH (**derivative 12-ii**). Solutions were loaded into cylindrical quartz cuvettes with a 5 mm path length. CD spectra were collected in the wavelength range 190-250

nm at four different temperatures: 273, 298, 310 and 333 K, using a scan speed of 50 nm min^{-1} and a bandwidth of 1 nm. Each reported spectrum corresponds to the average of 16 scans. Data processing was performed using the JASCO Spectral Analysis software: after background subtraction, spectra were smoothed using a FFT filtering algorithm. Results were expressed as molar ellipticity [Θ] deg cm^2 $dmol^{-1}$, and for HA-Arg-OH the values refer to the repeating disaccharide units.

2.2.18 Evaluation of Cytocompatibility of Electrospun Scaffolds

To evaluate scaffold biocompatibility, L929 murine fibroblasts were used. The cells were acquired from the American Type Culture Collection (ATCC, Rockville, MD, USA) and cultured in Dulbecco's Modified Eagle Medium High Glucose (DMEM, Merck Life Science S.r.l., Milan, Italy) supplemented with 10% fetal bovine serum (FBS, Merck Life Science S.r.l., Milan, Italy), 1% penicillin/streptomycin/amphotericin B (PSA, Merck Life Science S.r.l., Milan, Italy). Cultures were maintained at 37 °C in a humidified atmosphere containing 5% CO2 and sub-cultured upon reaching 80%-90% confluence. Electrospun scaffolds deposited onto 13 mm glass coverslips were sterilized by ultraviolet (UV) irradiation for 30 minutes prior to use. L929 fibroblasts were seeded onto each scaffold at a density of 3×10^4 cells per sample using a dropwise technique to ensure uniform initial adhesion. The seeded scaffolds were incubated for two hours under standard culture conditions (37 °C, 5% CO_2, humidified atmosphere). Following this adhesion period, 500 µL of fresh complete culture medium was carefully added to each well to fully immerse the scaffolds and support subsequent cell growth.

Cell viability was assessed using the MTT assay [3-(4,5-dimethylthiazol-2-yl)-2,5-diphenyltetrazolium bromide] test (Merck Life Science S.r.l., Milan, Italy) at 24- and 48-hours post-seeding. For each time point, 500 µL of a 1 mg/mL MTT solution prepared in serum-free high-glucose DMEM was added to each well and incubated at 37 °C for 2 hours. The resulting formazan crystals were solubilized in 500 µL of dimethyl sulfoxide (DMSO; Merck Life Science S.r.l., Milan, Italy). Absorbance was measured at 540 nm using a microplate reader (AMR-100, Biosigma, Verona, Italy). Viability data were normalized to cells cultured without scaffolds, which served as the internal control.

3. Results and Discussion

3.1 Semi-synthesis of HA-Arg-OH

To obtain HA-Arg-OH bioconjugates, four synthetic strategies were investigated. Each approach involved carbodiimide-mediated activation of HA carboxyl groups, followed by coupling with either side-chain-protected or free arginine. The strategies were designed to compare the degree of modification achieved on the HA backbone and the overall reaction yield.

The first synthetic strategy for obtaining the HA-Arg-OH bioconjugate involved the use of Fmoc-Arg(Pbf)-OH, in which the α-amino group and the guanidinium side chain are protected with Fmoc and Pbf, respectively. These protecting groups were selected to avoid undesired side reactions during the carbodiimide-mediated coupling step and to ensure selective derivatization of the HA backbone. In this approach, the Fmoc group was first removed using a 20% (v/v) piperidine solution in DMF (10 mL) [15], thereby exposing the α-amino group required for the subsequent amidation reaction with the carboxyl groups of the glucuronic acid residues of HA (Scheme 1). The **derivative 2** was obtained in quantitative yield.

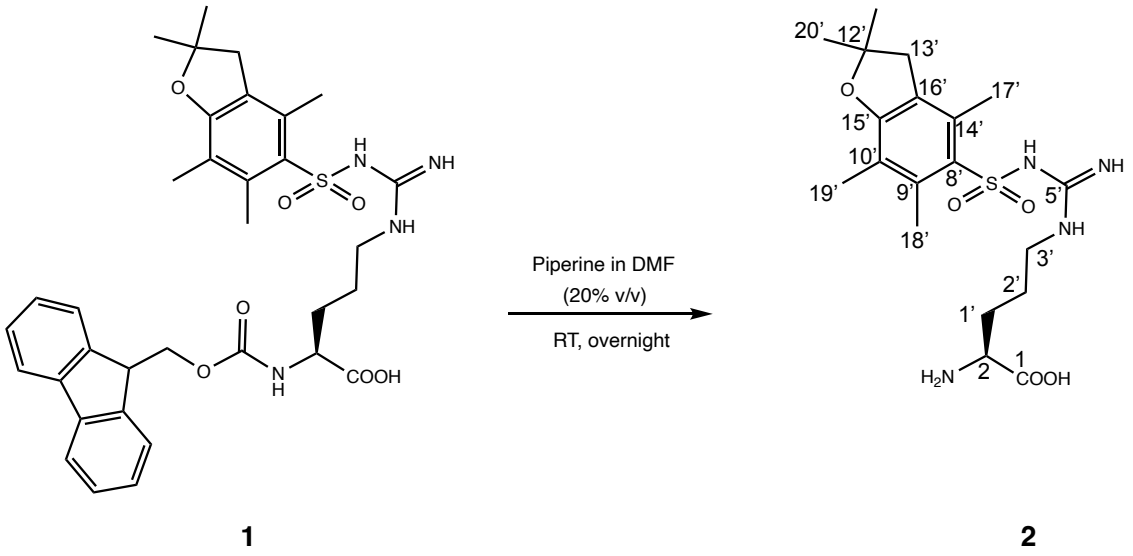

Scheme 1. Removal of the Fmoc protecting group from **derivative 1**.

The successful removal of the Fmoc protecting group was verified by ^{1}H-NMR analysis in DMSO-d_6 (Figure S1). In the spectrum, no aromatic signals attributable to the Fmoc group (δ_{DSS} = 7.94-7.27

ppm) were observed. Instead, the characteristic Pbf resonances appeared at δ_{DSS} = 2.48, 2.42, 2.08 and 1.48 ppm, corresponding to singlets assigned to the three CH_3 groups on the benzofuran aromatic ring and the two CH_3 groups of the dihydrofuran moiety, respectively.

These observations were further supported by the ^{13}C-NMR spectrum (Figure S2). The spectrum showed a signal at δ_{DSS} = 162.4 ppm corresponding to the carboxyl carbon of the N^G-Pbf-arginine product. The presence of the Pbf group was confirmed by the signals observed in the δ_{DSS} = 156.7-116.3 ppm region, as well as at δ_{DSS} = 19.03, 17.7, and 12.3 ppm, which were attributed to the aromatic carbons and the CH_3 groups of the benzofuran ring respectively. An additional signal at δ_{DSS} = 28.4 ppm corresponded to the CH_3 group of the dihydrofuran moiety. The main ^{1}H and ^{13}C-NMR signal assignments are summarized in Table 2.

Table 2. ^{1}H and ^{13}C-NMR chemical shift assignments of **derivative 2**.

Assignment	**^{1}H δ_{DSS} (ppm)**	**^{13}C δ_{DSS} (ppm)**
NH	8.23	-
NH	6.00-5.16	-
1	-	162.4
2	3.21	54.0
1'-2'	1.60–1.50	25.1, 24.5
3'	3.03	45.0
5′	-	157.4
8′	-	124.3
9′, 14′, 16′	-	137.3, 134.4, 131.4
10'	-	116.3
12'	-	86.3
13'	2.96	42.6
15'	-	156.7
17'	2.42	17.7
18'	2.48	19.03
19'	2.08	12.3
20'	1.48	28.4

Further confirmation of Fmoc removal was provided by the ATR-FTIR spectrum shown in Figure S3. As expected after the deprotection reaction, the characteristic C=O stretching band of the Fmoc group (~1705 cm^{-1}) was no longer observed. In contrast, the stretching bands (ν) of the aromatic C=C of the Pbf group (1540-1450 cm^{-1}) were clearly observed, along with the characteristic bands associated with N–H containing groups (Figure S3) [16]. The main IR band assignments are reported in Table 3.

Table 3. IR band assignments for **derivative 2** and commercial Fmoc-Arg(Pbf)-OH.

IR assignments Derivative 2 (red curve)	**Wavenumber (cm^{-1})**	**IR assignments Fmoc-Arg(Pbf)-OH (black curve)**	**Wavenumber (cm^{-1})**
ν (N-H)/ (O-H) (*)	3300-3200	ν (N-H)/ (O-H) (*)	3326
ν C-H (aliphatic) (*)	2930-2854	ν C-H (aliphatic) (*)	2925
ν_{as} (COO^-)(*)	1615	ν C=O (Fmoc) (*)	1705
δ N-H + ν C-N (guanidinium group) (*)	1543	ν C=C (aromatic) (*)	1573
ν C=C (aromatic) (*)	1540-1450	δ C-H (aromatic) (*)	1446
ν N-H (*)	1239	ν SO_2 (Pbf) (*)	1369
ν C-N (*)	1091	ν C-O (Fmoc) (*)	1243
ν C-O/ ν C-N (*)	1011-1035	ν C-N (*)	1091
γ C-H (aromatic) (*)	829-809	γ C-H (aromatic) (*)	740

The second synthetic strategy used to obtain an HA-Arg-OH bioconjugate involved the use of an α-amino acid protected both at the side chain and at the α-amino group with Cbz and Boc protecting groups, respectively (Boc-Arg(di-Z)-OH). The Boc group was removed by treatment with a 50% (v/v) TFA solution in CH_2Cl_2 (10 mL). The **derivative 4** was obtained in quantitative yield. The reaction scheme is shown in Scheme 2.

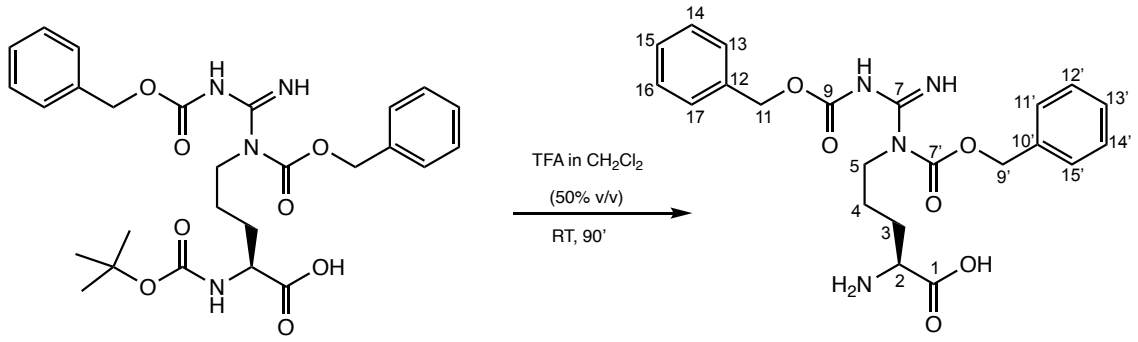

3 **4**

Scheme 2. Removal of the Boc protecting group from **derivative 3**.

^{1}H-NMR analysis in DMSO-d_6 confirmed the success of the deprotection. Figure S4 shows the proton NMR spectrum of **derivative 4**, in which the characteristic signals of the Boc group (δ_{DSS} = 1.30-1.43 ppm) were absent. In addition, the spectrum displayed signals at δ_{DSS} = 7.45-7.28 ppm and δ_{DSS} = 5.24 and 5.05 ppm, corresponding to the aromatic and benzylic protons of the Cbz groups, respectively. In addition, a multiplet at δ_{DSS} = 1.82-1.56 ppm was observed and can be attributed to the aliphatic methylene protons of the arginine side chain (H3 and H4).

The removal of the Boc protecting group was also confirmed by ^{13}C-NMR spectroscopy (Figure S5). In the corresponding spectrum, a signal at δ_{DSS} = 171.0 ppm was observed, attributable to the carboxyl carbon of the Arg(di-Z)-OH product. The presence of the Cbz groups was confirmed by the signals in the aromatic region (δ_{DSS} = 137.0-127.9 ppm), as well as by the resonances detected in the δ_{DSS} = 68.3-66.3 ppm region, corresponding to the benzylic carbon atoms of the two Cbz protecting groups. These data confirmed the successful Boc deprotection while preserving the integrity of the Cbz groups.

The main ^{1}H and ^{13}C-NMR signal assignments are summarized in Table 4.

Table 4. ^{1}H and ^{13}C-NMR chemical shift assignments of **derivative 4**.

Assignment	^{1}H δ_{DSS} (ppm)	^{13}C δ_{DSS} (ppm)
NH	9.25	-
NH	8.21	-
1	-	171.0
2	3.88	51.8
3	1.82–1.56	27.3
4	1.82–1.56	24.2
5	3.88	43.9
9	-	158.3
11	5.24	68.3
12-17	7.45–7.28	137.0–127.9
11'- 16'	7.45–7.28	128.0–127.9
7'	-	159.5
9'	5.05	66.3
10'	-	135.0

Additional confirmation of the successful removal of the Boc protecting group was obtained by ATR-FTIR spectroscopy (Figure S6). In the spectrum of Boc-Arg(di-Z)-OH (black curve), characteristic Boc-related bands were observed at 2976 cm^{-1} (aliphatic C-H stretching), 1685 cm^{-1} (carbonyl stretching, Boc/Cbz overlap), 1377 cm^{-1} (CH_3 bending), and 1250 cm^{-1} (C-O stretching), which were absent in **derivative 4**. Conversely, bands attributable to the Cbz groups were retained in **derivative 4**, namely 1663 cm^{-1} (C=O stretching), 1590-1440 cm^{-1} (aromatic C=C stretching), and 1173 cm^{-1} (benzylic C-O stretching). Band assignments are reported in Table 5.

Table 5. IR band assignments for **derivative 4** and commercial Boc-Arg(di-Z)-OH.

IR assignments Derivative 4 (red curve)	**Wavenumber (cm^{-1})**	**IR assignments Boc-Arg(di-Z)-OH (black curve)**	**Wavenumber (cm^{-1})**
v C-H (aromatic, Cbz) (*)	3029	*v* N-H (*)	3342
v C-H (aliphatic) (*)	2952	*v* C-H (Boc) (*)	2976
v C=O (Arg) (*)	1730	*v* C=O (Arg) (*)	1730
v C=O (Cbz) (*)	1663	*v* C=O (Boc, Cbz) (*)	1685
v C=C (aromatic, Cbz) (*)	1590-1440	*v* C=C (aromatic, Cbz) (*)	1608
v C-O (benzyloxy, Cbz)(*)	1173	δ CH_3 (Boc) (*)	1377
		v C-O (Boc) (*)	1250

The amidation of hyaluronic acid with Arg(Pbf)-OH was carried out in aqueous MES buffer using carbodiimide-mediated activation of carboxyl groups of the glucuronic acid units of HA (Scheme 3). After the addition of the amino acid derivative, the reaction mixture was adjusted to pH 6 with a freshly prepared 1 M NaOH solution and stirred overnight at room temperature. The crude mixture was subsequently neutralized, purified by dialysis against a 342 mM NaCl solution followed by H_2O, and finally freeze-dried to afford the HA-Arg(Pbf)-OH bioconjugate (**9-i**), which was obtained in quantitative yield.

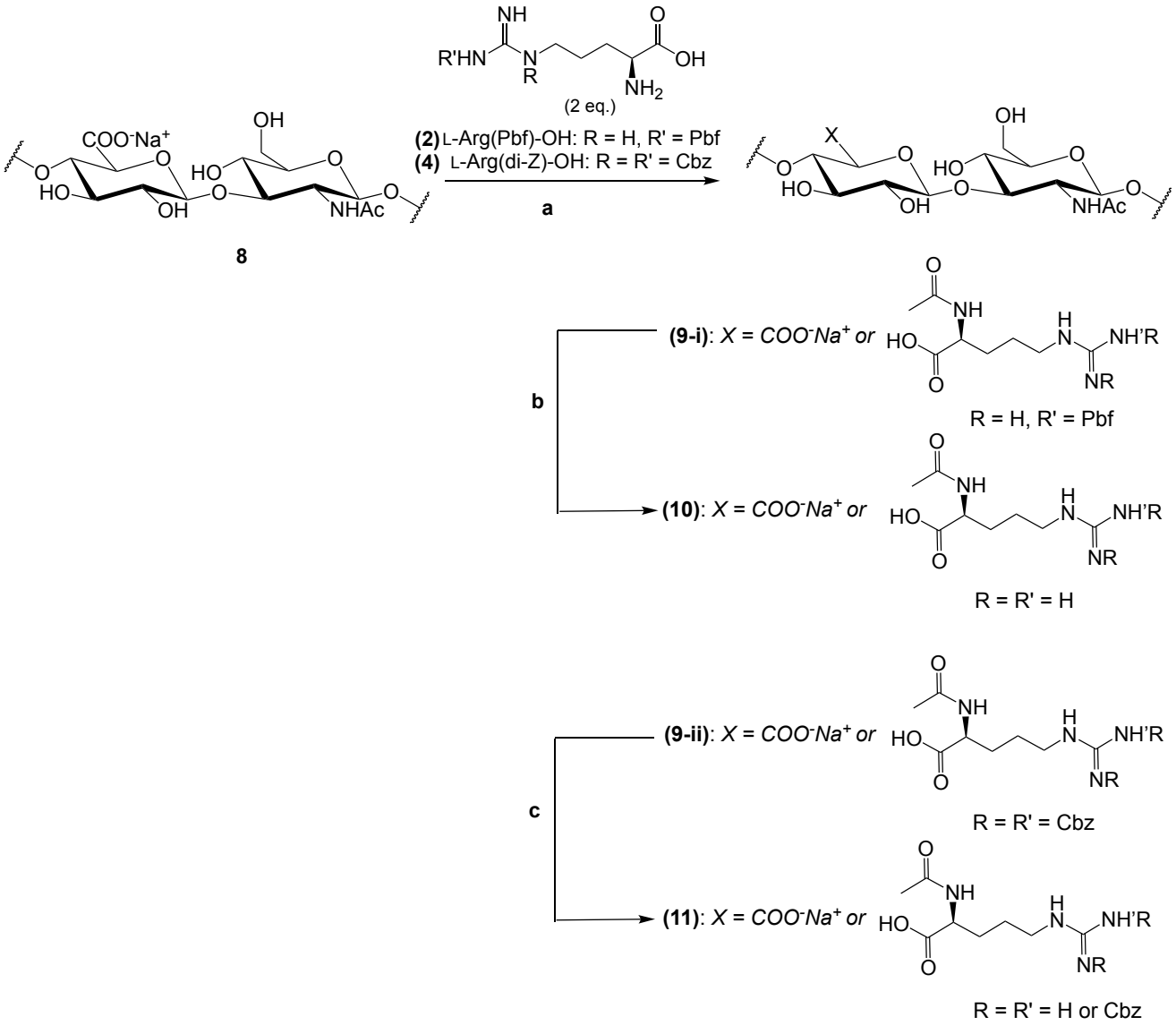

Scheme 3. Synthetic route for the preparation of HA-Arg-OH bioconjugates. **a)** EDC·HCl, s-NHS, MES, H_2O, pH = 6, room temperature, overnight; **b)** TFA, thioanisole, TIS, phenol, H_2O, room temperature, 3 h; **c)** H_2, Pd/C, EtOH/H_2O, room temperature, overnight.

The successful conjugation in **derivative 9-i** was confirmed by ^{1}H-NMR analysis (Figure 2), which shows resonances at δ_{DSS} = 2.54, 2.47, 2.09, and 1.48 ppm, attributable to the methyl groups of the Pbf protecting moiety. In addition, a signal at δ_{DSS} = 2.01 ppm, corresponding to the acetyl methyl group of the GlcNAc unit, was also observed.

The DS was 50%, as calculated according to Equation 5:

$$DS = \frac{(ICH_{3\ ortho}/2)}{(ICH_{3\ meta} + ICH_{3\ GlcNAc}) - (ICH_{3\ ortho}/2)} \quad (5)$$

$ICH_{3\ ortho}$ represents the integral of the methyl protons in the ortho position relative to the sulfonyl group of the Pbf moiety (δ_{DSS} = 2.54 and 2.47 ppm), $ICH_{3\ meta}$ corresponds to the methyl protons in meta position of the Pbf group (δ_{DSS} = 2.09 ppm, and $ICH_{3\ GlcNAc}$ refers to the acetyl methyl protons of the GlcNAc unit (δ_{DSS} = 2.01 ppm). The division by two accounts for the presence of two equivalent ortho methyl groups per Pbf substituent. The main ^{1}H-NMR signal assignments are summarized in Table 6.

Table 6. ^{1}H-NMR chemical shift assignments of **derivative 9-i**.

Assignment	**^{1}H δ_{DSS} (ppm)**
1 (GlcNAc)	4.54
1 (GlcA)	4.45
2-5 (GlcA)	4.0-3.20
2-6 (GlcNAc)	4.0-3.20
2	3.21
3’	3.07
18’	2.54
17’	2.47
19’	2.09
NHAc (GlcNAc)	2.01
12’+ 20’	1.48

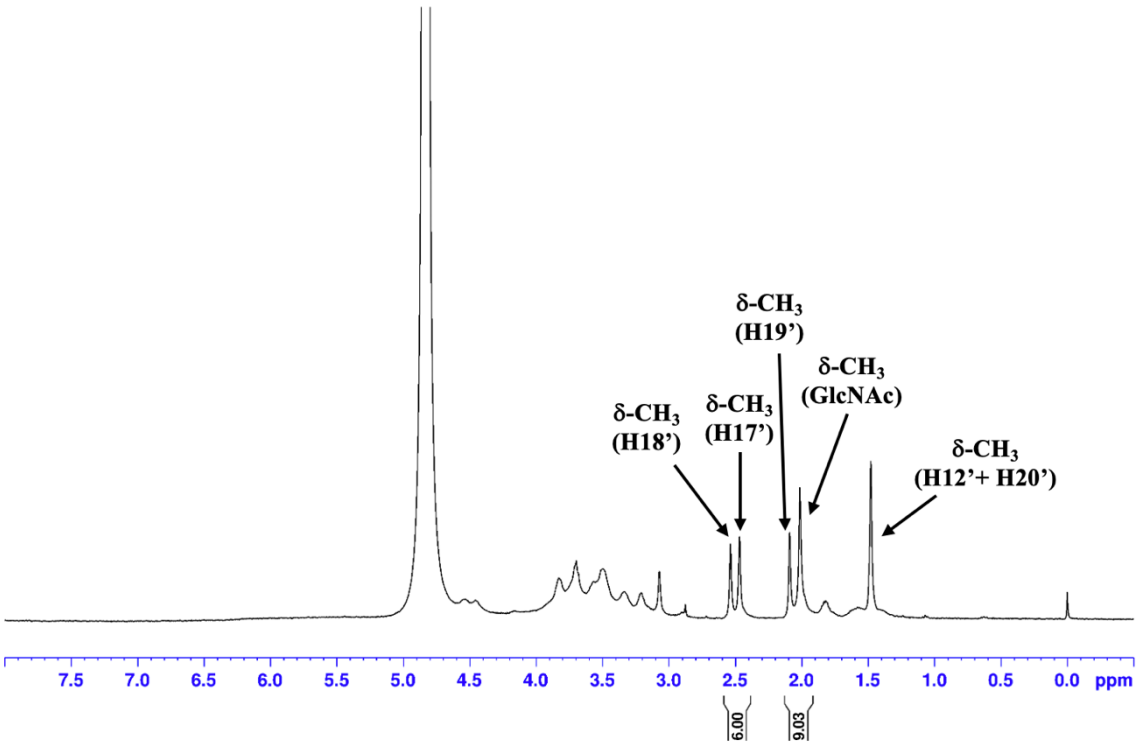

Figure 2. ^{1}H-NMR spectrum of **derivative 9-i** (400 MHz, D_2O, 298 K).

The conjugation of Arg(di-Z)-OH to HA was carried out under the same carbodiimide-mediated conditions previously described. After an overnight reaction, the mixture was neutralized, dialyzed and freeze-dried to afford the corresponding HA-Arg(di-Z)-OH conjugate (**9-ii**, Scheme 3), which was obtained in quantitative yield.

The successful conjugation in **derivative 9-ii** was confirmed by ^{1}H-NMR analysis (Figure 3), which revealed signals at δ_{DSS} = 7.53-7.30 ppm and δ_{DSS} = 5.33-5.06 ppm, attributable to the aromatic and benzylic protons of the Cbz protecting groups, respectively. The resulting DS was 50%, as calculated according to Equation 6:

$$DS = \frac{I_{Ar[Arg(di-Z)-OH]}/5}{ICH_{(GlcA+GlcNAc)}} \quad (6)$$

I_{Ar} represents the integral of the aromatic protons of the Cbz protecting groups (δ_{DSS} = 7.53-7.30 ppm), while $I_{CH\ (GlcA+GlcNAc)}$ corresponds to the combined integral of the anomeric protons of GlcA (δ_{DSS} = 4.45 ppm) and GlcNAc (δ_{DSS} = 4.54 ppm) of the hyaluronic acid backbone. The division by five accounts for the five equivalent aromatic protons of each Cbz group. The main ^{1}H-NMR signal assignments are summarized in Table 7.

Table 7. ^{1}H-NMR chemical shift assignments of **derivative 9-ii**.

Assignment	**^{1}H δ_{DSS} (ppm)**
1 (GlcNAc)	4.54
1 (GlcA)	4.45
2-5 (GlcA)	4.0-3.20
2-6 (GlcNAc)	4.0-3.20
12-17	7.53-7.30
11'-16'	7.53-7.30
9'	5.33-5.06
11	5.33-5.06
NHAc (GlcNAc)	2.01

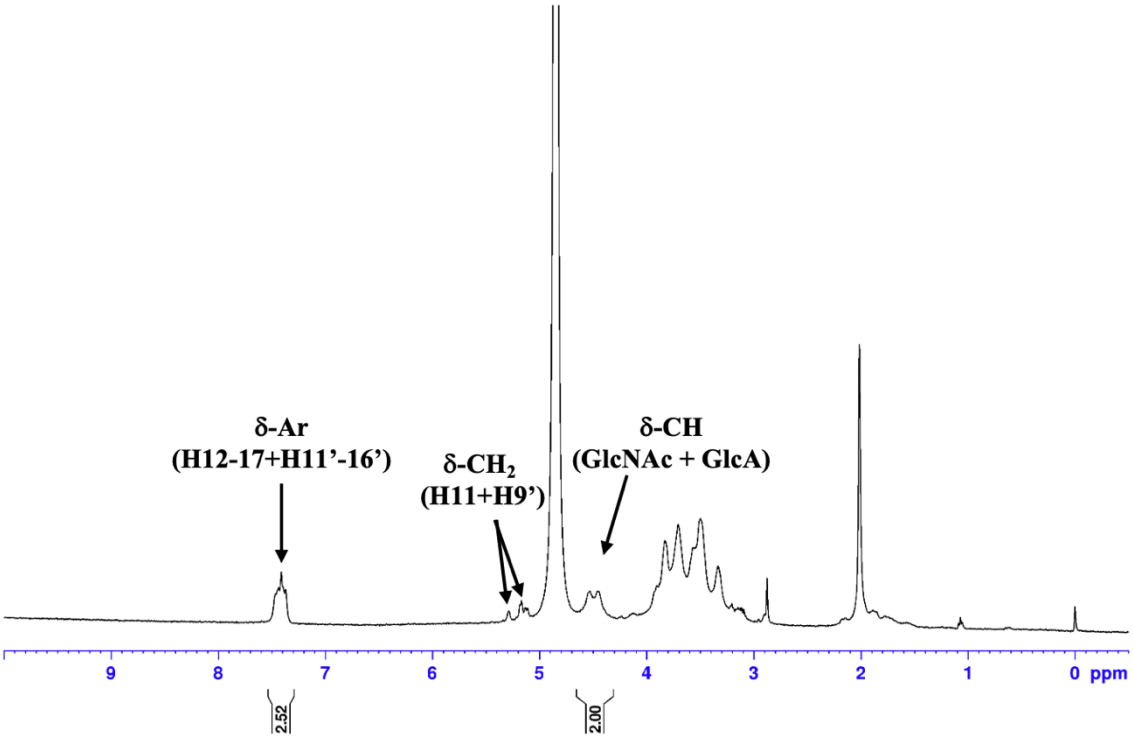

Figure 3. ^{1}H-NMR spectrum of **derivative 9-ii** (400 MHz, D_2O, 298 K).

Compound 9-i was subjected to Pbf deprotection using a TFA-based cleavage mixture containing phenol, thioanisole, TIS and water (11.25 mL). After reaction, the mixture was diluted, neutralized to pH 7, purified by dialysis, and freeze-dried. The deprotected **derivative 10** was obtained in quantitative yield (Scheme 3).

A comparison of the ^{1}H-NMR spectra (Figure S7) highlights the structural differences between native HA and the synthesized derivatives. In particular, the spectrum of **derivative 10** shows the complete disappearance of the characteristic Pbf signals observed in **derivative 9-i**, confirming the successful removal of the protecting group. The main ^{1}H-NMR signal assignments are summarized in Table 8.

Table 8. ^{1}H-NMR chemical shift assignments of **derivative 10**.

Assignment	**^{1}H δ_{DSS} (ppm)**
1 (GlcNAc)	4.54
1 (GlcA)	4.45
2-5 (GlcA)	4.0-3.20
2-6 (GlcNAc)	4.0-3.20
NHAc (GlcNAc)	2.01

Additional characterization was performed by ATR-FTIR spectroscopy, enabling the identification of specific functional groups in HA, **derivative 9-**i and **derivative 10** (Figure S8).

The ATR-FTIR spectra highlight the spectral changes associated with Pbf protection and subsequent deprotection. Compared to native HA, **derivative 9-i** (red curve) shows an additional band at 1547 cm^{-1}, attributable to ν C=C of the aromatic Pbf group (Table 9). After Pbf cleavage, the spectrum of **derivative 10** (blue curve) shows a marked decrease in the intensity of the aromatic C=C band, together with the appearance of bands attributable to the guanidinium group: ν C-N (guanidinium, 1197 cm^{-1}), a band at 840 cm^{-1} associated with guanidinium-related vibrations [16], and the asymmetric ν C-N/C=N stretching vibration at 1676 cm^{-1} [17]. In addition, the band observed at 1560 cm^{-1} is consistent with amide II (δ N-H + ν C-N).

Table 9. IR band assignments for **derivative 9-i** and **derivative 10.**

IR assignments Derivative 9-i (red curve)	**Wavenumber (cm^{-1})**	**IR assignments Derivative 10 (blue curve)**	**Wavenumber (cm^{-1})**
ν O-H (*)	3285	ν O-H (*)	3379
ν C=O (Amide I)(*)	1605	ν_{as} C-N/ C=N(*)	1676
ν C=C (aromatic, Pbf)(*)	1547	ν_{s} C-N/ C=N(*)	1623
ν C-O-C (*)	1152	δ N-H + ν C-N (amide II)(*)	1560
ν C-O (*)	1032	ν C-N (guanidinium) (*)	1197
		ν C-O-C (*)	1130
		γ N-H (guanidinium) (*)	840

Compound 9-ii was subjected to Cbz deprotection by catalytic hydrogenolysis using Pd/C in an EtOH/H_2O (1:1 v/v, 25 mL) mixture [18]. After completion of the reaction, the catalyst was filtered and the solution was purified by dialysis and freeze-dried. The deprotected **derivative 11** was obtained in 59% yield (Scheme 3). A comparison of the ^{1}H-NMR spectra of HA and **derivative 9-ii** shows the signals at δ_{DSS} = 7.53-7.30 ppm and 5.33-5.06 ppm, attributable to the aromatic and benzylic protons of the Cbz protecting group. In the spectrum of **derivative 11**, these Cbz resonances are still detectable, although with reduced intensity, indicating that the deprotection is only partial (Figure S9). The main ^{1}H-NMR signal assignments are summarized in Table 10.

Table 10. ^{1}H-NMR chemical shift assignments of **derivative 11**.

Assignment	^{1}H δ_{DSS} (ppm)
1 (GlcNAc)	4.54
1 (GlcA)	4.45
2-5 (GlcA)	4.0-3.20
2-6 (GlcNAc)	4.0-3.20
12-17	7.53-7.30
11'-16'	7.53-7.30
9'	5.33-5.06
11	5.33-5.06
NHAc (GlcNAc)	2.01

ATR-FTIR spectroscopy enables comparison of the spectra of HA, the conjugation **product 9-ii**, and the hydrogenolysis **product 11** (Figure S10). In **derivative 9-ii** (red curve), bands attributable to the Cbz protecting groups are clearly observed, including the carbonyl stretching band at 1716 cm^{-1} (ν C=O, Cbz), the aromatic ring stretching vibrations at 1510 cm^{-1} (ν C=C, aromatic, Cbz), and the benzylic C-O stretching band at 1241 cm^{-1} (ν C-O, benzylic, Cbz). In addition, the amide bond formed upon conjugation is evidenced by the amide I band at 1604 cm^{-1} (ν C=O). In the spectrum of **derivative 11** (blue curve), the Cbz-related bands are markedly reduced. The main IR assignment are reported in Table 11.

Table 11. IR band assignments for HA, **derivative 9-ii** and **derivative 11**.

IR assignments Derivative 9-ii (red curve)	**Wavenumber (cm^{-1})**	**IR assignments Derivative 11 (blue curve)**	**Wavenumber (cm^{-1})**
v O-H (*)	3372	*v* O-H (*)	3286
v C-H (aliphatic) (*)	2914	*v* C=O (Amide I)(*)	1609
v C=O (Cbz) (*)	1716	*v* C-O (*)	1023
v C=O (Amide I)(*)	1604		
v C=C (aromatic, Cbz) (*)	1510		
v C-O (benzylic, Cbz) (*)	1241		
v C-O-C (*)	1152		
v C-O (*)	1031		

The third synthetic strategy involved the use of Boc-Arg-OH. In this case, Boc deprotection was carried out at room temperature in a 45% (v/v) TFA solution in CH_2Cl_2 (10 mL), affording **derivative 6** (Scheme 4) in quantitative yield. The efficiency of the deprotection reaction was confirmed by ^{1}H-NMR spectroscopy (Figure S11).

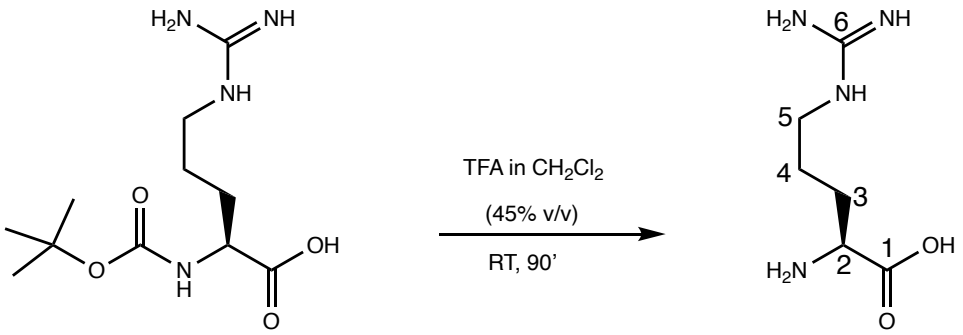

5 **6**

Scheme 4. Removal of the Boc protecting group from **derivative 5**.

The ^{1}H-NMR spectrum of **derivative 6** (Figure S11) shows characteristic resonances of the arginine moiety at δ_{DSS} = 3.95 ppm, corresponding to the methine proton (H2, C*H*), and at δ_{DSS} = 3.24, 1.95, and 1.70 ppm, corresponding to the methylene protons (CH_2, H5, H3, and H4, respectively). Additional evidence of the deprotection was provided by ^{13}C NMR analysis of **derivative 6** (Figure S12). Signals characteristic of the arginine backbone were observed, including a resonance at δ_{DSS} = 172.5 ppm, attributable to the carboxyl carbon, and additional signals in the aliphatic region at δ_{DSS}= 53.0, 40.4, 27.1, and 23.6 ppm, corresponding to the carbon atoms of the side chain. A signal at δ_{DSS} = 156.9 ppm is consistent with the guanidinium carbon. The main ^{1}H and ^{13}C-NMR signal assignments are summarized in Table 12.

Table 12. ^{1}H and ^{13}C-NMR chemical shift assignments of **derivative 6**.

Assignment	^{1}H δ_{DSS} (ppm)	^{13}C δ_{DSS} (ppm)
1	-	172.5
2	3.95	53.0
3	1.95	23.6
4	1.70	27.1
5	3.24	40.4
6	-	156.9

Further confirmation of Boc removal was provided by the ATR-FTIR spectrum shown in Figure S13. Boc removal in **derivative 6** (black curve) was confirmed by the presence of an intense band at ~3169 cm^{-1}, associated with the N-H stretching vibration, as well as by the absence of the characteristic absorptions at 1364 cm^{-1} and 1388 cm^{-1}, which were clearly visible in the spectrum of Boc-Arg-OH (red curve) and correspond to the CH_3 bending modes of the Boc tert-butyl group.
The remaining characteristic signals of the amino acid backbone are summarised in Table 13 [16].

Table 13. IR band assignments for Boc-Arg-OH and **derivative 6**.

IR assignments Derivative 6 (black curve)	Wavenumber (cm^{-1})	IR assignments Boc-Arg-OH (red curve)	Wavenumber (cm^{-1})
ν O-H (*)	3336	ν O-H (*)	3336
ν N-H (*)	3169	ν N-H (*)	3140
ν C-H (aliphatic) (*)	2944-2883	ν C-H (aliphatic) (*)	2970-2862
ν C=O (Amide I) (*)	1642	ν C=O (Boc) (*)	1668
ν N-C-N (guanidinium) (*)	1180	δ CH_3 (Boc) (*)	1388-1364
ν C-C (*)	1121	ν N-C-N (guanidinium)(*)	1160

After Boc deprotection, **compound 6** was coupled to HA using the previously described EDC/s-NHS activation procedure, affording **compound 12-i** with a yield of 54% (Scheme 5).

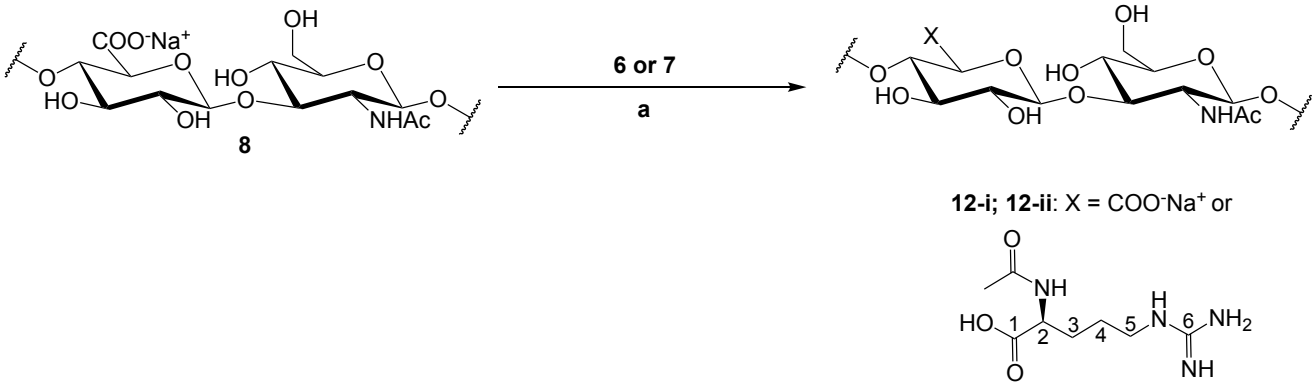

Scheme 5. Synthetic route for the preparation of HA-Arg-OH bioconjugates. **a)** EDC·HCl, s-NHS, MES, H_2O, pH = 6, room temperature, overnight

The successful conjugation in **derivative 12-i** was confirmed by the ^{1}H-NMR spectrum (Figure 4). In addition to the characteristic signals of the hyaluronic acid backbone, new resonances attributable to the arginine moiety were observed. In particular, the methine proton of arginine (H2) appeared at δ_{DSS} =4.25 ppm, while the methylene protons of the side chain were detected at δ_{DSS} = 3.20, 1.89, and 1.64 ppm, assigned to the H5, H3, and H4 protons of the arginine side chain, respectively.
The degree of substitution was determined to be 13%, as calculated according to Equation 7:

$$DS = \frac{ICH_{\,(Arg-OH)}}{ICH_{(GlcA+\,GlcNAc)}/2)} \quad (7)$$

$ICH_{\,(Arg-OH)}$ corresponds to the integral of the methine proton (H2) of the arginine moiety conjugated to HA (δ_{DSS} = 4.25 ppm), while $ICH_{(GlcA+\,GlcNAc)}$ represents the combined integral of the anomeric protons of GlcA (δ_{DSS} = 4.46 ppm) and GlcNAc (δ_{DSS} = 4.54 ppm) in the HA backbone. The division by two accounts for the two monosaccharide units forming the repeating disaccharide of hyaluronic acid. Although relatively modest, this degree of modification is close to the value considered optimal to avoid compromising the biological functionality of HA [19].
The main ^{1}H-NMR signal assignments are summarized in Table 14.

Table 14. [1]H-NMR chemical shift assignments of **derivative 12-i**.

Assignment	^1H δ_{DSS} (ppm)
1 (GlcNAc)	4.54
1 (GlcA)	4.46
2-5 (GlcA)	4.0-3.20
2-6 (GlcNAc)	4.0-3.20
2	4.25
5	3.20
3	1.89
4	1.64
NHAc (GlcNAc)	2.01

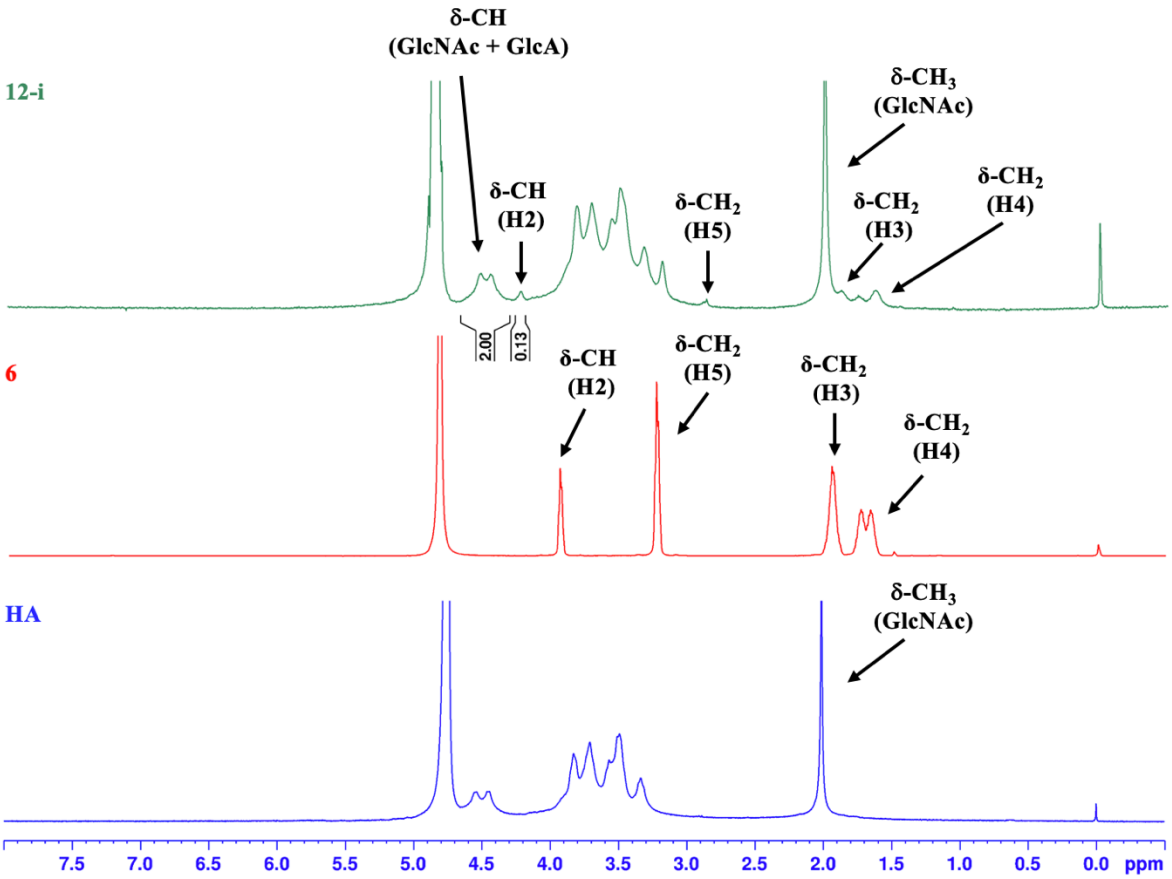

Figure 4. [1]H-NMR spectra of HA (black curve), **derivative 6** (red curve), and **derivative 12-i** (green curve) **(**400 MHz, D_2O, 298 K**)**.

Further confirmation of the successful conjugation was obtained by ATR-FTIR analysis (Figure 5).

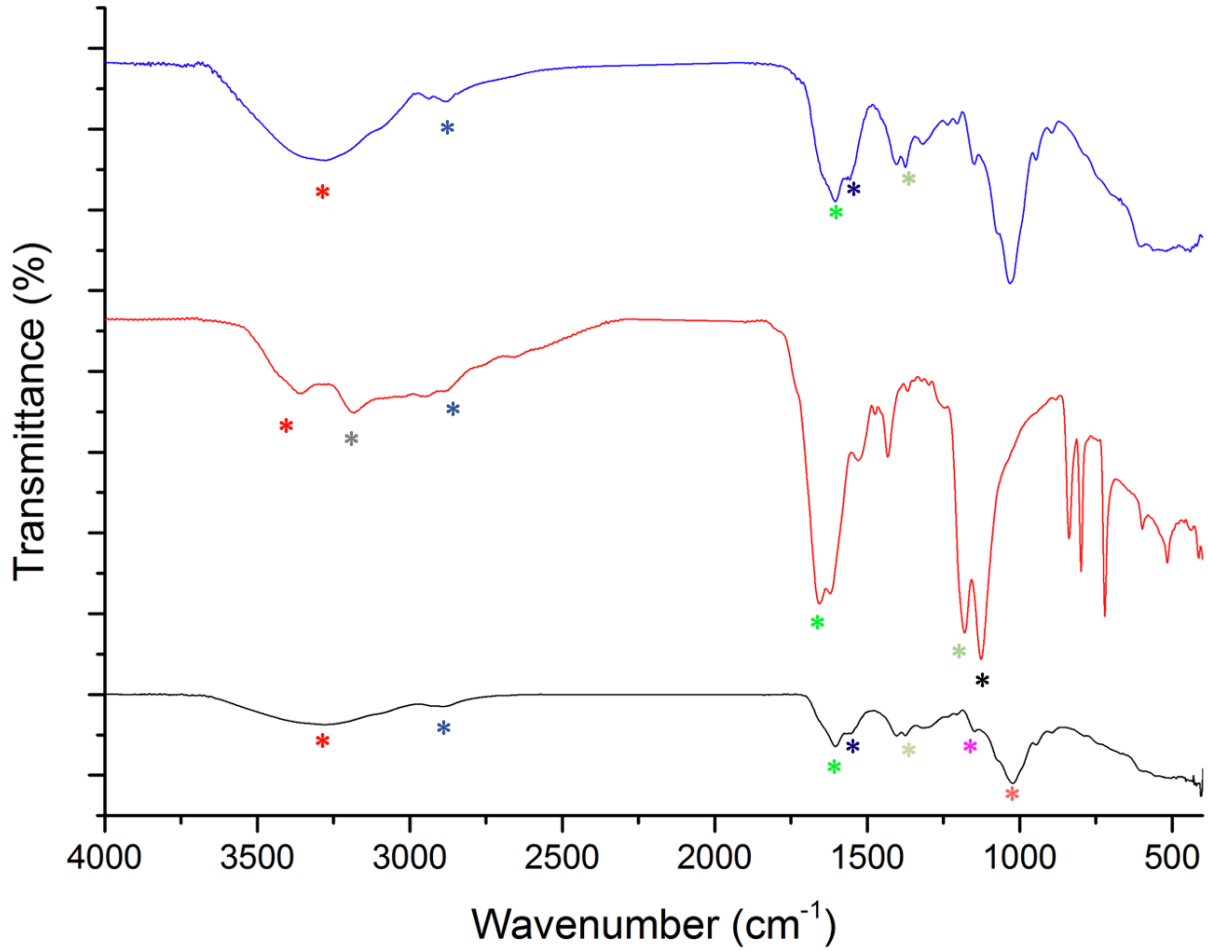

Figure 5. ATR-FTIR spectra of HA (black curve), **derivative 6** (red curve), and **derivative 12-i** (blue curve).

Figure 5 compares the ATR-FTIR spectra of native HA (black curve), **derivative 6** (red curve), and **derivative 12-i** (blue curve). The spectrum of HA exhibits the characteristic features of the polysaccharide backbone, including the broad O-H stretching band in the 3500-3000 cm^{-1} region, C-H stretching vibrations around 2876 cm^{-1}, the amide I band at ~1603 cm^{-1}, and the amide II band at ~1540 cm^{-1}. The spectrum of **derivative 12-i** retains the characteristic absorptions of the HA backbone, including the O-H stretching band and the amide I and II bands. Compared to native HA, slight variations in the shape of the bands associated with C-H stretching (~2884 cm^{-1}) and bending (~1384 cm^{-1}) vibrations were observed, suggesting the presence of the amino acid moiety within the HA repeating unit. The main IR band assignments for HA and **derivative 12-i** are summarized in Table 15. In contrast, **derivative 6** displays a distinct spectral profile associated with the free amino acid after Boc removal; its characteristic IR absorptions are reported separately in Table 13.

Table 15. IR band assignments for HA and **derivative 12-i**.

IR assignments HA (black curve)	**Wavenumber (cm^{-1})**	**IR assignments Derivative 12-i (blue curve)**	**Wavenumber (cm^{-1})**
ν O-H (*)	3284	ν O-H (*)	3311
ν C-H (aliphatic) (*)	2876	ν C-H (aliphatic) (*)	2884
ν C=O (Amide I) (*)	1603	ν C=O (Amide I) (*)	1606
δ N-H + ν N-C (Amide II) (*)	1540	δ N-H + ν N-C (Amide II) (*)	1552
δ C-H (*)	1377	δ C-H (*)	1384
ν C-O-C (*)	1146		
Ѵ C-O (*)	1014		

The fourth strategy for the preparation of the HA-Arg-OH bioconjugate involved the direct amidation of HA with commercial arginine hydrochloride (**compound 7**). In this approach, unprotected arginine was employed, thus avoiding any protection or deprotection steps before or after the coupling reaction. As in the previous strategies, the conjugation was carried out via carbodiimide-mediated activation of the HA carboxyl groups under aqueous conditions (Scheme 5). The resulting bioconjugate (**derivative 12-ii**) was obtained in 80% yield.

The successful formation of the HA-Arg-OH conjugate was confirmed by ^{1}H-NMR analysis (Figure 6). In addition to the characteristic resonances of the HA backbone, new signals attributable to the arginine moiety were clearly observed. In particular, the methine proton of arginine (H2) appeared at δ_{DSS} = 4.24 ppm, while the methylene protons of the side chain were detected at δ_{DSS} = 3.21 ppm (H5), 1.90 ppm (H3), and 1.65 ppm (H4), confirming the successful incorporation of arginine into the HA backbone. The DS was 16%, as calculated according to Equation 8:

$$DS = \frac{ICH_{(Arg-OH)}}{ICH_{(GlcA+GlcNAc)}/2} \quad (8)$$

$ICH_{(Arg-OH)}$ represents the integral of the methine proton (H2) of the conjugated arginine moiety (δ_{DSS} = 4.24 ppm), while $I_{CH\ (GlcA+GlcNAc)}$ corresponds to the combined integral of the anomeric protons of GlcA (δ_{DSS} = 4.46 ppm) and GlcNAc (δ_{DSS} = 4.54 ppm). The division by two accounts for the two monosaccharide units forming the repeating disaccharide of hyaluronic acid. A moderate DS was intentionally maintained to preserve the biological activity of hyaluronic acid, since HA binding to CD44 depends on the integrity of the GlcA carboxylate, the *N*-acetyl group of GlcNAc, and the HA-binding domain of the receptor [5, 20]. Literature reports indicate that limited derivatization does not compromise CD44 recognition, whereas extensive modification of the HA backbone can significantly reduce receptor affinity [19].

The main ^{1}H-NMR signal assignments are summarized in Table 16.

Table 16. ^{1}H-NMR chemical shift assignments of **derivative 12-ii**.

Assignment	^{1}H δ_{DSS} (ppm)
1 (GlcNAc)	4.54
1 (GlcA)	4.46
2-5 (GlcA)	4.0-3.20
2-6 (GlcNAc)	4.0-3.20
2	4.24
5	3.21
3	1.90
4	1.65
NHAc (GlcNAc)	2.01

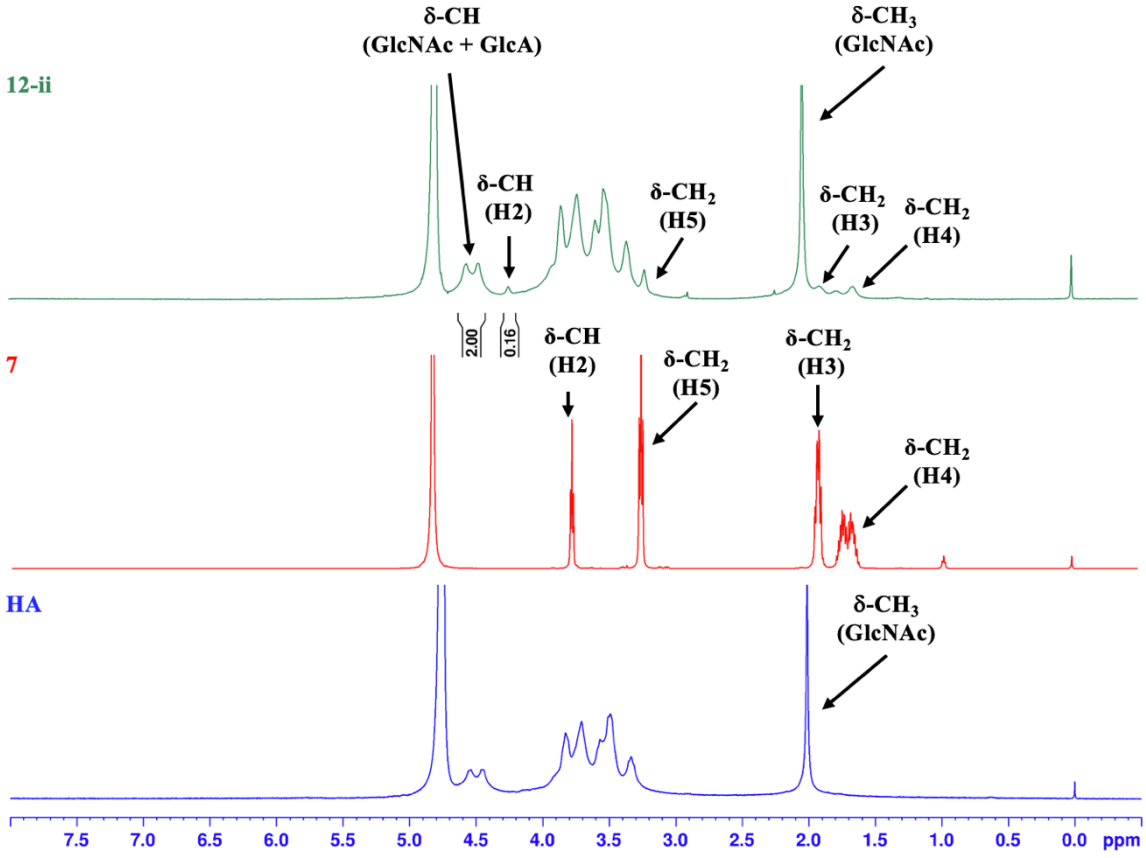

Figure 6. ^{1}H-NMR spectra of HA (blue curve), **compound 7** (red curve), and **derivative 12-ii** (green curve) (500 MHz, D_2O, 298 K).

ATR-FTIR analysis further characterized the bioconjugation process (Figure 7), which compares the spectra of native HA (black curve), **compound 7** (red curve), and **derivative 12-ii** (blue curve). The ATR-FTIR spectrum of HA (black curve) was discussed previously, and its main band assignments

are reported in Table 15. The spectrum of **compound 7** (red curve) displayed the expected vibrational features of free arginine, including N-H stretching of the primary amine and guanidinium groups at 3372 and 3262 cm^{-1}, aliphatic C-H stretching bands between 2929-2863 cm^{-1}, the carboxylic C=O stretch at 1670 cm^{-1}, and the C=N vibration of the guanidinium group at 1614 cm^{-1}. In the spectrum of **derivative 12-ii** (blue curve), the spectral profile was dominated by the HA backbone, as expected given the relatively low degree of substitution (DS 16%). Nevertheless, additional features consistent with the presence of arginine could be identified, including subtle but systematic variations in the C-H stretching region (2974-2895 cm^{-1}) and in the C-H bending region (around 1372 cm^{-1}). Although the distinct vibrational modes of free arginine were not directly observed due to their low relative intensity within the polymer matrix, the observed changes in the C-H regions, together with the NMR evidence, confirmed the successful conjugation of arginine to HA. The main IR band assignments are summarized in Table 17.

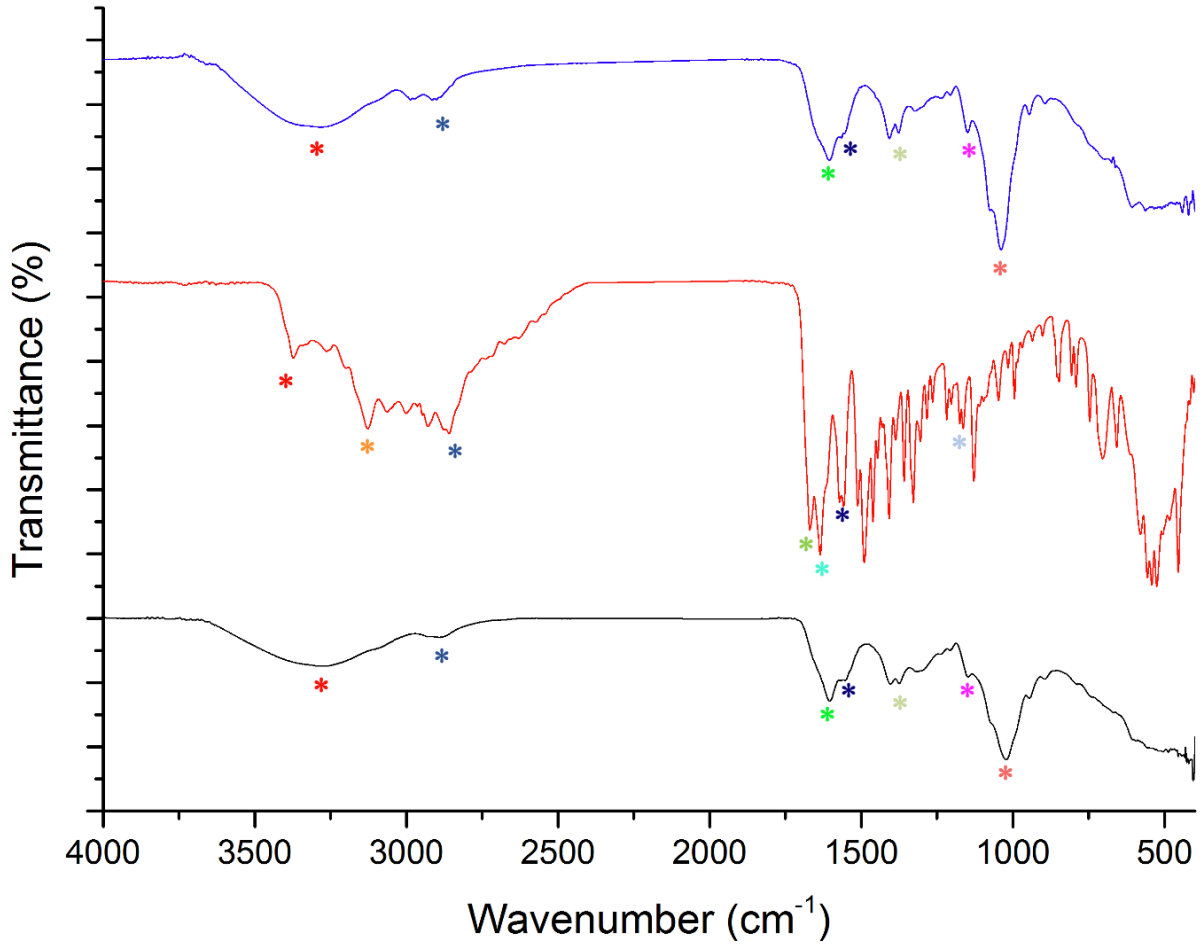

Figure 7. ATR-FTIR spectra of HA (black curve), **compound 7** (red curve), and **derivative 12-ii** (blue curve).

Table 17. IR band assignments for HA, **compound 7** and **derivative 12-ii**.

IR assignments Compound 7 (red curve)	**Wavenumber (cm^{-1})**	**IR assignments Derivative 12-ii (blue curve)**	**Wavenumber (cm^{-1})**
ν O-H/ ν N-H(*)	3372	ν O-H(*)	3289
ν N-H (guanidinium)(*)	3262	ν C-H (aliphatic)(*)	2974-2895
ν C-H (aliphatic)(*)	2929	ν C=O (Amide I) (*)	1613
ν C=O (COOH) (*)	1670	δ N-H + ν C-N (Amide II) (*)	1558
ν C=N (guanidium)(*)	1630	δ C-H (*)	1372
δ N-H + ν C-N (Amide II) (*)	1558	ν C-O-C (*)	1147
ν C-N (guanidinium) (*)	1174	ν C-O (*)	1021

3.2 Comparison of the Molecular Weight of HA-Arg-OH Derivatives

The flow times were measured for native HA and for the three HA-Arg-OH bioconjugates (**10, 11 and 12-ii**), synthesized through different strategies (Scheme 3 and 5). These measurements allowed the determination of their relative, specific, and reduced viscosities.

The flow times measured for native HA solutions at different concentrations are reported in Table 18 as T1, T2, and T3, together with the corresponding mean values and standard deviations.

For each solution, the flow time was measured in triplicate using an Ostwald viscometer. From the average flow times, the relative viscosity (η_{rel}), specific viscosity (η_{sp}), and reduced viscosity (η_{red}) were calculated and summarized in Table 19. The reduced viscosity values were plotted as a function of polymer concentration (Figure 8), and the intrinsic viscosity [η] was obtained from the intercept of the linear fit at zero concentration, as described in Section 2.2.14. Based on the intrinsic viscosity values, molecular weights were calculated using the Mark-Houwink-Sakurada equation, using the constants appropriate for each molecular-weight range.

- **HA:**

Table 18. Flow times (T1-T3), mean values, and standard deviations for HA solutions at different concentrations.

	T1 (s)	T2 (s)	T3 (s)	Mean (s)	SD (s)
Solvent (0.15 M NaCl)	118.85	119.82	119.66	119.44	±0.52
HA 1.0 mg/mL	159.69	159.53	160.50	159.91	±0.52
HA 0.75 mg/mL	150.73	151.54	151.79	151.35	±0.55
HA 0.50 mg/mL	138.00	138.98	139.68	138.89	±0.84
HA 0.25 mg/mL	123.62	124.72	124.49	124.28	±0.58

Table 19. Relative viscosity ($\boldsymbol{\eta_{rel}}$), specific viscosity ($\boldsymbol{\eta_{sp}}$), and reduced viscosity ($\boldsymbol{\eta_{red}}$) of HA solutions.

HA (mg/mL)	$\boldsymbol{\eta_{rel}}$	$\boldsymbol{\eta_{sp}}$	$\boldsymbol{\eta_{red}}$
1.0	1.34	0.34	338.77
0.75	1.27	0.27	356.21
0.5	1.16	0.16	325.57
0.25	1.04	0.04	161.86

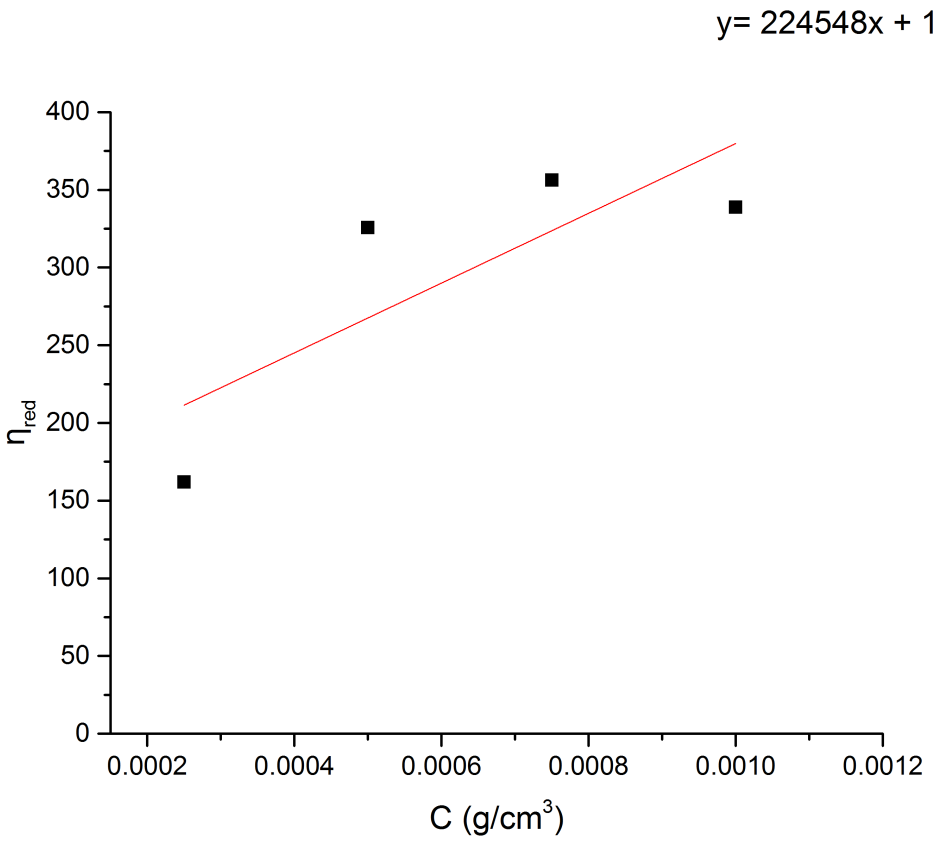

Figure 8. Reduced viscosity ($\boldsymbol{\eta_{red}}$) of HA solutions as a function of polymer concentration.

$[\eta]_{intrinsic}$ = 155.26 cm^3/g M_{HA} =45796 g/mol

The linear trend observed in the reduced viscosity as a function of concentration confirms the validity of the extrapolation procedure and supports the determination of the intrinsic viscosity [η].

Using the intrinsic viscosity value obtained from the extrapolation, the molecular weight of HA was calculated according to the Mark-Houwink-Sakurada equation, resulting in an estimated molecular weight of M_{HA}= 45796 g/mol.

The molecular weight of native hyaluronic acid determined by capillary viscometry (~ 4.6×10^4 g/mol, corresponding to 45796 g/mol) is lower than the nominal value reported by the manufacturer (186 kDa). Such discrepancies are not unexpected, as the molecular weight of hyaluronic acid is strongly method-dependent and is influenced by the definition of molecular weight considered (e.g., viscosity-average versus weight-average molecular weight), as well as by polymer conformation and intermolecular interactions in solution. Indeed, rheological and viscosimetric studies have shown that the effective molecular weight governing the macroscopic properties of HA solutions may differ

significantly from the nominal molecular weight, particularly when chain entanglement, chemical modification, or solution conditions are involved [21, 22].

- HA-Arg-OH **(Derivative 10)**

The flow times measured for **derivative 10** solutions at different concentrations are reported in Table 20. The corresponding relative, specific, and reduced viscosities are summarized in Table 21.

Table 20. Flow times (T1-T3), mean values, and standard deviations for the **derivative 10** solutions at different concentrations.

	T1 (s)	T2 (s)	T3 (s)	Mean (s)	SD (s)
Solvent (0.15 M NaCl)	82.69	82.55	82.00	82.52	±0.18
Derivative 10: 10 mg/mL	95.39	95.31	95.47	95.39	±0.08
Derivative 10: 7.5 mg/mL	92.62	93.31	92.93	92.95	±0.35
Derivative 10: 5.0 mg/mL	89.81	90.65	90.83	90.43	±0.54
Derivative 10: 2.5 mg/mL	87.71	88.00	87.51	87.74	±0.25

Table 21. Relative viscosity ($\boldsymbol{\eta_{rel}}$), specific viscosity ($\boldsymbol{\eta_{sp}}$), and reduced viscosity ($\boldsymbol{\eta_{red}}$) of **derivative 10**.

Derivative 10 (mg/mL)	$\boldsymbol{\eta_{rel}}$	$\boldsymbol{\eta_{sp}}$	$\boldsymbol{\eta_{red}}$
10	1.16	0.16	15.59
7.5	1.13	0.13	16.85
5.0	1.10	0.10	19.16
2.5	1.06	0.06	25.29

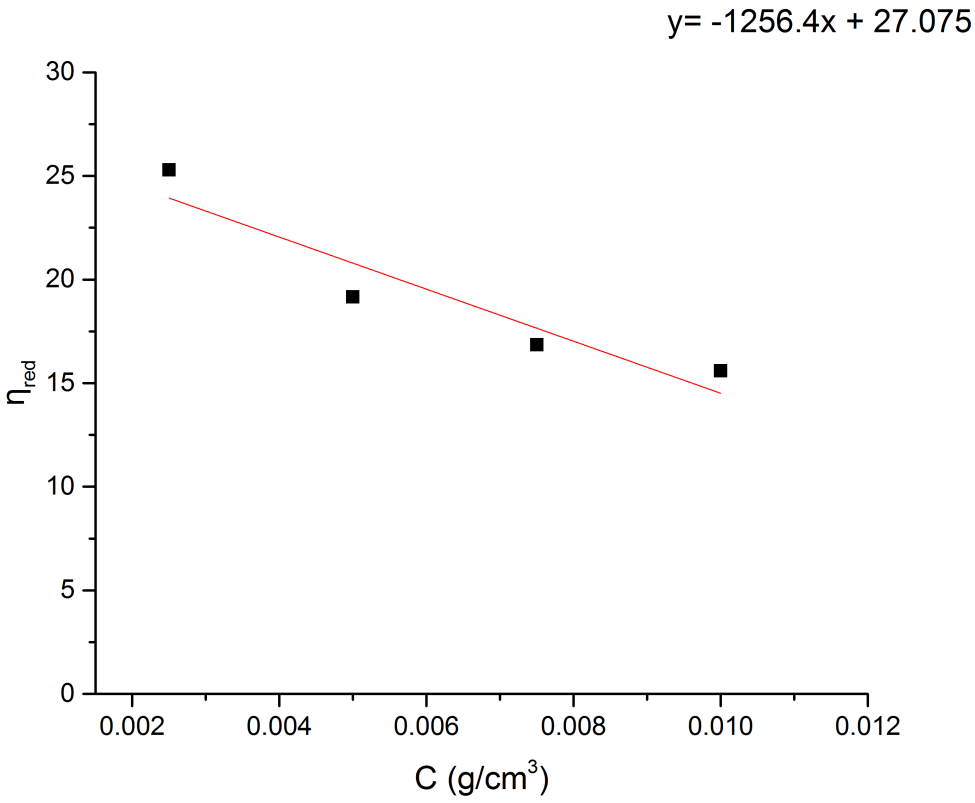

Figure 9. Reduced viscosity (η_{red}) of **derivative 10** solutions as a function of polymer concentration.

$[\eta]_{intrinsic} = 27.075\ cm^3/g$ $M_{\boldsymbol{derivative\ 10}} = 9552\ g/mol$

The intrinsic viscosity obtained for **derivative 10** was markedly lower than that of native HA, confirming that the polymer falls within the low-molecular-weight range. Therefore, the molecular weight was calculated using the Mark–Houwink–Sakurada parameters reported for low-molecular-weight hyaluronic acid in 0.15 M NaCl ($K = 6.54 \times 10^{-4}\ cm^3 \cdot g^{-1}$, $a = 1.16$). Based on these parameters, the molecular weight of derivative 10 was estimated to be 9552 g/mol.

This result suggests that the acidic Pbf deprotection conditions may have promoted partial depolymerization of the HA backbone.

- HA-Arg-OH (**Derivative 11**)

The flow times measured for **derivative 11** solutions at different concentrations are reported in Table 22. The corresponding relative, specific, and reduced viscosities are summarized in Table 23.

Table 22. Flow times (T1-T3), mean values, and standard deviations for the **derivative 11** solutions at different concentrations.

	T1 (s)	T2 (s)	T3 (s)	Mean (s)	SD (s)
Solvent (0.15 M NaCl)	118.85	119.82	119.66	119.44	±0.52
Derivative 11: 1.0 mg/mL	148.57	149.83	150.24	149.55	±0.87
Derivative 11: 0.75 mg/mL	141.77	142.49	141.48	141.91	±0.52
Derivative 11: 0.5 mg/mL	134.01	134.46	137.06	135.18	±1.65
Derivative 11: 0.25 mg/mL	121.77	123.36	125.36	123.49	±1.80

Table 23. Relative viscosity ($\boldsymbol{\eta_{rel}}$), specific viscosity ($\boldsymbol{\eta_{sp}}$), and reduced viscosity ($\boldsymbol{\eta_{red}}$) of **derivative 11**.

Derivative 11 (mg/mL)	$\boldsymbol{\eta_{rel}}$	$\boldsymbol{\eta_{sp}}$	$\boldsymbol{\eta_{red}}$
1.0	1.25	0.25	252.03
0.75	1.19	0.19	250.83
0.5	1.13	0.13	263.44
0.25	1.03	0.03	135.74

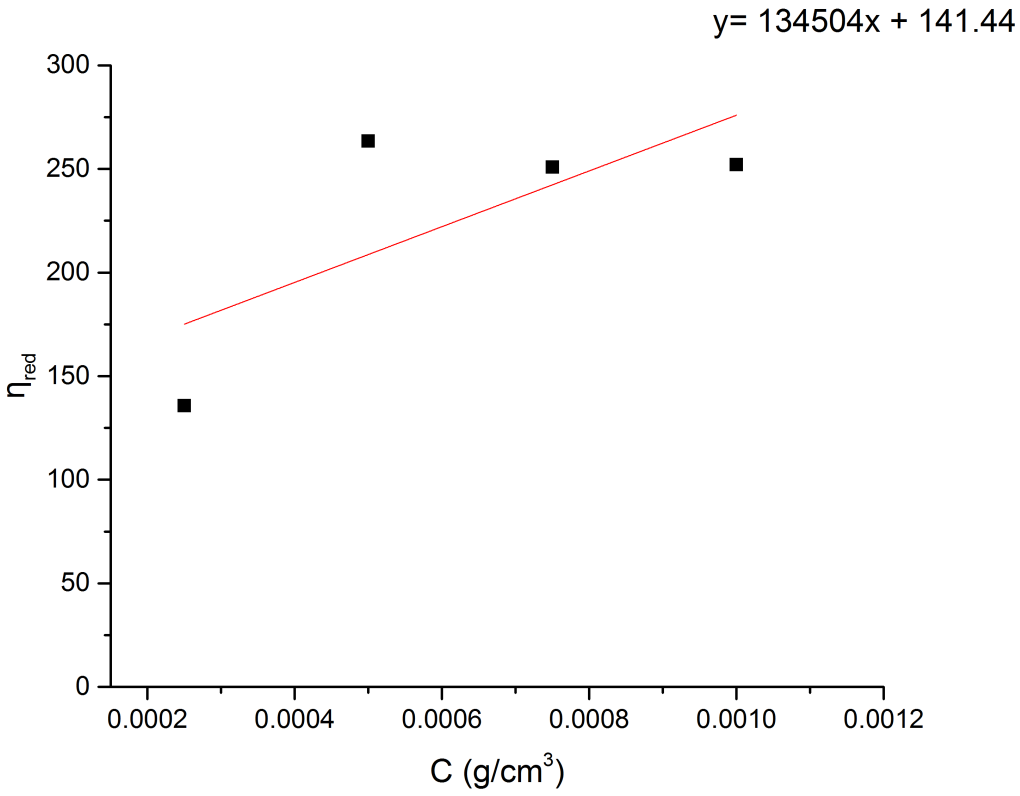

Figure 10. Reduced viscosity (η_{red}) of **derivative 11** solutions as a function of polymer concentration.

$[\eta]_{intrinsic}$ = 141.44 cm^3/g $\qquad\qquad$ $M_{\boldsymbol{derivative\ 11}}$ =40762 g/mol

The intrinsic viscosity obtained for **derivative 11** was lower than that of native HA but significantly higher than that of **derivative 10**, indicating a more limited depolymerization of the HA backbone under the employed reaction conditions; using the Mark-Houwink-Sakurada parameters appropriate for this molecular-weight range, the molecular weight of **derivative 11** was estimated to be 40762 g/mol.

- HA-Arg-OH (**Derivative 12-i**)

The flow times measured for **derivative 12-i** solutions at different concentrations are reported in Table 24. The corresponding relative, specific, and reduced viscosities are summarized in Table 25.

Table 24. Flow times (T1-T3), mean values, and standard deviations for the **derivative 12-i** solutions at different concentrations.

	T1 (s)	T2 (s)	T3 (s)	Mean (s)	SD (s)
Solvent (0.15 M NaCl)	118.85	119.82	119.66	119.44	0.52
Derivative 12-i: 1.0 mg/mL	170.32	168.68	165.75	168.25	2.32
Derivative 12-i: 0.75 mg/mL	146.48	147.65	148.41	147.51	0.97
Derivative 12-i: 0.5 mg/mL	131.11	135.59	137.06	134.59	3.10
Derivative 12-i: 0.25 mg/mL	126.03	126.90	128.06	126.99	1.02

Table 25. Relative viscosity ($\boldsymbol{\eta_{rel}}$), specific viscosity ($\boldsymbol{\eta_{sp}}$), and reduced viscosity ($\boldsymbol{\eta_{red}}$) of **derivative 12-i**.

Derivative 12-i (mg/mL)	$\boldsymbol{\eta_{rel}}$	$\boldsymbol{\eta_{sp}}$	$\boldsymbol{\eta_{red}}$
1.0	1.41	0.41	408.62
0.75	1.24	0.24	313.34
0.5	1.13	0.13	253.57
0.25	1.06	0.06	252.95

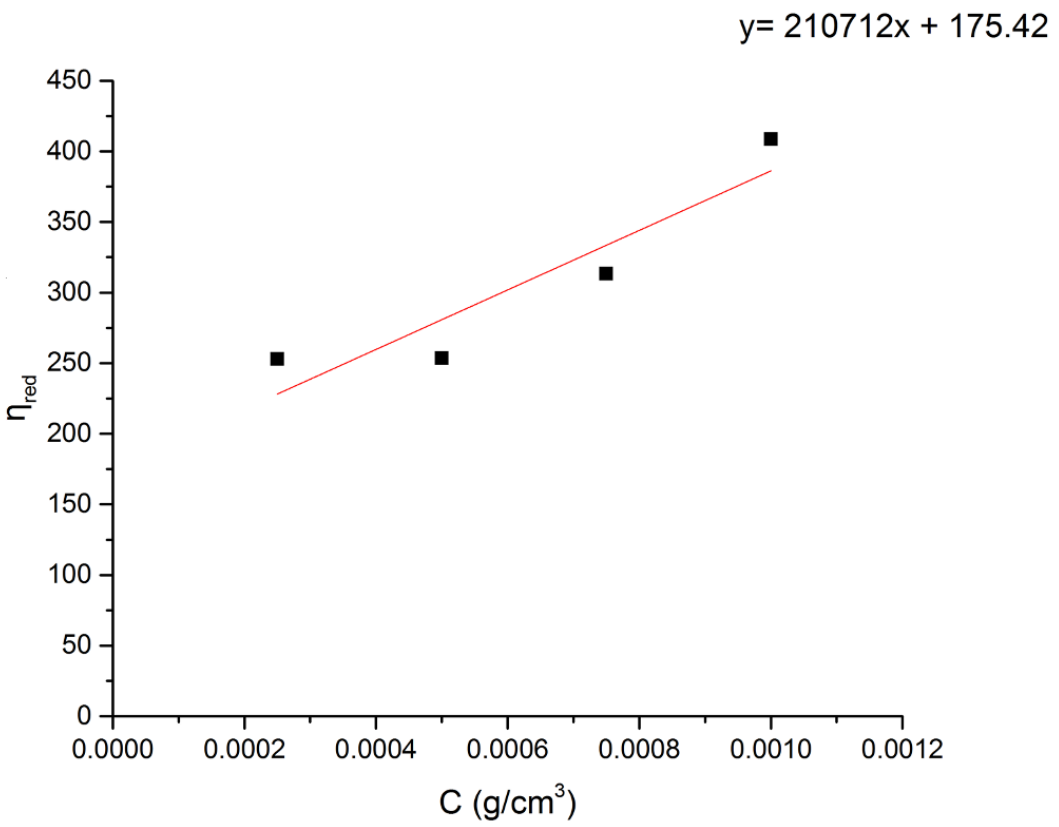

Figure 11. Reduced viscosity (η_{red}) of **derivative 12-i** solutions as a function of polymer concentration.

$[\eta]_{intrinsic}$ = 175.42 cm^3/g $M_{derivative\ 12-i}$ =53346 g/mol

The intrinsic viscosity obtained for **derivative 12-i** was higher than that of both **derivatives 10** and **11**, and slightly higher than that of native HA, indicating that the use of unprotected arginine preserved the polymer backbone and avoided significant depolymerization. Using the Mark-Houwink-Sakurada parameters appropriate for this molecular-weight range, the molecular weight of **derivative 12-i** was estimated to be 53346 g/mol.

The analysis of molecular weights estimated by capillary viscometry using an Ostwald viscometer revealed that the different synthetic strategies significantly influence the final properties of the hyaluronic acid–arginine bioconjugates (Table 26). **Derivative 10**, obtained using arginine protected with a Pbf group on the side chain and subsequently deprotected under acidic conditions, exhibited a markedly lower molecular weight compared to native HA. Similarly, **derivative 11**, synthesized using arginine protected with two Cbz groups and deprotected by hydrogenolysis, also showed a lower molecular weight than native HA, likely due to partial cleavage of glycosidic bonds in the

polysaccharide backbone during the deprotection steps. In contrast, **derivative 12-i**, prepared using unprotected arginine, displayed an increase in molecular weight relative to the starting HA, indicating a milder and more effective synthetic strategy. Overall, these results demonstrate that the reaction conditions employed in the different synthetic routes have a substantial impact on the structural integrity and final characteristics of the HA bioconjugates.

Table 26. Comparison of the molecular weights of **derivatives 10, 11** and **12-i** with HA.

Polymer	*M (g/mol)*	*K*	*a*
HA	45796	0.029	0.80
Derivative 10	9552	$6.54 \cdot 10^{-4}$	1.16
Derivative 11	40762	0.029	0.80
Derivative 12-i	53346	0.029	0.80

3.3 Raman Spectroscopy

Raman spectroscopy was used to further characterize arginine, HA, and the HA-Arg-OH bioconjugate. For these measurements, the HA-Arg-OH derivative synthesized using commercially available, unprotected L-arginine (**derivative 12-ii)** was selected as a representative sample. This choice was justified by the fact that the ATR-FTIR and NMR spectra of free L-arginine and L-arginine after deprotection were identical, indicating that the removal of protecting groups does not alter the vibrational fingerprint of arginine. For consistency across the different characterization techniques, this derivative was also used for subsequent experiments, unless otherwise specified.

The Raman spectrum of HA-Arg-OH (Figure 12, black curve) is dominated by the characteristic vibrational features of native hyaluronic acid (Figure 12, blue curve) [23,24], in agreement with the ATR-FTIR analysis. This behavior is expected, as the polymer is present at a much higher molecular weight and concentration compared to the conjugated amino acid, and therefore generates significantly stronger Raman scattering. This effect is well-documented in the vibrational spectroscopy of polysaccharide-amino acid conjugates. A comparison between HA and HA-Arg-OH reveals that the signals of the bioconjugate are systematically shifted to lower wavenumbers (Table 27). This negative Raman shift is a direct consequence of the conjugation process: the increased mass of the modified repeat units intrinsically lowers the vibrational frequencies, while the formation of new amide bonds and hydrogen-bonding interactions between HA and arginine slightly reduce the rigidity of the polymer backbone, further contributing to the downshift of the corresponding modes. Most of the Raman bands of both HA and HA-Arg-OH are located in two main spectral windows: 800-1640 cm^{-1} and 2800-3000 cm^{-1} [23]. These regions contain the major polysaccharide vibrational modes, including C-O-C bridges, ring deformations, C-H bending, C-N stretching, and the characteristic amide vibrations introduced by functionalization. A complete assignment of these signals is reported in Table 27.

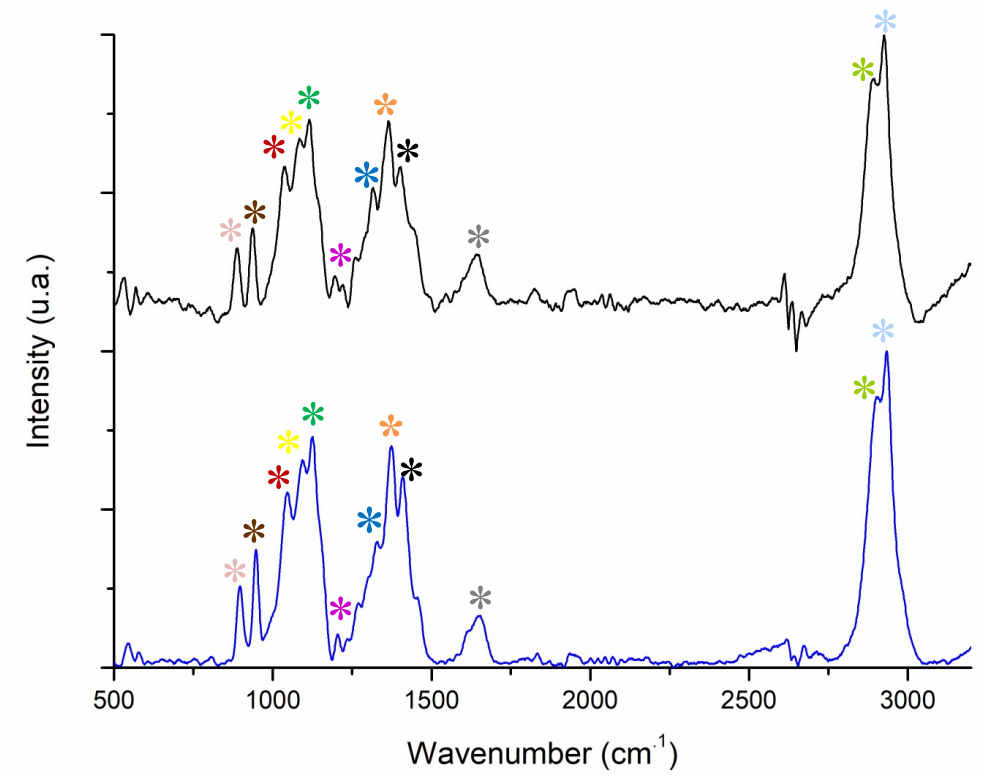

Figure 12. Raman spectra of HA (blue) and HA-Arg-OH (black). Amide C=O stretching vibration (grey star), amide C-N stretching vibration (black star), C-H stretching vibration (light green star), N-H stretching vibration (light blue star).

Table 27. Assignment of HA (blue curve) and HA-Arg-OH (black curve) functional groups to the corresponding Raman wavenumbers [23,24].

Wavenumber (cm^{-1})		**Assignments**
HA (blue curve)	HA-Arg-OH (black curve)	
895	887	δ C_1-H + ν C-O-C (*)
948	940	ν C-O-C bridge (*)
1047	1030	ν C-C and C-O (*)
1094	1087	δ C-OH (GlcNAc units) (*)
1126	1119	δ C_4-OH and δ C_4-H (*)
1203	1197	τ CH_2 (*)
1321	1312	δ C-H, Amide III (*)
1375	1363	δ C-H (*)
1406	1400	ν C-N and δ C-H (*)
1650	1644	ν C=C and ν C=O (*)
2902	2889	ν C-H (*)
2930	2920	ν N-H (*)

The Raman spectrum of pure arginine hydrochloride (Figure 13, red curve) is significantly richer in vibrational modes, particularly in the 500-1500 cm^{-1} region, where the most characteristic amino-acid functional group vibrations are found. These include guanidinium C-N and N-C-N modes, COO^- deformations, NH_2 wagging and rocking vibrations, and C-C skeletal stretching. The full vibrational assignment of arginine hydrochloride is reported in Table 28.

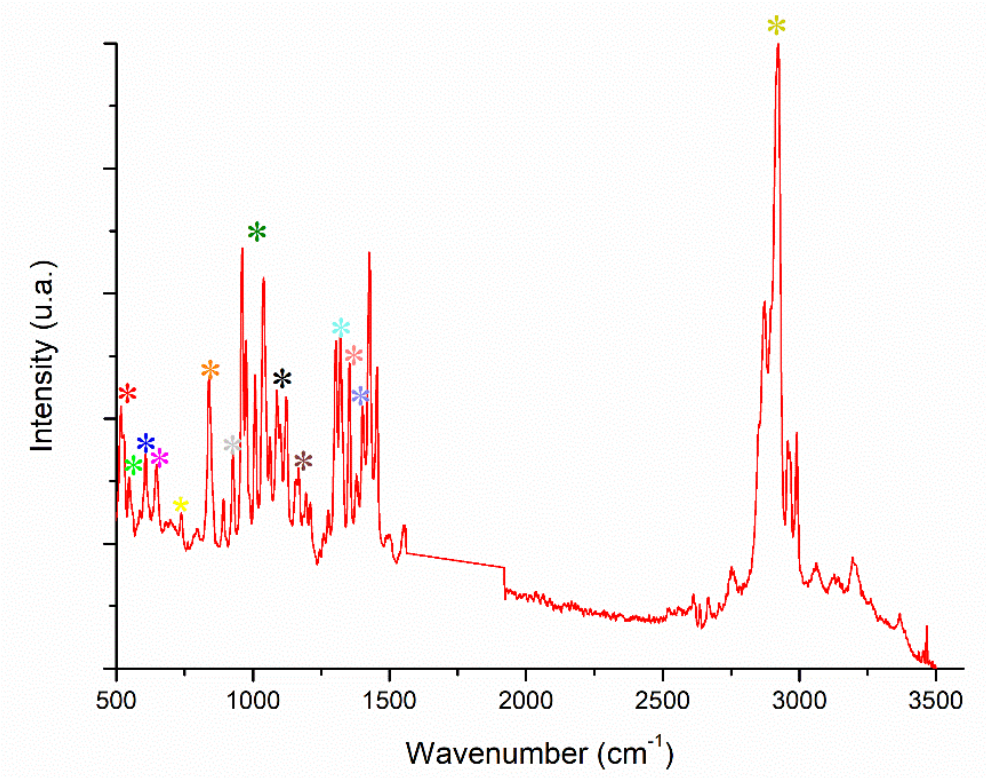

Figure 13. Raman spectra of arginine hydrochloride (red curve). C-N (guanidine) stretching vibration (brown star), C=O stretching vibration (orange star), -CH_2 stretching vibration (dark yellow star), C-N-C (guanidine) bending vibration (light green star).

Table 28. Assignment of arginine hydrochloride (red curve) functional groups to the corresponding Raman wavenumbers [25-27].

Wavenumber (cm^{-1})	**Assignments**	**Wavenumber (cm^{-1})**	**Assignments**
516	δ(N–H) (*)	965-1040	ν(C–C) (side chain)(*)
547	δ(N–C–N) guanidine (*)	1080-1124	ρ NH_3^+(*)
607	δ(COO^-)(*)	1168	ν(C–N) guanidine (*)
649	ν(C–$C_α$) (*)	1324	τ CH_2 (*)
738	ω (N-C-N) guanidine (*)	1355	ν C=O (*)
844	γ (COO^-) (*)	1399	δ(-CH_2) (*)
929	ω NH_2 (*)	2881-2993	ν(-CH_2) (*)

3.4 Circular Dichroism (CD)

Circular dichroism measurements were carried out in H_2O and phosphate-buffered saline (PBS, pH 7.0) to investigate the conformational behavior of arginine, native HA, and HA-Arg-OH as a function of temperature. The CD spectrum of arginine hydrochloride in aqueous solution (Figure 14A) displays, at 273 K, a positive band centered at approximately 201 nm, which is assigned to the π-π* transition. As the temperature increases from 273 to 310 K, a progressive decrease in the intensity of this band is observed. Both the temperature-dependent trend and the wavelength of the band maximum are consistent with the experimental and theoretical data reported by Wang et al. [28].

The CD spectrum of hyaluronic acid (Figure 14B) in aqueous solution shows a single negative band centered around 210 nm, commonly attributed to n→π* transitions of the amide chromophore in polysaccharides. As the temperature increases, the intensity of this band decreases (i.e., becomes less negative), indicating a gradual loss of local order without any cooperative conformational transition. This behavior is consistent with the findings of Staskus and Johnson [29], who reported that hyaluronic acid adopts a predominantly unordered (random-coil-like) conformation in water and exhibits only weak, non-cooperative CD changes.

The CD spectrum of the HA-Arg-OH conjugate (Figure 14C) closely resembles that of native HA, showing the same negative n→π* band at 210 nm but with a slightly more negative intensity. This modest increase suggests minor local ordering induced by arginine, while the overall temperature-dependent behavior remains comparable to HA, indicating that the conjugate still adopts a predominantly random-coil conformation in aqueous solution.

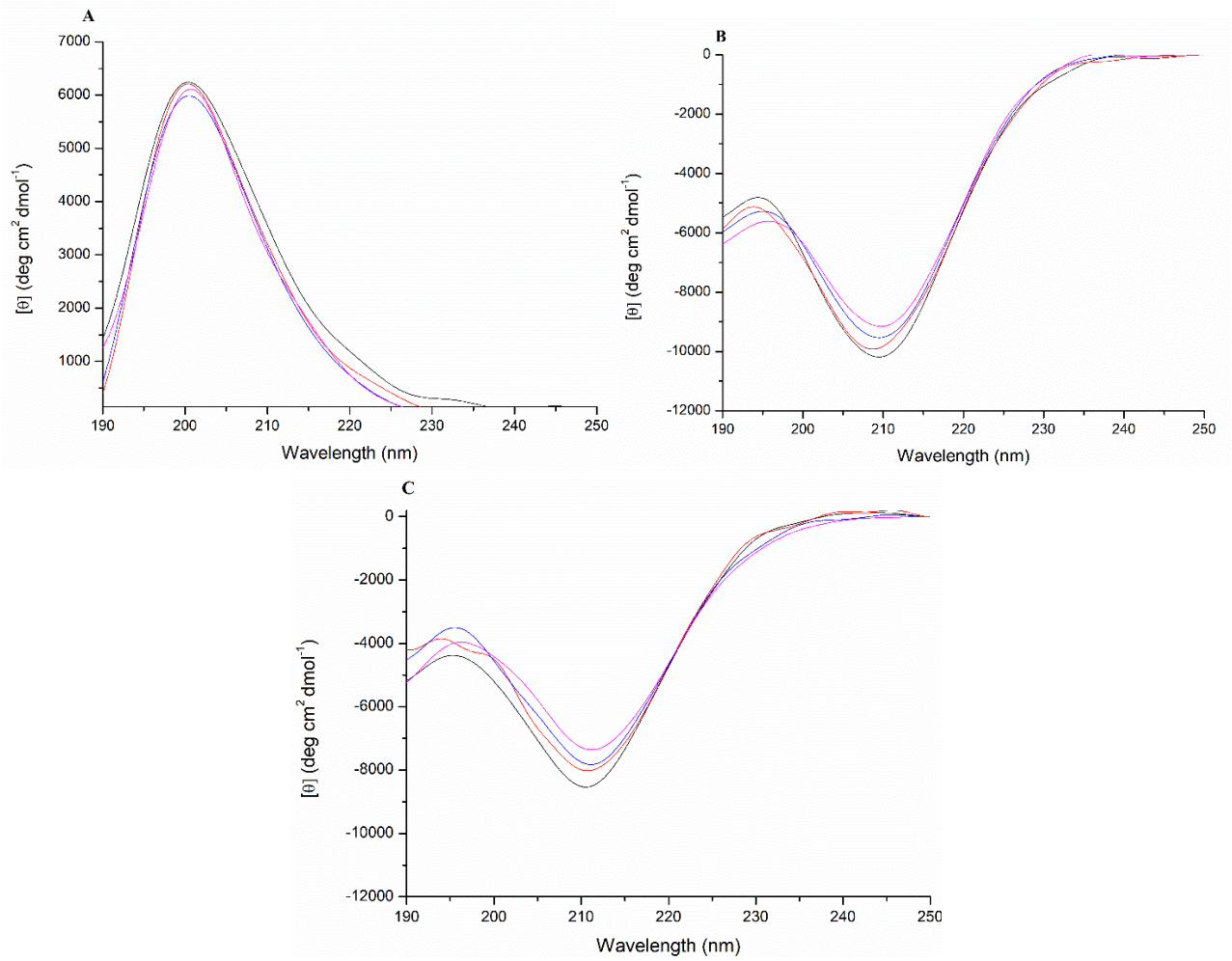

Figure 14. Temperature-dependent CD spectra in H_2O solution of: A) arginine hydrochloride, B) HA, C) HA-Arg-OH, recorded at 273 K (black), 298 K (red), 310 K (blue), and 333 K (purple).

In PBS solution, the CD spectra of arginine, native HA, and HA-Arg-OH were analyzed to evaluate whether the ionic environment modifies their conformational response to temperature.

The CD spectrum of arginine hydrochloride (Figure 15A) shows the characteristic positive band centered at 201 nm, which remains essentially unchanged in both position and shape over the temperature range studied. Only a slight decrease in ellipticity is observed upon heating, indicating that in PBS the conformational and electronic environment of arginine is only minimally affected by temperature.

The CD spectrum of hyaluronic acid in PBS solution (Figure 15B) displays a single negative band centered at approximately 209–210 nm, assigned to the n→π* transition of the amide chromophore. Upon heating, a gradual decrease in the intensity of this band is observed, without any shift in the wavelength of the band maximum. This behavior indicates a progressive loss of local order rather than a cooperative conformational transition.

The observed temperature-dependent trend is consistent with previous CD studies on hyaluronic acid in aqueous and buffered environments, which describe HA as adopting a predominantly unordered, random-coil–like conformation stabilized by hydrogen-bonding interactions along the polymer backbone [30]. The progressive decrease in ellipticity upon heating can be attributed to the weakening of these interactions, while the overall conformational organization of the polymer remains unchanged. Similarly, the HA-Arg-OH conjugate (Figure 15C) displays a negative band centered at 211 nm whose intensity diminishes with increasing temperature. The spectral shape and thermal behavior closely resemble those of native HA, consistent with a random-coil conformation preserved also in the presence of the arginine moiety.

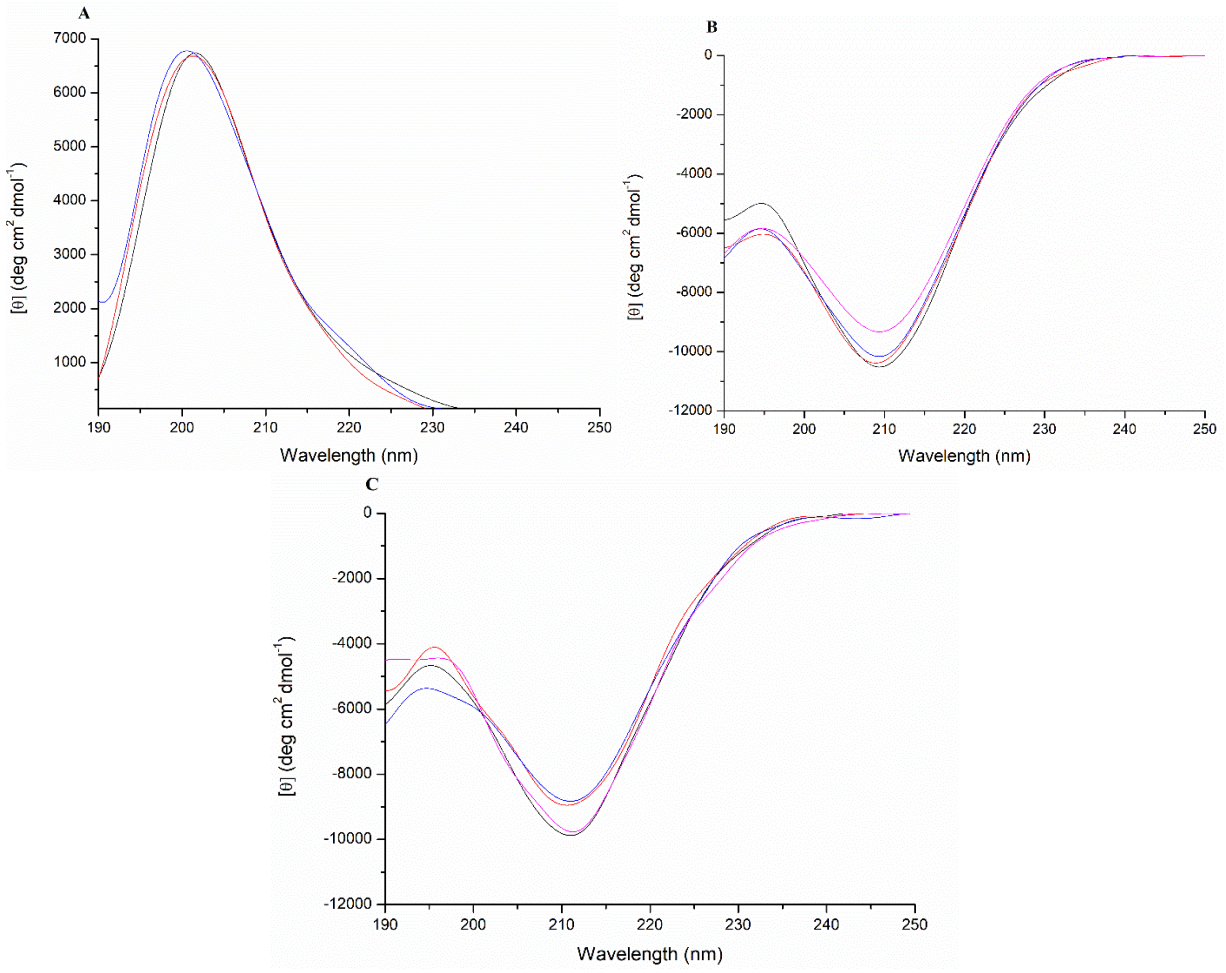

Figure 15. Temperature-dependent CD spectra in PBS solution of: A) arginine hydrochloride, B) HA, C) HA-Arg-OH recorded at 273 K (black), 298 K (red), 310 K(blue), and 333 K (purple).

Overall, for all three samples, the position of the CD bands (201 nm for arginine, 209 nm for HA, 211 nm for HA-Arg-OH) remains constant across temperatures, and the temperature-dependent

trends are analogous to those observed in water. These findings indicate that the ionic environment provided by PBS does not significantly influence the dominant conformational features of either L-arginine, HA, or HA-Arg-OH.

3.5 Electrospinning and Morphological Analysis of Electrospun Composites

The aim of this study was to fabricate asymmetric, bilayer electrospun scaffolds suitable for tissue engineering applications through the sequential electrospinning of biodegradable and bioactive polymers. This approach enables the controlled deposition of multiple layers, each designed to provide distinct biological and mechanical functions [31]. As reported in Table 1, the external hydrophobic layer was obtained by electrospinning a 12.0% w/V solution of PDLLA in HFP. The internal hydrophilic layers were produced from blends of semi-synthetic HA-Arg-OH conjugates (**derivative 12-ii**) and PVP prepared in an 80% v/v aqueous ethanol solution. The HA-Arg-OH component was incorporated at either 1% or 3% w/w, whereas PVP was used at 10% w/V. Independent optimization of the electrospinning parameters for the hydrophobic and hydrophilic formulations ensured process stability and yielded membranes with homogeneous macroscopic appearance.

At the microscopic level, SEM imaging was employed to assess the morphology of the electrospun scaffolds, with the aim of obtaining defect-free fibrous structures. All formulations produced continuous fibers with interconnected pores, characteristic of three-dimensional electrospun architectures (Figure 16). Since the results for the control scaffolds (PDLLA, PVP, PVP-HA 1%, and PVP-HA 3%) were discussed in Chapter 2, the present section focuses on the scaffolds incorporating HA-Arg-OH.

In particular, the PDLLA layer (Figure 16A) was characterized by nearly linear, smooth, and defect-free fibers. With respect to the hydrophilic layers, the electrospun scaffolds exhibited predominantly linear fiber orientation; however, the incorporation of HA or HA-based derivatives into the PVP matrix resulted in a slight fiber curling (Figure 16 B-F).

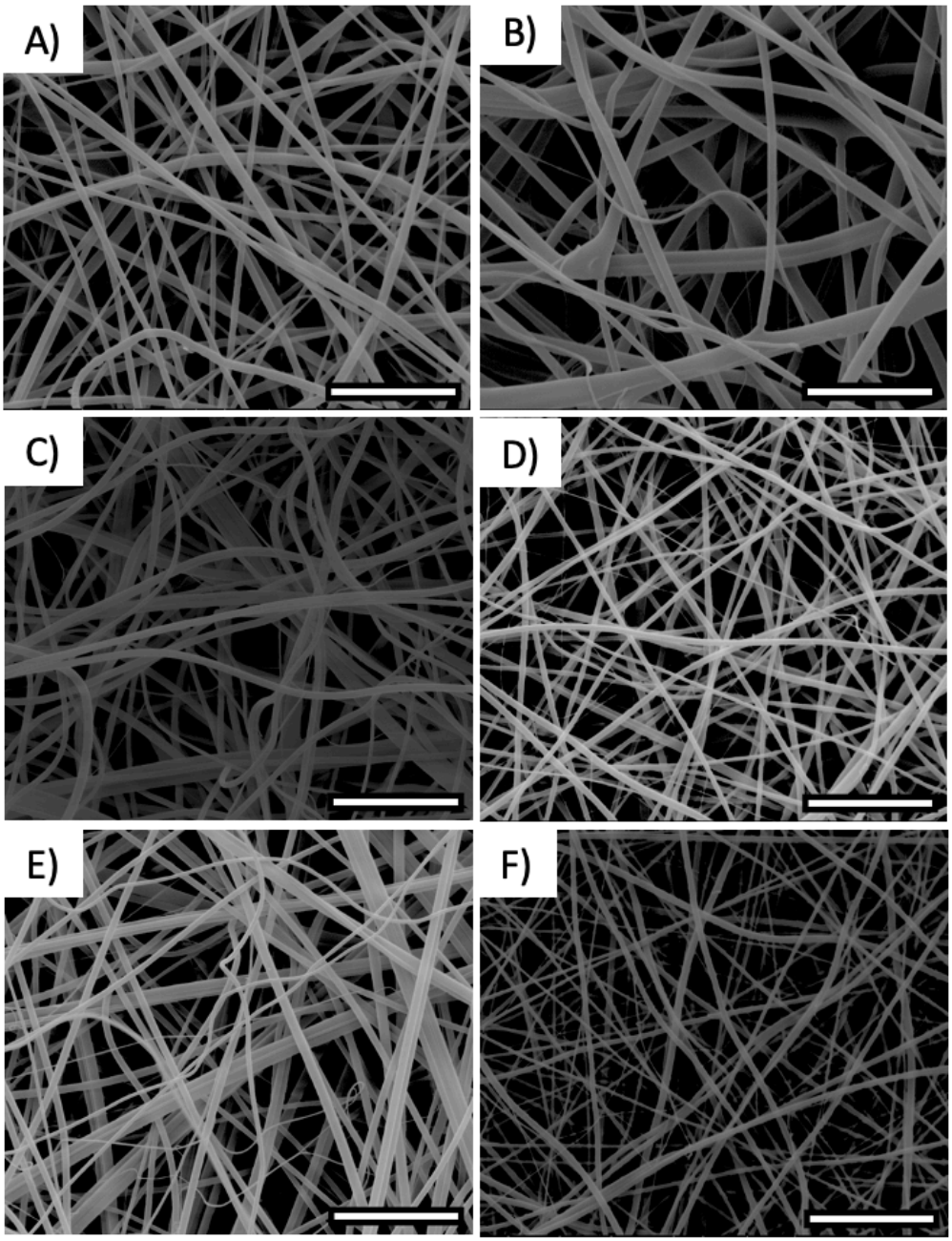

Figure 16. SEM images of electrospun scaffolds (bar: 20 μm). PDLLA (A), PVP (B), PVP-HA 1% (C), PVP-HA 3% (D), PVP-HA-Arg-OH 1% (E), PVP-HA-Arg-OH 3% (F).

A summary of the average fiber diameters for all analyzed samples is reported in Table 29.

Table 29. Average fiber diameter reported as mean value ± standard deviation.

Scaffold	Diameter (μm)	Standard deviation (μm)
PDLLA	1.23	0.64
PVP	1.56	0.79
PVP-HA 1%	1.31	0.51
PVP-HA 3%	0.95	0.24
PVP-HA-Arg-OH 1%	1.33	0.31
PVP-HA-Arg-OH 3%	1.21	0.30

Statistical evaluation was performed using a one-way analysis of variance (ANOVA), followed by Tukey's post hoc test to detect differences in fiber diameters (Figure 17).

The scaffold containing PVP-HA-Arg-OH 1% displayed an average fiber diameter of 1.33 ± 0.31 μm, significantly smaller than pure PVP (****, $p < 0.0001$), and comparable to the corresponding PVP-HA 1% formulation (1.31 ± 0.51 μm), for which no significant difference was observed.

This reduction in diameter is consistent with the well-documented increase in electrical conductivity introduced by HA, which enhances jet stretching during electrospinning [32]. Similarly, the PVP-HA-Arg-OH 3% scaffold exhibited a mean fiber diameter of 1.21 ± 0.30 μm, again significantly smaller than pure PVP (****, $p < 0.0001$). When comparing the two arginine-containing formulations, no statistically significant difference was detected between PVP-HA-Arg-OH 1% and PVP-HA-Arg-OH 3%, indicating that arginine concentration within this range does not substantially influence fiber thinning. Conversely, comparison between PVP-HA 3% and PVP-HA-Arg-OH 3% revealed a significant increase in fiber diameter (***, $p < 0.001$). This behavior aligns with literature evidence showing that the presence of arginine can lead to thicker fibers due to enhanced intermolecular interactions and modified viscoelastic properties of the precursor solution [33]. Overall, these results indicate that while HA incorporation generally leads to thinner fibers due to increased solution conductivity, the subsequent introduction of arginine partially counteracts this effect. The absence of significant differences between the 1% and 3% Arg-containing solutions suggests that, within this concentration range, arginine modulates fiber morphology in a concentration-independent manner.

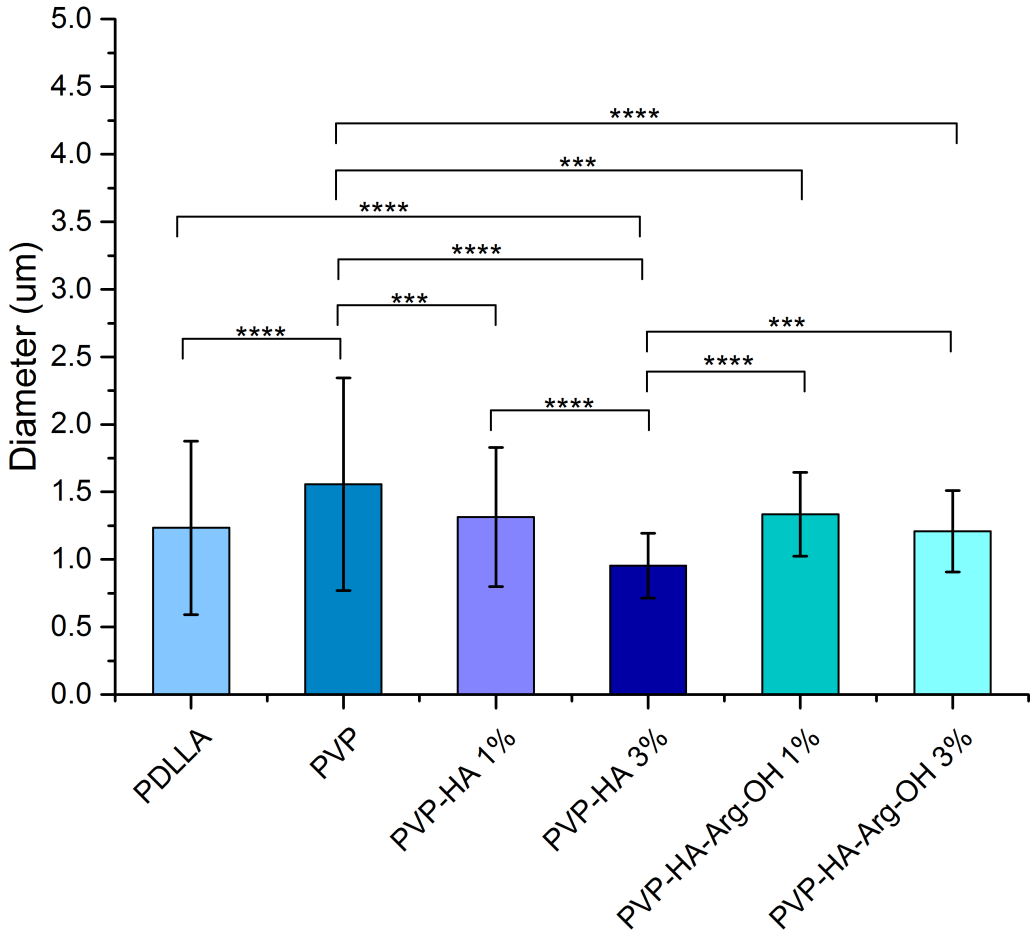

Figure 17. Histogram of average fiber diameter of electrospun scaffolds. Asterisks indicate the level of statistical significance among groups (***, $p < 0.001$; ****, $p < 0.0001$). Bars represent mean ± standard deviation obtained from 150 measurements per sample.

The effect of UV-induced crosslinking on fiber diameter was evaluated by comparing arginine-containing electrospun scaffolds before and after UV treatment. Statistical significance between non-crosslinked and crosslinked samples was assessed using a two-sample t-test, considering $p < 0.05$ as statistically significant.

For the PVP-HA-Arg-OH 3% formulation, UV crosslinking resulted in a clear increase in average fiber diameter. The non-crosslinked scaffold exhibited a mean diameter of 0.94 ± 0.19 µm, whereas the crosslinked sample showed a significantly higher value of 1.21 ± 0.30 µm (Figure 18; ****, $p < 0.0001$). A similar behavior was observed for the PVP-HA-Arg-OH 1% scaffolds. The non-crosslinked fibers showed an average diameter of 1.19 ± 0.26 µm, which increased to 1.33 ± 0.31 µm after UV crosslinking (Figure 18; ****, $p < 0.0001$). The observed increase in fiber diameter upon crosslinking can be attributed to the formation of covalent bonds within the polymer matrix, which reduce

chain mobility and increase the structural rigidity of the fibers. This stabilization can limit polymer chain rearrangement and relaxation, leading to a slight increase in the apparent fiber diameter.
This behavior is consistent with previous reports on electrospun polymeric and biopolymeric systems, where post-treatment crosslinking alters chain mobility and viscoelastic properties, often resulting in increased fiber diameter and modified morphology [34-36].

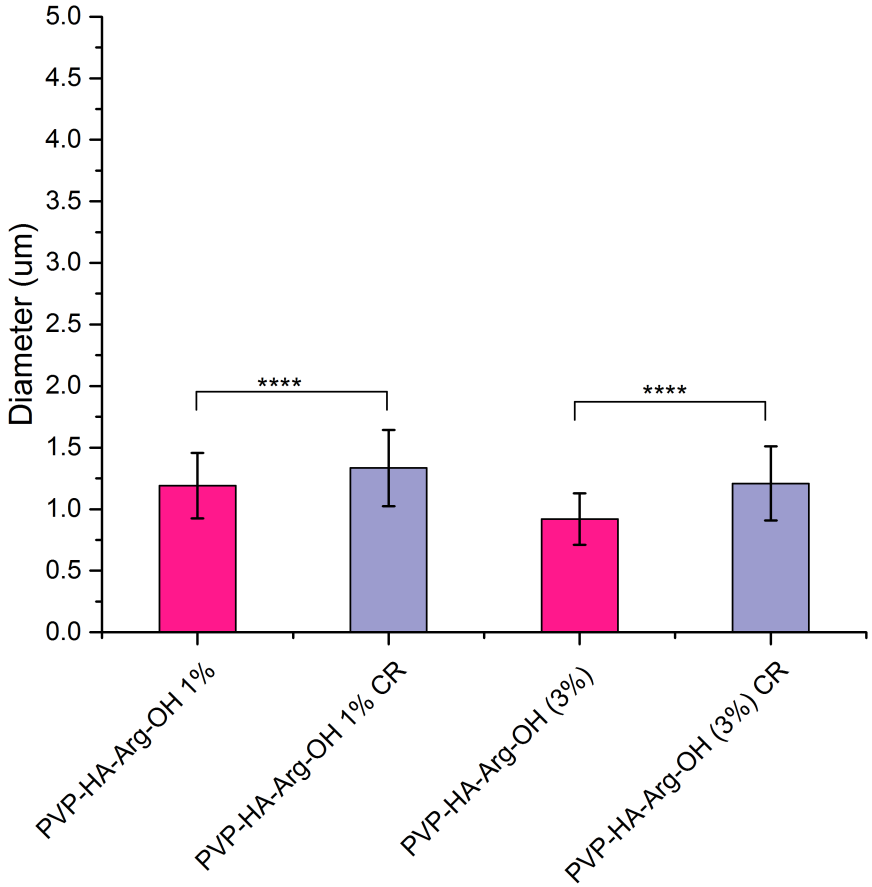

Figure 18. Histogram of average fiber diameter of electrospun scaffolds before and after UV-induced crosslinking ("CR" indicates crosslinked samples). Bars represent mean ± standard deviation obtained from 150 measurements per sample. Statistical analysis was performed using a two-sample t-test (**** $p < 0.0001$).

3.6 Biocompatibility Assessment

The cytocompatibility of the single-layer and bilayer electrospun scaffolds was assessed by quantifying L929 fibroblast viability at 24 and 48 hours post-seeding, using untreated cells as the 100% viability reference (Figure 19). Overall, the results confirmed that the majority of the tested formulations supported cell survival, although the magnitude of the response varied depending on the polymer composition and the presence of HA or its functionalized derivative, HA-Arg-OH.

Scaffolds composed solely of PDLLA or PVP showed a significant reduction in cell viability at both time points, indicating that these single-component matrices may induce an initial stress response in fibroblasts. The incorporation of HA into PVP improved the biological performance but did not fully restore viability to control levels, suggesting that HA alone only partially mitigates the cytotoxic effects of the polymer. A more favorable response was observed when HA-Arg-OH was added to PVP: at 24 hours, cell viability was comparable to the control, indicating that the arginine functionalized HA derivative enhances early cell–material interactions, possibly by improving hydration, surface charge, or protein adsorption. However, by 48 hours, viability decreased significantly, suggesting that the beneficial effect may be transient or that longer term interactions remain influenced by the underlying polymer matrix.

A similar trend was observed in the bilayer scaffolds. The PDLLA/PVP bilayer exhibited significantly reduced viability at both time points, consistent with the behavior of the individual components. The addition of HA improved cytocompatibility but did not eliminate the reduction in viability. Notably, the PDLLA/PVP bilayer containing HA-Arg-OH showed the most promising profile among the bilayer formulations: viability at 24 hours was statistically comparable to the control, indicating that HA-Arg-OH enhances the initial cell response even in more complex scaffold architectures. As observed in the single layer system, viability decreased significantly at 48 hours, suggesting that the long-term cytocompatibility of the bilayer structure may require further optimization.

Taken together, these findings highlight the importance of scaffold composition in modulating early fibroblast behavior. While PDLLA and PVP alone show limited cytocompatibility, the incorporation of HA, particularly HA-Arg-OH, can significantly improve the initial cellular response. The decline observed at 48 hours suggests that additional modifications, such as adjusting polymer ratios, tuning degradation kinetics, or optimizing surface functionalization, may be necessary to sustain long term biocompatibility. Nonetheless, the positive early response to HA-Arg-OH containing scaffolds indicates that functionalized HA derivatives represent a promising strategy for enhancing the biological performance of electrospun materials intended for tissue engineering applications.

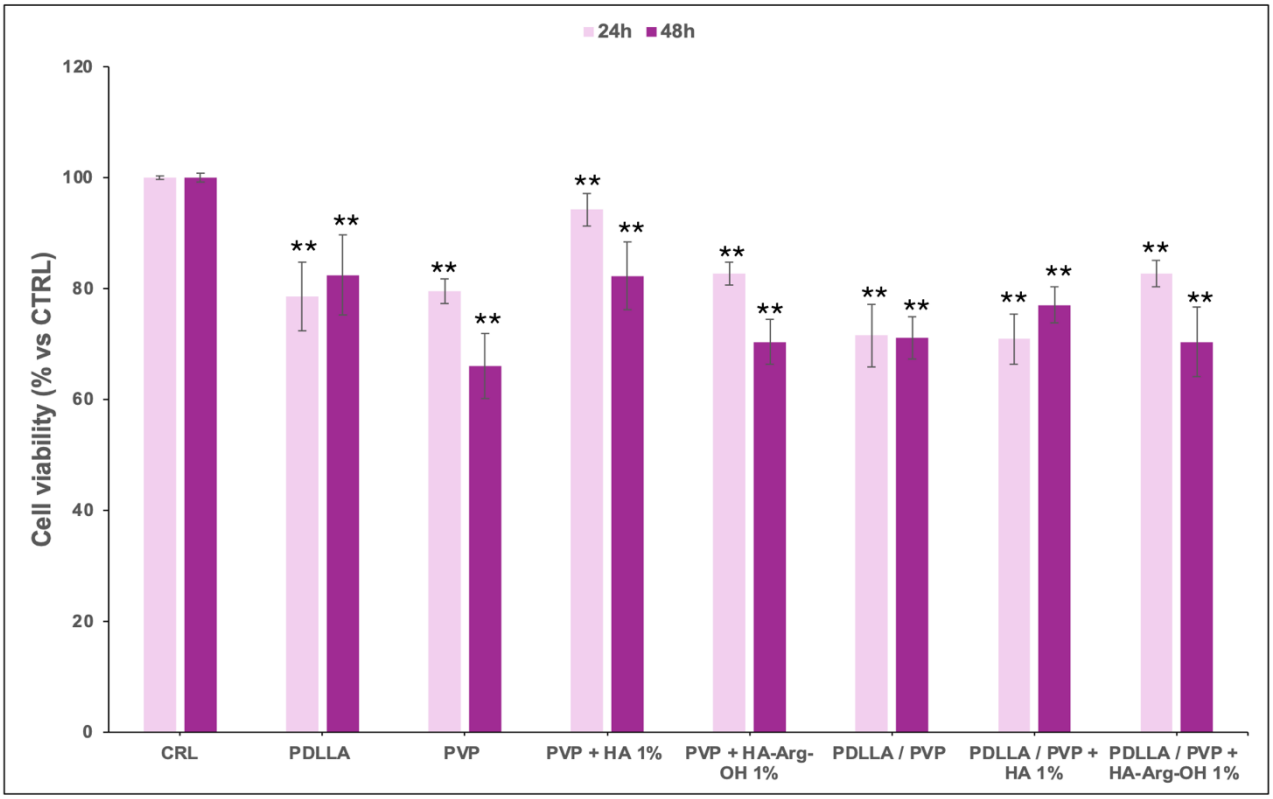

Figure 19. Cell viability of L929 fibroblasts cultured on various electrospun scaffold formulations at 24 and 48 hours. Bar graph showing cell viability (percentage of untreated cells) for seven treatment groups: untreated cells (CRL), PDLLA, PVP, PVP-HA 1%, PVP-HA-Arg-OH 1%, PDLLA/PVP, PDLLA/PVP-HA 1%, and PDLLA/PVP-HA-Arg-OH 1%. Error bars indicate standard deviation. Statistical significance is denoted as follows: **, $p < 0.01$.

4. Conclusions

In this chapter, the synthesis and characterization of hyaluronic acid–L-arginine bioconjugates were explored with the aim of developing bioactive molecules suitable for the fabrication of electrospun scaffolds for wound healing applications. Four different synthetic strategies were investigated, employing L-arginine in various protected forms (Pbf, Cbz, Boc) or already in its fully deprotected commercial form. All reactions were carried out through carbodiimide-mediated coupling in aqueous conditions.

^{1}H-NMR and ATR-FTIR analyses confirmed the successful formation of the amide bonds and, when required, the removal of the protecting groups. Capillary viscometry revealed substantial differences in molecular weight depending on the synthetic strategy employed. Bioconjugates derived from Pbf- or Cbz-protected arginine displayed a marked reduction in molecular weight compared to native HA, most likely due to the acidic or hydrogenolytic deprotection steps, which can promote cleavage of the glycosidic bond. In contrast, the approaches based on fully deprotected arginine, either obtained through mild Boc removal or used directly as commercial L-arginine hydrochloride, preserved the integrity of the polysaccharide backbone. This finding indicates that the use of free arginine represents the most effective route to obtain a stable bioconjugate without degradation of the hyaluronic acid matrix.

Further structural validation was provided by Raman spectroscopy, which showed the characteristic downshifts associated with chemical modification of the polysaccharide, and by circular dichroism, demonstrating that conjugation with arginine does not alter the overall conformational behavior of HA in either water or PBS.

The resulting bioconjugates were then incorporated into electrospinnable solutions by mixing HA-Arg-OH at 1% and 3% (w/w) with PVP in an ethanol/water mixture. These solutions were used to produce single-layer fibrous membranes as well as the hydrophilic top layer of bilayer scaffolds featuring a PDLLA support. SEM analysis revealed that the presence of the bioconjugate significantly affected fiber diameter and distribution. As expected, the addition of HA increased solution conductivity and favored the formation of thinner fibers, whereas the presence of arginine led to an increase in fiber diameter, likely due to enhanced intermolecular interactions and changes in solution viscosity. UV exposure, required to stabilize the membranes in aqueous environments, further increased fiber diameter in line with the reduced molecular mobility associated with crosslinking.

Biocompatibility assays performed with L929 fibroblasts further confirmed that scaffold composition plays a key role in modulating early cell response. In particular, HA-Arg-OH-containing scaffolds showed improved fibroblast viability at 24 h compared to the corresponding PVP-based formulations,

highlighting the beneficial role of arginine functionalization in enhancing the initial cytocompatibility of the electrospun matrices.

Overall, the results demonstrate that conjugation with free arginine is the most effective strategy for preserving the chemical integrity of hyaluronic acid and for obtaining derivatives compatible with the maintenance of its key biological properties. Spectroscopic and viscometric analyses confirmed the chemical and structural stability of the bioconjugate, while electrospinning experiments and subsequent morphological characterization showed that HA-Arg-OH can be incorporated into polymer matrices and processed into fibrous structures with a well-defined morphology.

Supporting Information

Design, Characterization, and Electrospinning of Hyaluronic Acid-Arginine Bioconjugates

Table of contents

Figure S1. ^{1}H-NMR spectrum of **derivative 2** (400 MHz, DMSO-d_6, 298 K).	**173**
Figure S2. ^{13}C-NMR spectrum of **derivative 2** (100 MHz, DMSO-d_6, 298 K).	**174**
Figure S3. ATR-FTIR spectra of **derivative 2** and commercial Fmoc-Arg(Pbf)-OH.	**175**
Figure S4. ^{1}H-NMR spectrum of **derivative 4** (500 MHz, DMSO-d_6, 298 K).	**176**
Figure S5. ^{13}C-NMR spectrum of **derivative 4** (125 MHz, DMSO-d_6, 298 K).	**177**
Figure S6. ATR-FTIR spectra of **derivative 4** and commercial Boc-Arg(di-Z)-OH.	**178**
Figure S7. ^{1}H-NMR spectra of HA, **derivative 9-i** and **derivative 10** (400 MHz, D_2O, 298 K).	**179**
Figure S8. ATR-FTIR spectra of HA, **derivative 9-i** and **derivative 10.**	**180**
Figure S9. ^{1}H-NMR spectra of HA, **derivative 9-ii** and **derivative 11** (400 MHz, D_2O, 298 K).	**181**
Figure S10. ATR-FTIR spectra of HA, **derivative 9-ii** and **derivative 11.**	**182**
Figure S11. ^{1}H-NMR spectra of **derivative 6** (400 MHz, D_2O, 298 K).	**183**
Figure S12. ^{13}C-NMR spectrum of **derivative 6** (100 MHz, DMSO-d_6, 298 K).	**184**
Figure S13. ATR-FTIR spectra of **derivative 6** and commercial **Boc-Arg-OH.**	**185**

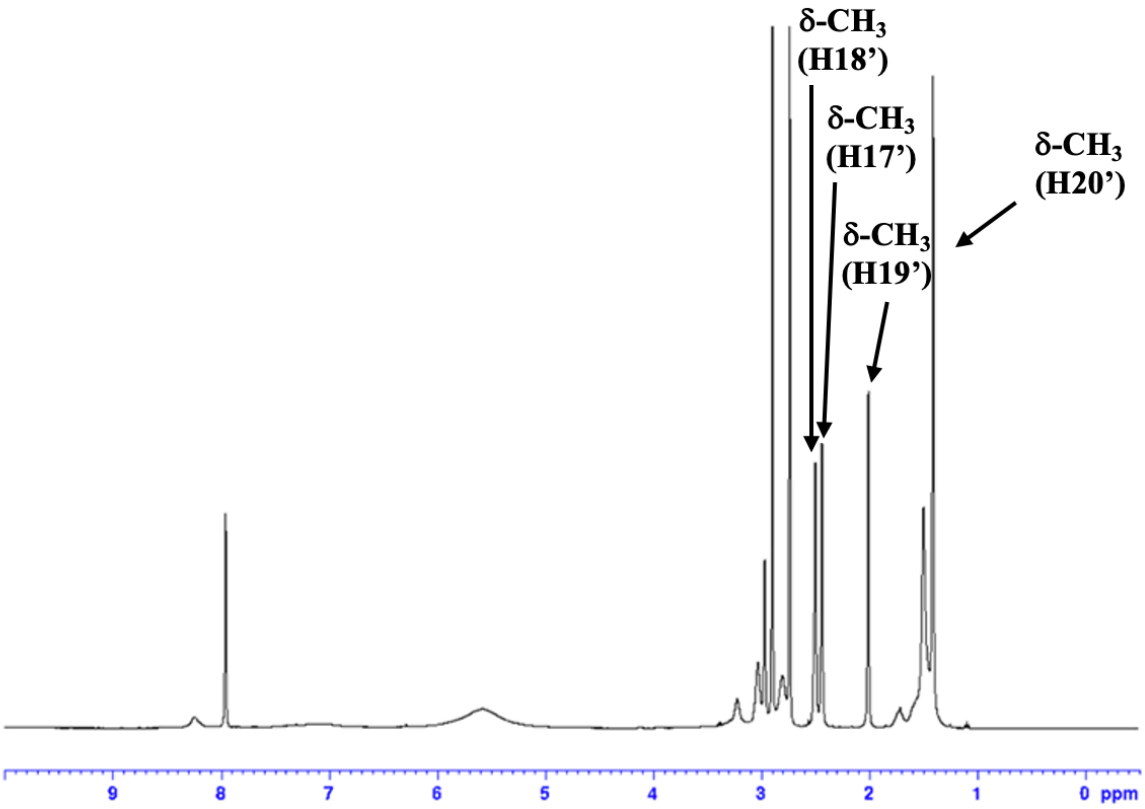

Figure S1. ^{1}H-NMR spectrum of **derivative 2** (400 MHz, DMSO-d_6, 298 K).

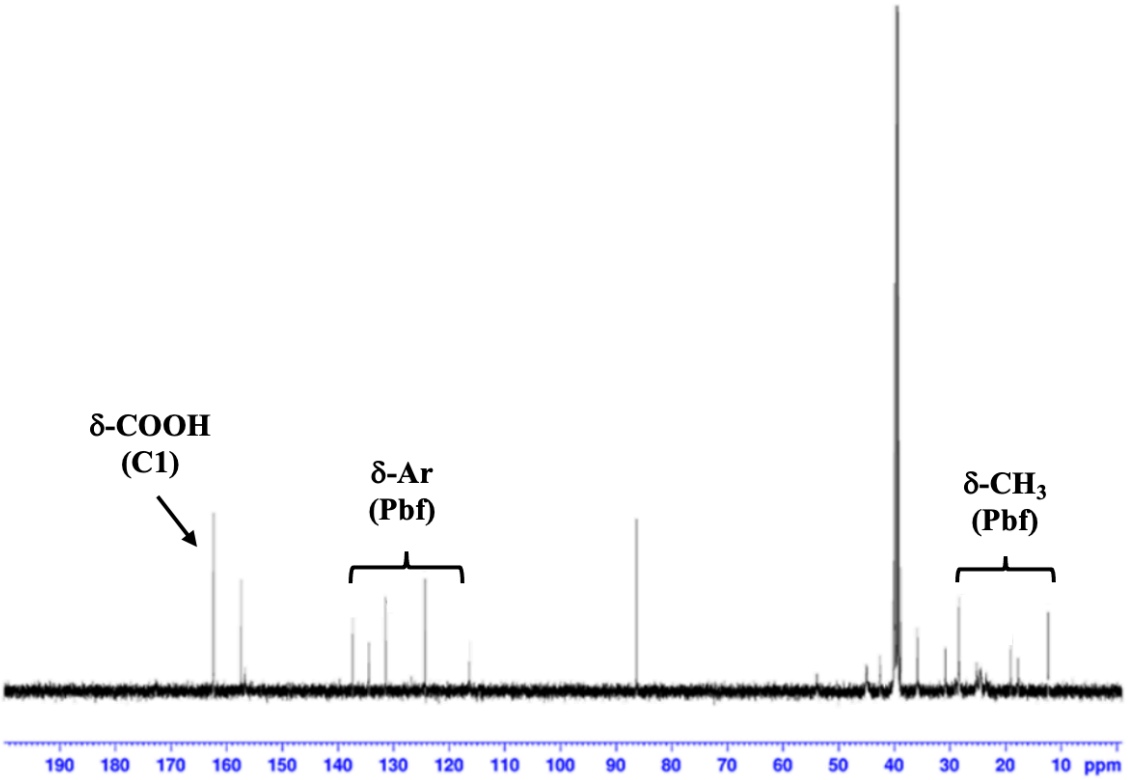

Figure S2. ^{13}C-NMR spectrum of **derivative 2** (100 MHz,DMSO-d_6, 298 K).

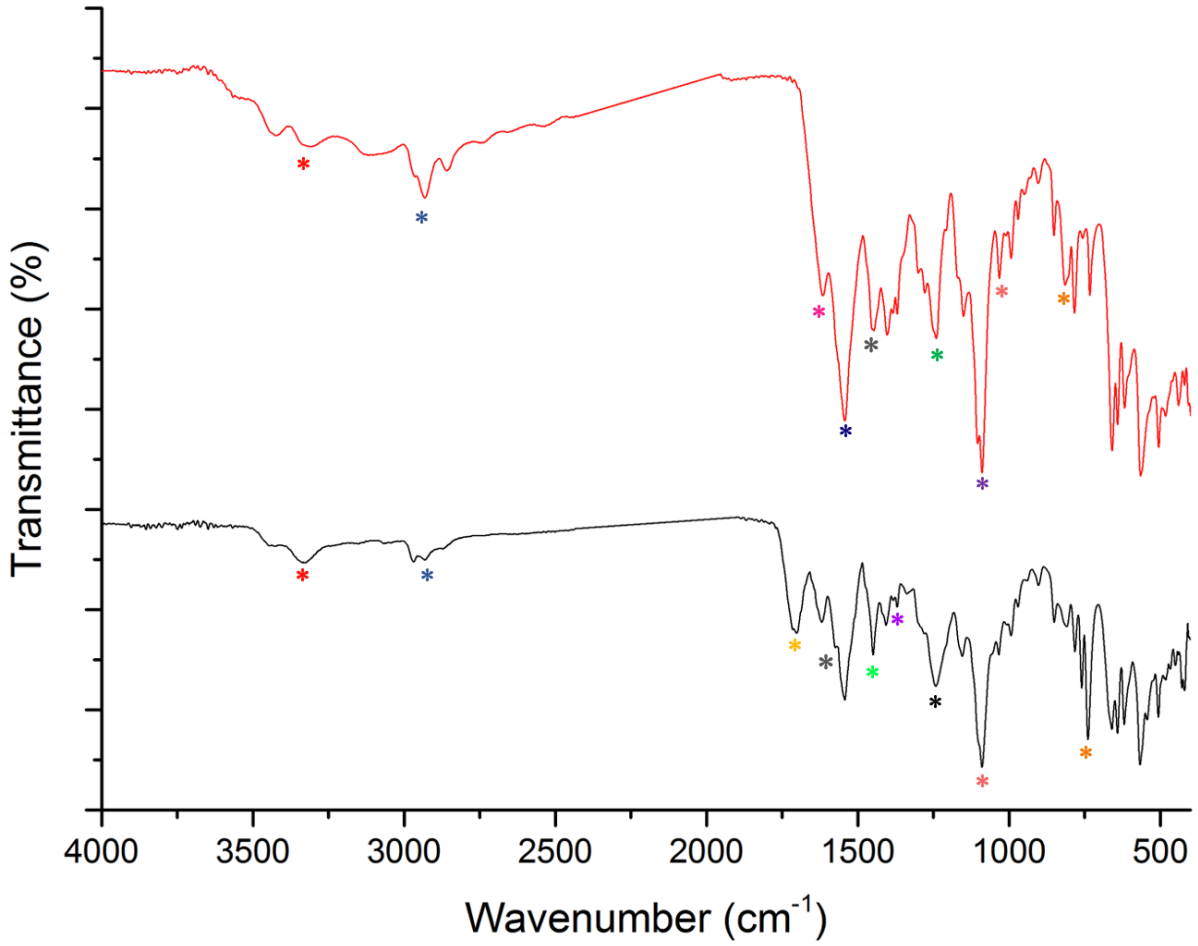

Figure S3. ATR-FTIR spectra of **derivative 2** (red curve) and commercial Fmoc-Arg(Pbf)-OH (black curve).

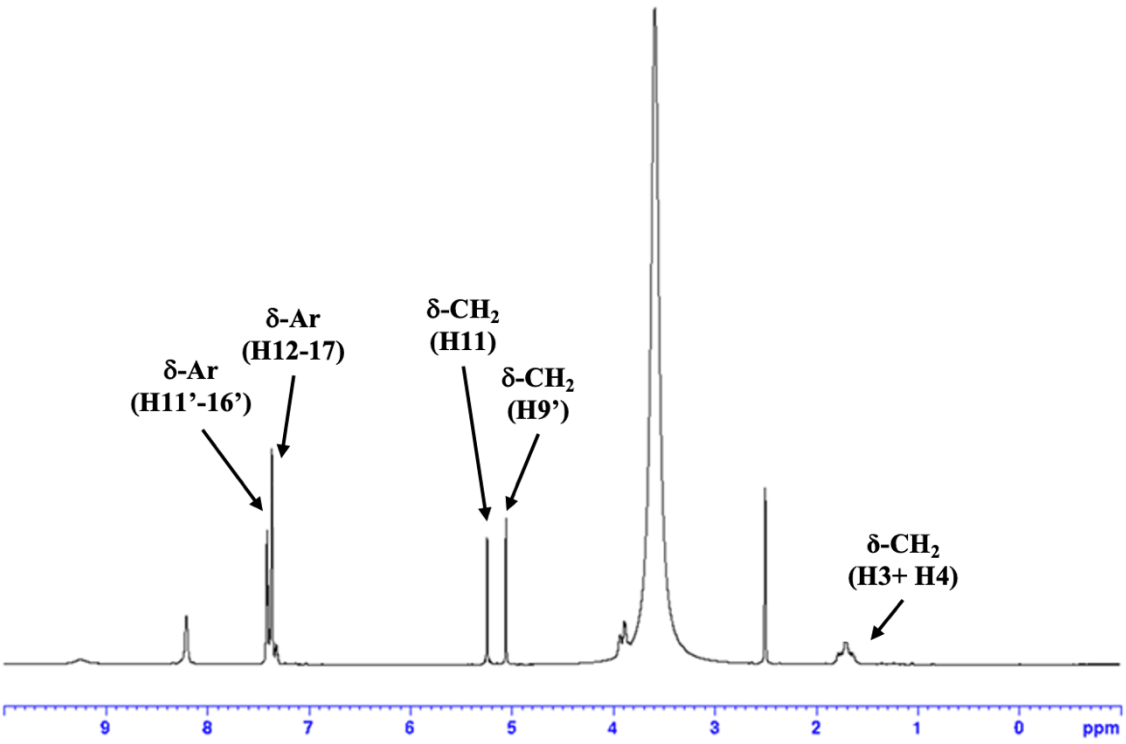

Figure S4. ^{1}H-NMR spectrum of **derivative 4** (500 MHz, DMSO-d_6, 298 K).

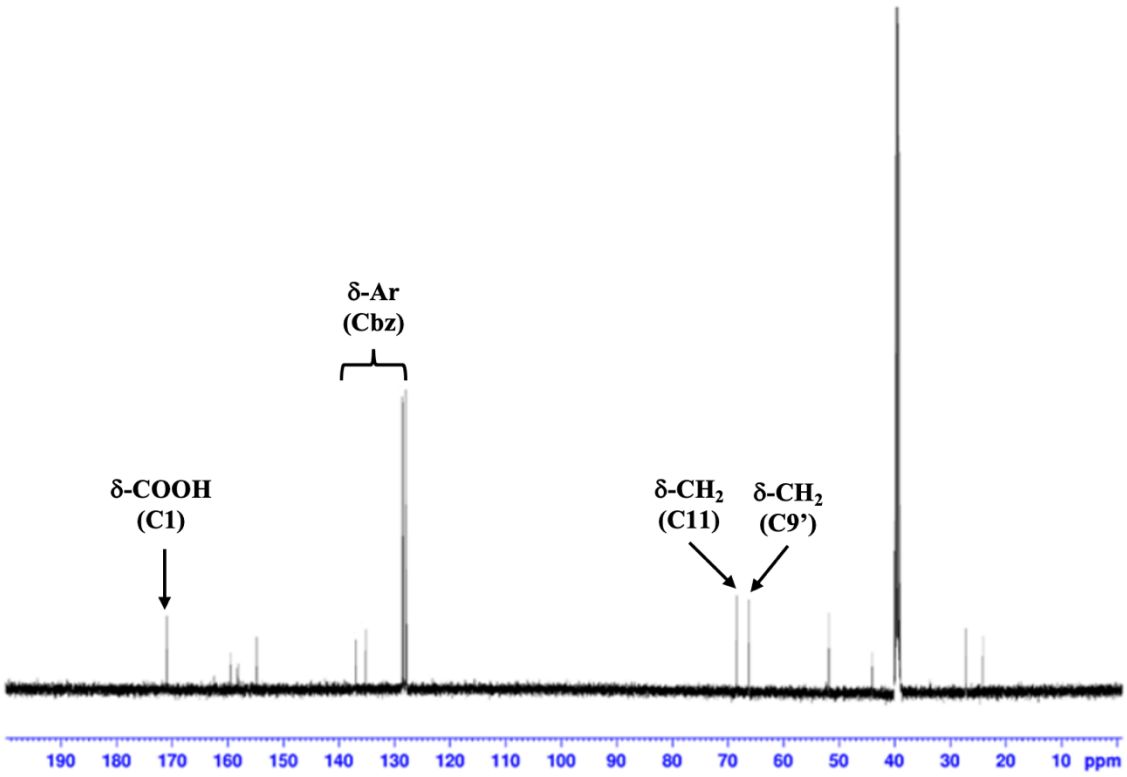

Figure S5. ^{13}C-NMR spectrum of **derivative 4** (125 MHz, DMSO-d_6, 298 K).

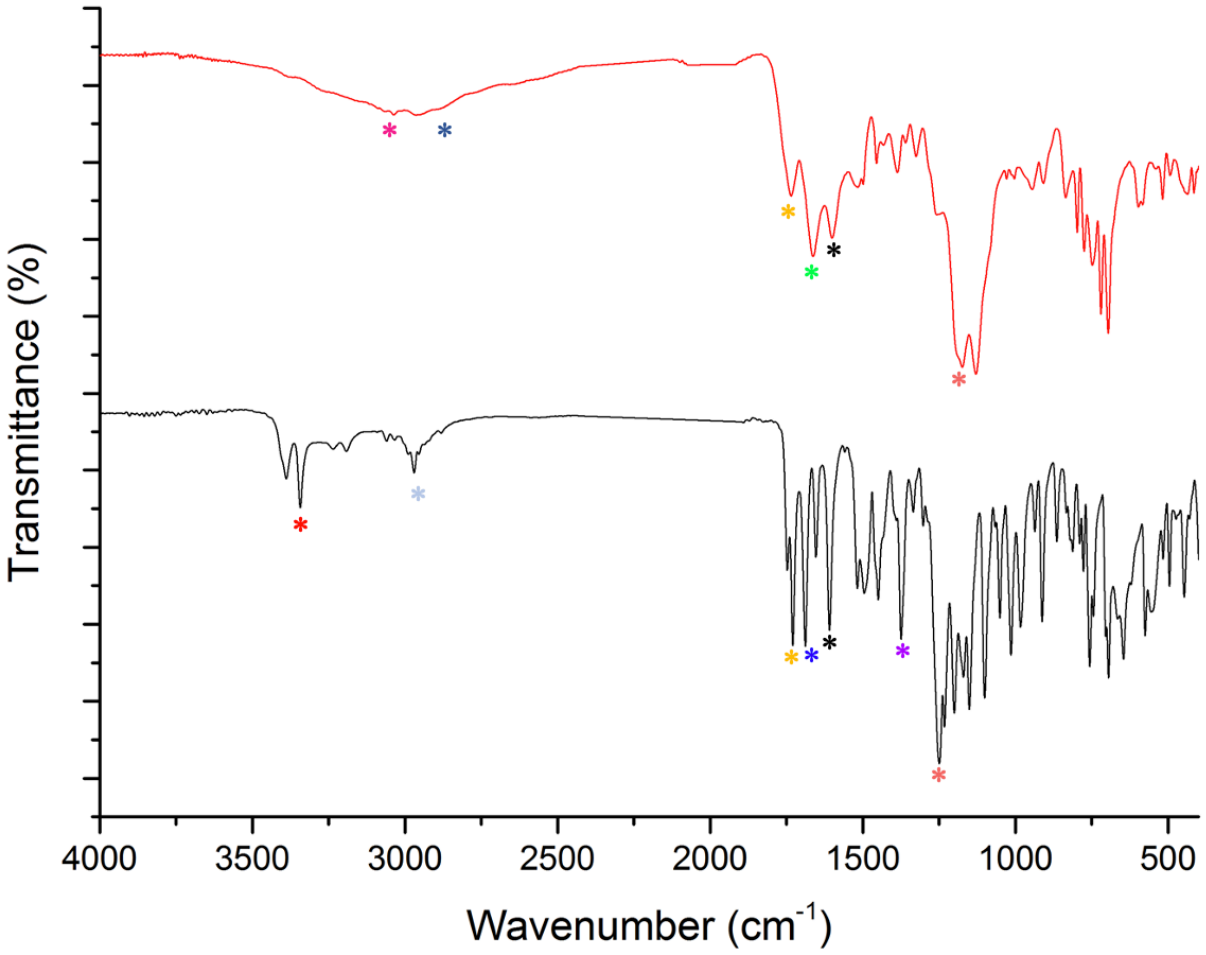

Figure S6. ATR-FTIR spectra of **derivative 4** (red curve) and commercial Boc-Arg(di-Z)-OH (black curve).

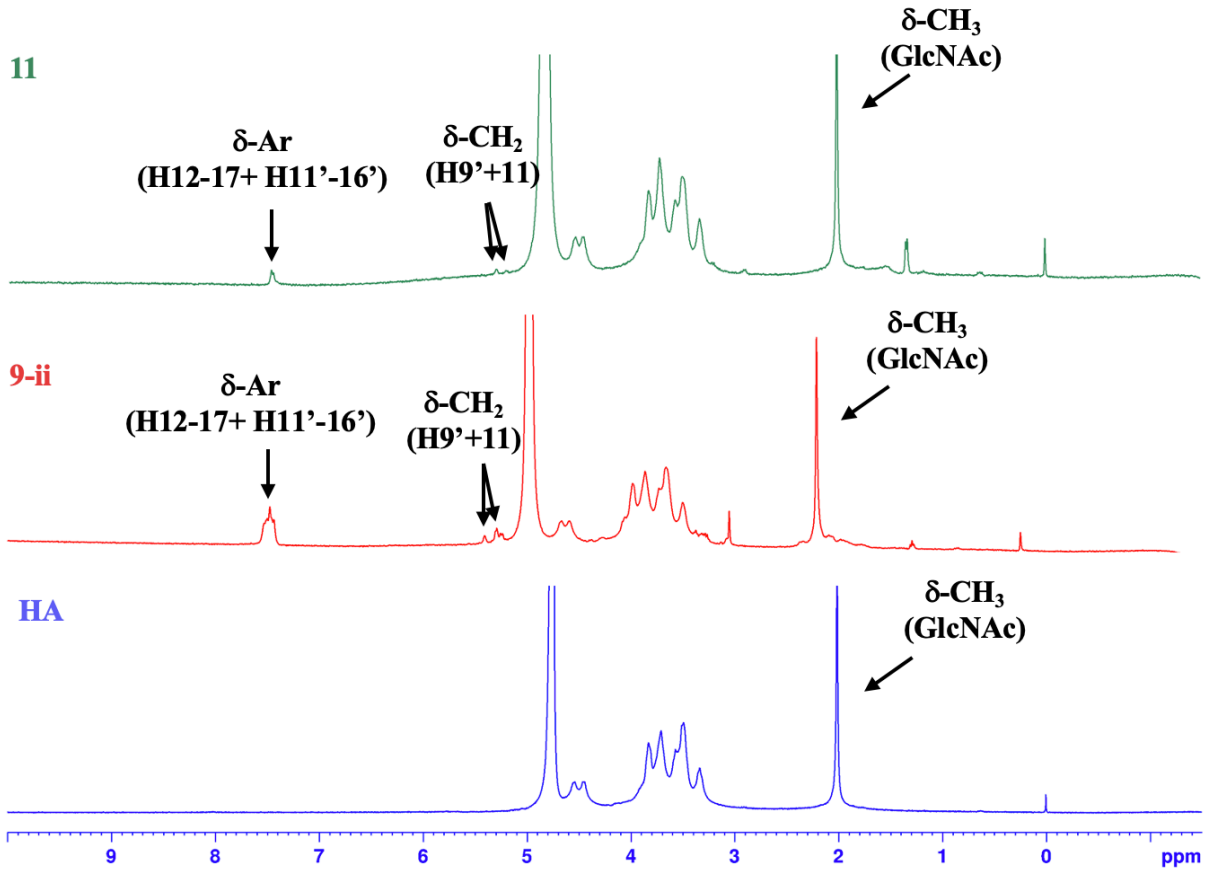

Figure S7. ^{1}H-NMR spectra of HA (blue curve), **derivative 9-i** (red curve) and **derivative 10** (green curve) (400 MHz, D_2O, 298 K).

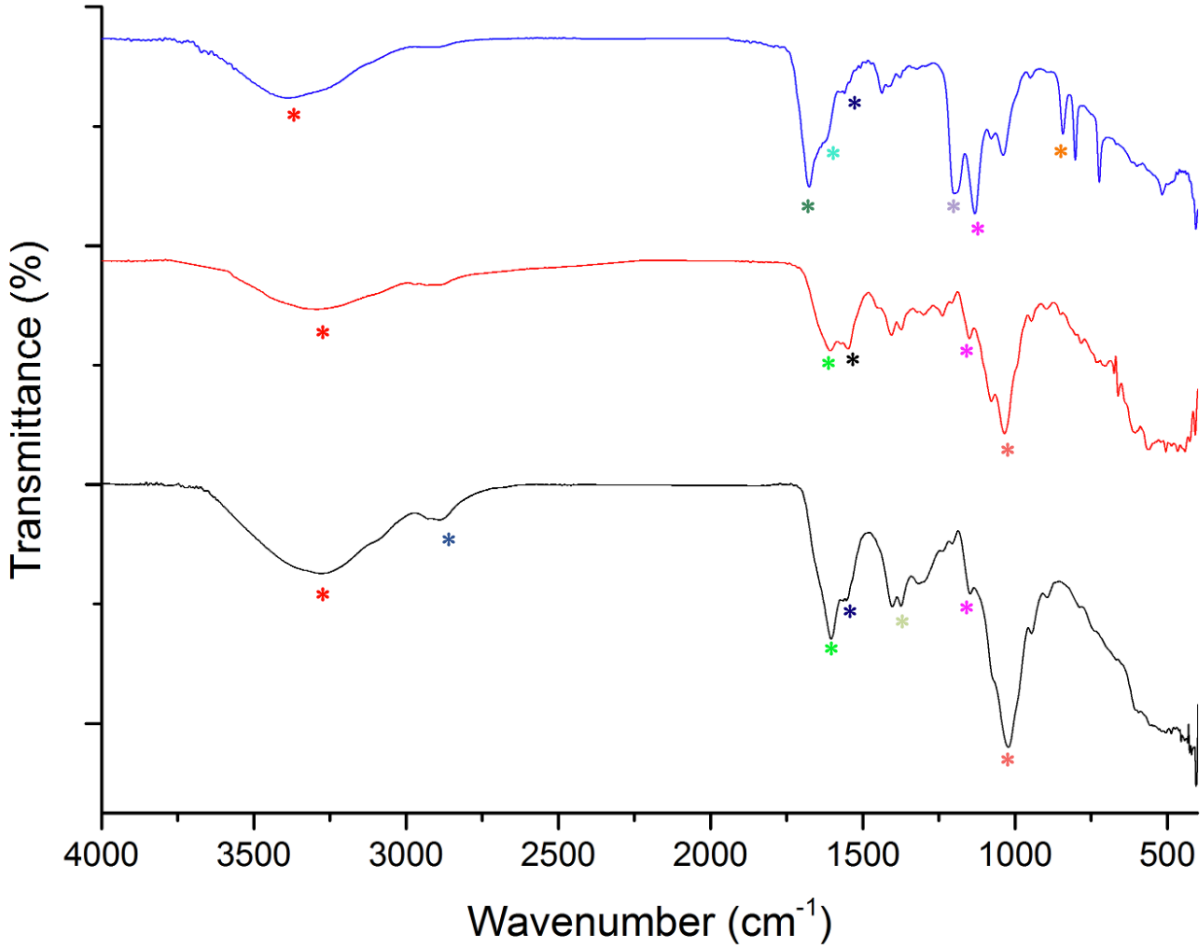

Figure S8. ATR-FTIR spectra of HA (black curve), **derivative 9-i** (red curve) and **derivative 10** (blue curve).

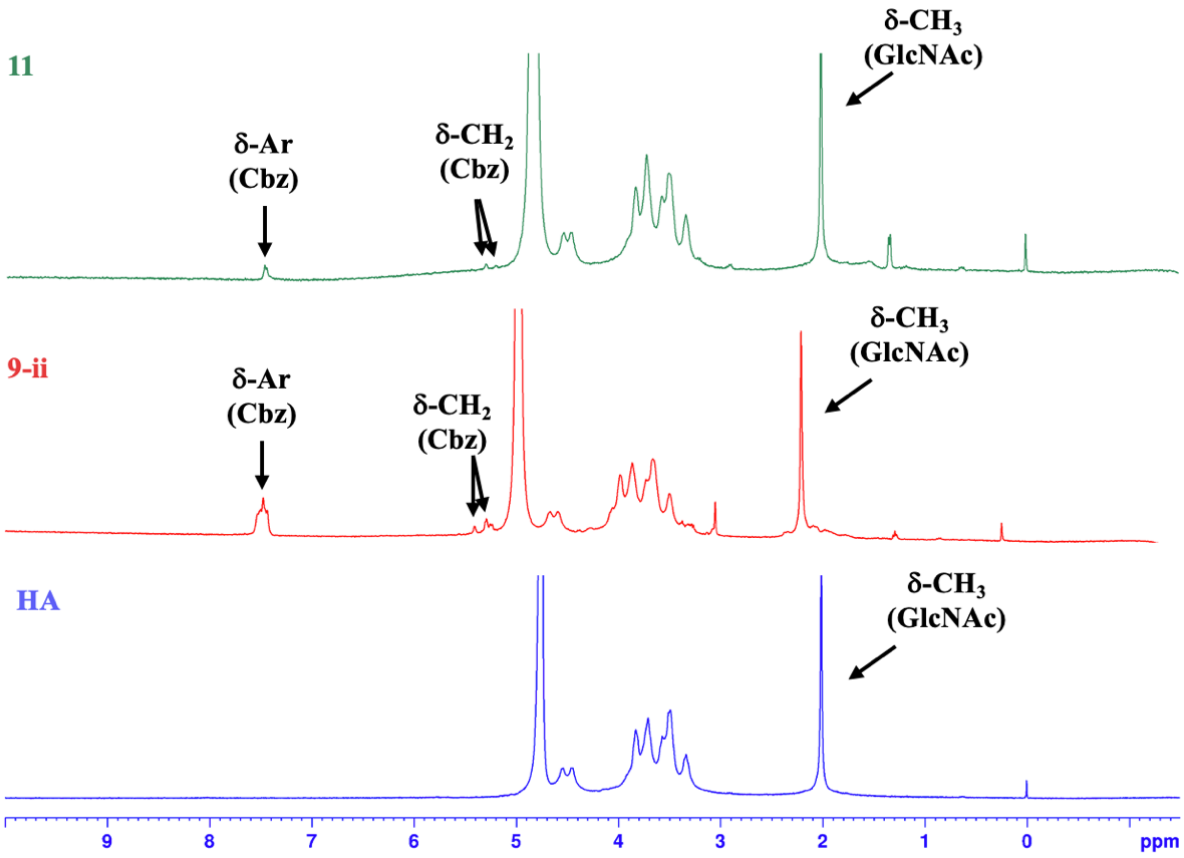

Figure S9. ^{1}H-NMR spectra of HA (black curve), **derivative 9-ii** (red curve) and **derivative 11** (green curve) (400 MHz, D_2O, 298 K).

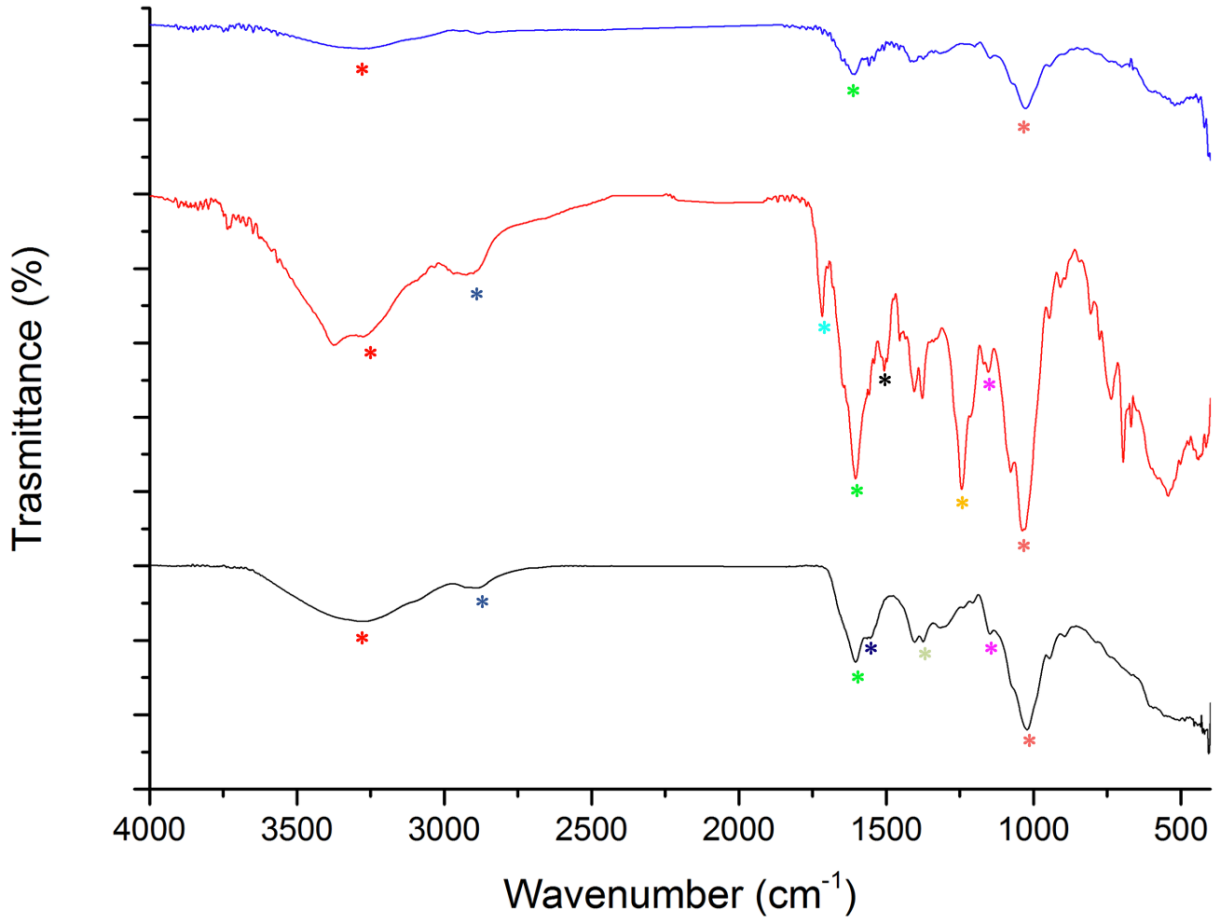

Figure S10. ATR-FTIR spectra of HA (black curve), **derivative 9-ii** (red curve) and **derivative 11** (blue curve).

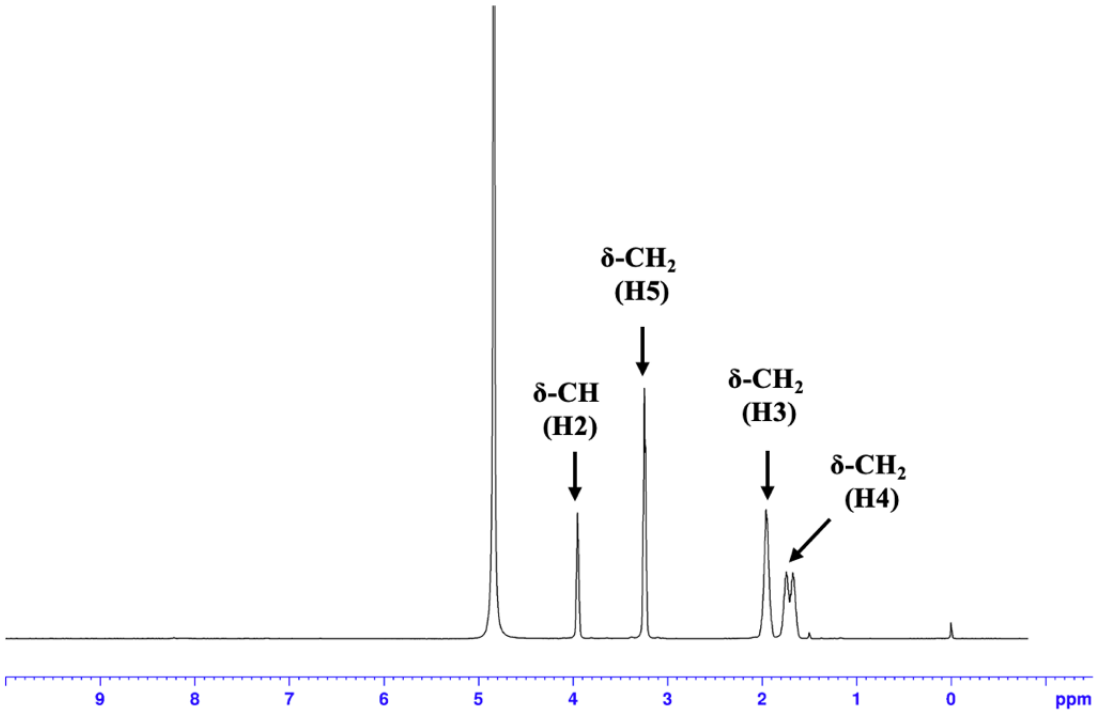

Figure S11. ^{1}H-NMR spectra of **derivative 6** (400 MHz, D_2O, 298 K).

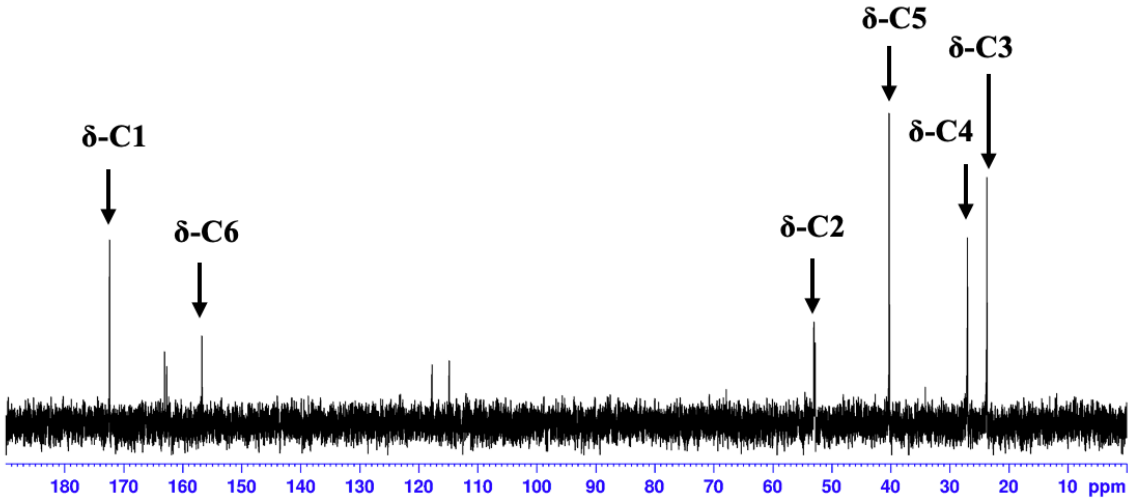

Figure S12. ^{13}C-NMR spectrum of **derivative 6** (100 MHz, DMSO-d_6, 298 K).

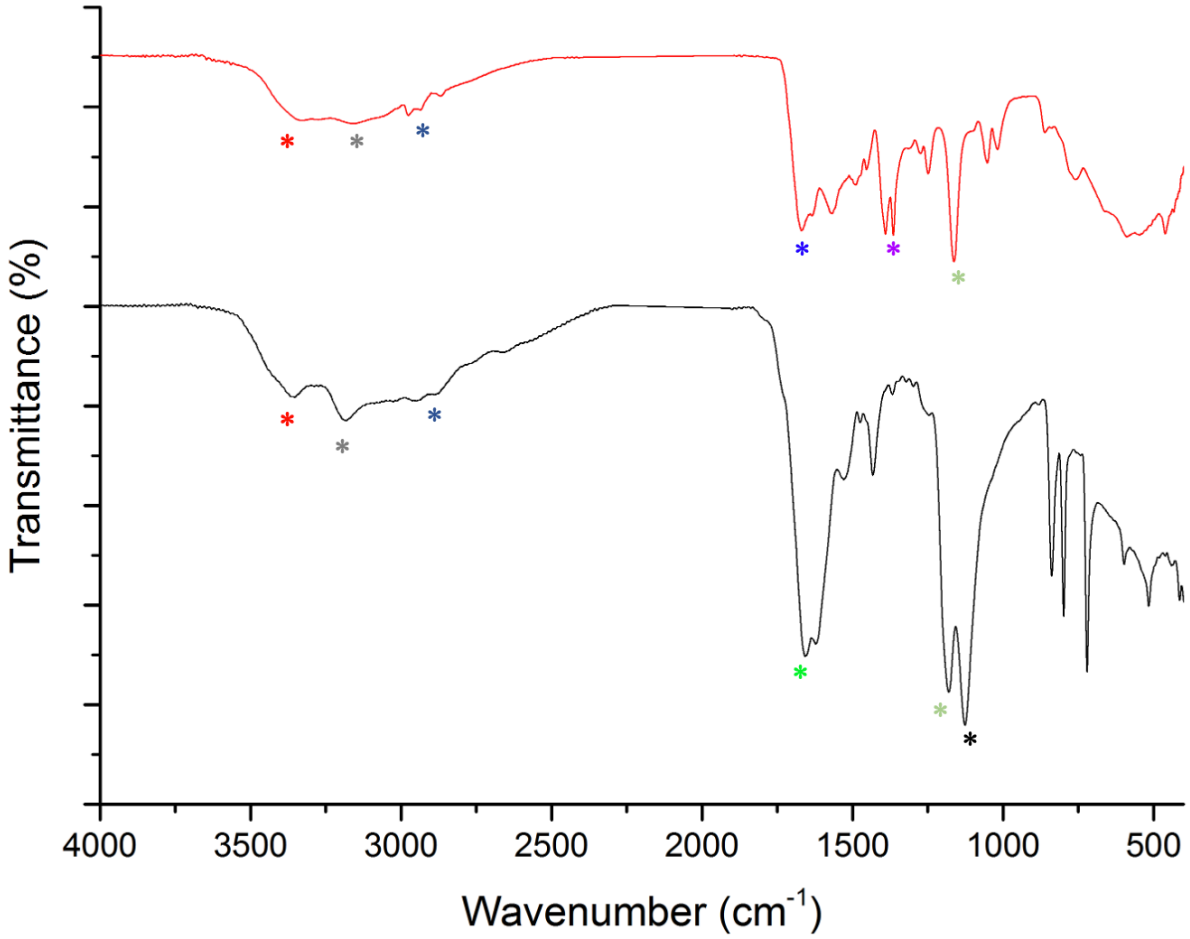

Figure S13. ATR-FTIR spectra of **derivative 6** (black curve) and commercial **Boc-Arg-OH** (red curve).

References

[1] Valachová K.; El Meligy M. A.; Šoltés L. *Hyaluronic acid and chitosan-based electrospun wound dressings: Problems and solutions.* International Journal of Biological Macromolecules, **2022**, 206, 74–91.

[2] Kim B. S.; Baez C. E.; Atala A. *Biomaterials for tissue engineering.* World Journal of Urology, **2000**, 18(1), 2–9.

[3] Keane T. J.; Badylak S. F. *Biomaterials for tissue engineering applications.* Seminars in Pediatric Surgery, **2014**, 23(3), 112–118.

[4] Scott J. E. *Extracellular matrix, supramolecular organisation and shape.* Journal of Anatomy, **1995**, 187(Pt 2), 259–269.

[5] Aya K. L.; Stern R. *Hyaluronan in wound healing: Rediscovering a major player.* Wound Repair and Regeneration, **2014**, 22(5), 579–593.

[6] Graça M. F. P.; Miguel S. P.; Cabral C. S. D.; Correia I. J. *Hyaluronic acid–based wound dressings: A review.* Carbohydrate Polymers, **2020**, 241, 116364.

[7] Pepe A.; Laezza A.; Armiento F.; Bochicchio B. *Chemical modifications in hyaluronic acid-based electrospun scaffolds.* ChemPlusChem, **2024**, 89(7), e202300599.

[8] Chircov C.; Grumezescu A. M.; Bejenaru L. E. *Hyaluronic acid-based scaffolds for tissue engineering.* Romanian Journal of Morphology and Embryology, **2018**, 59(1), 71–76.

[9] Witte M. B.; Barbul A. *Arginine physiology and its implication for wound healing.* Wound Repair and Regeneration, **2003**, 11(6), 419–423.

[10] Stechmiller J. K.; Childress B.; Cowan L. *Arginine supplementation and wound healing.* Nutrition in Clinical Practice, **2005**, 20(1), 52–61.

[11] Witte M. B.; Barbul A. *Role of nitric oxide in wound repair.* American Journal of Surgery, **2002**, 183(4), 406–412.

[12] Zhou Y.; Liu G.; Huang H.; Wu J. *Advances and impact of arginine-based materials in wound healing.* Journal of Materials Chemistry B, **2021**, 9, 6738–6750.

[13] Mariggiò M. A.; Cassano A.; Vinella A.; Vincenti A.; Fumarulo R.; Lo Muzio L.; Maiorano E.; Ribatti D.; Favia G. *Enhancement of fibroblast proliferation, collagen biosynthesis and production of growth factors as a result of combining sodium hyaluronate and amino acids.* International Journal of Immunopathology and Pharmacology, **2009**, 22(2), 485–492.

[14] Cowman M. K.; Mendichi R. *Methods for determination of hyaluronan molecular weight.* Chemistry and Biology of Hyaluronan, **2004**, 41–69.

[15] Szantai-Kis D. M.; Walters C. R.; Barrett T. M.; Hoang E. M.; Petersson E. J. *Improved Fmoc deprotection methods for the synthesis of thioamide-containing peptides and proteins.* Synlett, **2017**, 28, 1789–1794.

[16] Hernández B.; Pflüger F.; Derbel N.; De Coninck J.; Ghomi M. *Vibrational analysis of amino acids and short peptides in hydrated media. VI. Amino acids with positively charged side chains: L-lysine and L-arginine.* Journal of Physical Chemistry B, **2010**, 114, 1077–1088.

[17] Barth A. *The infrared absorption of amino acid side chains.* Progress in Biophysics and Molecular Biology, **2000**, 74, 141–173.

[18] Kozioł A.; Lendzion-Paluch A.; Manikowski A. *A fast and effective hydrogenation process of protected pentasaccharide: A key step in the synthesis of fondaparinux sodium.* Organic Process Research & Development, **2013**, 17, 869–875.

[19] Kwon M. Y.; Wang C.; Galarraga J. H.; Puré E.; Han L.; Burdick J. A. *Influence of hyaluronic acid modification on CD44 binding towards the design of hydrogel biomaterials.* Biomaterials, **2019**, 222, 119451.

[20] Banerji S.; Wright A. J.; Noble M.; Mahoney D. J.; Campbell I. D.; Day A. J.; Jackson D. G. *Structures of the CD44–hyaluronan complex provide insight into a fundamental carbohydrate–protein interaction.* Nature Structural & Molecular Biology, **2007**, 14, 234–239.

[21] Suárez-Hernández L. A.; Camacho-Ruíz R. M.; Arriola-Guevara E.; Padilla-Camberos E.; Kirchmayr M. R.; Corona-González R. I.; Guatemala-Morales G. M. *Validation of an analytical method for the simultaneous determination of hyaluronic acid concentration and molecular weight by size-exclusion chromatography.* Molecules, **2021**, 26, 5360.

[22] Ambrosio L.; Borzacchiello A.; Netti P. A.; Nicolais L. *Rheological study on hyaluronic acid and its derivative solutions.* Journal of Macromolecular Science, Part A, **1999**, 36(7–8), 991–1000.

[23] Essendoubi M.; Gobinet C.; Reynaud R.; Angiboust J. F.; Manfait M.; Piot O. *Human skin penetration of hyaluronic acid of different molecular weights as probed by Raman spectroscopy.* Skin Research and Technology, **2016**, 22, 55–62.

[24] Alkrad J. A.; Mrestani Y.; Stroehl D.; Wartewig S.; Neubert R. *Characterization of enzymatically digested hyaluronic acid using NMR, Raman, IR, and UV–Vis spectroscopies.* Journal of Pharmaceutical and Biomedical Analysis, **2003**, 31, 545–550.

[25] Petrosyan A. M.; Sukiasyan R. P. *Vibrational spectra of L-arginine nitrates.* Journal of Molecular Structure, **2008**, 874, 51–56.

[26] Faria J. L. B.; Freire P. T. C.; Gonçalves R. O.; Melo F. E. A.; Mendes Filho J.; Lima R. J. C.; Moreno A. J. D. *Polarized Raman spectra of L-arginine hydrochloride monohydrated single crystal.* Brazilian Journal of Physics, **2009**, 40, 288–294.

[27] Hernández B.; Pflüger F.; Adenier A.; Kruglik S. G.; Ghomi M. *Vibrational analysis of amino acids and short peptides in hydrated media. VIII. Amino acids with aromatic side chains: L-phenylalanine, L-tyrosine, and L-tryptophan.* Journal of Physical Chemistry B, **2010**, 114, 14202–14215.
[28] Wang L.; Zhang G.; Wang X.; Wang L.; Liu X.; Jin L.; Xu D. *Studies on the conformational transformations of L-arginine molecule in aqueous solution with temperature changing by circular dichroism spectroscopy and optical rotations.* Journal of Molecular Structure, **2012**, 1026, 71–77.
[29] Staskus P. W.; Johnson W. C. Jr. *Conformational transition of hyaluronic acid in aqueous–organic solvent monitored by vacuum ultraviolet circular dichroism.* Biochemistry, **1988**, 27, 2587–2593.
[30] Laezza A.; Pepe A.; Bochicchio B. *Elastin–hyaluronan bioconjugate as bioactive component in electrospun scaffolds.* Chemistry – A European Journal, **2022**, 28, e202201959.
[31] Morgado P. I.; Aguiar-Ricardo A.; Correia I. J. *Asymmetric membranes as ideal wound dressings: An overview on production methods, structure, properties and performance relationship.* Journal of Membrane Science, **2015**, 490, 139–151.
[32] Grimaudo M. A.; Concheiro A.; Alvarez-Lorenzo C. *Crosslinked hyaluronan electrospun nanofibers for ferulic acid ocular delivery.* Pharmaceutics, **2020**, 12, 274.
[33] Horakova J.; Oulehlova Z.; Novotny V.; Jencova V.; Mikes P.; Havlickova K.; Prochazkova R.; Heczkova B.; Hadinec P.; Sehr S.; Wendel H.-P.; Bell C.-M.; Krajewski S. *The assessment of electrospun scaffolds fabricated from polycaprolactone with the addition of L-arginine.* Biomedical Physics & Engineering Express, **2020**, 6, 025012.
[34] Meng L.; Arnoult O.; Smith M.; Wnek G. E. *Electrospinning of in situ crosslinked collagen nanofibers*. Journal of Materials Chemistry, **2012**, 22, 19412–19418.
[35] Yang B.; Wang J.; Chen X.; Zhao Y. *Effect of crosslinking on mechanical and biological properties of electrospun gelatin nanofibers.* Journal of Applied Polymer Science, **2008**, 110, 139–145.
[36] Zhou Y.; Yang D.; Chen H.; Liao Y.; Shao Z. *Electrospun poly(vinyl alcohol)/gelatin composite nanofibers and their crosslinking behavior.* Materials Science and Engineering C, **2011**, 31, 199–207.

Chapter 4

Design, Characterization, and Electrospinning of Hyaluronic Acid-Cysteine Bioconjugates

1. Introduction

In the previous chapters, different bioconjugation strategies between hyaluronic acid (HA) and amino acids were described, aimed at tuning the physicochemical and biological properties of HA-based scaffolds for tissue regeneration. This chapter focuses on cysteine, a sulfur-containing amino acid characterized by the presence of a thiol group (-SH), which provides unique chemical reactivity and biological functionality compared to the other amino acids investigated in this study.

L-cysteine is a semi-essential amino acid that plays a central role in cellular physiology, particularly in the regulation of the intracellular redox microenvironment. Its thiol group readily undergoes oxidation and participates in disulfide bond formation, contributing to protein structure and function. Moreover, cysteine is the main precursor of glutathione, a key antioxidant involved in cellular defense against reactive oxygen species (ROS), influencing proliferation, migration, and inflammatory processes relevant to wound healing [1–4].

These features make cysteine an attractive candidate for polymer functionalization. In particular, thiolated polymers (thiomers) exploit thiol groups to form disulfide bonds, resulting in enhanced mucoadhesion, improved matrix stability, and the possibility of redox-responsive crosslinking under physiological conditions [5].

Hyaluronic acid represents an ideal substrate for cysteine conjugation due to its reactive functional groups and its well-established role in tissue repair. Early studies demonstrated that HA-cysteine derivatives obtained via carbodiimide-mediated coupling exhibit enhanced mucoadhesion and matrix cohesion due to disulfide bond formation [6,7].

Subsequent studies further confirmed that HA-cysteine conjugates improve adhesion, resistance to degradation, and controlled release behavior. In wound healing applications, thiol-functionalized HA systems have been shown to combine the intrinsic bioactivity of HA with redox-responsive properties, enhancing tissue interaction and regeneration [8,9].

Although studies on electrospun HA-cysteine systems are still limited, cysteine-containing polymers have been successfully processed into nanofibrous scaffolds while preserving thiol functionality. Previous works demonstrated the electrospinning of cysteine-based materials, yielding fibers with maintained chemical reactivity and structural stability [10-12]. A recent review further highlights thiolated HA derivatives as promising candidates for electrospun scaffolds in tissue regeneration [13]. Based on this evidence, the bioconjugation of hyaluronic acid with cysteine represents a promising strategy to engineer electrospun scaffolds with tailored physicochemical and biological properties.

In this study, two bioconjugation strategies were employed to modify hyaluronic acid with cysteine. The first approach involved the use of ethyl ester-protected cysteine (CysOEt), followed by post-conjugation deprotection to obtain HA-Cys-OH, while the second approach utilized free cysteine. In

both cases, coupling was achieved via carbodiimide-mediated activation (EDC/s-NHS), yielding derivatives with controlled functionalization.

The resulting HA-Cys-OH bioconjugates were specifically designed for electrospinning-based scaffold fabrication. Both single-layer and bilayer architectures were developed to investigate the influence of scaffold structure on material performance. In particular, bilayer scaffolds were designed to mimic the hierarchical structure of the skin, consisting of a hydrophobic outer layer based on poly(D,L-lactide) (PDLLA) and a hydrophilic inner layer composed of HA-based bioconjugates blended with poly(vinylpyrrolidone) (PVP). Sequential electrospinning enabled the controlled deposition of distinct layers, while single-layer scaffolds served as simplified systems to evaluate the intrinsic properties of the materials.

Bioconjugation was confirmed by ^{1}H-NMR and ATR-FTIR analyses. The electrospun scaffolds were characterized in terms of morphology (SEM), fiber diameter, and the effect of cysteine functionalization and UV-induced crosslinking. Finally, cytocompatibility was assessed through fibroblast viability assays to evaluate the biological response to the developed materials.

2. Materials and Methods

2.1 Materials

All reagents and solvents were used as received unless otherwise stated. The term *"*pure H_2O*"* refers to ultrapure water obtained using a Millipore Milli-Q Gradient system.

Sodium hyaluronate (HA, Mw = 186 kDa) was a generous gift of Altergon Italia S.r.l.

L-Cysteine, L-Cysteine ethyl ester hydrochloride, sodium hydroxide (NaOH, ≥ 98%), polyvinylpyrrolidone (PVP), sodium 3-(trimethylsilyl) propane-1-sulfonate (98.0%, DSS), 2-(*N*-morpholino)ethanesulfonic acid monohydrate (MES·H_2O, ≥ 99.5%) and deuterium oxide (D_2O) were purchased from Sigma-Aldrich.

1-Ethyl-3-(3-dimethylaminopropyl) carbodiimide hydrochloride (EDC·HCl) and 1,1,1,3,3,3-Hexafluoro-2-propanol (HFP) were obtained from Iris Biotech GmbH, while *N*-hydroxysulfosuccinimide sodium salt (s-NHS) from Tokyo Chemical Industry (TCI).

Ethanol (EtOH; 96%) was obtained from VWR Chemicals and sodium chloride (NaCl, ≥ 99.5%) from Fluka. Poly(D,L-lactic acid) (PDLLA) was purchased from Formfutura.

2.2 Methods

2.2.1 General Methods

Centrifugation was performed using a Hermle (LaborTechnik GmbH) centrifuge (6000 rpm, room temperature, 40 min). Dialysis was carried out using a Slide-A-Lyzer™ Dialysis Cassette G2 with a molecular weight cut-off of 3.5 kDa. Lyophilization was conducted using a Christ Alpha 1-4 LD plus freeze dryer.

2.2.2 Nuclear Magnetic Resonance (NMR) Spectroscopy

NMR spectra were recorded using Varian Inova 500 MHz (^{1}H: 500 MHz, ^{13}C: 125 MHz) and 400 MHz (^{1}H: 400 MHz, ^{13}C: 100 MHz) spectrometers. Samples were prepared in D_2O. DSS (0.1 mM) was used as an internal standard for chemical shift calibration and referenced at δ_H = 0.00 ppm. The degree of substitution (DS) for the HA-Cys-OH derivatives was calculated relative to the disaccharide repeating unit.

2.2.3 Attenuated Total Reflectance Fourier Transform Infrared (ATR-FTIR) Spectroscopy

ATR-FTIR analyses were performed using a Jasco J-460 spectrometer (Jasco Europe Srl) equipped with an ATR PRO ONE single-reflection accessory fitted with a diamond crystal. Spectra were collected in the range of 4000-450 cm^{-1} with a spectral resolution of 2 cm^{-1}, averaging 256 scans for each measurement. A background spectrum was recorded prior to each acquisition and automatically subtracted from the corresponding sample spectrum.

2.2.4 Scanning Electron Microscopy (SEM)

SEM micrographs were obtained using a FEI Quanta 400 high-resolution field-emission scanning electron microscope (ESEM) operated at 20 kV and at various magnifications. Samples were sputter-coated with a thin layer of gold prior to imaging. The diameter of the fibers was evaluated using ImageJ software supplied with the DiameterJ plug-in. The sample size considered corresponds to 50 individual fibers measured from three different scaffolds, for a total of 150.

2.2.5 Bioconjugation of Cys-OEt with HA (4)

HA (136.74 mg, 0.341 mmol) was dispersed in 15 mL of H_2O and stirred at room temperature until complete dissolution. The resulting solution was then supplemented with aqueous EDC·HCl (3.26 mL, 0.682 mmol) and s-NHS (3.86 mL, 0.341 mmol), and the mixture was stirred for an additional 40 minutes. MES·H_2O (40.2 mg) and an aqueous solution of CysOEt (2 mL, 0.681 mmol) were added. The pH was carefully adjusted to 6.0 using freshly prepared 1 M NaOH. A clear solution was obtained, which was stirred overnight at room temperature. After approximately 22 hours, the reaction was brought to pH 7 with 1.0 M NaOH and subjected to dialysis, first against a 342 mM NaCl solution and subsequently against ultrapure water. The dialyzed solution was frozen and lyophilized to afford a white solid (103.64 mg, 75% yield).

^{1}H-NMR (400 MHz, D_2O, 25°C): δ_{DSS} = 4.54 ppm (H-1, GlcNAc), 4.45 ppm (H-1, GlcA), 4.00-3.20 ppm (H-2, H-3, H-4, H-5 GlcA; H-2, H-3, H-4, H-5, H-6 GlcNAc), 4.24 ppm (2H, q, CH_2 (H1',Cys-OEt)) , 2.89 ppm (2H, m, CH_2 (H3, Cys-OEt)), 2.01 ppm (NHAc, GlcNAc), 1.28 ppm (3H, t, CH_3, (H2', Cys-OEt)).

2.2.6 Deprotection of HA-Cys-OEt (5-i)

HA-Cys-OEt (103.80 mg, 0.232 mmol) was treated with 15 mL of 1.0 M NaOH solution to adjust the pH to 12. The solution was stirred for 6 h at room temperature and then 1 M HCl was added until

neutralization. Dialysis and subsequent freeze-drying yielded a white solid (91.13 mg, yield = 88%). ^{1}H-NMR (400 MHz, D_2O, 25°C): δ_{DSS} = 4.54 ppm (H-1, GlcNAc), 4.45 ppm (H-1, GlcA), 4.00-3.20 ppm (H-2, H-3, H-4, H-5 GlcA; H-2, H-3, H-4, H-5, H-6 GlcNAc), 2.89 ppm (2H, m, C*H*$_2$ (H3, Cys-OH), 2.01 ppm (NHAc, GlcNAc).

2.2.7 Bioconjugation of Cys-OH with HA (5-ii)

HA (100.43 mg, 0.250 mmol) was dispersed in 15 mL of H_2O and stirred at room temperature until complete dissolution. The resulting solution was then supplemented with aqueous EDC·HCl (2.40 mL, 0.500 mmol) and s-NHS (2.42 mL, 0.250 mmol), and the mixture was stirred for an additional 40 minutes. MES·H_2O (40.2 mg) and an aqueous solution of Cys-OH (2 mL, 0.500 mmol) were added. The pH was carefully adjusted to 6.0 using freshly prepared 1 M NaOH. A clear solution was obtained, which was left stirring overnight at room temperature. After approximately 22 hours, the reaction was brought to pH 7 with 1.0 M NaOH and subjected to dialysis, first against a 342 mM NaCl solution and subsequently against ultrapure water. The dialyzed solution was frozen and lyophilized to afford a white solid (66.98 mg, 64% yield).

^{1}H-NMR (400 MHz, D_2O, 25°C): δ_{DSS} = 4.54 ppm (H-1, GlcNAc), 4.45 ppm (H-1, GlcA), 4.00-3.20 ppm (H-2, H-3, H-4, H-5 GlcA; H-2, H-3, H-4, H-5, H-6 GlcNAc), 2.90 ppm (2H, m, C*H*$_2$ (H3, Cys-OH)), 2.01 ppm (NHAc, GlcNAc).

2.2.8 Electrospinning

Electrospinning was carried out using a Gamma High Voltage generator (Linari Engineering, Italy) integrated into a horizontal electrospinning system. The composition of the electrospinning solutions is reported in Table 1.

Table 1. Composition of the electrospinning solutions.

Hydrophobic layer						
Scaffold	**PDLLA (% w/V)**		**HFP (mL)**			**Final volume (mL)**
PDLLA	12.0		3.0			3
Hydrophilic layer						
Scaffold	**PVP (% w/V)**	**HA (% w/w)**	**HA-Cys-OH (% w/w)**	**H_2O (mL)**	**EtOH (mL)**	**Final volume (mL)**
PVP-HA-Cys-OH 1%	10.0	-	1.0	0.6	2.4	3
PVP-HA-Cys-OH 3%	10.0	-	3.0	0.6	2.4	3

In the case of the hydrophobic layer, PDLLA (360 mg) was dissolved in HFP (3 mL) and kept under magnetic stirring overnight at T= 37 °C. The solution was loaded into a 10 mL glass syringe with a 20 G stainless-steel needle, and electrospun at 17 kV with a flow rate of 1.0 mL/h. The collector consisted of a circular copper plate (90 mm diameter) covered with aluminum foil and positioned 19 cm from the needle tip.

For the hydrophilic layer, the preparation of the electrospinning solutions followed the general protocol described below. HA-Cys-OH (**derivative 5-ii**; 1.0 or 3.0 mg), corresponding to 1% or 3% (w/w) with respect to PVP, was dissolved in H_2O (0.6 mL) and stirred for 2 h at room temperature. In parallel, PVP (100 or 300 mg) was dissolved in EtOH (0.9 mL) under the same conditions. The two solutions were then combined and further diluted with EtOH (1.5 mL). The mixture was then stirred overnight at 37°C, loaded into a 10 mL glass syringe fitted with a 20 G stainless-steel needle, and electrospun at 19 kV with a flow rate of 0.5 mL/h. The collector consisted of a circular copper plate (90 mm diameter) covered with aluminum foil and positioned 19 cm from the needle tip.

To prevent the complete dissolution of the electrospun PVP-based layers, the obtained scaffolds were subjected to ultraviolet (UV) irradiation (254 nm) using a multiray reactor (Helios Italquartz, Milan, Italy) for 60 minutes, corresponding to a UV dose of 169.2 mJ/cm^2.

For cytocompatibility evaluation, the scaffolds were directly electrospun onto 13 mm glass coverslips. In this case, the electrospun volume was reduced to 1.0 mL for each layer, while maintaining the same solution composition and electrospinning parameters described above. Due to the reduced volume, the resulting scaffolds were exposed to UV irradiation for 15 minutes, corresponding to a UV dose of 42.3 mJ/cm^2.

2.2.9 Evaluation of Cytocompatibility of Electrospun Scaffolds

To evaluate scaffold biocompatibility, L929 murine fibroblasts were used. The cells were acquired from the American Type Culture Collection (ATCC, Rockville, MD, USA) and cultured in Dulbecco's Modified Eagle Medium High Glucose (DMEM, Merck Life Science S.r.l., Milan, Italy) supplemented with 10% fetal bovine serum (FBS, Merck Life Science S.r.l., Milan, Italy), 1% penicillin/streptomycin/amphotericin B (PSA, Merck Life Science S.r.l., Milan, Italy). Cultures were maintained at 37 °C in a humidified atmosphere containing 5% CO2 and sub-cultured upon reaching 80-90% confluence. Electrospun scaffolds deposited onto 13 mm glass coverslips were sterilized by ultraviolet (UV) irradiation for 30 minutes prior to use. L929 fibroblasts were seeded onto each scaffold at a density of 3×10^4 cells per sample using a dropwise technique to ensure uniform initial adhesion. The seeded scaffolds were incubated for two hours under standard culture conditions (37

°C, 5% CO_2, humidified atmosphere). Following this adhesion period, 500 µL of fresh complete culture medium was carefully added to each well to fully immerse the scaffolds and support subsequent cell growth.

Cell viability was assessed using the MTT assay [3-(4,5-dimethylthiazol-2-yl)-2,5-diphenyltetrazolium bromide] test (Merck Life Science S.r.l., Milan, Italy) at 24 and 48 hours post-seeding. For each time point, 500 µL of a 1 mg/mL MTT solution prepared in serum-free high-glucose DMEM was added to each well and incubated at 37 °C for 2 hours. The resulting formazan crystals were solubilized in 500 µL of dimethyl sulfoxide (DMSO; Merck Life Science S.r.l., Milan, Italy). Absorbance was measured at 540 nm using a microplate reader (AMR-100, Biosigma, Verona, Italy). Viability data were normalized to cells cultured without scaffolds, which served as the internal control.

3. Results and Discussion

3.1 Semi-synthesis of HA-Cys-OH

To obtain HA-Cys-OH bioconjugates, two different L-cysteine derivatives were explored: L-cysteine ethyl ester hydrochloride, used in its protected form, and free L-cysteine. The use of both derivatives enabled a direct comparison of the bioconjugation outcomes in terms of reaction yield and the degree of substitution (DS) achieved on the HA backbone.

In both cases, cysteine was conjugated to hyaluronic acid via carbodiimide-mediated amidation. The carboxyl groups of HA were activated using the EDC/s-NHS coupling system, allowing the nucleophilic attack of the cysteine amino group and the formation of a stable amide bond.

The first strategy involved the use of cysteine ethyl ester (Cys-OEt) and was carried out in aqueous MES buffer (pH 6) through activation of the GlcA carboxylate (Scheme 1). After addition of the amino acid, the reaction mixture was maintained at the same pH with a freshly prepared 1.0 M NaOH solution and stirred overnight at room temperature. The crude product was then neutralized, purified by dialysis against a 342 mM NaCl solution followed by H_2O, and finally freeze-dried to afford the HA-Cys-OEt bioconjugate (**derivative 4**), which was obtained with a 75% yield.

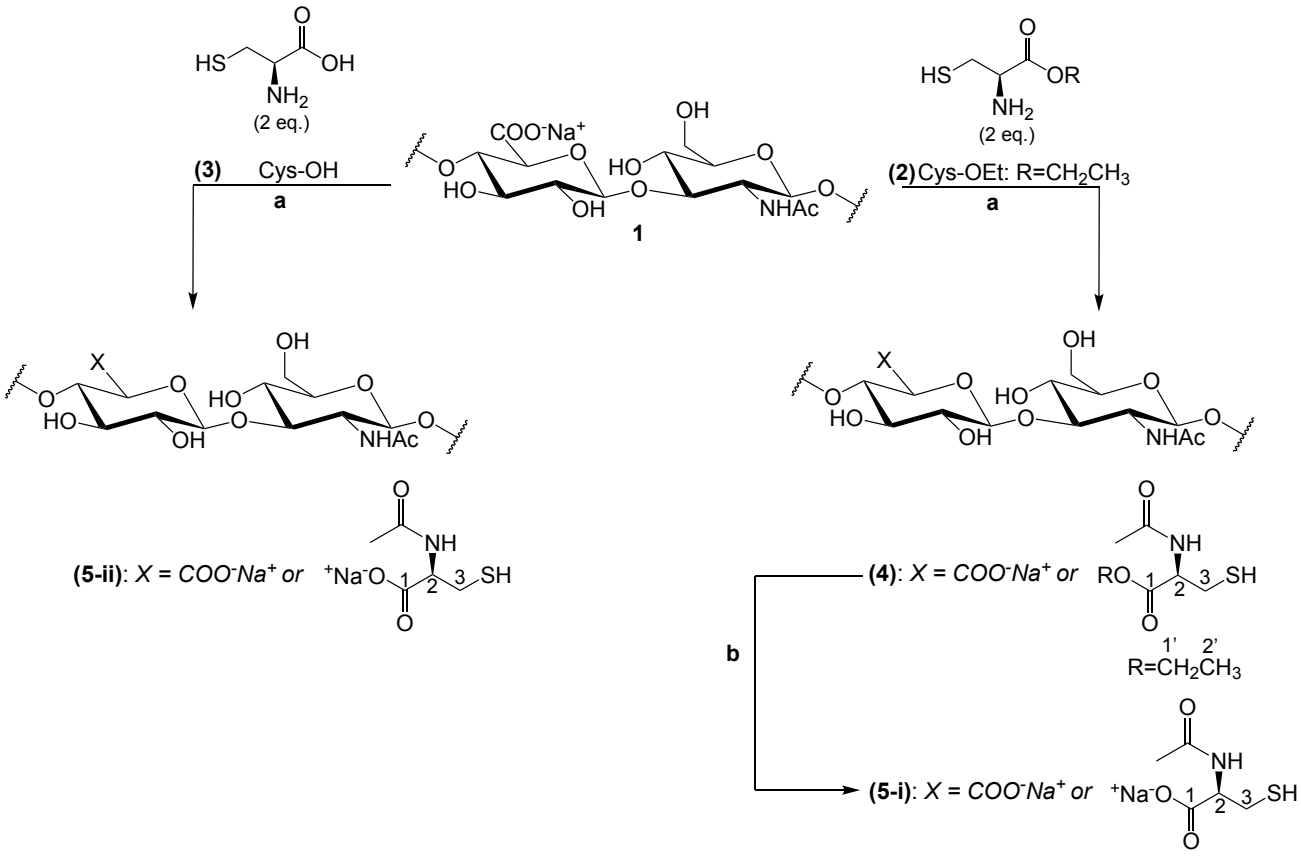

Scheme 1. Semi-synthesis of derivative HA-Cys-OH. a: EDC·HCl, s-NHS, MES, H_2O, pH = 6, room temperature, overnight; b: NaOH, H_2O, pH = 12, overnight, 6h.

The successful bioconjugation of **derivative 4** was confirmed by ^{1}H-NMR analysis (Figure 1). In addition to the characteristic resonances of the HA backbone, including the broad signals of the sugar ring protons in the 4.0-3.20 ppm region, a singlet corresponding to the *N*-acetyl methyl group of the GlcNAc unit was observed at δ_{DSS} = 2.01 ppm.

New resonances attributable to the Cys-OEt moiety were clearly detected. In particular, a signal at δ_{DSS} = 1.28 ppm, corresponding to the methyl group (CH_3) of the ethyl ester, was observed.

The DS value was 15%, as calculated according to Equation 1:

$$DS = \frac{ICH_{3\ (Cys-OEt)}/3}{ICH_{3\ (GlcNAc)}/3} \qquad (1)$$

$ICH_{3\ (Cys-OEt)}$ represents the integral of the methyl protons of the ethyl ester group of the Cys-OEt moiety (δ_{DSS} =1.28 ppm), while $ICH_{3\ (GlcNAc)}$ corresponds to the integral of the acetyl methyl protons of the GlcNAc unit (δ_{DSS} = 2.01 ppm).

The main ^{1}H-NMR signal assignments are summarized in Table 2.

Table 2. ^{1}H-NMR chemical shift assignments of **derivative 4**.

Assignment	^{1}H δ_{DSS} (ppm)
1 (GlcNAc)	4.54
1 (GlcA)	4.45
2-5 (GlcA)	4.0-3.20
2-6 (GlcNAc)	4.0-3.20
1’	4.24
3	2.89
NHAc (GlcNAc)	2.01
2’	1.28

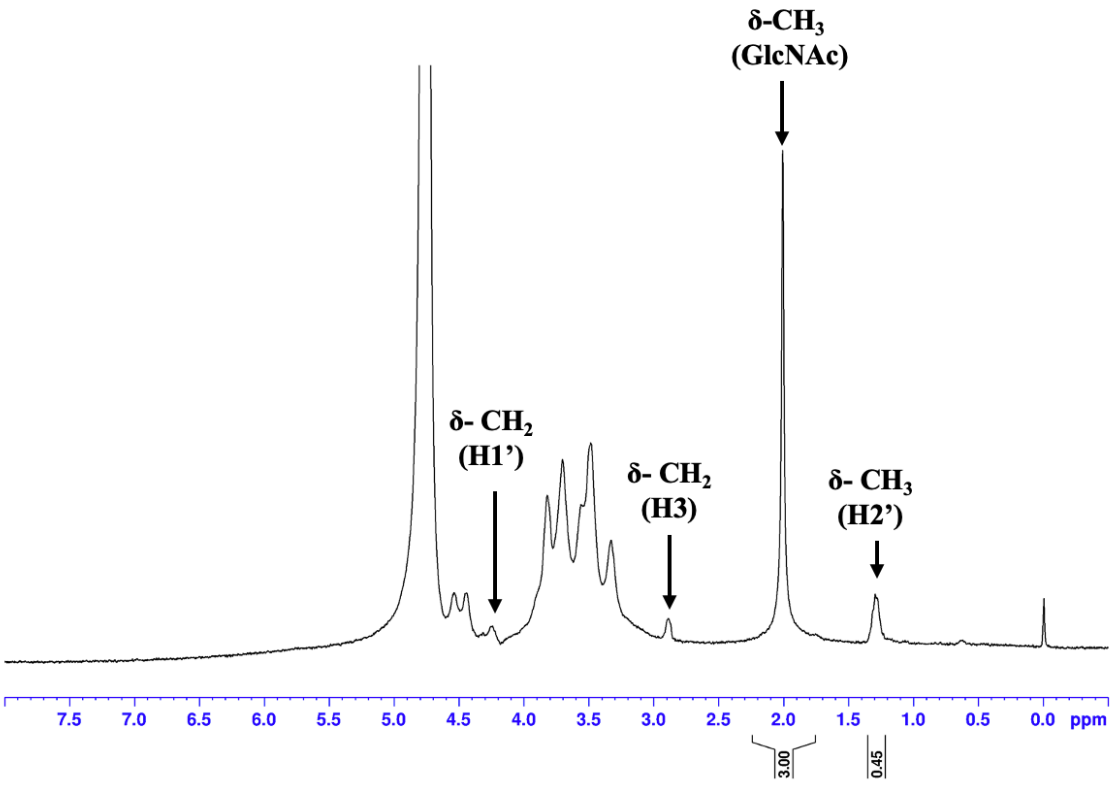

Figure 1. ^{1}H-NMR spectrum of **derivative 4** (400 MHz, D_2O, 25°C).

Derivative 4 was subsequently subjected to saponification by treatment with a 1.0 M NaOH solution to adjust the pH to 12. The reaction mixture was then neutralized, dialyzed, and finally freeze-dried to obtain **derivative 5-i** (Scheme 1) with a yield of 88%.

The successful removal of the ethyl group was confirmed by ^{1}H-NMR (Figure S1). Compared to **derivative 4**, the characteristic signals of the ethyl ester group at δ_{DSS} = 4.24 ppm and 1.28 ppm were no longer observed, indicating saponification of the Cys-OEt moieties. The remaining cysteine signal corresponding to the CH_2 at δ_{DSS} = 2.89 ppm was still present, confirming preservation of the cysteine side chain after hydrolysis. The main ^{1}H-NMR signal assignments are summarized in Table 3.

Table 3. ^{1}H-NMR chemical shift assignments of **derivative 5-i**.

Assignment	^{1}H δ_{DSS} (ppm)
1 (GlcNAc)	4.54
1 (GlcA)	4.45
2-5 (GlcA)	4.0-3.20
2-6 (GlcNAc)	4.0-3.20
3	2.89
NHAc (GlcNAc)	2.01

The formation of the **derivative 5-i** was supported by ATR-FTIR analysis (Figure S2). The spectrum of native HA (black curve) exhibits the characteristic absorption bands of the polysaccharide backbone, including the broad O-H stretching band at 3284 cm^{-1}, the C-H stretching vibration at 2876 cm^{-1}, and the typical amide I and amide II bands at 1603 cm^{-1} and 1540 cm^{-1}, respectively.

The ATR-FTIR spectrum of **derivative 5-i** (red curve) retains the characteristic absorption bands of the HA backbone, indicating that the polysaccharide structure is preserved after saponification. Compared to native HA, **derivative 5-i** shows an aliphatic C-H stretching band at 2912 cm^{-1}, which slightly differs from that observed for HA. In addition, variations in both the position and shape of the amide I and amide II bands are observed, with absorptions at 1617 cm^{-1} and 1391 cm^{-1}, respectively, suggesting the presence of cysteine moieties within the HA backbone.

In contrast to the ATR-FTIR spectrum of commercial Cys-OEt (blue curve), **derivative 5-i** does not exhibit the characteristic ester carbonyl band at 1739 cm^{-1} [14], supporting the successful removal of the ethyl ester group during saponification. The main IR band assignments for HA, derivative 5-i and commercial Cys-OEt are summarized in Table 4.

Table 4. IR bands assignments for HA, **derivative 5-i** and commercial Cys-OEt.

IR assignments HA (black curve)	**Wavenumber (cm^{-1})**	**IR assignments Derivative 5-i (red curve)**	**Wavenumber (cm^{-1})**	**IR assignments Cys-OEt (blue curve)**	**Wavenumber (cm^{-1})**
ν O-H (*)	3284	ν O-H (*)	3302	ν C-H (aliphatic)(*)	2889
ν C-H (aliphatic)(*)	2876	ν C-H (aliphatic)(*)	2912	ν S-H (*)	2473
ν C=O (Amide I)(*)	1603	ν C=O (Amide I)(*)	1617	ν C=O (Ester) (*)	1739
δ N-H + ν N-C (Amide II) (*)	1540	δ N-H + ν N-C (Amide II)(*)	1391	ν C-S (*)	607
δ C-H (*)	1377	ν C-O-C (*)	1155		
ν C-O-C (*)	1146	ν C-O (*)	1047		
ν C-O (*)	1014				

The second strategy to obtain HA-Cys-OH bioconjugate involved the use of free L-cysteine (Cys-OH) and was carried out using the same EDC/NHS-mediated coupling approach (Scheme 1). After an overnight reaction, the mixture was neutralized, purified by dialysis, and freeze-dried to afford **derivative 5-ii** with a 64% yield.

The successful bioconjugation of **derivative 5-ii** was confirmed by ^{1}H-NMR analysis (Figure 2). In addition to the characteristic HA resonances, a signal appeared at δ_{DSS} = 2.90 ppm, which was assigned to the methylene protons of the cysteine residue.

The resulting DS was 23%, as calculated according to Equation 2:

$$DS = \frac{ICH_{2\,(Cys-OH)}/2}{ICH_{3(GlcNAc)}/3} \quad (2)$$

$I_{CH_2(Cys-OH)}$ represents the integral of the cysteine methylene signal at δ_{DSS} = 2.90 ppm, while $I_{CH_3(GlcNAc)}$ corresponds to the integral of the *N*-acetyl methyl protons of the GlcNAc unit at δ_{DSS} = 2.01 ppm.

The main ^{1}H-NMR signal assignments are summarized in Table 5.

Table 5. ^{1}H-NMR chemical shift assignments of **derivative 5-ii**.

Assignment	**^{1}H δ_{DSS} (ppm)**
1 (GlcNAc)	4.54
1 (GlcA)	4.45
2-5 (GlcA)	4.0-3.20
2-6 (GlcNAc)	4.0-3.20
3	2.90
NHAc (GlcNAc)	2.01

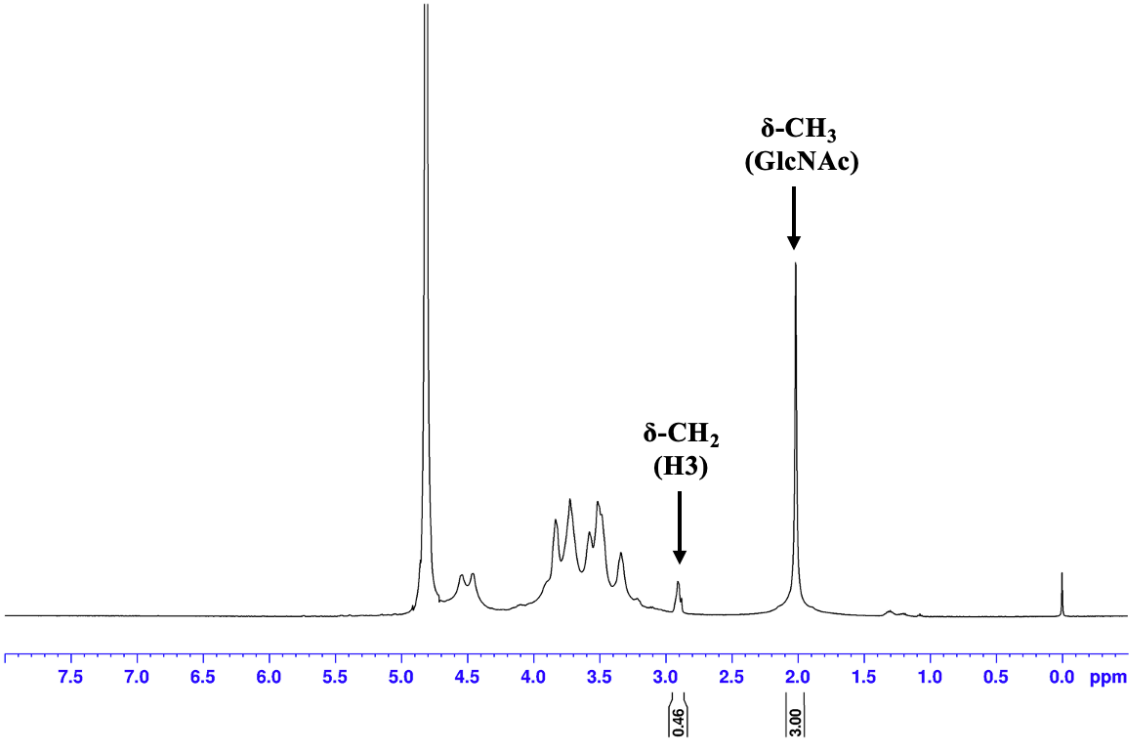

Figure 2. ^{1}H-NMR spectrum of **derivative 5-ii** (400 MHz, D_2O, 25°C).

Further confirmation of the successful conjugation was obtained by ATR-FTIR analysis (Figure S3), which compares the spectra of HA (black curve), **derivative 5-ii** (red curve), and commercial Cys-OH (blue curve). The characteristic IR features of native HA have been previously discussed (Table 4).

Compared to native HA, **derivative 5-ii** shows an aliphatic C-H stretching band at 2880 cm^{-1}, slightly shifted with respect to HA, together with small differences in the position and shape of the amide I and amide II bands (1611 cm^{-1} and 1555 cm^{-1}, respectively). These variations are consistent with the presence of cysteine moieties in the modified HA structure. In addition, the appearance of a band at 666 cm^{-1}, attributable to ν(C-S), further supports cysteine incorporation.

The spectrum of commercial Cys-OH (blue curve) displays the characteristic vibrational bands of the amino acid, such as the asymmetric N-H stretching of the amino group at ~3380 cm^{-1}, the S-H stretching vibration at ~2556 cm^{-1}, and the C-S stretching band at ~655 cm^{-1} [15] which are consistent with those observed in the **derivative 5-ii**. The main IR band assignments for **derivative 5-ii** and commercial Cys-OH are summarized in Table 6.

Table 6. IR bands assignments for HA**, derivative 5-ii** and commercial Cys-OH.

IR assignments Derivative 5-ii (red curve)	**Wavenumber (cm^{-1})**	**IR assignments Commercial Cys-OH (blue curve)**	**Wavenumber (cm^{-1})**
ν O-H (*)	3270	*ν* N-H (*)	3380
ν C-H (aliphatic)(*)	2880	ν C-H (aliphatic)(*)	2879
ν C=O (Amide I)(*)	1611	*ν* S-H (*)	2556
δ N-H + ν N-C (Amide II) (*)	1555	δ (N-H) (*)	1571
δ C-H (*)	1372	*ν* C-S (*)	655
ν C-S (*)	666		

3.2 Electrospinning and Morphological Analysis of Electrospun Composites

The objective of this part of the work was to develop asymmetric bilayer electrospun scaffolds for tissue engineering by sequentially electrospinning biodegradable and bioactive polymeric layers, following the same strategy previously described [16]. This multilayer approach allows the combination of materials with different physicochemical properties within a single construct, enabling the modulation of both mechanical behavior and biological functionality.

As summarized in Table 1, the outer hydrophobic layer was fabricated by electrospinning a 12.0% w/V solution of PDLLA in HFP, while the inner hydrophilic layers were obtained from blends of semi-synthetic HA-Cys-OH conjugates (**derivative 5-ii**) and PVP dissolved in an 80% v/v aqueous ethanol solution. The HA-Cys-OH derivative was used at either 1% or 3% w/w, whereas PVP was maintained at a concentration of 10% w/V. The electrospinning parameters for the hydrophobic and hydrophilic solutions were independently optimized to ensure a stable process and to obtain membranes with uniform macroscopic appearance.

The morphology of the electrospun scaffolds was evaluated by SEM analysis to verify the formation of continuous and defect-free fibrous structures. All the investigated formulations yielded interconnected fibrous networks typical of electrospun architectures (Figure 3). Since the morphological features of the control scaffolds (PDLLA, PVP, PVP-HA 1%, and PVP-HA 3%) have already been discussed in Chapter 2, the present section specifically addresses the scaffolds incorporating the HA-Cys-OH derivative.

The PDLLA layer (Figure 3A) consisted of smooth, nearly linear fibers without visible defects. In contrast, the hydrophilic layers displayed a predominantly linear fiber arrangement; however, the addition of HA or HA-based cysteine derivatives to the PVP matrix induced a slight degree of fiber curling, as observed in Figure 3B-F. This effect is consistent with the incorporation of hydrophilic macromolecules within the spinning solution and did not compromise the overall fibrous morphology of the scaffolds.

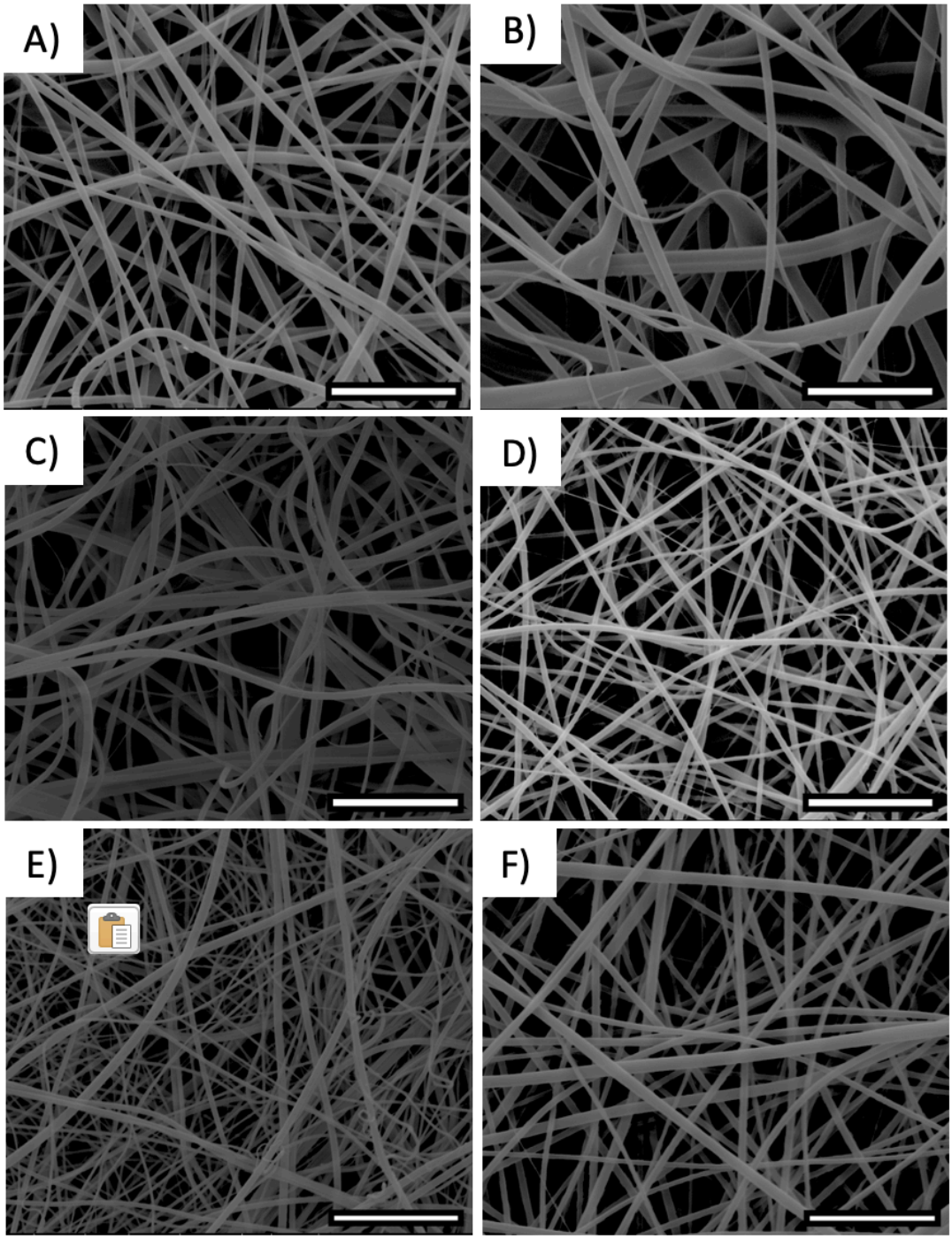

Figure 3. SEM images of electrospun scaffolds (bar: 20 μm). PDLLA (A), PVP (B), PVP-HA 1% (C), PVP-HA 3% (D), PVP-HA-Cys-OH 1% (E), PVP-HA-Cys-OH 3% (F).

A summary of the average fiber diameters for all analyzed samples is reported in Table 7.

Table 7. Average fiber diameter reported as mean value ± standard deviation.

Scaffold	Diameter (μm)	Standard deviation (μm)
PDLLA	1.23	0.64
PVP	1.56	0.79
PVP-HA 1%	1.31	0.51
PVP-HA 3%	0.95	0.24
PVP-HA-Cys-OH 1%	1.46	0.26
PVP-HA-Cys-OH 3%	1.67	0.35

Statistical evaluation was performed using a one-way analysis of variance (ANOVA), followed by Tukey's post hoc test to detect differences in fiber diameters (Figure 4).

The PVP-HA-Cys-OH 1% scaffold exhibited an average fiber diameter of 1.46 ± 0.26 μm, which is significantly higher than that of the corresponding PVP-HA 1% formulation (1.31 ± 0.51 μm) (****, $p < 0.0001$).

At higher concentration, the PVP-HA-Cys-OH 3% scaffold showed a further increase in fiber diameter (1.67 ± 0.35 μm), which is significantly higher than that of PVP-HA 3% (0.95 ± 0.24 μm) (****, $p < 0.0001$). This behavior may be attributed to the introduction of cysteine moieties, which can enhance intermolecular interactions and alter the viscoelastic properties of the electrospinning solution, ultimately affecting fiber formation.

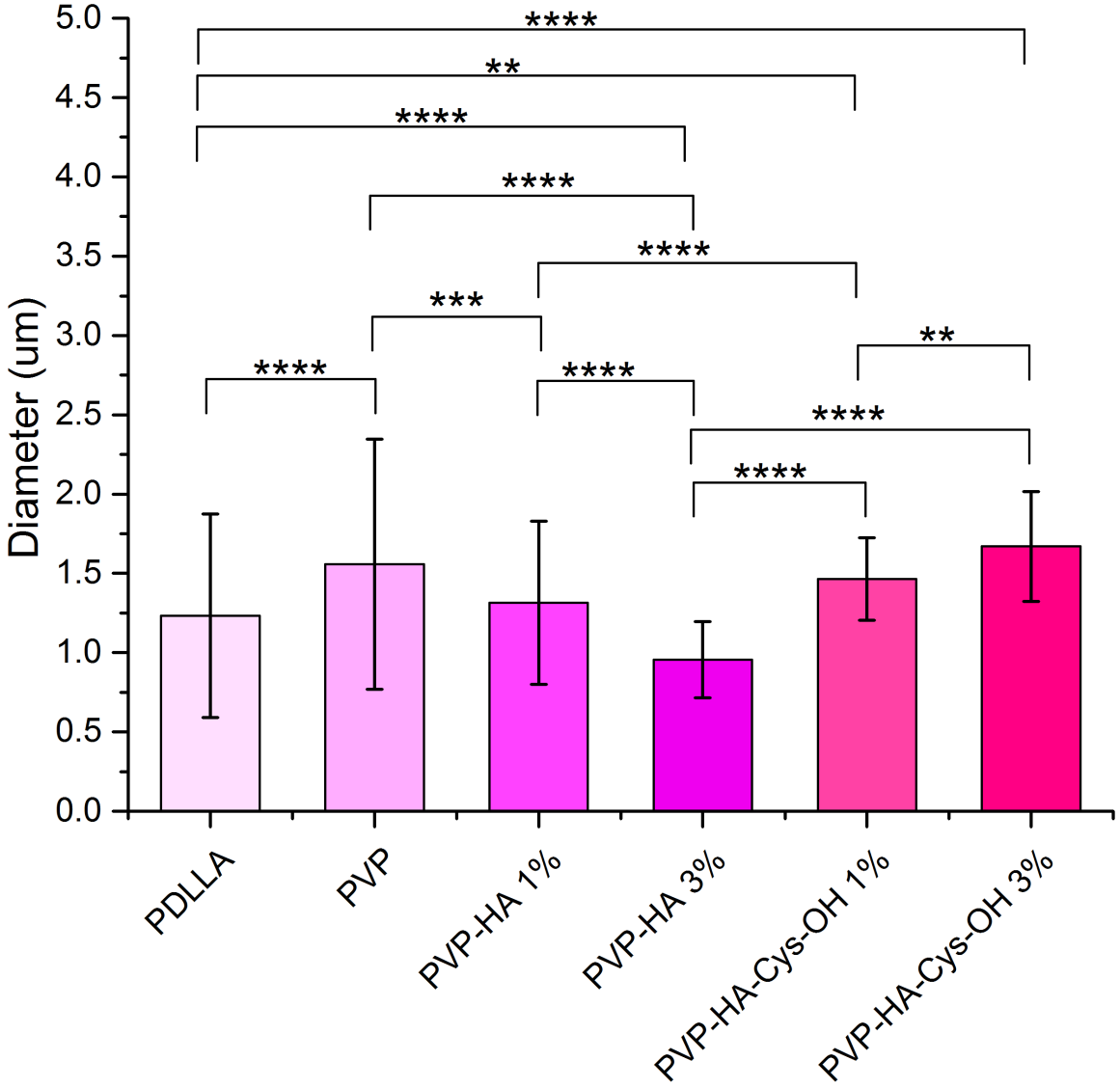

Figure 4. Histogram of average fiber diameter of electrospun scaffolds. Asterisks indicate the level of statistical significance among groups (**p < 0.01, ***, p < 0.001; ****, p < 0.0001). Bars represent mean ± standard deviation obtained from 150 measurements per sample.

The effect of UV-induced crosslinking on fiber diameter was investigated by comparing cysteine-containing electrospun scaffolds before and after UV treatment. Statistical significance between non-crosslinked and crosslinked samples was assessed using a two-sample t-test, considering $p < 0.05$ as statistically significant.

For the PVP-HA-Cys-OH 3% formulation, UV crosslinking led to a marked increase in the average fiber diameter. The non-crosslinked scaffold exhibited a mean diameter of 1.16 ± 0.33 µm, while the crosslinked sample showed a significantly higher value of 1.67 ± 0.35 µm (Figure 5; ****, $p < 0.0001$).

A similar behavior was observed for the PVP-HA-Cys-OH 1% scaffolds. The non-crosslinked fibers showed an average diameter of 1.39 ± 0.34 µm, which increased to 1.46 ± 0.26 µm after UV crosslinking (Figure 5; ****, $p < 0.0001$).

The observed increase in fiber diameter upon crosslinking can be attributed to the formation of covalent bonds within the polymer matrix, which reduces chain mobility and increases the structural rigidity of the fibers. This stabilization can limit polymer chain rearrangement and relaxation, leading to a slight increase in the apparent fiber diameter.

This behavior is consistent with previous reports on electrospun polymeric and biopolymeric systems, where post-treatment crosslinking alters chain mobility and viscoelastic properties, often resulting in increased fiber diameter and modified morphology [17-19].

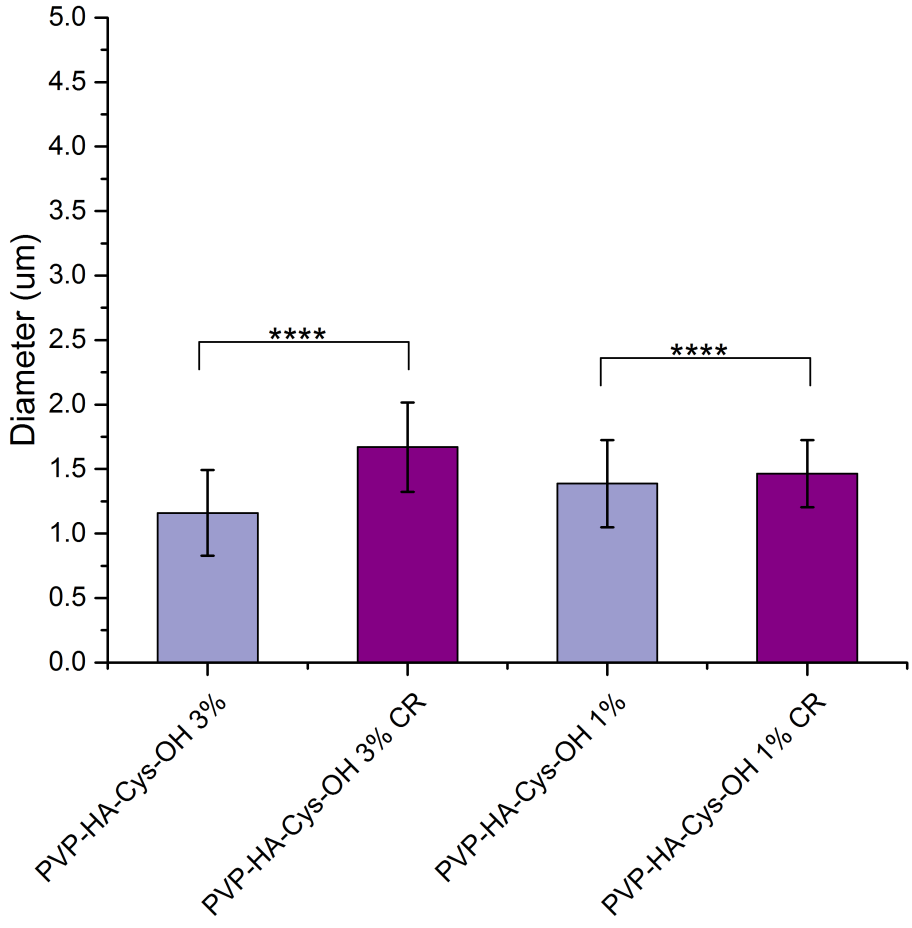

Figure 5. Histogram of average fiber diameter of electrospun scaffolds before and after crosslinking ("CR" indicates crosslinked samples). Bars represent mean ± standard deviation obtained from 150 measurements per sample. Statistical analysis was performed using a two-sample t-test. (**** $p < 0.0001$).

3.3 Biocompatibility Assessment

The biocompatibility of the single-layer and bilayer electrospun scaffolds was assessed by evaluating L929 fibroblast viability at 24 and 48 hours post-seeding, with untreated cells used as the 100% viability reference (Figure 6). Overall, the results confirmed that the majority of the tested formulations supported cell survival, although the extent of cytocompatibility varied depending on the polymer composition and the presence of functional additives.

At both time points, scaffolds composed solely of PDLLA or PVP induced a significant reduction in cell viability compared to the control, indicating that these single-component matrices may exert a mild cytotoxic effect during the early phases of cell–material interaction. The incorporation of HA into PVP improved the biological response, although viability remained significantly lower than the control at both 24 and 48 hours.

Interestingly, the addition of HA-Cys-OH to PVP resulted in a more favorable outcome: at 24 hours, cell viability was comparable to the control, suggesting that the thiolated HA derivative may mitigate the initial stress associated with polymer exposure. However, by 48 hours, viability decreased significantly, indicating that the beneficial effect may be transient or dependent on early cell–matrix interactions.

The bilayer scaffolds demonstrated a similar trend. The PDLLA/PVP bilayer showed significantly reduced viability at both time points, consistent with the behavior of the individual components. The incorporation of HA into the bilayer improved cytocompatibility but did not fully restore viability to control levels.

Notably, the PDLLA/PVP bilayer containing HA-Cys-OH exhibited the most promising profile among the bilayer formulations: viability at 24 hours was statistically comparable to the control, suggesting that the presence of thiolated HA may enhance the initial cell response by improving hydration, protein adsorption, or matrix compliance. However, as observed in the single-layer PVP-HA-Cys-OH scaffold, viability decreased significantly at 48 hours, indicating that longer-term interactions may still be influenced by the underlying polymeric structure.

Taken together, these findings highlight the importance of scaffold composition in modulating early cell behavior. While PDLLA and PVP alone show limited cytocompatibility, the incorporation of HA, particularly HA-Cys-OH, can transiently improve cell viability, especially during the initial 24-hour period. The decline observed at 48 hours suggests that further optimization of polymer ratios, crosslinking density, or degradation kinetics may be required to sustain long-term cytocompatibility. Nonetheless, the positive early response to HA-Cys-OH-containing scaffolds indicates that functionalized HA derivatives represent a promising strategy for enhancing the biological performance of electrospun materials intended for tissue engineering applications.

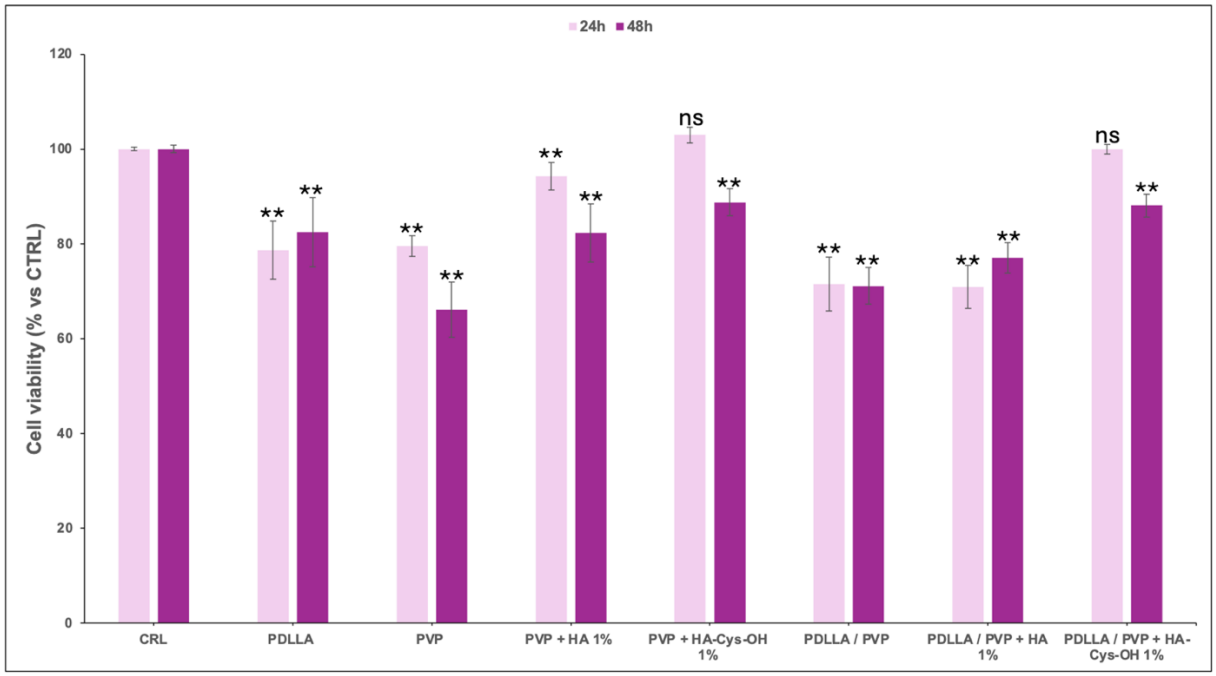

Figure 6. Cell viability of L929 fibroblasts cultured on various electrospun scaffold formulations at 24 and 48 hours. Bar graph showing cell viability (percentage of untreated cells) for seven treatment groups: untreated cells (CRL), PDLLA, PVP, PVP-HA 1%, PVP-HA-Cys-OH 1%, PDLLA/PVP, PDLLA/PVP-HA 1%, and PDLLA/PVP-HA-Cys-OH 1%. Error bars indicate standard deviation. Statistical significance is denoted as follows: **, $p < 0.01$, ns = not significant.

4. Conclusions

In this chapter, the bioconjugation of hyaluronic acid with L-cysteine was successfully achieved through carbodiimide-mediated coupling, yielding HA-Cys-OH derivatives with controlled degrees of substitution. Two conjugation strategies were explored, namely the use of L-cysteine ethyl ester followed by saponification and the direct coupling of free L-cysteine, allowing a comparative evaluation of reaction efficiency in terms of yield and degree of modification. The bioconjugation route involving the cysteine ethyl ester resulted in an HA-Cys-OH derivative with a degree of substitution of 15% and high yields in both the coupling and deprotection steps. In contrast, the direct coupling of free L-cysteine led to a higher degree of substitution (23%) with a good overall yield (64%), indicating a more efficient and straightforward conjugation strategy for the functionalization of the hyaluronic acid backbone.

Spectroscopic analyses by ^{1}H-NMR and ATR-FTIR confirmed the successful introduction of cysteine moieties along the HA backbone, as evidenced by the appearance of characteristic cysteine-related signals and vibrational bands.

The resulting HA-Cys-OH bioconjugates were effectively processed into nanofibrous scaffolds by electrospinning, both as single-layer hydrophilic membranes and as asymmetric bilayer constructs combined with a PDLLA hydrophobic layer. SEM analysis demonstrated that all formulations produced continuous, defect-free fibrous networks with interconnected porosity, confirming the suitability of cysteine-modified HA for electrospinning-based scaffold fabrication.

Quantitative analysis of fiber diameters revealed that the incorporation of HA-Cys-OH into PVP-based electrospinning solutions influenced fiber morphology. Compared to the corresponding PVP-HA formulations, cysteine-containing scaffolds generally exhibited higher average fiber diameters, although the magnitude of this effect depended on the HA-Cys-OH content and was not statistically significant in all comparisons. These results indicate that cysteine modification modulates fiber morphology without inducing a uniform or linear trend with increasing derivative concentration.

The influence of UV-induced crosslinking on scaffold morphology was also investigated. UV treatment resulted in an increase in fiber diameter for both HA-Cys-OH formulations, with a more pronounced effect observed at higher derivative content. This behavior is consistent with the formation of covalent crosslinks within the polymer matrix, which reduce chain mobility and limit jet stretching during electrospinning. At lower HA-Cys-OH concentrations, the effect of UV crosslinking was statistically significant but quantitatively modest, suggesting a concentration-dependent response of the system.

Biocompatibility assays performed with L929 fibroblasts further demonstrated that scaffold composition significantly influences early cell response. In particular, HA-Cys-OH containing

scaffolds showed improved fibroblast viability at 24 hours compared to the corresponding PVP-based formulations, highlighting the potential of thiolated HA derivatives to enhance the initial cytocompatibility of electrospun matrices.

Overall, the results presented in this chapter demonstrate that cysteine-functionalized hyaluronic acid can be successfully integrated into electrospun scaffold architectures, enabling modulation of fiber morphology and responsiveness to post-processing treatments such as UV crosslinking. The combination of HA bioactivity with cysteine-derived thiol functionality provides a versatile platform for the development of electrospun scaffolds with tunable structural properties, which may be advantageous for future applications in tissue regeneration and wound healing.

Supporting Information

Design, Characterization, and Electrospinning of Hyaluronic Acid-Cysteine Bioconjugates

Table of contents

Figure S1. ^{1}H-NMR spectrum of **derivative 5-i** (400 MHz, D_2O, 25°C).	**216**
Figure S2. ATR-FTIR spectra of HA **derivative 5-i** and commercial Cys-OEt	**217**
Figure S3. ATR-FTIR spectra of HA, **derivative 5-ii** and commercial Cys-OH.	**218**

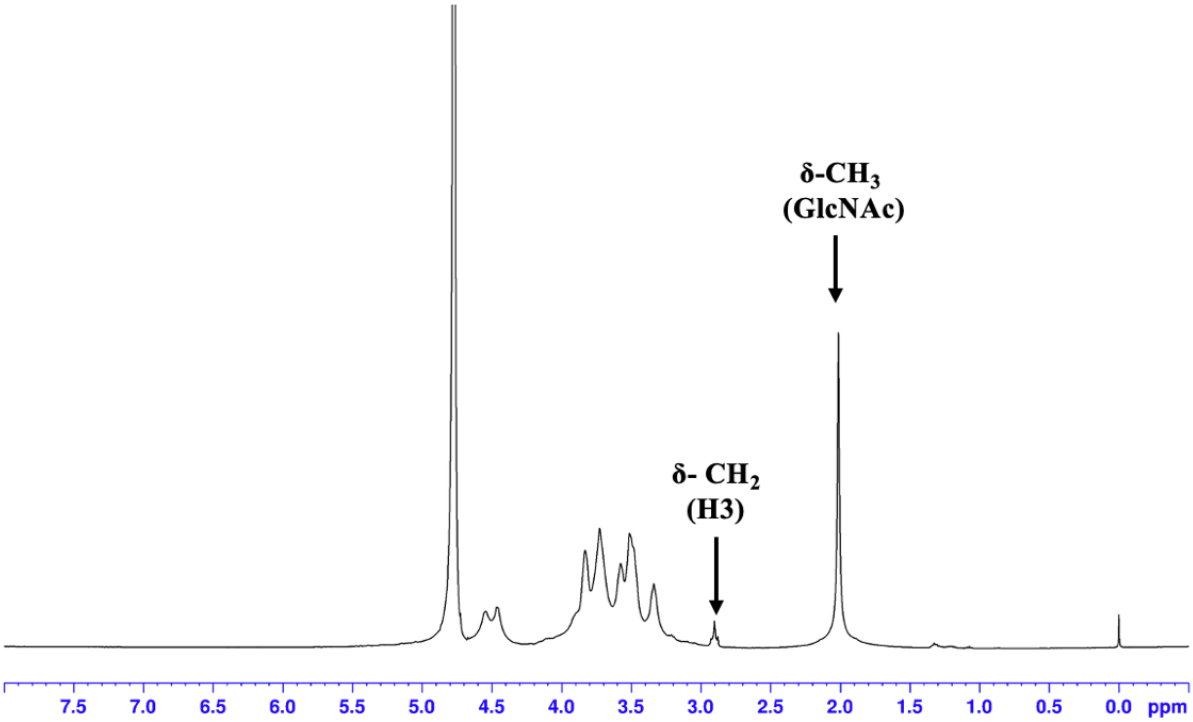

Figure S1. ^{1}H-NMR spectrum of **derivative 5-i** (400 MHz, D_2O, 25°C).

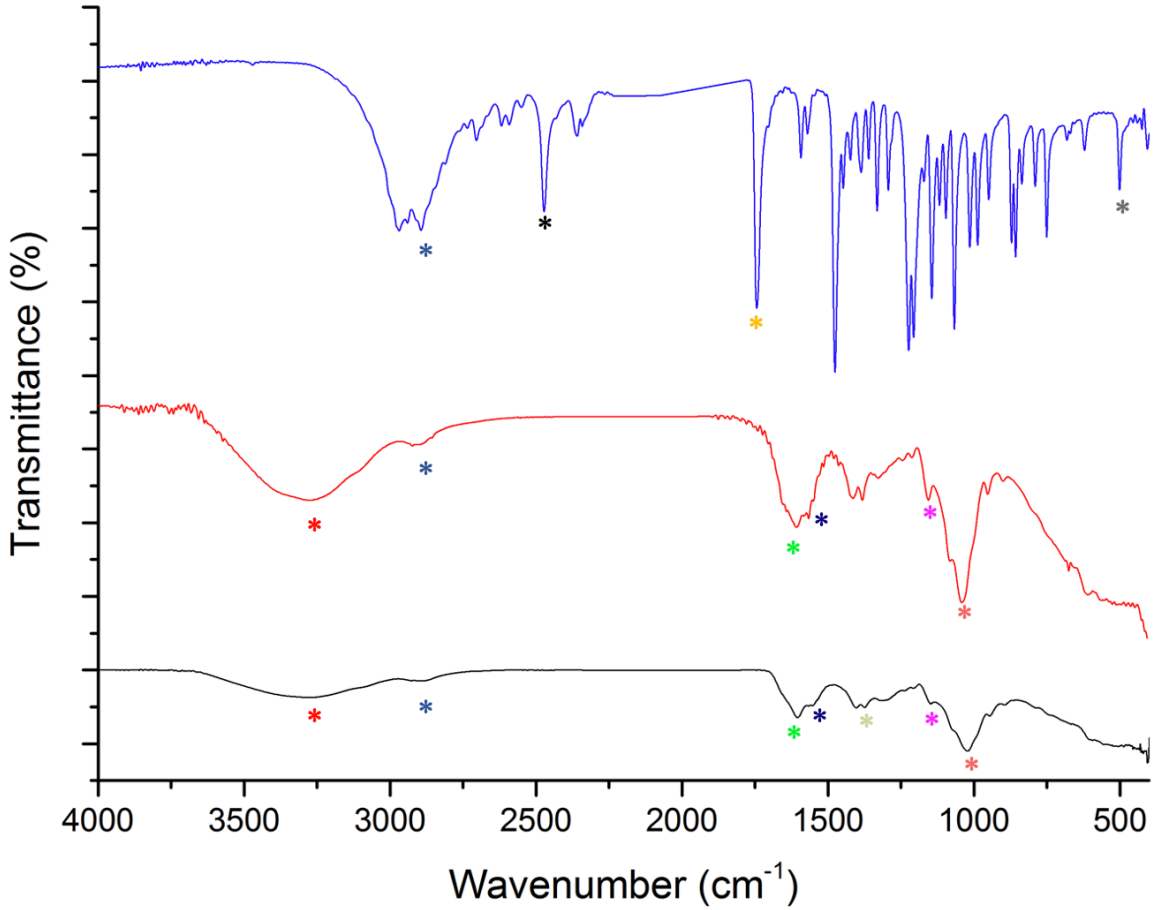

Figure S2. ATR-FTIR spectra of HA (black curve) **derivative 5-i** (red curve) and commercial Cys-OEt (blue curve).

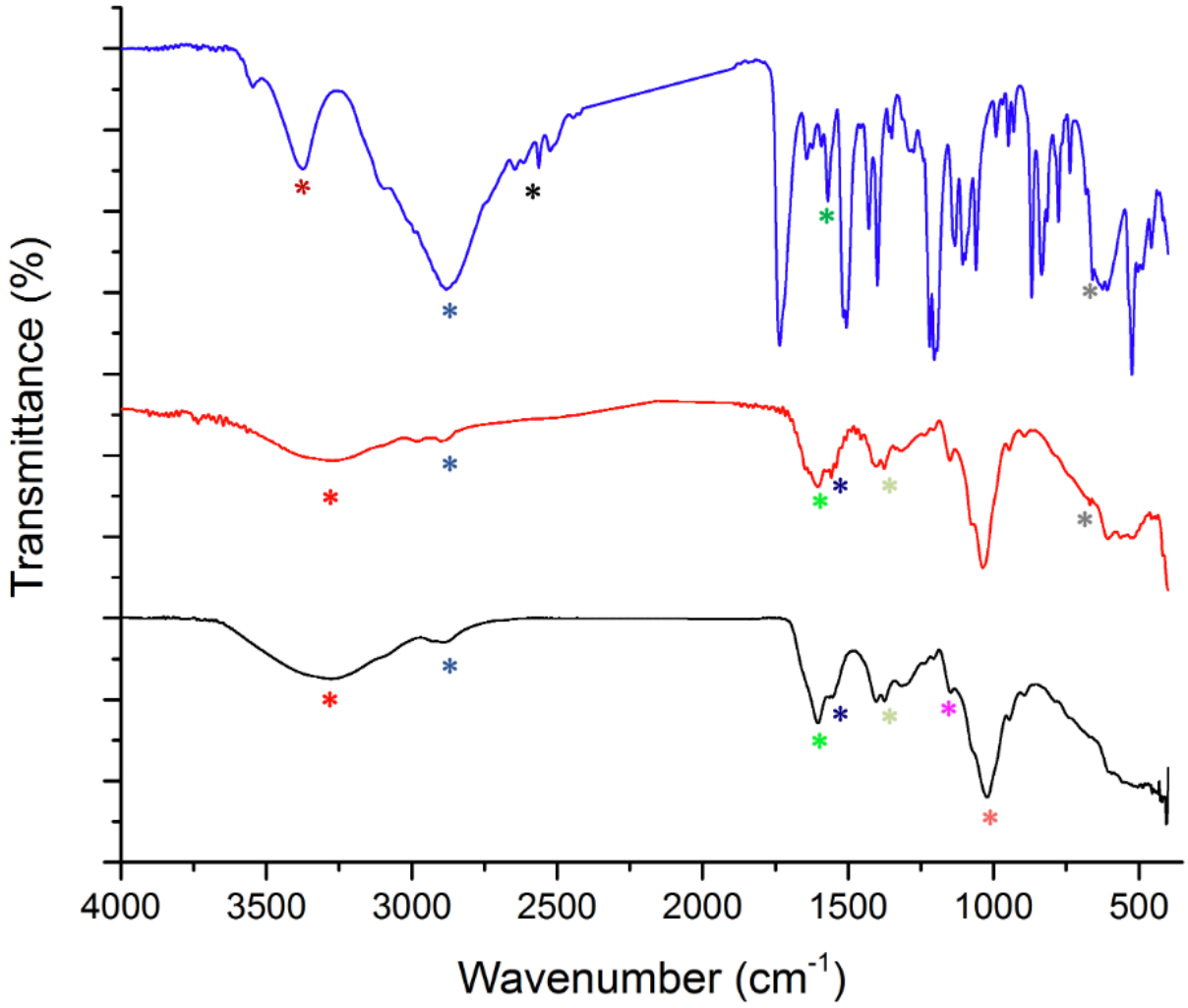

Figure S3. ATR-FTIR spectra of HA (black curve), the **derivative 5-ii** (red curve) and commercial Cys-OH (blue curve)

References

[1] Li T.; Wang L.; Hu Q.; Liu S.; Bai X.; Xie Y.; Zhang T.; Bo S.; Gao X.; Wu S.; Li G.; Wang Z. *Neuroprotective roles of L-cysteine in attenuating early brain injury and improving synaptic density via the CBS/H_2S pathway following subarachnoid hemorrhage in rats.* Frontiers in Neurology, **2017**, 8, 176.

[2] Yang M.; Huang C.; Luo W.; Gong P.; Huang B.; Yao Y. *L-cysteine rescues radiation-induced ferroptosis and boosts wound healing through fibroblasts proliferation and migration.* Biochemical and Biophysical Research Communications, **2025**, 10;784:152599.

[3] Paul B. D.; Sbodio J. I.; Snyder S. H. *Cysteine metabolism in neuronal redox homeostasis.* Trends in Pharmacological Sciences, **2018**, 39, 513–524.

[4] Ukaegbu K.; Allen E.; Svoboda K. K. H. *Reactive oxygen species and antioxidants in wound healing: Mechanisms and therapeutic potential.* International Wound Journal, **2025**, 22(5):e70330.

[5] Bernkop-Schnürch A. *Thiomers: A new generation of mucoadhesive polymers.* Advanced Drug Delivery Reviews, **2005**, 57, 1569–1582.

[6] Kafedjiiski K.; Jetti R. K. R.; Föger F.; Hoyer H.; Werle M.; Hoffer M.; Bernkop-Schnürch A. *Synthesis and in vitro evaluation of thiolated hyaluronic acid for mucoadhesive drug delivery.* International Journal of Pharmaceutics, **2007**, 343, 48–58.

[7] Bernkop-Schnürch A, Kast CE, Guggi D. *Permeation enhancing polymers in oral delivery of hydrophilic macromolecules: thiomer/GSH systems.* Journal of Controlled Release**. 2003**;93(2):95–103.

[8] Li X.; Yu G.; Jin K.; Yin Z. *Hyaluronic acid–L-cysteine conjugate exhibits controlled-release potential for mucoadhesive drug delivery.* Pharmazie, **2012**, 67(3):224-8.

[9] Yang X.; Wang B.; Peng D.; Nie X.; Wang J.; Yu C.-Y.; Wei H. *Hyaluronic acid-based injectable hydrogels for wound dressing and localized tumor therapy: A review.* Advanced NanoBiomed Research, **2022**, 2, 2200124.

[10] Lu, T., Sun, J., Dong, X. et al. *PLLA-PCys co-electrospun fibers for capture and elution of glutathione S-transferase.* Sci. China Ser. B-Chem*,* **2009***,* 52, 2033–2037.

[11] Ben Khalifa E.; Cecone C.; Rzig B.; Mori G.; Cesano F.; Malandrino M.; Bracco P.; Magnacca G. *Electrospun maltodextrin fibers for efficient removal of nanoparticles, atenolol, and crystal violet: Preparation and characterization.* ACS Omega, **2025**, 10(42).

[12] Ben Khalifa E.; Cecone C.; Rzig B.; Azaiez S.; Cesano F.; Malandrino M.; Bracco P.; Magnacca G. *Green surface modification of polyvinyl alcohol fibers and its application for dye removal using Doehlert experimental design.* Reactive and Functional Polymers, **2023**, 193, 105763.

[13] Pepe A.; Laezza A.; Armiento F.; Bochicchio B. *Chemical modifications in hyaluronic acid-based electrospun scaffolds.* ChemPlusChem, **2024**, 89, e202300599.

[14] Defonsi Lestard M. E.; Díaz S. B.; Puiatti M.; Echeverría G. A.; Piro O. E.; Pierini A. B.; Altabef A. B.; Tuttolomondo M. E. *Vibrational and structural behavior of L-cysteine ethyl ester hydrochloride in the solid state and in aqueous solution.* Journal of Physical Chemistry A, **2013**, 117(51), 14243–14252.

[15] Parker S. F. *Assignment of the vibrational spectrum of L-cysteine.* Chemical Physics, **2013**, 424, 75–79.

[16] Morgado P. I.; Aguiar-Ricardo A.; Correia I. J. *Asymmetric membranes as ideal wound dressings: An overview on production methods, structure, properties and performance relationship.* Journal of Membrane Science, **2015**, 490, 139–151.

[17] Meng L.; Arnoult O.; Smith M.; Wnek G. E. *Electrospinning of in situ crosslinked collagen nanofibers*. Journal of Materials Chemistry, **2012**, 22, 19412–19418.

[18] Yang B.; Wang J.; Chen X.; Zhao Y. *Effect of crosslinking on mechanical and biological properties of electrospun gelatin nanofibers.* Journal of Applied Polymer Science, **2008**, 110, 139–145.

[19] Zhou Y.; Yang D.; Chen H.; Liao Y.; Shao Z. *Electrospun poly(vinyl alcohol)/gelatin composite nanofibers and their crosslinking behavior.* Materials Science and Engineering C, **2011**, 31, 199–207.

Chapter 5

Characterization of Electrospun Hyaluronic Acid-Based Bioconjugate Scaffolds

1. Introduction

The characterization of electrospun scaffolds represents a critical step in assessing their suitability for biomedical applications, particularly in wound healing and tissue regeneration. Scaffold surface chemistry, wettability, and chemical stability play a central role in regulating cell–material interactions, influencing key biological processes such as cell adhesion, survival, and phenotypic response. For this reason, a comprehensive physicochemical characterization is essential when developing functionalized electrospun systems intended for biological use.

In this chapter, electrospun scaffolds with different architectures and surface chemistries were systematically investigated. Hydrophilic formulations based on PVP, either alone or combined with HA or HA bioconjugated with amino acids (HA-AA), were compared with hydrophobic PDLLA scaffolds. In addition, bilayer scaffold systems were developed by combining a mechanically stable PDLLA bottom layer with a functional hydrophilic PVP-based top layer. This architectural strategy allowed direct exposure of the bioactive surface while preserving the overall mechanical integrity and handling properties of the system.

The physicochemical characterization focused on surface wettability, chemical composition, and chemical stability following UV sterilization. Static contact angle measurements were performed to evaluate surface hydrophilicity before and after UV exposure. Raman spectroscopy, coupled with principal component analysis (PCA), was applied to UV-crosslinked electrospun scaffolds to investigate compositional differences and to assess whether UV sterilization (60 seconds) induced detectable chemical modifications.

Finally, a preliminary biological evaluation was conducted using human dermal fibroblasts to qualitatively assess early cell–material interactions among the different scaffold formulations. This analysis aimed to explore cell adhesion, spatial distribution, and the expression of markers associated with apoptosis and fibroblast activation, providing initial insights into the biocompatibility and limitations of the developed scaffold systems.

All experimental activities described in this chapter were carried out at the Natural and Medical Sciences Institute (NMI) and at the University of Tübingen (Germany).

2. Materials and Methods

2.1 Materials

All reagents, consumables, and cell culture media were used as received unless otherwise specified. Ultrapure water refers to sterile, autoclaved water.

Primary human dermal fibroblasts isolated from foreskin tissue were obtained from the in-house cell culture facility.

Dulbecco's Modified Eagle Medium (DMEM, high glucose, 1×), GlutaMAX™-I (100×), Dulbecco's phosphate-buffered saline (DPBS, 1×, without Ca^{2+} and Mg^{2+}), fetal bovine serum (FBS, heat-inactivated and sterile filtered), penicillin–streptomycin solution (10,000 U mL^{-1}), and trypsin–EDTA solution (0.25%) were purchased from Gibco (Thermo Fisher Scientific).

Trypan Blue solution (0.4%), Alexa Fluor®-conjugated secondary antibodies, and ProLong™ Diamond Antifade Mountant were obtained from Invitrogen (Thermo Fisher Scientific). 4′,6-Diamidino-2-phenylindole (DAPI), Triton™ X-100, and Tween® 20 were purchased from Sigma-Aldrich.

Paraformaldehyde (PFA) solution (4% w/V in DPBS, pH 7.2) was freshly prepared in-house.

Tryptone Soya Agar (TSA) and Tryptone Soya Broth (TSB) were purchased from Carl Roth (Germany), while Sabouraud Dextrose Agar (SDA) and Sabouraud Dextrose Broth (SDB) were obtained from Sigma-Aldrich (Germany).

Collagen R solution (0.2% in 0.1% acetic acid, sterile) was purchased from SERVA Electrophoresis (Germany). Sodium alginate (Protanal LF 10/60 FT) was supplied by FMC BioPolymer (Norway).

Yeast extract, sodium chloride (NaCl), and ethanol (EtOH) were obtained from Carl Roth (Germany).

Microscope glass slides (SuperFrost™ Plus and cut-frosted slides) were purchased from Epredia, while glass coverslips (25 × 75 mm) were obtained from Knittel Glass. CellCrown™ inserts were purchased from Scaffdex (Finland).

2.2 Methods

2.2.1 Scaffold fabrication and composition

Electrospun scaffolds were fabricated as single-layer or bilayer systems combining a hydrophobic PDLLA layer with a hydrophilic PVP-based layer.

In the bilayer configuration, scaffolds were initially fabricated with the hydrophobic PDLLA layer deposited as the top layer and the hydrophilic PVP-based formulation as the bottom layer. This initial bilayer configuration was used for sterility testing.

However, these bilayer scaffolds exhibited limited stability upon exposure to aqueous environments, resulting in poor hydration resistance. For this reason, the bilayer architecture was subsequently inverted, with PDLLA deposited as the bottom layer and the PVP-based formulation as the top layer, to improve structural stability while maintaining direct exposure of the hydrophilic functional surface. These scaffolds were subjected to UV-induced crosslinking at 254 nm for 1 h, corresponding to a cumulative UV dose of 169.2 mJ cm^{-2}.

Following optimization of the scaffold architecture, the inverted bilayer scaffolds were used for contact angle measurements and cell culture experiments.

The hydrophobic layer consisted of a PDLLA solution (12% w/V) prepared in hexafluoro-2-propanol (HFP). The hydrophilic layer was based on PVP (10% w/V) dissolved in a water/ethanol mixture (20:80 v/v) and was formulated either without additives, with hyaluronic acid (HA), or with hyaluronic acid bioconjugated with amino acids (HA-AA).

HA and HA-AA were incorporated into the PVP solutions at a concentration of 3% (w/w) relative to the PVP mass. HA-AA refers to hyaluronic acid functionalized with glycine (HA-Gly-OH), cysteine (HA-Cys-OH), or arginine (HA-Arg-OH), respectively.

All polymer solutions were prepared under magnetic stirring at room temperature until complete dissolution and were subsequently used for the fabrication of single-layer or bilayer electrospun scaffolds. The detailed compositions of the electrospinning solutions used in this study are reported in Table 1.

Electrospinning parameters (applied voltage, flow rate, tip-to-collector distance, and collector type) were kept constant for all formulations and are described in detail in previous chapters.

Table 1. Composition of electrospinning solutions used for scaffold fabrication. HA-AA indicates HA bioconjugated with glycine (HA-Gly-OH), cysteine (HA-Cys-OH), or arginine (HA-Arg-OH).

Hydrophobic layer						
Scaffold	**PDLLA (% w/V)**			**HFP (mL)**		**Final volume (mL)**
PDLLA	12.0			3.0		3
Hydrophilic layer						
Scaffold	**PVP (% w/V)**	**HA (% w/w)**	**HA-AA (% w/w)**	**H_2O (mL)**	**EtOH (mL)**	**Final volume (mL)**
PVP	10.0	-		0.6	2.4	3
PVP-HA	10.0	3.0	-	0.6	2.4	3
PVP-HA-Gly-OH	10.0	-	3.0	0.6	2.4	3
PVP-HA-Cys-OH	10.0	-	3.0	0.6	2.4	3
PVP-HA-Arg-OH	10.0	-	3.0	0.6	2.4	3

2.2.2 Sterility Test

Scaffold sterilization was performed by ultraviolet (UV) irradiation using a UV crosslinker system (Bio-Link, Vilber) operating at a wavelength of 254 nm. Three irradiation times were investigated—30 seconds, 60 seconds, and 5 minutes—corresponding to irradiation doses of 3.0, 6.0, and 30.0 mJ cm^{-2}, respectively. The aim of this study was to identify the minimum UV dose required to achieve complete microbial inactivation while preserving scaffold integrity.

Sterility was evaluated by means of a microbiological assay performed according to the general principles of ISO 11737-1:2006 (determination of bioburden) and ISO 11737-2:2009 (evaluation of sterilization efficacy). Following UV treatment, scaffolds were immersed in Tryptic Soy Broth (TSB) and incubated for 24 h at 30-32 °C to allow the release and proliferation of any microorganisms potentially present on the scaffold surface. Subsequently, 100 µL of the resulting suspension was plated onto sterile Tryptic Soy Agar (TSA) plates and evenly spread using a Drigalski spatula previously disinfected with 70% ethanol and flame-sterilized.

The agar plates were incubated at 30-32 °C and inspected after 24 and 48 h to assess the presence or absence of microbial growth.

For each experimental condition, three independent replicates were analyzed. Non-sterilized scaffolds were used as positive controls to confirm the presence of initial bioburden, while UV-sterilized scaffolds

represented the experimental groups. It should be noted that UV irradiation was applied either as a short treatment for sterilization purposes (6.0 mJ cm^{-2}) or as a prolonged exposure (169.2 mJ cm^{-2}) to induce crosslinking of the hydrophilic layers, depending on the specific experimental purpose.

2.2.3 Water Contact Angle Measurement

Surface wettability of the electrospun scaffolds was evaluated by water contact angle (WCA) measurements performed in static sessile drop mode on UV-crosslinked bilayer scaffolds using a Drop Shape Analyzer (DSA25E, KRÜSS). A 2 µL droplet of ultrapure water was deposited onto the scaffold surface using an automated syringe system.

The contact angle was recorded 10 s after droplet deposition to standardize the measurement and minimize the influence of rapid absorption phenomena occurring on highly hydrophilic fibrous surfaces. For each scaffold type and experimental condition, three independent scaffolds were analyzed, and three contact angle measurements were collected at different locations on each scaffold surface to account for local heterogeneities inherent to electrospun fibrous structures. Results are reported as mean ± standard deviation (SD).

Prior to statistical analysis, data distribution was evaluated for normality (Shapiro-Wilk test). Depending on the data distribution, parametric (unpaired two-tailed Student's t-test) or non-parametric statistical tests were applied accordingly. Statistical significance was set at $p < 0.05$.

2.2.4 Raman Spectroscopy and Principal Component Analysis (PCA)

Raman analysis was performed on previously UV-crosslinked electrospun scaffolds, analyzed before UV sterilization (No UV) and after UV sterilization at 254 nm for 60 seconds, using a confocal Raman microscope (inVia™, Renishaw) equipped with a 785 nm diode laser and a 600 lines mm^{-1} grating (GOLD 785 nm). Spectra were acquired in extended mode over the range 50-2275 cm^{-1}, with the spectral center set at 1250 cm^{-1}. The instrument was calibrated prior to each measurement session using the internal Renishaw calibration routine. Samples were placed on standard glass microscope slides and analyzed in confocal mode.

To account for the intrinsic heterogeneity of the fibrous scaffolds, Raman maps were acquired over a 50 × 50 µm area for each sample. For each scaffold type, three independent areas were analyzed, and three technical acquisitions were performed per area, resulting in a total of nine Raman maps per scaffold formulation.

For each Raman map, individual spectra were extracted and the area under the curve (AUC) was calculated. Spectra presenting AUC values below the median of the corresponding dataset were excluded to remove spectra dominated by background signals or edge artefacts. From the remaining spectra, 200 spectra were randomly selected for subsequent analysis. For each scaffold type and experimental condition, mean spectra and standard deviations were calculated.

Prior to multivariate analysis, spectra were pre-processed by baseline correction and normalization. Pre-processed spectra were imported into The Unscrambler X software (CAMO Analytics), and principal component analysis (PCA) was applied to evaluate spectral variability, compare scaffold formulations, and assess the effects of surface functionalization and UV sterilization. PCA score plots and loading plots were generated using The Unscrambler X, while graphical representations of averaged spectra and statistical analyses were performed using GraphPad Prism.

2.2.5 Cell Seeding and Culture Conditions

Human dermal fibroblasts (HDFs) were cultured in Dulbecco's Modified Eagle Medium (DMEM) supplemented with 10% fetal bovine serum (FBS), 1% GlutaMAX™, and 1% penicillin–streptomycin. Cells were maintained under standard culture conditions (37 °C, 5% CO_2) in a humidified incubator.

Prior to seeding onto the scaffolds, cells were washed with Dulbecco's phosphate-buffered saline (DPBS), detached using trypsin–EDTA, neutralized with complete culture medium, and counted using the Trypan Blue exclusion method.

Sterile electrospun scaffolds were trimmed to fit CellCrown™ inserts and placed into 24-well plates. All scaffolds used for biological evaluation were UV-crosslinked prior to cell seeding in order to ensure structural stability under culture conditions. Each scaffold was pre-hydrated with 200 µL of complete culture medium prior to cell seeding. The investigated scaffold types corresponded to the compositions reported in Table 1 and included single-layer PDLLA scaffolds, single-layer PVP scaffolds, and bilayer scaffolds composed of a PDLLA bottom layer combined with PVP-based hydrophilic top layers with or without hyaluronic acid (HA) or HA bioconjugated with amino acids (HA-Gly-OH, HA-Cys-OH, and HA-Arg-OH).

The seeding density was calculated based on the effective scaffold surface area (~1.6 cm^2), resulting in approximately 12,800 cells per scaffold (corresponding to ~8,000 cells cm^{-2}). After cell seeding, samples were incubated for 1, 3, 4, or 7 days prior to further analysis.

2.2.6 Immunofluorescence

After 1, 3, 4, and 7 days of culture, electrospun scaffolds were gently washed with DPBS and fixed with 4% (w/V) paraformaldehyde. Samples were subsequently permeabilized using Triton™ X-100 and processed for immunofluorescence staining.

Immunofluorescence staining was performed using three markers: 4′,6-diamidino-2-phenylindole (DAPI) for nuclear visualization, an anti-cleaved caspase-3 primary antibody to detect apoptotic cells, and α-smooth muscle actin conjugated with fluorescein isothiocyanate (α-SMA–FITC) to identify activated fibroblasts and myofibroblast-like phenotypes.

The anti-cleaved caspase-3 primary antibody (rabbit) was applied at a dilution of 1:100 and detected using an Alexa Fluor®-conjugated anti-rabbit IgG secondary antibody. A secondary-only control was included for each staining session by omitting the primary antibody and incubating samples exclusively with the secondary antibody, allowing the evaluation of scaffold autofluorescence and potential non-specific binding.

All incubation steps were carried out under the conditions recommended by the manufacturers. Each incubation was followed by thorough washing with DPBS to remove unbound reagents and reduce background fluorescence.

After staining, scaffolds were removed from the CellCrown™ holders, mounted on glass microscope slides using ProLong™ Diamond Antifade Mountant, covered with a coverslip, and sealed with clear nail polish.

Fluorescence imaging was performed using a confocal laser scanning microscope (Zeiss LSM) operated with Zen 2.3 software. Samples were imaged with the cell-facing surface oriented toward the objective. Excitation wavelengths were set at 405 nm for DAPI, 488 nm for FITC, and 594 nm for Alexa Fluor 594, with corresponding emission detection ranges of 410-484 nm, 499-571 nm, and 606-735 nm, respectively. A pinhole size of approximately 1 Airy unit was used for all channels, and non-descanned detectors were selected to enhance signal collection from the highly scattering fibrous scaffolds. Acquisition parameters were kept constant within each experimental series to allow qualitative comparison between samples.

3. Results and discussion

3.1 Sterilization of Electrospun Scaffolds

Sterilization represents a critical step in the preparation of electrospun scaffolds intended for biological investigations, as microbial contamination may alter cell behavior and compromise the reliability and reproducibility of subsequent experiments. Two scaffold configurations were evaluated: (i) a single-layer PDLLA scaffold and (ii) a bilayer scaffold composed of a hydrophobic PDLLA top layer and a hydrophilic PVP/HA bottom layer. For each configuration, three independent samples (n=3) were analyzed.

All scaffolds were sterilized by UV irradiation at 254 nm using three different exposure times (30 seconds, 60 seconds, and 5 minutes) in order to assess the effectiveness of the treatment as a function of irradiation dose. Following UV exposure, sterility was evaluated by incubating the scaffolds in Tryptic Soy Broth (TSB) and subsequently plating the suspension onto agar plates to detect potential microbial growth.

Non-sterilized PDLLA scaffolds consistently exhibited visible microbial growth, confirming the presence of initial bioburden. In contrast, all UV-sterilized PDLLA samples showed no detectable microbial colonies at either 24 or 48 h of incubation, regardless of the irradiation time applied. These results demonstrate that even the shortest UV sterilization (30 seconds) was sufficient to achieve complete sterilization of the single-layer PDLLA scaffolds (Figure S1-S7).

A similar trend was observed for the bilayer PVP-HA scaffolds. Non-sterilized samples displayed extensive bacterial growth, whereas all UV-sterilized samples remained sterile at all inspection time points. The absence of microbial colonies at all tested irradiation times indicates that UV sterilization was equally effective across both scaffold configurations (Figure S8-S14).

Although complete sterilization was achieved for all investigated exposure times, an irradiation time of 60 seconds was selected as the reference UV sterilization condition for all subsequent experiments described in this chapter. This choice was based on the cumulative UV dose delivered rather than on exposure time alone. According to the literature, germicidal efficacy is primarily governed by the total UV-C dose (expressed in mJ cm^{-2}), largely independent of the applied intensity or exposure duration, in

accordance with the Bunsen-Roscoe reciprocity law. Reported UV-C doses in the range of approximately 6-7 mJ cm^{-2} are commonly associated with effective microbial inactivation on surfaces [1].

The observed effectiveness of UV-C treatment under all tested conditions is consistent with the well-established ability of UV-C radiation to inactivate microorganisms on exposed surfaces [2].

3.2 Final Scaffolds Compositions

During preliminary experiments, single-layer hydrophilic scaffolds based on PVP, PVP-HA, and PVP-HA-amino acid conjugates exhibited limited structural stability upon exposure to aqueous environments. In particular, the absence of a mechanically supporting layer resulted in poor handling properties and limited mechanical integrity, which could compromise the reliability and reproducibility of subsequent surface and biological analyses.

To overcome these limitations, a novel bilayer scaffold architecture was designed, in which the hydrophilic formulation was deposited as the top layer and supported by the hydrophobic PDLLA bottom layer. This configuration markedly improved the mechanical stability and handling properties of the scaffolds, enabling their manipulation and subsequent experimental characterization under aqueous conditions.

This behavior may be explained by the high hydrophilicity of PVP- and HA-based formulations, which can rapidly absorb water and show reduced structural stability in aqueous environments, leading to swelling, partial dissolution, or gel-like behavior, especially in the absence of a supporting hydrophobic layer [3-4].

In addition to the inverted arrangement, the hydrophilic components were exposed to UV irradiation. Scaffolds were exposed to UV irradiation at 254 nm for 1 hour, corresponding to a total UV dose of 169.2 mJ cm^{-2}, to induce crosslinking of the hydrophilic layers. This treatment was applied to all hydrophilic single-layer scaffolds and to the hydrophilic top layers of the corresponding bilayer scaffolds intended for water contact angle (WCA) measurements, Raman spectroscopy, and biological evaluation. A possible explanation is that UV treatment promoted partial stabilization of the hydrophilic layer. This hypothesis is consistent with the known ability of PVP to undergo radical-induced crosslinking, which can reduce polymer solubility and favor hydrogel network formation [5]

The final scaffold formulations selected for subsequent surface, chemical, and biological analyses are summarized in Table 2.

Table 2. Electrospun scaffold formulations.

Scaffolds Type	Bottom Layer	Top Layer
Double Layer	PDLLA (12% w/V)	PVP (10% w/V)
Double Layer	PDLLA (12% w/V)	PVP (10% w/V) + HA (3% w/w)
Double Layer	PDLLA (12% w/V)	PVP (10% w/V) + HA-Cys-OH (3% w/w)
Double Layer	PDLLA (12% w/V)	PVP (10% w/V) + HA-Arg-OH (3% w/w)
Double Layer	PDLLA (12% w/V)	PVP (10% w/V) + HA-Gly-OH (3% w/w)

The scaffold configurations, UV treatment, and corresponding experimental analyses are summarized in Table 3.

Table 3. Scaffold configurations, UV crosslinking conditions, and experimental analyses.

Scaffold Type	Layer Configuration	Crosslinking	Experimental Analysis
Single-Layer PDLLA	PDLLA	Not applied	Sterility, Contact angle, Cell culture
Single-Layer PVP-Based	PVP or PVP-based	Applied	Raman
Bilayer (Initial Configuration)	PDLLA top / PVP-based bottom	Not applied	Sterility
Bilayer (Inverted Configuration)	PDLLA bottom / PVP-based top	Applied	Contact angle, Cell culture, Raman

3.3 Water Contact Angle Measurement

All water contact angle measurements (WCA) were performed only on UV-crosslinked scaffolds in order to ensure sufficient structural stability during the measurements. Contact angle measurements were carried out to evaluate the surface wettability of the electrospun scaffolds before and after UV sterilization. For each scaffold type, three independent scaffolds were analyzed, and three contact angle measurements were collected from different regions of each scaffold surface (n = 9). Results are reported as mean ± standard deviation.

For the single-layer PDLLA scaffold, contact angle values remained consistently high under all UV sterilization conditions, reflecting the intrinsic hydrophobic nature of the polymer. Untreated samples exhibited a contact angle of 131.5 ± 10.7°. Following UV sterilization, a slight increase was observed after 30 seconds (140.3 ± 6.4°), while values of 129.3 ± 14.1° and 128.5 ± 8.0° were measured after 60 seconds and 5 minutes, respectively (Figure 1A). However, none of these variations were statistically significant, indicating that UV sterilization at 254 nm did not induce appreciable changes in the surface wettability of PDLLA. This behavior is consistent with the limited susceptibility of PDLLA to UV-induced chemical modifications under the applied conditions.

In contrast, the bilayer scaffold featuring a PVP top layer exhibited a gradual increase in contact angle with increasing UV sterilization time. Untreated samples displayed a mean contact angle of 57.07 ± 17.51°, in agreement with the hydrophilic nature of PVP. After 30 seconds of UV sterilization, the contact angle increased to 63.74 ± 16.11°, while a value of 69.88 ± 11.62° was measured after 60 seconds. The highest contact angle was observed following 5 minutes of UV sterilization (73.27 ± 5.07°), representing the only statistically significant increase compared to the untreated condition (Figure 1B). Although a clear trend of increasing contact angle with UV sterilization time was observed, the overall variation remained moderate. The relatively large standard deviations suggest that wettability is influenced by the combined effects of fibrous morphology, local surface heterogeneity, and the layered scaffold architecture.

For the bilayer scaffold composed of a PVP-HA hydrophilic top layer, untreated samples exhibited a low contact angle (36.75 ± 19.41°), consistent with the highly hydrophilic character of the formulation. UV sterilization for 30 seconds resulted in a marked increase in contact angle (60.91 ± 7.79°), and a comparable value was observed after 60 seconds of UV sterilization (59.90 ± 21.01°). Both conditions showed statistically significant differences relative to the untreated samples. After 5 minutes of UV

sterilization, the contact angle decreased slightly to 50.40 ± 12.33°, although this variation was not statistically significant (Figure 1C). Overall, UV sterilization induced an increase in contact angle values at shorter exposure times, while longer exposure did not further enhance this effect.

Taken together, the data suggest that scaffold wettability is primarily governed by the chemical composition of the exposed top layer, with HA-containing formulations contributing to the overall hydrophilic character of the bilayer systems.

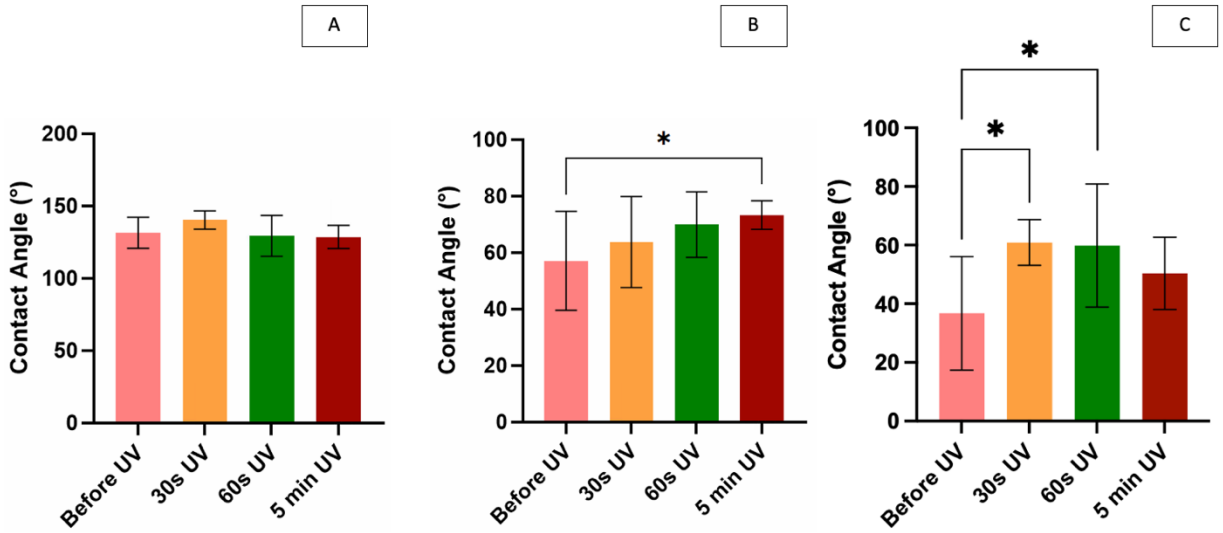

Figure 1. Static water contact angle measurements of electrospun scaffolds subjected to UV sterilization. (A) Single-layer PDLLA scaffolds. (B) Bilayer scaffolds with a PVP top layer. (C) Bilayer scaffolds with a PVP-HA top layer. Data are presented as mean ± SD. Asterisks indicate statistically significant differences compared with the untreated samples (*, $p < 0.05$).

PVP-HA-Cys-OH bilayer scaffold exhibited moderate variability in contact angle values across the different UV sterilization conditions. Untreated samples showed a contact angle of 49.01 ± 15.70°, which increased to 66.47 ± 28.12° after 30 seconds of UV sterilization. The values measured after 60 seconds (60.59 ± 10.34°) and 5 min (56.79 ± 8.08°) remained within a comparable range (Figure 2A). However, none of the observed differences were statistically significant.

PVP-HA-Arg-OH bilayer scaffold showed an overall increase in contact angle following UV sterilization. Untreated samples displayed a contact angle of 45.59 ± 17.44°, which increased to 59.08 ± 6.37° after 30 seconds and to 70.34 ± 11.61° after 60 seconds of UV sterilization. After 5 minutes of UV sterilization, the contact angle was 60.25 ± 8.55°, remaining higher than the untreated condition (Figure

2B). Statistical analysis revealed significant differences between the untreated samples and those exposed for 60 seconds or 5 minutes.

PVP-HA-Gly-OH bilayer scaffold exhibited the largest variability among the investigated formulations. Untreated samples showed a relatively high contact angle of 128.2 ± 12.61° whereas significantly lower values were measured after 30 seconds (63.89 ± 8.88°) and 60 seconds (62.15 ± 10.05°) of UV sterilization. The contact angle measured after 5 minutes (74.44 ± 9.30°) also remained lower than that of the untreated samples, although this difference was not statistically significant (Figure 2C). Overall, UV sterilization resulted in lower and more consistent contact angle values for this formulation.

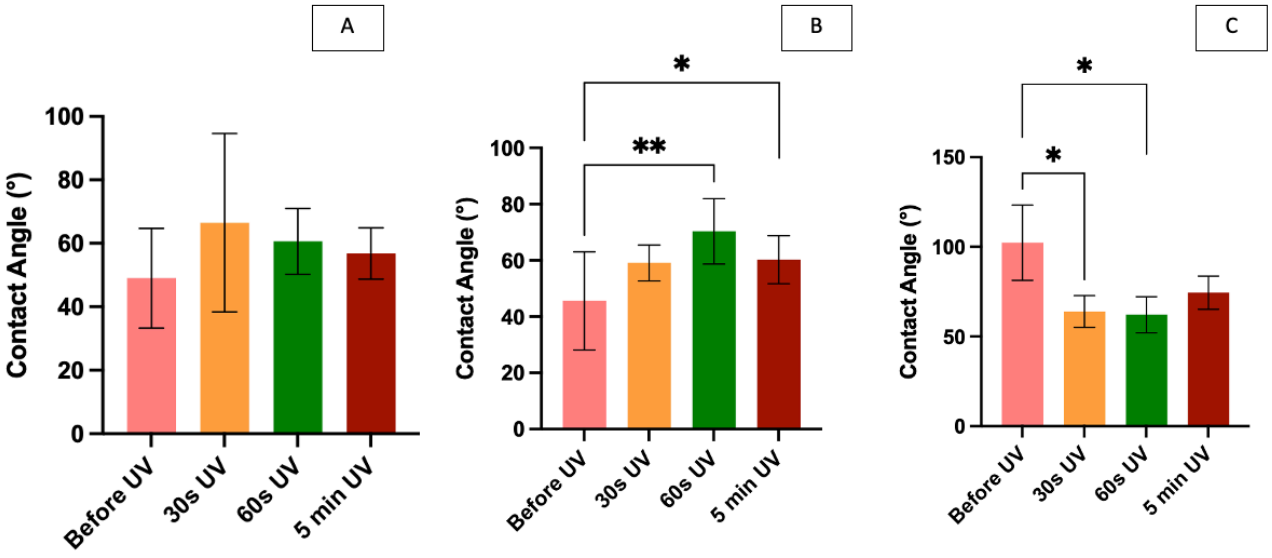

Figure 2. Static water contact angle measurements of electrospun scaffolds subjected to UV sterilization. (A) Bilayer scaffolds with a PVP-HA-Cys-OH top layer. (B) Bilayer scaffolds with a PVP-HA-Arg-OH top layer. (C) Bilayer scaffolds with a PVP-HA-Gly-OH top layer. Data are presented as mean ± SD. Asterisks indicate statistically significant differences compared with the untreated samples (*, $p < 0.05$, **, $p < 0.01$).

A summary of the contact angle values obtained under the different UV sterilization conditions is reported in Table 4.

Table 4. Static contact angle values (mean ± SD) of UV-crosslinked scaffolds under different UV sterilization conditions. Single-layer PDLLA refers to monolayer hydrophobic scaffolds, whereas PDLLA/PVP-based formulations denote bilayer scaffolds composed of a PDLLA bottom layer and a hydrophilic PVP-based top layer.

Scaffold	Untreated (°)	30 s (°)	60 s (°)	5 min (°)
Single layer PDLLA	131.5 ± 10.7	140.3 ± 6.4	129.3 ± 14.1	128.5 ± 8.0
PDLLA/PVP	57.07 ± 17.51	63.74 ± 16.11	69.88 ± 11.62	73.27 ± 5.07
PDLLA/PVP-HA	36.75 ± 19.41	60.91 ± 7.79	59.90 ± 21.01	± 12.33
PDLLA/ PVP-HA-Cys-OH	49.01 ± 15.70	66.47 ± 28.12	60.59 ± 10.34	56.79 ± 8.08
PDLLA/PVP-HA-Arg-OH	45.59 ± 17.44	59.08 ± 6.37	70.34 ± 11.61	± 8.55
PDLLA/ PVP-HA-Gly-OH	128.2 ± 12.61	63.89 ± 8.88	62.15 ± 10.05	74.44 ± 9.30

Overall, contact angle measurements revealed that scaffold surface wettability is primarily governed by the chemical nature of the exposed top layer, with hydrophobic PDLLA surfaces remaining largely unaffected by UV sterilization, while PVP-based hydrophilic layers exhibited a moderate increase in contact angle following UV exposure. The incorporation of hyaluronic acid and HA-amino acid derivatives further modulated surface wettability, although no uniform trend was observed across all formulations. The relatively large standard deviations observed for several samples reflect the intrinsic heterogeneity of electrospun fibrous structures, as well as the combined influence of surface chemistry, fiber morphology, and layered architecture. Importantly, UV irradiation induced only moderate and formulation-dependent changes in wettability, without significantly compromising the overall hydrophilic character of the functionalized bilayer scaffolds.

A one-way ANOVA revealed a significant effect of scaffold formulation on contact angle values under untreated conditions (Figure 3; ****, $p < 0.0001$). Post hoc Tukey analysis demonstrated that PDLLA differed significantly from all hydrophilic PVP-based systems (****, $p < 0.0001$), confirming the expected contrast between hydrophobic PDLLA and hydrophilic PVP-based surfaces.

Among HA-containing scaffolds, native PVP-HA, PVP-HA-Cys-OH, and PVP-HA-Arg-OH did not show statistically significant differences between each other, indicating that cysteine and arginine functionalization do not substantially modify baseline wettability relative to native HA.

In contrast, PVP-HA-Gly-OH exhibited significantly higher contact angle values compared to all other PVP-based formulations (****, $p < 0.0001$) and was not statistically different from PDLLA. This

indicates that glycine functionalization results in a surface behavior that deviates markedly from the expected hydrophilic character of HA-containing systems.

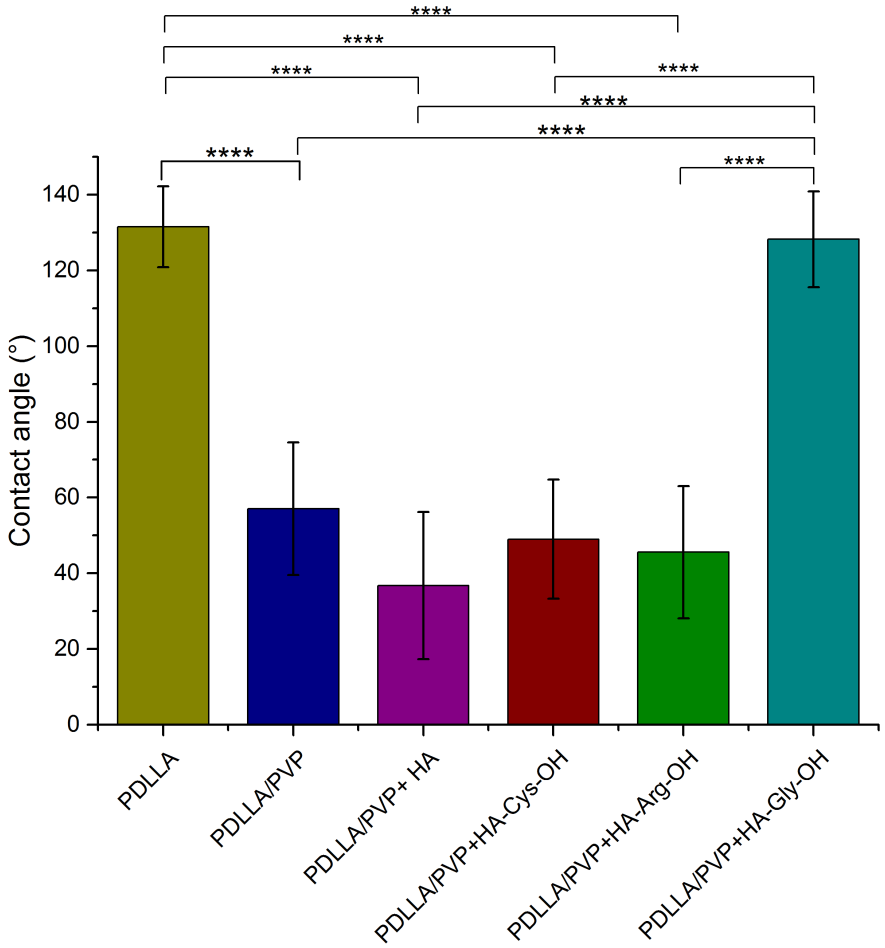

Figure 3. Static water contact angle values of untreated electrospun scaffolds including single-layer PDLLA and bilayer scaffolds composed of a PDLLA bottom layer and a hydrophilic PVP-based top layer (PVP, PVP-HA, PVP-HA-Cys-OH, PVP-HA-Arg-OH, and PVP-HA-Gly-OH). Data are presented as mean ± SD. Statistical analysis was performed using one-way ANOVA followed by Tukey's multiple comparison test. Asterisks indicate statistically significant differences between groups (****, $p < 0.0001$).

Following 30 seconds of UV exposure, a one-way ANOVA revealed a significant overall effect of scaffold formulation on contact angle values (Figure 4; ****, $p < 0.0001$). Post hoc Tukey analysis demonstrated that all bilayer PVP-based scaffolds differed significantly from the single-layer PDLLA

control (****, $p < 0.0001$), confirming the persistent contrast between hydrophobic and hydrophilic surfaces after UV treatment.

However, no statistically significant differences were observed among the PVP-based formulations themselves, indicating that short UV exposure does not induce measurable differentiation in wettability between native HA and HA-amino acid derivatives.

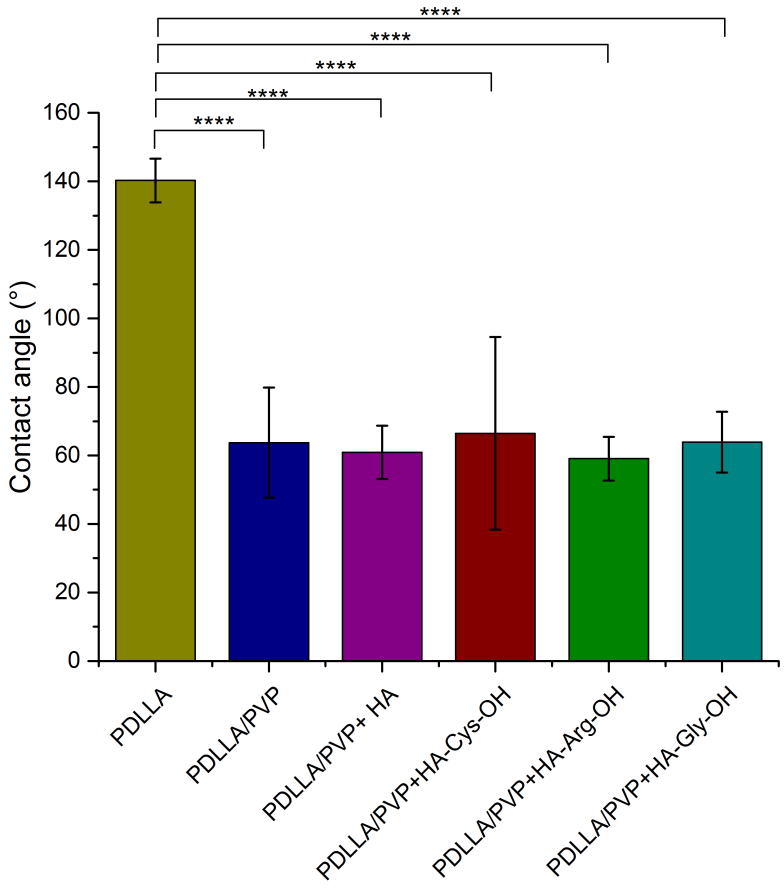

Figure 4. Static water contact angle values of electrospun scaffolds after 30 s UV sterilization, including single-layer PDLLA and bilayer scaffolds composed of a PDLLA bottom layer and a hydrophilic PVP-based top layer (PVP, PVP-HA, PVP-HA-Cys-OH, PVP-HA-Arg-OH, and PVP-HA-Gly-OH). Data are presented as mean ± SD. Statistical analysis was performed using one-way ANOVA followed by Tukey's multiple comparison test. Asterisks indicate statistically significant differences between groups (****, $p < 0.0001$).

A similar statistical pattern was observed for longer UV exposure times (Figures 5 and 6). One-way ANOVA revealed a significant effect of scaffold formulation on contact angle values (****, $p < 0.0001$). Post hoc Tukey analysis confirmed that all bilayer PVP-based scaffolds differed significantly from the single-layer PDLLA control, while no statistically significant differences were detected among the PVP-based formulations themselves.

These results indicate that increasing UV exposure time from 30 seconds to 60 seconds and 5 minutes does not produce additional differentiation in wettability among scaffolds containing native HA and HA-amino acid derivatives. Instead, the main distinction remains between the hydrophobic PDLLA surface and the hydrophilic PVP-based bilayer systems.

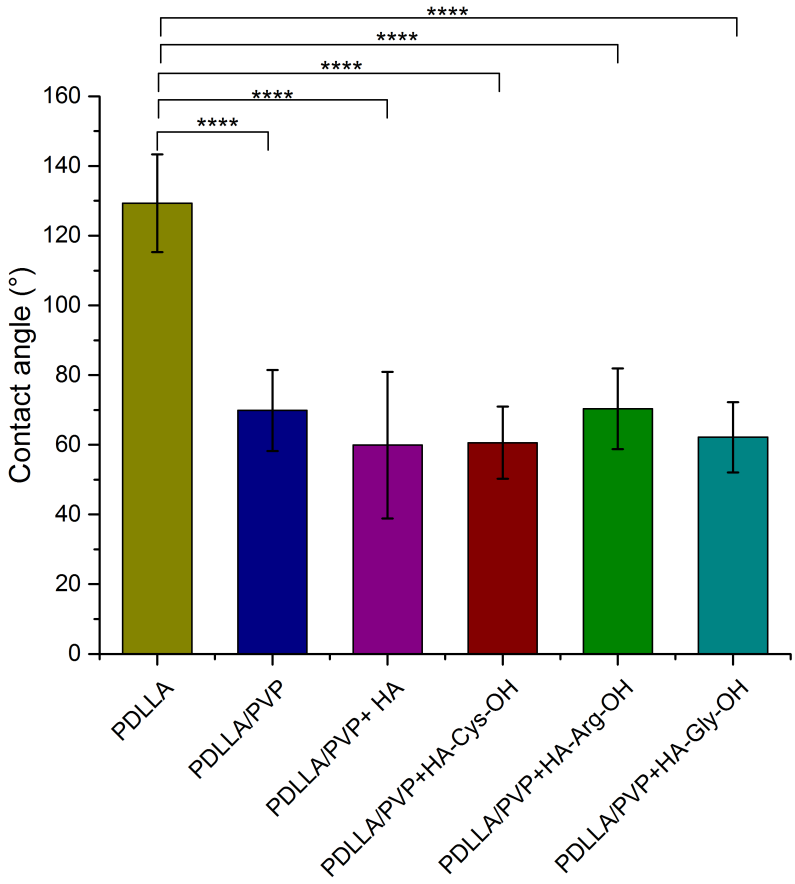

Figure 5. Static water contact angle values of electrospun scaffolds after 60 s UV sterilization, including single-layer PDLLA and bilayer scaffolds composed of a PDLLA bottom layer and a hydrophilic PVP-based top layer (PVP, PVP-HA, PVP-HA-Cys-OH, PVP-HA-Arg-OH, and PVP-HA-Gly-OH). Data are presented as mean ± SD. Statistical analysis was performed using one-way ANOVA followed by Tukey's multiple comparison test. Asterisks indicate statistically significant differences between groups (****, $p < 0.0001$).

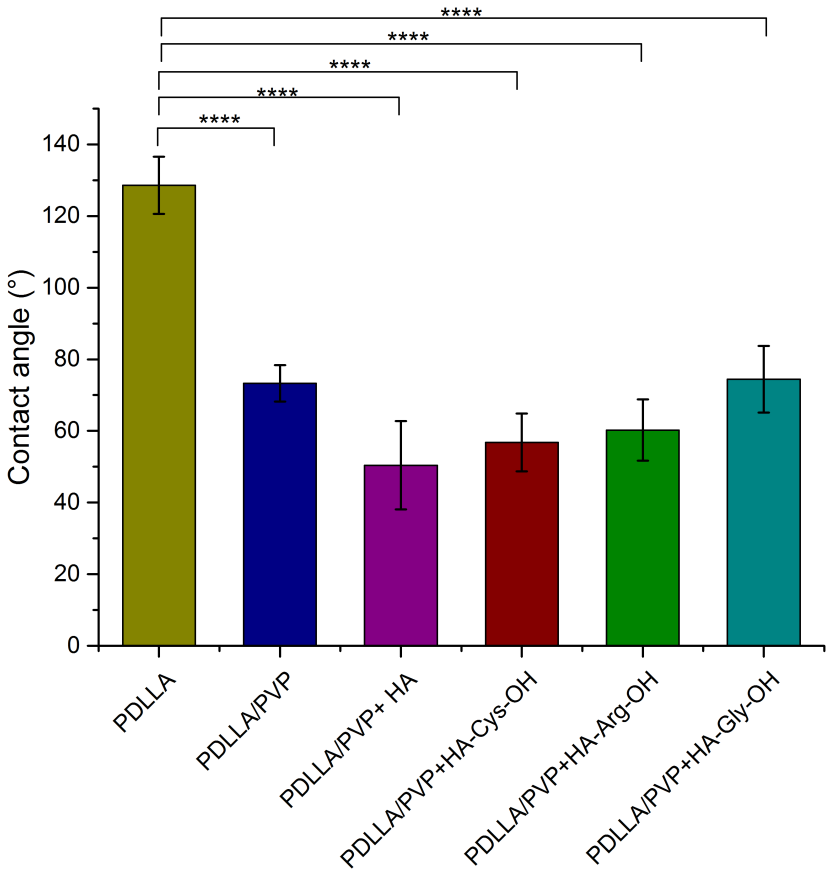

Figure 6. Static water contact angle values of electrospun scaffolds after 5 min UV sterilization, including single-layer PDLLA and bilayer scaffolds composed of a PDLLA bottom layer and a hydrophilic PVP-based top layer (PVP, PVP-HA, PVP-HA-Cys-OH, PVP-HA-Arg-OH, and PVP-HA-Gly-OH). Data are presented as mean ± SD. Statistical analysis was performed using one-way ANOVA followed by Tukey's multiple comparison test. Asterisks indicate statistically significant differences between groups (****, $p < 0.0001$).

3.4 Raman Spectroscopy and Principal Component Analysis (PCA)

Raman spectroscopy combined with principal component analysis (PCA) was employed to investigate chemical differences between scaffolds containing non-functionalized hyaluronic acid (PVP-HA) and those functionalized with cysteine (PVP-HA-Cys-OH). This multivariate approach enabled a comprehensive evaluation of the Raman dataset and facilitated the identification of subtle but systematic compositional differences, despite the strong spectral overlap among PVP, HA, and HA-amino acid derivatives.

PCA revealed a clear and reproducible separation between the two scaffold types. The first principal component (PC-1), accounting for 11% of the total variance, represented the primary axis discriminating between PVP-HA and PVP-HA-Cys-OH samples.

In the PC-1 score plot (Figure 7C), spectra corresponding to PVP-HA-Cys-OH scaffolds were consistently shifted toward positive PC-1 values, whereas PVP-HA spectra clustered predominantly in the negative PC-1 region. This separation was statistically significant (***, $p < 0.001$), indicating that cysteine functionalization induces detectable and systematic changes in the Raman spectral response of the scaffolds.

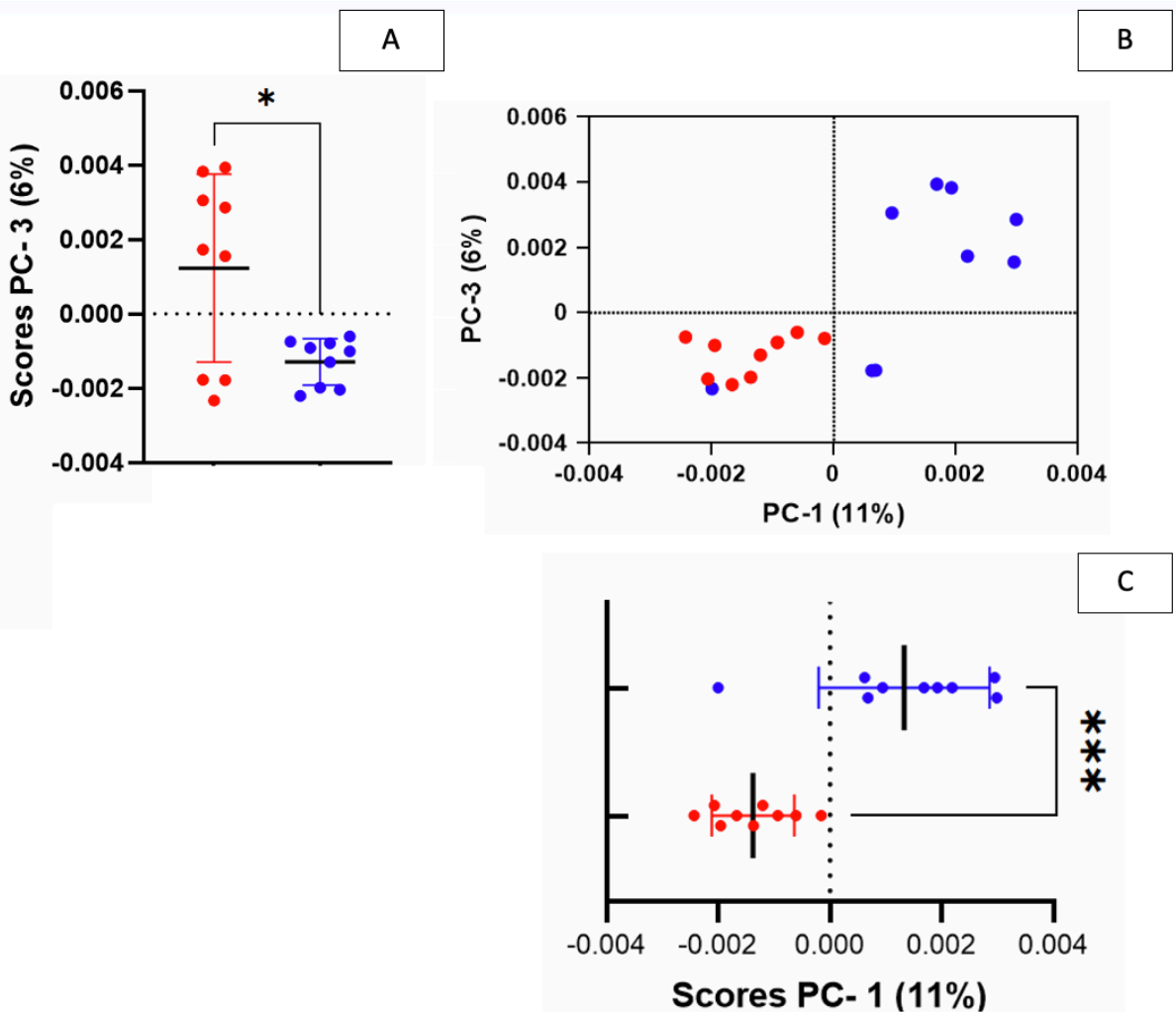

Figure 7. PCA of Raman spectra acquired from electrospun PVP-HA (red symbols) and PVP-HA-Cys-OH (blue symbols) scaffolds. (A) PC-3 score distribution for the two scaffold formulations (unpaired Student's t-test; *, $p < 0.05$). (B) PC-1 versus PC-3 score plot showing the separation between the two groups. (C) PC-1 score distribution highlighting the main spectral difference between PVP-HA and PVP-HA-Cys-OH scaffolds (unpaired Student's t-test; ***, $p < 0.001$).

Because all scaffold formulations contained 10% (w/V) PVP, PVP-related Raman contributions were expected to be present in the spectral dataset. In particular, characteristic PVP bands, including the carbonyl stretching vibration in the ~1660-1680 cm^{-1} region and CH_2 deformation modes around 1420-1470 cm^{-1}, were observed in the PC-1 loadings. These features are consistent with the common polymeric matrix shared by all samples [6].

The PC-1 versus PC-3 score plot (Figure 7B) further confirmed the separation between the two scaffold formulations. PVP-HA samples clustered predominantly in the lower-left quadrant, whereas PVP-HA-

Cys-OH samples were shifted toward the upper-right region of the plot. PC-3 accounted for 6% of the total variance and contributed to the discrimination between the two materials. Consistently, the PC-3 score distribution (Figure 7A) showed significantly higher PC-3 values for PVP-HA scaffolds compared to PVP-HA-Cys-OH (*, $p < 0.05$).

To investigate the spectral origin of the differences captured along PC-1, the corresponding loadings plot was examined (Figure 8). Relevant contributions were observed in several spectral regions, including approximately 600-700 cm^{-1}, 830-900 cm^{-1}, and 1300-1500 cm^{-1}. These wavenumber ranges are commonly associated with vibrational modes reported for cysteine-containing structures in the literature [7-10]. Overall, the loadings profile supports the presence of compositional differences between PVP-HA and PVP-HA-Cys-OH scaffolds at the multivariate level.

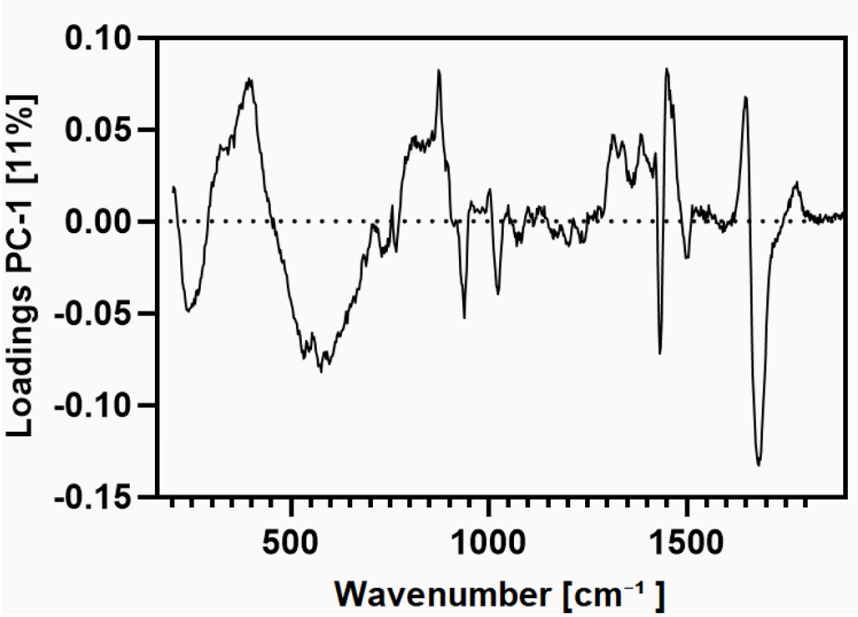

Figure 8. PC-1 loadings plot derived from PCA of Raman spectra acquired from electrospun PVP-HA and PVP-HA-Cys-OH scaffolds.

The average Raman spectra (Figure 9) showed that PVP-HA-Cys-OH samples exhibited an overall higher signal intensity across the fingerprint region compared with PVP-HA, while the general spectral profile remained similar between the two groups. These qualitative observations are consistent with the distributed spectral contributions highlighted by the PCA.

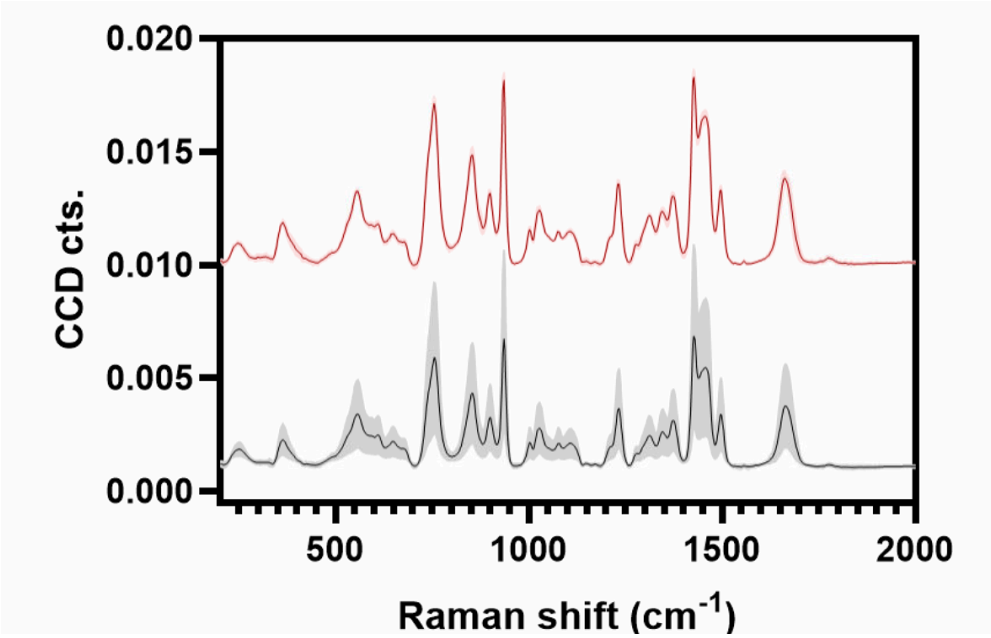

Figure 9. Average Raman spectra of electrospun PVP-HA and PVP-HA-Cys-OH scaffolds. The PVP-HA-Cys-OH spectrum is shown in red, while the PVP-HA spectrum is shown in black.

PCA was also applied to investigate the spectral differences between scaffolds containing non-functionalized hyaluronic acid (PVP-HA) and those functionalized with arginine (PVP-HA-Arg-OH), in order to assess whether arginine bioconjugation induces detectable chemical modifications in the Raman spectral response of the electrospun scaffolds.

PCA revealed a clear separation between the two scaffold formulations. The first principal component (PC-1), accounting for 52% of the total variance, represented the main axis discriminating between PVP-HA and PVP-HA-Arg-OH samples.

In the PC-1 score plot (Figure S15C), spectra corresponding to PVP-HA-Arg-OH scaffolds consistently exhibited higher PC-1 values compared to PVP-HA samples. This difference was highly significant (***, $p < 0.001$), indicating a clear and reproducible distinction between the two formulations along the component explaining the largest fraction of the spectral variance.

The combined PC-1 versus PC-2 score plot (Figure S15B) further confirmed this separation. PVP-HA spectra clustered predominantly on the left side of the plot, whereas PVP-HA-Arg-OH spectra were shifted toward the right, highlighting a robust multivariate difference between the two sample groups.

Although to a lesser extent, PC-2 also contributed to the discrimination between the materials. PC-2 explained 4% of the total variance, and the corresponding score distribution (Figure S15A) showed

significantly higher PC-2 values for PVP-HA samples compared to PVP-HA-Arg-OH (**, $p < 0.01$), suggesting the presence of additional, more subtle spectral differences captured by this component.

To investigate the spectral origin of the separation observed along PC-1, the corresponding loadings plot was examined (Figure S16). A pronounced contribution was observed in the region around 880-900 cm^{-1}, which is consistent with Raman features commonly reported for arginine side-chain vibrations, particularly those associated with C-N and C-C stretching modes of the guanidinium group. Additional, weaker contributions were observed in the 1045-1085 cm^{-1} range, which overlaps with spectral regions where C-N-related vibrational modes of arginine are typically reported [11]. Overall, the loadings profile supports the presence of compositional differences between PVP-HA and PVP-HA-Arg-OH scaffolds at the multivariate level.

The average Raman spectra (Figure S17) showed that both groups shared a comparable overall spectral profile, which is expected given their common polymeric matrix. However, small but reproducible intensity differences were observed in specific regions. In particular, PVP-HA-Arg-OH samples (red) exhibited slightly higher signal intensity in the 800-900 cm^{-1} range and in the low-frequency region below 500 cm^{-1}. An additional difference was observed in the 1700-1800 cm^{-1} region, where the PVP-HA-Arg-OH spectra displayed a weak feature that was absent in the PVP-HA spectra (black). Although subtle, these variations are consistent with the multivariate differences highlighted by the PCA and support the presence of chemical modifications associated with arginine functionalization.

PCA was also applied to investigate the spectral differences between scaffolds containing non-functionalized hyaluronic acid (PVP-HA) and those functionalized with glycine (PVP-HA-Gly-OH).

The first principal component (PC-1), accounting for 12% of the total variance, represented the main axis responsible for the separation between the two scaffold formulations. In the PC-1 score plot (Figure S18C), PVP-HA-Gly-OH samples exhibited consistently higher PC-1 values compared to PVP-HA, with a highly significant difference (***, $p < 0.001$). This result indicates that glycine functionalization, despite inducing minimal compositional differences, produces a reproducible multivariate distinction in the Raman spectral dataset.

The combined PC-1 versus PC-6 score plot (Figure S18B) further supported this separation. PVP-HA samples clustered predominantly on the left side of the plot, whereas PVP-HA-Gly-OH samples were shifted toward the right region, highlighting a clear separation between the two formulations along PC-1.

PC-6 accounted for 2% of the total variance and provided a secondary contribution to group discrimination. As shown in the PC-6 score distribution (Figure S18A), PVP-HA-Gly-OH samples displayed significantly higher PC-6 values compared to PVP-HA (**, $p < 0.01$), suggesting the presence of additional, subtle spectral differences associated with glycine functionalization.

In the PC-1 loadings plot (Figure S19), relevant contributions were observed in the 900-1000 cm^{-1} region, which falls within spectral intervals where glycine-related Raman activity has been reported. Additional variations were observed in the 400-700 cm^{-1} and 1300-1500 cm^{-1} regions, which also include vibrational modes previously associated with this amino acid [12]. Overall, the loadings profile supports the presence of subtle compositional differences between PVP-HA and PVP-HA-Gly-OH scaffolds at the multivariate level.

The average Raman spectra of PVP-HA and PVP-HA-Gly-OH (Figure S20) appeared nearly identical, with no visually appreciable differences in peak positions or relative intensities. This strong spectral overlap indicates that glycine functionalization introduces only very subtle chemical modifications that are not directly detectable in the raw Raman spectra. PCA enabled the detection of these weak variations, as evidenced by the separation observed along PC-1 and PC-6.

To better understand the contribution of the polymeric matrix to the observed spectral variability, additional comparisons were performed between scaffolds composed of PVP alone and those containing HA.

In the specific case of scaffolds containing non-functionalized HA, comparison with PVP alone revealed clear differences in the main PCA components. The first principal component (PC-1), accounting for 13% of the total variance, showed a distinct separation between the two groups, with PVP-HA samples exhibiting significantly higher PC-1 values compared to pure PVP (**, $p < 0.01$; Figure 10C). This result indicates that the incorporation of HA induces detectable Raman spectral variations already along the primary principal component.

This separation was further confirmed in the PC-1 versus PC-2 score plot (Figure 10B), where PVP spectra clustered predominantly on the left side of the plot, while PVP-HA spectra were shifted toward the right. PC-2, explaining 6% of the total variance, also contributed to the differentiation between the two materials. As shown in the corresponding score distribution (Figure 10A), HA-containing scaffolds displayed significantly higher PC-2 values than pure PVP (*, $p < 0.05$). Taken together, these results highlight the overall spectral differences introduced by the presence of hyaluronic acid within the polymeric matrix.

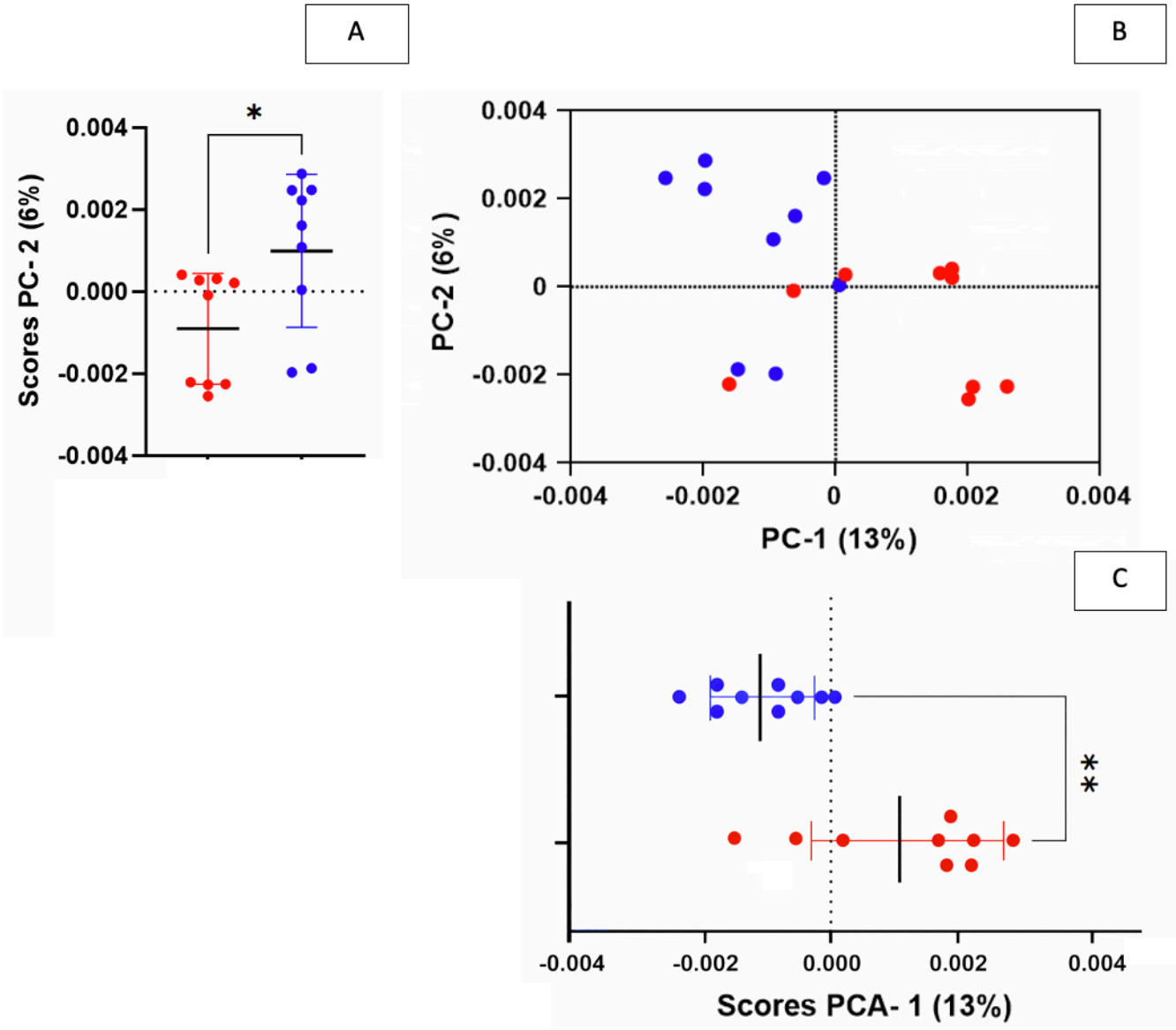

Figure 10. PCA of Raman spectra acquired from electrospun PVP (red symbols) and PVP-HA (blue symbols) scaffolds. (A) PC-2 score distribution for the two scaffold formulations (unpaired Student's t-test, *, $p < 0.05$). (B) PC-1 versus PC-2 score plot showing the separation between the two groups. (C) PC-1 score distribution highlighting the main spectral difference between PVP and PVP-HA scaffolds (unpaired Student's t-test, **, $p < 0.01$).

The PC-1 loadings plot (Figure 11A) exhibited marked contributions in several spectral regions, including approximately 950 cm^{-1}, 1040-1100 cm^{-1}, 1350-1450 cm^{-1}, and around 1660 cm^{-1}. These intervals fall within the Raman fingerprint region of hyaluronic acid and include vibrational modes commonly reported for polysaccharides, such as C-O and C-C stretching vibrations (~950-1100 cm^{-1}),

CH and CH_2 bending modes (1350-1450 cm^{-1}), and amide-related contributions near 1660 cm^{-1} [9]. These spectral regions also partially overlap with characteristic Raman bands of PVP. These features primarily reflect overall compositional differences between PVP and PVP-HA scaffolds at the multivariate level. The average spectra (Figure 11B) highlighted clear qualitative differences between PVP and PVP-HA scaffolds. Samples containing HA exhibited a richer and more structured fingerprint region, consistent with the presence of the polysaccharide, whereas PVP alone displayed a simpler spectral profile with fewer intense features. These qualitative observations are in agreement with the multivariate separation captured by PCA.

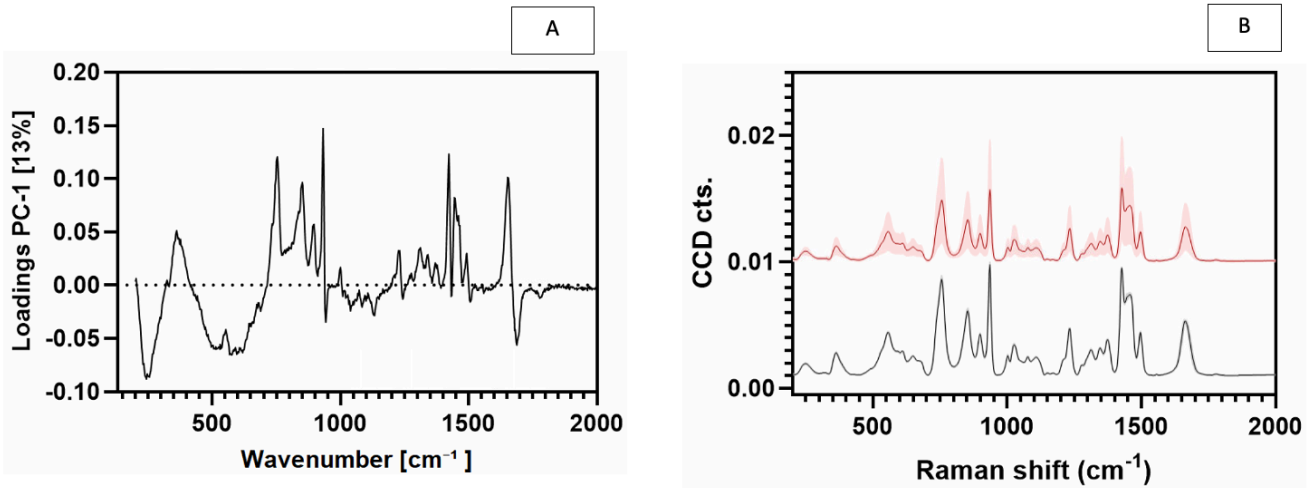

Figure 11. Raman analysis of electrospun PVP and PVP-HA scaffolds. (A) PC-1 loadings plot derived from PCA of Raman spectra acquired from electrospun PVP and PVP-HA scaffolds. (B) Average Raman spectra of electrospun PVP and PVP-HA scaffolds. The spectrum of PVP-HA is shown in red, while the spectrum of PVP is shown in black.

PCA was used to compare the Raman spectra of scaffolds composed of PVP alone with those containing hyaluronic acid functionalized with cysteine (PVP-HA-Cys-OH). The first principal component (PC-1), accounting for 11% of the total variance, clearly separated the two groups. As shown in Figure S21C, PVP-HA-Cys-OH samples exhibited significantly higher PC-1 scores compared to pure PVP (**, $p < 0.01$), indicating that HA-Cys-OH incorporation introduces detectable spectral modifications relative to the PVP matrix.

The combined PC-1 versus PC-2 score plot (Figure S21B) further confirmed this separation. PVP spectra clustered predominantly at negative PC-1 values, whereas PVP-HA-Cys-OH samples were shifted

toward the positive PC-1 region. PC-2, explaining 8% of the total variance, provided a secondary contribution to group discrimination, with PVP-HA-Cys-OH scaffolds displaying slightly higher PC-2 scores compared to PVP (*, $p < 0.05$; Figure S21A).

The PC-1 loadings plot (Figure S22A) displayed contributions distributed across multiple regions of the Raman fingerprint, reflecting the overall spectral differences introduced by the incorporation of HA-Cys-OH into the PVP matrix. Overall, the loadings pattern supports the presence of compositional differences between PVP and PVP-HA-Cys-OH scaffolds at the multivariate level. The loadings pattern should therefore be interpreted as a global spectral signature distinguishing the composite material from pure PVP rather than as evidence of cysteine-specific Raman bands.

The average Raman spectra (Figure S22B) provided a qualitative comparison between the two sample groups. The PVP-HA-Cys-OH scaffold exhibited a more articulated and structured fingerprint region, with additional small spectral features distributed across the 600-1600 cm^{-1} range, compared with the smoother spectral profile of PVP alone. Although differences in absolute intensity were observed, the overall spectral patterns clearly differentiated the two materials, in agreement with the PCA results.

PCA was employed to compare the Raman spectra of scaffolds composed of PVP alone with those containing hyaluronic acid functionalized with arginine (PVP-HA-Arg-OH). The first principal component (PC-1), accounting for 55% of the total variance, clearly separated the two groups (Figure S23C). PVP-HA-Arg-OH samples exhibited significantly higher PC-1 values than pure PVP (**, $p < 0.01$), indicating that arginine functionalization introduces pronounced and distributed spectral differences relative to the PVP matrix.

This separation was further confirmed by the PC-1 versus PC-5 score plot (Figure S23B), where PVP spectra clustered toward negative PC-1 values, whereas PVP-HA-Arg-OH samples were shifted toward the positive region. Although PC-5 explained only 1% of the total variance, it also contributed to group discrimination, with PVP-HA-Arg-OH scaffolds displaying significantly higher PC-5 scores than PVP (**, $p < 0.01$; Figure S23A), reflecting minor yet systematic secondary spectral variations.

The PC-1 loadings plot (Figure S24A) displayed contributions distributed across the Raman fingerprint region, reflecting broad spectral differences between PVP and PVP-HA-Arg-OH scaffolds. Some loading features appeared in spectral regions around 850-900 cm^{-1}, 1000-1100 cm^{-1}, and 1300-1500 cm^{-1}, where HA- or arginine-related vibrations are commonly reported. Overall, the loadings profile supports the presence of pronounced compositional differences between PVP and PVP-HA-Arg-OH scaffolds at the multivariate level.

The average Raman spectra (Figure S24B) revealed marked differences between pure PVP and PVP-HA-Arg-OH scaffolds. The PVP spectrum exhibited sharp and well-defined peaks across the fingerprint region, whereas the PVP-HA-Arg-OH spectrum showed a broader and more complex profile, with additional features distributed throughout the 400-1700 cm^{-1} range. These differences were particularly evident in the 800-1000 cm^{-1} and 1300-1500 cm^{-1} regions. Although no specific vibrational assignment can be made, the overall spectral pattern clearly distinguishes PVP-HA-Arg-OH from PVP, in agreement with the strong separation captured by PC-1 in the PCA analysis.

PCA was also applied to compare the Raman spectra of pure PVP with those of PVP blended with glycine-functionalized hyaluronic acid (PVP-HA-Gly-OH). In contrast to comparisons involving HA or HA-Arg-OH, the first principal component (PC-1) accounted for a relatively small fraction of the total variance (11%), indicating that the spectral differences induced by glycine functionalization are comparatively subtle.

In the PC-1 score plot (Figure S25C), PVP-HA-Gly-OH samples exhibited moderately higher PC-1 values than pure PVP, with a statistically significant difference (**, $p < 0.01$). Although significant, this separation reflects a weaker chemical contrast than that observed for scaffolds functionalized with other amino acids.

The PC-1 versus PC-2 score plot (Figure S25B) confirmed this trend, with PVP samples clustering predominantly at negative PC-1 values and PVP-HA-Gly-OH samples shifted toward positive values, albeit with a narrower dispersion. PC-2, accounting for 7% of the total variance, provided an additional contribution to group discrimination. As shown in the corresponding score distribution (Figure S25A), PVP-HA-Gly-OH samples displayed significantly higher PC-2 scores compared to pure PVP (****, $p < 0.0001$), suggesting the presence of minor but consistent spectral variations not fully captured by PC-1 alone.

The PC-1 loadings plot (Figure S26A) displayed contributions distributed across several regions of the Raman fingerprint, particularly within the 600-900 cm^{-1}, 900-1200 cm^{-1}, and 1300-1500 cm^{-1} intervals. These spectral regions fall within ranges where both hyaluronic acid and HA-amino acid derivatives are known to exhibit Raman activity. Overall, the loadings profile supports the presence of subtle compositional differences between PVP and PVP-HA-Gly-OH scaffolds at the multivariate level. The average Raman spectra of PVP and PVP-HA-Gly-OH (Figure S26B) appeared highly similar in terms of peak positions and overall spectral profile. The most evident differences were related to signal intensity and band shape: pure PVP exhibited sharper and more intense peaks, whereas PVP-HA-Gly-OH showed

the same spectral features with lower intensity and slightly broader bands. These variations are consistent with the incorporation of HA-Gly-OH into the polymeric matrix but do not allow the direct identification of glycine-specific vibrational modes from the raw spectra. Overall, the strong spectral similarity confirms that glycine functionalization induces only very subtle chemical changes, which become detectable primarily through multivariate analysis rather than direct spectral inspection.

PCA was employed to assess whether 60 seconds UV sterilization affected the Raman spectral profile of PVP-HA-Arg-OH scaffolds. No separation between UV-sterilized and untreated samples was observed in the multivariate space. This behavior is evidenced by the overlap of PCA score distributions and score plots, as well as by highly similar PC loadings and average Raman spectra. Overall, these results indicate that UV sterilization does not induce detectable chemical modifications within the sensitivity of the technique in arginine-functionalized scaffolds (Figures 12 and 13).

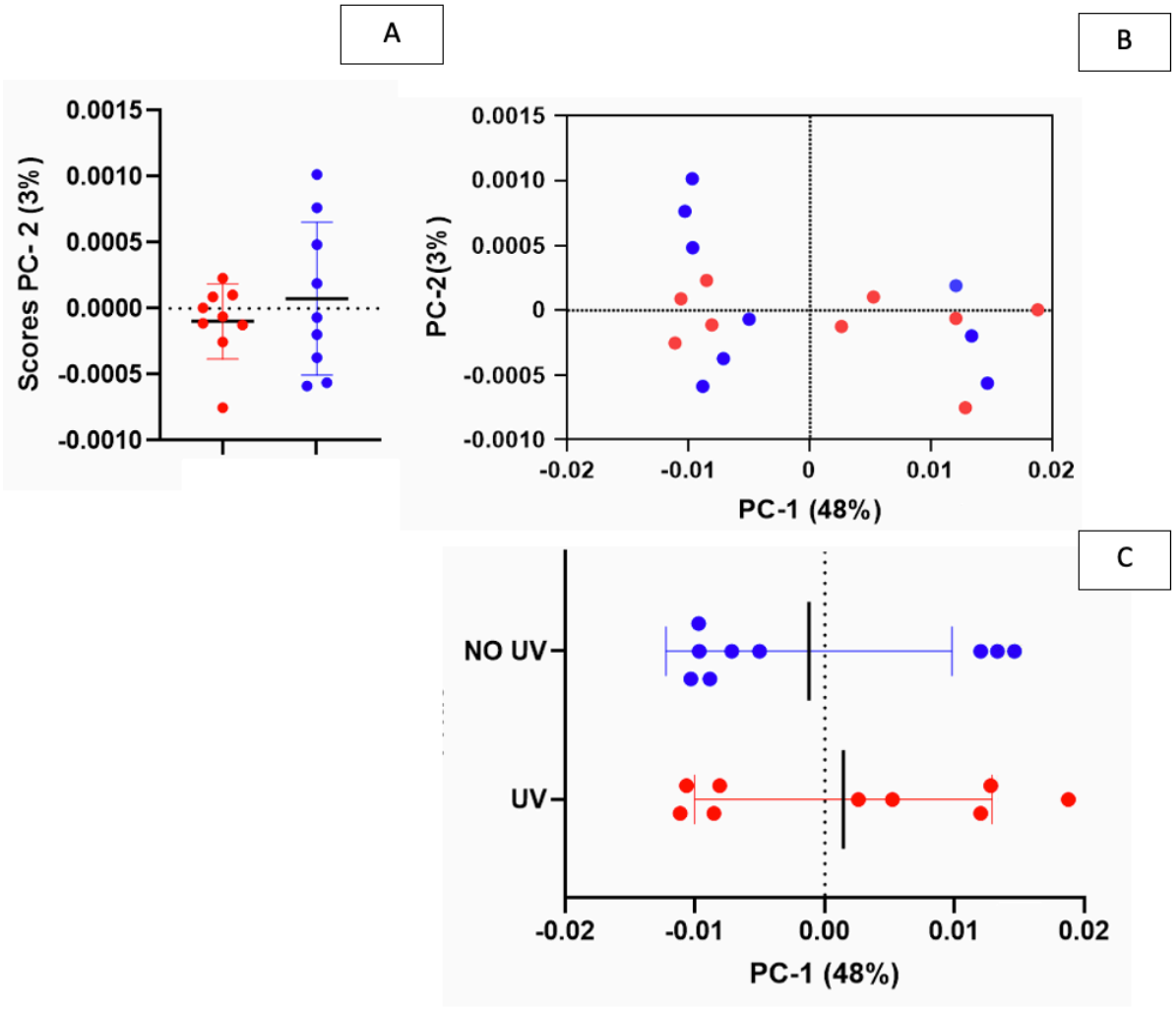

Figure 12. PCA of Raman spectra acquired from electrospun PVP-HA-Arg-OH scaffolds subjected to UV sterilization (60 s) and corresponding non-sterilized controls. (A) PC-2 score distribution for UV-sterilized and untreated samples (paired Wilcoxon test; n.s.). (B) PC-1 versus PC-2 score plot showing the overlap between the two groups. (C) PC-1 score distribution for UV-sterilized and untreated samples (paired Wilcoxon test; n.s.).

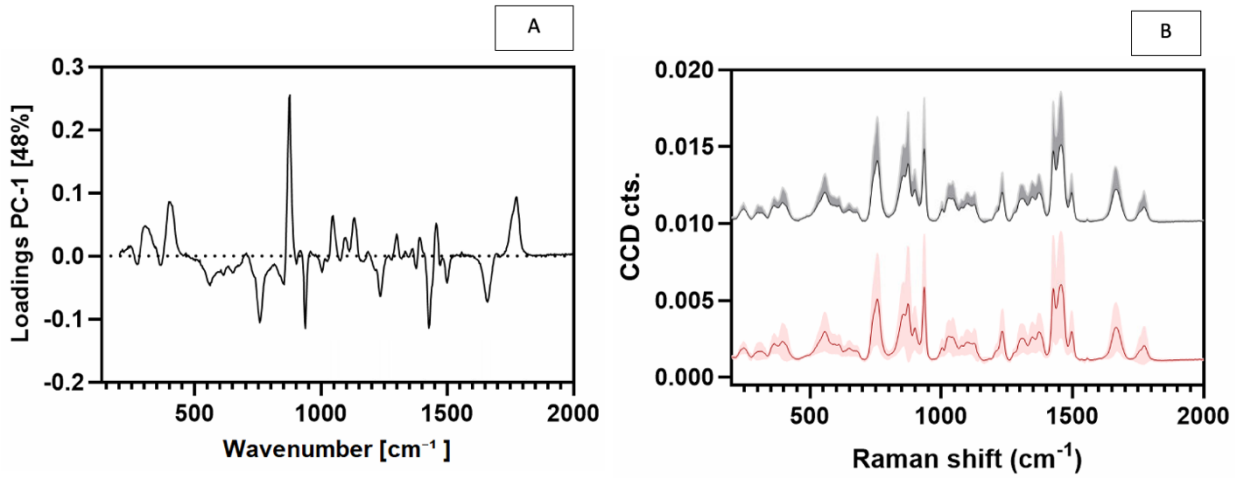

Figure 13. Raman analysis of electrospun scaffolds before and after UV sterilization. (A) PC-1 loadings plot obtained from PCA of Raman spectra acquired from electrospun scaffolds. (B) Average Raman spectra of electrospun scaffolds before and after UV sterilization. Non-UV spectra are shown in black, while UV-sterilized spectra are shown in red.

A similar analysis was performed on pure PVP scaffolds. PCA revealed overlapping score distributions, PC loadings, and average Raman spectra for UV-treated and untreated samples, indicating the absence of UV-induced chemical changes. This confirms that the polymeric matrix remains chemically stable under the applied sterilization conditions (Figures S27 and S28).

A comparable behavior was observed for PVP-HA scaffolds. PCA was performed to evaluate whether UV sterilization affected the Raman spectral profile of these systems. No statistically significant differences were detected between UV-sterilized and untreated samples. Score distributions and score plots showed substantial overlap between the two conditions, indicating the absence of UV-induced multivariate separation (Figures S29 and S30).

Consistently, PC loadings and average Raman spectra displayed highly similar profiles, with identical peak positions and only minor, non-systematic intensity variations. Overall, these results indicate that UV sterilization for 60 s does not induce detectable chemical changes in PVP-HA scaffolds.

The effect of UV sterilization on HA-functionalized scaffolds was further evaluated by Raman PCA for PVP-HA-Cys-OH and PVP-HA-Gly-OH systems. In both cases, PCA score distributions showed substantial overlap between UV-sterilized and untreated samples, indicating the absence of UV-induced multivariate separation (Figures S31-S34).

Consistently, PC loadings and average Raman spectra displayed highly similar spectral profiles for UV-treated and untreated samples, with identical peak positions and only minor, non-systematic intensity variations. No UV-dependent peak shifts or systematic spectral changes were observed.

Overall, these results confirm that UV sterilization under the applied conditions does not induce detectable chemical modifications in HA-amino acid functionalized scaffolds.

3.5 Biological Evaluation of the Electrospun Scaffolds

To perform an exploratory qualitative assessment of early cell–material interactions, a preliminary biological evaluation was carried out using human dermal fibroblasts (HDFs). The aim of this analysis was to qualitatively investigate cell presence, spatial distribution, and the expression of selected markers associated with apoptosis and fibroblast activation on the different electrospun scaffold formulations, as well as to identify potential limitations related to scaffold composition and architecture.

After the defined incubation times, the scaffolds were processed for immunofluorescence staining using three complementary markers:

• DAPI, used to visualize cell nuclei and assess cell presence and spatial distribution;
• Cleaved caspase-3, employed as a qualitative marker of apoptosis to detect potential cell death;
• α-SMA-FITC, used to evaluate the expression of α-smooth muscle actin, a marker associated with fibroblast activation and differentiation toward a myofibroblast phenotype.

For each experimental condition, a negative control image of the cleaved caspase-3 channel was acquired to exclude potential background fluorescence and non-specific signal arising from the scaffold material. Immunofluorescence staining was performed for all scaffold formulations after 1, 3, 4, and 7 days of culture. However, confocal imaging did not reveal a clear or consistent time-dependent trend. In several samples and time points, cells were not clearly detectable. This limitation may be related to changes occurring during cell culture conditions, likely associated with the formation of a highly hydrated gel-like layer on the scaffold surface.

Confocal images acquired using the Zeiss LSM microscope showed that single-layer PDLLA scaffolds exhibited a relatively high number of DAPI-positive signals, suggesting the presence of cell nuclei distributed along the fibrous surface. The image shown corresponds to 1 day of culture (Figure 14). However, DAPI staining alone does not allow definitive conclusions regarding cell adhesion, morphology, or viability. In this case, the spatial overlap between nuclear staining and cytoplasmic markers (α-SMA or cleaved caspase-3) was only partial and not consistently identifiable, limiting the interpretation of effective cell adhesion and cellular organization.

A cleaved caspase-3 signal was detectable in some regions; however, its intensity was comparable to that observed in the corresponding control images. This makes it difficult to determine whether the detected fluorescence reflects genuine apoptotic activity or background-related signal arising from the scaffold. In this context, cleaved caspase-3 was employed as a qualitative screening marker, and the primary

observation is the absence of clear or widespread apoptotic signaling rather than evidence of apoptosis. Similarly, the α-SMA signal appeared weak and punctate, preventing confident identification of activated fibroblasts or well-defined myofibroblast-like phenotypes.

Overall, these observations suggest a possible presence of cells on PDLLA scaffolds; however, the limited definition of cytoplasmic markers and the absence of a clear temporal trend do not allow firm conclusions to be drawn regarding cell adhesion, viability, or functional state.

A representative merged confocal image is shown in Figure 14A, while the corresponding cleaved caspase-3 control is reported in Figure 14B.

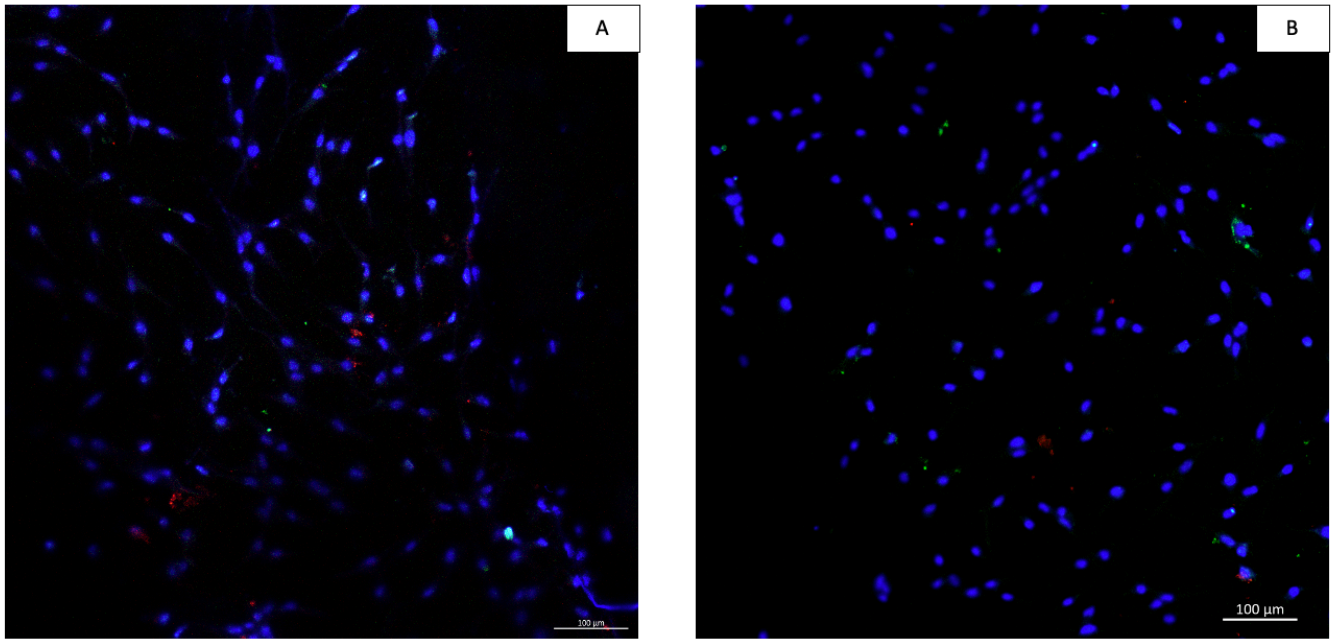

Figure 14. Confocal images of single-layer PDLLA scaffolds stained with DAPI (blue), cleaved caspase-3 (red), and α-SMA-FITC (green). (A) Merged image including all fluorescence channels. (B) Cleaved caspase-3 negative control acquired in the absence of the primary antibody. Scale bar: 100 µm.

In the images of the bilayer scaffolds with a PVP surface layer, a noticeably lower apparent cell density was observed compared with the single-layer PDLLA samples, as indicated by the reduced number of DAPI-stained nuclei (blue). The representative image shown corresponds to 3 days of culture (Figure 15A). Weak red and green fluorescence signals were detectable in some regions; however, they were poorly defined and not consistently present across the scaffold surface. Only a limited number of cells

exhibited partial signal overlap, and both the intensity and spatial distribution of these signals were insufficient to allow reliable interpretation of apoptosis or fibroblast activation. In the corresponding secondary-only control (Figure 15B), DAPI-positive nuclei were visible, while no specific signal was detected in the cleaved caspase-3 channel, indicating negligible scaffold autofluorescence and non-specific secondary antibody binding. Overall, although faint fluorescence signals were occasionally observed, the results remain qualitative and do not permit definitive conclusions regarding cell activation or apoptotic processes on the PVP-containing bilayer scaffolds.

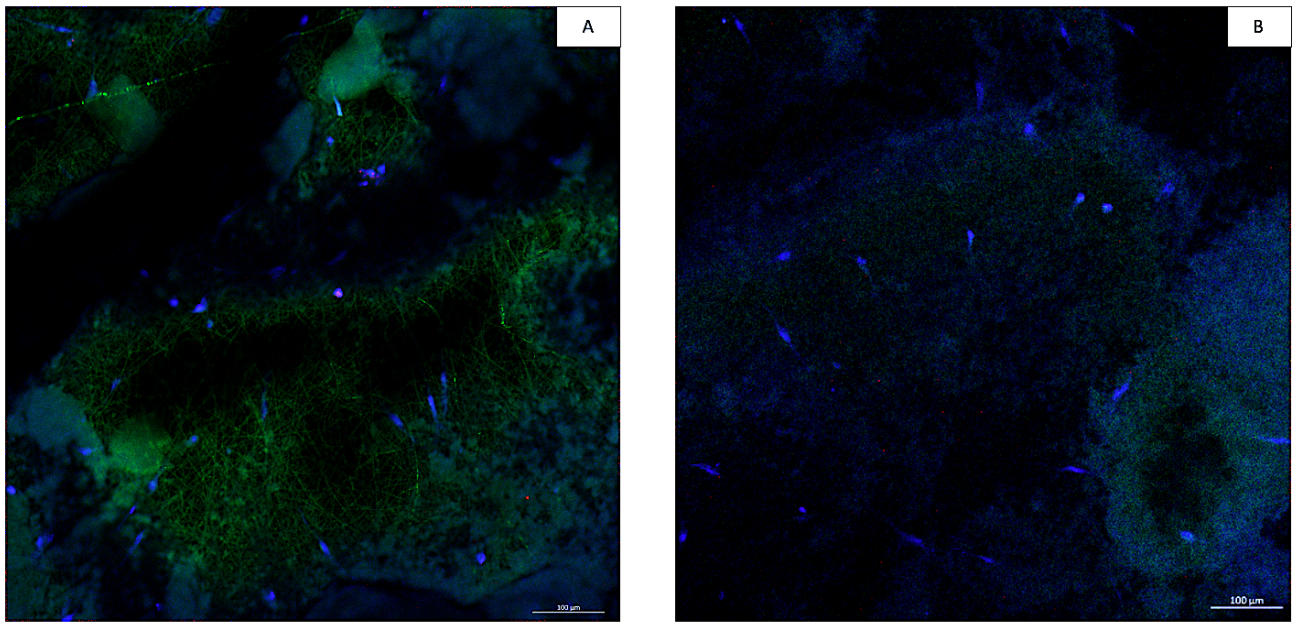

Figure 15. Confocal images of bilayer PVP-based scaffolds stained with DAPI (blue), cleaved caspase-3 (red), and α-SMA-FITC (green). (A) Merged image showing all fluorescence channels. (B) Cleaved caspase-3 negative control acquired in the absence of the specific primary antibody. Scale bar: 100 µm.

In the bilayer samples containing a hyaluronic acid–based top layer, with or without amino acid functionalization, no clearly recognizable cellular structures were observed. The images showed few or no visible nuclei (DAPI, blue) and only faint or diffuse signals in the additional fluorescence channels, without reliable morphological features indicative of cell adhesion or spreading. The representative image shown was acquired after 1 day of culture (Figure 16A), while the corresponding caspase-3 negative control is shown in Figure 16B.

Throughout the culture period, a visible and reproducible gel-like layer formed on the surface of these scaffolds, likely resulting from the combined presence and high hydrophilicity of hyaluronic acid and PVP. This phenomenon represents a critical limitation of the highly hydrophilic PVP/HA-based top layers and is likely to have hindered effective cell adhesion and/or cell survival. A similar behavior was observed for scaffolds containing amino acid–modified hyaluronic acid, independently of the incubation time (1, 3, 4, or 7 days).

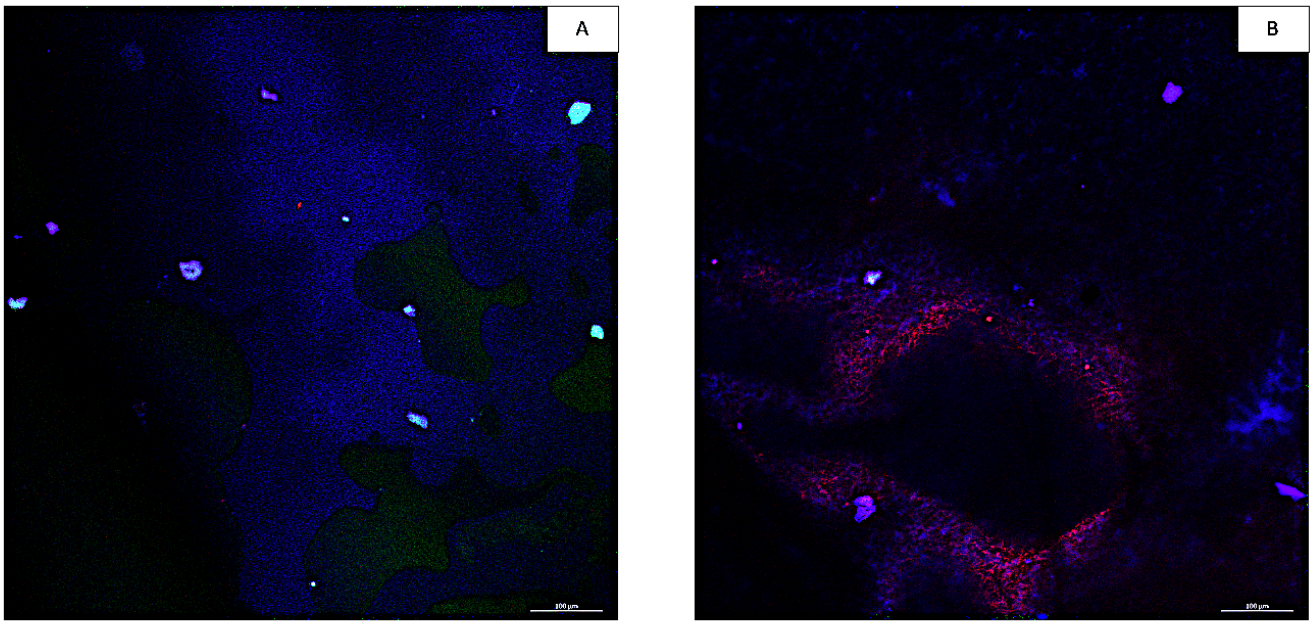

Figure 16. Confocal images of bilayer PVP-HA scaffolds stained with DAPI (blue), cleaved caspase-3 (red), and α-SMA-FITC (green). (A) Merged image showing all fluorescence channels. (B) Cleaved caspase-3 negative control acquired in the absence of the primary antibody. Scale bar: 100 µm.

Overall, this exploratory qualitative biological evaluation indicates that while single-layer PDLLA and, to a lesser extent, PVP-based bilayer scaffolds may support limited cell presence, highly hydrophilic HA-containing top layers present significant challenges for cell adhesion under the investigated conditions. These findings highlight the importance of balancing surface bioactivity with structural and physicochemical stability and provide valuable guidance for the further optimization of scaffold architecture and surface composition.

4. Conclusions

In this chapter, a comprehensive physicochemical and preliminary biological characterization of functionalized electrospun scaffolds was performed to evaluate the effects of scaffold architecture, surface functionalization, and UV sterilization on surface properties, chemical stability, and early cell–material interactions.

UV irradiation at 254 nm proved to be an effective sterilization method for both single-layer and bilayer electrospun scaffolds, achieving complete microbial inactivation already at short exposure times. Based on sterility testing, a UV exposure time of 60 seconds was selected as the standard sterilization condition for subsequent analyses. Raman spectroscopy combined with PCA demonstrated that UV sterilization at 254 nm for 60 seconds did not induce detectable chemical modifications in any of the investigated formulations, including pure PVP, PVP-HA, and HA-amino acid functionalized scaffolds (glycine, cysteine, and arginine). These results confirm the chemical stability of the materials under the applied sterilization conditions and support the suitability of UV treatment for further biological investigations.

Contact angle measurements highlighted clear differences in surface wettability among the different scaffold architectures and compositions. As expected, single-layer PDLLA scaffolds exhibited a highly hydrophobic behavior that was not affected by UV exposure. In contrast, bilayer scaffolds with hydrophilic PVP-based top layers displayed significantly lower contact angle values, confirming the effective exposure of the functional surface. The incorporation of HA and HA-amino acid conjugates further modulated surface wettability, although relatively large standard deviations were observed, reflecting the intrinsic heterogeneity of electrospun fibrous systems. UV irradiation induced moderate changes in wettability for some formulations, particularly those containing HA or HA-amino acid derivatives, without compromising the overall hydrophilic character of the functionalized surfaces.

Raman spectroscopy coupled with multivariate analysis proved to be a powerful tool for detecting compositional differences between scaffold formulations. PCA consistently discriminated between PVP scaffolds and those containing HA, as well as between non-functionalized HA and HA bioconjugated with glycine, cysteine, and arginine. Although strong spectral overlap among PVP, HA, and HA-amino acid derivatives prevented the unambiguous assignment of individual Raman bands to specific amino acid vibrations, the reproducible multivariate separation observed across all comparisons confirms that bioconjugation induces detectable chemical modifications at the spectral level. The extent of these differences varied among the amino acids, with arginine-functionalized scaffolds showing the most pronounced separation, while glycine-functionalized systems exhibited more subtle changes that were detectable primarily through multivariate analysis.

Preliminary biological evaluation using human dermal fibroblasts provided qualitative insights into cell–material interactions but also highlighted important limitations. While DAPI-positive nuclei were observed on single-layer PDLLA and, to a lesser extent, on bilayer scaffolds with a PVP surface layer, the expression of cytoplasmic markers associated with apoptosis or fibroblast activation was weak and inconsistent, preventing definitive conclusions regarding cell viability or functional state. In bilayer scaffolds containing HA or HA-amino acid derivatives, cell adhesion was markedly reduced, and a reproducible gel-like layer formed on the scaffold surface during culture. This phenomenon is likely associated with the highly hydrophilic and partially soluble nature of the PVP/HA-based top layers and consequently hindered effective cell attachment and survival.

Overall, the results presented in this chapter demonstrate that the developed electrospun scaffolds can be effectively sterilized without altering their chemical composition and that surface functionalization with HA and HA-amino acid derivatives produces measurable changes in wettability and Raman spectral profiles. At the same time, the biological findings underscore the need for further optimization of scaffold architecture and surface stability to improve cell adhesion and functionality. These findings provide a solid foundation for the subsequent development and rational optimization of bioactive electrospun scaffolds aimed at wound-healing applications.

Supporting Information

Characterization of Electrospun Hyaluronic Acid-Based Bioconjugate Scaffolds

Table of contents

Figure S1. Sterility test plates of single-layer PDLLA scaffolds after 30 seconds of UV sterilization, incubated for 24 h.	**265**
Figure S2. Sterility test plates of single-layer PDLLA scaffolds after 60 seconds of UV sterilization, incubated for 24 h.	**265**
Figure S3. Sterility test plates of single-layer PDLLA scaffolds after 5 minutes of UV sterilization, incubated for 24 h.	**265**
Figure S4. Sterility test plates of single-layer PDLLA scaffolds after 30 seconds of UV sterilization, incubated for 48 h.	**266**
Figure S5. Sterility test plates of single-layer PDLLA scaffolds after 60 seconds of UV sterilization, incubated for 48 h	**266**
Figure S6. Sterility test plates of single-layer PDLLA scaffolds after 5 minutes of UV sterilization, incubated for 48 h	**266**
Figure S7. Sterility test plates of single-layer PDLLA scaffolds without UV treatment. A), B), and C) correspond to independent samples after 24 h of incubation.	**267**
Figure S8. Sterility test plates of bilayer PVP-HA scaffolds after 30 seconds of UV sterilization, incubated for 24 h.	**267**
Figure S9. Sterility test plates of bilayer PVP-HA scaffolds after 60 seconds of UV sterilization, incubated for 24 h.	**268**
Figure S10. Sterility test plates of bilayer PVP-HA scaffolds after 5 minutes of UV sterilization, incubated for 24 h.	**268**
Figure S11. Sterility test plates of bilayer PVP-HA scaffolds after 30 seconds of UV sterilization, incubated for 48 h	**269**
Figure S12. Sterility test plates of bilayer PVP-HA scaffolds after 60 seconds of UV sterilization, incubated for 48 h.	**269**
Figure S13. Sterility test plates of bilayer PVP-HA scaffolds after 5 minutes of UV sterilization, incubated for 48 h.	**270**

Figure S14. Sterility test plates of bilayer PVP-HA scaffolds without UV treatment. A), B), and C) correspond to independent samples after 24 h of incubation.	**271**
Figure S15. PCA of Raman spectra acquired from electrospun PVP-HA and PVP-HA-Arg-OH scaffolds. (A) PC-2 score distribution for the two scaffold formulations. (B) PC-1 versus PC-2 score plot showing the separation between the two groups. (C) PC-1 score distribution highlighting the main spectral difference between PVP-HA and PVP-HA-Arg-OH scaffolds.	**272**
Figure S16. PC-1 loadings plot obtained from PCA of Raman spectra acquired from electrospun PVP-HA and PVP-HA-Arg-OH scaffolds.	**273**
Figure S17. Average Raman spectra of electrospun PVP-HA and PVP-HA-Arg-OH scaffolds.	**273**
Figure S18. PCA of Raman spectra acquired from electrospun PVP-HA and PVP-HA-Gly-OH scaffolds. (A) PC-6 score distribution for the two scaffold formulations. (B) PC-1 versus PC-6 score plot showing the separation between the two groups. (C) PC-1 score distribution highlighting the main spectral difference between PVP-HA and PVP-HA-Gly-OH scaffolds.	**274**
Figure S19. PC-1 loadings plot obtained from PCA of Raman spectra acquired from electrospun PVP-HA and PVP-HA-Gly-OH scaffolds.	**275**
Figure S20. Average Raman spectra of electrospun PVP-HA and PVP-HA-Gly-OH scaffolds.	**275**
Figure S21. PCA of Raman spectra acquired from electrospun PVP and PVP-HA-Cys-OH scaffolds. (A) PC-2 score distribution for the two scaffold formulations. (B) PC-1 versus PC-2 score plot showing the separation between the two groups. (C) PC-1 score distribution highlighting the main spectral difference between PVP and PVP-HA-Cys-OH scaffolds.	**276**
Figure S22. Raman analysis of electrospun PVP and PVP-HA-Cys-OH scaffolds. (A) PC-1 loadings plot obtained from PCA of Raman spectra acquired from electrospun PVP and PVP-HA-Cys-OH scaffolds. (B) Average Raman spectra of electrospun PVP and PVP-HA-Cys-OH scaffolds.	**277**

Figure S23. PCA of Raman spectra acquired from electrospun PVP and PVP-HA-Arg-OH scaffolds. (A) PC-5 score distribution for the two scaffold formulations. (B) PC-1 versus PC-5 score plot showing the separation between the two groups. (C) PC-1 score distribution highlighting the main spectral difference between PVP and PVP-HA-Arg-OH scaffolds.	**278**
Figure S24. Raman analysis of electrospun PVP and PVP-HA-Arg-OH scaffolds. (A) PC-1 loadings plot obtained from PCA of Raman spectra acquired from electrospun PVP and PVP-HA-Arg-OH scaffolds. (B) Average Raman spectra of electrospun PVP and PVP-HA-Arg-OH scaffolds.	**279**
Figure S25. PCA of Raman spectra acquired from electrospun PVP and PVP-HA-Gly-OH scaffolds. (A) PC-2 score distribution for the two scaffold formulations. (B) PC-1 versus PC-2 score plot showing the separation between the two groups. (C) PC-1 score distribution highlighting the main spectral difference between PVP and PVP-HA-Gly-OH scaffolds.	**280**
Figure S26. Raman analysis of electrospun PVP and PVP-HA-Gly-OH scaffolds. (A) PC-1 loadings plot obtained from PCA of Raman spectra acquired from electrospun PVP and PVP-HA-Gly-OH scaffolds. (B) Average Raman spectra of electrospun PVP and PVP-HA-Gly-OH scaffolds.	**281**
Figure S27. PCA of Raman spectra acquired from electrospun PVP scaffolds subjected to UV sterilization (60 s) and corresponding non-sterilized controls. (A) PC-2 score distribution for UV-sterilized and untreated samples. (B) PC-1 versus PC-2 score plot showing the overlap between the two groups. (C) PC-1 score distribution for UV-sterilized and untreated samples.	**282**
Figure S28. Raman analysis of electrospun PVP scaffolds before and after UV sterilization (60 s). (A) PC-1 loadings plot obtained from PCA of Raman spectra acquired from electrospun PVP scaffolds. (B) Average Raman spectra of electrospun PVP scaffolds before and after UV sterilization.	**283**
Figure S29. PCA of Raman spectra acquired from electrospun PVP-HA scaffolds subjected to UV sterilization (60 s) and corresponding non-sterilized controls. (A) PC-2 score distribution for UV-sterilized and untreated samples. (B)	**284**

PC-1 versus PC-2 score plot showing the overlap between the two groups. (C) PC-1 score distribution for UV-sterilized and untreated samples.	
Figure S30. Raman analysis of electrospun PVP-HA scaffolds before and after UV sterilization. (A) PC-1 loadings plot obtained from PCA of Raman spectra acquired from electrospun PVP-HA scaffolds. (B) Average Raman spectra of electrospun PVP-HA scaffolds before and after UV sterilization.	**285**
Figure S31. PCA of Raman spectra acquired from electrospun PVP-HA-Cys-OH scaffolds subjected to UV sterilization (60 s) and corresponding non-sterilized controls. (A) PC-2 score distribution for UV-sterilized and untreated samples. (B) PC-1 versus PC-2 score plot showing the overlap between the two groups. (C) PC-1 score distribution for UV-sterilized and untreated samples.	**286**
Figure S32. Raman analysis of electrospun PVP-HA-Cys-OH scaffolds before and after UV sterilization. (A) PC-1 loadings plot obtained from PCA of Raman spectra acquired from electrospun PVP-HA-Cys-OH scaffolds. (B) Average Raman spectra of electrospun PVP-HA-Cys-OH scaffolds before and after UV sterilization.	**287**
Figure S33. PCA of Raman spectra acquired from electrospun PVP-HA-Gly-OH scaffolds subjected to UV sterilization (60 s) and corresponding non-sterilized controls. (A) PC-2 score distribution for UV-sterilized and untreated samples. (B) PC-1 versus PC-2 score plot showing the overlap between the two groups. (C) PC-1 score distribution for UV-sterilized and untreated samples.	**288**
Figure S34. Raman analysis of electrospun PVP-HA-Gly-OH scaffolds before and after UV sterilization. (A) PC-1 loadings plot obtained from PCA of Raman spectra acquired from electrospun PVP-HA-Gly-OH scaffolds. (B) Average Raman spectra of electrospun PVP-HA-Gly-OH scaffolds before and after UV sterilization.	**289**

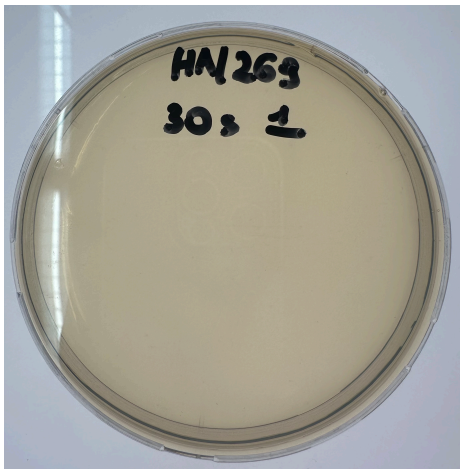

Figure S1. Sterility test plates of single-layer PDLLA scaffolds after 30 seconds of UV sterilization, incubated for 24 h.

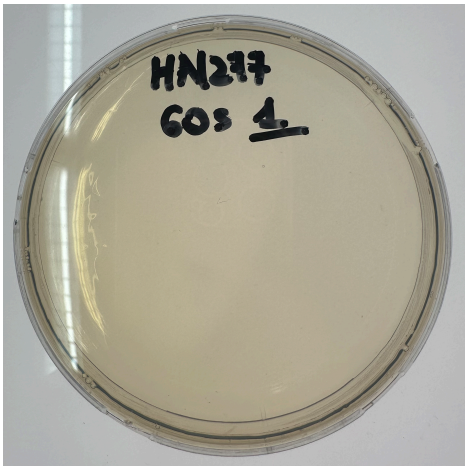

Figure S2. Sterility test plates of single-layer PDLLA scaffolds after 60 seconds of UV sterilization, incubated for 24 h.

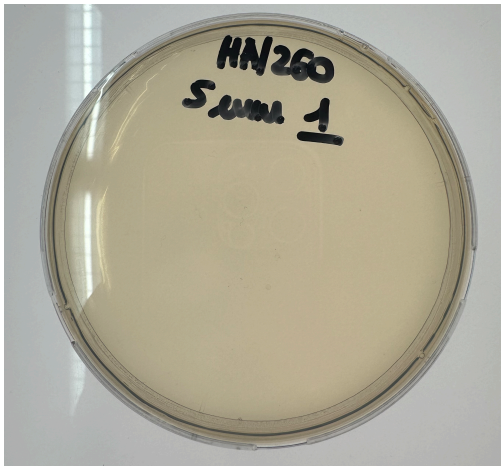

Figure S3. Sterility test plates of single-layer PDLLA scaffolds after 5 minutes of UV sterilization, incubated for 24 h.

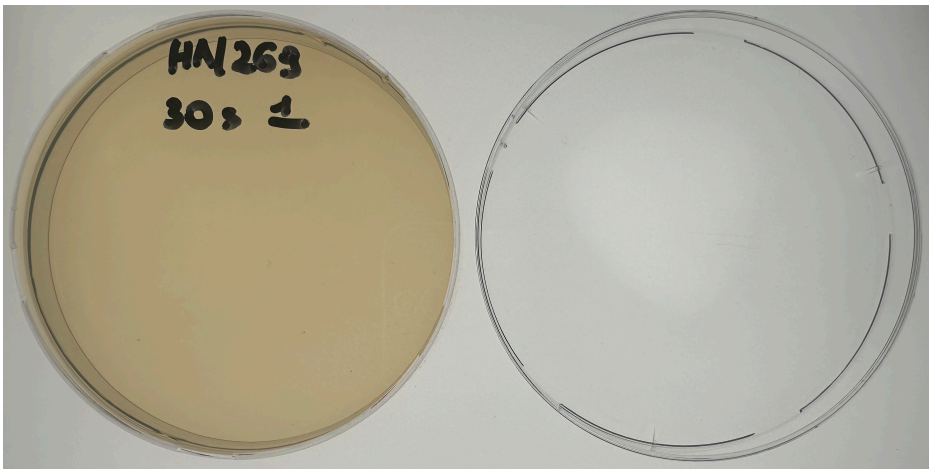

Figure S4. Sterility test plates of single-layer PDLLA scaffolds after 30 seconds of UV sterilization, incubated for 48 h.

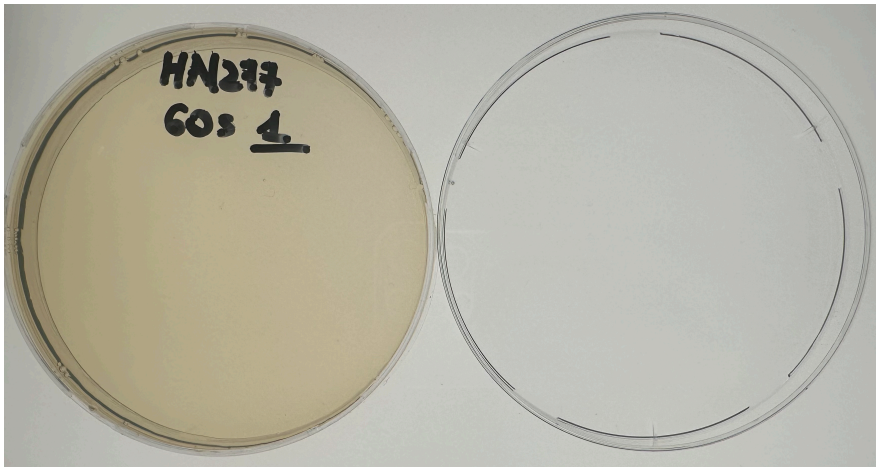

Figure S5. Sterility test plates of single-layer PDLLA scaffolds after 60 seconds of UV sterilization, incubated for 48 h.

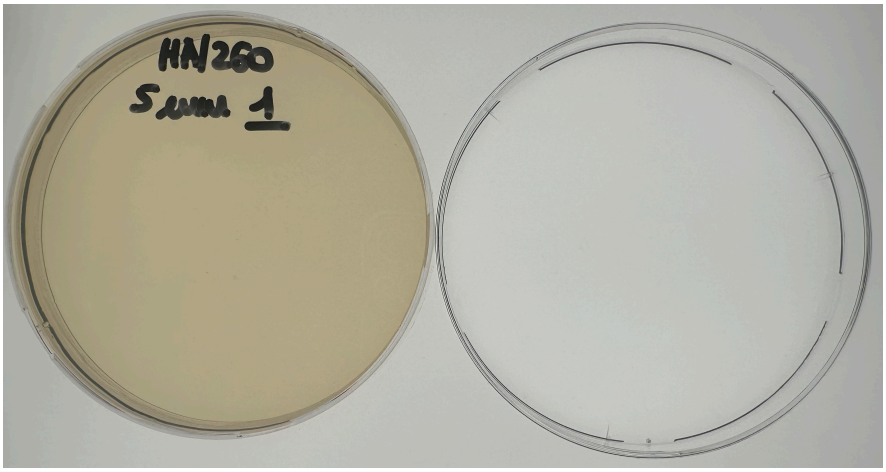

Figure S6. Sterility test plates of single-layer PDLLA scaffolds after 5 minutes of UV sterilization, incubated for 48 h.

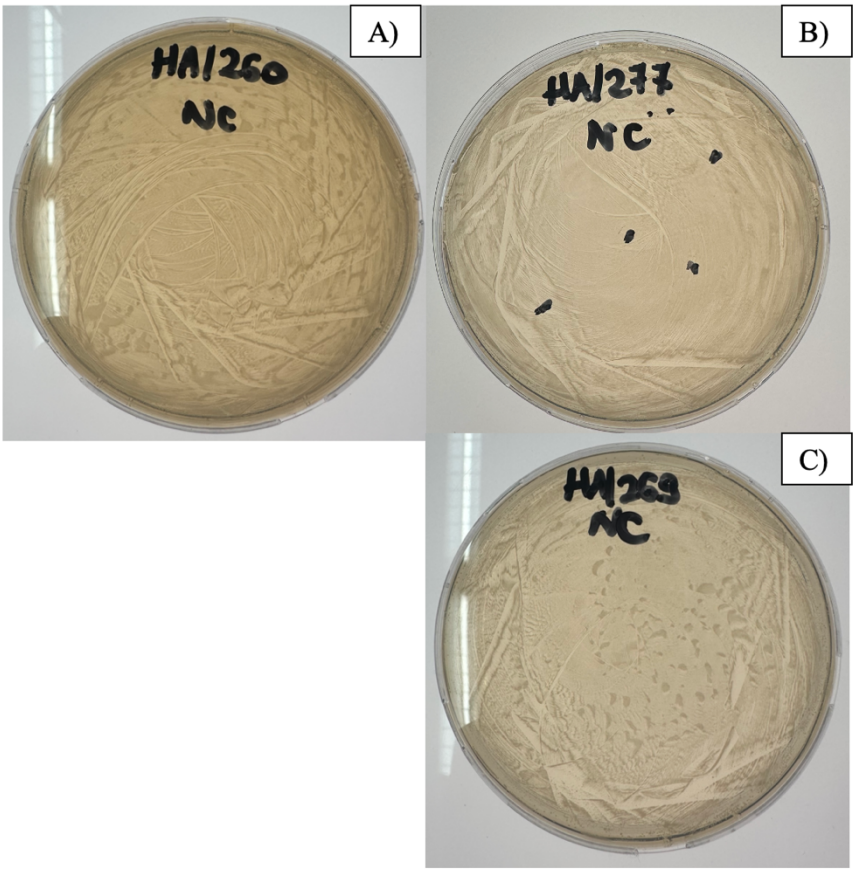

Figure S7. Sterility test plates of single-layer PDLLA scaffolds without UV treatment. A), B), and C) correspond to independent samples after 24 h of incubation.

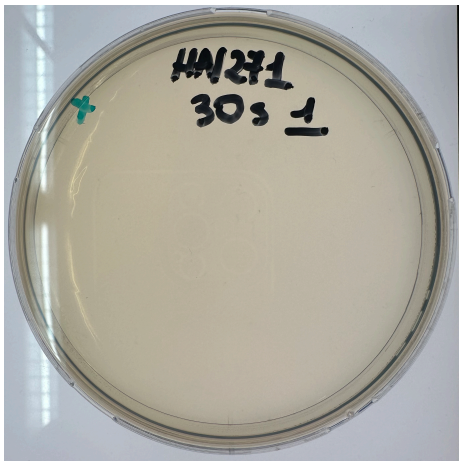

Figure S8. Sterility test plates of bilayer PVP-HA scaffolds after 30 seconds of UV sterilization, incubated for 24 h.

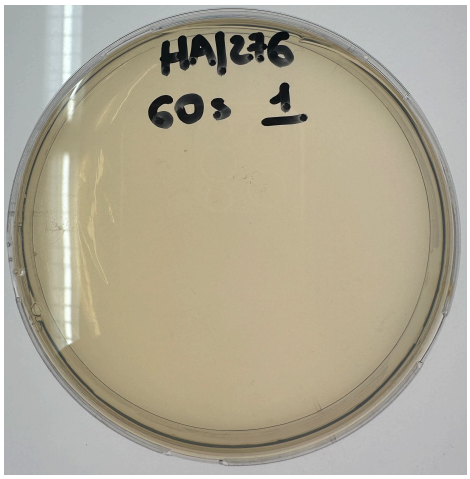

Figure S9. Sterility test plates of bilayer PVP-HA scaffolds after 60 seconds of UV sterilization, incubated for 24 h.

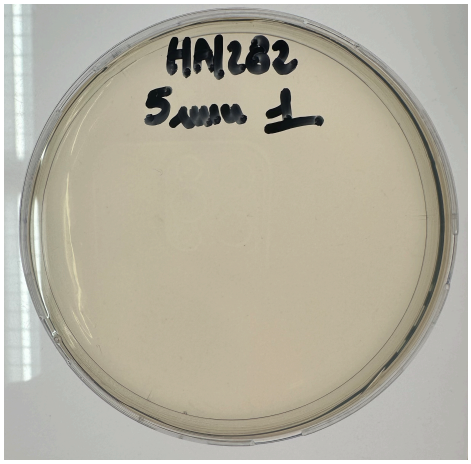

Figure S10. Sterility test plates of bilayer PVP-HA scaffolds after 5 minutes of UV sterilization, incubated for 24 h.

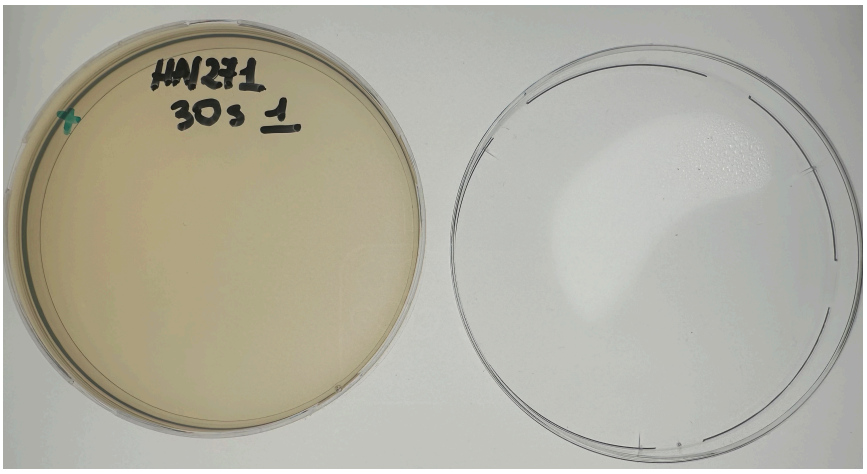

Figure S11. Sterility test plates of bilayer PVP-HA scaffolds after 30 seconds of UV sterilization, incubated for 48 h.

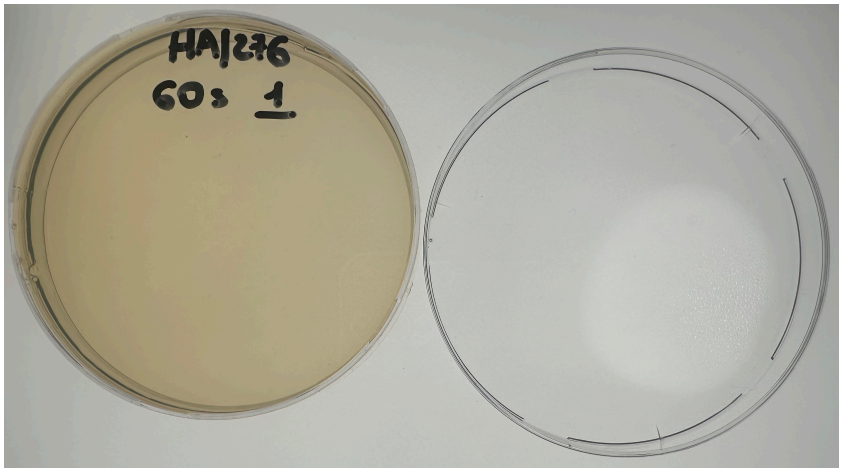

Figure S12. Sterility test plates of bilayer PVP-HA scaffolds after 60 seconds of UV sterilization, incubated for 48 h.

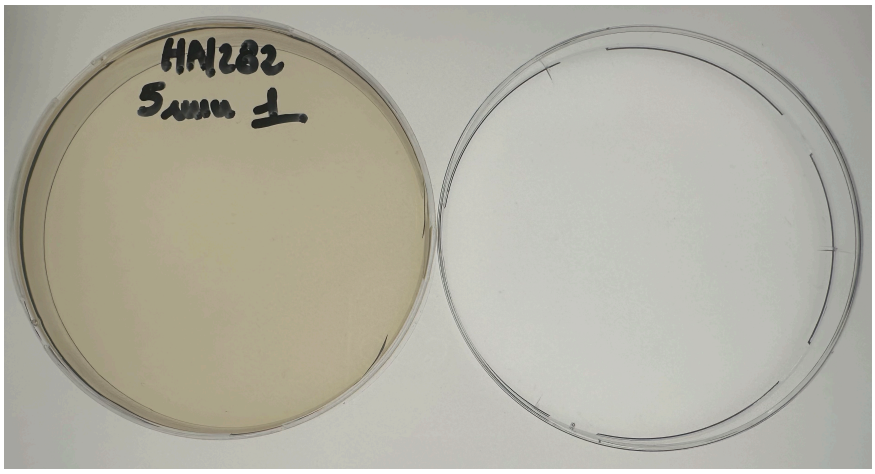

Figure S13. Sterility test plates of bilayer PVP-HA scaffolds after 5 minutes of UV sterilization, incubated for 48 h.

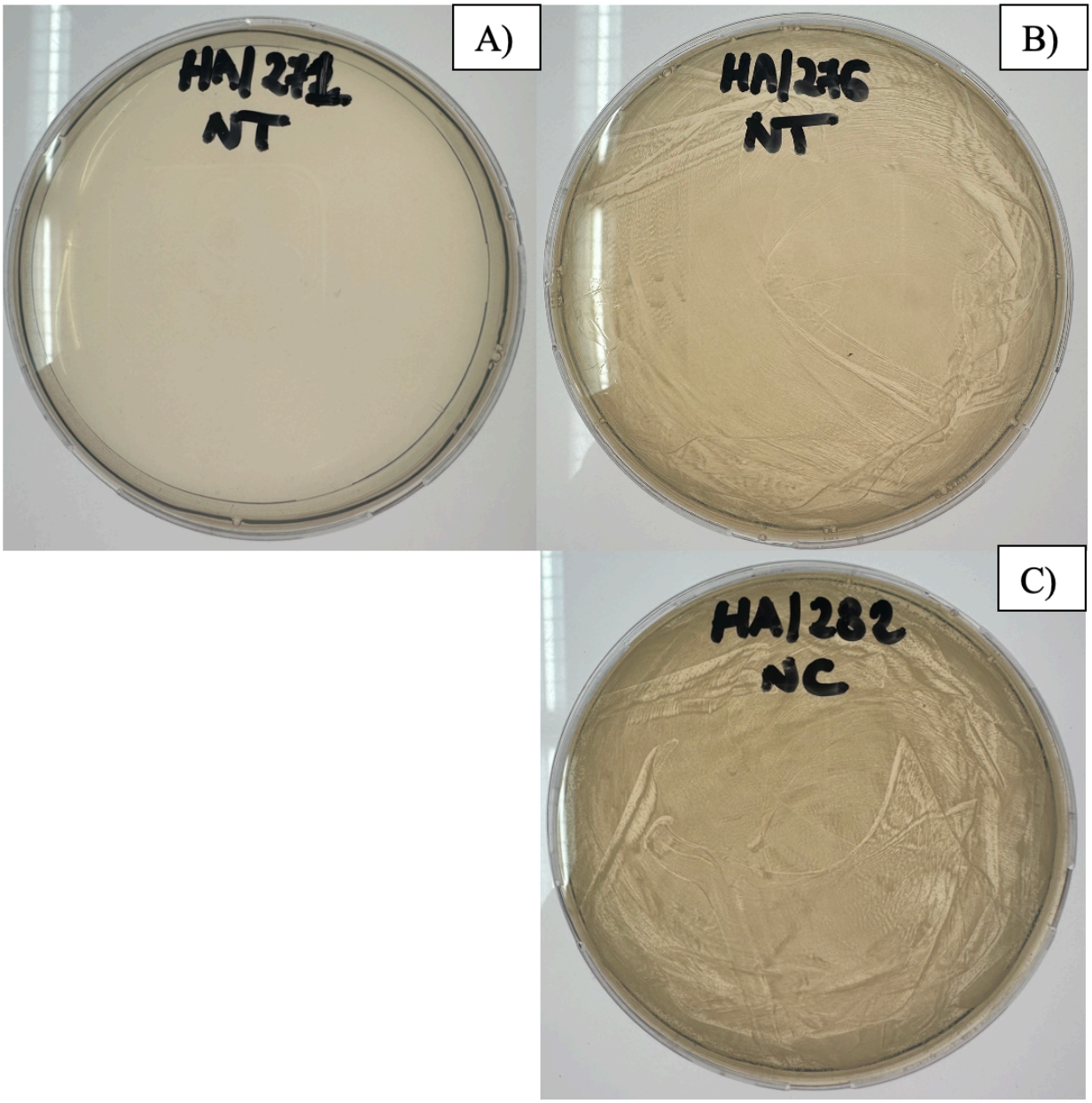

Figure S14. Sterility test plates of bilayer PVP-HA scaffolds without UV treatment. A), B), and C) correspond to independent samples after 24 h of incubation.

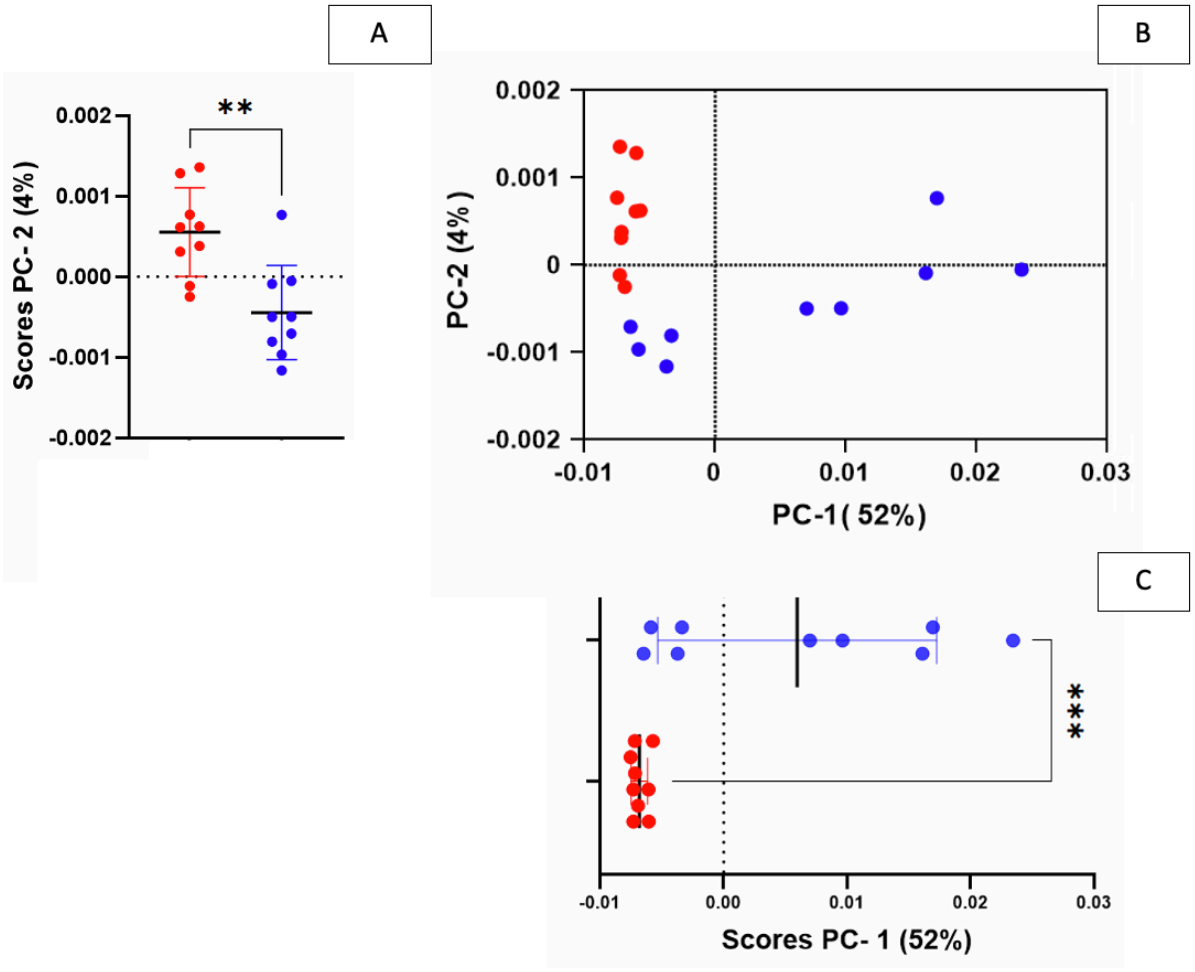

Figure S15. PCA of Raman spectra acquired from electrospun PVP-HA (red symbols) and PVP-HA-Arg-OH (blue symbols) scaffolds. (A) PC-2 score distribution for the two scaffold formulations (unpaired Student's t-test, **, $p < 0.01$). (B) PC-1 versus PC-2 score plot showing the separation between the two groups. (C) PC-1 score distribution highlighting the main spectral difference between PVP-HA and PVP-HA-Arg-OH scaffolds (unpaired Student's t-test, ***, $p < 0.001$).

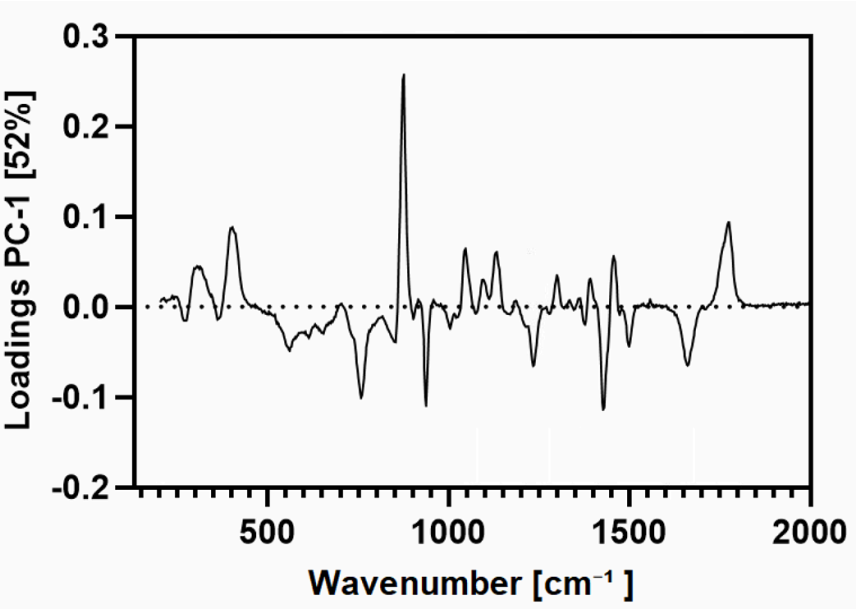

Figure S16. PC-1 loadings plot derived from PCA of Raman spectra acquired from electrospun PVP-HA and PVP-HA-Arg-OH scaffolds.

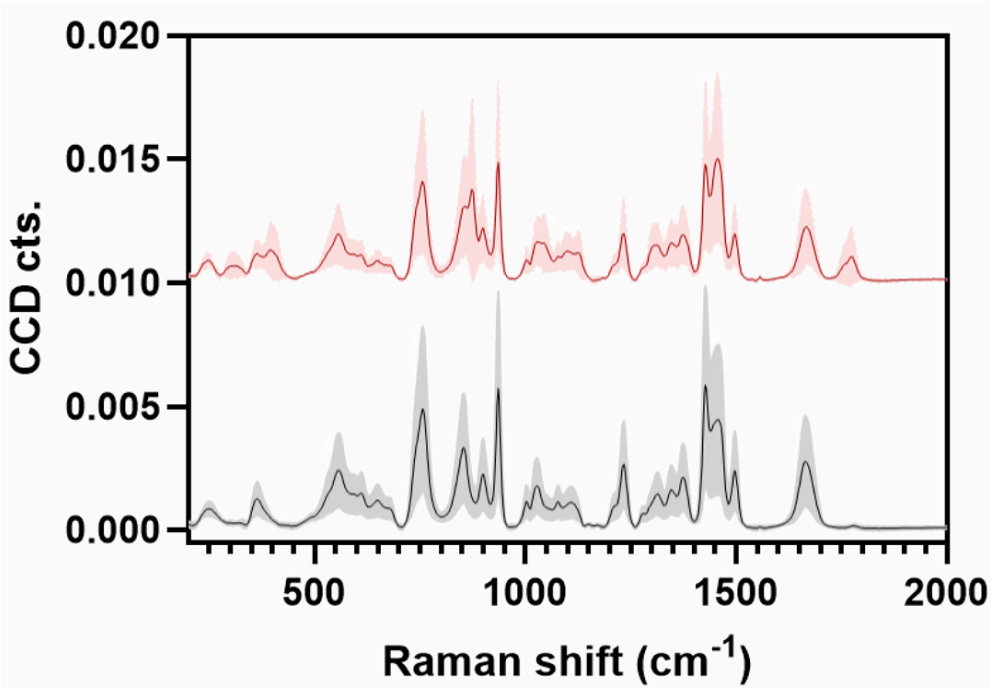

Figure S17. Average Raman spectra of electrospun PVP-HA and PVP-HA-Arg-OH scaffolds. The spectrum of PVP-HA-Arg-OH is shown in red, while the spectrum of PVP-HA is shown in black.

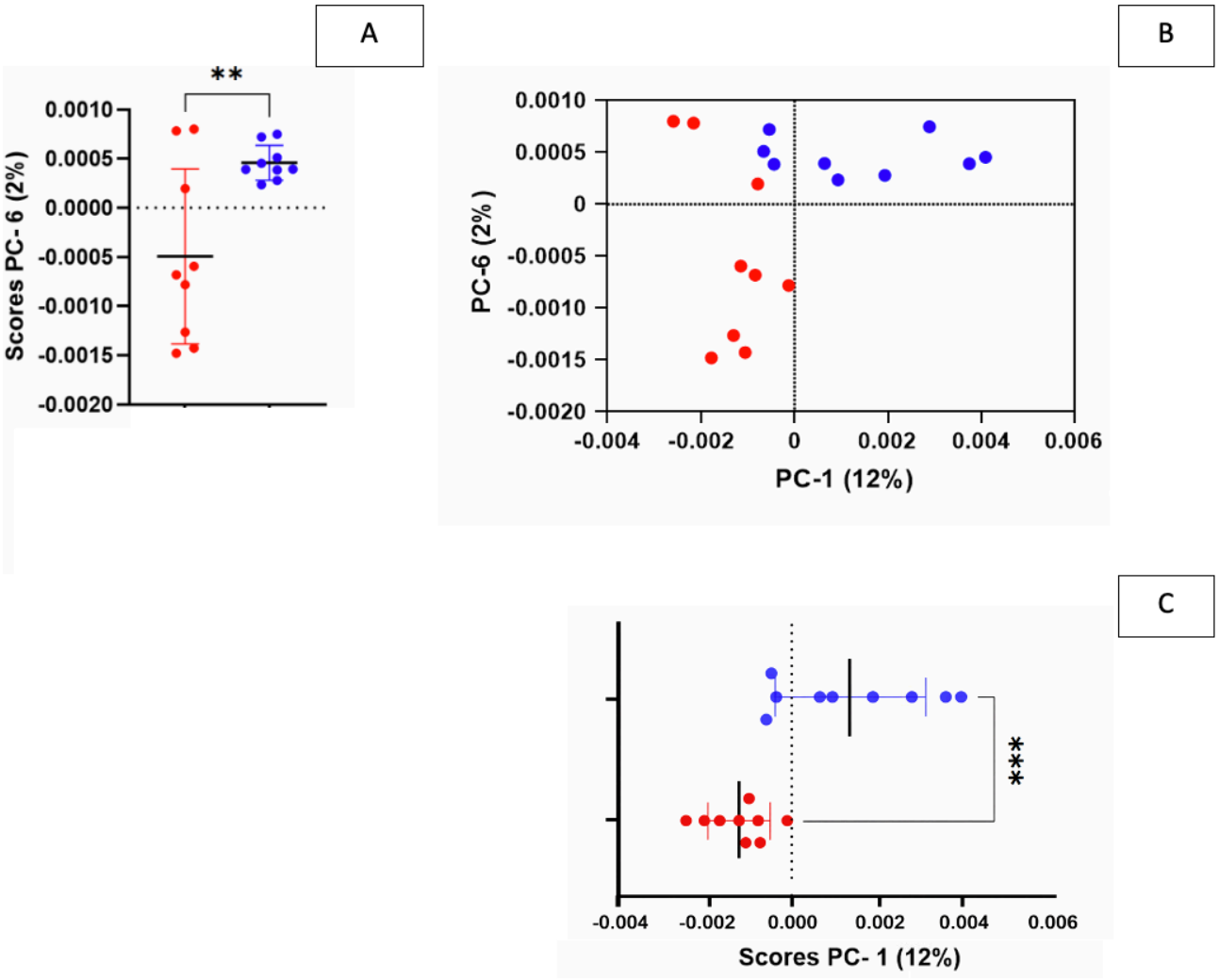

Figure S18. PCA of Raman spectra acquired from electrospun PVP-HA (red symbols) and PVP-HA-Gly-OH (blue symbols) scaffolds. (A) PC-6 score distribution for the two scaffold formulations (unpaired Student's t-test, **, $p < 0.01$). (B) PC-1 versus PC-6 score plot showing the separation between the two groups. (C) PC-1 score distribution highlighting the main spectral difference between PVP-HA and PVP-HA-Gly-OH scaffolds (unpaired Student's t-test, ***, $p < 0.001$).

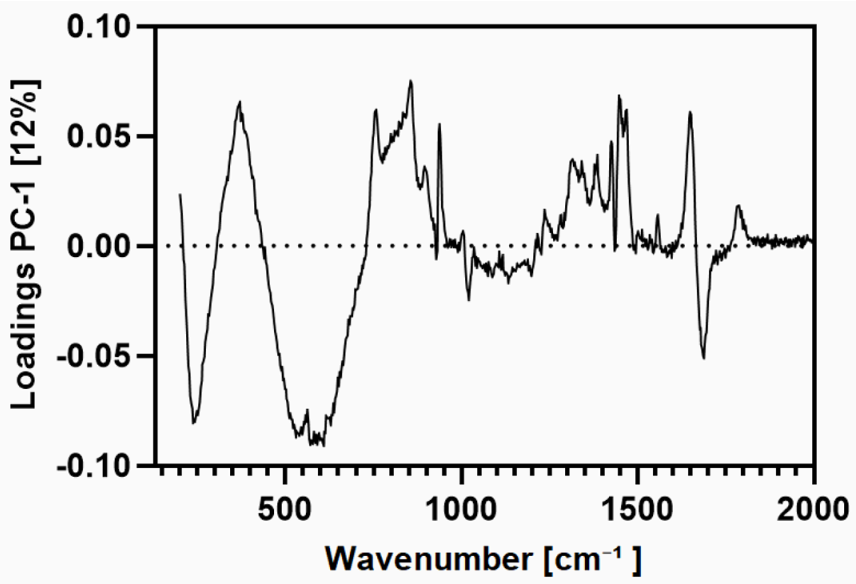

Figure S19. PC-1 loadings plot derived from PCA of Raman spectra acquired from electrospun PVP-HA and PVP-HA-Gly-OH scaffolds.

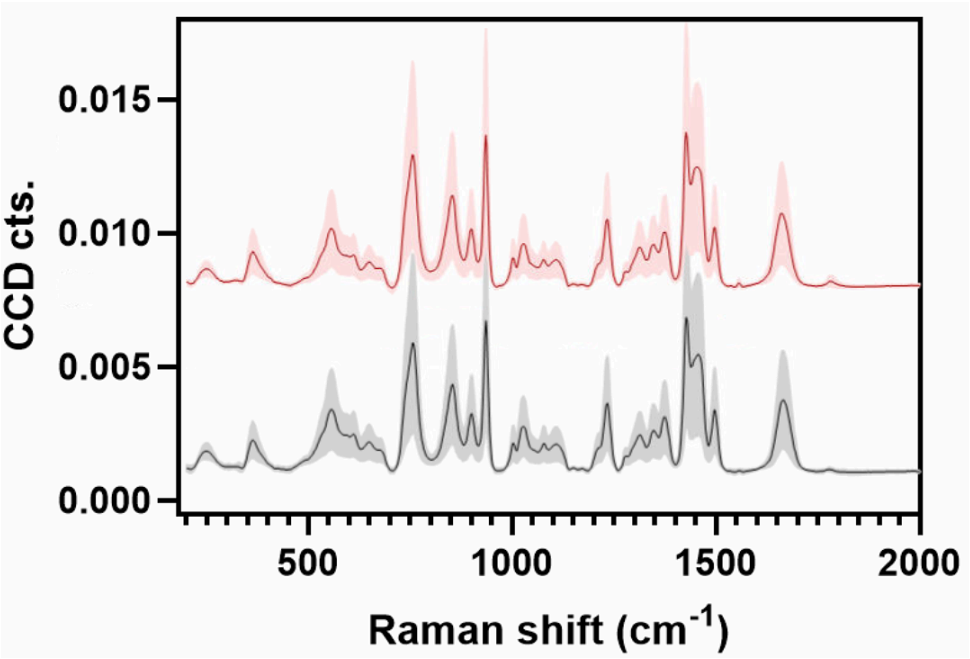

Figure S20. Average Raman spectra of electrospun PVP-HA and PVP-HA-Gly-OH scaffolds. The spectrum of PVP-HA-Gly-OH is shown in red, while the spectrum of PVP-HA is shown in black.

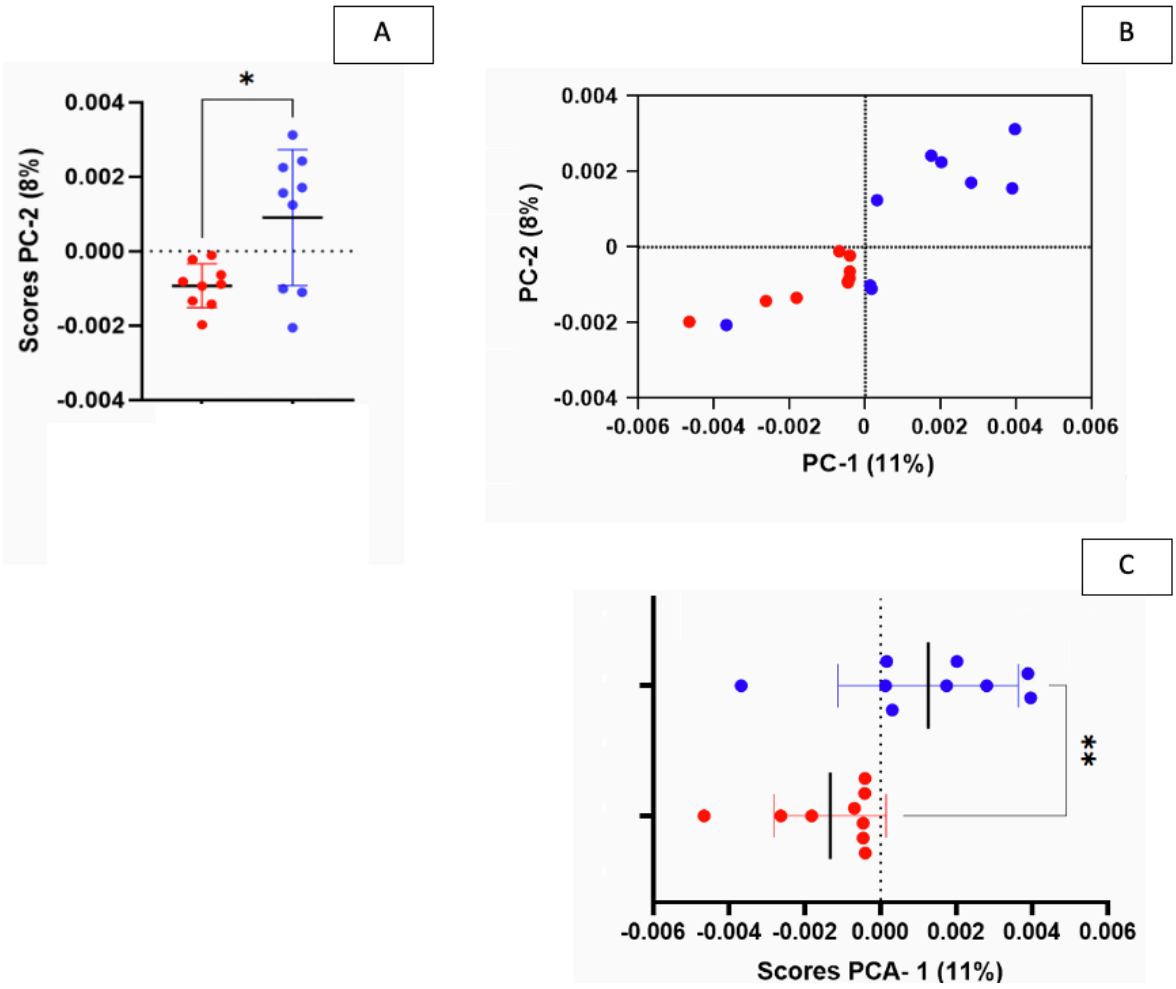

Figure S21. PCA of Raman spectra acquired from electrospun PVP (red symbols) and PVP-HA-Cys-OH scaffolds (blue symbols). (A) PC-2 score distribution for the two scaffold formulations (unpaired Student's t-test, *, $p < 0.05$). (B) PC-1 versus PC-2 score plot showing the separation between the two groups. (C) PC-1 score distribution highlighting the main spectral difference between PVP and PVP-HA-Cys-OH scaffolds (unpaired Student's t-test, **, $p < 0.01$).

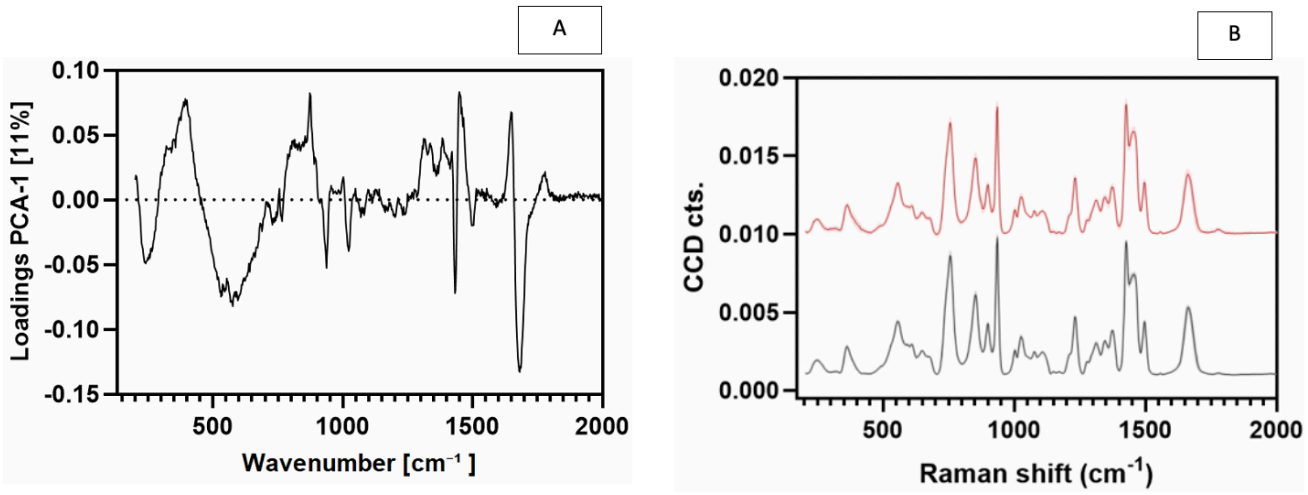

Figure S22. Raman analysis of electrospun PVP and PVP-HA-Cys-OH scaffolds. (A) PC-1 loadings plot derived from PCA of Raman spectra acquired from electrospun PVP and PVP-HA-Cys-OH scaffolds. (B) Average Raman spectra of electrospun PVP and PVP-HA-Cys-OH scaffolds. The spectrum of PVP-HA-Cys-OH is shown in red, while the spectrum of PVP is shown in black.

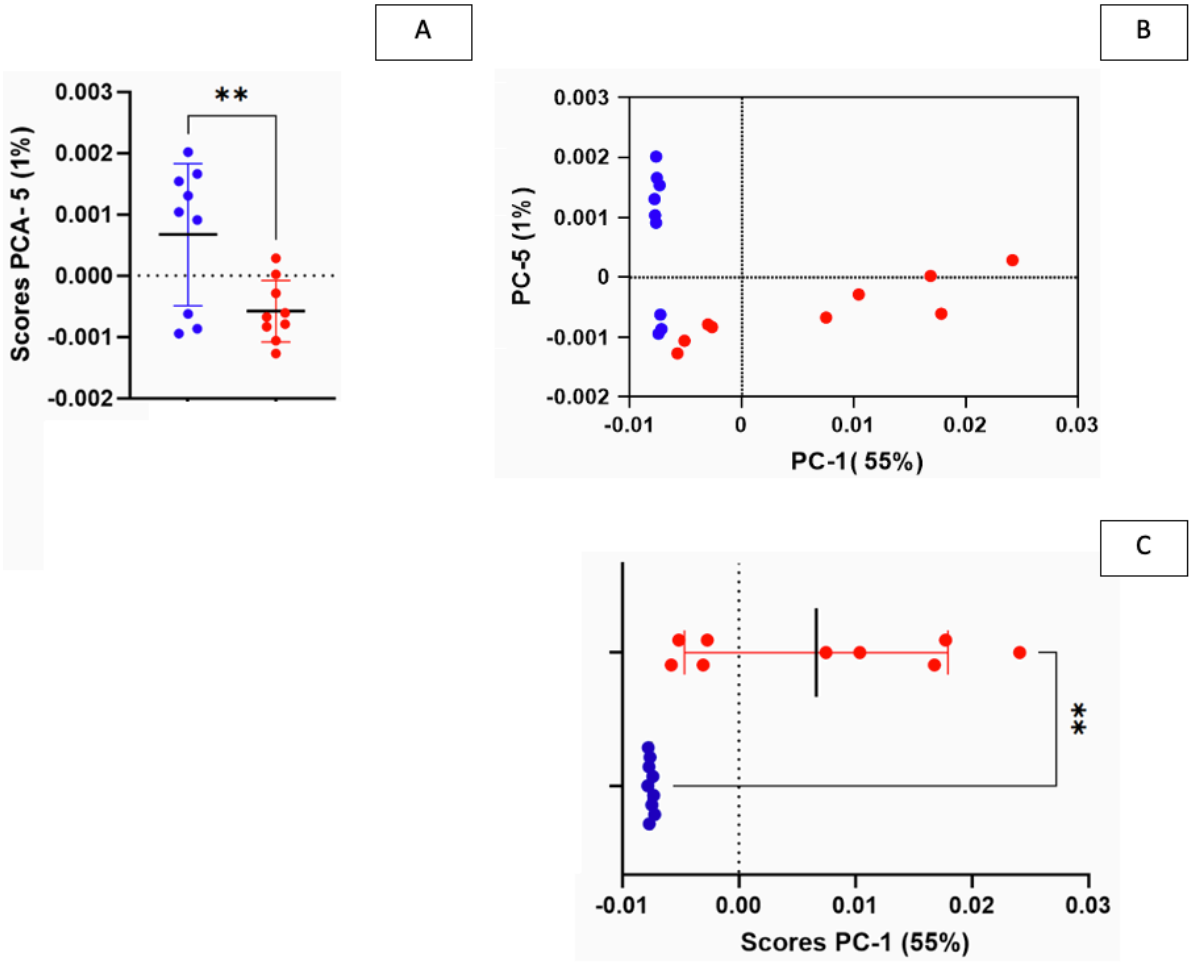

Figure S23. PCA of Raman spectra acquired from electrospun PVP (red symbols) and PVP-HA-Arg-OH (blue symbols) scaffolds. (A) PC-5 score distribution for the two scaffold formulations (unpaired Student's t-test; **, $p < 0.01$). (B) PC-1 versus PC-5 score plot showing the separation between the two groups. (C) PC-1 score distribution highlighting the main spectral difference between PVP and PVP-HA-Arg-OH scaffolds (unpaired Student's t-test; **, $p < 0.01$).

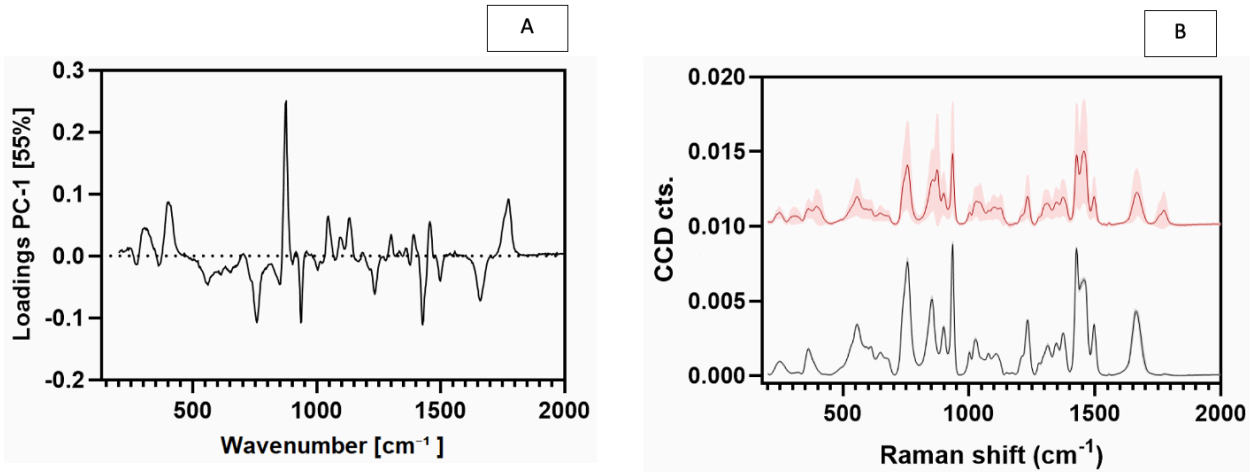

Figure S24. Raman analysis of electrospun PVP and PVP-HA-Arg-OH scaffolds. (A) PC-1 loadings plot obtained from PCA of Raman spectra acquired from electrospun PVP and PVP-HA-Arg-OH scaffolds. (B) Average Raman spectra of electrospun PVP and PVP-HA-Arg-OH scaffolds. The PVP-HA-Arg-OH spectrum is shown in red, while the PVP spectrum is shown in black.

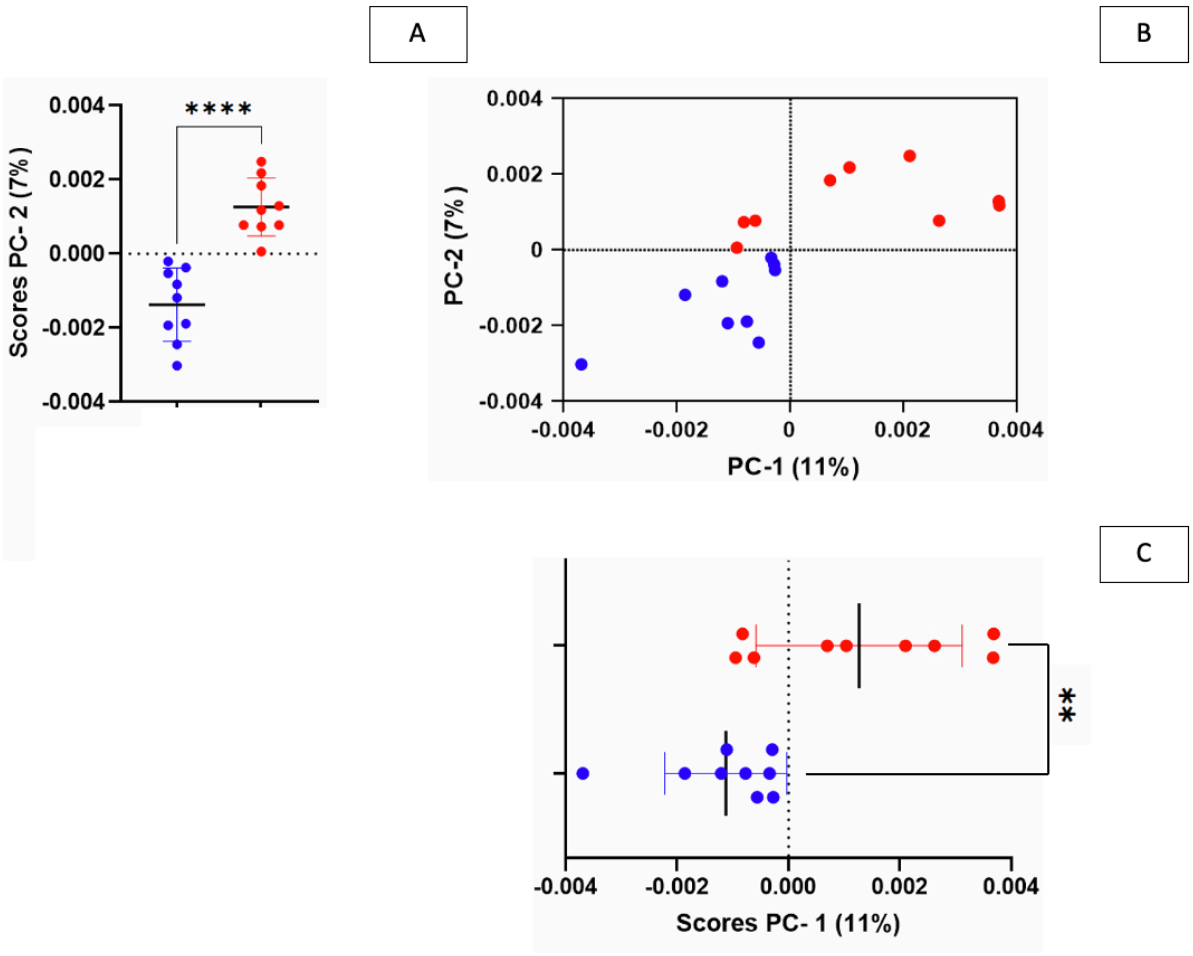

Figure S25. PCA of Raman spectra acquired from electrospun PVP (black symbols) and PVP-HA-Gly-OH (red symbols) scaffolds. (A) PC-2 score distribution for the two scaffold formulations (unpaired Student's t-test; ****, $p < 0.0001$). (B) PC-1 versus PC-2 score plot showing the separation between the two groups. (C) PC-1 score distribution highlighting the main spectral difference between PVP and PVP-HA-Gly-OH scaffolds (unpaired Student's t-test; **, $p < 0.01$).

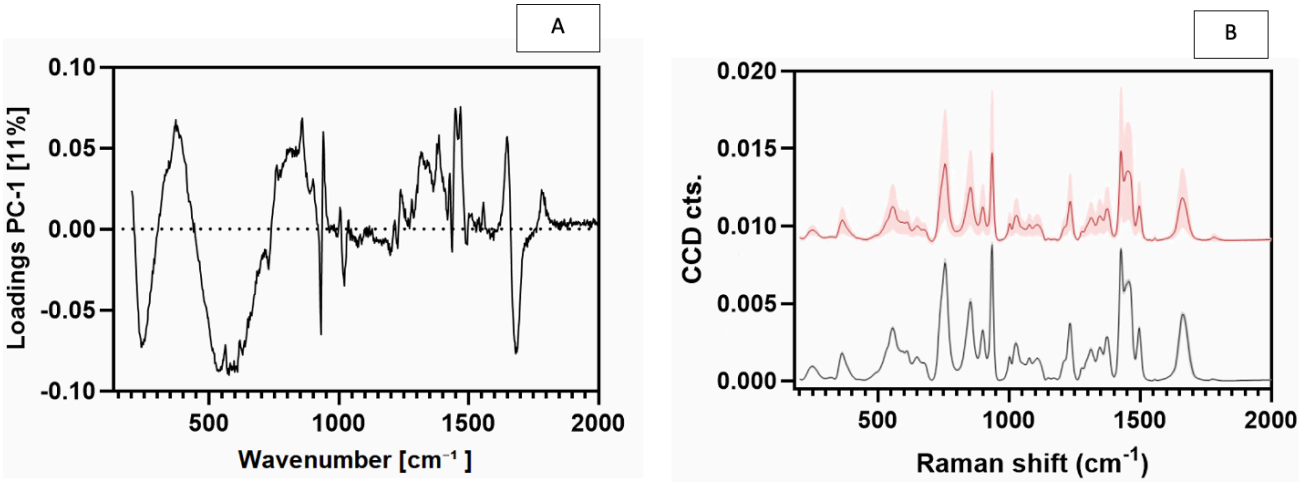

Figure S26. Raman analysis of electrospun PVP and PVP-HA-Gly-OH scaffolds. (A) PC-1 loadings plot obtained from PCA of Raman spectra acquired from electrospun PVP and PVP-HA-Gly-OH scaffolds. (B) Average Raman spectra of electrospun PVP and PVP-HA-Gly-OH scaffolds. The PVP-HA-Gly-OH spectrum is shown in red, while the PVP spectrum is shown in black.

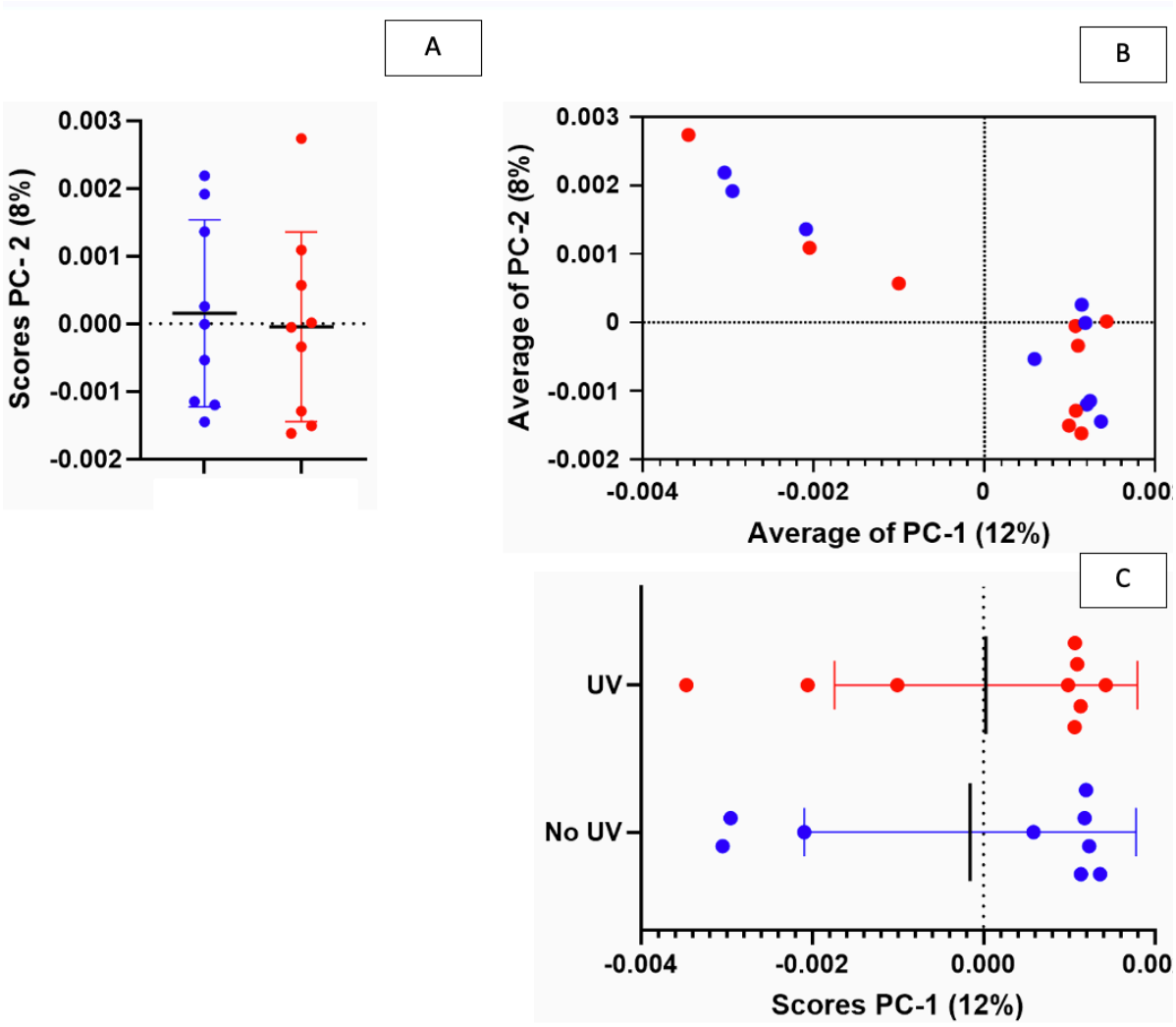

Figure S27. PCA of Raman spectra acquired from electrospun PVP scaffolds subjected to UV sterilization (60 s) and corresponding non-sterilized controls. (A) PC-2 score distribution for UV-sterilized and untreated samples (paired t-test; n.s.). (B) PC-1 versus PC-2 score plot showing the overlap between the two groups. (C) PC-1 score distribution for UV-sterilized and untreated samples (paired Wilcoxon test; n.s.).

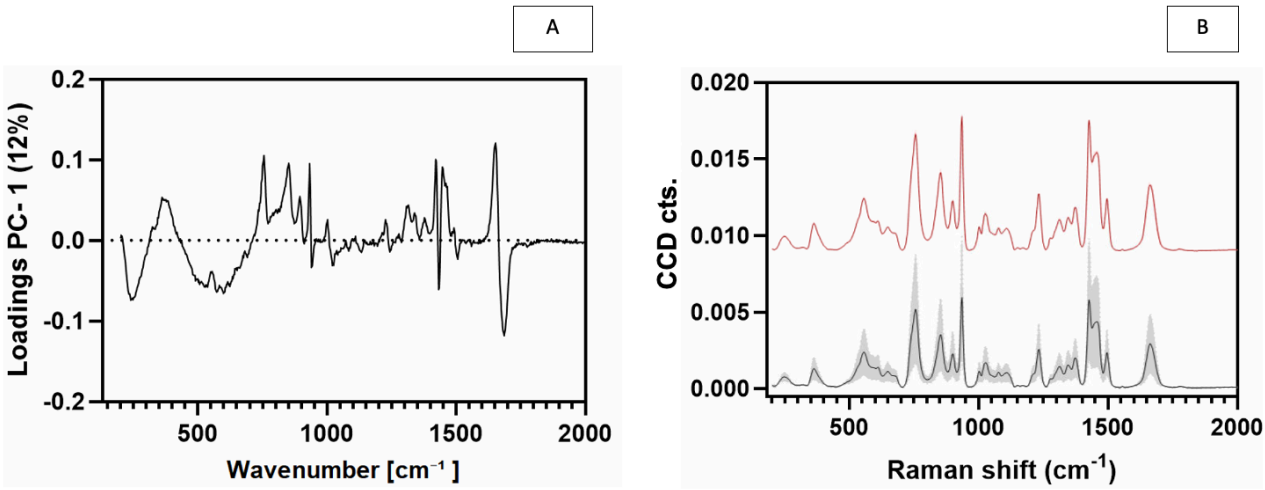

Figure S28. Raman analysis of electrospun PVP scaffolds before and after UV sterilization (60 s). (A) PC-1 loadings plot obtained from PCA of Raman spectra acquired from electrospun PVP scaffolds. (B) Average Raman spectra of electrospun PVP scaffolds before and after UV sterilization. Non-UV spectra are shown in black, while UV-sterilized spectra are shown in red.

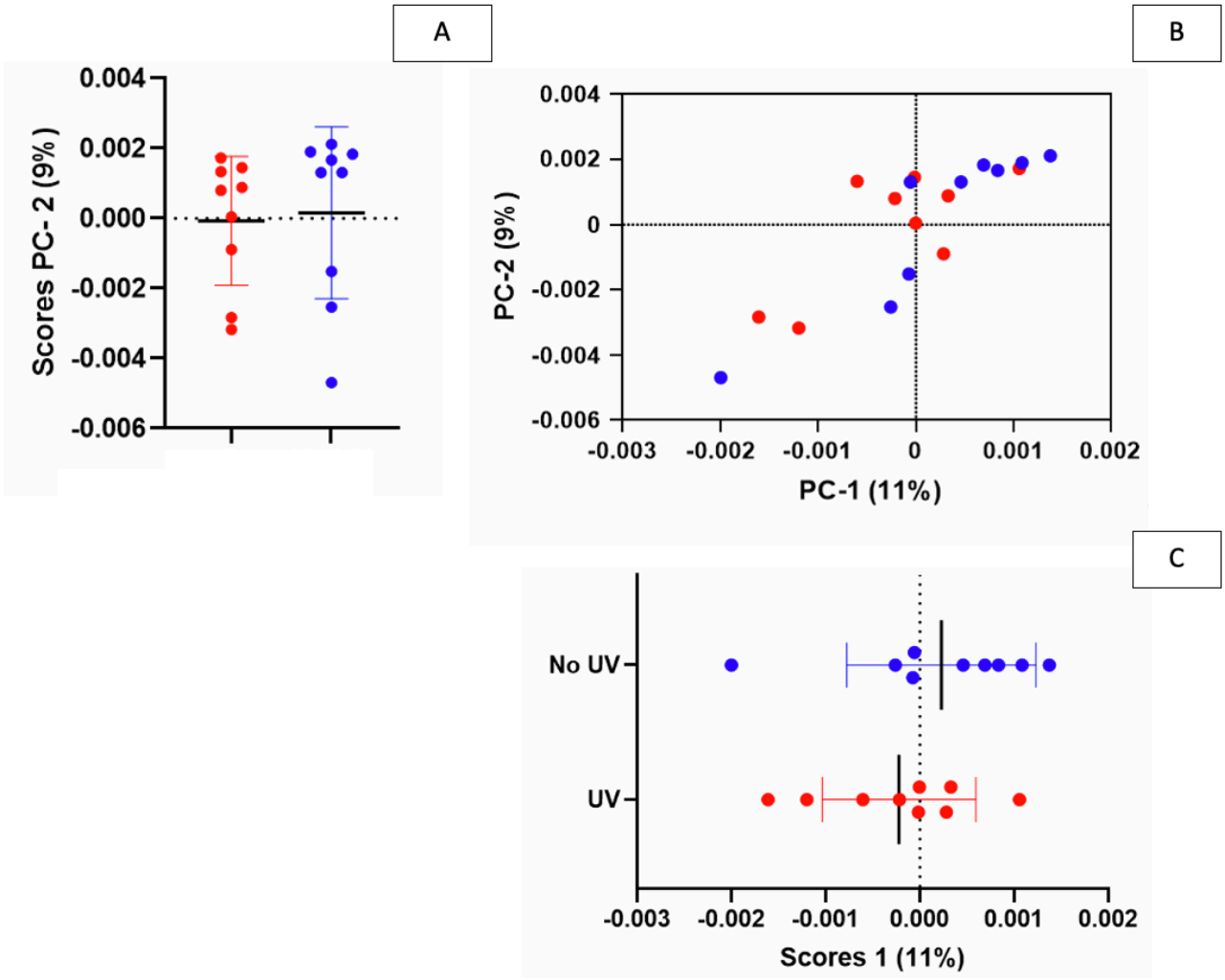

Figure S29. PCA of Raman spectra acquired from electrospun PVP-HA scaffolds subjected to UV sterilization (60 s) and corresponding non-sterilized controls. (A) PC-2 score distribution for UV-sterilized and untreated samples (paired Wilcoxon test; n.s.). (B) PC-1 versus PC-2 score plot showing the overlap between the two groups. (C) PC-1 score distribution for UV-sterilized and untreated samples (paired Wilcoxon test; n.s.).

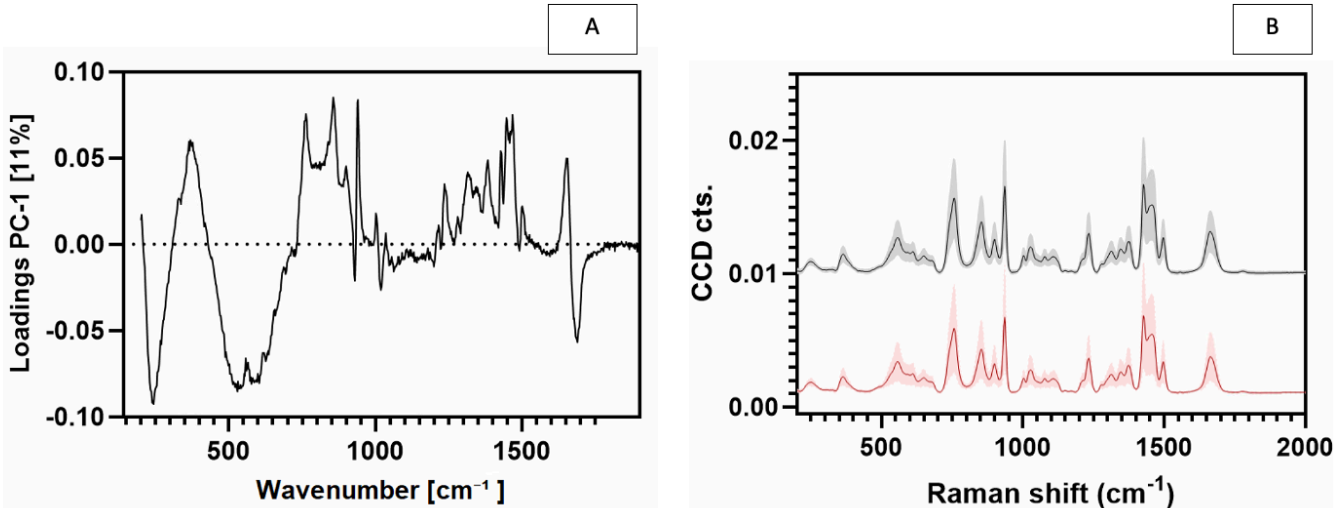

Figure S30. Raman analysis of electrospun PVP-HA scaffolds before and after UV sterilization. (A) PC-1 loadings plot obtained from PCA of Raman spectra acquired from electrospun PVP-HA scaffolds. (B) Average Raman spectra of electrospun PVP-HA scaffolds before and after UV sterilization. Non-UV spectra are shown in black, while UV-sterilized spectra are shown in red.

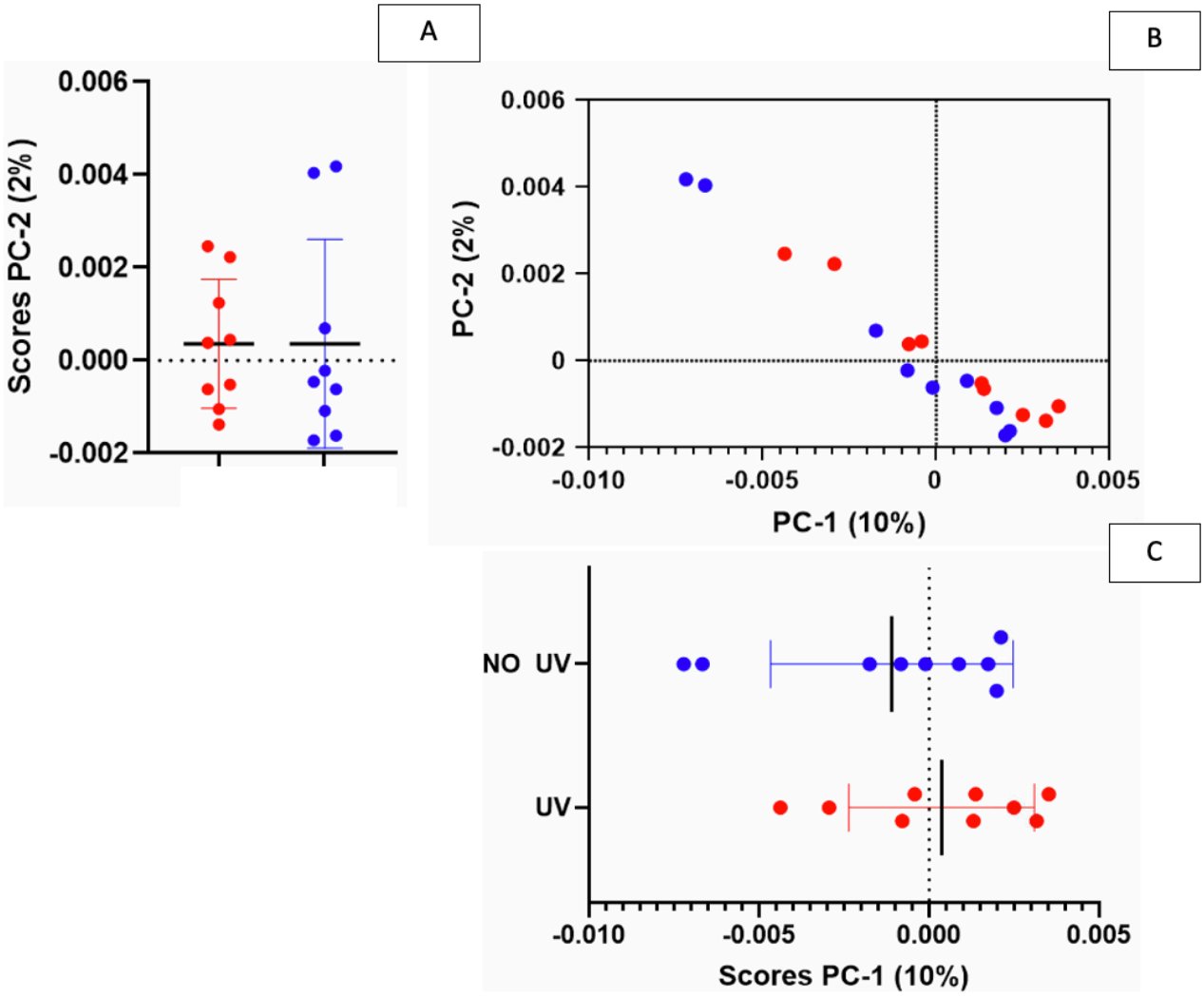

Figure S31. PCA of Raman spectra acquired from electrospun PVP-HA-Cys-OH scaffolds subjected to UV sterilization (60 s) and corresponding non-sterilized controls. (A) PC-2 score distribution for UV-sterilized and untreated samples (paired Wilcoxon test; n.s.). (B) PC-1 versus PC-2 score plot showing the overlap between the two groups. (C) PC-1 score distribution for UV-sterilized and untreated samples (paired Wilcoxon test; n.s.).

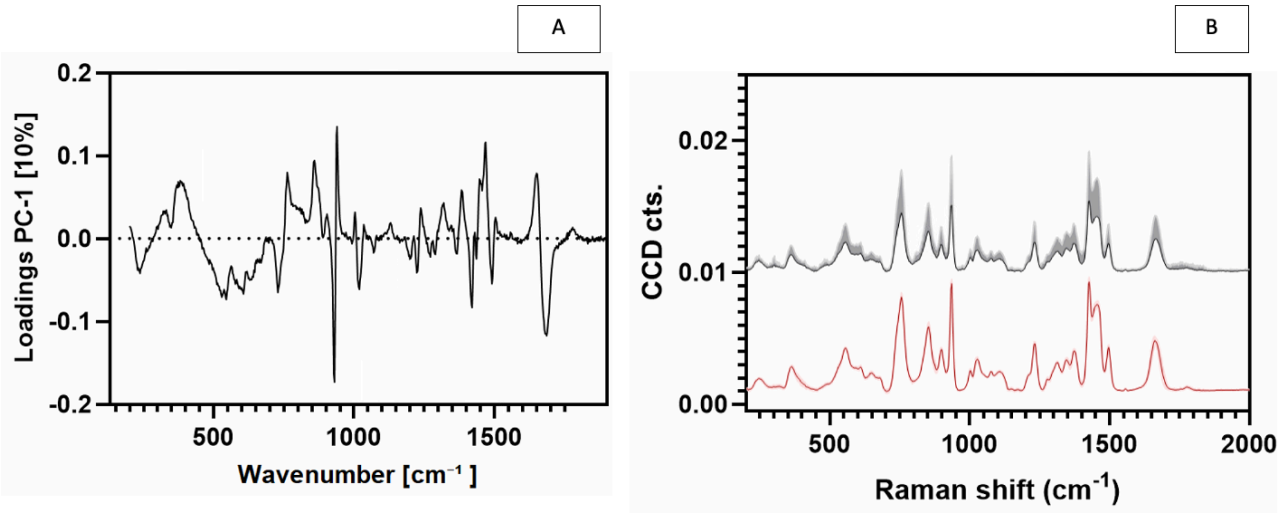

Figure S32. Raman analysis of electrospun PVP-HA-Cys-OH scaffolds before and after UV sterilization. (A) PC-1 loadings plot obtained from PCA of Raman spectra acquired from electrospun PVP-HA-Cys-OH scaffolds. (B) Average Raman spectra of electrospun PVP-HA-Cys-OH scaffolds before and after UV sterilization. Non-UV spectra are shown in black, while UV-sterilized spectra are shown in red.

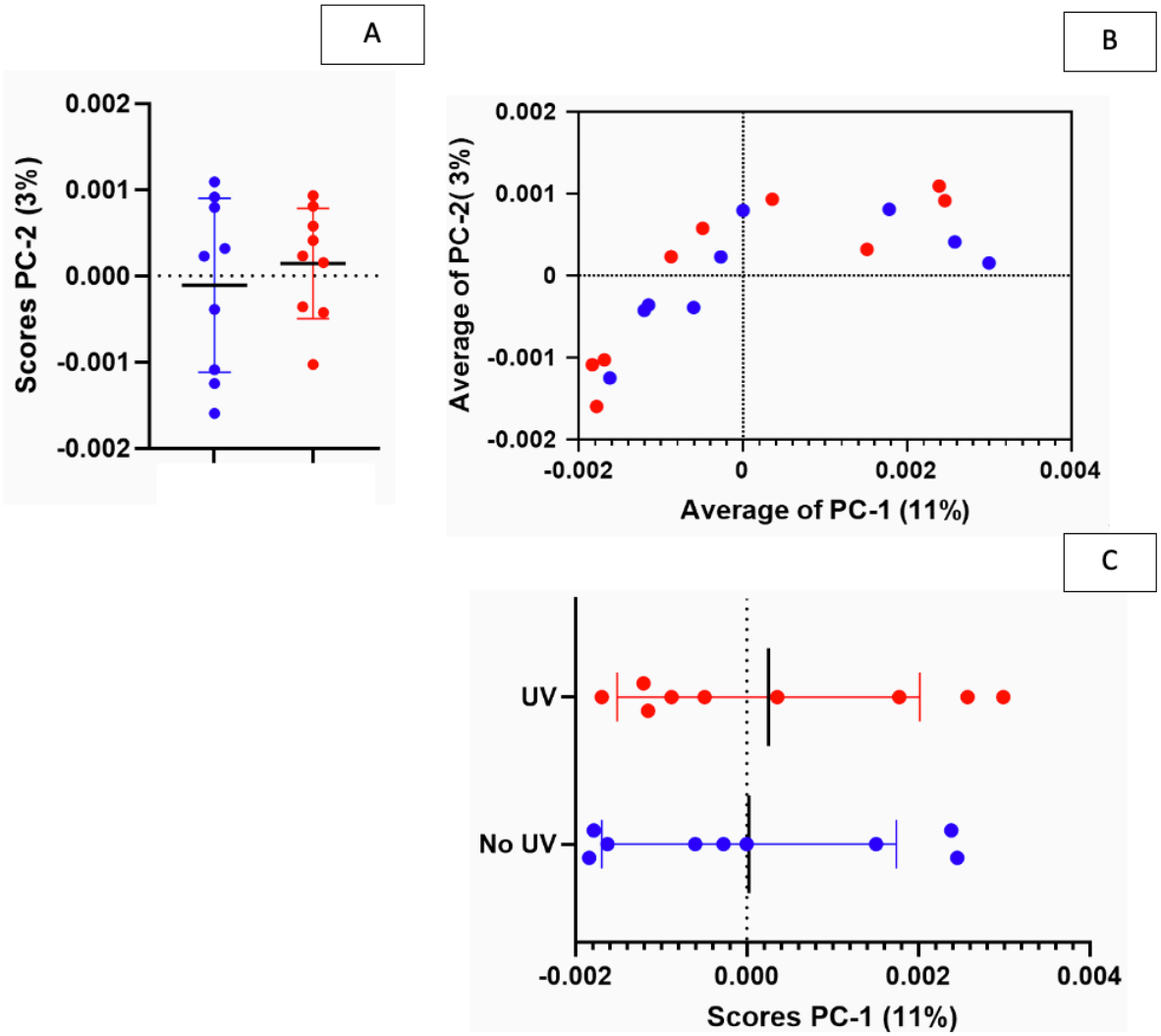

Figure S33. PCA of Raman spectra acquired from electrospun PVP-HA-Gly-OH scaffolds subjected to UV sterilization (60 s) and corresponding non-sterilized controls. (A) PC-2 score distribution for UV-sterilized and untreated samples (paired t-test; n.s.). (B) PC-1 versus PC-2 score plot showing the overlap between the two groups. (C) PC-1 score distribution for UV-sterilized and untreated samples (paired t-test; n.s.).

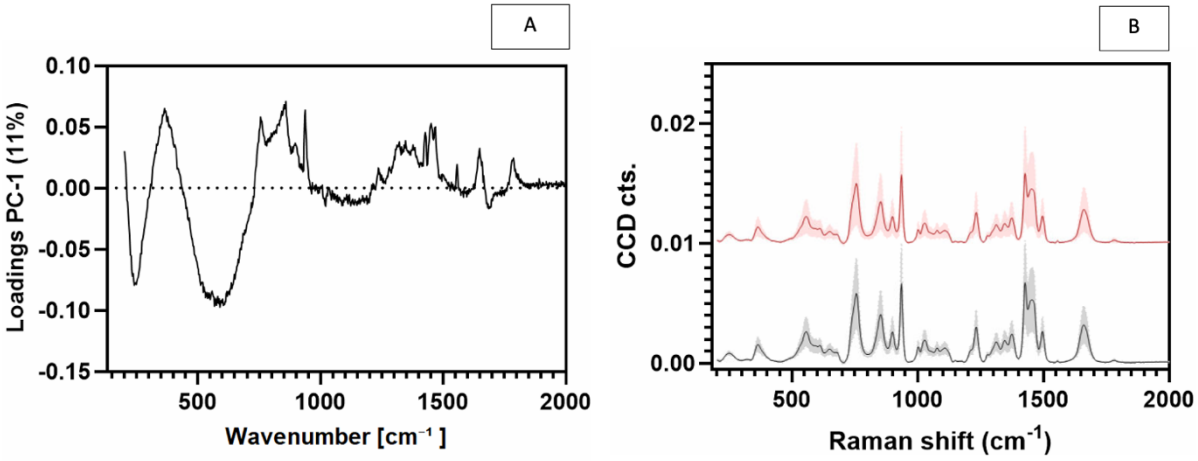

Figure S34. Raman analysis of electrospun PVP-HA-Gly-OH scaffolds before and after UV sterilization. (A) PC-1 loadings plot obtained from PCA of Raman spectra acquired from electrospun PVP-HA-Gly-OH scaffolds. (B) Average Raman spectra of electrospun PVP-HA-Gly-OH scaffolds before and after UV sterilization. Non-UV spectra are shown in black, while UV-sterilized spectra are shown in red.

References

[1] Malayeri A. H.; Mohseni M.; Cairns B.; Bolton J. R.; Chevrefils G.; Caron E.; Barbeau B.; Wright H.; Linden K. G. *Fluence (UV-C dose) required to achieve incremental log inactivation of bacteria, protozoa, viruses and algae.* International Ultraviolet Association News, **2016**, 18(3).

[2] Ploydaeng M, Rajatanavin N, Rattanakaemakorn P. *UV-C light: A powerful technique for inactivating microorganisms and the related side effects to the skin.* Photodermatol Photoimmunol Photomed. **2021** Jan;37.

[3] López-Calderón, H.D.; Avilés-Arnaut, H.; Galán-Wong, L.J.; Almaguer-Cantú, V.; Laguna-Camacho, J.R.; Calderón-Ramón, C.; Escalante-Martínez, J.E.; Arévalo-Niño, K. *Electrospun Polyvinylpyrrolidone-Gelatin and Cellulose Acetate Bi-Layer Scaffold Loaded with Gentamicin as Possible Wound Dressing*. Polymers **2020**, *12*, 2311.

[4] Pepe A, Laezza A, Armiento F, Bochicchio B. *Chemical Modifications in Hyaluronic Acid-Based Electrospun Scaffolds.* Chempluschem. **2024** Jul;89(7):e202300599.

[5] Barros, J. A. G.; Fechine, G. J. M.; Alcantara, M. R.; Catalani, L. H. *Poly(N-vinyl-2-pyrrolidone) hydrogels produced by Fenton reaction,* Polymer **2006**, 47, 8414–8419.

[6] Fini A.; Cavallari C.; Ospitali F. *Raman and thermal analysis of indomethacin/PVP solid dispersion enteric microparticles.* European Journal of Pharmaceutics and Biopharmaceutics, **2008**, 70(1), 409–420.

[7] Parker S. F. *Assignment of the vibrational spectrum of L-cysteine.* Chemical Physics, **2013**, 424, 75–79.

[8] Farrokhpour H.; Jalali F.; Atta-Figueroa S.; et al. *Theoretical spectroscopic study of L- and D-cysteine on Au/Ag nanoclusters: Raman and IR assignments.* Journal of Physical Chemistry A, **2024**, 128, 3285–3300.

[9] Movasaghi Z.; Rehman S.; Rehman I. U. *Raman spectroscopy of biological tissues.* Applied Spectroscopy Reviews, **2007**, 42, 493–541.

[10] Essendoubi M.; Gobinet C.; Reynaud R.; Angiboust J. F.; Manfait M.; Piot O. *Human skin penetration of hyaluronic acid of different molecular weights as probed by Raman spectroscopy.* Skin Research and Technology, **2016**, 21, 416–425.

[11] Aliaga A. E.; Garrido C.; Leyton P.; Díaz G. F.; Gómez-Jeria J. S.; Aguayo T.; Clavijo E.; Campos-Vallette M. M.; Sánchez-Cortés S. *SERS and theoretical studies of arginine.* Spectrochimica Acta Part A: Molecular and Biomolecular Spectroscopy, **2010**, 76, 458–463.

[12] Zhu G.; Zhu X.; Fan Q.; Wan X. *Raman spectra of amino acids and their aqueous solutions.* Spectrochimica Acta Part A: Molecular and Biomolecular Spectroscopy, **2011**, 78(3), 1187–1195.

Chapter 6

Design and Characterization of Hyaluronic Acid-Amino Acid Bioconjugates

1. Introduction

The present chapter focuses on the systematic functionalization of hyaluronic acid with L-amino acids through carbodiimide-mediated coupling. In previous chapters, the chemical modification of hyaluronic acid has been introduced as an effective strategy to modulate its structural and physicochemical properties. The introduction of amino acid residues with different chemical structures and protecting groups can influence the efficiency of carbodiimide-mediated coupling and the resulting degree of substitution, as the chemical nature of the nucleophilic partner and its reactivity significantly affect amide bond formation. EDC/s-NHS chemistry is widely used to activate carboxyl groups for coupling with primary amines, and studies on polysaccharide–amino acid conjugates indicate that esterified amino acid derivatives may exhibit different reactivity and conjugation efficiencies compared to free amino acids under similar conditions [1-2].

The conjugation of amino acids represents a straightforward chemical approach to introduce side-chain functionalities with diverse steric and chemical characteristics along the hyaluronic acid backbone. Depending on the amino acid structure and form employed, such modifications may influence intermolecular interactions and the overall chemical behavior of the resulting HA derivatives [3-5].

The amino acids selected in this study—L-valine, L-methionine, L-leucine, and L-phenylalanine—were chosen as representative examples of aliphatic and aromatic residues characterized by increasing side-chain size and hydrophobicity. Although they share the same α-amino acid backbone, these molecules differ in steric hindrance and side-chain functionality, providing structurally distinct substituents along the hyaluronic acid backbone.

Here, a series of hyaluronic acid-amino acid bioconjugates was synthesized using valine, methionine, leucine, and phenylalanine as model amino acids. For selected systems, both amino acid methyl esters and the corresponding free amino acids were employed in order to compare their impact on the conjugation process. The resulting HA derivatives were characterized by ^{1}H-NMR and ATR-FTIR spectroscopy to confirm successful functionalization, quantify the degree of substitution, and verify the preservation of the hyaluronic acid backbone after chemical modification.

2. Materials and Methods

2.1 Materials

Sodium hyaluronate (HA, Mw = 186 kDa) was a generous gift of Altergon Italia S.r.l.

Sodium hydroxide (NaOH, ≥98%), sodium 3-(trimethylsilyl)propane-1-sulfonate (DSS, 98.0%), 2-(*N*-morpholino)ethanesulfonic acid monohydrate (MES·H_2O, ≥99.5%), and deuterium oxide (D_2O), as well as L-methionine ethyl ester hydrochloride, L-leucine methyl ester hydrochloride, L-valine methyl ester hydrochloride, L-phenylalanine, L-leucine, and L-valine were purchased from Sigma-Aldrich.

1-Ethyl-3-(3-dimethylaminopropyl)carbodiimide hydrochloride (EDC·HCl) was obtained from Iris Biotech GmbH, while *N*-Hydroxysulfosuccinimide sodium salt (s-NHS) was purchased from Tokyo Chemical Industry (TCI).

2.2 Methods

2.2.1 General Methods

Centrifugation was performed using a Hermle (LaborTechnik GmbH) centrifuge (6000 rpm, room temperature, 40 min). Dialysis was carried out using a Slide-A-Lyzer™ Dialysis Cassette G2 with a molecular weight cut-off of 3.5 kDa. Lyophilization was conducted using a Christ Alpha 1-4 LD plus freeze dryer.

2.2.2 Nuclear Magnetic Resonance (NMR) Spectroscopy

NMR spectra were recorded using Varian Inova 500 MHz (^{1}H: 500 MHz, ^{13}C: 125 MHz) and 400 MHz (^{1}H: 400 MHz, ^{13}C: 100 MHz) spectrometers. Samples were prepared in D_2O. DSS (0.1 mM) was used as an internal standard for chemical shift calibration and referenced at δ_H = 0.00 ppm. The degree of substitution (DS) for the HA-amino acid derivatives was calculated relative to the disaccharide repeating unit.

2.2.3 Attenuated Total Reflectance Fourier Transform Infrared (ATR-FTIR) Spectroscopy

ATR-FTIR analyses were performed using a Jasco J-460 spectrometer (Jasco Europe Srl) equipped with an ATR PRO ONE single-reflection accessory fitted with a diamond crystal. Spectra were

collected in the range of 4000-450 cm^{-1} with a spectral resolution of 2 cm^{-1}, averaging 256 scans for each measurement. A background spectrum was recorded prior to each acquisition and automatically subtracted from the corresponding sample spectrum.

2.2.4 Bioconjugation of Val-OMe with HA (4)

HA (101.85 mg, 0.251 mmol) was dispersed in 15 mL of H_2O and stirred at room temperature until complete dissolution. The resulting solution was then supplemented with aqueous EDC·HCl (2.40 mL, 0.503 mmol) and s-NHS (2.43 mL, 0.251 mmol), and the mixture was stirred for an additional 40 minutes. MES·H_2O (40.3 mg) and an aqueous solution of valine methyl ester hydrochloride (Val-OMe; 2 mL, 0.503 mmol) were added. The pH was carefully adjusted to 6.0 using freshly prepared 1 M NaOH. A clear solution was obtained, which was left stirring overnight at room temperature. After approximately 22 hours, the reaction was brought to pH 7 with 1.0 M NaOH and subjected to dialysis, first against a 342 mM NaCl solution and subsequently against H_2O. The dialyzed solution was frozen and freeze-dried to afford a white solid (69.70 mg, 67% yield).

^{1}H-NMR (400 MHz, D_2O, 25°C): δ_{DSS} = 4.54 ppm (H-1, GlcNAc), 4.45 ppm (H-1, GlcA), 4.15 ppm (1H, m, C*H* (H2, Val-OMe)), 4.00-3.20 ppm (H-2, H-3, H-4, H-5 GlcA; H-2, H-3, H-4, H-5, H-6 GlcNAc), 3.74 ppm (3H, s, CH_3 (H1', Val-OMe)), 2.01 ppm (NHAc, GlcNAc), 0.93 ppm (6H, d, CH_3 (H4 + H5, Val-OMe)).

2.2.5 Deprotection of HA-Val-OMe (5-i)

HA-Val-OMe (61.04 mg, 0.168 mmol) was treated with 15 mL of 1.0 M NaOH solution to adjust pH to 12. The solution was stirred for 6 h at room temperature and then 1 M HCl was added until neutralization. Dialysis and subsequent freeze-drying yielded a white solid (42.95 mg, yield = 63%).

^{1}H-NMR (400 MHz, D_2O, 25°C): δ_{DSS} = 4.54 ppm (H-1, GlcNAc), 4.45 ppm (H-1, GlcA), 4.15 ppm (1H, m, C*H* (H2, Val-OH)), 4.00-3.20 ppm (H-2, H-3, H-4, H-5 GlcA; H-2, H-3, H-4, H-5, H-6 GlcNAc), 2.01 ppm (NHAc, GlcNAc), 0.93 ppm (6H, d, CH_3 (H4 + H5, Val-OH)).

2.2.6 Bioconjugation of Val-OH with HA (5-ii)

HA (101.85 mg, 0.251 mmol) was dispersed in 15 mL of H_2O and stirred at room temperature until complete dissolution. The resulting solution was then supplemented with aqueous EDC·HCl (2.40 mL, 0.503 mmol) and s-NHS (2.43 mL, 0.251 mmol), and the mixture was stirred for an additional 40 minutes. MES·H_2O (40.3 mg) and an aqueous solution of valine (Val-OH; 2 mL, 0.503 mmol) were added. The pH was carefully adjusted to 6.0 using freshly prepared 1 M NaOH. A clear solution

was obtained, which was left stirring overnight at room temperature. After approximately 22 hours, the reaction was brought to pH 7 with 1.0 M NaOH and subjected to dialysis, first against a 342 mM NaCl solution and subsequently against H_2O. The dialyzed solution was frozen and freeze-dried to afford a white solid (70.50 mg, 77% yield).

^{1}H-NMR (400 MHz, D_2O, 25°C): δ_{DSS} = 4.54 ppm (H-1, GlcNAc), 4.45 ppm (H-1, GlcA), 4.11 ppm (1H, m, C*H* (H2, Val-OH)), 4.00-3.20 ppm (H-2, H-3, H-4, H-5 GlcA; H-2, H-3, H-4, H-5, H-6 GlcNAc), 2.88 ppm (1H, m, C*H* (H3, Val-OH)), 2.01 ppm (NHAc, GlcNAc), 0.94 ppm (6H, d, CH_3 (H4 + H5, Val-OH)).

2.2.7 Bioconjugation of Met-OEt with HA (7)

HA (101.16 mg, 0.252 mmol) was dispersed in 15 mL of H_2O and stirred at room temperature until complete dissolution. The resulting solution was then supplemented with aqueous EDC·HCl (2.44 mL, 0.504 mmol) and s-NHS (2.43 mL, 0.253 mmol), and the mixture was stirred for additional 40 minutes. MES·H_2O (40.3 mg) and an aqueous solution of methionine ethyl ester hydrochloride (Met-OEt; 2 mL, 0.504 mmol) were added. The pH was carefully adjusted to 6.0 using freshly prepared 1 M NaOH. A clear solution was obtained, which was left stirring overnight at room temperature. After approximately 22 hours, the reaction was brought to pH 7 with 1.0 M NaOH and subjected to dialysis, first against a 342 mM NaCl solution and subsequently against H_2O. The dialyzed solution was frozen and freeze-dried to afford a white solid (67.12 mg, 61% yield).

^{1}H-NMR (400 MHz, D_2O, 25°C): δ_{DSS} = 4.54 ppm (H-1, GlcNAc), 4.45 ppm (H-1, GlcA), 4.25 ppm (2H, q, CH_2 (H1′, Met-OEt)), 4.00-3.20 ppm (H-2, H-3, H-4, H-5 GlcA; H-2, H-3, H-4, H-5, H-6 GlcNAc), 2.61 ppm (2H, m, CH_2 (H4, Met-OEt)), 2.10 ppm (2H, m, CH_2 (H3, Met-OEt)), 2.01 ppm (NHAc, GlcNAc), 1.28 ppm (3H, t, CH_3 (H2′, Met-OEt)).

2.2.8 Deprotection of HA-Met-OEt (8)

HA-Met-OEt (60.26 mg, 0.137 mmol) was treated with 15 mL of 1.0 M NaOH solution to adjust the pH to 12. The solution was stirred for 6 h at room temperature and then 1 M HCl was added until neutralization. Dialysis and subsequent freeze-drying yielded a white solid (44.74 mg, yield = 80%).

^{1}H-NMR (400 MHz, D_2O, 25°C): δ_{DSS} = 4.54 ppm (H-1, GlcNAc), 4.45 ppm (H-1, GlcA), 4.00-3.20 ppm (H-2, H-3, H-4, H-5 GlcA; H-2, H-3, H-4, H-5, H-6 GlcNAc), 2.56 ppm (2H, m, CH_2 (H4, Met-OH)), 2.11 ppm (2H, m, CH_2 (H3, Met-OH)), 2.01 ppm (NHAc, GlcNAc).

2.2.9 Bioconjugation of Leu-OMe with HA (11)

HA (101.35 mg, 0.253 mmol) was dispersed in 15 mL of H_2O and stirred at room temperature until complete dissolution. The resulting solution was then supplemented with aqueous EDC·HCl (2.42 mL, 0.505 mmol) and s-NHS (2.44 mL, 0.253 mmol), and the mixture was stirred for additional 40 minutes. MES·H_2O (42.8 mg) and an aqueous solution of leucine methyl ester hydrochloride (Leu-OMe; 2 mL, 0.505 mmol) were added. The pH was carefully adjusted to 6.0 using freshly prepared 1 M NaOH. A clear solution was obtained, which was left stirring overnight at room temperature. After approximately 22 hours, the reaction was brought to pH 7 with 1.0 M NaOH and subjected to dialysis, first against a 342 mM NaCl solution and subsequently against H_2O. The dialyzed solution was frozen and freeze-dried to afford a white solid (71.23 mg, 60% yield).

^{1}H-NMR (400 MHz, D_2O, 25°C): δ_{DSS} = 4.54 ppm (H-1, GlcNAc), 4.45 ppm (H-1, GlcA), 3.73 ppm (3H, s, CH_3 (H1', Leu-OMe)); 4.00-3.20 ppm (H-2, H-3, H-4, H-5 GlcA; H-2, H-3, H-4, H-5, H-6 GlcNAc), 2.01 ppm (NHAc, GlcNAc), 0.91 ppm (6H, d, CH_3, (H5 + H6, Leu-OMe)).

2.2.10 Deprotection of HA-Leu-OMe (12-i)

HA-Leu-OMe (69.85 mg, 0.145 mmol) was treated with 15 mL of 1.0 M NaOH solution to adjust pH to 12. The solution was stirred for 6 h at room temperature and then 1 M HCl was added until neutralization. Dialysis and subsequent freeze-drying yielded a white solid (51.50 mg, yield = 78%).

^{1}H-NMR (400 MHz, D_2O, 25°C): δ_{DSS} = 4.54 ppm (H-1, GlcNAc), 4.45 ppm (H-1, GlcA), 4.00-3.20 ppm (H-2, H-3, H-4, H-5 GlcA; H-2, H-3, H-4, H-5, H-6 GlcNAc), 2.01 ppm (NHAc, GlcNAc), 0.91 ppm (6H, d, CH_3, (H5 + H6, Leu-OH)).

2.2.11 Bioconjugation of Leu-OH with HA (12-ii)

HA (100.60 mg, 0.251 mmol) was dispersed in 15 mL of H_2O and stirred at room temperature until complete dissolution. The resulting solution was then supplemented with aqueous EDC·HCl (2.48 mL, 0.502 mmol) and s-NHS (2.43 mL, 0.251 mmol), and the mixture was stirred for additional 40 minutes. MES·H_2O (41.51 mg) and an aqueous solution of leucine (Leu-OH; 3 mL, 0.502 mmol) were added. The pH was carefully adjusted to 6.0 using freshly prepared 1 M NaOH. A clear solution was obtained, which was left stirring overnight at room temperature. After approximately 22 hours, the reaction was brought to pH 7 with 1.0 M NaOH and subjected to dialysis, first against a 342 mM NaCl solution and subsequently against H_2O. The dialyzed solution was frozen and freeze-dried to afford a white solid (77.35 mg, 78% yield).

^{1}H-NMR (400 MHz, D_2O, 25°C): δ_{DSS} = 4.54 ppm (H-1, GlcNAc), 4.45 ppm (H-1, GlcA), 4.00-3.20 ppm (H-2, H-3, H-4, H-5 GlcA; H-2, H-3, H-4, H-5, H-6 GlcNAc), 2.01 ppm (NHAc, GlcNAc), 1.65 ppm (1H, m, C*H* (H4, Leu-OH)), 0.92 ppm (6H, d, CH_3, (H5 + H6, Leu-OH)).

2.2.12 Bioconjugation of Phe-OH with HA (14)

HA (100.90 mg, 0.252 mmol) was dispersed in 15 mL of H_2O and stirred at room temperature until complete dissolution. The resulting solution was then supplemented with aqueous EDC·HCl (2.49 mL, 0.504 mmol) and s-NHS (2.44 mL, 0.252 mmol), and the mixture was stirred for additional 40 minutes. MES·H_2O (43.9 mg) and an aqueous solution of phenylalanine (Phe-OH; 3 mL, 0.504 mmol) were added. The pH was carefully adjusted to 6.0 using freshly prepared 1 M NaOH. A clear solution was obtained, which was left stirring overnight at room temperature. After approximately 22 hours, the reaction was brought to pH 7 with 1.0 M NaOH and subjected to dialysis, first against a 342 mM NaCl solution and subsequently against H_2O. The dialyzed solution was frozen and freeze-dried to afford a white solid (86.77 mg, 81% yield).

^{1}H-NMR (400 MHz, D_2O, 25°C): δ_{DSS} = 7.33 ppm (m, 5H, aromatic protons, Phe-OH); 4.54 ppm (H-1, GlcNAc), 4.45 ppm (H-1, GlcA), 4.00-3.20 ppm (H-2, H-3, H-4, H-5 GlcA; H-2, H-3, H-4, H-5, H-6 GlcNAc), 2.01 ppm (NHAc, GlcNAc).

3. Results and Discussion

3.1 Semi-synthesis of HA-Val-OH

To obtain HA-Val-OH bioconjugates, two different valine forms were employed**,** namely valine L-methyl ester hydrochloride (Val-OMe) and free L-valine, enabling a direct comparison of the bioconjugation efficiency and the degree of substitution (DS) achieved on the hyaluronic acid backbone. In both cases, valine was covalently conjugated to hyaluronic acid via carbodiimide-mediated amidation. The carboxyl groups of HA were activated using the EDC/s-NHS coupling system, allowing nucleophilic attack by the valine amino group and the formation of a stable amide bond.

The first strategy involved the use of Val-OMe and was carried out in aqueous MES buffer through activation of the GlcA carboxylate (Scheme 1). After addition of the amino acid, the reaction mixture was adjusted to pH 6 with a freshly prepared 1.0 M NaOH solution and stirred overnight at room temperature. The crude product was then neutralized, purified by dialysis and finally freeze-dried to afford the HA-Val-OMe bioconjugate (**derivative 4**), which was obtained with a 67 % yield.

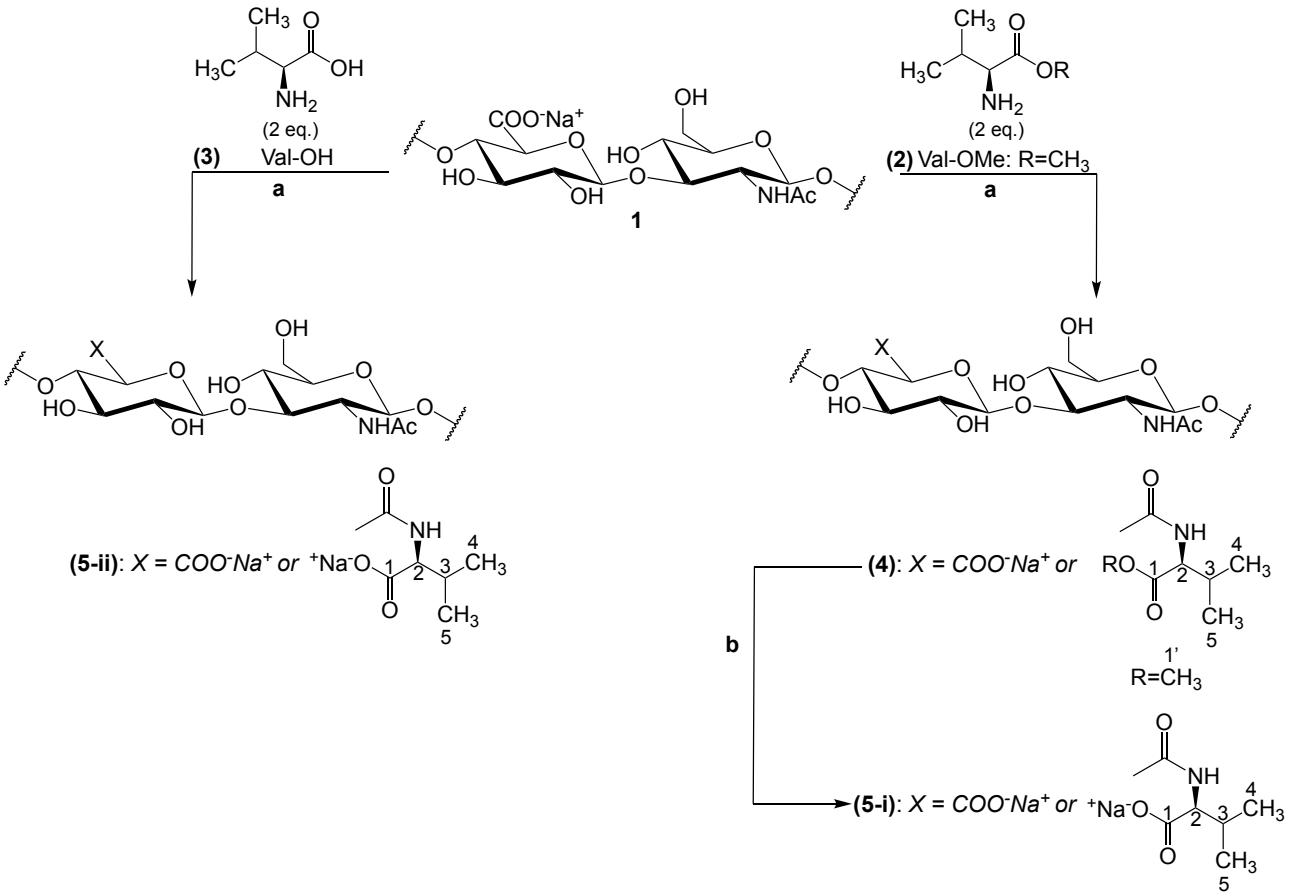

Scheme 1. Semi-synthesis of derivative HA-Val-OH. a: EDC·HCl, s-NHS, MES, H_2O, pH = 6, room temperature, overnight; b: NaOH, H_2O, pH = 12, RT, 6h.

The successful bioconjugation of **derivative 4** was confirmed by ^{1}H-NMR analysis (Figure 1). In addition to the characteristic resonances of the HA backbone, including the broad signals of the sugar ring protons in the 4.00-3.20 ppm region, a singlet corresponding to the *N*-acetyl methyl group of the GlcNAc unit was observed at δ_{DSS} = 2.01 ppm. New resonances attributable to the valine methyl ester moiety were clearly detected. In particular, a signal at δ_{DSS} = 3.74 ppm was assigned to the methyl group of the ester (C*H*$_3$, Val-OMe). Although this resonance partially overlaps with the HA signals in the 3.2-4.0 ppm region, it remains distinguishable from the native HA spectrum.

A multiplet at δ_{DSS} = 4.15 ppm was assigned to the methine proton (C*H*) adjacent to the amino group of valine. Moreover, a doublet at δ_{DSS} = 0.93 ppm, integrating for six protons, was attributed to the two methyl groups of the isopropyl side chain of valine, confirming the successful conjugation of Val-OMe onto the HA backbone.

The DS was 51%, as calculated according to Equation 1:

$$DS = \frac{ICH_{3\ (Val-OMe)}/6}{ICH_{3\ (GlcNAc)}/3} \qquad (1)$$

$ICH_{3\ (Val-OMe)}$ represents the integral of the six equivalent protons of the two methyl groups of the valine isopropyl moiety (0.93 ppm), while $ICH_{3\ (GlcNAc)}$ corresponds to the integral of the acetyl methyl protons of the GlcNAc unit (δ_{DSS} = 2.01 ppm).

The main ^{1}H-NMR signal assignments are summarized in Table 1.

Table 1. ^{1}H-NMR chemical shift assignments of **derivative 4**.

Assignment	**^{1}H δ_{DSS} (ppm)**
1 (GlcNAc)	4.54
1 (GlcA)	4.45
2-5 (GlcA)	4.0-3.20
2-6 (GlcNAc)	4.0-3.20
2	4.15
1’	3.74
NHAc (GlcNAc)	2.01
4+5	0.93

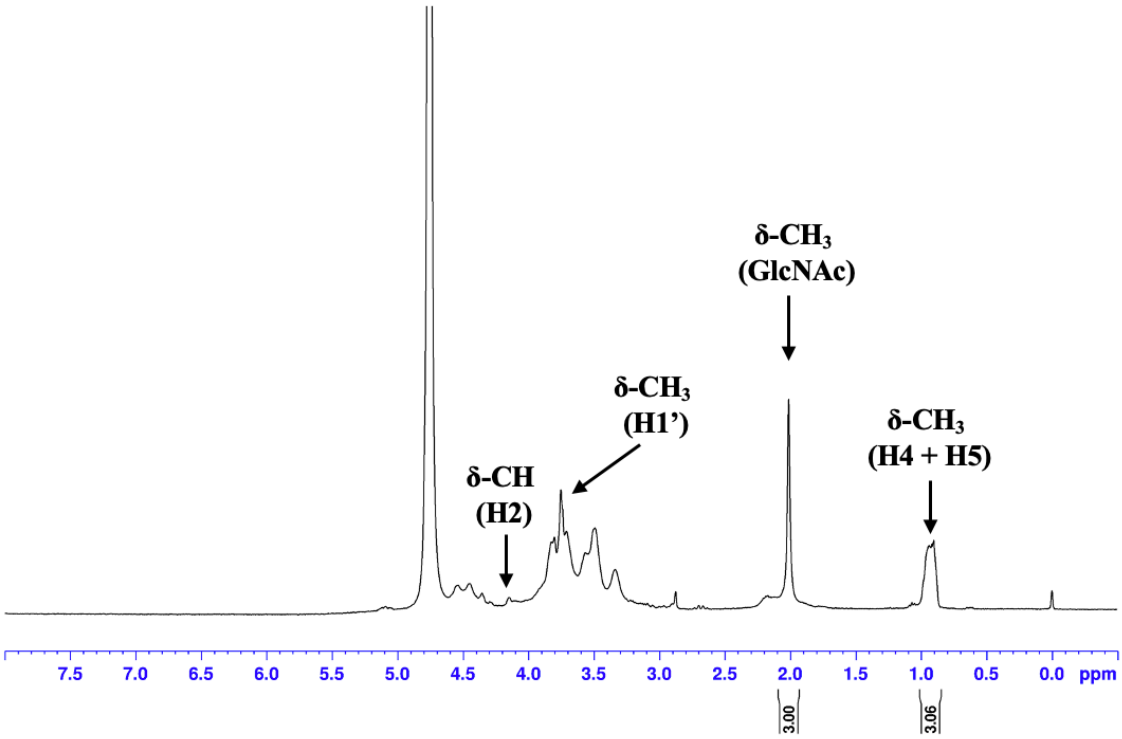

Figure 1. ^{1}H-NMR spectrum of **derivative 4** (400 MHz, D_2O, 25°C).

Derivative 4 was subsequently subjected to saponification by treatment with a 1.0 M NaOH solution to adjust the pH to 12. The reaction mixture was then neutralized, dialyzed, and finally freeze-dried to obtain **derivative 5-i** (Scheme 1) with a yield of 63%.

The successful removal of the methyl ester group was confirmed by ^{1}H-NMR analysis (Figure S1). In comparison with **derivative 4**, the characteristic singlet of the ester methyl group at δ_{DSS} = 3.74 ppm was no longer observed, indicating complete saponification of the Val-OMe moieties. The remaining valine signals were still detectable, including the methine proton adjacent to the amino group at δ_{DSS} = 4.15 ppm and the doublet corresponding to the two isopropyl methyl groups at δ_{DSS} = 0.94 ppm, confirming the preservation of the valine side chain after hydrolysis.

The main ^{1}H-NMR signal assignments are summarized in Table 2.

Table 2. ^{1}H-NMR chemical shift assignments of **derivative 5-i**.

Assignment	**^{1}H δ_{DSS} (ppm)**
1 (GlcNAc)	4.54
1 (GlcA)	4.45
2-5 (GlcA)	4.0-3.20
2-6 (GlcNAc)	4.0-3.20
2	4.15
NHAc (GlcNAc)	2.01
4+5	0.93

Successful deprotection of Val-OMe was supported by ATR-FTIR spectroscopy through the disappearance of the ester carbonyl band at ~1739 cm^{-1} (Figure S2), in agreement with literature IR data reported for aliphatic ester carbonyl stretching vibrations [6].

Compared to commercial Val-OMe (blue curve), the ATR-FTIR spectrum of **derivative 5-i** (red curve) no longer showed the characteristic ester carbonyl signal. This observation, together with the appearance of the carboxylate doublet at 1604 and 1405 cm^{-1}, assigned to the asymmetric and symmetric stretching vibrations of COO^{-} groups [7], was consistent with ester hydrolysis during deprotection.

Moreover, in comparison with the ATR-FTIR spectrum of hyaluronic acid (black curve), **derivative 5-i** displayed changes in the aliphatic C-H stretching region, suggesting the introduction of additional alkyl moieties associated with valine residues upon conjugation. The main IR band assignments are summarized in Table 3.

Table 3. IR bands assignments for HA, **derivative 5-i** and commercial Val-OMe.

IR assignments HA (black curve)	**Wavenumber (cm^{-1})**	**IR assignments Derivative 5-i (red curve)**	**Wavenumber (cm^{-1})**	**IR assignments Val-OMe (blue curve)**	**Wavenumber (cm^{-1})**
ν O-H (*)	3284	ν O-H (*)	3267	ν C-H (aliphatic)(*)	2973–2820
ν C-H (aliphatic) (*)	2876	ν C-H (aliphatic)(*)	2897	ν C=O (Ester) (*)	1739
ν C=O (Amide I) (*)	1603	ν_{AS} (COO^-)(*)	1604	δ (N-H) (*)	1595
δ N-H + ν N-C (Amide II) (*)	1540	δ N-H + ν N-C (Amide II) (*)	1558	δ (N-H) + δ CH_3(*)	1435
δ C-H (*)	1377	ν_S (COO^-)(*)	1405		
ν C-O-C (*)	1146	ν C-O-C(*)	1148		
ν C-O (*)	1014				

The second strategy to obtain HA-Val-OH bioconjugate involved the use of free valine (Val-OH) and was carried out using the same EDC/s-NHS-mediated coupling approach (Scheme 1). After an over-night reaction, the mixture was neutralized, purified by dialysis, and freeze-dried to afford **derivative 5-ii** with a yield of 77%.

The successful bioconjugation of **derivative 5-ii** was confirmed by ^{1}H-NMR analysis (Figure 2). In addition to the characteristic resonances of the HA backbone, new signals attributable to the valine residue were observed. In particular, a doublet at δ_{DSS} = 0.94 ppm, integrating for six protons, was assigned to the two methyl groups of the isopropyl side chain of valine, while a multiplet at δ_{DSS} = 4.11 ppm corresponded to the methine proton (CH) adjacent to the amino group. Moreover, a multiplet at δ_{DSS} = 2.88 ppm was attributed to the methine proton of the isopropyl group, further confirming the presence of valine grafted onto the HA backbone.

The resulting degree of substitution (DS) was 17%, as calculated according to Equation 2:

$$DS = \frac{ICH_{3\,(Val-OH)}/6}{ICH_{3\,(GlcNAc)}/3} \quad (2)$$

$ICH_{3\,(Val-OH)}$ represents the integral of the six equivalent protons of the two methyl groups of the valine isopropyl moiety (0.94 ppm), while $ICH_{3\,(GlcNAc)}$ corresponds to the integral of the acetyl methyl protons of the GlcNAc unit (δ_{DSS} = 2.01 ppm).

The main ^{1}H-NMR signal assignments are summarized in Table 4.

Table 4. [1]H-NMR chemical shift assignments of **derivative 5-ii**.

Assignment	^1H δ_{DSS} (ppm)
1 (GlcNAc)	4.54
1 (GlcA)	4.45
2-5 (GlcA)	4.0-3.20
2-6 (GlcNAc)	4.0-3.20
2	4.11
NHAc (GlcNAc)	2.01
3	2.88
4+5	0.94

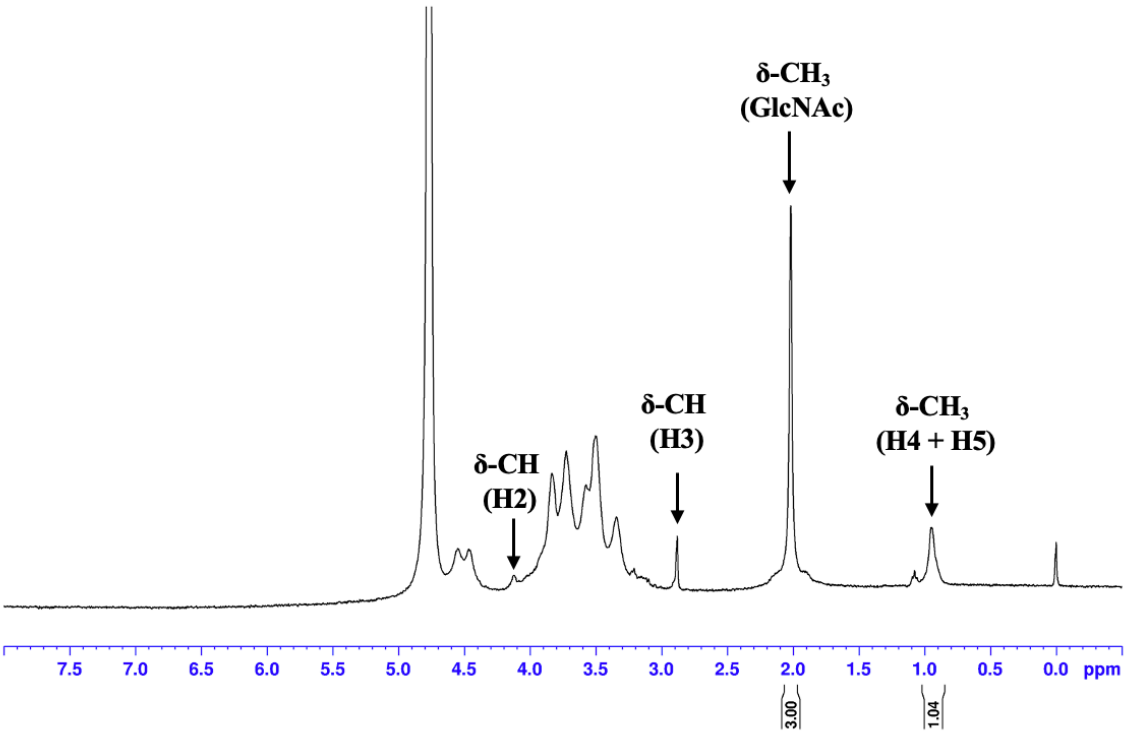

Figure 2. [1]H-NMR spectrum of **derivative 5-ii** (400 MHz, D_2O, 25°C).

The successful conjugation of valine to hyaluronic acid was further supported by ATR-FTIR analysis (Figure S3).

Compared to native hyaluronic acid (black curve), the ATR-FTIR spectrum of **derivative 5-ii** (red curve) showed noticeable changes in the spectral profile, particularly in the aliphatic C-H stretching region and in the N-H-related bands, consistent with the contribution of the valine isopropyl side chain [8].

Slight changes in the Amide I and Amide II regions were observed, which are consistent with the presence of additional amide linkages. However, due to overlap with native HA amide bands, ATR-FTIR provides complementary evidence, while the conjugation was primarily confirmed by ^{1}H-NMR.

For comparison, the ATR-FTIR spectrum of commercial Val-OH (blue curve) is also reported as a reference, highlighting the characteristic vibrational regions of free valine, particularly those associated with aliphatic C-H stretching and carboxylate vibrations. The main IR band assignments are reported in Table 5.

Table 5. IR bands assignments for **derivative 5-ii** and commercial Val-OH.

IR assignments Derivative 5-ii (red curve)	**Wavenumber (cm^{-1})**	**IR assignments Val-OH (blue curve)**	**Wavenumber (cm^{-1})**
ν O-H (*)	3280	ν C-H (aliphatic) (*)	2933
ν C-H (aliphatic) (*)	2882	ν_{AS} (COO^-) (*)	1579
ν C=O (Amide I) (*)	1608	δ (N-H) (*)	1563
δ N-H + ν N-C (Amide II) (*)	1535	δ (N-H) + δ CH (*)	1424
ν_S (COO^-) (*)	1405	ν_S (COO^-) (*)	1394
ν C-O-C (*)	1151		
ν C-O (*)	1030		

3.2 Semi-synthesis of HA-Met-OH

To obtain HA-Met-OH bioconjugates, L-methionine ethyl ester hydrochloride (Met-OEt) was employed as the amino acid source, and a single conjugation strategy was adopted.

Met-OEt was covalently conjugated to HA via carbodiimide-mediated amidation. The carboxyl groups of HA were activated using the EDC/s-NHS coupling system, enabling the nucleophilic attack of the amino group of Met-OEt and the formation of a stable amide bond.

The conjugation reaction was carried out in aqueous MES buffer through activation of the GlcA carboxylate groups (Scheme 2). After addition of methionine ethyl ester hydrochloride, the reaction mixture was adjusted to pH 6 using a freshly prepared 1.0 M NaOH solution and stirred overnight at room temperature. The reaction was then neutralized, purified by dialysis and finally freeze-dried to obtain the **derivative 7,** with a yield of 61%.

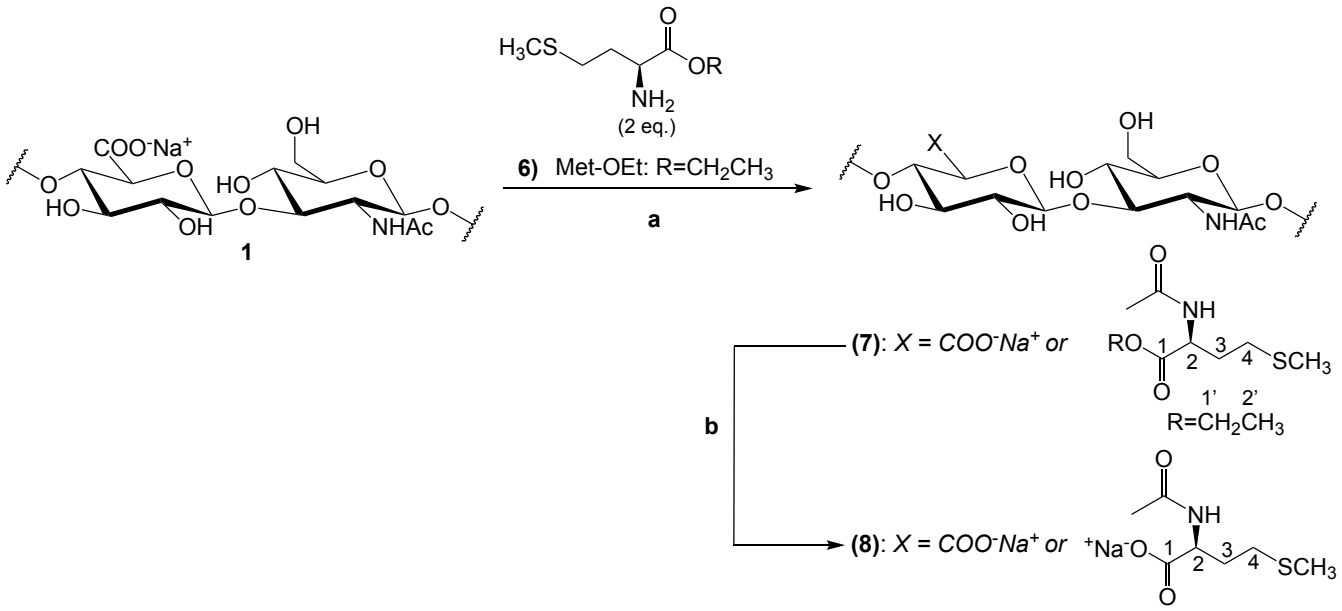

Scheme 2. Semi-synthesis of derivative HA-Met-OH. a: EDC·HCl, s-NHS, MES, H_2O, pH = 6, room temperature, overnight; b: NaOH, H_2O, pH = 12, RT, 6h.

The successful bioconjugation of **derivative 7** was confirmed by ^{1}H-NMR analysis (Figure 3). In addition to the characteristic resonances of the HA backbone, new resonances attributable to the methionine ethyl ester moiety were clearly detected. In particular, a signal at δ_{DSS} = 1.28 ppm was assigned to the methyl group of the ethyl ester, while signals at δ_{DSS} = 2.61 ppm and δ_{DSS} = 2.10 ppm were assigned to the methylene protons of the methionine side chain (H4 and H3, respectively), confirming the presence of methionine grafted onto the HA backbone.

The DS was 31%, as calculated according to Equation 3:

$$DS = \frac{ICH_{3\ (Met-OEt)}}{\left[ICH_{3\ (GlcNAc)} + ICH_{2\ (Met-OEt)}\right] + \frac{2}{3}ICH_{3\ (Met-OEt)}} \qquad (3)$$

Where $ICH_{3\ (Met-OEt)}$ is the integral of the methyl protons of the ethyl ester group of methionine (δ_{DSS} = 1.28 ppm), $CH_{3\ (GlcNAc)}$ is the integral of the *N*-acetyl methyl protons of the GlcNAc unit of hyaluronic acid (δ_{DSS} = 2.01 ppm) and $CH_{2\ (Met-OEt)}$ is the integral of the methionine methylene protons assigned as H3 (δ_{DSS} = 2.10 ppm).

The main ^{1}H-NMR signal assignments are summarized in Table 6.

Table 6. ^{1}H-NMR chemical shift assignments of **derivative 7**.

Assignment	**^{1}H δ_{DSS} (ppm)**
1 (GlcNAc)	4.54
1 (GlcA)	4.45
2-5 (GlcA)	4.0-3.20
2-6 (GlcNAc)	4.0-3.20
1’	4.25
NHAc (GlcNAc)	2.01
4	2.61
3	2.10
2’	1.28

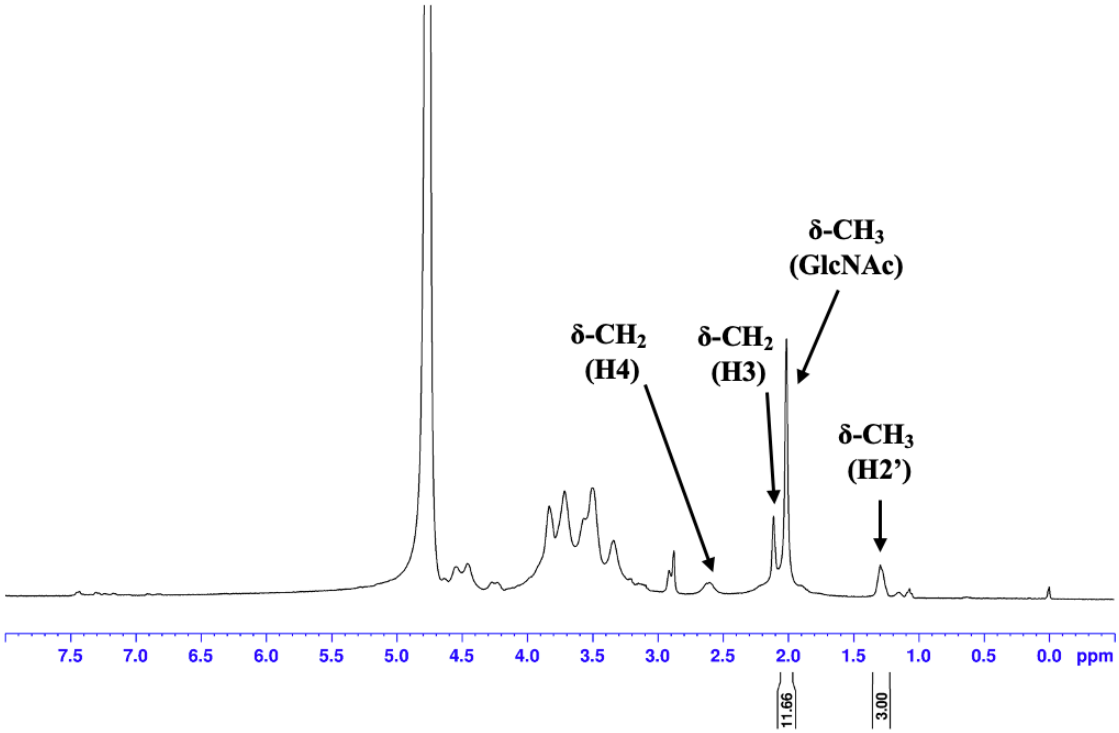

Figure 3. ^{1}H-NMR spectrum of **derivative 7** (400 MHz, D_2O, 25°C).

Derivative 7 was subsequently subjected to saponification by treatment with a 1.0 M NaOH solution to adjust the pH to 12. The reaction mixture was then neutralized, dialyzed, and finally freeze-dried to obtain **derivative 8** (Scheme 2) with a yield of 80%.

The successful removal of the ethyl ester group was confirmed by ^{1}H-NMR analysis (Figure S4). Compared to **derivative 7**, the characteristic signals of the ethyl ester moiety, previously observed at δ_{DSS} = 1.28 ppm and δ_{DSS} = 4.25 ppm, were no longer detected, indicating complete saponification of the Met-OEt groups. The remaining methionine signals were still observed, including resonances at δ_{DSS} = 2.56 ppm and δ_{DSS} = 2.11 ppm, assigned to the methylene protons H4 and H3 of the methionine side chain, respectively. The *N*-acetyl methyl signal of the GlcNAc unit was retained at δ_{DSS} = 2.01 ppm, confirming the presence of the HA backbone after hydrolysis.

The main ^{1}H-NMR signal assignments are summarized in Table 7.

Table 7. ^{1}H-NMR chemical shift assignments of **derivative 8**.

Assignment	^{1}H δ_{DSS} (ppm)
1 (GlcNAc)	4.54
1 (GlcA)	4.45
2-5 (GlcA)	4.0-3.20
2-6 (GlcNAc)	4.0-3.20
NHAc (GlcNAc)	2.01
4	2.56
3	2.11

ATR-FTIR analysis was performed to compare native HA, **derivative 8** and commercial Met-OEt (Figure S5); the main band assignments are summarized in Table 8, while the characteristic features of native HA have been discussed previously.

The ATR-FTIR spectrum of **derivative 8** (red curve) closely resembles that of native HA (black curve). Due to the strong overlap of HA bands in the fingerprint region, no distinct new absorptions attributable to methionine could be clearly identified.

Moreover, the ester carbonyl absorption at ~1737 cm^{-1}, clearly visible in the spectrum of commercial Met-OEt (blue curve), is absent in **derivative 8**, indicating hydrolysis of the ethyl ester group. However, successful methionine conjugation was primarily confirmed by ^{1}H-NMR analysis.

Table 8. IR bands assignments for **derivative 8** and commercial Met-OEt.

IR assignments Derivative 8 (red curve)	**Wavenumber (cm^{-1})**	**IR assignments Met-OEt (blue curve)**	**Wavenumber (cm^{-1})**
ν O-H (*)	3323	ν C-H (aliphatic) (*)	2885
ν C-H (aliphatic) (*)	2892	ν C=O (Ester) (*)	1737
ν C=O (Amide I) (*)	1602	δ (N-H) (*)	1577
δ N-H + ν C-N (Amide II)(*)	1556	ν C-S (*)	667
δ C-H (*)	1412		
ν C-O-C (*)	1151		
ν C-O (*)	1038		

3.3 Semi-synthesis of HA-Leu-OH

To obtain HA-Leu-OH bioconjugates, L-leucine methyl ester and free L-leucine were used. In both cases, leucine was covalently conjugated to hyaluronic acid via carbodiimide-mediated amidation. The carboxyl groups of HA were activated using the EDC/s-NHS chemistry, allowing nucleophilic attack by the leucine amino group and the formation of a stable amide bond.

The first strategy involved the use of Leu-OMe and was carried out in aqueous MES buffer through activation of the GlcA carboxylate (Scheme 3). After addition of the amino acid, the reaction mixture was adjusted to pH 6 with a freshly prepared 1.0 M NaOH solution and stirred overnight at room temperature. The crude product was then neutralized, purified by dialysis and finally freeze-dried to afford the HA-Leu-OMe bioconjugate (**derivative 11**), which was obtained with a 60% yield.

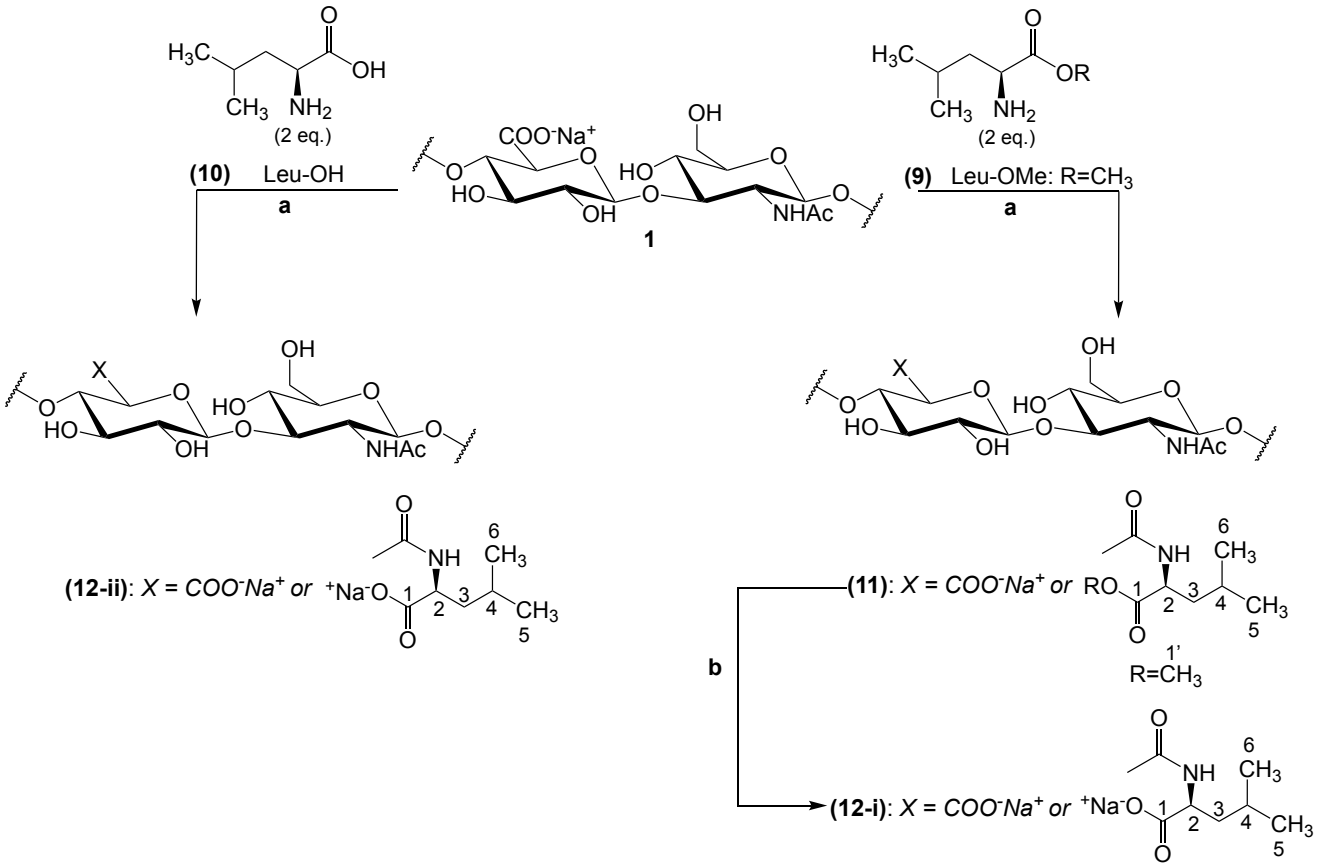

Scheme 3. Semi-synthesis of derivative HA-Leu-OH. a: EDC·HCl, s-NHS, MES, H_2O, pH = 6, room temperature, overnight; b: NaOH, H_2O, pH = 12, RT, 6h.

The successful bioconjugation of **derivative 11** was confirmed by ^{1}H-NMR analysis (Figure 4). In addition to the characteristic resonances of the HA backbone, new resonances attributable to the Leu-

OMe moiety were clearly detected. In particular, a signal at δ_{DSS} = 3.73 ppm, assigned to the methoxy group of the methyl ester (H1'), was observed. Moreover, a signal at δ_{DSS} = 0.91 ppm, attributed to the two equivalent methyl groups (6H, H5 + H6) of the isobutyl side chain, further confirmed the presence of leucine units covalently bound to the HA backbone.

The DS of **derivative 11** was 63%, as calculated according to Equation 4:

$$DS = \frac{ICH_{3\ (Leu-OMe)}/6}{ICH_{3\ (GlcNAc)}/3} \quad (4)$$

where $ICH_{3\ (Leu-OMe)}$ corresponds to the integral of the signal at δ_{DSS} = 0.91 ppm, assigned to the two equivalent methyl groups of the leucine side chain, while $ICH_{3\ (GlcNAc)}$ corresponds to the integral of the signal at δ_{DSS} = 2.01 ppm, attributed to the *N*-acetyl methyl group of the GlcNAc unit.

The main ^{1}H-NMR signal assignments are summarized in Table 9.

Table 9. ^{1}H-NMR chemical shift assignments of **derivative 11**.

Assignment	**^{1}H δ_{DSS} (ppm)**
1 (GlcNAc)	4.54
1 (GlcA)	4.45
2-5 (GlcA)	4.0-3.20
2-6 (GlcNAc)	4.0-3.20
NHAc (GlcNAc)	2.01
1'	3.73
5+6	0.91

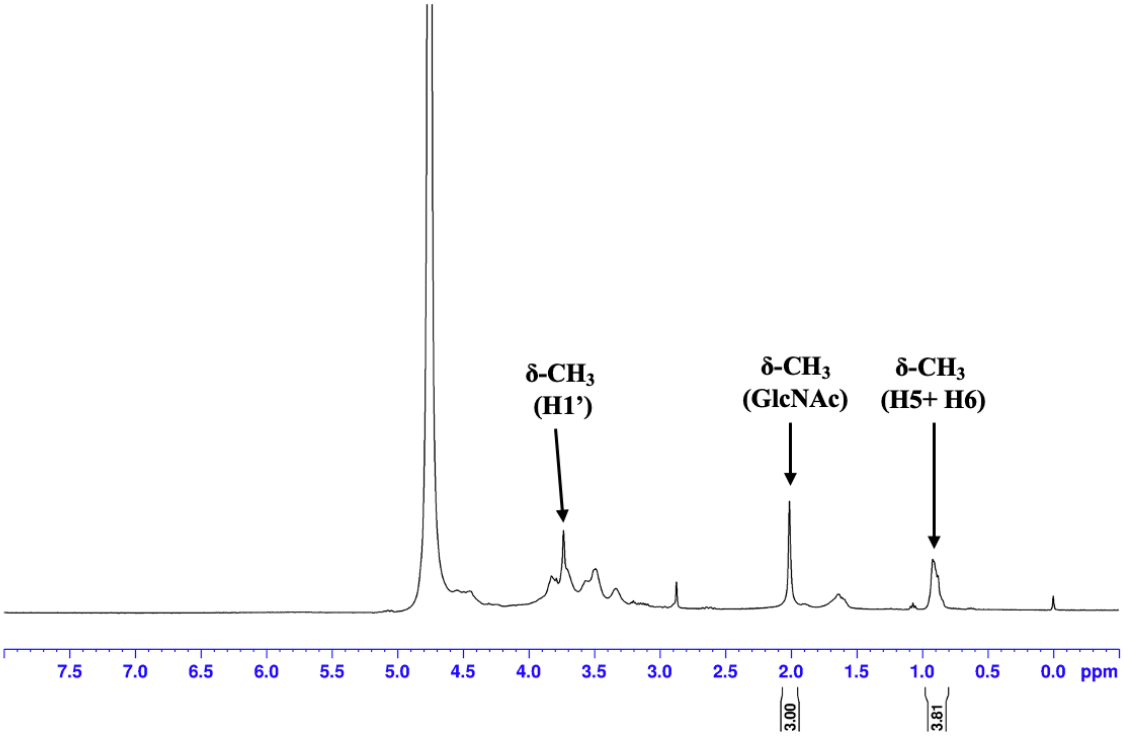

Figure 4. ^{1}H-NMR spectrum of **derivative 11** (400 MHz, D_2O, 25°C).

Derivative 11 was subsequently subjected to saponification by treatment with a 1.0 M NaOH solution to adjust the pH to 12, in order to remove the methyl ester protecting group. The reaction mixture was then neutralized, dialyzed, and finally freeze-dried to obtain **derivative 12-i** with a yield of 78% (Scheme 3).

The successful removal of the methyl ester group was confirmed by ^{1}H-NMR analysis (Figure S6). The disappearance of the methoxy ester signal at δ_{DSS} = 3.73 ppm confirmed the deprotection of the methyl ester group. In addition, the persistence of the characteristic leucine signals, including the resonance at δ_{DSS} = 0.91 ppm, assigned to the two equivalent methyl groups of the isobutyl side chain, confirmed the preservation of the leucine structure after hydrolysis.

The main ^{1}H-NMR signal assignments are summarized in Table 10.

Table 10. ^{1}H-NMR chemical shift assignments of **derivative 12-i**.

Assignment	^{1}H δ_{DSS} (ppm)
1 (GlcNAc)	4.54
1 (GlcA)	4.45
2-5 (GlcA)	4.0-3.20
2-6 (GlcNAc)	4.0-3.20
NHAc (GlcNAc)	2.01
5+6	0.91

Further confirmation of successful bioconjugation and subsequent saponification was obtained by ATR-FTIR analysis of HA-Leu-OH (**derivative 12-i**) and commercial Leu-OMe spectra, shown in Figure S7. The main IR band assignments are summarized in Table 11.

The spectrum of **derivative 12-i** (red curve) displays the signals related to the polysaccharide backbone of HA and a modification of the band shape due to C-H bending, which could be attributed to the presence of the six protons of the isobutyl side chain of leucine.

Successful deprotection was supported by the absence of the ester carbonyl band at ~1733 cm^{-1} in **derivative 12-i**, whereas this band is clearly present in the spectrum of commercial Leu-OMe (blue curve).

Table 11. IR bands assignments for **derivative 12-i** and commercial Leu-OMe.

IR assignments Derivative 12-i (red curve)	Wavenumber (cm^{-1})	IR assignments Leu-OMe (blue curve)	Wavenumber (cm^{-1})
ν O-H (*)	3304	ν C-H (aliphatic) (*)	2858
ν C-H (aliphatic) (*)	2884	ν C=O (Ester) (*)	1733
ν C=O (Amide I) (*)	1614	δ (N-H) (*)	1594
δ N-H + ν N-C (Amide II)(*)	1552	ν C-N (*)	1031
δ C-H (*)	1376		
ν C-O-C (*)	1146		
ν C-O (*)	1034		

The second strategy to obtain HA-Leu-OH bioconjugate involved the use of free leucine (Leu-OH) and was carried out using the same EDC/s-NHS-mediated coupling approach (Scheme 3). After an overnight reaction, the mixture was neutralized, purified by dialysis, and freeze-dried to obtain **derivative 12-ii** with a yield of 78%.

The successful bioconjugation of **derivative 12-ii** was confirmed by ^{1}H-NMR analysis (Figure 5). In addition to the characteristic resonances of the HA backbone, new signals attributable to the leucine residue were detected. In particular, a signal at δ_{DSS} = 1.65 ppm was assigned to the methine proton (C*H*, H4) of the isobutyl side chain, which is adjacent to the two methyl groups. Moreover, a signal at δ_{DSS} = 0.92 ppm, integrating for six protons, was assigned to the two equivalent methyl groups of the isobutyl side chain, confirming the successful grafting of leucine onto the HA backbone.

The DS was 10 %, as calculated according to Equation 5:

$$DS = \frac{ICH_{3\ (Leu-OH)}/6}{ICH_{3\ (GlcNAc)}/3} \quad (5)$$

where $ICH_{3\ (Leu-OH)}$ corresponds to the integral of the signal at δ_{DSS} = 0.92 ppm, assigned to the two equivalent methyl groups of the leucine side chain, while $ICH_{3\ (GlcNAc)}$ corresponds to the integral of the signal at δ_{DSS} = 2.01 ppm, attributed to the *N*-acetyl methyl group of the GlcNAc unit.

The main ^{1}H-NMR signal assignments are summarized in Table 12.

Table 12. ^{1}H-NMR chemical shift assignments of **derivative 12-ii**.

Assignment	**^{1}H δ_{DSS} (ppm)**
1 (GlcNAc)	4.54
1 (GlcA)	4.45
2-5 (GlcA)	4.0-3.20
2-6 (GlcNAc)	4.0-3.20
NHAc (GlcNAc)	2.01
4	1.65
5+6	0.92

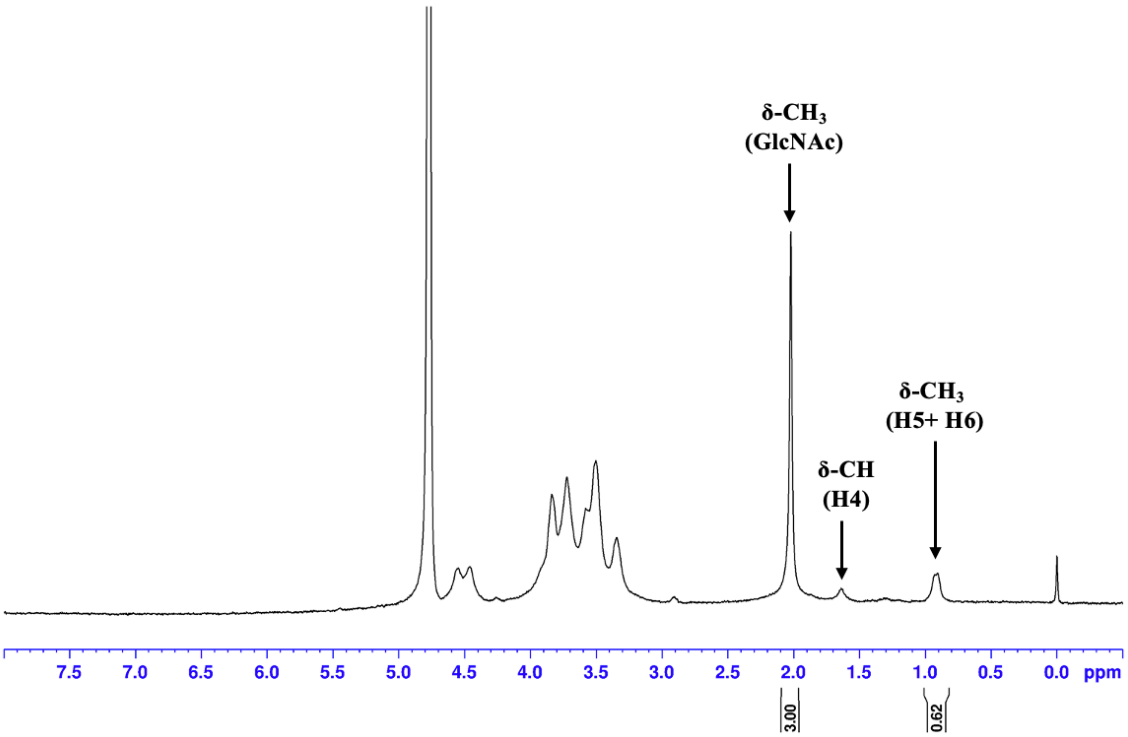

Figure 5. ^{1}H-NMR spectrum of **derivative 12-ii** (400 MHz, D_2O, 25°C).

The successful conjugation of leucine to hyaluronic acid in **derivative 12-ii** was supported by ATR-FTIR analysis (Figure S8).

Compared to commercial Leu-OH (blue curve), which showed the characteristic carboxylate bands at 1602 and 1405 cm^{-1} assigned to ν_{AS} (COO^-) and ν_S(COO^-), respectively, the spectrum of **derivative 12-ii** (red curve) showed changes in the Amide I/Amide II regions consistent with additional amide linkages.

In the spectrum of derivative 12-ii, a change in the shape of the ν (C=O) (Amide I) band at 1605 cm^{-1} and of the δ N-H + ν C-N (Amide II) band at 1553 cm^{-1} supports the formation of additional amide bonds between hyaluronic acid and leucine. The main IR band assignments are reported in Table 13.

Table 13. IR bands assignments for **derivative 12-ii** and commercial Leu-OH.

IR assignments Derivative 12-ii (red curve)	**Wavenumber (cm^{-1})**	**IR assignments Leu-OH (blue curve)**	**Wavenumber (cm^{-1})**
ν O-H (*)	3279	ν C-H (aliphatic) (*)	2868
ν C-H (aliphatic) (*)	2888	ν_{AS} (COO^-) (*)	1602
ν C=O (Amide I) (*)	1605	δ (N-H) (*)	1562
δ N-H + ν N-C (Amide II) (*)	1553	ν_S (COO^-) (*)	1405
ν_S (COO^-) (*)	1373		
ν C-O-C (*)	1072		
ν C-O (*)	1035		

3.4 Semi-synthesis of HA-Phe-OH

To obtain HA-Phe-OH bioconjugates, free L-phenylalanine **(**Phe-OH**)** was covalently conjugated to hyaluronic acid via carbodiimide-mediated amidation. The carboxyl groups of HA were activated using the EDC/s-NHS coupling system, allowing the nucleophilic attack of the amino group of phenylalanine and the formation of a stable amide bond.

The reaction was carried out in aqueous MES buffer through activation of the GlcA carboxylate (Scheme 4). After addition of the amino acid, the reaction mixture was adjusted to **pH 6** with a freshly prepared 1.0 M NaOH solution and stirred overnight at room temperature. The crude product was subsequently neutralized, purified by dialysis to remove unreacted reagents and low-molecular-weight by-products, and finally freeze-dried to obtain **derivative 14** with a yield of 81%.

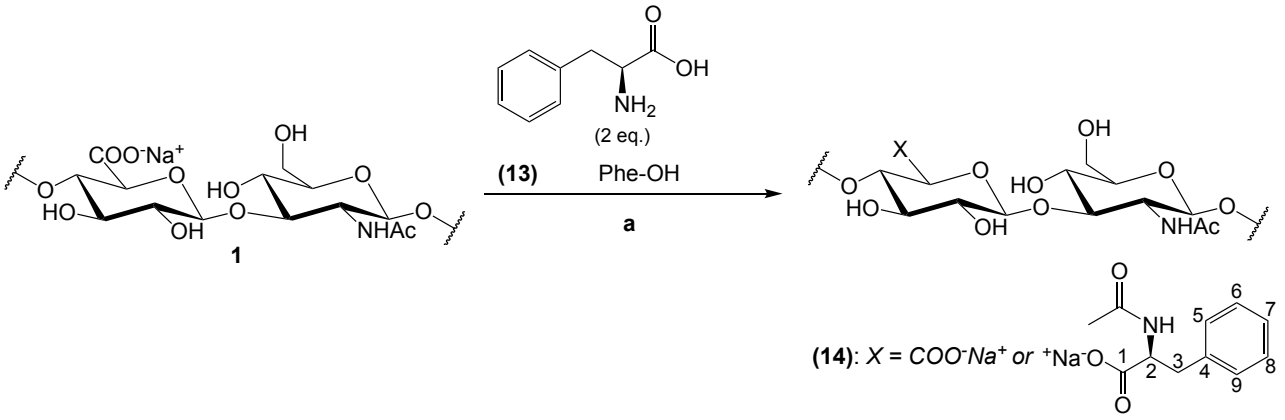

Scheme 4. Semi-synthesis of derivative HA-Phe-OH. a: EDC·HCl, s-NHS, MES, H_2O, pH = 6, room temperature, overnight.

The successful bioconjugation of **derivative 14** was confirmed by ^{1}H-NMR analysis (Figure 6). In addition to the characteristic resonances of the HA backbone, a signal at δ_{DSS} = 7.33 ppm was observed and assigned to the aromatic protons of the phenylalanine residue, confirming the coupling of phenylalanine units onto the HA backbone. The remaining aliphatic protons of phenylalanine were expected to resonate in the 2.9-4.3 ppm region, where they partially overlapped with the signals of the HA backbone and therefore could not be uniquely assigned.

The DS of **derivative 14** was 15%, as calculated according to Equation 6:

$$DS = \frac{I_{Ar(Phe-OH)}/5}{ICH_{3\ (GlcNAc)}/3} \quad (6)$$

Where $I_{Ar(Phe-OH)}$ is the integral of the aromatic proton signal of phenylalanine at δ_{DSS} = 7.33 ppm, while $ICH_{3\ (GlcNAc)}$ is the integral of the *N*-acetyl methyl group of the GlcNAc unit at δ_{DSS} = 2.01 ppm. The main ^{1}H-NMR signal assignments are summarized in Table 14.

Table 14. ^{1}H-NMR chemical shift assignments of **derivative 14**.

Assignment	**^{1}H δ_{DSS} (ppm)**
Aromatic protons	7.33
1 (GlcNAc)	4.54
1 (GlcA)	4.45
2-5 (GlcA)	4.0-3.20
2-6 (GlcNAc)	4.0-3.20
NHAc (GlcNAc)	2.01

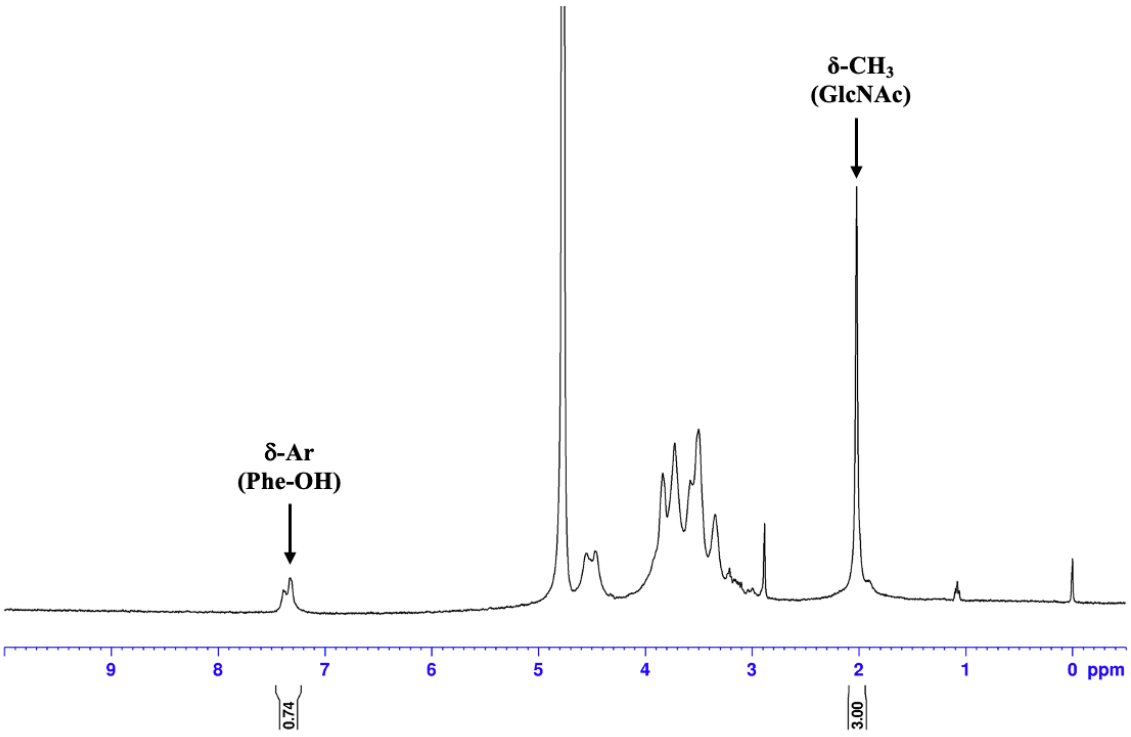

Figure 6. ^{1}H-NMR spectrum of **derivative 14** (400 MHz, D_2O, 25°C).

The successful conjugation of phenylalanine to hyaluronic acid was supported by ATR-FTIR analysis (Figure S9).

Compared to commercial Phe-OH (blue curve), which exhibited the characteristic carboxylate bands at 1623 and 1408 cm^{-1} assigned to $\nu_{AS}(COO^-)$ and $\nu_S(COO^-)$, respectively, the spectrum of the HA-Phe-OH derivative (red curve) showed changes in the Amide I and Amide II regions consistent with additional amide linkages.

In the spectrum of derivative 14, the presence of the ν(C=O) (Amide I) band at 1606 cm^{-1} and the δ N-H + ν C-N (Amide II) band at 1553 cm^{-1} supports the formation of an amide bond, due to the successful bioconjugation to HA. The main IR band assignments are reported in Table 15.

Table 15. IR bands assignments for **derivative 14** and commercial Phe-OH.

IR assignments Derivative 14 (red curve)	**Wavenumber (cm^{-1})**	**IR assignments Phe-OH (blue curve)**	**Wavenumber (cm^{-1})**
ν O-H (*)	3273	ν C-H (aliphatic) (*)	2957
ν C-H (aliphatic) (*)	2880	ν_{AS} (COO^-) (*)	1623
ν C=O (Amide I) (*)	1606	δ (N-H) (*)	1556
δ N-H + ν N-C (Amide II) (*)	1553	ν_S (COO^-) (*)	1408
ν_S (COO^-) (*)	1405		
ν C-O-C (*)	1076		
ν C-O (*)	1030		

All HA bioconjugates obtained in this chapter, along with the corresponding derivatives, are summarized in Table 16, including their yields and degrees of modification.

Table 16. Summary of the HA-bioconjugates.

Sample	Derivative	Yield	DS
HA-Val-OH	**5-i**	67%	51%
HA-Val-OH	**5-ii**	77%	17%
HA-Met-OH	**8**	61%	31%
HA-Leu-OH	**12-i**	60%	63%
HA-Leu-OH	**12-ii**	78%	10%
HA-Phe-OH	**14**	81%	15%

4. Conclusions

In this chapter, a study on the semi-synthesis and characterization of hyaluronic acid-amino acid bioconjugates was presented. A series of HA derivatives functionalized with L-valine, L-methionine, L-leucine, and L-phenylalanine were successfully prepared through carbodiimide-mediated amidation, exploiting the carboxyl groups of the glucuronic acid units along the HA backbone.

For valine and leucine, two different conjugation strategies were explored, namely the use of amino acid methyl esters followed by alkaline saponification and the direct coupling of the free amino acids. This comparative approach allowed a direct evaluation of the influence of the amino acid form on the efficiency of the bioconjugation reaction and on the resulting degree of substitution. In both cases, higher DS values were obtained when ester-protected amino acids were employed, suggesting a beneficial role of esterification in enhancing the apparent reactivity of the amino group and reducing competing side reactions during coupling. Conversely, direct conjugation of free amino acids led to lower substitution degrees, likely due to competing ionic interactions and reduced reactivity under aqueous conditions, consistent with previous reports on carbodiimide-mediated coupling in water [2].

HA-amino acid bioconjugates were thoroughly characterized by ^{1}H-NMR spectroscopy, which provided clear evidence of successful grafting through the appearance of characteristic resonances attributable to the amino acid side chains. Quantitative analysis of the NMR spectra enabled the determination of the degree of substitution for each derivative, confirming the tunability of the functionalization process depending on the amino acid structure and conjugation strategy. ATR-FTIR spectroscopy further supported the formation of new amide bonds, where applicable, the complete removal of ester protecting groups.

Overall, this chapter demonstrates the effectiveness of carbodiimide-mediated coupling as a versatile strategy for the controlled functionalization of hyaluronic acid with structurally diverse amino acids. The degree of substitution can be modulated by varying the amino acid form and the conjugation approach, enabling fine control over the chemical structure of the resulting HA derivatives.

The introduction of amino acid moieties with different side-chain characteristics represents a straightforward chemical modification that may influence intermolecular interactions and the solution properties of hyaluronic acid, while preserving the integrity of the polysaccharide backbone. These features make the synthesized HA-amino acid bioconjugates suitable for further investigation in subsequent processing and formulation studies.

Supporting Information

Design and Characterization of Hyaluronic Acid-Amino Acid Bioconjugates

Table of contents

Figure S1. ^{1}H-NMR spectrum of **derivative 5-i** (400 MHz, D_2O, 25°C).	**323**
Figure S2. ATR-FTIR spectra of HA, the **derivative 5-i** and commercial Val-OMe.	**324**
Figure S3. ATR-FTIR spectra of HA, the **derivative 5-ii** and commercial Val-OH.	**325**
Figure S4. ^{1}H-NMR spectrum of **derivative 8** (400 MHz, D_2O, 25°C).	**326**
Figure S5. ATR-FTIR spectra of HA, **derivative 8** and commercial Met-OEt.	**327**
Figure S6. ^{1}H-NMR spectrum of **derivative 12-i** (400 MHz, D_2O, 25°C).	**328**
Figure S7. ATR-FTIR spectra of HA, **derivative 12-i** and commercial Leu-OMe.	**329**
Figure S8. ATR-FTIR spectra of HA, the **derivative 12-ii** and commercial Leu-OH.	**330**
Figure S9. ATR-FTIR spectra of HA, the **derivative 14** and commercial Phe-OH.	**331**

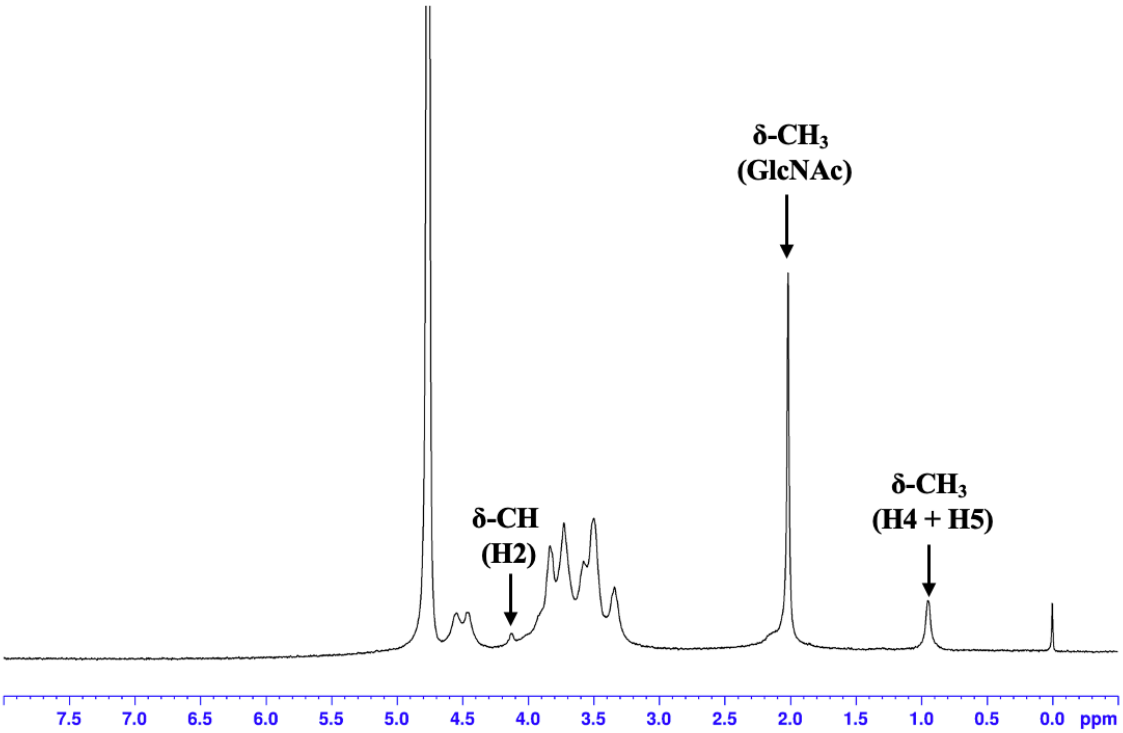

Figure S1. ^{1}H-NMR spectrum of **derivative 5-i** (400 MHz, D_2O, 25°C).

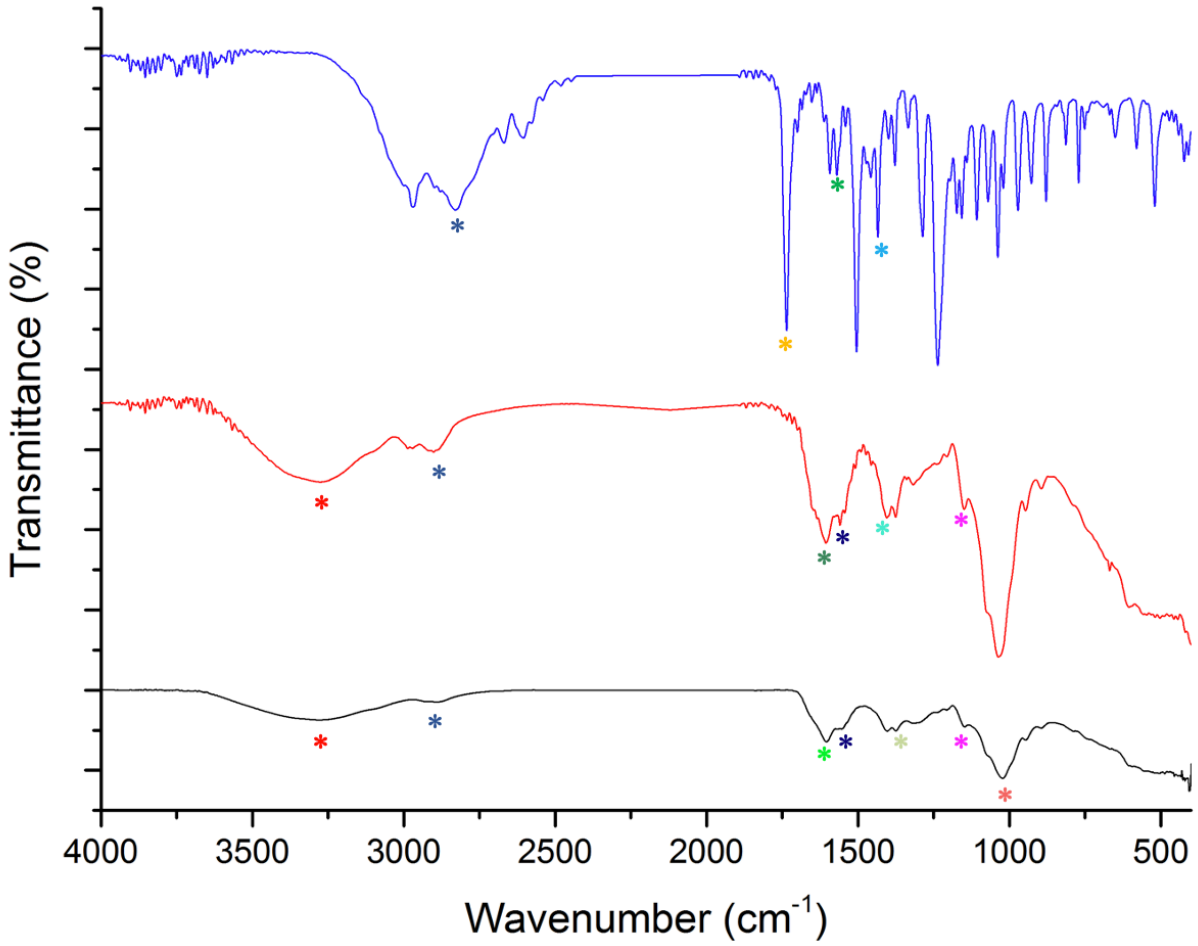

Figure S2. ATR-FTIR spectra of HA (black curve), the **derivative 5-i** (red curve) and commercial Val-OMe (blue curve).

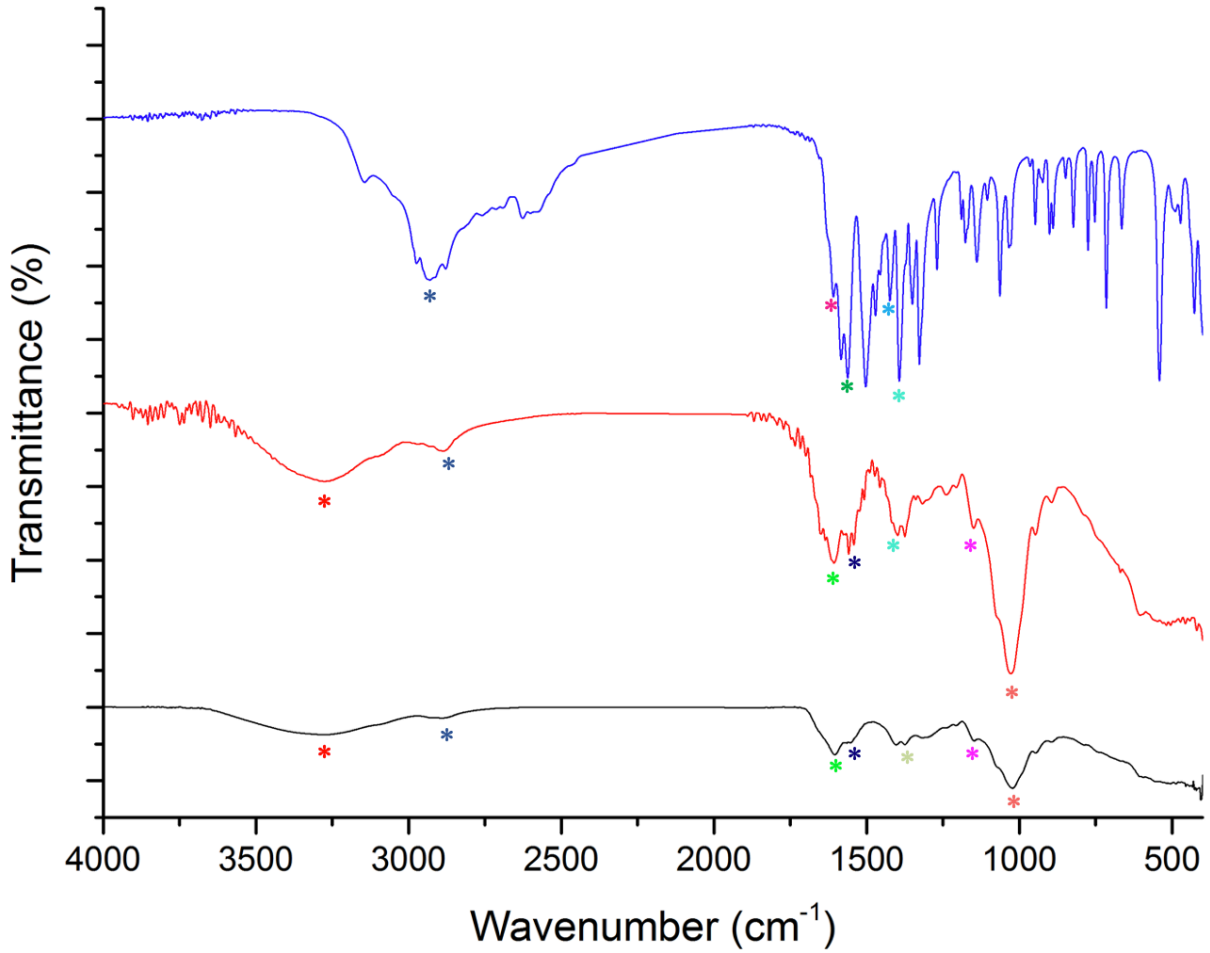

Figure S3. ATR-FTIR spectra of HA (black curve), the **derivative 5-ii** (red curve) and commercial Val-OH (blue curve).

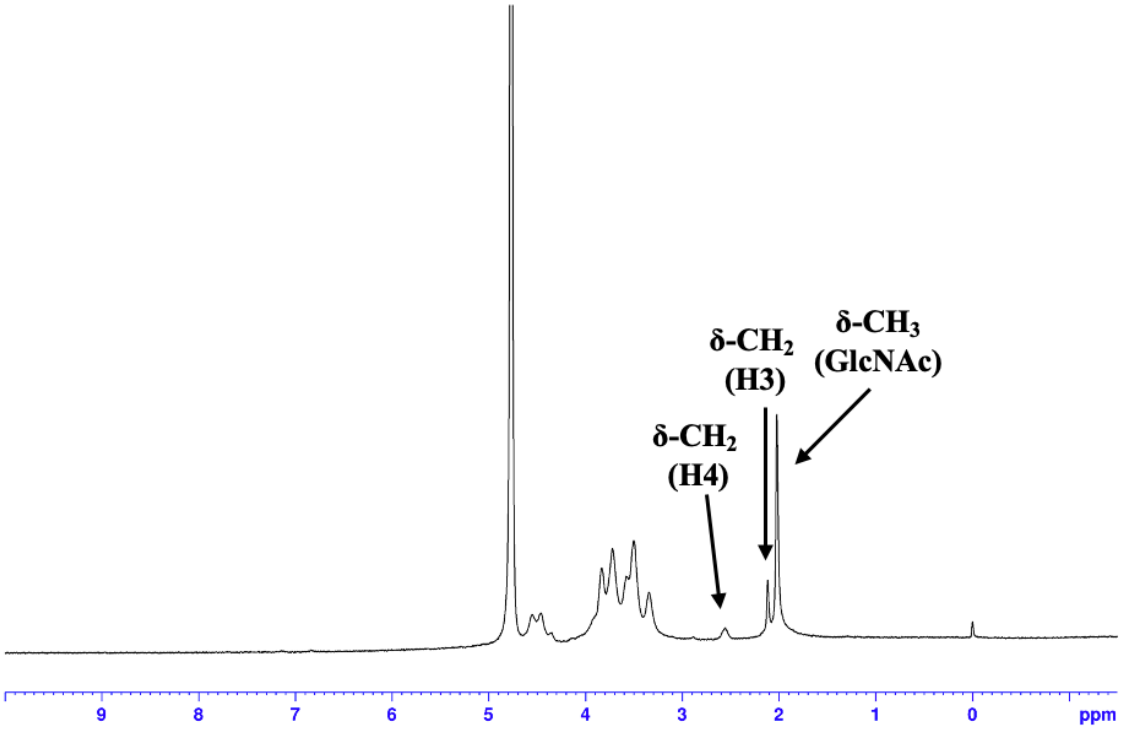

Figure S4. ^{1}H-NMR spectrum of **derivative 8** (400 MHz, D_2O, 25°C).

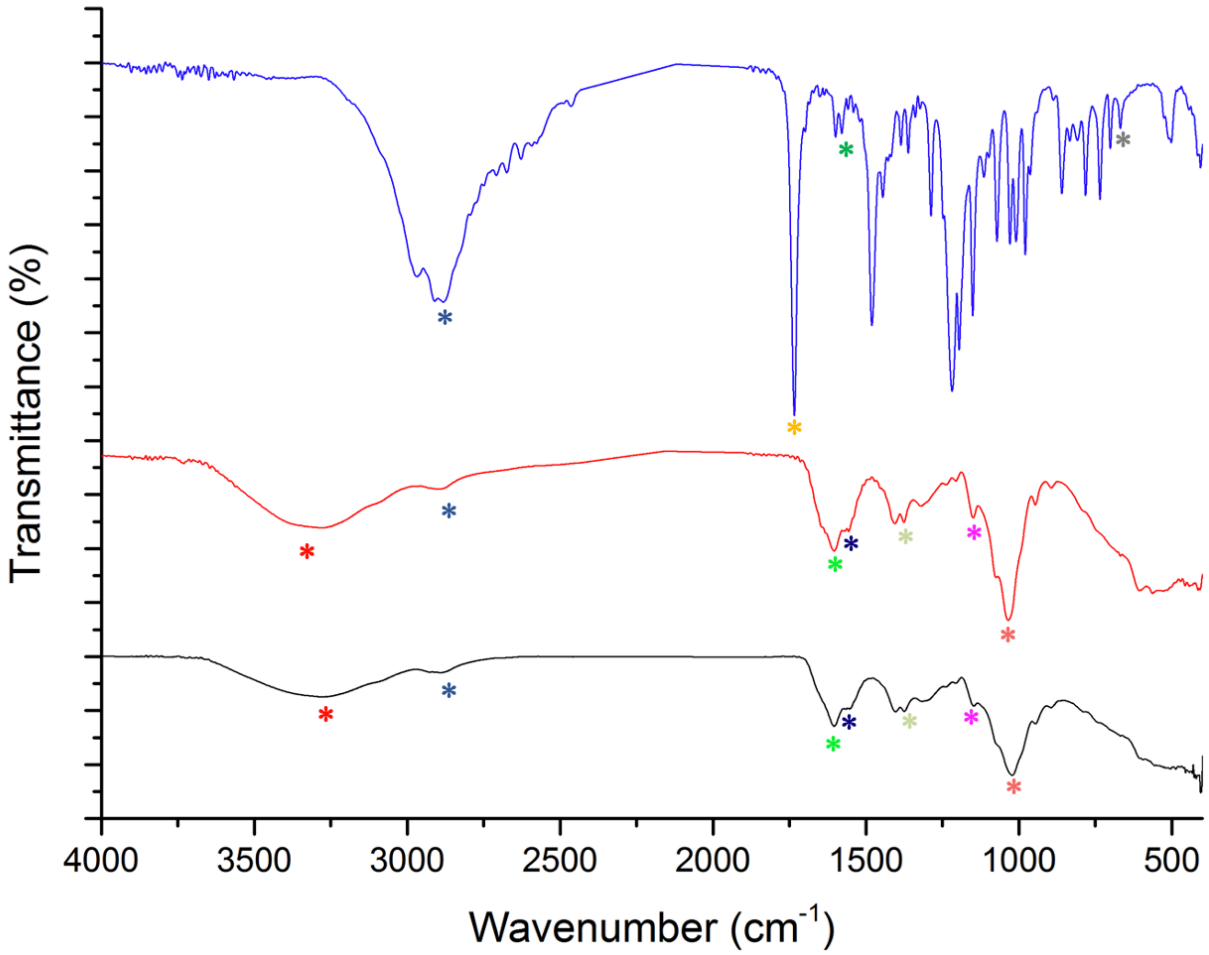

Figure S5. ATR-FTIR spectra of HA (black curve), **derivative 8** (red curve) and commercial Met-OEt (blue curve)

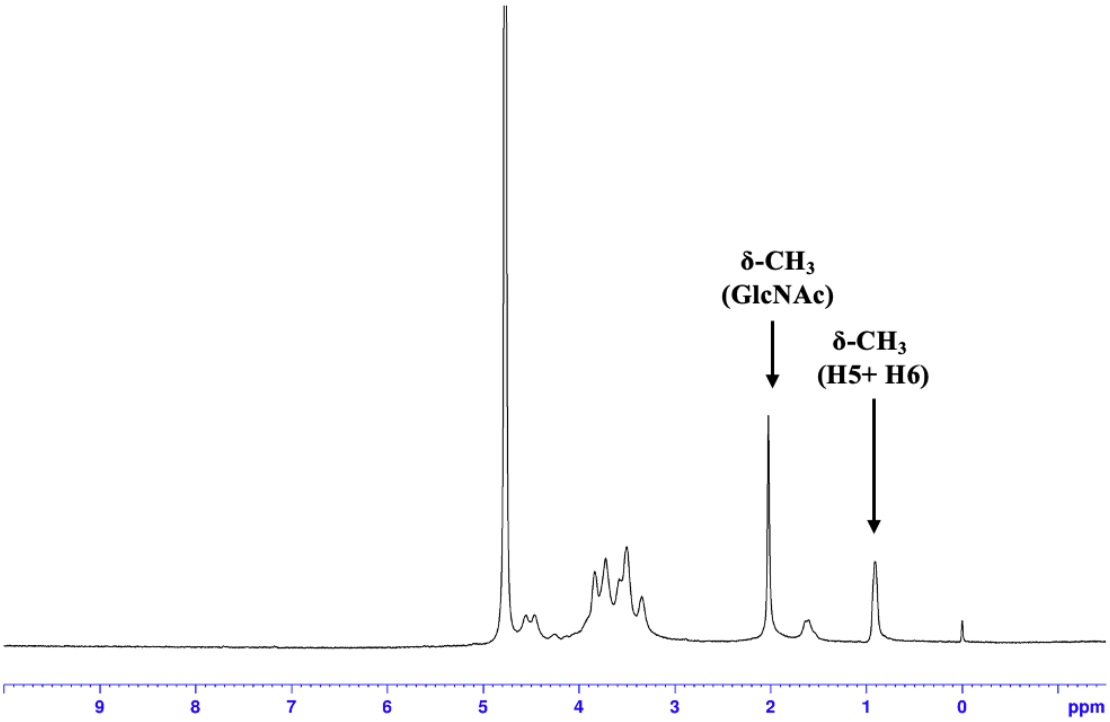

Figure S6. ^{1}H-NMR spectrum of **derivative 12-i** (400 MHz, D_2O, 25°C).

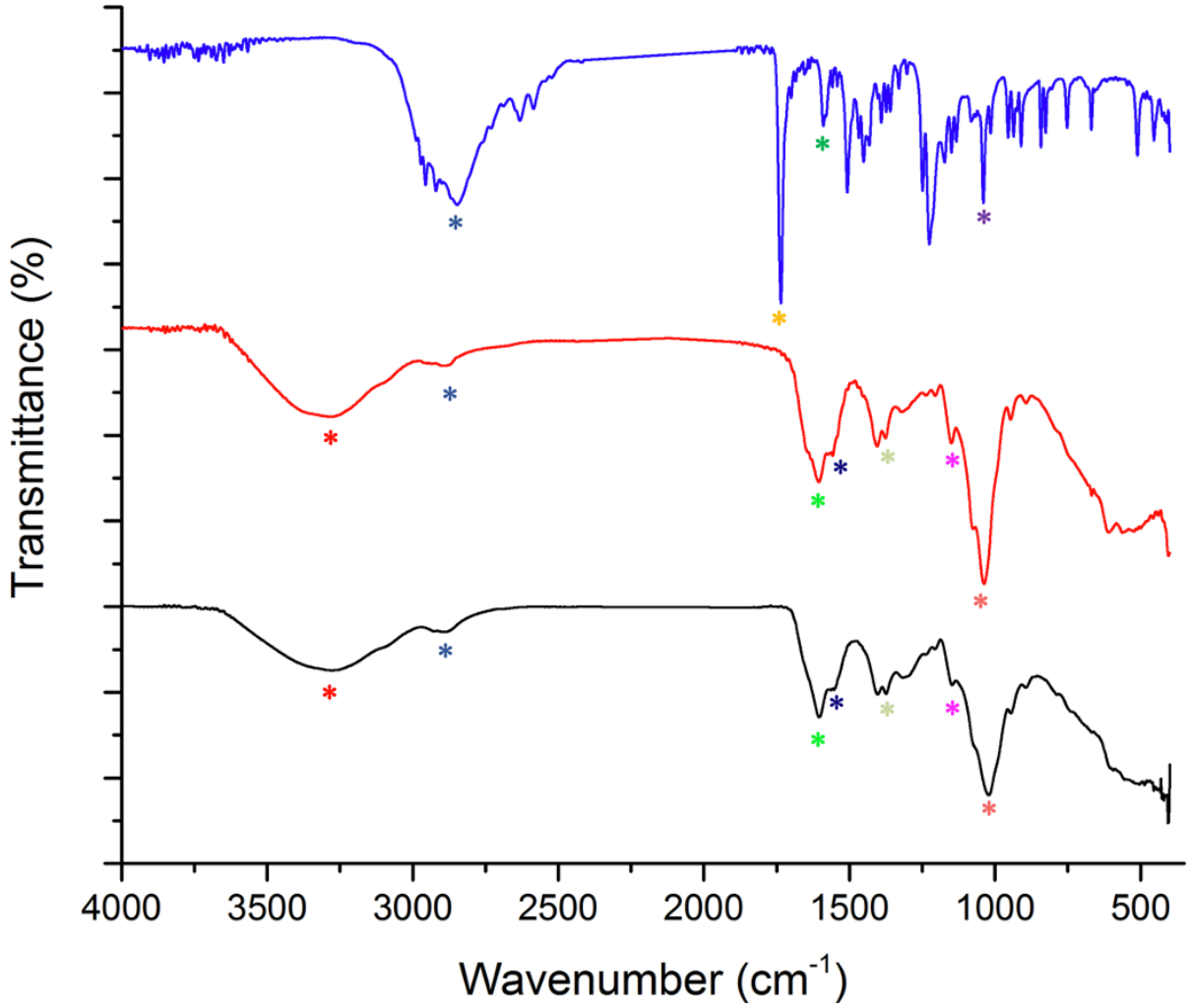

Figure S7. ATR-FTIR spectra of HA (black curve), **derivative 12-i** (red curve) and commercial Leu-OMe (blue curve).

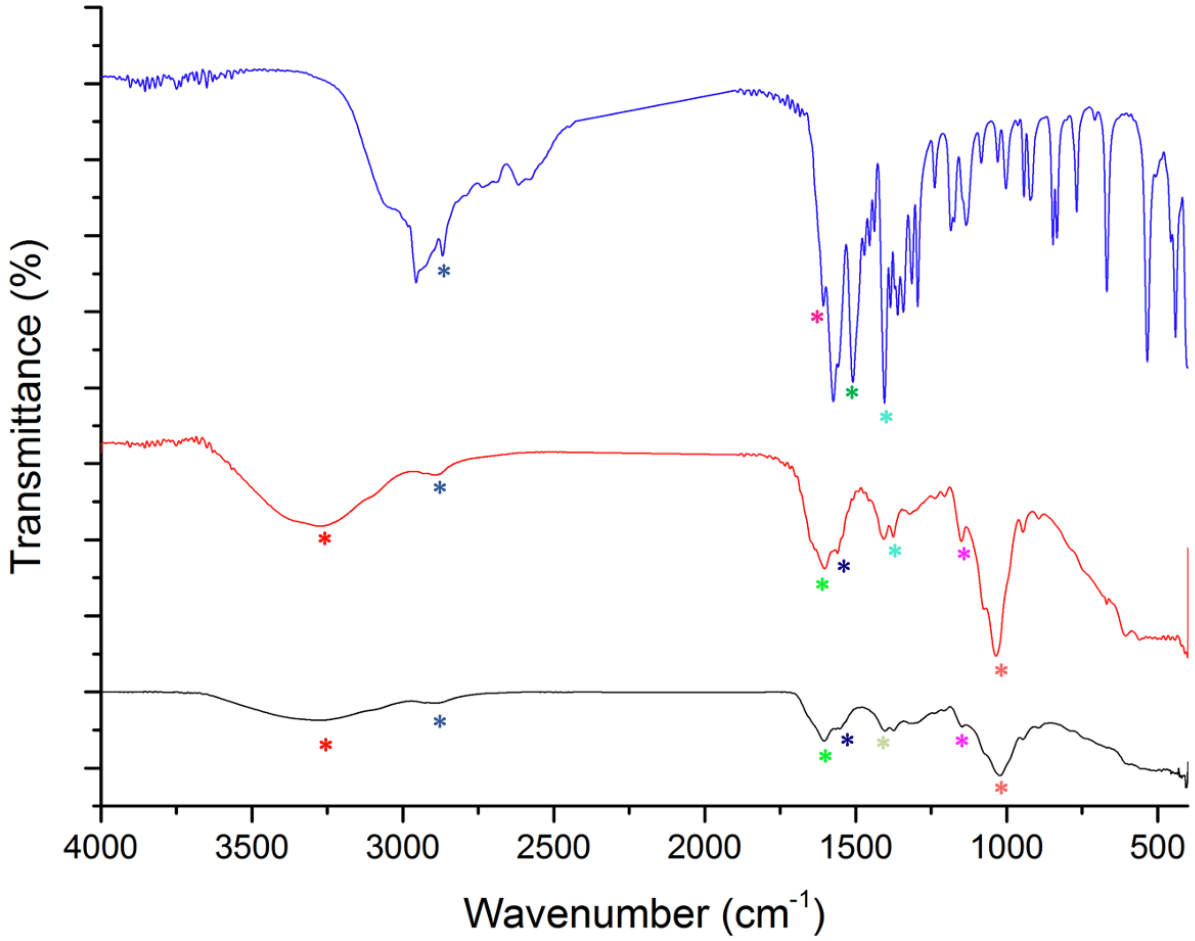

Figure S8. ATR-FTIR spectra of HA (black curve), the **derivative 12-ii** (red curve) and commercial Leu-OH (blue curve).

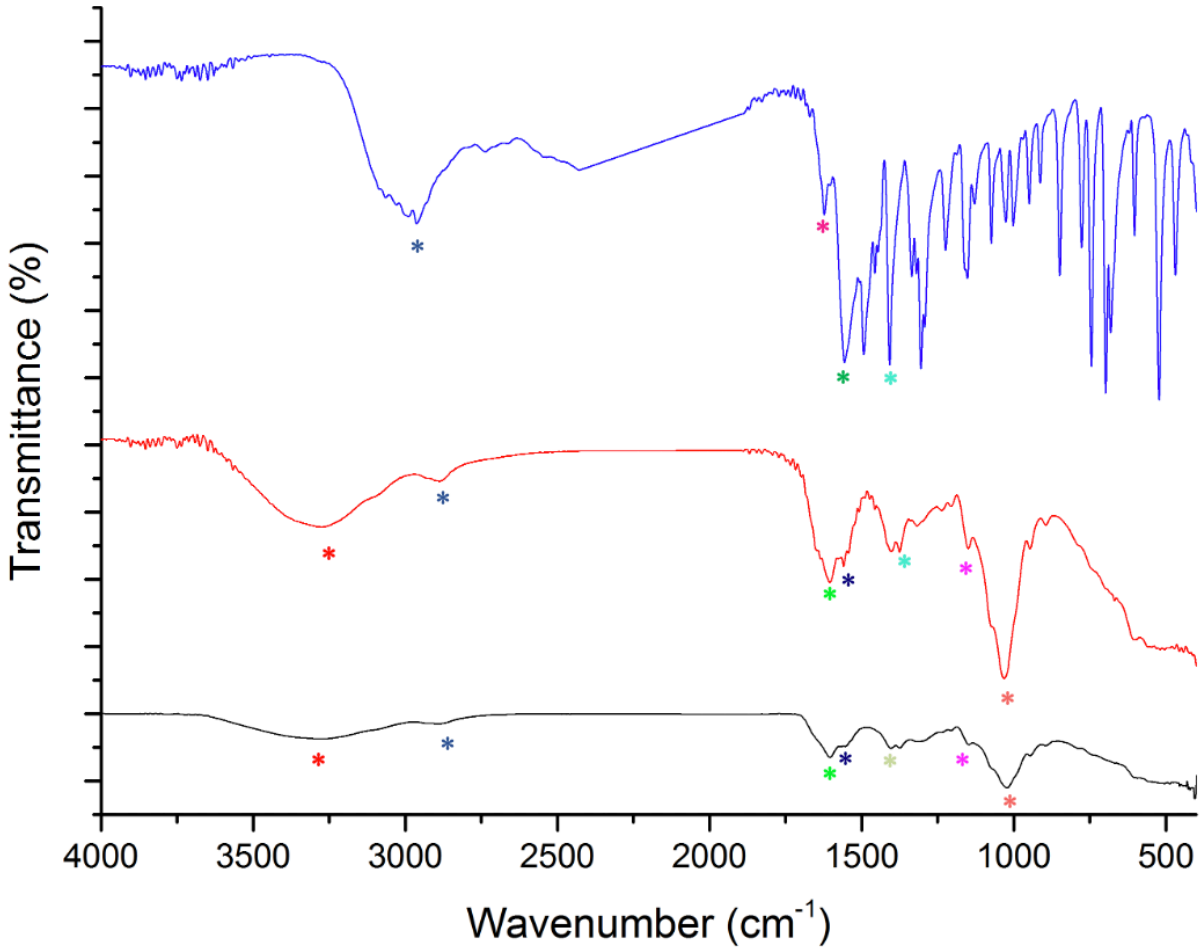

Figure S9. ATR-FTIR spectra of HA (black curve), the **derivative 14** (red curve) and commercial Phe-OH (blue curve).

References

[1] Khalilov L. M. *Modification of hyaluronic acid with aromatic amino acids.* Russian Journal of Bioorganic Chemistry, **2005**, 31, 512–518.

[2] Gürer F.; Kargl R.; Bračič M.; Makuc D.; Thonhofer M.; Plavec J.; Mohan T.; Kleinschek K. S. *Water-based carbodiimide mediated synthesis of polysaccharide–amino acid conjugates: Deprotection, charge and structural analysis.* Carbohydrate Polymers, **2021**, 267, 118226.

[3] Prestwich G. D. *Hyaluronic acid-based clinical biomaterials derived for cell and molecule delivery in regenerative medicine.* Journal of Controlled Release, **2011**, 155, 193–199.

[4] Burdick J. A.; Prestwich G. D. *Hyaluronic acid hydrogels for biomedical applications.* Advanced Materials, **2011**, 23, H41–H56.

[5] Schanté C. E.; Zuber G.; Herlin C.; Vandamme T. F. *Chemical modifications of hyaluronic acid for the synthesis of derivatives for biomedical applications.* Carbohydrate Polymers, **2011**, 85, 469–489.

[6] Edington S. C.; Flanagan J. C.; Baiz C. R. *An empirical IR frequency map for ester C=O stretching vibrations.* Journal of Physical Chemistry A, **2016**, 120, 3888–3896.

[7] Barth A. *The infrared absorption of amino acid side chains.* Progress in Biophysics and Molecular Biology, **2000**, 74(3–5), 141–173.

[8] Coates J. *Interpretation of infrared spectra: A practical approach.* Encyclopedia of Analytical Chemistry, **2000**, 10815–10837.

Chapter 7

A Study on Thiol-Michael Addition to Semi-Synthetic Elastin-Hyaluronan Material for Electrospun Scaffolds

Dr. Antonio Laezza[a], Prof. Antonietta Pepe[a], Nicola Solimando[b], Francesca Armiento [a], Floriane Oszust[c], Prof. Laurent Duca[c], Prof. Brigida Bochicchio[a]

[a] Department of Science, University of Basilicata, Viale dell'Ateneo Lucano 10, 85100, Potenza (Italy)
[b] Altergon Italia S.r.l.Zona Industriale ASI, Morra De Sanctis, 83040, Italy
[c] MEDyC UMR CNRS 7369, "Matrice Extracellulaire et Dynamique Cellulaire", University of Reims Champagne-Ardenne, Team 2 "Matrix Ageing and Vascular Remodelling" 51100, Reims, France

The content of this chapter has been published in ChemPlusChem
DOI: 10.1002/cplu.202300662

Abstract

Thiol-Michael addition is a chemical reaction extensively used for conjugating peptides to polysaccharides with applications as biomaterials. In the present study, for designing a bioactive element in electrospun scaffolds as wound dressing material, a chemical strategy for the semi-synthesis of a hyaluronan-elastin conjugate containing an amide linker (ELAHA) was developed in the presence of tris(2-carboxyethyl)phosphine hydrochloride (TCEP · HCl). The bioconjugate was electrospun with poly-D,L-lactide (PDLLA), obtaining scaffolds with appealing characteristics in terms of morphology and cell viability of dermal fibroblast cells. For comprehending the factors influencing the efficiency of the bioconjugation reaction, thiolated amino acids were also investigated as nucleophiles toward hyaluronan decorated with Michael acceptors in the presence of TCEP · HCl through the evaluation of byproducts formation.

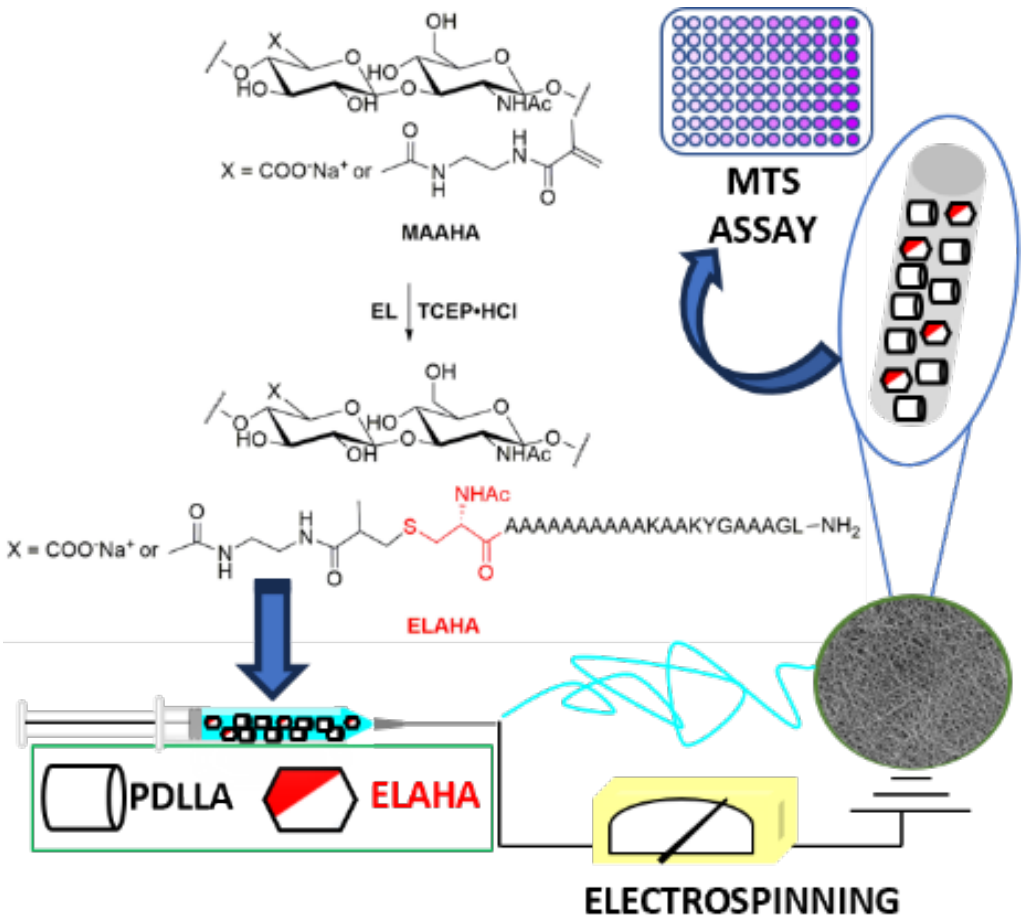

Elastin and hyaluronan have been coupled exploiting a phosphine-mediated thiol-Michael reaction. The conjugate has been blended and electrospun with poly-D,L-lactide (PDLLA), obtaining scaffolds whose morphology and cell viability are influenced by the extent of the peptide coupling. Therefore, the efficiency of the thiol-Michael reaction has been investigated under different conditions.

1. Introduction

Peptide-polymer conjugates are attractive materials in biomedical applications, [1] ranging from drug discovery and delivery to tissue engineering. The bioconjugates show enhanced properties in comparison to peptides alone, which show sensitivity to organic solvents, temperature and pH. Among naturally sourced polymers, polysaccharides, are strongly appealing for conjugation with peptides due to their biocompatibility and biodegradability characteristics [2],

Considering the different chemical strategies for polysaccharides-peptide conjugation, [2b,3] the Michael-type addition has been widely used for the advantageous mild reaction conditions, high reactivity and bio-orthogonality [4]. In this reaction, thiols react with electron-poor "ene" groups such as acrylates, methacrylates and methacrylamidates under basic conditions without requiring free radicals and affording derivatives with stable thioether bonds. Typically, the thiol groups are inserted into peptide chains through cysteine residues at a specific position, whereas Michael acceptor "ene" groups consist of a suitably decorated polysaccharide backbone [2b]. Although acrylates are more reactive than methacrylates into thiol-Michael addition, the hydrolysis resistance of their adducts is reduced in comparison with the methacrylate ones, [4] which in turn are more sensitive to the hydrolysis respect to the methacrylamide counterparts [5]. In the field of wound healing, materials relying on the cleavage of chemical bonds under the influence of pH for a precise drug delivery to wounded sites are continuously under study [6]. Moreover, for the treatment of wounds, the design of materials inspired by the extracellular matrix (ECM) components, such as elastin and hyaluronan (HA), is intriguing. As a matter of fact, systems composed of HA and elastin have been developed for tissue engineering, such as films and hydrogels, [7] and their application specifically in wound healing is still limited [8]. The fibrous elastin protein is responsible for the resilience and elastic recoil of tissues lost after a skin injury. Analogously, the glycosaminoglycan (GAG) plays several roles in the processes after a skin injury, from the hemostasis to the remodelling [9]. Regarding the fabrication methodology, the electrospinning process allowed the production of nanofibrous biomaterials possessing a beneficial porous structure with a high surface-to-volume ratio. Air and water transport, characteristics of electrospun fibers, allows a moist environment fundamental for cell proliferation, lowering the chance of infection. On the other hand, porous structure reproduces the tridimensionality of ECM, facilitating cell adhesion, migration, and proliferation [10].

In the last decades, the interest towards producing nonwoven fabrics obtained from recombinant and synthetic sourced elastin for wound treatment has grown [11] since these materials have exhibited good cell colonization. Electrospun elastin scaffolds reported poor contraction after cell colonization, differently from collagen ones, which reported, in some cases, a reduction larger than 50 % of the original size [12]. As other ECM component, HA is conveniently usable in creating electrospun

nanofibers for wound healing due to its influence on inflammation, cell migration and proliferation, angiogenesis, and re-epithelialization processes [13]. However, HA aqueous solutions' high viscosity and surface tension impair the electrospinning of this polysaccharide in its natural conditions and by itself. Many strategies have been applied to overcome this drawback, including using organic solvent mixtures, blending HA with other polymers and its backbone modification [14]. The insertion of methacrylate, acrylate or thiol pending groups on HA [7c,15] for a Michael-type reaction has been reported, either at the carboxylic function of D-glucuronic acid (GlcA) or at primary hydroxyl of the *N*-acetyl-D-glucosamine (GlcNAc) units of the glycosaminoglycan. The subsequent coupling has been usually carried out with a subsequent coupling with a cysteine [16] or with a Michael-acceptor-containing peptide, [17] respectively. Based on the skills acquired in amino acids, [18] peptides, [19] and protein [20] conjugation to carbohydrates, and starting from the semi-synthesis of ELAHA, herein we present a study exploiting the reactivity of methacrylamide and methacrylate linkers in the presence of a water-soluble alkylphosphine such as TCEP · HCl. This latter is typically employed both as a catalyst [21] and as reducing agent [22] in bioconjugation reactions, even though its efficiency is controversial. Several examples of low functionalization, for example, have been reported in the presence of maleimide, suggesting a possible side reaction between TCEP · HCl and thiol-Michael type donor [23]. Herein, we have explored the feasibility of Michael-type thiol-ene reaction for the production of a bioconjugate constituted of an elastin-derived peptide grafted to hyaluronic acid. The final product would benefit biocompatibility and bioactivity properties as well. In this work, a methacrylamide moiety has been inserted into the glycosaminoglycan carboxylic function on GlcA unit. The obtained methacrylamide-decorated hyaluronan derivative (MAAHA), based on the conditions reported in our recent work,[19a] has been covalently conjugated in the presence of alkylphosphine to the peptide corresponding to the region 302–322 of human tropoelastin (HTE) promoting cell attachment and spreading [24].

The sequence of the peptide (C)AAAAAAAAAAKAAKYGAAAGL (**1**) after the insertion of a cysteine at the C-terminus to carry out Michael-type addition. The nonquantitative bioconjugation between **1** and MAAHA has encouraged us to investigate and compare the efficiency of the Michael addition reaction of MAAHA and a methacrylate-decorated hyaluronan (MAHA) with L-cysteine (Cys) and *N*-acetyl-L-cysteine (NAcCys) amino acids. The semi-synthetic derivatives were characterized by nuclear magnetic resonance (NMR), attenuated total reflectance Fourier transform infrared (ATR-FTIR) spectroscopy and then electrospun with racemic PDLLA to obtain scaffolds, whose morphology was investigated by scanning electron microscopy (SEM). Finally, with the perspective of applications as wound dressing materials, the electrospun scaffolds underwent a cytotoxic analysis and were compared with the ones containing bioconjugates obtained from MAHA polysaccharide.

2. Results and Discussion

2.1 Semi-synthesis of Polysaccharide Derivatives

The strategy for semi-synthesizing elastin-hyaluronan glycoconjugate, exploiting thiol Michael-type addition, started with the amidation at the carboxyl group of GlcA unit of HA by the insertion of methacrylamide moiety. This was accomplished in water in the presence of 2-aminoethylmethacrylamide hydrochloride (2-AEMAA · HCl), *N*-(3-(dimethylamino)propyl)-*N*′-ethylcarbodiimide reagent (EDC · HCl) and *N*-hydroxysulfosuccinimide (s-NHS) at pH=6.8, (Scheme 1a). After overnight reaction at room temperature, dialyses and subsequent freeze-drying furnished MAAHA derivative **2** in quantitative mass yield and with a degree of substitution ($DS_{methacryl}$) of 0.30, as calculated by ^{1}H-NMR (Figure 1).

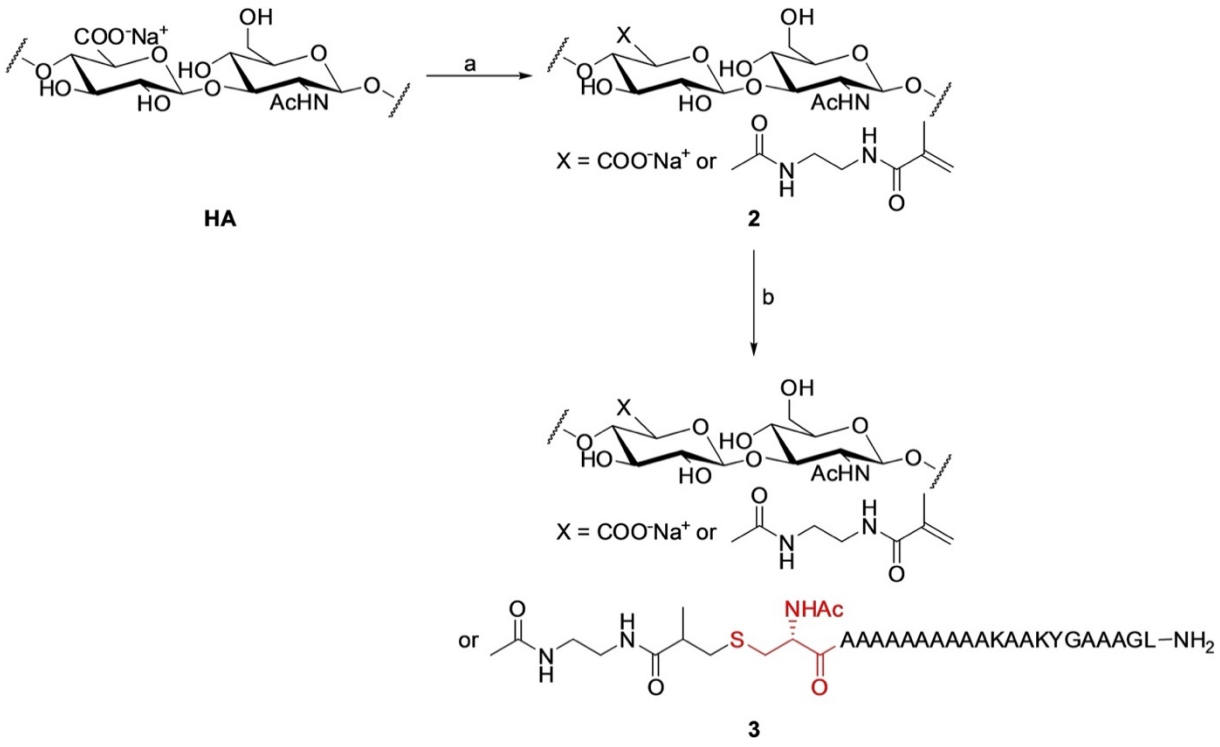

Scheme 1. Semi-synthesis of derivative **3**.a) 2-AEMAA · HCl, EDC, s-NHS, H_2O, RT, pH=6.8, overnight, yield=79 %, $DS_{methacryl}$=0.30; b)**1**, TCEP · HCl, H_2O, RT, pH=8.9, 2d, yield=41 %, $DS_{methacryl}$ = 0.06, $DS_{addition}$ = 0.24.

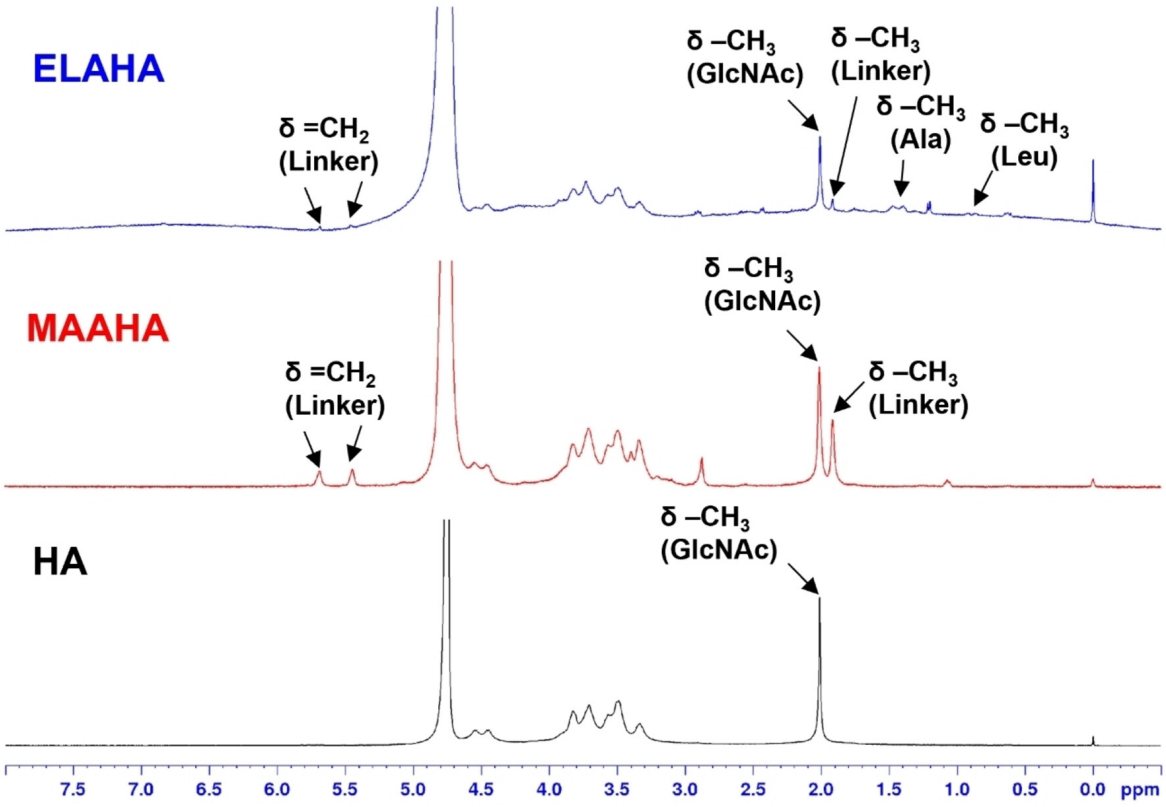

Figure 1. ^{1}H-NMR spectra of HA (black), derivative **2** (MAAHA, red), and derivative **3** (ELAHA, blue) (400 MHz, D_2O, 298 K).

The amide bond formation in MAAHA (**2**) was confirmed by ^{1}H-NMR spectrum for the presence of signals at δ_{DSS}=1.91 ppm, δ_{DSS}=5.69 ppm, and δ_{DSS}=5.45 ppm, respectively associated to the $-CH_3$, and $=CH_2$ groups, of methacrylamide linker. The $DS_{methacryl}$ of derivative **2** was calculated by comparing the ^{1}H-NMR vinyl (δ_{DSS}=5.69, or 5.45 ppm) integrals with that obtained by the sum of HA and 2-AEMAA acetyl signals (δ_{DSS}=2.01 and 1.91 ppm) (Figure S1) by Equation 1

$$DS_{\,methacryl} = \frac{3I_{\,CH\,(2-AEMAA)}}{I_{[CH3\;\;(GlcN\,Ac)+CH3(2-AEMAA)]} - 3I_{\,CH(2-AEMAA)}} \qquad (1)$$

Where *I*CH(2-AEMAA) represents the proton integral of the 2-AEMAA methine proton, while *I*CH_3(GlcNAc) and *I*CH_3(2-AEMAA) represent the proton integrals of the methyl groups of GlcNAc and 2-AEMAA, respectively.

Derivative **2** was coupled to the cysteine thiol at the N-terminal residue of elastin-derived peptide **1** (Scheme 1b) to obtain ELAHA (**3**). The ^{1}H-NMR of this compound (Figure 1, blue) showed a non-quantitative functionalization by the presence of 2-AEMAA groups, such as the methyl at δ_{DSS}=1.91

ppm and the smaller vinyl signals, which entail respectively a $DS_{methacryl}$=0.06 and a $DS_{addition}$=0.24. The latter has been calculated by the difference of vinyl signals intensity after and before the coupling. The bioconjugation was confirmed further by the peptide side chain signals, such as the $-CH_3$ groups of alanine and leucine residues, respectively, at δ_{DSS}=1.54–1.30 ppm, δ_{DSS}=0.91, and δ_{DSS}=0.86 ppm. The reactivity of acceptors into the thiol-Michael addition is related to the electronic feature of the substituent linked to the C=C bond:[25] at any given pH the reaction proceeds rapidly with acceptors bearing esters, slower with amides or methacrylates. In contrast, the slowest rates were calculated for methacrylamides, due to the poor electronegativity of amides [26].

Therefore, to evaluate how the coupling conditions affected ELAHA semi-synthesis, two thiols such as Cys and NAcCys, were studied as donors in the presence of MAAHA (**2**) or MAHA (**4**) as acceptors (Figure 2).

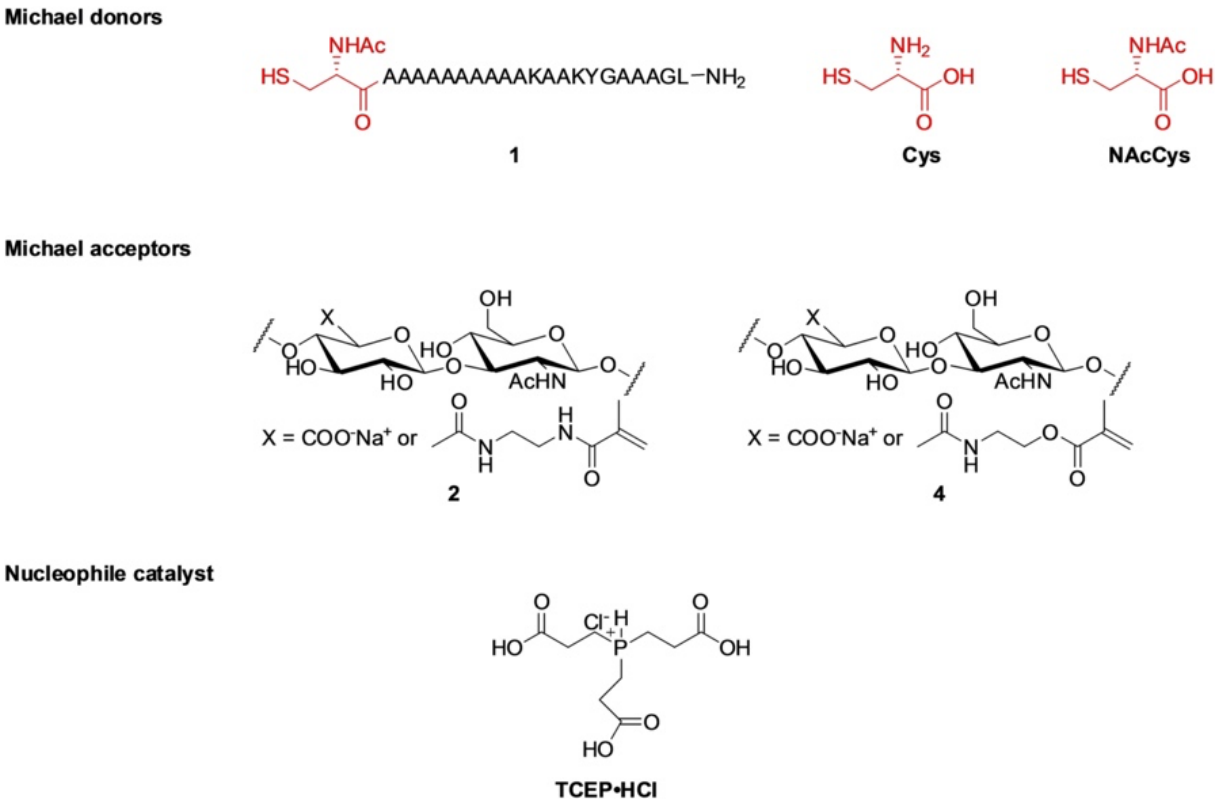

Figure 2. Michael donors, acceptors and nucleophile catalyst used in the study.

MAHA has been synthesized under conditions recently reported [19a] with a $DS_{methacryl}$=0.19 (Figure S2).

All the reactions were carried out for two days at room temperature in H_2O at pH=8.9, where the acceptor/donor/nucleophile ratios investigated were 1 : 1.3 : 1.9 and 1 : 1.5 : 2.25, as reported in Table 1. The conjugation of Cys with MAAHA afforded derivatives **5-i**,**ii** (Scheme 2a,b) in 77 % and 41 % mass yield.

Table 1 Coupling conditions, yield and structural data of derivatives **5-8** in the thiol-Michael addition study.

Sample	Acceptor	Donor	Acceptor/Donor/Nucleophile Ratio	Donor/Nucleophile Ratio	Yield	$DS_{methacryl}$	$DS_{addition}$
3	MAAHA	EL	1:1.3:1.9	1:1.5	41%	0.06	0.24
5-i	MAAHA	Cys	1:1.3:1.9	1:1.5	77%	0.13	0.17
5-ii	MAAHA	Cys	1:1.5:2.25	1:1.5	41%	0.06	0.24
6-i	MAHA	Cys	1:1.3:1.9	1:1.5	68%	-	0.19
6-ii	MAHA	Cys	1:1.5:2.25	1:1.5	50%	-	0.19
7-i	MAAHA	NAcCys	1:1.3:1.9	1:1.5	44%	0.07	0.23
7-ii	MAAHA	NAcCys	1:1.5:2.25	1:1.5	57%	0.07	0.23
8-i	MAHA	NAcCys	1:1.3:1.9	1:1.5	91%	-	0.19
8-ii	MAHA	NAcCys	1:1.5:2.25	1:1.5	86%	-	0.19

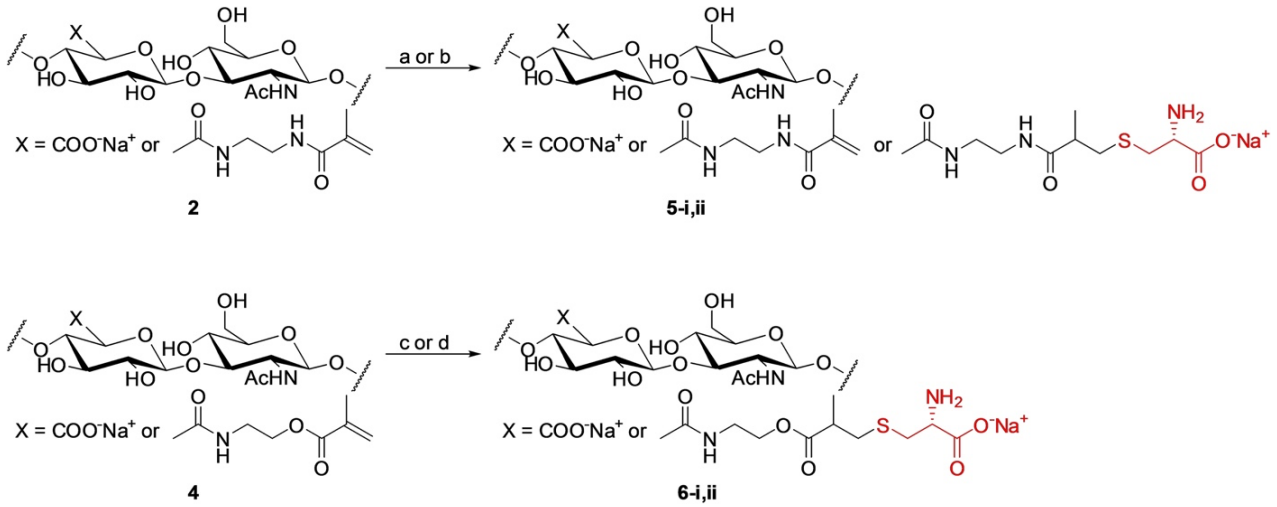

Scheme 2. Cys investigation as Michael donor: a) Cys (1.3 eq), TCEP · HCl (1.9 eq), H_2O, RT, pH=8.9, 2d, yield: 77 %, $DS_{methacryl}$=0.13, $DS_{addition}$=0.17; b) Cys (1.5 eq), TCEP · HCl (2.25 eq), H_2O, RT, pH=8.9, 2d, yield: 41 %, $DS_{methacryl}$=0.06, $DS_{addition}$=0.24; c) Cys (1.3 eq), TCEP · HCl (1.9 eq), H_2O, RT, pH=8.9, 2d, yield: 68 %, $DS_{addition}$=0.19; d) Cys (1.5 eq), TCEP · HCl (2.25 eq), H_2O, RT, pH=8.9, 2d, yield: 50 %, $DS_{addition}$=0.19.

Analogously with ELAHA, they showed a nonquantitative functionalization by the presence of 2-AEMAA groups, which entail a $DS_{methacryl}$=0.13 and 0.06 and a $DS_{addition}$=0.17 and 0.24, for **5-I** and **5-ii**, respectively (Figure S3, red and blue curves).

The reactivity of Cys with the acceptor MAHA afforded derivatives **6-i**,**ii** (Scheme 2c,d). In this case a disappearance of vinyl signals was noted and a $DS_{addition}$=0.19 (Figure S4, red and blue curves) was obtained for both the compounds, which were collected in 68 % and 50 % mass yield.

The presence in peptide **1** of the L-cysteine, acetylated at the amino group in the final step of SPPS, suggested us to employ *N*-acetyl-L-cysteine as a model amino acid playing the role of a donor. The conjugation of NAcCys with MAAHA afforded derivatives **7-i**,**ii** (Scheme 3a,b) respectively in 44 % and 57 % mass yield and with a $DS_{methacryl}$=0.07 and a $DS_{addition}$=0.23 as calculated by ^{1}H-NMR (Figure S5, red and blue curves) applying Equation 2.

$$DS_{\ methacryl} = \frac{3I_{\ CH\ (2-AEMAA)}}{I_{[CH3\ \ (GlcN\ Ac)+CH3(N\ AcCys)+CH3\ (2-AEMAA)]} - 6I_{\ CH(2-AEMAA)}}$$

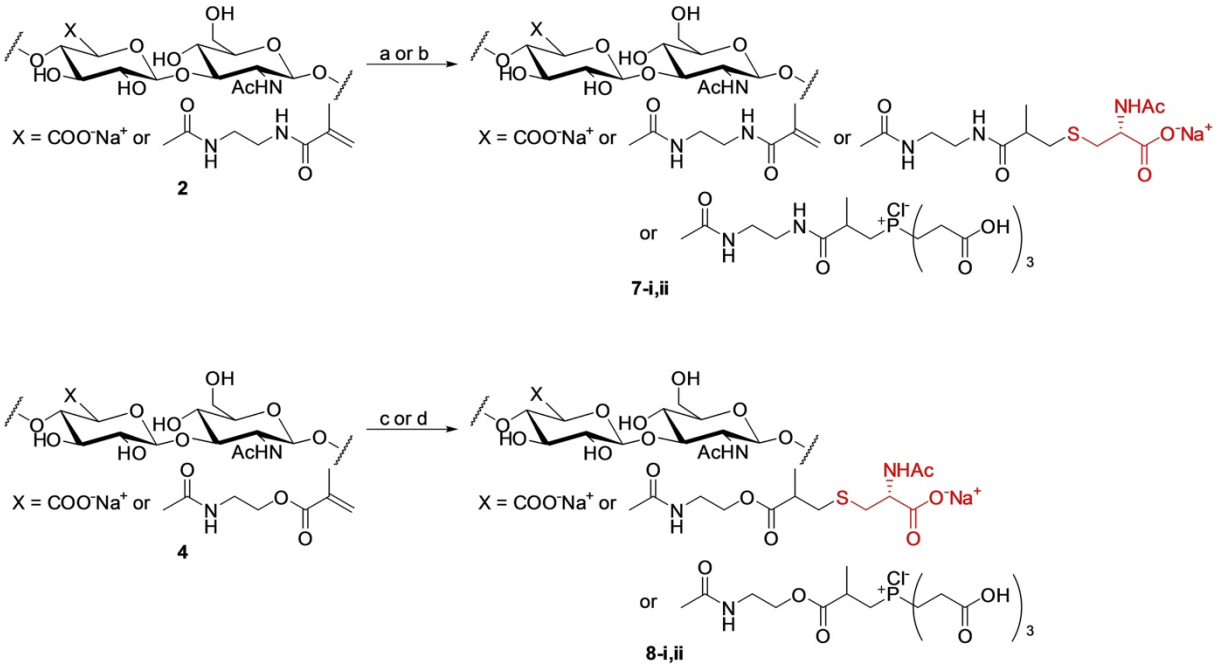

Scheme 3. NAcCys investigation as Michael donor: a) NAcCys (1.3 eq), TCEP · HCl (1.9 eq), H_2O, RT, pH=8.9, 2d, yield: 44 %, $DS_{methacryl}$=0.07, $DS_{addition}$=0.23; b) NAcCys (1.5 eq), TCEP · HCl (2.25 eq), H_2O, RT, pH=8.9, 2d, yield: 57 %, $DS_{methacryl}$=0.07, $DS_{addition}$=0.23; c) NAcCys (1.3 eq), TCEP · HCl (1.9 eq), H_2O, RT, pH=8.9, 2d, yield: 91 %, $DS_{addition}$=0.19; d) NAcCys (1.5 eq), TCEP · HCl (2.25 eq), H_2O, RT, pH=8.9, 2d, yield: 86 %, $DS_{addition}$=0.19.

When NAcCys reacted with MAHA (Scheme 3c,d) , derivatives **8-i**–**ii** were respectively obtained in 91 % and 86 % mass yield with a quantitative functionalization and a $DS_{addition}$=0.19 (Figure S6, red and blue curves). However, the absence of isolated protons ascribable to the thiolated amino acids did not allow the evaluation of functionalization; for this reason, correlation spectroscopy 2D-NMR (COSY) analyses were conducted. The derivatives obtained after Cys bioconjugation (Figures S7–S10) displayed a correlation between the methylene protons density at δ_{DSS}=3.11 ppm and that at δ_{DSS}=3.93 ppm in the typical region of the H_α proton of the thiolated amino acid, suggesting its presence on the polysaccharide backbone. In the case of NAcCys bioconjugation (Figures S11–S13), a correlation was detected between the methylene protons at δ_{DSS}=2.88 ppm and the H_α proton of the amino acid at δ_{DSS}=4.37 ppm. The exception is represented by the sample **8-i**, where the presence of NAcCys is not evident (data not shown). In both cases, the upfield shift of H_α amino acids might suggest the Michael addition occurrence [27]. Moreover, the depletion of vinyl signals does not exclude the presence of side products formed in the thiol-Michael reactions. ^{1}H-NMR spectra of the amino acid-hyaluronan derivatives, indeed, displayed signals in the region 2.70–2.00 ppm, possibly related to contaminants; therefore, ^{31}P-NMR experiments were conducted to evaluate the presence of undesired products. The same analysis was conducted on ELAHA, which displayed the absence of any signal related to phosphorus adducts (Figure S14). Regardless of the acceptor and the reaction conditions, the conjugations with Cys showed two phosphorus signals at δ_{DSS}=58.2 ppm and δ_{DSS}=52.8 ppm, consistent with oxidized (TCEP=O) and the thiophosphine byproducts (TCEP=S), respectively (Figure S15–S16) [28]. These confirmed the absence of hyaluronan-phosphine adducts (**5-i**,**ii** and **6-i**,**ii**, Scheme 2). A different behavior has been noted with the NAcCys conjugation, where the formation of phosphonium ester adducts has been detected. In the case of the MAAHA acceptor, the adduct has formed independently from the equivalents of the catalyst and the ^{31}P-NMR spectra (Figure S17) showed a signal at δ_{DSS}=34.5 ppm in agreement with literature data [29]. When the same reaction was conducted on MAHA, the formation of phosphonium ester was dependent on the equivalent of the catalyst (Figure S18). The ^{31}P-NMR spectra showed signals in the range of δ_{DSS}=34.7–33.6 ppm: these signals could be associated with a different protonation level of the phosphorus adduct (**7-i**,**ii** and **8-i**,**ii**, Scheme 3) [30].

Cys is more acidic than NAcCys; hence, the thiol group is mainly present as more nucleophilic thiolate at the given pH. However, a selectivity for the Cys is evident in the addition on the methacrylate and on the methacrylamide acceptors.

Besides the thiol/thiolate ratio [26], a combination of vinyl, catalyst and reaction conditions [31] influences the reaction mechanism. Because of the higher electron-withdrawing capability, the

methacrylate is more reactive than the methacrylamide, which could be generally affected by the formation of byproducts for the competition of nucleophile initiator with the thiolate.

It is worth noting that the pH plays a pivotal role in the reaction efficiency. In the cysteine-containing derivatives, the phosphonium ester side products are absent due to the faster addition kinetic to the vinyl groups of the thiolate than the phosphine; the only difference in the conjugation could be attributed to the electron-withdrawing feature of the acceptors.

Notably, despite the different acceptors' electrophilicity, when NAcCys has been used as a model, the byproducts formation is influenced by the higher thiol/thiolate ratio by the excess of phosphine catalyst. These findings confirm the controversial role of TCEP · HCl in the catalysis of thiol-Michael addition on polysaccharides [32]. Generally, organophosphines can be considered efficient catalysts in the thiol-Michael addition, even if their high reactivity tends to induce side reactions. In recent years, several theoretical and experimental approaches have been adopted to deepen the factors involved in the nucleophilic pathway and in the generation of byproducts [27b,33].

2.2 ATR-FTIR Analysis

The characterization of HA, MAAHA and ELAHA was further carried out by ATR-FTIR (Figure S19), allowing the assignment of specific functional groups on the polysaccharide backbones. HA spectrum (black curve) shows in the 3500–3000 cm^{-1} region a broad band attributed to the stretching of carbohydrate O−H, as well as, C=O (amide I, filled green circle) and C−N (amide II, filled orange circle) bands of acetamido groups stretching vibrations are observed at ~1605 and ~1550 cm^{-1}, respectively. Derivative **2** spectrum (MAAHA, red curve) proved the occurrence of methacrylamidation by the slight shift peak of the amide I band (filled green circle) to ~1610 cm^{-1} caused by the inductive effect of the methyl group of the linker.

Several findings confirmed the peptide presence in derivative **3** (ELAHA, blue curve). First of all, the sharpening of the band at ~3269 cm^{-1} due to N−H stretching (filled blue circle) of the peptide amide is evident. It appears in the same region where the O−H stretching of pristine HA (black curve) and the derivative **2** (MAAHA, red curve) were present as a broad band at ~3281 cm^{-1}.

Moreover, the amide I band (filled green circle) is shifted to ~1622 cm^{-1}. This one, together with the amide II band at ~1516 cm^{-1} (filled orange circle) are assigned to the peptide **1**.

Further proof derives from the band at ~1450 cm^{-1} (filled gray circle) in the purple curve associated with the asymmetric C−H_3 bending vibration of alanine residues, which are present in peptide **1** spectrum (purple curve) and absent in HA and derivative **2** curves.

2.3 Morphological Analysis

HA, derivatives **2** and **3** were blended with PDLLA and electrospun, with the process parameters listed in Table 2, fulfilling the aim to produce electrospun scaffolds made of biodegradable and bio-active polymers. 1,1,1,3,3,3-hexafluoro-2-propanol (HFP) was chosen because of its ability to solubilize both elastin peptides and PDLLA as pure solvent [34] and in aqueous solutions [19a]. The electrospinning parameters were tuned to ensure process stability, providing macroscopically uniform structures. Herein, to dissolve HA, derivatives **2** and **3**, HFP was mixed with H_2O: HP (HA/PDLLA), MAHP (MAAHA/PDLLA) and EAHP (ELAHA/PDLLA) blends were prepared by dissolving in 80 % (V/V) HFP aqueous solution either HA, MAAHA or ELAHA and PDLLA to a final concentration of 0.24 % and 12.0 % (w/V), respectively. In the same way, the P scaffold, containing pristine PDLLA, was prepared by dissolving the polymer in 80 % (V/V) HFP aqueous solution to a final concentration of 12.0 % (w/V).

Table 2 Composition, process parameters and morphology of electrospun scaffolds

Scaffolds[a]	Composition	Polymer weight ratio (w/w)	Final polymer concentration % (w/V)	Electrospinning process parameters				Average fiber diameter[b] (nm)
				V (kV)	N (G)	d (cm)	F (mL/h)	
P[c]	PDLLA	-	12.00	19	18	19	0.5	447.65 ± 121.09
HP[c]	HA/PDLLA	1:50	12.24	19	18	19	0.5	416.61 ± 34.15
MAHP	MAAHA/PDLLA	1:50	12.24	19	18	19	0.5	410.35 ± 8.36
EAHP	ELAHA/PDLLA	1:50	12.24	19	18	19	0.5	455.74 ± 17.23

[a] P: (poly-lactic acid), HP: (hyaluronic acid/poly-lactic acid), MAHP: (methacrylamidated hyaluronic acid/poly-lactic acid), EAHP: (elastin-conjugated hyaluronic acid/poly-lactic acid), [b] Mean value±standard deviation (n>100 from three different images). [c] Average fiber diameter of P and HP are taken as a reference from [19a].

Scanning electron microscopy investigated the morphology of the scaffolds with particular attention to the assessment of any defect (beads), the fibers' orientation, and the diameter distribution. Concerning the detection of beads, the SEM image of the electrospun P scaffold (Figure 3A) showed a three-dimensional microstructure enriched with interconnected pores and bead-on-string morphology that typically arises when the surface tension of the liquid overcomes the charge repulsion and viscous forces [35].

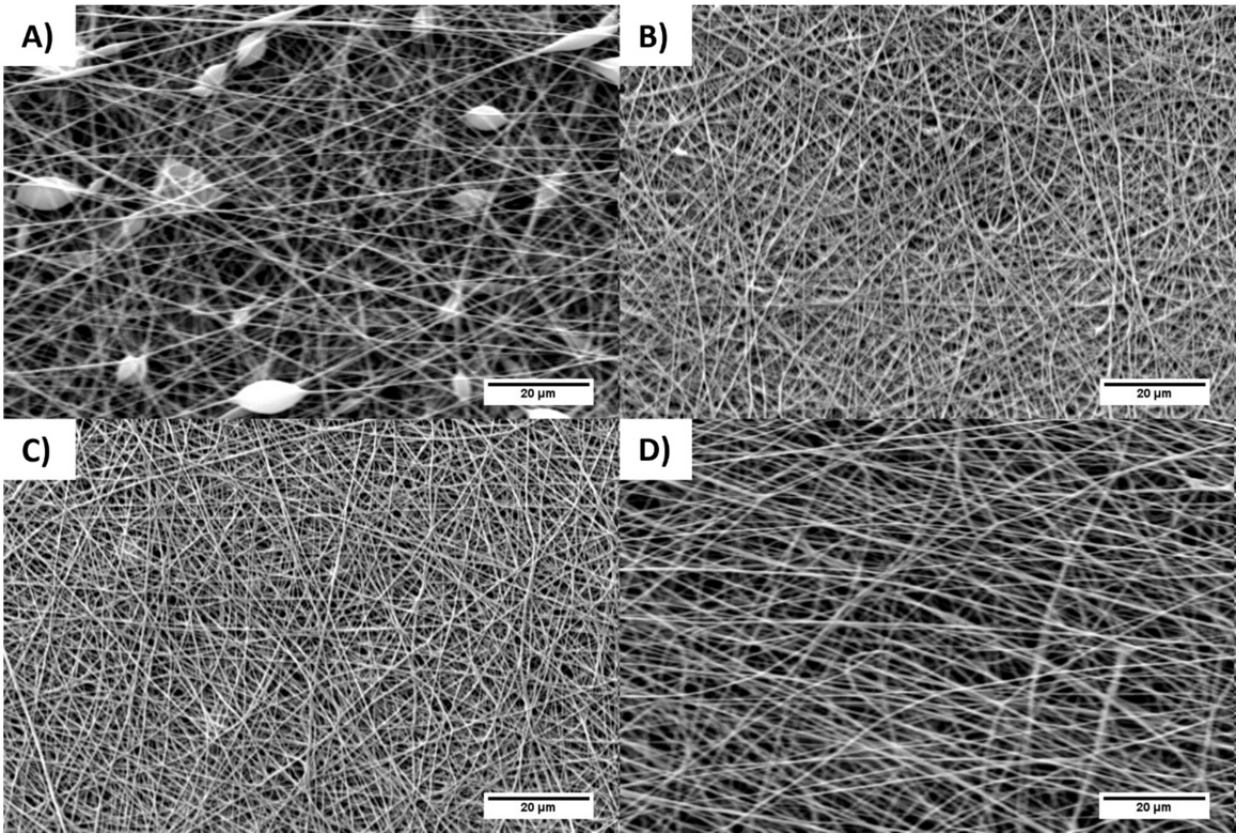

Figure 3. SEM images of electrospun scaffolds. P (A), HP (B), MAHP (C), EAHP (D); (bar: 20 µm). Images A and B are taken from [19a].

Generally, the surface tension and viscosity of the electrospinnable mixture depend on the polymer and the solvent system used, as well as the charge density is dependent on the applied voltage. The presence of H_2O increases the surface tension as opposed to pure HFP solution, leading to beads formation in the nanofibrous morphology [36]. Nevertheless, HP, MAHP and EAHP scaffolds displayed fibers with a linear trend, without beads, suggesting an increase of electrospun solution viscosities, differently from the scaffold P solution, and the effective dispersion of the polysaccharides and semi-synthetic derivatives in the mixture due to the absence of defects (Figure 3B-D). Moreover, for EAHP scaffold, the fibers appeared slightly curled. The average diameters of fibers as function of frequency (Figures S20A–B) showed a normal distribution around a mean value of 448±121, 417±34, 410±8, and 456±17 nm for P, HP, MAHP, and EAHP electrospun scaffolds, respectively, as reported in Table 2.

The differences in the fibers' diameter between the scaffolds were evaluated by statistical analyses using the one-way Analysis of Variance (ANOVA) method and Tukey's Test. Between P and HP as well as P and MAHP membranes, a significant decrease was observed for *, $p \leq 0.05$ (from 448±121 to 417±34, and from 448±121 to 410±8), whereas for **, $p \leq 0.01$ a statistical reduction in average diameter was found by comparison of P and MAHP membranes (Figure S21) (from 448±121 to

410±8). Even though by blending HA and MAAHA with PDLLA, the viscosity of the solution should rise, with a relative increase of nanofibers diameter, the observed data could be the results of humidity increasing, which allows elongation of the charged jet to continue longer and thereby to form thinner fibers [37] However, the substantial standard deviation (SD) related to the measure of scaffold P should be taken into account due to bead formation.

Differently from previous studies [19a], in the case of EAHP scaffold, the presence of ELAHA glycoconjugate induced a significant increase of average fibers diameter with *, $p \leq 0.05$ and ** $p \leq 0.01$ respect to HP and MAHP, as reported in Table 2 (from 417±34 to 456±17, and from to 456±17, respectively). Since P, HP, MAHP, and EAHP membranes have been electrospun using the same process parameters, this finding should be imputable to specific solution physical properties changes due to the nonquantitative conjugation of peptide **1** in ELAHA derivative.

As a matter of fact, the acidity of the HFP/H_2O solution should give rise to positively charged ϵ-amine of Lys residues with a consequent increase of solution conductivity and a reduction in the average diameter. Typically, in fact, the increase of charge density in the electrospun solution affords the formation nanofibers with smaller diameter. In our case, instead, the nonquantitative functionalization of derivative **2** with elastin peptide afforded a low charge density of the solution with a consequent increase of nanofibers diameter [38].

Overall, the morphology of HP, MAHP and EAHP scaffolds is characterized by the absence of defects and the presence of interconnected nanofibers, which well mimic the ECM three-dimensional structure as well as enable oxygen and vapor permeation in wound dressing applications. These aspects are pivotal for optimal wound dressing design. Moreover, as reported by Kenar and co-workers [39], the found values of the average fibers diameter of the produced membranes (326-569 nm) render the scaffolds good candidates for tissue engineering applications.

2.4 Cytotoxicity Assay

A 3-(4,5-dimethylthiazol-2-yl)-5-(3-carboxymethoxyphenyl)-2-(4-sulfophenyl)-2H-tetrazolium (MTS) assay was performed to evaluate the absence of cytotoxicity of the scaffolds.

Both with the employment of a methacrylate and methacrylamide moieties in the chemical strategy, the results of the cytotoxicity assay showed no negative influence of the extracts on the metabolic activity of dermal fibroblast cells (Table S1 and Figures S22A-B) After 24 h (Figure S22A), the cells in the extraction medium of scaffold P showed a statistically lower metabolic activity (P=90±6%) than the medium and the positive gelatin control for *, $p \leq 0.05$. When pristine HA and methacrylated HA were co-electrospun with PDLLA, a metabolic activity (HP = 95±1% and MHP = 92±5%, respectively) not significantly different to the medium and positive control was reported. In the case of methacrylamidated HA, instead, a statistically lower metabolic activity (MAHP = 91±5%) than the

medium and the positive control for *, $p \leq 0.05$. The derivative obtained after the conjugation with EL were co-electrospun with PDLLA, and both reported a metabolic activity not statistically different metabolic activity to the medium and the positive control (EHP = 94±5% and EAHP = 96±4).

After 48 h (Figure S22B), all the scaffolds reported a similar metabolic activity to the medium and the positive gelatin control, except MAHP with a value of 85±5% that was statistically different for *, $p \leq 0.05$ and **, $p \leq 0.01$.

According to ISO 10993-5 : 2009, the extract shows no cytotoxic potential if the relative viability is not reduced below 70 %. This condition was met in all the scaffolds that were spun out of polymers, which were previously described as mostly biocompatible. No cytotoxicity on fibroblast cells was observed for PDLLA scaffolds and PLA/HA composites [40].

3. Conclusions

A semi-synthetic ELAHA bioconjugate has been obtained and described here by exploiting the reactivity of a methacrylamide linker on MAAHA. Simultaneously, because of the low reactivity of the linker, Cys and NAcCys have been investigated in a study on the thiol-Michael addition, where the efficiencies of MAAHA and MAHA have been compared. The study displayed that the different reactivity and efficiency are related to a combination of pH, electron-withdrawing properties of the linkers and the phosphine catalyst excess.

Moreover, to pursue the attractive properties of hyaluronan-elastin materials in wound healing applications, a set of bio-inspired electrospun scaffolds composed of HA, MAAHA, ELAHA, and PDLLA have been produced, evaluating their morphology. The nonquantitative functionalization in the derivative ELAHA affected the morphology, increasing the diameter of the fibers.

At the same time, the cell viability on the electrospun scaffolds has been evaluated, demonstrating the increase of the cells' metabolic activity in the case of the scaffolds containing semi-synthetic derivatives compared to those containing pure HA, even though not significantly.

4. Experimental Section

Materials: Commercial-grade reagents and solvents were used without further purification, except where otherwise indicated. The term "pure H_2O" refers to water purified by a Millipore Milli-Q Gradient system. HA (Mw=186 KDa) medical device grade was a generous gift of Altergon Italia SrL. 2-AEMAA · HCl, MTS Assay Kit, 3-(Trimethylsilyl)propionic-2,2,3,3-d_4 acid sodium salt (DSS), NAcCys, Cys, sodium chloride (NaCl), sodium hydroxide pellets (NaOH) were purchased from Sigma Aldrich. HFP and EDC · HCl were purchased from Iris Biotech GmbH, and s-NHS was purchased from TCI Chemicals.

Peptide **1** was synthesized as recently reported.[1] Dulbecco's modified Eagle's medium, fetal bovine serum, penicillin-streptomycin, TCEP · HCl were purchased from ThermoFisher Scientific. PDLLA (EasyFil PLA, transparent pellets, molecular weight: 126 kDa, density: 1240 kg/m^3) was obtained from FormFutura.

Dermal fibroblasts cells (20.000 cells/well) were purchased from PromoCell.

Dialyses were conducted on Slide-A-LyzersTM Dialysis Cassette G2 2.0 kDa cut-off membranes at 25 °C for MAAHA and MAHA and 3.5 kDa for ELAHA. Freeze-drying was performed with a Christ Alpha 1–4 LD plus freeze-dryer.

NMR Spectroscopy: NMR spectra were recorded on 500 MHz (^{1}H: 500 MHz), 400 MHz (^{1}H: 400 MHz, ^{31}P: 162 MHz) Varian Inova instruments in D_2O (DSS 10 mM as internal standard, δ_H=0 ppm, δ_C=0 ppm).

COSY experiments were performed using spectral widths of either 3750 Hz in both dimensions, using data sets of 2048×256 points. $DS_{methacryl}$ and $DS_{addition}$ of **2**, **3**, **4**, **5-i**,**ii**, **6-i**,**ii**, **7-i**,**ii** and **8-i**,**ii** are attributed to disaccharide repeating units.

ATR-FTIR Spectroscopy: ATR spectra were recorded on a model J-460 instrument (Jasco Europe Srl) equipped with an ATR PRO ONE Single-reflection ATR accessory using a single crystal diamond ATR prism. Spectra were acquired in the region from 4000 to 450 cm^{-1} with a spectral resolution of 2 cm^{-1} and 256 scans. Background spectra were recorded each time and then subtracted from the sample spectra.

SEM Analysis: SEM images were acquired with a voltage of 20 kV and different magnifications, after gold sputter-coating on a Philips, FEI ESEM XL30 instrument. The diameter of the fibers was

evaluated, on three images for each scaffold, using ImageJ software supplied with the DiameterJ plug-in (n>100).

MTS Assay: Scaffolds were sterilized during 24 h using UV irradiation (254 nm) then placed in sterile 24-wells plate. Wells containing gelatin coating were coated during 1 h at 37 °C before cells seeding. The fabricated scaffolds were tested for biocompatibility. For this purpose, a cytotoxicity test has been performed using an MTS assay. Each polymer was incubated for 24 h at 37 °C and 5 % CO_2 in Dulbecco's modified Eagle's medium and 1 % penicillin-streptomycin before seeding cells. Dermal fibroblasts cells were then cultured for 24 h and 48 h on the different scaffolds with sterile cell culture medium supplemented with 10 % fetal bovine serum. The cell culture medium alone served as a negative control. Subsequently, the MTS assay was performed according to the manufacturer's protocol (100 µL of MTS were added to each well and incubated for 2 h at 37 °C). The absorbance of the soluble formazan produced by the cellular reduction of MTS was measured at 490 nm (n=3). The cell viability was determined by the absorption of the samples relative to the control.

General procedure for the Thiol-Michael addition study: The thiol donor and TCEP · HCl were mixed and dissolved in pure H_2O obtaining respectively a 32 mM and 47 mM solution. After five minutes it was added to an 8.4 mM solution either of **2** or **4**, and the pH was adjusted to 8.9 with freshly prepared 1.0 M NaOH solution. After 48 h at room temperature the mixture was neutralized with HCl 0.1 M solution and dialyzed against NaCl 150 mM solution for 2 days, and against H_2O for further 2 days. The subsequent freeze-drying yielded a white solid with TCEP=O and TCEP=S as impurities in the derivatives.

Acknowledgments

The authors thank Altergon SrL (Morra De Sanctis, AV, Italy) for hyaluronic acid supply and Mr. Alessandro Laurita (Microscopy Center, University of Basilicata, Potenza, Italy) for SEM images. The authors are grateful for the financial support by PON R&I2014–2020 (cod: PON_ARS01_01081 and Azione IV.6) from MUR and for the PhD scholarship of FA supported by INPS.

Conflict of interest

The authors declare no conflict of interest.

Data Availability Statement

The data that support the findings of this study are available from the corresponding author upon reasonable request.

Supporting Information

A Study on Thiol-Michael Addition to Semi-Synthetic Elastin-Hyaluronan Material for Electrospun Scaffolds

Antonio Laezza, Antonietta Pepe, Nicola Solimando, Francesca Armiento, Floriane Oszust, Laurent Duca, and Brigida Bochicchio*

Table of Contents

Experimental section	**354**
Figure S1. ^{1}H-NMR spectrum of derivative **2.**	**358**
Figure S2. ^{1}H-NMR spectrum of derivative **4.**	**359**
Figure S3. ^{1}H-NMR spectra of derivatives **2, 5-i,** and **5-ii.**	**360**
Figure S4. ^{1}H-NMR spectra of derivatives **4, 6-i,** and **6-ii.**	**361**
Figure S5. ^{1}H-NMR spectra of derivatives **2, 7-i,** and **7-ii.**	**362**
Figure S6. ^{1}H-NMR spectra of derivatives **4, 8-i,** and **8-ii.**	**363**
Figure S7. COSY spectrum magnification of derivative **5-i.**	**364**
Figure S8. COSY spectrum magnification of derivative **5-ii.**	**365**
Figure S9. COSY spectrum magnification of derivative **6-i.**	**366**
Figure S10. COSY spectrum magnification of derivative **6-ii.**	**367**
Figure S11 COSY spectrum magnification of derivative **7-i.**	**368**
Figure S12 COSY spectrum magnification of derivative **7-ii.**	**369**
Figure S13 COSY spectrum magnification of derivative **8-ii.**	**370**
Figure S14. ^{31}P-NMR spectra of derivative **3** and **TCEP·HCl.**	**371**
Figure S15. ^{31}P-NMR spectra of **TCEP·HCl**, derivatives **5-i**, and **5-ii.**	**372**
Figure S16. ^{31}P-NMR spectra of **TCEP·HCl**, derivatives **6-i**, and **6-ii.**	**373**
Figure S17. ^{31}P-NMR spectra of **TCEP·HCl,** derivatives **7-i**, and **7-ii.**	**374**
Figure S18. ^{31}P-NMR spectra of **TCEP·HCl,** derivatives 8**-i**, and **8-ii.**	**375**
Figure S19. ATR-FTIR spectra of **HA,** derivative **2,** peptide **1** and derivative **3.**	**376**
Figure S20A. Histogram of the frequency as a function of fibers diameter of electro-spun scaffold MAHP.	**377**
Figure S20B. Histogram of the frequency as a function of fibers diameter of electro-spun scaffold EAHP.	**378**
Figure S21 Histogram of average fibers diameter of electrospun scaffolds.	**379**
Figure S22A. Cell viability on electrospun scaffolds after 24 h.	**380**
Figure S22B. Cell viability on electrospun scaffolds after 48 h.	**381**
Table S1. MTS assay on electrospun scaffolds.	**382**

Experimental section

Materials: Commercial-grade reagents and solvents were used without further purification, except where otherwise indicated. The term "pure H_2O" refers to water purified by a Millipore Milli-Q Gradient system. Hyaluronic acid sodium salt (Mw = 186 KDa) medical device grade was a generous gift of Altergon Italia SrL. 2-Aminoethylmethacrylamide hydrochloride (≥98.0%, 2-AEMAA), 3-(4,5-dimethylthiazol-2-yl)-5-(3-carboxymethoxyphenyl)-2-(4-sulfophenyl)-2H-tetrazolium (MTS), 3-(Trimethylsilyl)propionic-2,2,3,3-d_4 acid sodium salt (98.0%, DSS), *N*-acetyl-L-cysteine (≥98.0%, NAcCys), L-cysteine (≥97.0%, Cys), sodium chloride (≥99.0%, NaCl), sodium hydroxide pellets (≥98.0%, NaOH) were purchased from Sigma Aldrich. 1-Hydroxybenzotriazole hydrate (≥98%, HOBt), was furnished by Fluka. 1,1,1,3,3,3-hexafluoro-2-propanol (HFP) and *N*-(3-(Dimethylamino)propyl)-*N*'-ethylcarbodiimide hydrochloride (EDC·HCl) were purchased from Iris Biotech GmbH, and *N*-Hydroxysulfosuccinimide sodium salt (>98%, s-NHS) was purchased from TCI Chemicals.

Peptide **1** was synthesized as recently reported.[1] Dulbecco's modified Eagle's medium, fetal bovine serum, penicillin−streptomycin, Tris(2-carboxyethyl)phosphine hydrochloride (TCEP·HCl) was purchased from ThermoFisher Scientific. PDLLA (EasyFil PLA, transparent pellets, molecular weight: 126 kDa, density: 1240 kg/m^3) was obtained from FormFutura.

Dermal fibroblasts cells (20.000 cells/wel) were purchased from PromoCell.

Dialyses were conducted on Slide-A-LyzerTM Dialysis Cassette G2 2.0 kDa cut-off membranes at 25 °C for MAAHA and MAHA and 3.5 kDa for ELAHA. Freeze-drying was performed with a Christ Alpha 1-4 LD plus freeze-dryer.

Nuclear magnetic resonance (NMR) spectroscopy: NMR spectra were recorded on 500 MHz (^{1}H: 500 MHz), 400 MHz (^{1}H: 400 MHz, ^{31}P: 162 MHz) Varian Inova instruments in D_2O (DSS 10 mM as internal standard, δ_H = 0 ppm, δ_C = 0 ppm).

Gradient selected correlation spectroscopy (COSY) experiments were performed using spectral widths of either 3750 Hz in both dimensions, using data sets of 2048×256 points. The degrees of substitution ($DS_{methacryl}$ and $DS_{addition}$) of **2**, **3**, **4**, **5-i,ii**, **6-i,ii**, **7-i,ii** and **8-i,ii** are attributed to disaccharide repeating units.

Attenuated Total Reflectance Fourier Transform Infrared (ATR-FTIR) Spectroscopy: ATR spectra were recorded on a model J-460 instrument (Jasco Europe Srl) equipped with an ATR PRO ONE Single-reflection ATR accessory using a single crystal diamond ATR prism. Spectra were

acquired in the region from 4000 to 450 cm^{-1} with a spectral resolution of 2 cm^{-1} and 256 scans. Background spectra were recorded each time and then subtracted from the sample spectra.

Scanning electron microscopy (SEM): SEM images were acquired with a voltage of 20 kV and different magnifications, after gold sputter-coating on a Philips, FEI ESEM XL30 instrument. The diameter of the fibers was evaluated, on three images for each scaffold, using ImageJ software supplied with the DiameterJ plug-in (n > 100).

MTS Assay: Scaffolds were sterilized during 24 h using UV irradiation (254 nm) then placed in sterile 24-wells plate. Wells containing gelatin coating were coated during 1 h at 37 °C before cells seeding. The fabricated scaffolds were tested for biocompatibility. For this purpose, a cytotoxicity test has been performed using an MTS assay. Each polymer was incubated for 24 h at 37 °C and 5% CO_2 in Dulbecco's modified Eagle's medium and 1% penicillin−streptomycin. Dermal fibroblasts cells were then cultured for 24 h and 48 h with the sterile filtered extraction medium supplemented with 10% fetal bovine serum. The medium without polymer extract served as a negative control. Subsequently, the MTS assay was performed according to the manufacturer's protocol (100 µL of MTS were added to each well and incubated for 2 h at 37 °C). The absorbance of the soluble formazan produced by the cellular reduction of MTS was measured at 490 nm (n = 3). The cell viability was determined by the absorption of the samples relative to the control.

Synthesis of derivative 2: Sodium hyaluronate (202.95 mg, 0. 506 mmol) was suspended in pure H_2O (30.0 mL) and stirred at room temperature up to complete dissolution, then treated with a 49.6 mM EDC (20.4 mL, 1.01 mmol) and 24.8 mM s-NHS (20.4 mL, 0.506 mmol) solution. After five minutes a 122.2 mM 2-AEMAA (8.4 mL, 1.01 mmol) was added to the reaction mixture resulting in a molar ratio of 1:2:2 (s-NHS:EDC:2-AEMAA), obtaining a clear solution. Few drops of freshly prepared 1.0 M NaOH solution were then added to adjust pH to 6.5, and stirring was continued overnight. After ~ 20 h, the crude was neutralized by HCl 1.0 M and centrifuged, the supernatant was dialyzed against NaCl 150 mM solution for 2 days, and against H_2O for further 2 days. The subsequent freeze-drying yielded a white solid (174.35 mg, yield: 79%). ^{1}H-NMR (400 MHz, D_2O): δ_{DSS} = 5.69 (CH_a Linker), 5.45 (CH_b Linker), 4.55 (H-1 GlcNAc), 4.46 (H-1 GlcA), 4.00-3.20 (H-2, H-3, H-4, H-5 GlcA, H-2, H-3, H-4, H-5, H-6 GlcNAc, CH_{2a}, CH_{2b} Linker), 2.01 (CH_3 GlcNAc), 1.91 (CH_3 Linker).

Synthesis of derivative 3: Derivative **2** (9.05 mg, 0.021 mmol) was suspended in pure H_2O (1.5 mL) and stirred at room temperature up to complete dissolution. Peptide **1** (52.29 mg, 0.028 mmol) synthesized by Solid Phase Peptide Synthesis (SPPS), with a purity of 97% and chemical structure assessed by High-Performance Liquid Chromatography (HPLC) and Matrix-Assisted Laser Desorption/Ionization-Time of Flight (MALDI-TOF) mass spectrometry, respectively[29] and TCEP·HCl (12.01 mg, 0.042 mmol) were simultaneously dissolved in pure H_2O (2.0 mL) at room temperature obtaining a 13.95 mM and 20.96 mM solution. After five minutes this solution was added to **2** and the pH was adjusted to 8.9 with freshly prepared 1.0 M NaOH solution. After 48 h at room temperature the mixture was neutralized with HCl 0.1 M solution and dialyzed against NaCl 150 mM solution for 2 days, and against H_2O for further 2 days. The subsequent freeze-drying yielded a white solid (9.28 mg, yield: 41%).^{1}H-NMR (400 MHz, D_2O): δ_{DSS} = 5.69 (CH_a Linker), 5.45 (CH_b Linker), 4.55 (H-1 GlcNAc), 4.46 (H-1 GlcA), 4.00-3.20 (17H), 2.16-1.91 (CH_3 GlcNAc, CH_3 NAcCys, CH_3 Linker), 1.53-1.31 (H_α+H_β Leu, H_β+H_γ+H_δ Lys, CH_3 Ala, CH_3 Linker), 0.89 (CH_3 Leu)

Synthesis of derivative 4: Sodium hyaluronate (183.42 mg, 0.457 mmol) was suspended in pure H_2O (27.1 mL) and stirred at room temperature up to complete dissolution, then treated with a 49.6 mM EDC (18.4 mL, 0.914 mmol) and 24.8 mM s-NHS (18.4 mL, 0.457 mmol) solution. After five minutes a 122.2 mM 2-AEMA (7.5 mL, 0.914 mmol) was added to the reaction mixture resulting in a molar ratio of 1:2:2 (s-NHS:EDC:2-AEMA), obtaining a yellowish suspension. Few drops of freshly prepared 1.0 M NaOH solution were then added to adjust pH to 6.5, and stirring was continued overnight. After ~ 20 h, the crude was neutralized by HCl 1.0 M and centrifuged, the supernatant was dialyzed against NaCl 150 mM solution for 2 days, and against H2O for further 2 days. The subsequent freeze-drying yielded a white solid (188.62 mg, yield: 98%).^{1}H NMR (400 MHz, D_2O): δ_{DSS}= 6.13 (CH_a Linker), 5.73 (CH_b Linker), 4.55 (H-1 GlcNAc), 4.46 (H-1 GlcA), 4.23 (CH_{2a} Linker), 4.00-3.24 (H-2, H-3, H-4, H-5 GlcA, H-2, H-3, H-4, H-5, H-6 GlcNAc, CH_{2b} Linker), 2.01 (CH_3 GlcNAc), 1.91 (CH_3 Linker).

General procedure for the Thiol-Michael addition study: The thiol donor and TCEP•HCl were mixed dissolved in pure H_2O obtaining respectively a 32 mM and 47 mM solution. After five minutes it was added to an 8.4 mM solution either of **2** or **4**, and the pH was adjusted to 8.9 with freshly prepared 1.0 M NaOH solution. After 48 h at room temperature the mixture was neutralized with HCl 0.1 M solution and dialyzed against NaCl 150 mM solution for 2 days, and against H_2O for further 2 days. The subsequent freeze-drying yielded a white solid with TCEP=O and TCEP=S as impurities in the derivatives.

5-i: (54.23 mg, yield: 77%) ^{1}H-NMR (400 MHz, D_2O): δ_{DSS} = 5.69 (C*H*$_a$ Linker), 5.45 (C*H*$_b$ Linker), 4.55 (H-1 GlcNAc), 4.46 (H-1 GlcA), 4.00-3.20 (H-2, H-3, H-4, H-5 GlcA, H-2, H-3, H-4, H-5, H-6 GlcNAc, C*H*$_{2a}$, C*H*$_{2b}$ Linker, H$_\alpha$ Cys), 2.01 (C*H*$_3$ GlcNAc), 1.91 (C*H*$_3$ Linker), 1.31 (C*H*$_3$ Linker). ^{31}P-NMR (162 MHz, D_2O): δ_{DSS} = 58.21 (TCEP=O), 52.83 (TCEP=S).

5-ii: (28.92 mg, yield: 41%) ^{1}H-NMR (400 MHz, D_2O): δ_{DSS} = 5.69 (C*H*$_a$ Linker), 5.45 (C*H*$_b$ Linker), 4.55 (H-1 GlcNAc), 4.46 (H-1 GlcA), 4.00-3.20 (H-2, H-3, H-4, H-5 GlcA, H-2, H-3, H-4, H-5, H-6 GlcNAc, C*H*$_{2a}$, C*H*$_{2b}$ Linker, H$_\alpha$ Cys), 2.01 (C*H*$_3$ GlcNAc), 1.91 (C*H*$_3$ Linker), 1.31 (C*H*$_3$ Linker). ^{31}P-NMR (162 MHz, D_2O): δ_{DSS} = 58.21 (TCEP=O), 52.83 (TCEP=S).

6-i: (26.03 mg, yield: 68%) ^{1}H-NMR (400 MHz, D_2O): δ_{DSS} = 4.55 (H-1 GlcNAc), 4.46 (H-1 GlcA), 4.00-3.20 (H-2, H-3, H-4, H-5 GlcA, H-2, H-3, H-4, H-5, H-6 GlcNAc, C*H*$_{2a}$, C*H*$_{2b}$ Linker, H$_\alpha$ Cys), 2.01 (C*H*$_3$ GlcNAc), 1.31 (C*H*$_3$ Linker). ^{31}P-NMR (162 MHz, D_2O): δ_{DSS} = 58.21 (TCEP=O), 52.83 (TCEP=S).

6-ii: (26.09 mg, yield: 50%) ^{1}H-NMR (400 MHz, D_2O): δ_{DSS} = 4.55 (H-1 GlcNAc), 4.46 (H-1 GlcA), 4.00-3.20 (H-2, H-3, H-4, H-5 GlcA, H-2, H-3, H-4, H-5, H-6 GlcNAc, C*H*$_{2a}$, C*H*$_{2b}$ Linker, H$_\alpha$ Cys), 2.01 (C*H*$_3$ GlcNAc), 1.31 (C*H*$_3$ Linker). ^{31}P-NMR (162 MHz, D_2O): δ_{DSS} = 58.21 (TCEP=O), 52.83 (TCEP=S).

7-i: (18.55 mg, yield: 44%) ^{1}H-NMR (400 MHz, D_2O): δ_{DSS} = 5.69 (C*H*$_a$ Linker), 5.45 (C*H*$_b$ Linker), 4.55 (H-1 GlcNAc), 4.46 (H-1 GlcA), 4.00-3.20 (H-2, H-3, H-4, H-5 GlcA, H-2, H-3, H-4, H-5, H-6 GlcNAc, C*H*$_{2a}$, C*H*$_{2b}$ Linker, H$_\alpha$ NAcCys), 2.01 (C*H*$_3$ GlcNAc, C*H*$_3$ NAcCys), 1.91 (C*H*$_3$ Linker), 1.31 (C*H*$_3$ Linker). ^{31}P-NMR (162 MHz, D_2O): δ_{DSS} = 58.21 (TCEP=O), 52.83 (TCEP=S), 34.51 (Phosphonium ester adduct).

7-ii: (33.19 mg, yield: 57%)^{1}H-NMR (400 MHz, D_2O): δ_{DSS} = 5.69 (C*H*$_a$ Linker), 5.45 (C*H*$_b$ Linker), 4.55 (H-1 GlcNAc), 4.46 (H-1 GlcA), 4.00-3.20 (H-2, H-3, H-4, H-5 GlcA, H-2, H-3, H-4, H-5, H-6 GlcNAc, C*H*$_{2a}$, C*H*$_{2b}$ Linker, H$_\alpha$ NAcCys), 2.01 (CH$_3$ GlcNAc, C*H*$_3$ NAcCys), 1.91 (CH$_3$ Linker), 1.31 (C*H*$_3$ Linker). ^{31}P-NMR (162 MHz, D_2O): δ_{DSS} = 58.21 (TCEP=O), 52.83 (TCEP=S), 34.51 (Phosphonium ester adduct).

8-i: (12.70 mg, yield: 91%) ^{1}H-NMR (400 MHz, D_2O): δ_{DSS} = 4.55 (H-1 GlcNAc), 4.46 (H-1 GlcA), 4.00-3.20 (H-2, H-3, H-4, H-5 GlcA, H-2, H-3, H-4, H-5, H-6 GlcNAc, C*H*$_{2a}$, C*H*$_{2b}$ Linker, H$_\alpha$ NAcCys), 2.01 (C*H*$_3$ GlcNAc, C*H*$_3$ NAcCys), 1.31 (C*H*$_3$ Linker). ^{31}P-NMR (162 MHz, D_2O): δ_{DSS} = 58.21 (TCEP=O), 52.83 (TCEP=S), 34.51 (Phosphonium ester adduct).

8-ii: (12.44 mg, yield: 86%) ^{1}H-NMR (400 MHz, D_2O): δ_{DSS} = 4.55 (H-1 GlcNAc), 4.46 (H-1 GlcA), 4.00-3.20 (H-2, H-3, H-4, H-5 GlcA, H-2, H-3, H-4, H-5, H-6 GlcNAc, C*H*$_{2a}$, C*H*$_{2b}$ Linker, H$_\alpha$ NAcCys), 2.01 (3H, C*H*$_3$ GlcNAc, C*H*$_3$ NAcCys), 1.31 (CH$_3$ Linker). ^{31}P-NMR (162 MHz, D_2O): δ_{DSS} = 58.21 (TCEP=O), 52.83 (TCEP=S), 34.51 (Phosphonium ester adduct)

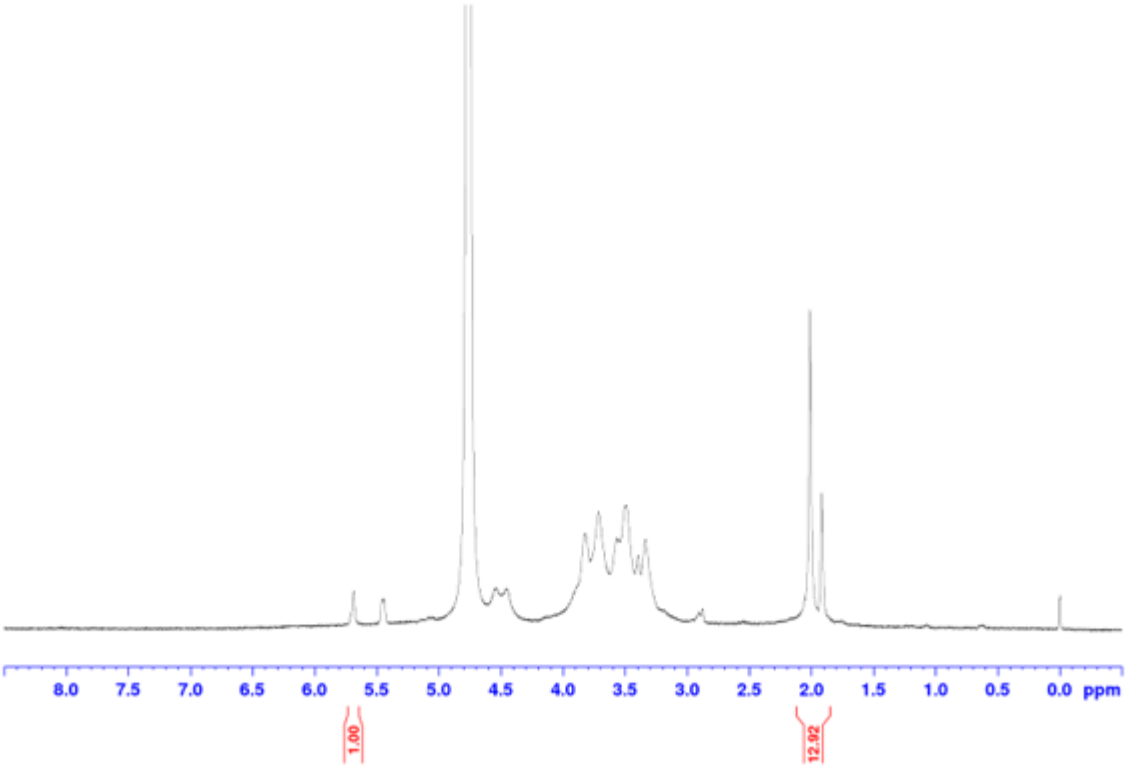

Figure S1. ^{1}H-NMR spectrum of derivative **2** (400 MHz, D_2O, 298 K).

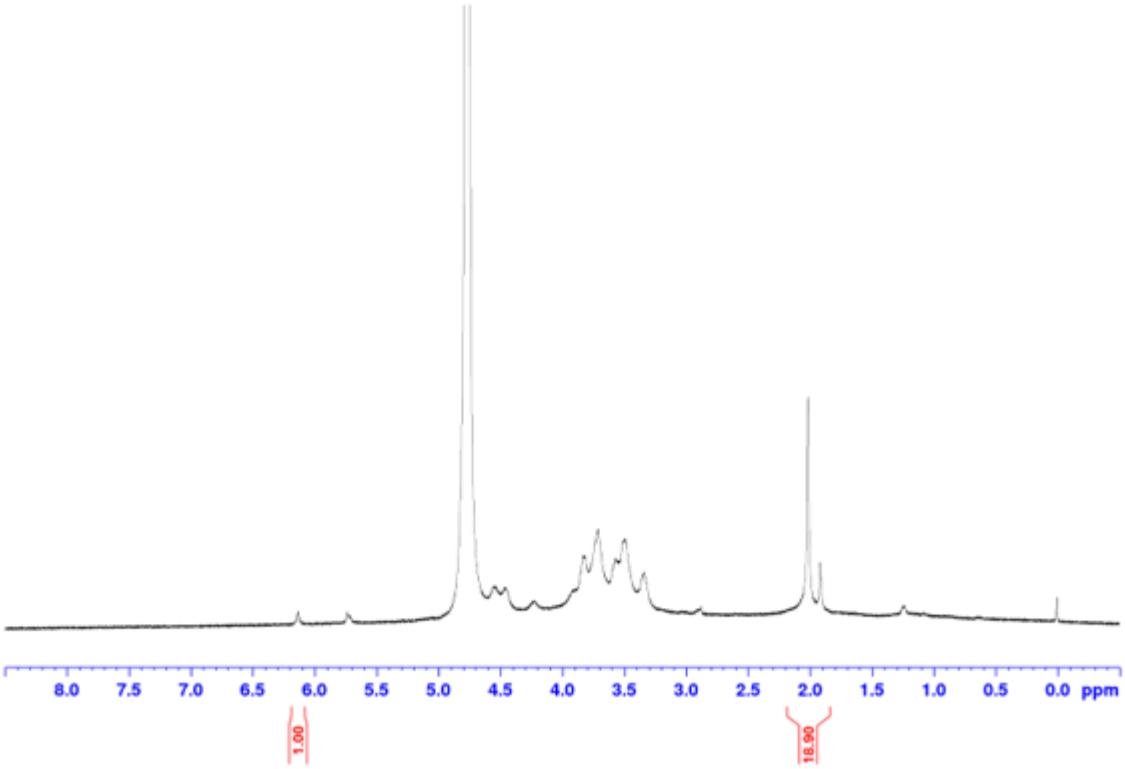

Figure S2. ^{1}H-NMR spectrum of derivative **4** (400 MHz, D_2O, 298 K).

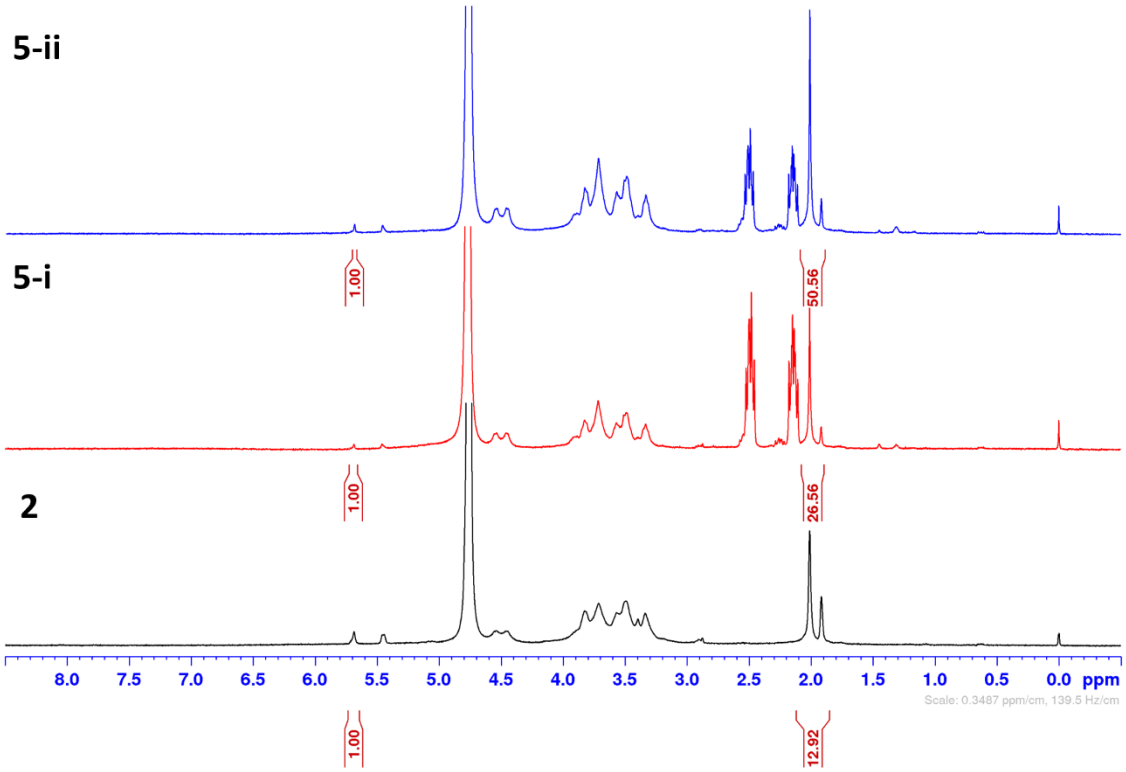

Figure S3. [1]H-NMR spectra of derivatives **2, 5-i, 5-ii** (400 MHz, D_2O, 298 K).

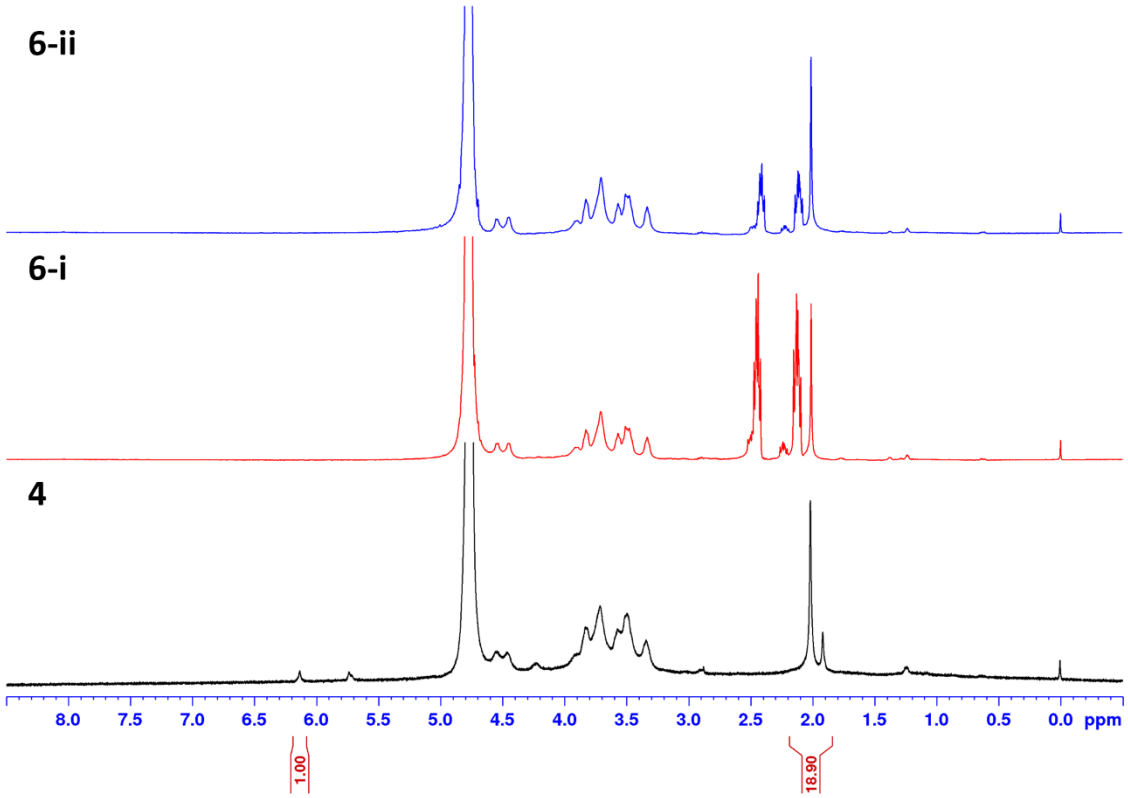

Figure S4. ^{1}H-NMR spectra of derivatives **4, 6-i, 6-ii** (400 MHz, D_2O, 298 K).

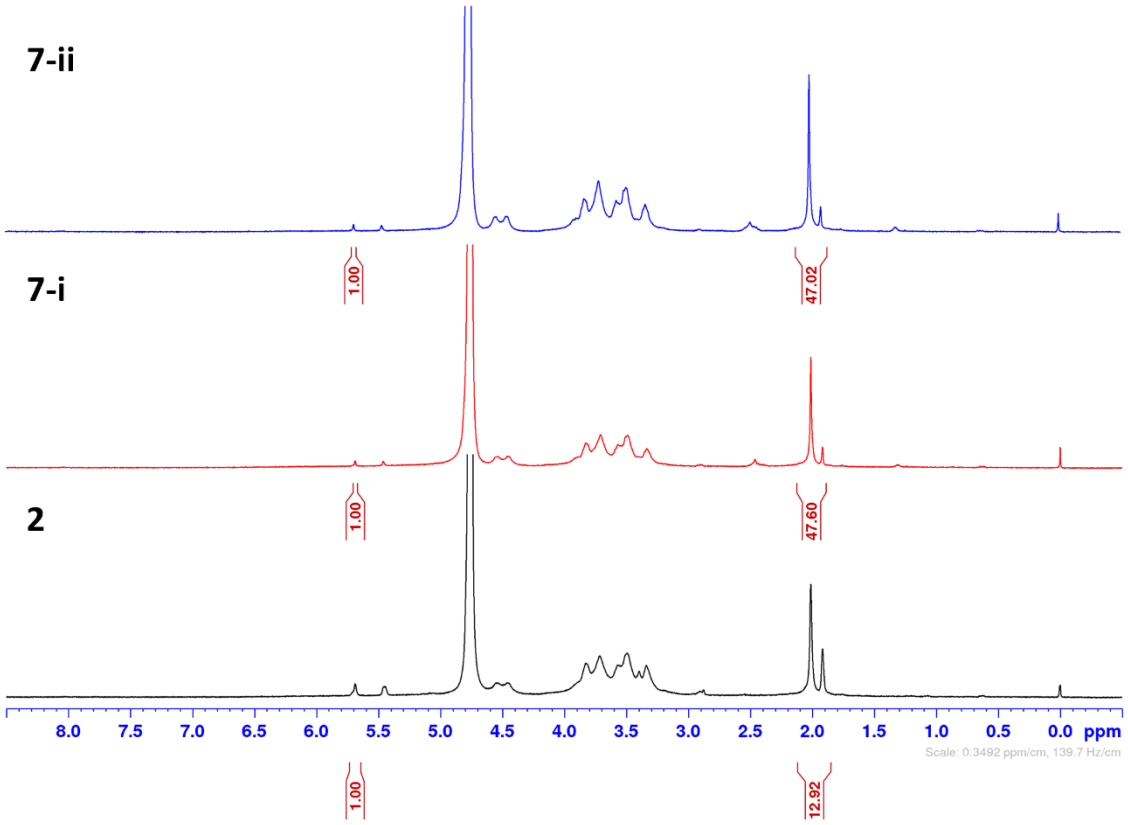

Figure S5. ^{1}H-NMR spectra of derivatives **2, 7-i,** and **7-ii** (400 MHz, D_2O, 298 K).

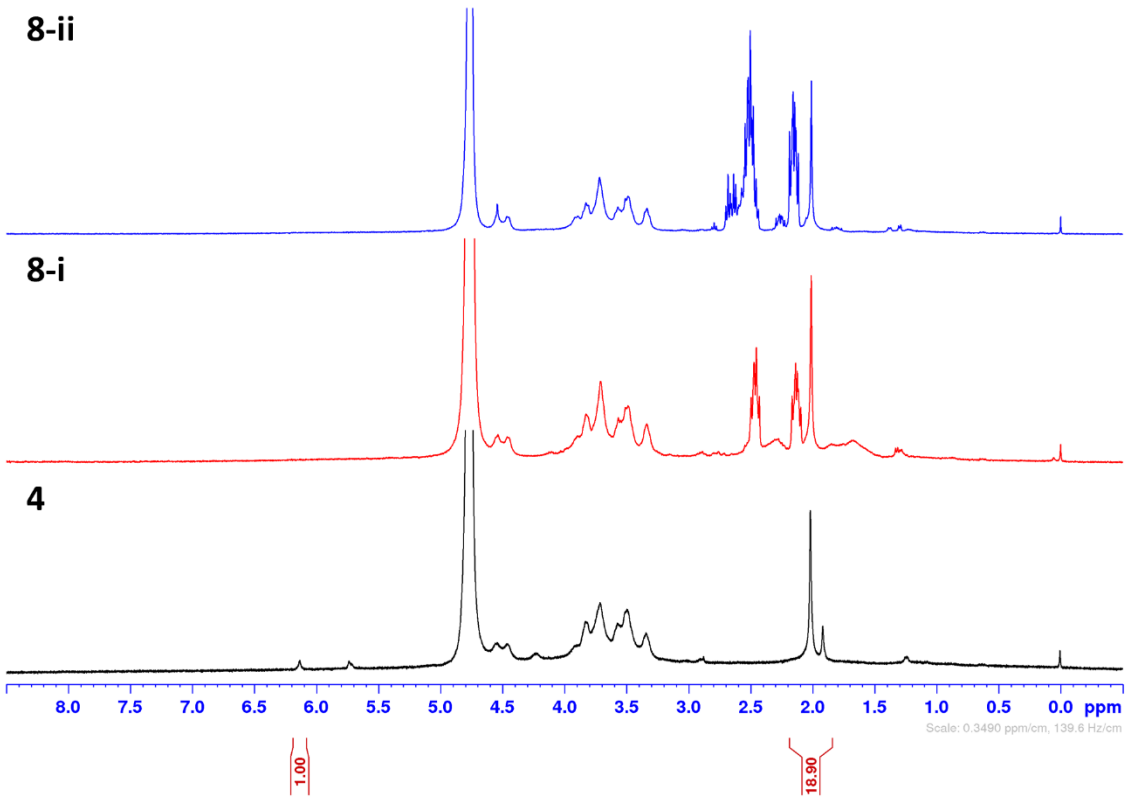

Figure S6. ^{1}**H**-NMR spectra of derivatives **4, 8-i, 8-ii** (400 MHz, D_2O, 298 K).

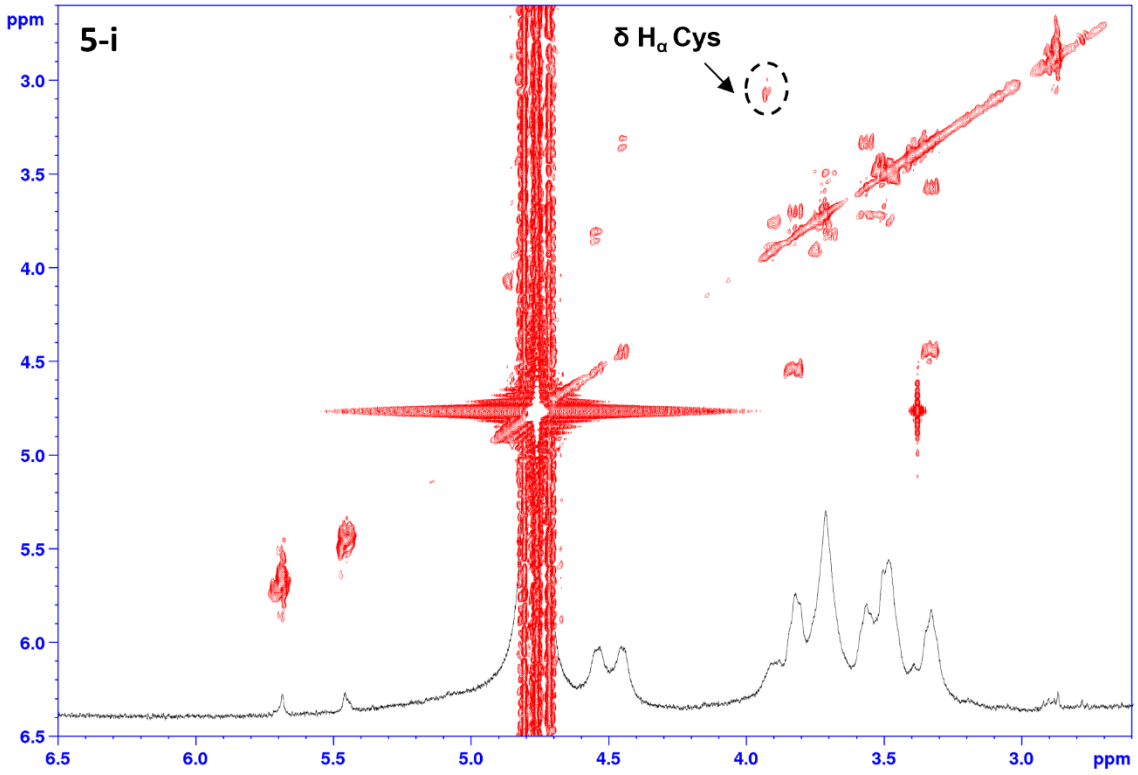

Figure S7. COSY spectrum magnification of derivative **5-i.**

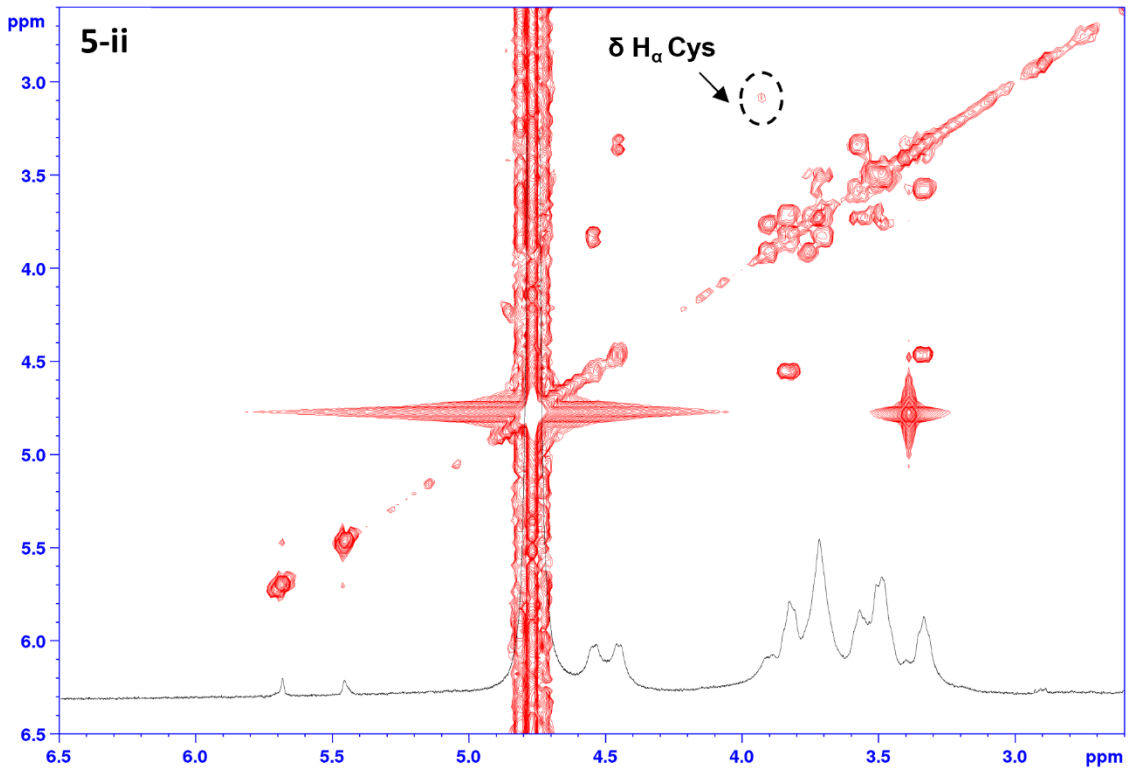

Figure S8. COSY spectrum magnification of derivative **5-ii.**

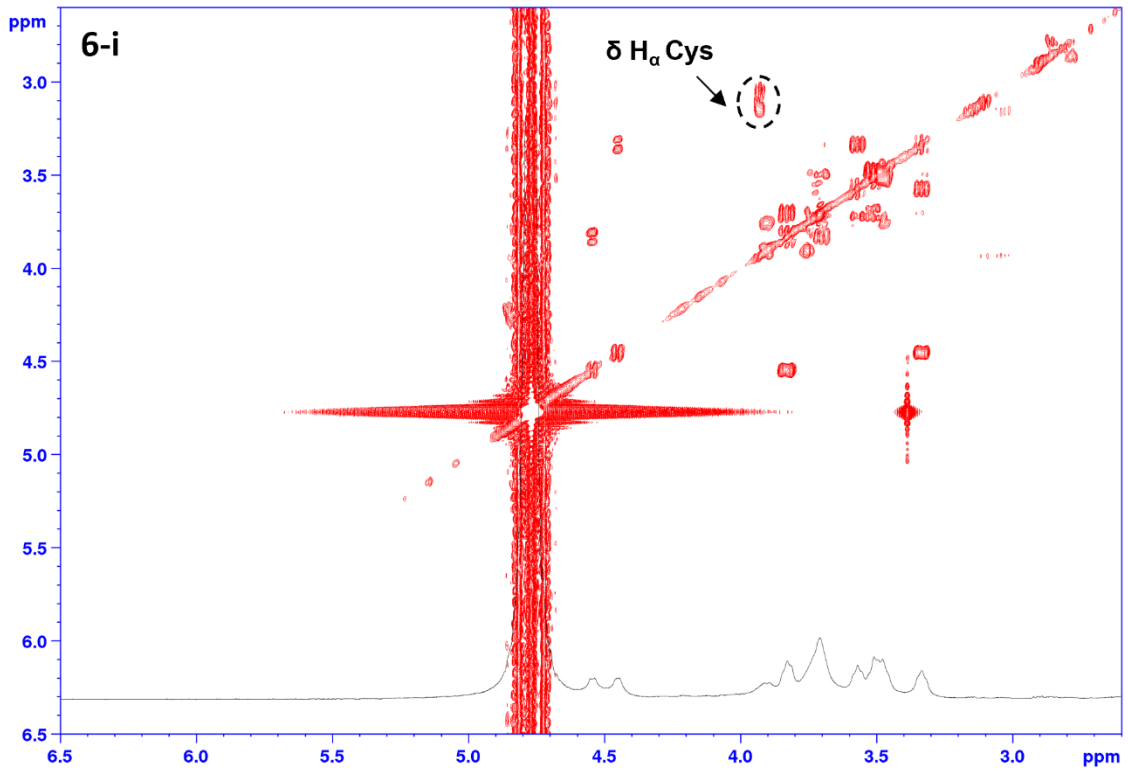

Figure S9. COSY spectrum magnification of derivative **6-i.**

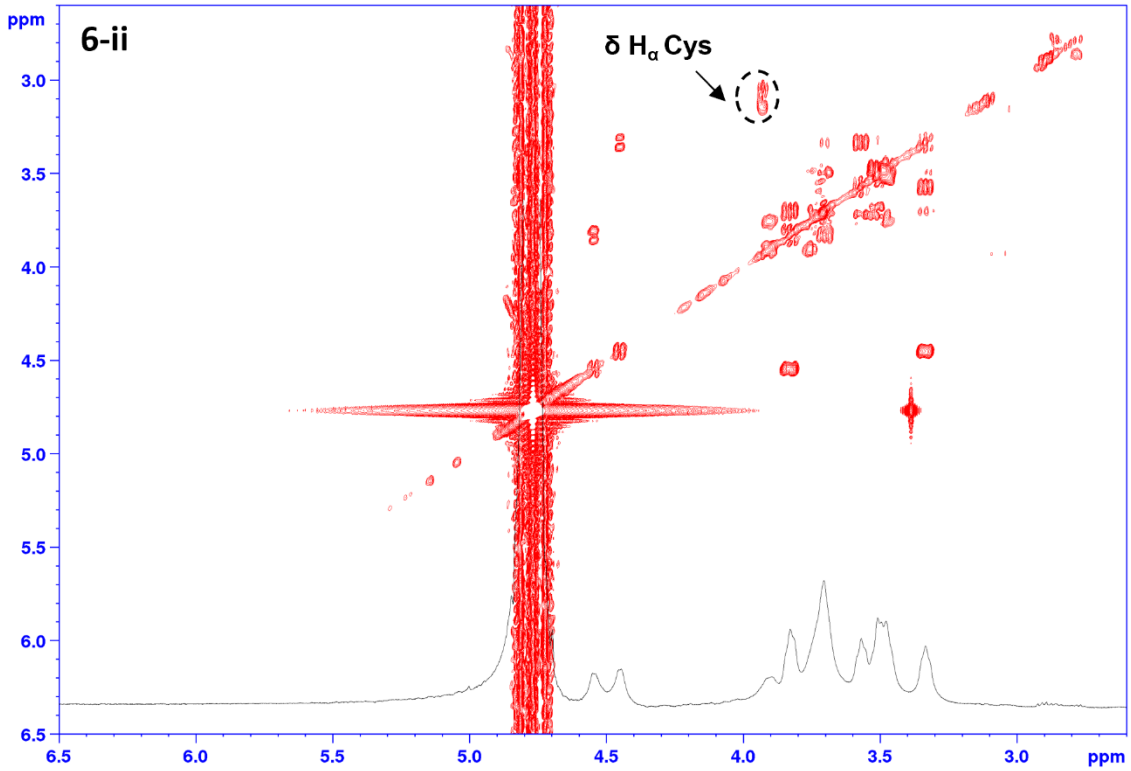

Figure S10. COSY spectrum magnification of derivative **6-ii.**

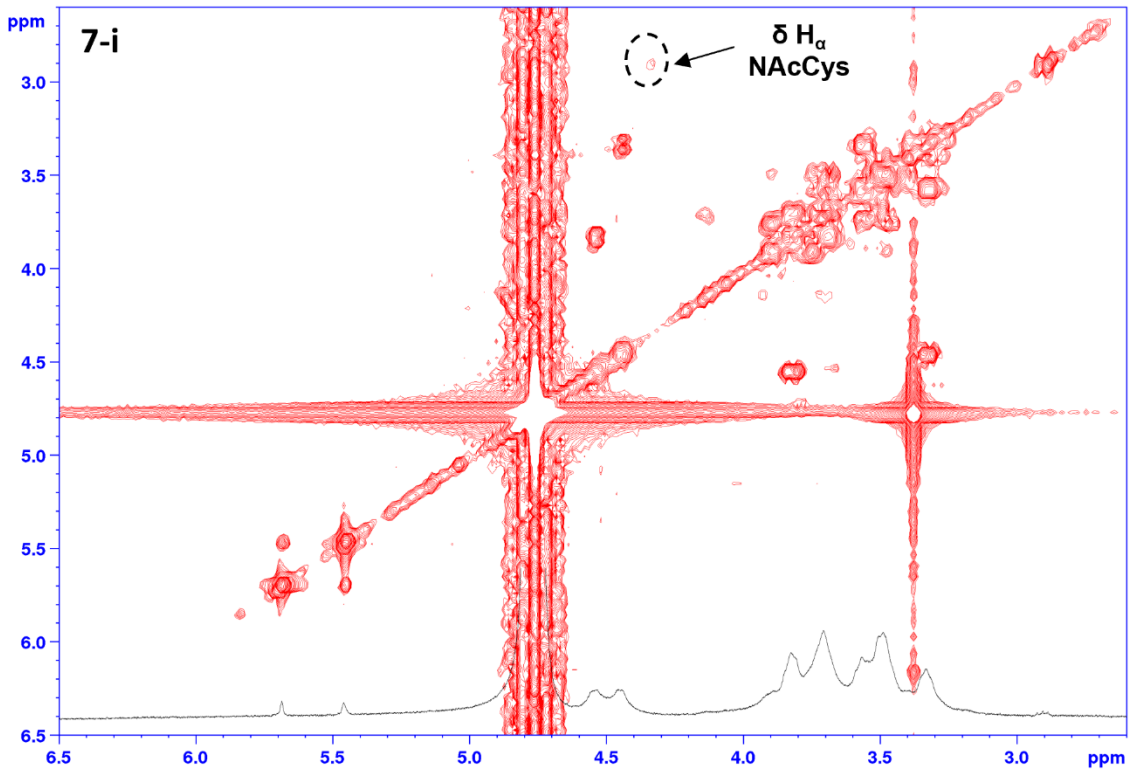

Figure S11. COSY spectrum magnification of derivative **7-i.**

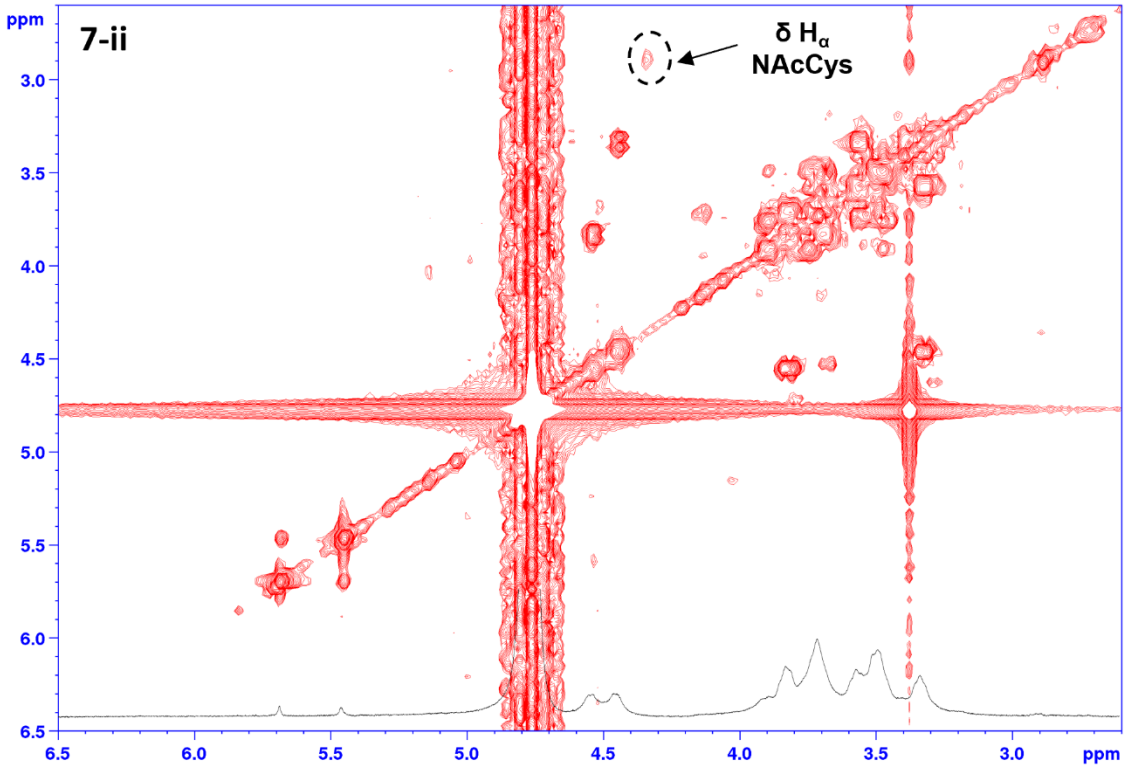

Figure S12. COSY spectrum magnification of derivative **7-ii.**

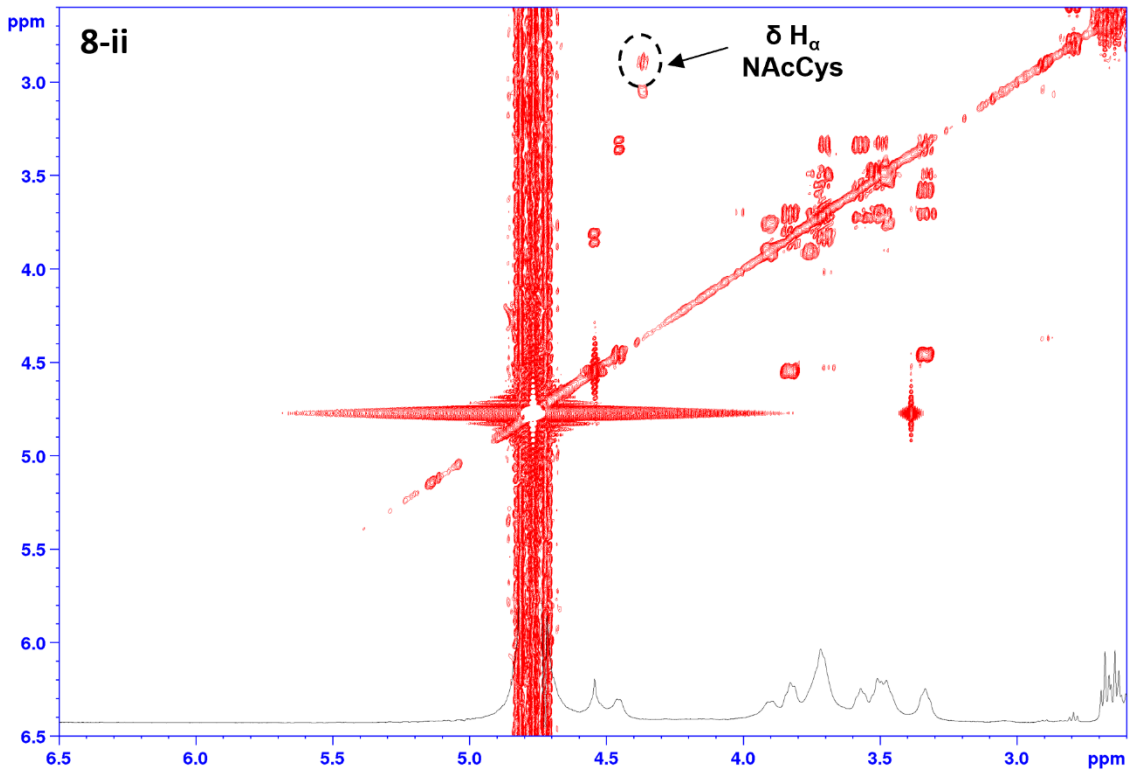

Figure S13. COSY spectrum magnification of derivative **8-ii.**

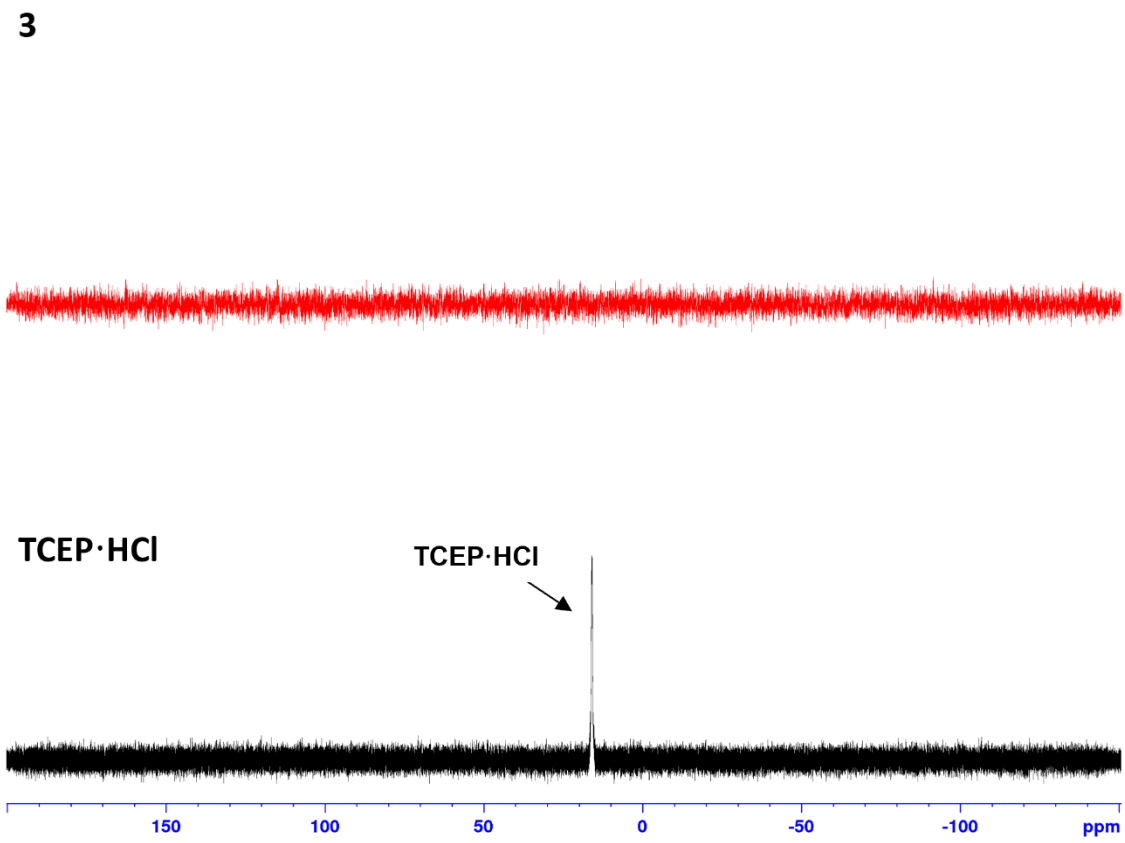

Figure S14. ^{31}P-NMR spectra of derivative **3** and TCEP·HCl.

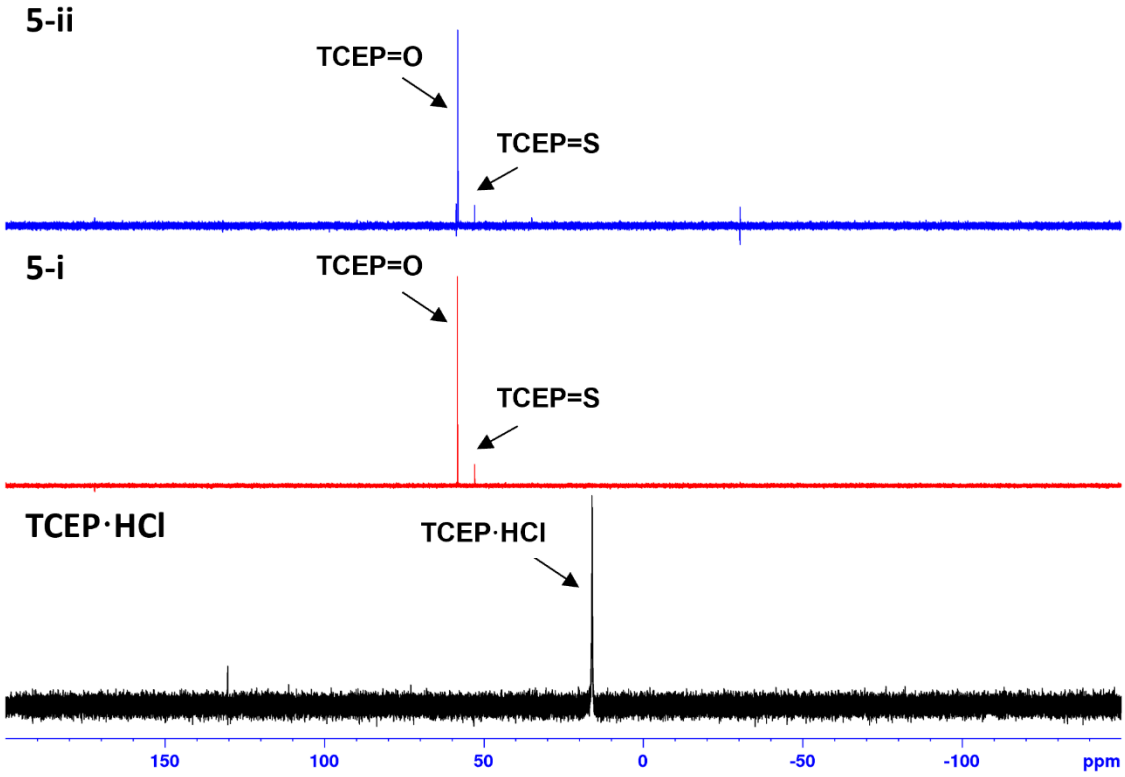

Figure S15. ^{31}P-NMR spectra of **TCEP·HCl**, derivatives **5-i**, and **5-ii** (162 MHz, D_2O, 298 K).

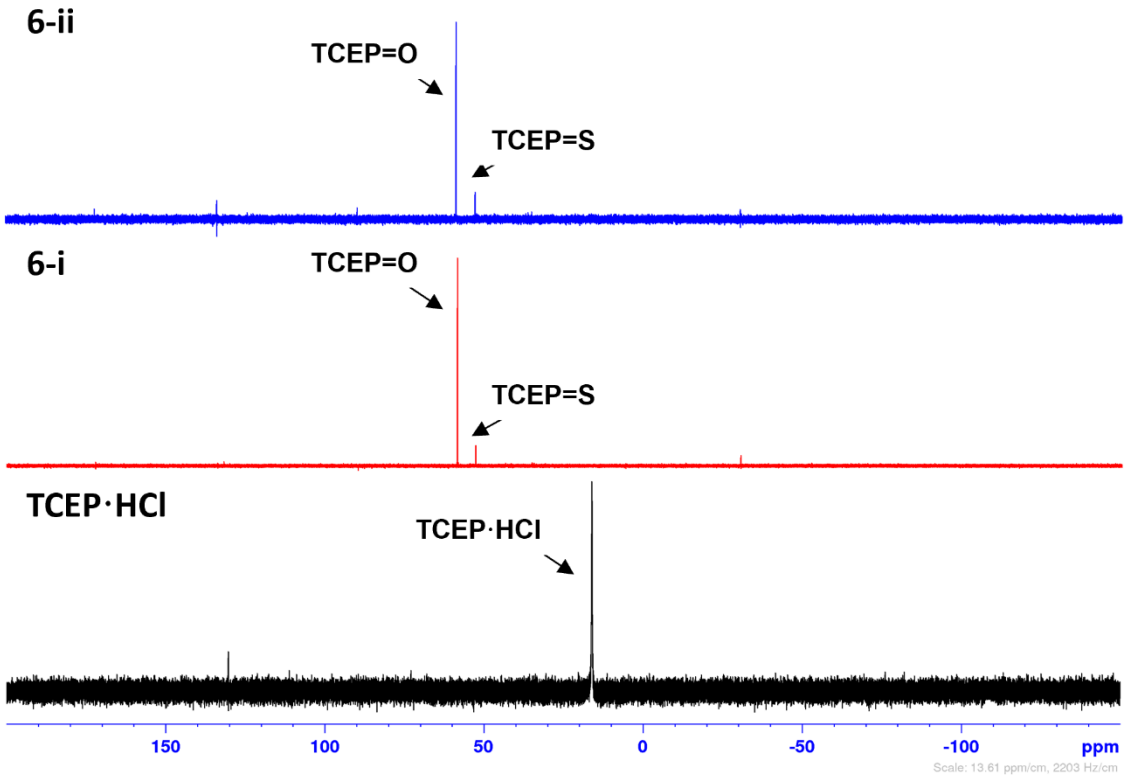

Figure S16. ^{31}P-NMR spectra of **TCEP·HCl**, derivatives **6,i** and **6,ii** (162 MHz, D_2O, 298 K).

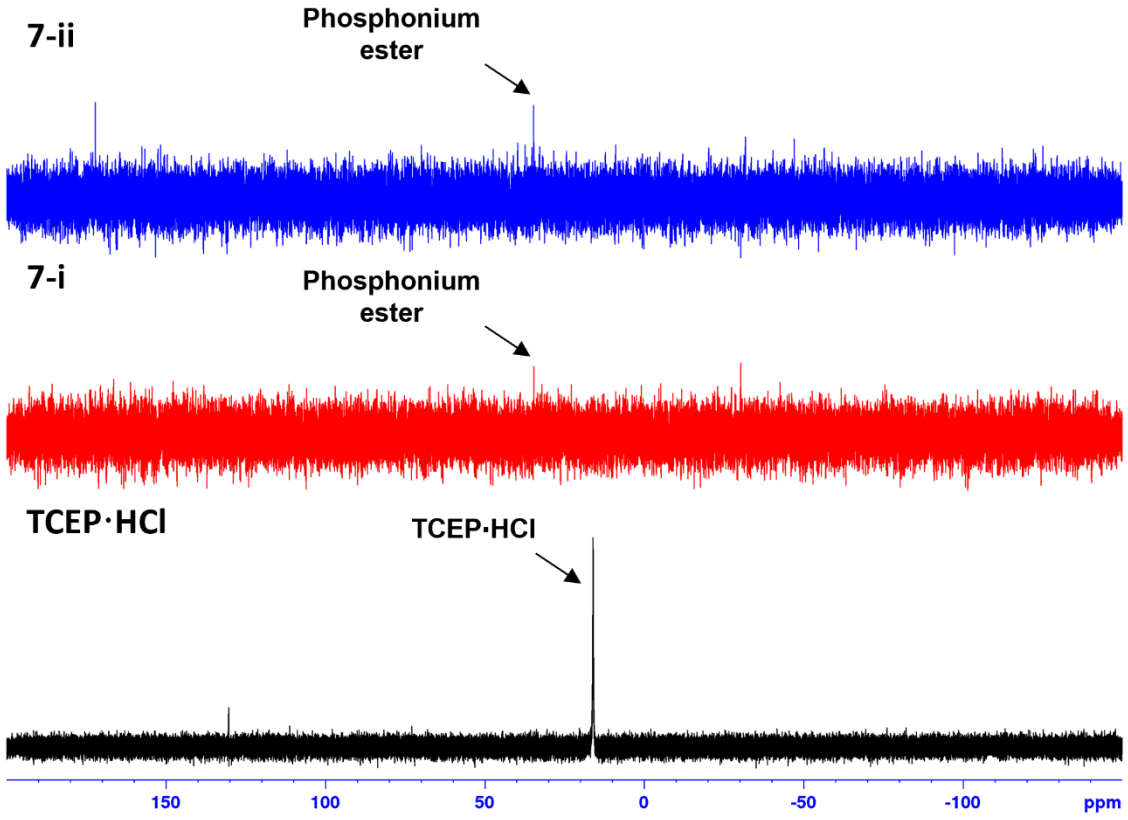

Figure S17. ^{31}P-NMR spectra of **TCEP·HCl**, derivatives **7,i** and **7,ii** (162 MHz, D_2O, 298 K).

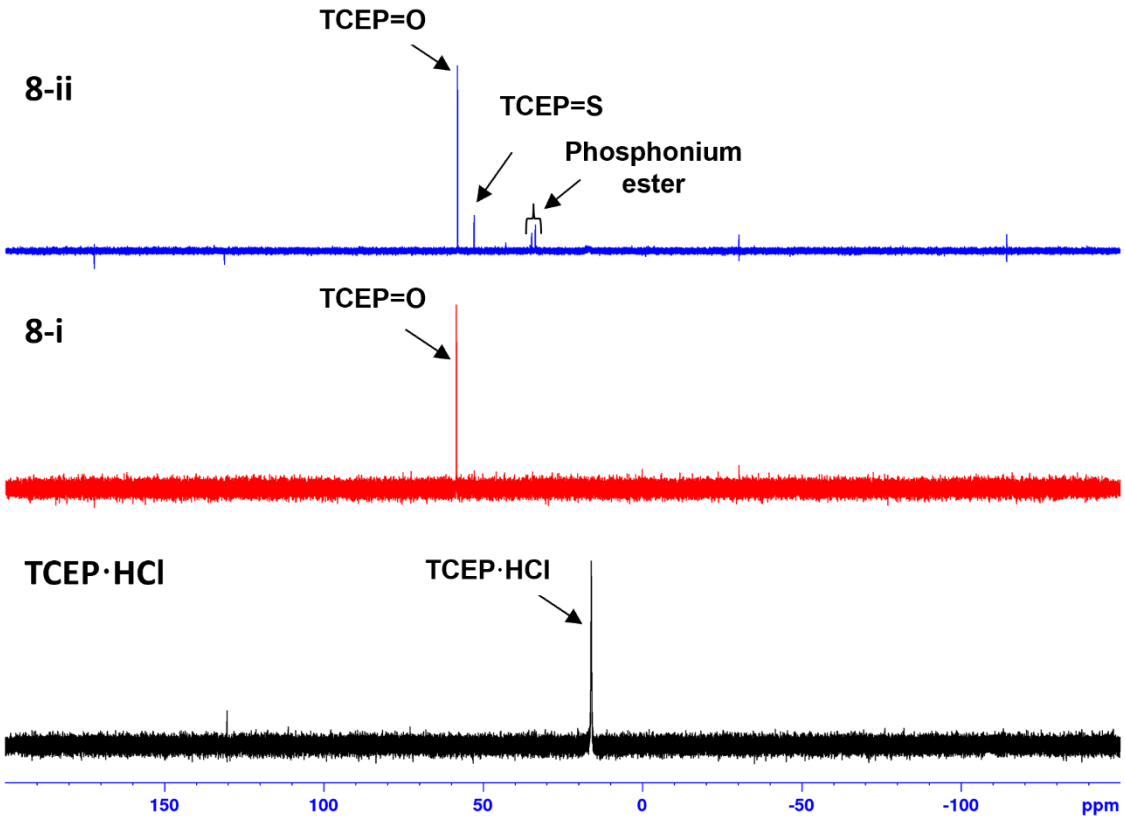

Figure S18. ^{31}P-NMR spectra of **TCEP·HCl**, derivatives **8,i** and **8,ii** (162 MHz, D_2O, 298 K).

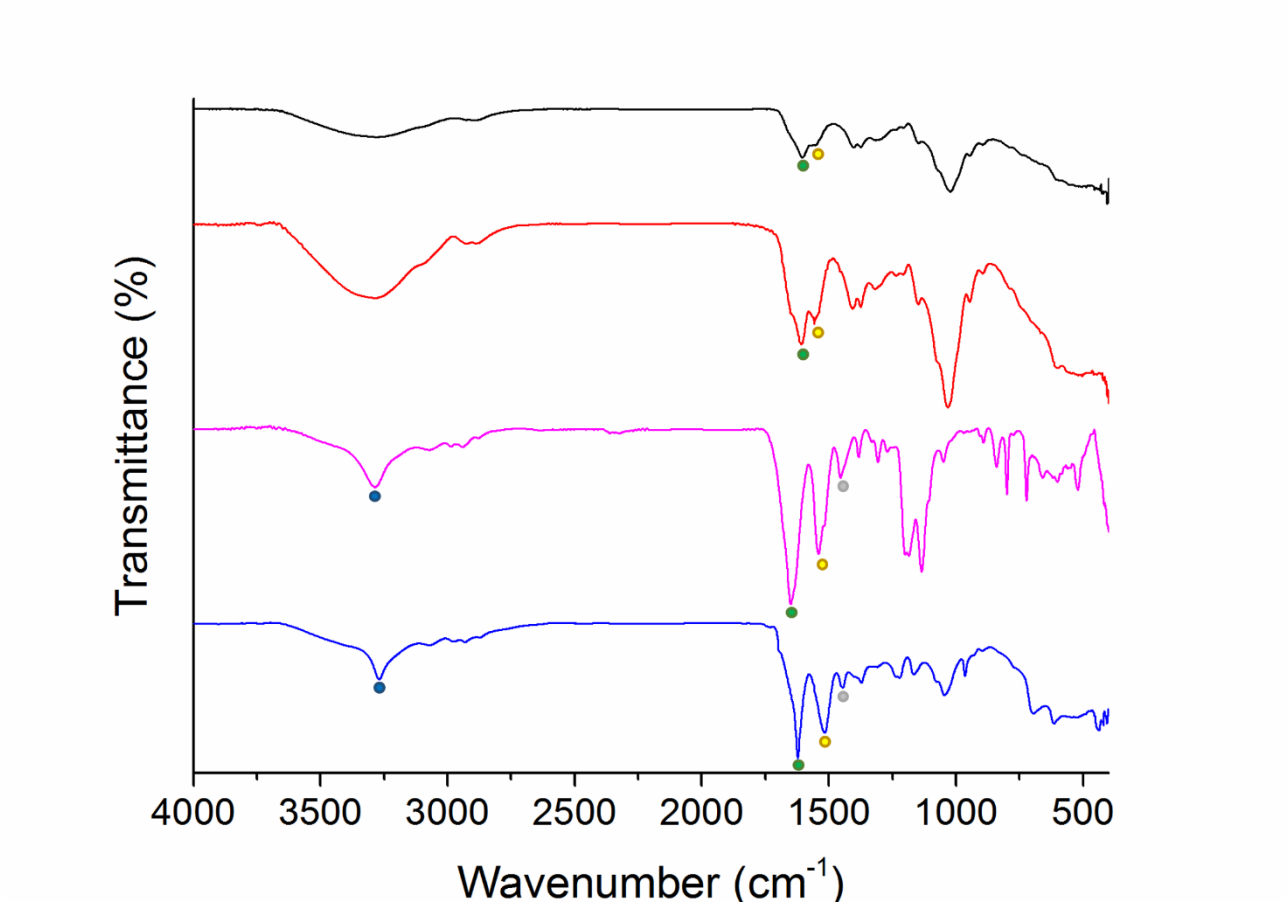

Figure S19. ATR spectra of HA (black), derivative **2** (MAAHA,red), peptide **1** (EL, purple), and derivative **3**, (ELAHA,blue).N-H stretching vibration band (filled blue circle), amide C=O stretching vibration (filled green circle), amide C-N stretching vibration (filled yellow circle), C-H_3 bending vibration (filled gray circle).

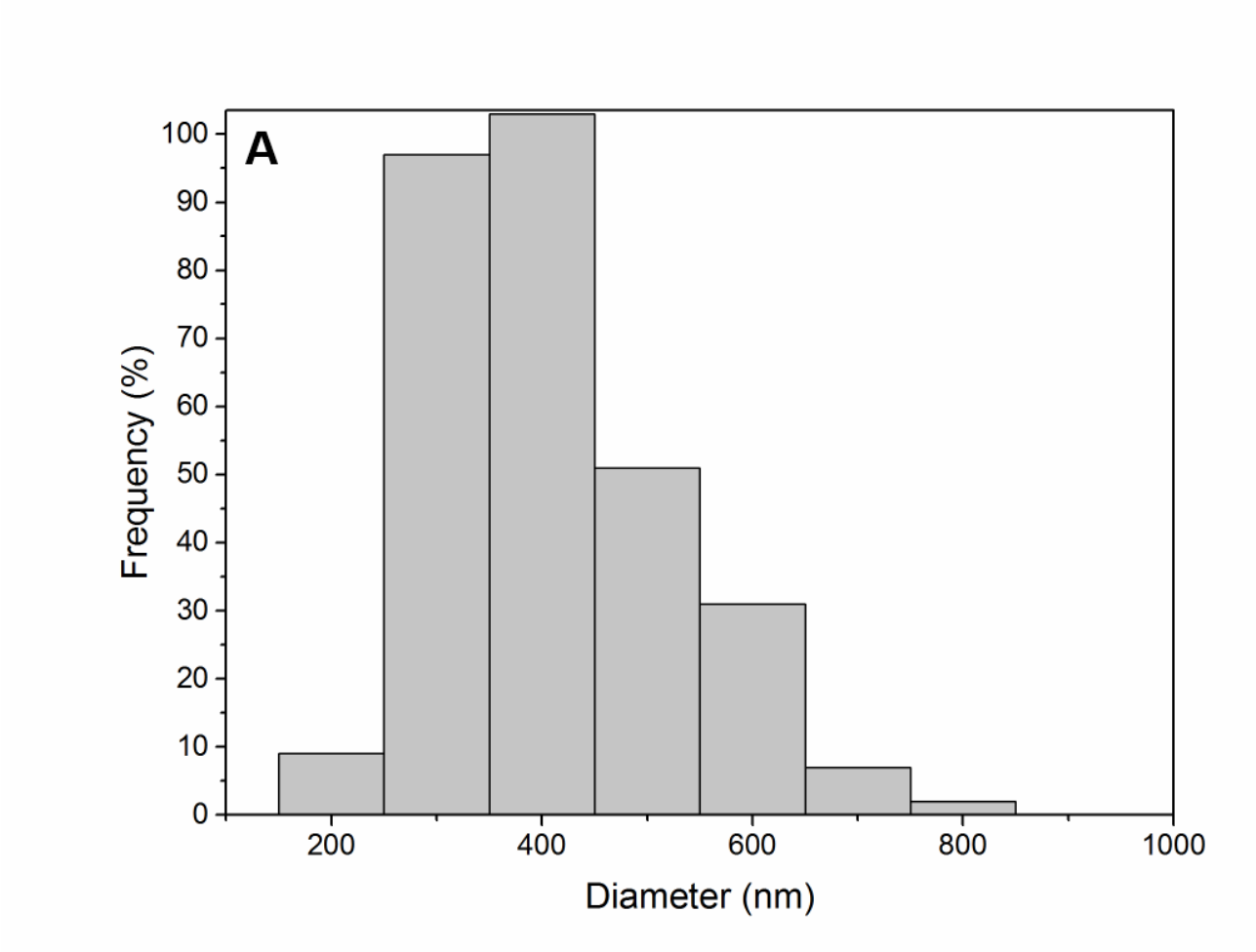

Figure S20A. Histogram of the frequency as a function of fibers diameter of electrospun scaffold MAHP.

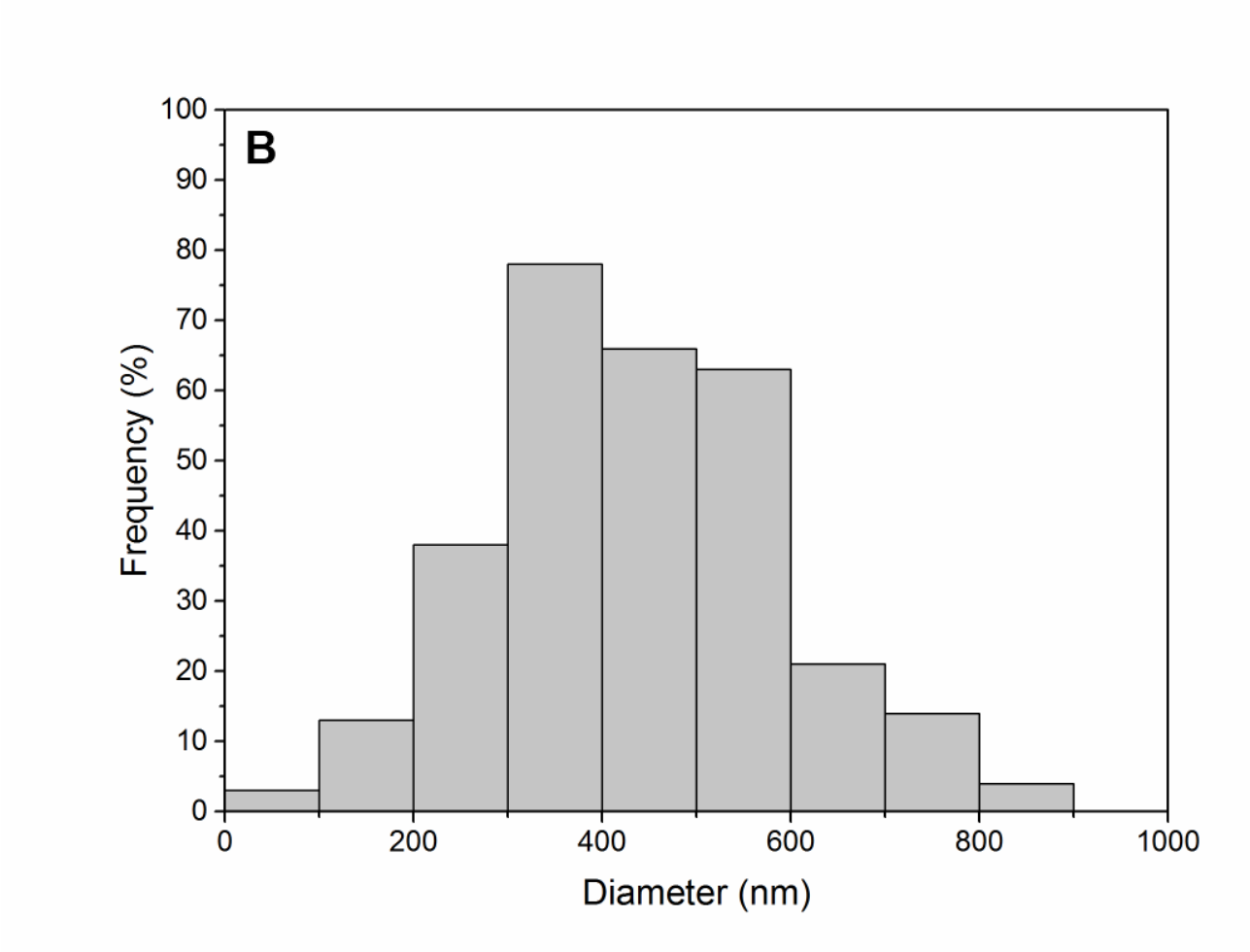

Figure S20B. Histogram of the frequency as a function of fibers diameter of electrospun scaffold EAHP.

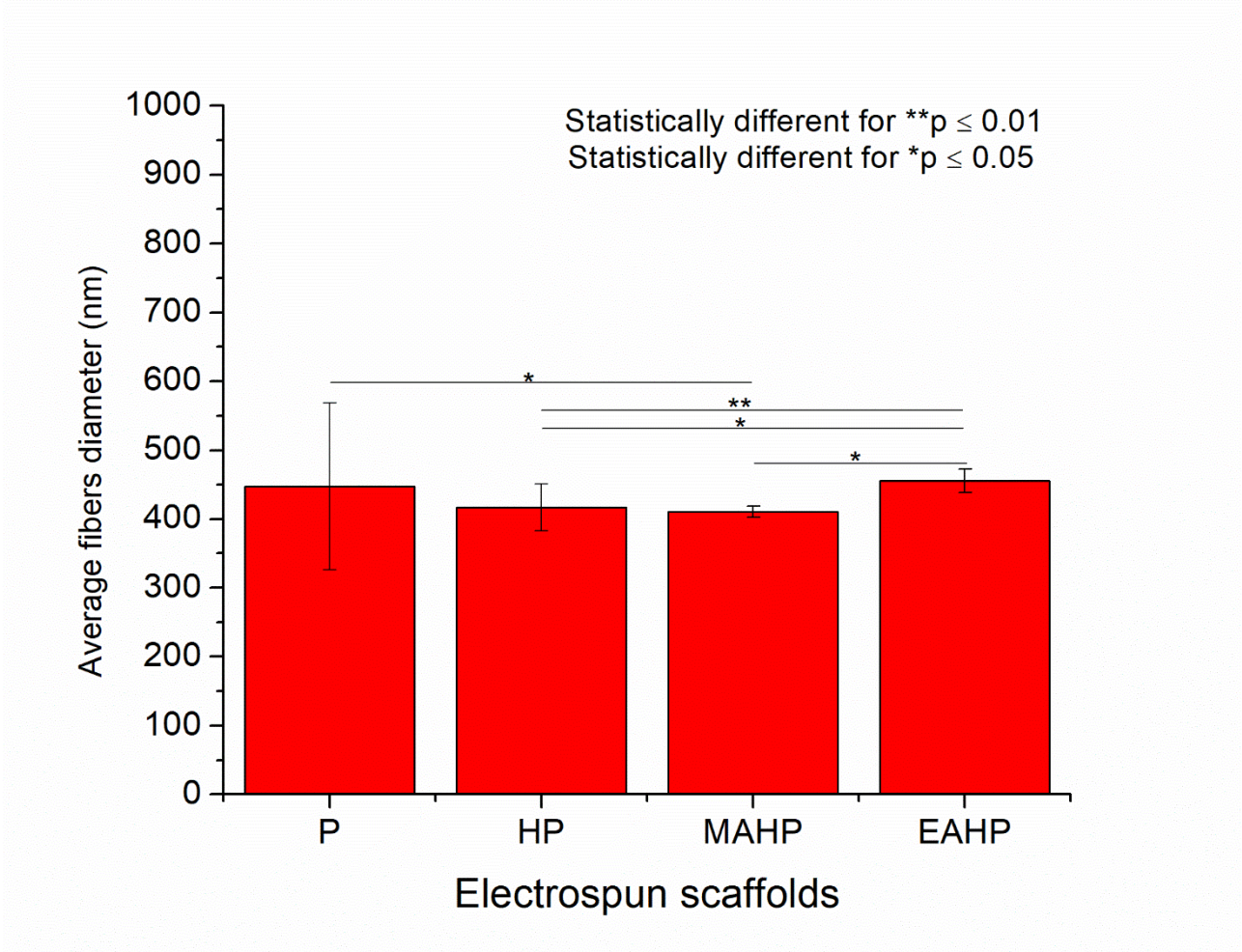

Figure S21. Histogram of average fibers diameter of electrospun scaffolds.

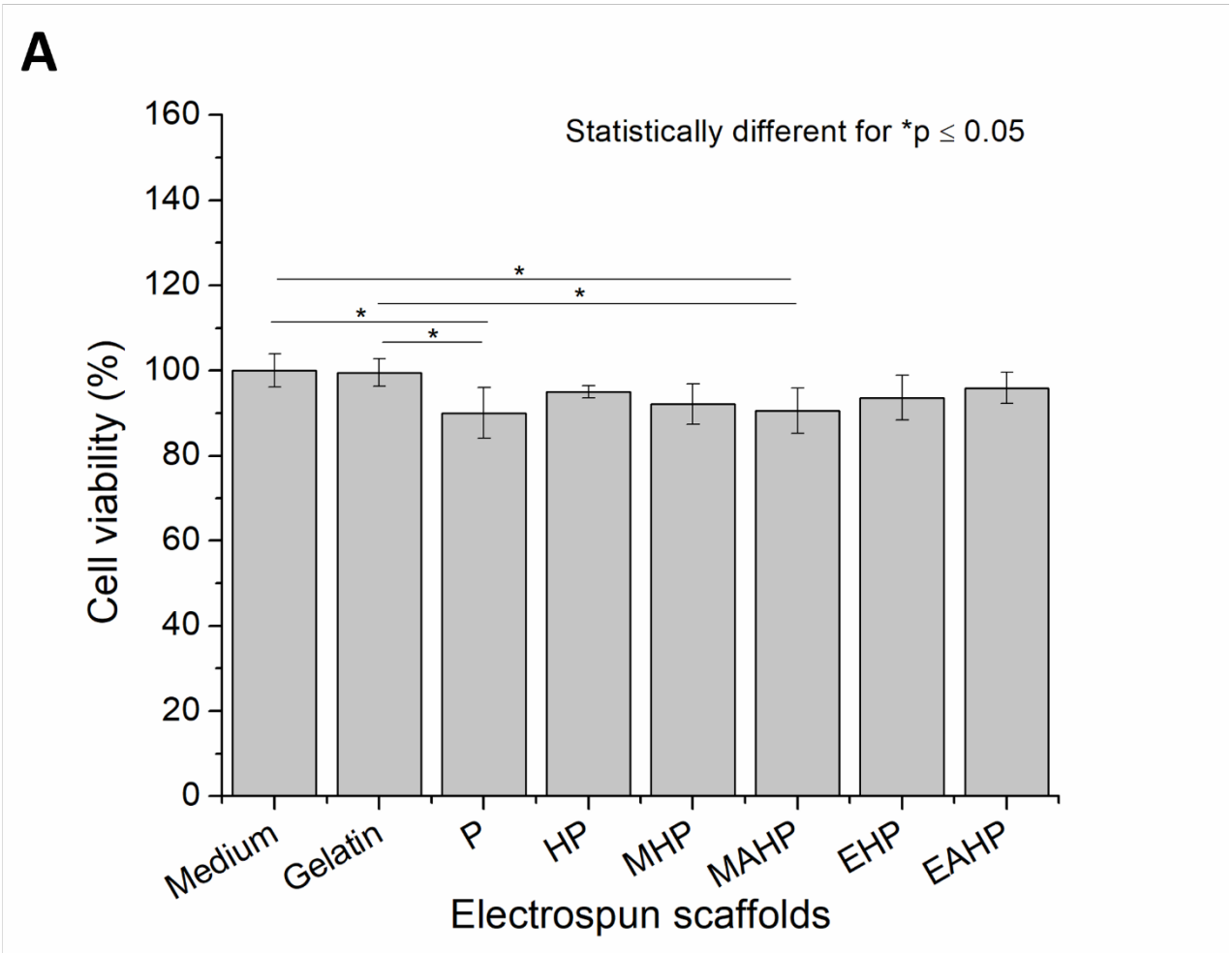

Figure S22A. Cell viability on electrospun scaffolds after 24 h.

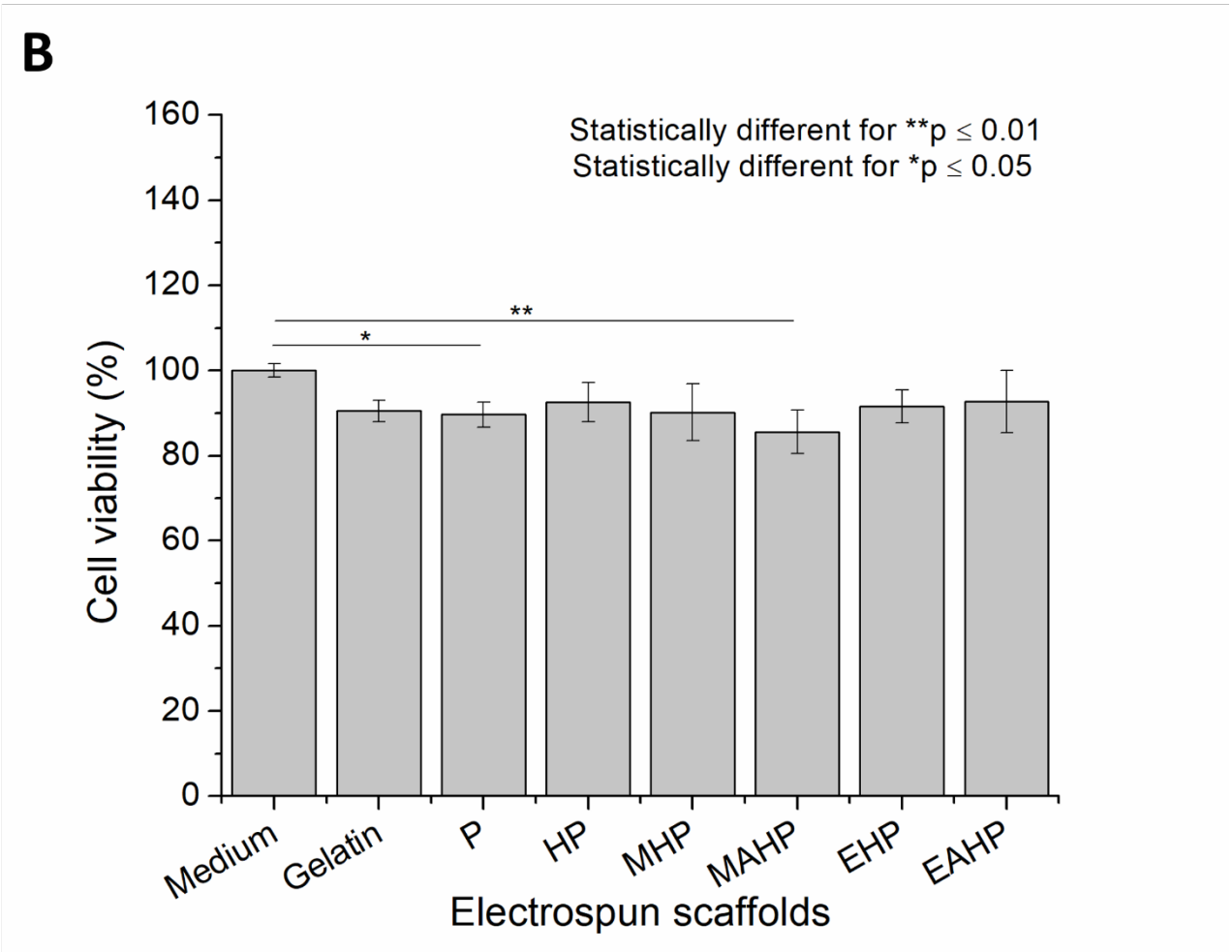

Figure S22B. Cell viability on electrospun scaffolds after 48 h.

Table S1. MTS assay on electrospun scaffolds.

Scaffolds	Cell viability 24 h (%)	Cell viability 48 h (%)
Medium (Control)	100.00 ± 3.89	100.00 ± 1.61
Gelatin (Control)	99.49 ± 3.28	90.49 ± 2.57
P	90.04 ± 5.94	89.64 ± 2.96
HP	94.98 ± 1.38	92.58 ± 4.55
MHP	92.07 ± 4.75	90.13 ± 6.65
MAHP	90.57 ± 5.36	85.54 ± 5.08
EHP	93.60 ± 5.29	91.52 ± 3.86
EAHP	95.91 ± 3.69	92.73 ± 7.31

[1] A. Laezza, A. Pepe, B. Bochicchio, *Chem. Eur. J.* **2022**, *28*, e202201959

References

[1] Krishna O.D., Kiick K.L. *Protein- and peptide-modified synthetic polymeric biomaterials.* Biopolymers, **2020**; 94(1): 32–48.

[2] Hersh, J., Broyles, D., Capcha, J. M. C., Dikici, E., Shehadeh, L. A., Daunert, S., & Deo, S. *Peptide-modified biopolymers for biomedical applications***.** ACS Applied Bio Materials**,** 2021**, 4(1), 229–251.**

[2b] Song H.-Q., Fan Y., Hu Y., Cheng G., Xu F.-J. *Polysaccharide–Peptide Conjugates: A Versatile Material Platform for Biomedical Applications.* Adv. Funct. Mater., **2021**; 31: 2005978

[3] Mohan T., Kleinschek K.S., Kargl R. *Polysaccharide–peptide conjugates: Chemistry, properties and applications.* Carbohydrate Polymers, **2022**; 280: 118875.

[4] Nair D.P., Podgórski M., Chatani S., Gong T., Xi W., Fenoli C.R., Bowman C.N. *The Thiol–Michael Addition Click Reaction: A Powerful and Widely Used Tool in Materials Chemistry.* Chemistry of Materials, **2013**; 26(1): 724–744.

[5] Redondo, J. A., Navarro, R., Martínez-Campos, E., Pérez-Perrino, M., París, R., López-Lacomba, J. L., & Gallardo, A. *Prodendronic polyamines from stable or labile methacrylates obtained by selective Michael addition onto asymmetric diacrylic compounds*. Journal of Polymer Science Part A: Polymer Chemistry, **2014**, 52(16), 2297–2305.

[6] Li H., Li B., Lv D., Li W., Lu Y., Luo G. *Biomaterials releasing drug responsively to promote wound healing via regulation of pathological microenvironment.* Advanced Drug Delivery Reviews, **2023**; 196: 114778.

[7a] Shirzaei Sani E., Portillo-Lara R., Spencer A., Yu W., Geilich B.M., Noshadi I., Webster T.J., Annabi N. *Engineering adhesive and antimicrobial hyaluronic acid/elastin-like polypeptide hybrid hydrogels for tissue engineering applications.* ACS Biomaterials Science & Engineering, **2018**; 4(7): 2528–2540.

[7b] Zhu, D., Wang, H., Trinh, P., Heilshorn, S. C., & Yang, F. *Elastin-like protein–hyaluronic acid (ELP–HA) hydrogels with decoupled mechanical and biochemical cues for cartilage regeneration*. Biomaterials, **2017**; 127, 132–140.

[7c] Wang M., Deng Z., Guo Y., Xu P. *Designing functional hyaluronic acid–based hydrogels for cartilage tissue engineering.* Materials Today Bio, **2022**; 17: 100495.

[8a] Fiorica, C., Palumbo, F. S., Pitarresi, G., Allegra, M., Puleio, R., & Giammona, G. *Hyaluronic acid and α-elastin based hydrogel for three dimensional culture of vascular endothelial cells*. Journal of Drug Delivery Science and Technology, **2018**; 46, 28–33.

[8b] Palumbo F.S., Pitarresi G., Fiorica C., Rigogliuso S., Ghersi G., Giammona G. *Chemical hydrogels based on a hyaluronic acid-graft-α-elastin derivative as potential scaffolds for tissue engineering.* Materials Science and Engineering: C, **2013**; 33(5): 2541–2549.

[9] Graça M.F.P., Miguel S.P., Cabral C.S.D., Correia I.J. *Hyaluronic acid–based wound dressings: A review.* Carbohydrate Polymers, **2020**; 241: 116364.

[10a] Rahmati M., Mills D.K., Urbanska A.M., Saeb M.R., Venugopal J.R., Ramakrishna S., Mozafari M. *Electrospinning for tissue engineering applications.* Progress in Materials Science, **2021**; 117: 100721.

[10b] Gao, C., Zhang, L., Wang, J., Jin, M., Tang, Q., Chen, Z., Cheng, Y., Yang, R., & Zhao, G. *Electrospun nanofibers promote wound healing: theories, techniques, and perspectives*. **Journal of** Materials Chemistry B, **2021**, 9(14), 3106–3130.

[10c] Keirouz, A., Chung, M., Kwon, J., Fortunato, G., & Radacsi, N. *2D and 3D electrospinning technologies for the fabrication of nanofibrous scaffolds for skin tissue engineering: A review*. WIREs Nanomedicine and Nanobiotechnology, **2020**, 12, e1626.

[10d] Memic, A., Abudula, T., Mohammed, H. S., Joshi Navare, K., Colombani, T., & Bencherif, S. A. *Latest progress in electrospun nanofibers for wound healing applications*. ACS Applied Bio Materials, **2019**, 2, 952–969.

[11a] Rodriguez-Cabello J.C., Gonzalez De Torre I., González-Pérez M., González-Pérez F., Montequi I. *Fibrous scaffolds from elastin-based materials.* Frontiers in Bioengineering and Biotechnology, **2021**; 9: 652384.

[11b] Akhmetova, A., & Heinz, A. *Electrospinning proteins for wound healing purposes: opportunities and challenges*. Pharmaceutics, **2021**, 13(1), 4.

[11c] Khadka, D. B., Cross, M. C., & Haynie, D. T. *A synthetic polypeptide electrospun biomaterial*. ACS Applied Materials & Interfaces, **2011**, 3(8), 2994–3001.

[12] Powell H.M., Boyce S.T. *Engineered human skin fabricated using electrospun collagen–PCL blends: morphogenesis and mechanical properties.* Tissue Engineering Part A, **2009**; 15(8): 2177–2187.

[13] Frenkel J.S. *The role of hyaluronan in wound healing.* International Wound Journal, **2014**; 11(2): 159–163.

[14] Castro K.C., Campos M.G.N., Mei L.H.I. *Hyaluronic acid electrospinning: Challenges, applications in wound dressings and new perspectives.* International Journal of Biological Macromolecules, **2021**; 173: 251–266.

[15] Schuurmans C.C.L., Mihajlovic M., Hiemstra C., Ito K., Hennink W.E., Vermonden T. *Hyaluronic acid and chondroitin sulfate (meth)acrylate-based hydrogels for tissue engineering: Synthesis,*

characteristics and pre-clinical evaluation. Biomaterials, **2021**; 268: 120602.
[16a] Tsanaktsidou E., Kammon O., Kiparissides C. *On the synthesis and characterization of bio-functional hyaluronic acid-based injectable hydrogels for the repair of cartilage lesions.* European Polymer Journal, **2019**; 114: 47–56.
[16b] Oh, E. J., Kim, J. W., Kong, J. H., Ryu, S. H., & Hahn, S. K. *Signal transduction of hyaluronic acid–peptide conjugate for formyl peptide receptor-like 1 receptor*. Bioconjugate Chemistry, **2008**, 19(12), 2401–2408.
[17] Fowler E.W., Ravikrishnan A., Witt R.L., Pradhan-Bhatt S., Jia X. *RGDSP-decorated hyaluronate hydrogels facilitate rapid 3D expansion of amylase-expressing salivary gland progenitor cells.* ACS Biomaterials Science & Engineering, **2021**; 7(12): 5749–5761.
[18] Laezza A., Casillo A., Cosconati S., Biggs C.I., Fabozzi A., Paduano L., Iadonisi A., Novellino E., Gibson M.I., Randazzo A., Corsaro M.M., Bedini E. *Decoration of chondroitin polysaccharide with threonine: Synthesis, conformational study, and ice-recrystallization inhibition activity.* Biomacromolecules, **2017**; 18(8): 2267–2276.
[19a] Laezza A., Pepe A., Bochicchio B. *Elastin–hyaluronan bioconjugate as bioactive component in electrospun scaffolds.* Chemistry – A European Journal, **2022**; 28(58): e202201959.
[19b] Piccirillo, G., Pepe, A., Bedini, E., & Bochicchio, B. *Photoinduced thiol–ene chemistry applied to the synthesis of self-assembling elastin-inspired glycopeptides*. Chemistry – A European Journal, **2017**, 23(11), 2648–2659.
[20] Pepe A., Laezza A., Ostuni A., Scelsi A., Laurita A., Bochicchio B. *Bioconjugation of carbohydrates to gelatin sponges promoting 3D cell cultures.* Biomimetics (Basel), **2023**; 8(2): 193.
[21] Li, G. Z., Randev, R. K., Soeriyadi, A. H., Rees, G., Boyer, C., Tong, Z., & Haddleton, D. M. *Investigation into thiol-(meth)acrylate Michael addition reactions using amine and phosphine catalysts*. Polymer Chemistry, **2010**, 1(8), 1196–1204.
[22] Burns J.A., Butler J.C., Moran J., Whitesides G.M. *Selective reduction of disulfides by tris(2-carboxyethyl)phosphine.* Journal of Organic Chemistry, **1991**; 56(8): 2648–2650.
[23] Kantner T., Watts A.G. *Characterization of reactions between water-soluble trialkylphosphines and thiol alkylating reagents: implications for protein–conjugation reactions.* Bioconjugate Chemistry, **2016**; 27(10): 2400–2406.
[24] Lee P., Yeo G.C., Weiss A.S. *A cell adhesive peptide from tropoelastin promotes sequential cell attachment and spreading via distinct receptors.* FEBS Journal, **2017**; 284(14): 2216–2230.
[25] Chan, J. W., Hoyle, C. E., Lowe, A. B., & Bowman, M. *Nucleophile-initiated thiol–Michael reactions: effect of organocatalyst, thiol, and ene*. Macromolecules, **2010**, 43(15), 6381–6388.

[26] Gennari A., Wedgwood J., Lallana E., Francini N., Tirelli N. *Thiol-based Michael-type addition: A systematic evaluation of its controlling factors.* Tetrahedron, **2020**; 76(47): 131637.

[27a] Okamoto H., Taniguchi T., Takekuma M., Mashio A.S., Wong K.H., Hasegawa H., Nishimura T., Maeda K. *Revisiting the synthesis of cellulose acrylate and its modification via Michael addition reactions.* Biomacromolecules, **2023**; 24(8): 3767–3774.

[27b] Frayne, S. H., & Northrop, B. H. *Evaluating nucleophile byproduct formation during phosphine- and amine-promoted thiol–methyl acrylate reactions*. The Journal of Organic Chemistry, **2018**, 83(17), 10370–10382.

[28] Cumnock K., Tully T., Cornell C., Hutchinson M., Gorrell J., Skidmore K., Chen Y., Jacobson F. *Trisulfide modification impacts the reduction step in antibody–drug conjugation process.* Bioconjugate Chemistry, **2013**; 24(7): 1154–1160.

[29] Lee Y.J., Kurra Y., Liu W.R. *Phospha–Michael addition as a new click reaction for protein functionalization.* ChemBioChem, **2016**; 17(6): 456–461.

[30] Krężel A., Latajka R., Bujacz G.D., Bal W. *Coordination properties of tris(2-carboxyethyl)phosphine, a newly introduced thiol reductant, and its oxide.* Inorganic Chemistry, **2003**; 42(6): 1994–2003.

[31a] Northrop B.H., Frayne S.H., Choudhary U. *Thiol–maleimide "click" chemistry: evaluating the influence of solvent, initiator, and thiol on the reaction mechanism, kinetics, and selectivity.* Polymer Chemistry, **2015**; 6(18): 3415–3430.

[31b] Chatani, S., Sheridan, R. J., Podgórski, M., Nair, D. P., & Bowman, C. N. *Temporal control of thiol-click chemistry*. Chemistry of Materials, **2013**, 25(19), 3897–3901.

[32a] Tallec G., Loh C., Liberelle B., Garcia-Ac A., Vo Duy S., Sauvé S., Banquy X., Murschel F., De Crescenzo G. *Adequate reducing conditions enable conjugation of oxidized peptides to polymers by one-pot thiol click chemistry.* Bioconjugate Chemistry, **2018**; 29(11): 3866–3876.

[32b] Tang, Q., Cao, B., Lei, X., Sun, B., Zhang, Y., & Cheng, G. *Dextran–peptide hybrid for efficient gene delivery*. Langmuir, **2014**, 30(18), 5202–5208.

[33a] Desmet G.B., Sabbe M.K., D'Hooge D.R., Espeel P., Celasun S., Marin G.B., Du Prez F.E., Reyniers M.F. *Thiol–Michael addition in polar aprotic solvents: nucleophilic initiation or base catalysis?* Polymer Chemistry, **2017**; 8(8): 1341–1352.

[33b] Chatani, S., Nair, D. P., & Bowman, C. N. *Relative reactivity and selectivity of vinyl sulfones and acrylates towards the thiol–Michael addition reaction and polymerization*. Polymer Chemistry, **2013**, 4(4), 1048–1055.

[34a] Ciarfaglia N., Laezza A., Lods L., Lonjon A., Dandurand J., Pepe A., Bochicchio B. *Thermal and dynamic mechanical behavior of poly(lactic acid) (PLA)-based electrospun scaffolds for tissue engineering.* Journal of Applied Polymer Science, **2021**; 138(44): e51313.

[34b] Ciarfaglia, N., Pepe, A., Piccirillo, G., Laezza, A., Daum, R., Schenke-Layland, K., & Bochicchio, B. *Nanocellulose and elastin act as plasticizers of electrospun bioinspired scaffolds*. ACS Applied Polymer Materials, **2020**, 2(11), 4836–4847.

[35] Williams G.R., Raimi-Abraham B.T., Luo C.J. *Nanofibres in Drug Delivery.* UCL Press, London, **2018**, p. 24.

[36] Fong H., Chun I., Reneker D.H. *Beaded nanofibers formed during electrospinning.* Polymer, **1999**, 40(16): 4585–4592.

[37] Tripatanasuwan S., Zhong Z.X., Reneker D.H. *Effect of evaporation and solidification of the charged jet in electrospinning of poly(ethylene oxide) aqueous solution.* Polymer, **2007**, 48(19): 5742–5746.

[38] Han S.O., Youk J.H., Min K.D., Kang Y.O., Park W.H. *Electrospinning of cellulose acetate nanofibers using a mixed solvent of acetic acid/water: Effects of solvent composition on the fiber diameter.* Materials Letters, **2008**, 62(4–5): 759–762.

[39] Kenar H., Yilmaz Ozdogan C., Dumlu C., Doger E., Torun Kose G., Hasirci V. *Microfibrous scaffolds from poly(L-lactide-co-ε-caprolactone) blended with xeno-free collagen/hyaluronic acid for improvement of vascularization in tissue engineering applications.* Materials Science and Engineering: C, **2019**, 97: 31–44.

[40] Antunes, J. C., Oliveira, J. M., Reis, R. L., Soria, J. M., Gómez-Ribelles, J. L., & Mano, J. F. *Novel poly(L-lactic acid)/hyaluronic acid macroporous hybrid scaffolds: characterization and assessment of cytotoxicity*. Journal of Biomedical Materials Research Part A, **2010**, 94(3), 856–869.

Conclusions and Future Perspectives

This PhD thesis investigated the chemical modification of hyaluronic acid through carbodiimide-mediated coupling with selected L-amino acids and an elastin-derived peptide, with the aim of generating chemically defined hyaluronic acid derivatives.

A systematic investigation of the bioconjugation reactions showed that the efficiency of functionalization and the resulting degree of substitution depend on the specific system investigated and on the chosen coupling strategy. Comparative analyses of different amino acids, protecting group approaches, and reaction conditions indicated that no general trend can be universally applied, highlighting the need for case-by-case experimental optimization.

All synthesized derivatives were thoroughly characterized by spectroscopic techniques, confirming successful grafting and the preservation of the polysaccharide backbone.

In addition to chemical synthesis and characterization, selected hyaluronic acid bioconjugates were successfully processed into fibrous scaffolds by electrospinning. This demonstrated the compatibility of chemically modified glycosaminoglycans with electrospinning-based fabrication techniques and allowed the production of nanofibrous materials while retaining the chemical features introduced through bioconjugation.

To improve the structural integrity and handling properties of the resulting materials, asymmetric bilayer scaffolds were developed by combining a mechanically stable hydrophobic layer with a functional hydrophilic layer containing hyaluronic acid or its bioconjugates.

The electrospun systems were characterized using complementary physicochemical techniques, confirming the incorporation of hyaluronic acid derivatives within the fibrous structures and providing insight into their morphological and surface properties. Overall, these results demonstrate the feasibility of processing selected hyaluronic acid bioconjugates by electrospinning, in addition to their characterization in solution.

From a future perspective, several aspects of this work could be further developed. On the chemical side, additional optimization of the bioconjugation strategies could be explored to improve reaction efficiency and to expand the range of biomolecular moieties that can be introduced onto the hyaluronic acid backbone, including alternative amino acids, peptides, or other functional moieties.

With respect to materials processing, the stabilization of highly hydrophilic hyaluronic acid–based layers emerged as a key challenge. Future studies may therefore investigate alternative crosslinking strategies, controlled spatial confinement of hyaluronic acid derivatives, or modified scaffold architectures to better balance chemical functionality and physical stability.

Following further optimization of scaffold composition and stability, future investigations may include biological tests on selected scaffold formulations. Such studies could contribute to elucidating how molecular-level chemical modifications influence cell–material interactions, once the chemical and structural parameters of the system are adequately controlled.

Acknowledgements

First of all, I would like to thank INPS for funding my PhD through the project *"Bi-hyaluronic: Hyaluronic acid-inspired biomaterials"*, providing a fundamental opportunity for my scientific and professional development.

I would like to express my sincere gratitude to Prof. Brigida Bochicchio, my PhD supervisor, for her continuous guidance and support, as well as for accompanying me throughout the development of this work.

I also thank my co-supervisors, Prof. Antonietta Pepe for her availability and scientific contribution, and Dr. Antonio Laezza, to whom I am particularly grateful for his valuable support in the laboratory and for his significant contribution to my training.

I would like to thank Altergon Italia S.r.l. for giving me the opportunity to experience the industrial environment, enriching my training and providing an applied perspective to my research activity.

My sincere thanks go to Prof. Katja Schenke-Layland for welcoming me into her laboratory in Tübingen and at NMI, allowing me to carry out part of my research in a stimulating and highly qualified international environment.

I would also like to thank Prof. Giovanna Calabrese from the University of Messina for her contribution to the biological analyses.

Finally, I would like to thank all those who, in various ways, contributed to the completion of this work.